Scuola Internazionale Superiore di Studi Avanzati - Trieste

Formation of disc galaxies from cosmological simulations: galactic outflows and chemical evolution

Author: **Milena Valentini**

Supervisors: Prof. Stefano Borgani,
Prof. Alessandro Bressan,
Dr. Giuseppe Murante

International School for Advanced Studies

SISSA/ISAS

A thesis submitted in fulfilment of the requirements for the degree of Doctor Philosophiae

in ASTROPHYSICS and COSMOLOGY

October 2018

SISSA - Via Bonomea 265 - 34136 TRIESTE - ITALY

To Nicola

Abstract

In this Thesis, I study the formation of late-type galaxies and the role that feedback from stars and supermassive black holes (SMBHs) plays in galaxy evolution across cosmic time. By carrying out cosmological hydrodynamical simulations, I investigate how different processes, such as the cosmological gas accretion from the large scale environment, star formation and chemical enrichment, stellar and AGN (Active Galactic Nucleus) feedback, affect the early stages of forming galaxies and contribute to determine their present-day properties.

Driven by the challenging task of simulating late-type galaxies with a limited bulge and a dominant disc in a cosmological context, I study the impact of galactic outflow modelling on the formation and evolution of a disc galaxy. I find that galactic outflows regulate the timing of gas accretion and determine the star formation history of the forming galaxy. Also, I quantify the strong interplay between the adopted hydrodynamical scheme and the sub-resolution model describing star formation and stellar feedback.

Throughout this Thesis, I devote particular emphasis to connect chemical evolution and gas dynamics, in order to interpret observations of metal abundance in the interstellar medium (ISM) and circumgalactic medium (CGM). I investigate the metal content of gas and stars, and explore how the variation of the essential elements contributing to define the model of chemical evolution determine final metal abundance trends. The investigation that I present is guided by observations and focusses on the results at redshift $z = 0$, with particular emphasis on the role played by the high-mass end of the IMF.

Moreover, I introduce a novel methodology to generate synthetic stars from star particles. The technique that I developed takes properties of star particles from simulations as input and allows to obtain a catalogue of mock stars, provided with photometric properties, whose characteristics are drawn from the input features. The ultimate goal of this method is to translate the populations of star particles of a simulation into stellar populations, thereby enabling a direct and accurate comparison with observations. This technique will be of paramount importance with ongoing survey data releases (e.g. GAIA and surveys of resolved stellar populations).

Also, I investigate the role of AGN feedback in regulating the formation and evolution of late-type galaxies. I introduce a new model aimed at investigating the interaction between the central SMBH and the various gas phases which coexist in the ISM of the host galaxy.

Contents

List of Figures

List of Tables

List of Abbreviations

AC . . . . . Artificial conduction

AGB . . . . . Asymptotic giant branch

AGN . . . . . Active galactic nucleus

AMD . . . . . Age-metallicity distribution

AV . . . . . Artificial viscosity

BH . . . . . Black hole

CDM . . . . . Cold dark matter

CGM . . . . . Circumgalactic medium

CMB . . . . . Cosmic microwave background

CMD . . . . . Colour magnitude diagram

DE . . . . . Dark Energy

DM . . . . . Dark Matter

FRW . . . . . Friedmann-Robertson-Walker

ICs . . . . . Initial conditions

ISM . . . . . Interstellar medium

ΛCDM . . . . Λ cold dark matter

MAH . . . . . Mass accretion history

MDF . . . . . Metallicity distribution function

MW . . . . . Milky Way

PM . . . . . Particle Mesh

SFR . . . . . Star formation rate

SMBH . . . . . Supermassive black hole

SN . . . . . Supernova

SPH . . . . . Smoothed Particle Hydrodynamics

SSP . . . . . Simple stellar population

Publication list

This Thesis presents the main results of the research that I carried out during my Ph.D., working with Professors Stefano Borgani, Alessandro Bressan, and Giuseppe Murante. The work accomplished during these years yielded the following papers published on refereed journals and a paper in preparation, on which Chapters 6, 7, 8, and 9 are based:

- **Valentini Milena**, Murante Giuseppe, Borgani Stefano, Monaco Pierluigi, Bressan Alessandro, and Beck Alexander M.; ***On the effect of galactic outflows in cosmological simulations of disc galaxies***; 2017; MNRAS, volume 470, page 3167

- **Valentini Milena**, Bressan Alessandro, Borgani Stefano, Murante Giuseppe, Girardi Léo, and Tornatore Luca; ***Colour-magnitude diagram in simulations of galaxy formation***; 2018; MNRAS, volume 480, page 722

- **Valentini Milena**, Borgani Stefano, Bressan Alessandro, Murante Giuseppe, Tornatore Luca, and Pierluigi Monaco; ***Chemical evolution of disc galaxies from cosmological simulations***; 2018; submitted to MNRAS, under revision

- **Valentini Milena**, Murante Giuseppe, Borgani Stefano, Bressan Alessandro, Granato Gian Luigi, Brighenti Fabrizio, Lapi Andrea, and Monaco Pierluigi; ***On the impact of AGN feedback on forming galaxies and their multiphase ISM across cosmic time***; in preparation

Another result of my research, not included in this Thesis, is the published work:

- **Valentini Milena** & Brighenti Fabrizio; ***AGN-stimulated cooling of hot gas in elliptical galaxies***; 2015; MNRAS, volume 448, page 1979

This Thesis

1

Introduction

The Universe's mass and energy budget is constituted of ordinary matter only for 4.9%. What primarily contributes to this inventory is the dark energy (DE, 68.3%), that is responsible for the accelerated expansion of the Universe and that hampers gravity. The third component is the dark matter (DM), that accounts for 26.8% (Planck Collaboration et al., 2016b) of the Universe's budget and that interacts only gravitationally. We do not know the nature of DM and DE, and we only have indirect evidence of both so far. We are thus experiencing an apparent paradox: while living in the era of precision cosmology and knowing cosmological parameters with high accuracy, we only understand what less than 5% of our Universe is made of. As almost all the ordinary matter constitutes galaxies and resides in their surroundings, galaxies are fundamental to study indirectly the other components. Galaxies are indeed considered probes to explore the Universe, to investigate its evolution, and play a key role in astrophysics and cosmology.

Within the aforementioned well-established, standard cosmological framework, increasing attention has been progressively focused on investigating how galaxies form and evolve across cosmic time. One of the most challenging tasks in the study of galaxy formation is to understand – or corroborate the established comprehension of – how gaseous, and thus stellar, discs form. The formation of discs is indeed of paramount importance for the overall theory of galaxy formation and evolution, and not only for the investigation of the formation of spiral galaxies. Indeed, according to the current accepted scenario, elliptical galaxies are the outcome of the merging of disc proto-galaxies occurred at relatively high redshift. When focussing on the formation of late-type galaxies, a deep understanding of how radially extended discs form poses significant challenges.

To this end, cosmological hydrodynamical simulations represent the state-of-the-art methodology to capture the complexity of galaxy formation. They are indeed

essential to follow the non-linear growth of initial density perturbations and to investigate the formation of cosmic structures, accounting for the simultaneous evolution of DM and baryons. The series of complex processes through which galaxies form and evolve involves a large dynamical range of spatial scales: cosmological hydrodynamical simulations are therefore required to effectively describe the Mpc scale where DM clusters as well as the kpc scale where the baryonic physics plays a crucial role in addition to gravity, while also accounting for the pc scale (and below) where star formation occurs. The numerical modelling of physics – especially of those phenomena that take place below the resolution limit of cosmological simulations – has thus deserved increasing focus. Indeed, it is crucial to self-consistently implement within cosmological simulations processes such as hot gas cooling, the consequent star formation, and the resulting feedback both in energy and in metals. In this way, cosmological hydrodynamical simulations provide us with invaluably powerful predictions.

Finally, comparing these theoretical, numerical predictions to observations allows us to gain insight on the physical mechanisms that drive galaxy formation and evolution, and to interpret the observational evidence.

This is the general framework in which my work fits. In this Thesis, I will mainly concentrate on the formation and evolution of disc galaxies from a theoretical and numerical perspective, making extensive use of cosmological hydrodynamical simulations. Particular focus is on the investigation of how galactic outflows determine disc galaxy evolution, and to the chemical evolution of late-type galaxies, as it emerges from the distribution of heavy elements in the interstellar medium (ISM) and in stars.

The open challenges that I address with this Thesis are the following: what is the impact of galactic outflows on the formation of late-type galaxies? How can the observed distribution of metals in gas and stars constrain the scenario of disc galaxy formation and evolution? How does the coupling of AGN (active galactic nucleus) feedback energy with the different phases of the ISM contribute to determine the present-day properties of spiral galaxies?

This Thesis is structured in three parts and is organised as follows.

In the *first part*, I outline the broad framework within which this Thesis locates, reviewing observational and theoretical evidence that is of interest for the discussion of my results.

- In Chapter 2, I introduce the general features of disc galaxies: the theoretical scenario for their formation is presented, and the main observational properties of late-type galaxies in the local Universe are described.

- Chapter 3 is focused on the contribution added by cosmological simulations to the state of the art in the understanding of the galaxy formation process. I discuss how and why is challenging to simulate galaxies in a cosmological context, and the importance of the numerical modelling of astrophysical processes such as the stellar feedback.

The *second part* is devoted to present the methodology that I adopted to achieve results.

- In Chapter 4, I briefly review the basis of numerical cosmology and the essentials of computational fluid dynamics, with critical focus on Smoothed Particle Hydrodynamics (SPH).
- In Chapter 5, I introduce in detail the simulations setup: the state-of-the-art Lagrangian code GADGET3 that I use to carry out the simulations whose results are presented in this Thesis, the adopted implementation of SPH, the sub-resolution model for hot gas cooling, star formation, stellar feedback, and chemical evolution, along with the initial conditions.

The *third part* is constituted by the results of the original work that I present in this Thesis.

- Chapter 6 is devoted to the numerical modelling of stellar feedback in cosmological simulations of disc galaxies. I explore different feedback schemes and investigate the requirements for galactic outflow models to lead to the formation of disc dominated galaxies. Also, I quantify the impact of the hydrodynamic solver on final results by simulating disc galaxies with two different SPH implementations.
- In Chapter 7, I investigate the gas and stellar metal content in simulated disc galaxies. I compare predictions from simulations to observations from our Galaxy and from late-type galaxies in the local Universe, in order to interpret and quantify the effect of the different components entering the chemical evolution modelling, e.g. the assumed initial mass function, on the process of chemical enrichment.
- In Chapter 8, I introduce a novel approach that allows to perform a comparison as accurate as possible between simulation output and observations of stars. I present a method that I developed to compare the outcome of cosmological simulations, that provide a coarse sampling of stellar populations by means of star particles corresponding to simple stellar populations, with observations, that resolve single stars within stellar populations.
- Chapter 9 reports on how I included the effect of AGN feedback within the sub-resolution model adopted for simulations of galaxies. Here, I investigate how different ways of coupling AGN feedback energy to the different phases of the ISM across cosmic time impact on the final properties of simulated galaxies and their central black holes (BHs).
- In Chapter 10 I draw conclusions. I outline the general scenario and the implications that the work presented in this Thesis suggests, and discuss how it contributes to the understanding of late-type galaxy formation and evolution. Also, I illustrate how the results presented pave the way to future work, outlining forthcoming directions of investigation.

Finally, Appendix A summarises the essentials of cosmology to which I refer throughout the Thesis when considering the formation of galaxies in cosmological simulations.

Part I

General background

2

Late-type galaxies in the local Universe

This Thesis adds a contribution to the study of the formation of disc galaxies and investigates how different processes impact on their present-day properties. The goal of this Chapter is to give an overview of disc galaxies (Section 2.1), to outline the theoretical framework in which their formation fits (Sections 2.2 and 2.3), and to review the main properties of disc galaxies in the local Universe that emerge from observations (Section 2.4).

Contents

2.1 The diversity of the galaxy population

Galaxies are bright structures that populate the Universe. They are visible as they are made up of baryonic matter, i.e. gas and stars that emit electro-

magnetic radiation.

As every population, the galaxy population exhibits an interesting diversity: galaxies with different morphology live in differently crowded environments, galaxies with different content show peculiar colours, galaxies with distinct size and internal activity behave in dissimilar ways and have various ages. The galaxy population is sliced in three main categories according to their morphology: elliptical galaxies, disc or spiral galaxies (see Figure 2.1), and irregular galaxies (Blanton & Moustakas, 2009; Mo et al., 2010, and references therein).

Disc galaxies have the bulk of their gas and stars distributed on a rotating disc, where a spiral pattern is usually evident. Some stars are also arranged in a central, spheroidal component, the bulge. Gaseous and stellar discs in spiral galaxies are rotationally supported structures in centrifugal equilibrium, as the gravitational acceleration that gas and stars experience is counterbalanced by the centrifugal acceleration in the rotating reference system. Therefore, the circular velocity $v_{\rm circ}$ that they are observed to rotate with is:

$$V_{\rm circ} = \left(\frac{G\, M_{\rm tot}(r)}{r} \right)^{1/2} \quad , \tag{2.1}$$

r being the distance from the galaxy centre, G the gravitational constant, and $M_{\rm tot}(r)$ the total dynamical mass enclosed within the considered radius. Therefore, $M_{\rm tot}$ accounts for both baryons and DM: the first evidence that galaxies are embedded within DM haloes comes indeed from the discrepancy between the observed circular velocity and that expected if the motion were driven by luminous matter alone. Rotation curves of spirals are characterised by a steep increase in the innermost regions, followed by a flat profile that declines mildly towards large radii. They are usually computed from combined observations of both stars or ionised gas, and neutral hydrogen, that extends further than the stellar disc. Through the mass modelling of different galaxy components, namely gas, stars and DM, split contribution to the total rotation curve can be retrieved. The relative contribution of the baryonic matter to the total mass budget of the system is often appreciated by analysing the mass-to-light ratio, M/L. Typical stellar massess of disc galaxies range between $10^9 \lesssim M_* \lesssim 10^{11}$ M$_\odot$, the M/L ratios reaching 10 or even beyond.

The galaxy population in the nearby Universe is mainly contributed by disc galaxies. They contain $\sim 65\%$ of the current mass in stars and amount to $\sim$ 70 % of the intermediate-mass galaxies with stellar mass between $3 \cdot 10^{10} \div 3 \cdot 10^{11}$ M$_\odot$ (Hammer et al., 2005).

Surface brightness profiles of observed spiral galaxies are roughly exponential, and can be described as (Mo et al., 2010):

$$I(r) = I_0 \exp\!\left(-\frac{r}{R_{\rm d}}\right) \quad , \qquad \text{where} \qquad I_0 = \frac{L}{2\,\pi\, R_{\rm d}^2} \quad . \tag{2.2}$$

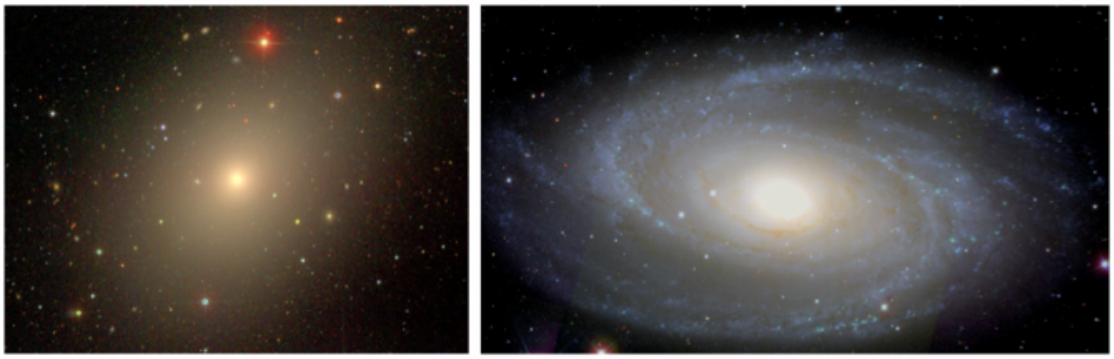

Figure 2.1: The elliptical galaxy NGC 4636 (left) and the spiral galaxy M 81 (right), observed within the Sloan Digital Sky Survey (York et al., 2000).

In equation (2.2), I_0 is the central surface brightness, L is the total luminosity, R_d is the disc scale length, ranging from few to ~ 10 kpc according to the galaxy size. With a similar exponential law the surface mass density is modelled, too.

The central spheroidal component of disc galaxies is called bulge and hosts a supermassive black hole (SMBH) in the centre (see Gadotti & Kauffmann, 2009; Kormendy & Ho, 2013, for a review, and Section 2.4.5). Classical bulges are featureless spheroids embedded within the galaxy disc: they are made up of old stars whose motion is supported by velocity dispersion, and likely have a formation history similar to that of elliptical galaxies (Renzini, 1999). Both these systems possibly formed as a consequence of a major merger (Kormendy & Ho, 2013). Pseudo-bulges have an oblate shape and an exponential surface brightness profile. They are the result of a secular evolution internal to the host galaxy itself and their properties do not correlate with the SMBH's ones as classical bulges do (Gadotti, 2009; Kormendy & Bender, 2012). Stars in pseudo-bulges are usually characterised by lower velocity dispersions than in classical bulges.

Galaxies can also host bars in their innermost regions, where stars move with particularly elongated orbits (Kormendy & Kennicutt, 2004; Gadotti, 2008). They are thought to originate through the dynamical instability of a rotationally supported disc, and contain a stellar mass that amounts to $\sim 10\%$ of that in spiral discs (Gadotti, 2009).

Since this Thesis focuses on spiral galaxies, a brief overview of their main observational properties will be given in the following Sections. For now, it is worth noting that disc galaxies differ from ellipticals for a number of properties: colours, star formation history and stellar ages, characteristic scaling relations, spectra and luminosities, metallicity and dust content, environment where they reside. For instance, disc galaxies are usually observed in regions that do not have a high galaxy number density (e.g. Dressler, 1980).

On the other hand, elliptical galaxies are usually more massive systems, with stellar mass up to $M_* \sim 10^{12}$ $\mathrm{M}_\odot$, often living in groups and clusters. They have their mass arranged in a smooth spheroidal structure: stars are supported by

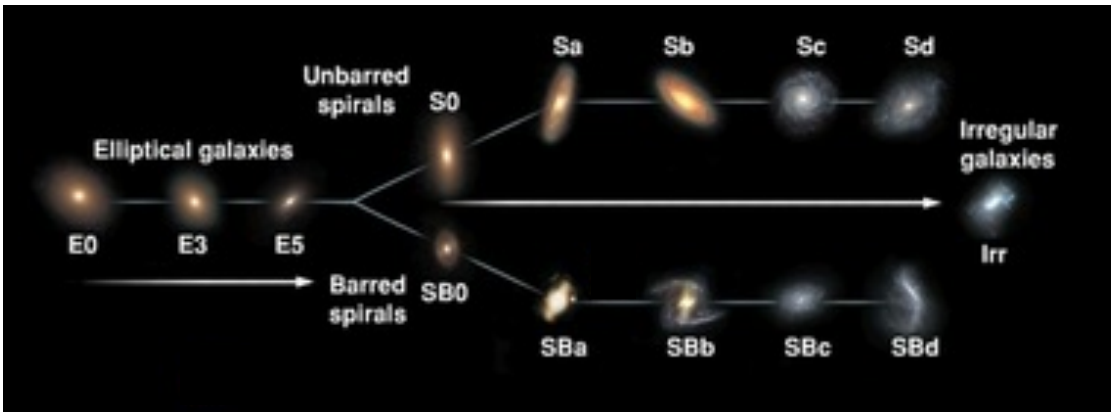

Figure 2.2: Representative illustration of the Hubble (1936) diagram.

internal pressure as their velocity dispersion dominates over the rotation velocity. The surface brightness radial profile $I(r)$ of elliptical galaxies is well described by the Sersic (1968) profile:

$$I(r) = I_0 \exp\left[-\beta_\mathrm{n}\left(\frac{r}{R_\mathrm{e}}\right)^{1/n}\right] = I(R_\mathrm{e}) \exp\left[-\beta_\mathrm{n}\left(\frac{r}{R_\mathrm{e}}\right)^{1/n} - 1\right] \ , \qquad (2.3)$$

where I_0 is the central surface brightness, R_e is the effective or half-light radius, and β_n a fitting parameter. In equation (2.3), n is the Sersic index, that is related to the concentration of light and that usually ranges between 2 and 10 for ellipticals. Isophotes of the majority of elliptical galaxies are found to be well described assuming $n = 4$ (de Vaucouleurs, 1948), with $\beta_4 = 7.67$.

Half-way between disc and elliptical galaxies, lenticular or S0 galaxies have a rough and faint disc, no spiral arms and a dominant bulge component. The third broad class is constituted by irregular galaxies. They lack a defined shape, are usually less massive than spirals, and characterised by a large gas fraction and ongoing star formation.

The morphological classification of galaxies is usually displayed through the Hubble diagram or tuning fork (Hubble, 1936). Figure 2.2 shows the Hubble sequence, where elliptical galaxies locate from left to right according to their flatness and elongation. Disc galaxies occupy the upper or lower branch of the fork depending on whether or not they have a bar. They arrange according to the prominence of their bulge (bulgeless spirals are on the far right), and the tight or loose winding of spiral arms. The prominence of the bulge component is usually quantified through the bulge-over-total mass ratio, B/T. In observations it is usually derived from the photometry and adopt values ranging between 0.5 and 0.7 as a threshold to distinguish between disc and elliptical galaxies, the latter class being characterised by B/T approaching unity.

Albeit this classification neither captures the whole complexity of galaxies nor accounts for transitional systems that are interacting and experiencing merging

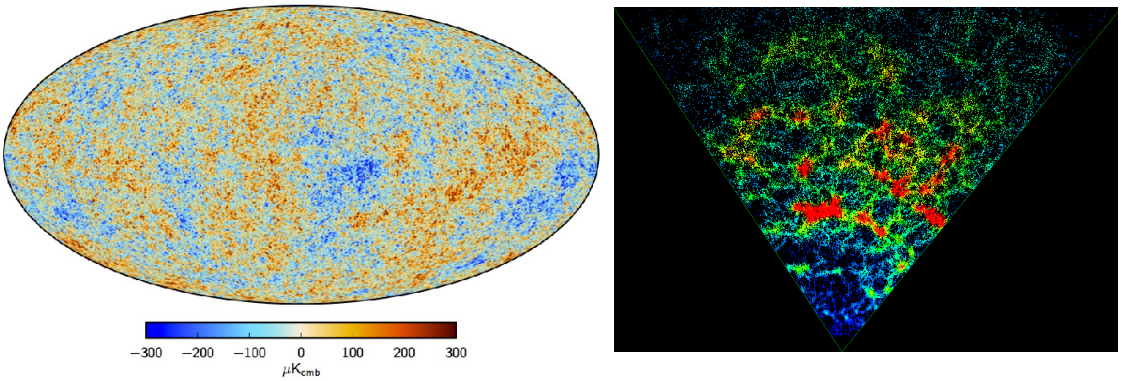

Figure 2.3: *Left:* Temperature map of the CMB, on the left (Planck Collaboration et al., 2016a). Penzias & Wilson (1965) first came across this background radiation. The map shows an almost homogeneous early Universe, with tiny density fluctuations. *Right:* For comparison, the clustered matter distribution in the present-day ($z \sim 0.1$) Universe as observed within the 2dF Galaxy Redshift Survey (Colless et al., 2001, image adapted from *www.2dfgrs.net*).

events, it is widely adopted. Also, it originated the dichotomy between early-type and late-type galaxies. Hubble indeed first thought the diagram was an evolutionary sequence, where early-type galaxies at the left evolved into late-type galaxies at the right of the tuning fork's pivot. This is not the accepted scenario of galaxy evolution anymore (e.g. Kormendy & Bender, 2012), still elliptical and spiral galaxies are usually referred to as early- and late-type galaxies, respectively.

2.2 Growth of cosmic structures

The tiny temperature fluctuations imprinted on the almost perfect blackbody emission of the CMB ($\Delta T_{\rm CMB}/T_{\rm CMB} \simeq 10^{-5}$, being $T_{\rm CMB} \simeq 2.73$ K today, see Section A.2) correspond to density perturbations that evolve and grow until they originate the cosmic structures in our Universe that we observe today (see Figure 2.3).

Density fluctuations are studied by means of the overdensity field (see Section A.2), that at a given time can be cast as:

$$\delta(\mathbf{x}) = \frac{\rho(\mathbf{x})}{\bar{\rho}} - 1 \ , \tag{2.4}$$

where $\rho(\mathbf{x})$ is the matter density distribution at the position $\mathbf{x}$, and $\bar{\rho}$ is the mean background density.

As log as $\delta(\mathbf{x}) \ll 1$, the evolution of density fluctuations is described within the linear regime (see Section A.2). When relaxing the assumption $\delta(\mathbf{x}) \ll 1$ and leaving the linear regime, it is not possible to capture analytically the complex evolution of perturbations (see also Section A.3): in order to investigate their further growth and possible collapse, we have to resort to numerical simulations (see also Section 3.1).

A fundametal scale determines whether a perturbation can undergo collapse or not. This is the Jeans scale. A matter fluctuation whose density is larger than that of the background medium is expected to collapse, unless the motion of particles within the perturbation is able to counteract gravity and make the perturbation dissolve. The Jeans scale can be computed by balancing energies, forces, or timescales involved in the process. A possible straightforward way is to consider the equation that describes the temporal evolution of $\delta(\mathbf{x})$ (see equation (A.13) in Section A.2 for further details). For a single mode $\delta_{\rm k}$ whose wavenumber is k, in Fourier space, the temporal evolution of density fluctuations reads:

$$\ddot{\delta}_{\rm k} + 2\,H\,\dot{\delta}_{\rm k} + \delta_{\rm k}\left(\frac{k^2\,c_{\rm s}^2}{a^2} - 4\,\pi\,G\,\bar{\rho}\right) = 0 \ , \tag{2.5}$$

where H is the Hubble parameter, $a(t)$ is the expansion or scale factor (see Section A.1), and $c_{\rm s}$ is the sound speed of the component whose fluctuations are considered. By ignoring at first the expansion of the Universe, equation (2.5) reduces to a wave equation, and $(k^2\,c_{\rm s}^2/a^2 - 4\,\pi\,G\,\bar{\rho}) = 0$ defines a characteristic mode $k_{\rm J}$. This can be translated in a critical wavelength $\lambda_{\rm J}$, the Jeans scale:

$$\lambda_{\rm J} = \frac{2\,\pi\,a}{k_{\rm J}} = \left(\frac{\pi\,c_{\rm s}^2}{G\,\bar{\rho}}\right)^{1/2} \ . \tag{2.6}$$

If $\lambda < \lambda_{\rm J}$, the pressure counterbalancing gravity makes the perturbation oscillate. If instead $\lambda \gg \lambda_{\rm J}$ the perturbation grows as time passes. The Jeans scale has been here retrieved assuming no expansion: $\lambda_{\rm J} = \sqrt{24}/5\,[(\pi\,c_{\rm s}^2)/(G\,\bar{\rho})]^{1/2}$ when the contribution from the expansion is included. (Coles & Lucchin, 2002).

In this way, a corresponding mass threshold is set, the Jeans mass:

$$M_{\rm J} = \frac{4\,\pi}{3}\,\bar{\rho}\left(\frac{\lambda_{\rm J}}{2}\right)^3 \ . \tag{2.7}$$

A fluctuation whose mass exceeds $M_{\rm J}$ can collapse, the gravity being not counterbalanced by the pressure support. This mass threshold assumes different values at different cosmic epoch.

In the commonly adopted model for structure formation, initial perturbations grow within a non-relativistic matter dominated Universe that is undergoing expansion. This process occurs via gravitational instability. DM is the first component to decouple from radiation, so DM perturbations first grow and enter the non-linear regime.

The Jeans mass as derived above in equation (2.7) has been obtained by balancing the fluid pressure and the gravitational pull. DM being a pressureless fluid, the equation for the Jeans mass has to be modified. In particular, the Jeans mass for the DM can be defined as (Coles & Lucchin, 2002):

$$M_{\rm J,DM} = \frac{1}{6}\,\pi\,m_{\rm DM}\,n_{\rm DM}\,\lambda_{\rm J,DM}^3 \ , \tag{2.8}$$

where $m_{\rm DM}$ and $n_{\rm DM}$ are the mass and the number density of the considered DM particles, respectively, and $\lambda_{\rm J,DM}$ is the Jeans length for DM, defined as:

$$\lambda_{\rm J,DM} = v_{\rm DM} \left(\frac{\pi}{G\,\bar{\rho}} \right)^{1/2} \quad . \tag{2.9}$$

Equation (2.9) is similar to the Jeans length for a collisional fluid (see equation (2.6)), except that for DM the sound speed is replaced by the mean velocity of the DM particles. This relies on the assumption that DM particles have a velocity distribution in random directions that acts as a pressure support. Due to this velocity distribution, DM perturbations can be dissipated or damped by the particle motion, a phenomenon referred to as free-streaming. Therefore, a free-streaming scale below which perturbations are damped and do not grow can be defined as:

$$\lambda_{\rm FS} \simeq a(t) \int_0^t \frac{v_{\rm DM}}{a(t')}\, dt' \quad , \tag{2.10}$$

where $a(t)$ is the expansion or scale factor (see Section A.1). Equation (2.10) sets a characteristic mass, the free-streaming mass $M_{\rm FS}$, in the same way as equation (2.8), where $\lambda_{\rm J,DM}$ is replaced by $\lambda_{\rm FS}$. The mass of a DM perturbation has to be compared with the free-streaming mass scale: DM perturbations with mass exceeding $M_{\rm FS}$ can grow.

The typical mass of the first haloes experiencing collapse depends on the nature of DM. Within the ΛCDM scenario, DM is cold, meaning that it is constituted of particles that are non-relativistic at decoupling. This has key consequences on the framework of structure formation, since the velocity of DM particles translates directly in a minimum $M_{\rm J,DM}$ (equation (2.8)) and free-streaming mass. Small density fluctuations with typical mass of $10^5 \div 10^6$ $M_\odot$ are the first ($z \sim 30 \div 20$) to be amplified due to gravitational instability (e.g. Barkana & Loeb, 2001, for a review, and references therein). As a consequence, they grow, leave the linear regime and first condense out of the Hubble flow. Larger haloes form later either through the merging of smaller haloes or as a consequence of the collapse of larger fluctuations in the DM. This is the hierarchical or bottom-up scenario for structure formation, for CDM (White & Rees, 1978; Kauffmann & White, 1993; Lacey & Cole, 1993).

On the other hand, if one assumed hot DM whose particles (e.g. massive neutrinos) are still relativistic at decoupling, a top-down scenario for structure formation would result, in which smaller structures form later as a consequence of the fragmentation of larger ones. This is the consequence of a significantly larger free-streaming mass scale $M_{\rm FS}$.

Assuming the ΛCDM scenario, DM perturbations grow, undergo a gravitational collapse and experience a violent relaxation. Since DM is collisionless and dissipationless, its collapse does not produce shocks, still it relaxes and reaches a condition of quasi-equilibrium, originating DM haloes.

Soon after the recombination ($z_{\rm rec} \sim 1100$), baryonic matter decouples from radiation ($z_{\rm dec} \sim 300$). At this time DM perturbations in the Universe already

form a distribution of potential wells that exert a gravitational pull on the baryonic component. Baryonic fluctuations can thus grow in the existing dark matter potential wells: as a final result, baryons flow towards the innermost regions of DM haloes, and undergo a dissipative collapse. The kinetic energy of the collapsing gas is transformed into thermal energy as strong shocks originate. Gas is thus shock-heated and this prevents further collapse. The gas is heated to the so-called virial temperature, $T_{\rm vir}$, that is related to the physical properties of the host halo. If we assume that gas is in equilibrium after the collapse and consider a static system that is not subject to external pressure, the virial theorem ensures what follows. The gas thermal energy matches the potential energy that the gas mass $M_{\rm gas}$ gains during the gravitational collapse within the halo of mass $M_{\rm DM}$, so that:

$$\frac{3 \cdot M_{\rm gas} K_{\rm B} T_{\rm vir}}{\mu\, m_{\rm p}} = \frac{G\, M_{\rm gas} M_{\rm DM}}{R_{\rm vir}} \ . \tag{2.11}$$

In equation (2.11), $K_{\rm B}$, μ, $m_{\rm p}$, and $R_{\rm vir}$ are the Boltzmann constant, the mean molecular weight, the proton mass, and the virial radius, respectively. The virial radius is defined as the radius that encloses an overdensity of $\delta_{\rm vir} \simeq 200$ times the critical density at that time (see Section A.3, where virial quantities are accurately derived). $M_{\rm gas}$ and $M_{\rm DM}$ are considered within $R_{\rm vir}$. In this way we obtain:

$$T_{\rm vir} = \frac{G\, \mu\, m_{\rm p}}{3 \cdot K_{\rm B} R_{\rm vir}} M_{\rm DM} = \frac{\mu\, m_{\rm p}}{3 \cdot K_{\rm B}} V_{\rm c,DM}^2 \ , \tag{2.12}$$

where $V_{\rm c,DM}$ is the equivalent Keplerian circular velocity of the DM halo and represents an alternative measure of the halo mass (e.g. Navarro, 1998). Linking the gas temperature to the host halo mass is crucial: theoretical models indeed provide the mass function of collapsed objects, i.e. the comoving number density $n(M_{\rm DM}, z)$ of haloes of mass $M_{\rm DM}$ within the range $[M_{\rm DM}, M_{\rm DM}+{\rm d}m]$, at a given redshift (Press & Schechter, 1974; Barkana & Loeb, 2001; Sheth & Tormen, 2002). This piece of information needs to be connected to the properties of the gas within DM haloes.

Gas at the virial temperature is expected to cool down to lower temperatures as a consequence of radiative cooling. This process is usually described according to the cooling function Λ (that is shown in Figure 2.4; e.g. Dalgarno & McCray, 1972; Sutherland & Dopita, 1993; Barkana & Loeb, 2001), so that $n^2\,\Lambda$ represents the cooling rate per unit volume, n being the gas number density. The cooling function $\Lambda(T, Z, \rho, z)$ depends on gas temperature, on metallicity and ionization degree, on density (unless the collisional ionization equilibrium is assumed), and on cosmic time.

Radiative cooling occurs on a characteristic timescale, the cooling time, that is defined as the time over which radiative losses become relevant for the energetic budget of the system. It can be expressed as the specific gas enthalpy over the energy radiated per unit volume, assuming the cooling to occur at constant pressure. It can be cast as:

$$t_{\rm cool} = \frac{5\, n\, K_{\rm B} T}{n^2\, \Lambda} \ , \tag{2.13}$$

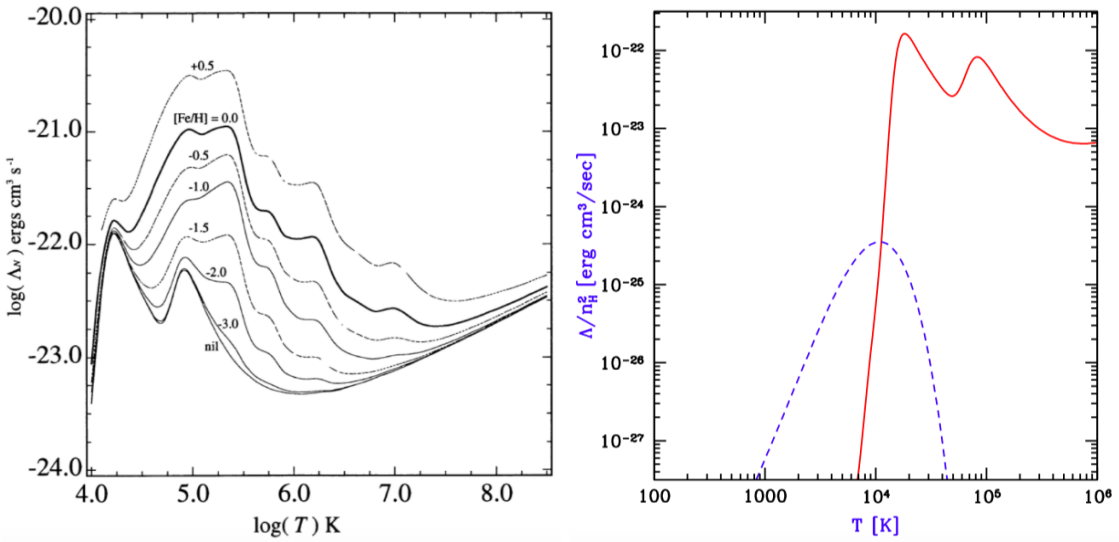

Figure 2.4: *Left:* Cooling function $\Lambda(T, Z)$ as a function of the temperature for different values of metallicity (Sutherland & Dopita, 1993). *Right:* contribution from hydrogen and helium (red) and molecular hydrogen (blue) to the cooling function of primordial gas (Barkana & Loeb, 2001). Note that what Barkana & Loeb (2001) define as Λ is the volume cooling rate (in erg s^{-1} cm^{-3}), at variance with the formalism adopted in Sections 2.2 and 4.2.

where n is the gas number density, considering electron and ion number densities to be comparable. The effectiveness of cooling is also remarkably dependent on the availability of molecular hydrogen, that is the main coolant if the gas has a primordial chemical composition (see Figure 2.4), especially at high redshift, when first structures are characterised by $T_{\rm vir} \lesssim 10^4$ K (Fuller & Couchman, 2000; Ciardi & Ferrara, 2005, for a review). If cooling is slow or inefficient (i.e. $H_0^{-1} > t_{\rm cool} > t_{\rm dyn}$, where the dynamical time $t_{\rm dyn} \propto (G\,\rho)^{-1/2}$), the virialised gas within the halo settles in hydrostatic equilibrium, as its pressure gradient counterbalances gravity. In this regime, cooling is allowed, but gas contraction is slow due to thermal support. Should the cooling be effective (i.e. $t_{\rm cool} < t_{\rm dyn}$), the gas cloud undergoes further collapse, almost free falling directly to the centre. As the gas density further increases, protostellar clouds likely collapse and possibly fragment. Stars finally form out of the collapsed molecular clouds (Abel et al., 1998; Bromm et al., 1999; Nishi & Susa, 1999; Abel et al., 2000; Yoshida et al., 2008).

As soon as star formation is onset in the innermost regions of these structures, protogalaxies appear. Different evolutionary paths will lead these protogalaxies to end up in the variety of galaxies and cosmic structures that we observe.

2.3 Formation of disc galaxies: theoretical scenario

The overview outlined in Appendix A and in Section 2.2 summarises the general picture for structure formation. The angular momentum plays a crucial role in

determining what is the fate of the gas within DM haloes and in what structure the protogalactic gas cloud will end up. Being this Thesis focused on spiral galaxies, the main aspects of the scenario for the formation of disc galaxies are briefly reviewed in this Section.

Albeit it has been extensively investigated for decades (since Efstathiou & Jones, 1980; Fall & Efstathiou, 1980), the scenario that leads to the formation of spiral galaxies has not been definitively assessed yet, as several details are still debated. The traditional picture is that the protogalactic cloud has an initial high angular momentum, so that the dissipative collapse that it experiences ends up with a centrifugally supported disc (Mo et al., 2010). It is generally assumed that the host DM halo and the infalling gas initially share the same specific (i.e. per unit mass) angular momentum. Both DM and gas likely have been provided with it as a consequence of external tidal torques exerted by the surrounding proto-structures and perturbations in the large scale environment (Peebles, 1969; Fall & Efstathiou, 1980; Porciani et al., 2002). Besides the asymmetry in the ambient matter distribution, mergers can also supply angular momentum, since the resulting system collects the angular momentum initially deposited in the orbits of the structures that merged (Gardner, 2001). Once the gas cloud falls within the halo, it cools efficiently, loosing energy and thereby the pressure support. As a consequence, it starts to contract. Since the cooling gas emits photons isotropically, its angular momentum is conserved during the collapse. As the gas cloud contracts, it spins up and flattens. Meanwhile, its angular momentum is transported towards the innermost regions of the halo where the galaxy forms. The gas cooled out and arranged in the disc undergoes further contraction until the surface density of the disc increases enough to form stars. This picture for disc galaxy formation was first introduced by Fall & Efstathiou (1980), and later revised and further developed by Mo et al. (1998); van den Bosch et al. (2002); Dutton et al. (2007); Dutton & van den Bosch (2012).

In order to quantify the importance of rotation in DM haloes, the dimensionless spin parameter λ is commonly adopted (Peebles, 1969). It reads:

$$\lambda = \frac{J_{\rm DM}\,|E_{\rm DM}|^{1/2}}{G\,M_{\rm DM}^{5/2}}\ , \tag{2.14}$$

where $J_{\rm DM} = |\mathbf{J}_{\rm DM}|$ and $E_{\rm DM}$ are the angular momentum and total energy of the halo, respectively. $M_{\rm DM}$ is the halo mass within the virial radius $R_{\rm vir}$ (see equation (2.11) and Section A.3). A corresponding quantity $\lambda_{\rm d}$ can be defined to measure the rotational support of the stellar disc. Numerical simulations investigated the spin parameter in DM haloes and found its distribution to be well described by a log-normal distribution with mean $\bar{\lambda} \simeq 0.035$, dispersion $\sigma_{\ln\lambda} \simeq 0.5$, and no significant dependence on redshift, halo mass or environment (Barnes & Efstathiou, 1987; Lemson & Kauffmann, 1999; Bullock et al., 2001; Macciò et al., 2007).

Further insight into the formation of the galaxy discs and the evolution of their size can be gained when properties of the disc are connected to the properties of the

host halo across time. Mo et al. (1998) presented a model for the formation of disc galaxies and computed analytically the scale radius of a stellar galaxy disc that forms within a DM halo. They assumed that the halo has a NFW profile[1] (Navarro et al., 1996) and that the disc is a stable, self-gravitating system, centrifugally supported and with an exponential surface density profile. Also, they made the hypothesis that the angular momentum $J_{\rm d}$ of the disc is a fraction $j_{\rm d}$ of that of the halo:

$$J_{\rm d} = j_{\rm d}\, J_{\rm DM} \ , \tag{2.16}$$

and that a fraction $m_{\rm d}$ of the halo mass is settled in the disc, so that:

$$M_{\rm d} = m_{\rm d}\, M_{\rm DM} \ . \tag{2.17}$$

Using equations (2.14), (2.16), and (2.17) it is possible to relate $J_{\rm d}$ to the spin parameter of the halo:

$$\lambda = \frac{1}{j_{\rm d}} \frac{J_{\rm d}\, |E_{\rm DM}|^{1/2}}{G\, M_{\rm DM}^{5/2}} \ . \tag{2.18}$$

Being $F_{\rm E}$ a factor that depends on the halo density profile and that allows to write the energy of the halo as:

$$E_{\rm DM} = -\frac{M_{\rm DM}\, V_{\rm c,\,DM}^2}{2}\, F_{\rm E} \ , \tag{2.19}$$

where $V_{\rm c,\,DM}$ is the circular velocity of the DM halo (see equation (2.12)), and assuming that $F_{\rm R}$ is a function that accounts for the halo density profile and self-gravity of the disc, and that allows to cast the total angular momentum of the disc as:

$$J_{\rm d} = 2\, M_{\rm d}\, R_{\rm d}\, V_{\rm c,\,DM}\, F_{\rm R} \ , \tag{2.20}$$

then, from equation (2.20), the expected scale length (see Section 2.1) of stellar discs at a given time reads:

$$R_{\rm d} = \frac{J_{\rm d}}{2\, M_{\rm d}\, V_{\rm c,\,DM}\, F_{\rm R}} \ . \tag{2.21}$$

Using equations (2.16) and (2.17), equation (2.21) becomes:

$$R_{\rm d} = \frac{j_{\rm d}}{m_{\rm d}} \frac{J_{\rm DM}}{2\, M_{\rm DM}\, V_{\rm c,\,DM}\, F_{\rm R}} \ ; \tag{2.22}$$

[1] The NFW (Navarro et al., 1996) profile for DM haloes at any time can be cast as:

$$M_{\rm NFW}(r) \ = \ M_{\rm vir}\, \frac{f(y)}{f(c)} \ , \ \text{where:} \ f(y) = \ln(1+y) - \frac{y}{(1+y)} \ , \ y = \frac{r}{r_{\rm s}} = \frac{c\, r}{R_{\rm vir}} \ , \ c = \frac{R_{\rm vir}}{r_s} \ , \tag{2.15}$$

$r_{\rm s}$ being the scale radius and c the concentration parameter, that are the two parameters entering in the definition of the NFW profile. More massive haloes are less concentrated than less massive ones at the same redshift (e.g. Bullock et al., 2001).

by plugging equation (2.19) into equation (2.14), it is possible to express:

$$J_{\rm DM} = \frac{\lambda\, G\, M_{\rm DM}^2\, \sqrt{2}}{F_{\rm E}^{1/2}\, V_{\rm c,\,DM}} \ , \tag{2.23}$$

so that the expected scale length of stellar discs at a given time reads (Mo et al., 1998):

$$R_{\rm d} = \frac{1}{\sqrt{2}} \left(\frac{j_{\rm d}}{m_{\rm d}} \right) \lambda\, R_{\rm vir}\, F_{\rm E}^{-1/2}\, F_{\rm R}^{-1} \ . \tag{2.24}$$

Assuming the NFW profile, for instance, $F_{\rm E}$ is a function of the concentration parameter (see equation (2.15) and see Mo et al. (1998) for further details). The redshift evolution is encoded within virial quantities (see Section A.3). The key results of Mo et al. (1998) are the following: first, the extent of the stellar disc is dependent on the angular momentum of DM and gas. Second, the typical assembly redshift for stellar discs is $z \lesssim 1$. Also, assuming $j_{\rm d} = m_{\rm d} \simeq 0.05$, their model predictions are in agreement with observations.

While the aformentioned seminal model captures several aspects of disc galaxy formation, some of its assumptions are not adequate at capturing the complexity of the disc formation process. One issue deals with the adiabatic contraction, that is the hypothesis that the system adjusts itself adiabatically as a consequence of the assembly of the disc (Blumenthal et al., 1984; Dutton et al., 2007). The formation of a central galaxy perturbs the underlying DM distribution and induces transformations on it: as a result, the halo contracts in the innermost regions at early stage (Blumenthal et al., 1986). On the other hand, the evolution of the galaxy at later times makes the DM density profile expand, especially because of mass loss and galactic winds (e.g. Tonini et al., 2006; Di Cintio et al., 2014). These processes are highly sensitive to the formation history of the system.

Also, the hypothesis that $m_{\rm d} = j_{\rm d}$ has been thouroughly investigated. This assumption translates in the requirement that the specific angular momentum of baryons is equal to that of the DM halo. However, $(j_{\rm d}/m_{\rm d}) \neq 1$ is possible either because there is an exchange of angular momentum between DM and baryons, or because of processes that eject baryons selectively. For instance, the effect of the dynamical friction results in a specific angular momentum of baryons that is lower than that of the DM halo (Navarro & White, 1994; Sommer-Larsen et al., 1999a; Dutton & van den Bosch, 2012). Galactic outflows are instead able to remove selectively low angular momentum gas (Maller & Dekel, 2002; Governato et al., 2010; Übler et al., 2014; Genel et al., 2015; Teklu et al., 2015).

As for the transport of angular momentum within the disc itself, possible mechanisms that may play a role are gas viscosity (Lin & Pringle, 1987) and stellar scattering (Sellwood & Binney, 2002). Although stellar scattering and radial migration are found to play a supporting role in redistributing the angular momentum within the disc (Roškar et al., 2008), these mechanisms are considered to be not efficient (Mo et al., 2010). Indeed, the lowest energy state for a given angular momentum J would be the configuration where a central black hole (BH)

of mass $M_{\rm BH}$ resides at the centre and a small blob of mass ΔM is orbiting around it (i.e. $J = \Delta M\,(G\,M_{\rm BH}\,r)^{1/2}$, r describing the Keplerian orbit). In order to reach this lowest energy configuration, mass should spiral in towards the BH and be accreted. However, mass can only flow inwards while loosing angular momentum, which is transferred outwards in the meanwhile. Galaxy discs are far from this prediction, as their mass is distributed in the disc following an almost exponential profile (Section 2.1). This evidence is considered a proof that the transport of angular momentum is not effective.

A viable channel to allow the formation of extended stellar discs is the accretion of high angular momentum gas at low redshift. This reservoir of gas has been first assumed to come from the outermost regions of the halo (Fall, 1979). Later on, numerical simulations have shown that the large scale structure can provide high angular momentum gas through cold flows (Brooks et al., 2009; Pichon et al., 2011; Dubois et al., 2014; Codis et al., 2015). The large scale structure is indeed made up of a network of filaments containing gas that is cooling because of radiative losses. As this gas cools, it streams towards the inner regions of haloes where galaxies are forming, advecting the angular momentum originally gained because of tidal torques.

Another possible channel that contributes to the formation of extended discs is the re-accretion at low-redshift of gas that has been expelled from the forming galaxy at high-redshift, especially as a consequence of early bursts of star formation. The gas that is re-accreted falls back onto the galaxy at quite large distances from the galaxy centre, as a result of its high angular momentum. Galactic outflows (see Section 2.4.4) play a fundamental role in promoting gas expulsion and in allowing gas re-accretion: this topic will be thouroughly addressed in Chapters 6.

Several processes contribute to the formation and assembly of disc galaxies over cosmic time, such as accretion of gas from the large scale environment, merging with other galaxies or smaller substructures, star formation and feedback. Their interaction is complex, and still far from being completely understood.

2.4 Disc galaxies: observational results

In this Section, I briefly review the main observational properties and features of disc galaxies in the local Universe. The overview is far from being comprehensive: deeper insight can be obtained from the reviews by e.g. Kennicutt (1998a); Sofue & Rubin (2001); Blanton & Moustakas (2009); Putman et al. (2012); Kormendy & Ho (2013).

2.4.1 The multiphase ISM

The recent availability of multiwavelength high-quality observations from different galaxy surveys (e.g. SDSS (Sloan Digital Sky Survey, York et al., 2000), FIRES (Faint InfraRed Extragalactic Survey, Franx et al., 2000), 2dF (Two-degree-Field) Galaxy Redshift Survey (Colless et al., 2001), GEMS (Galaxy Evolution from Morphology and SEDs, Rix et al., 2004), GASP (Gassendi HAlpha survey of SPirals, Epinat et al., 2008), AMIGA (Analysis of the interstellar Medium of Isolated GAlaxies, Lisenfeld et al., 2011), COLD GASS (CO Legacy Data base for the GALEX Arecibo SDSS Survey, Saintonge et al., 2011)) opened the possibility to investigate the properties of stars and gas in nearby galaxies accurately.

Spiral galaxies have a complex multiphase interstellar medium (ISM). It is made up of cold ($T \lesssim 10^4$ K), warm ($T \sim 10^4 \div 10^5$ K) and hot ($T \gtrsim 10^5$ K) gas, that can be molecular, neutral or ionised. Overall, different phases are considered to be in pressure equilibrium. The ISM is embedded within the galaxy hot corona ($T \sim 10^6$ K), that continues and extends towards the circumgalactic medium (CGM), without definite borders in between (Fukugita & Peebles, 2006). This diffuse and hot gas is approximately at virial temperature and constitutes the galaxy gaseous halo, that is considered to be extended from the proximity of the stellar disc out to the virial radius (few hundreds of kpc, Putman et al., 2012). Metal poor gas from the intergalactic medium (IGM), that represents the reservoir of baryons out of which galaxies form, is continuously accreted through the CGM: it reaches star-forming regions in the galaxy disc, thus sustaining star formation (Tumlinson et al., 2011). Properties of the ISM control and drive processes within the galaxy. Meanwhile, the structure of the ISM is shaped and maintained by ongoing injections of energy and momentum, the so-called feedback processes resulting from galaxy evolution. Above all, stellar evolution contributes to provide the ISM with energy and to pollute it with metals, the stars aging and possibly exploding as SNe.

Atomic gas, mainly constituted of neutral hydrogen (H I), is detected through the 21 cm emission line and reveals that gaseous discs in spiral galaxies are usually more radially extended than their stellar counterpart (Bosma, 1981; Oosterloo et al., 2007). Also, the H I emission shows that gaseous discs often appear warped, flared, and extend up to ~ 3 kpc above the galactic plane (Sancisi, 1976; Matthews & Wood, 2003; Sancisi et al., 2008; O'Brien et al., 2010; Bosma, 2017). Extraplanar gas can also be ionised due to incident stellar radiation (Bizyaev et al., 2017) and can be arranged in gas streams (Martínez-Delgado et al., 2010).

Molecular hydrogen (H_2) primarily contributes to the molecular gas, that is commonly investigated through the CO molecule transition lines. It traces the location of recent sites of star formation along spiral arms (Wong & Blitz, 2002; Kennicutt, 1998b; Kennicutt et al., 2007; Leroy et al., 2008), as stars originate within giant molecular clouds. The latter are associations that contain the majority of H_2: their mass and size distributions show that typically GMCs are few tens of pc wide and a have mass $\lesssim 10^6$ $M_\odot$ (Heyer & Dame, 2015).

The star formation rate (SFR) correlates with the total (molecular plus atomic) gas surface density $\Sigma_{\rm gas}$, albeit the correlation is even tighter when the H_2 alone is considered (Wong & Blitz, 2002; Kennicutt et al., 2007; Bigiel et al., 2008). Schmidt (1959) introduced a fitting formula for the SFR surface density $\Sigma_{\rm SFR}$, where $\Sigma_{\rm SFR} \propto \Sigma_{\rm gas}^{n}$, the so-called Schmidt-Kennicutt relation. A commonly adopted value is $n \simeq 1.4$ (Kennicutt et al., 2007). The value of the slope n spans the range $0.9 \div 1.7$ (Kennicutt, 1998a), depending especially on the considered tracer of SFR (Buat et al., 1989; Kennicutt, 1989; Buat, 1992).

Interestingly, Blitz & Rosolowsky (2006) showed that the interstellar gas pressure determines the ratio between atomic and molecular gas surface densities (this piece of information will be exploited in Section 5.3). They found that the molecular gas fraction is proportional to the hydrostatic pressure of gas in the galaxy disc, by analysing a sample of local spiral galaxies, including our Milky Way (MW), whose mean metallicity ranges from solar down to ~ 0.2 solar.

The ratio between gas and stellar mass is usually referred to as gas richness. Observations show that low-mass galaxies are both atomic gas richer and molecular gas richer than more massive spirals (Lisenfeld et al., 2011; Saintonge et al., 2011; Jiang et al., 2015). H_2 richness, however, flattens below stellar masses $M_* \sim 10^{10}$ $M_\odot$. Low mass galaxies are therefore richer in atomic gas, but not as efficient as higher mass systems at converting it into the molecular form: this results in a lower SFR and a lower efficiency of coverting baryons into stars (Blanton & Moustakas (2009); see also Section 2.4.2). Also gas in more massive galaxies is more enriched in metals (mass-metallicity relation, e.g. Tremonti et al., 2004; Kewley & Ellison, 2008).

2.4.2 Scaling relations

A simple yet straightforward and powerful method to appreciate how galaxies evolve is to analyse their scaling relations. Scaling relations describe correlations between global properties of galaxies, such as their luminosity, stellar mass, rotation speed, and size. The size is usually expressed by means of either the scale radius or the half-mass (effective) or optical radius, the latter being scaled versions of $R_{\rm d}$. Some among the most well established observed scaling relations in disc galaxies are the following.

The velocity - luminosity, or velocity - stellar mass relation is the so-called Tully-Fisher relation (Tully & Fisher, 1977): it indicates that the total luminosity of the galaxy correlates with its rotation speed (see Figure 2.5), i.e. $L \propto V_{\rm circ}^{\alpha}$, where $\alpha \simeq 2.5 \div 4$ (Bell & de Jong, 2001; Vogt et al., 2004; Courteau et al., 2007; Pizagno et al., 2007; Dutton et al., 2007; Reyes et al., 2011; Torres-Flores et al., 2011; Lapi et al., 2018). The value of the slope depends on the passband where the magnitude of the galaxy is determined (Pierce & Tully, 1992). A similar relation can be predicted as follows. Requiring the balance between the centrifugal and the gravitational acceleration, $V_{\rm circ}^2(r) \propto M_{\rm tot}(r)/r$ (equation (2.1)); also, the luminosity can be written in terms of central surface brightness as $L(r) \propto I_0\, r^2$. If one assumes

that the mass over light ratio M/L (see Section 2.1) is roughly constant (but see Bell et al., 2003; Courteau et al., 2007), then $L \propto V_{\rm circ}^4$. The Tully-Fisher relation is commonly cast in terms of stellar mass of the galaxy, rather than luminosity (see also Sections 6.5.2 and 6.5.3.2). This relation is often investigated by considering both the stellar and gas mass (baryonic Tully-Fisher relation): in this way it pertains to galaxies whose baryonic mass ranges between $\sim 10^7$ M$_\odot$ and $\sim 10^{11.5}$ M$_\odot$ (McGaugh et al., 2000; Verheijen, 2001a; Stark et al., 2009; Hall et al., 2012). Lower mass systems would otherwise be offset if stars rather than baryons are considered, as they are characterised by a larger amount of cold gas and lower efficiencies in converting it to stars. The total luminosity of the galaxy should correlate with the circular velocity evaluated at a distance that encompasses the entire galaxy; instead, $V_{\rm circ}$ is usually evaluated where it reaches its maximum or at a distance multiple of the disc scale radius $R_{\rm d}$. Besides being used to determine distances to galaxies, this relation is key as it relates the luminosity of the galaxy to its dynamical mass. Also, the slope, (small) scatter, zero point, and colour trends of this relation encode valuable information on the scenario of disc galaxy formation (e.g. Courteau et al., 2007).

The scale radius - velocity and scale radius - luminosity relations show that the more extended the stellar disc, the larger the galaxy rotation speed (and therefore, the dynamical mass of the galaxy) and the higher its luminosity (see Figure 2.5). Also, the size - luminosity relation is often cast in terms of size versus stellar mass. Interestingly, if one considers the size - stellar mass relation in terms of central surface density ($\Sigma_0 \propto M_*/R_{\rm d}^2$) versus stellar mass, it emerges how the surface density flattens as the stellar mass approaches $M_* \sim 10^{11}$ M$_\odot$. This is interpreted as follows: extended spiral galaxies experience a quiet low-redshift star formation, and this prevents them to increase promptly their stellar mass, at variance with ellipticals of the same stellar mass (e.g. Lapi et al., 2018).

The stellar mass - halo mass relation is related to the star formation efficiency or baryon conversion efficiency. It highlights that a lower fraction of the original baryon content of the halo is converted into stars within lower mass spirals (e.g. Dutton et al., 2011a; Huang et al., 2017).

The stellar to virial velocity ratio - stellar mass relation shows that the optical velocity ($V_{\rm circ}$ evaluated at $r \sim 2.2\,R_{\rm d}$) is an accurate tracer of $V_{\rm c,DM}$ (equation (2.12)). This relation implies a connection between the kinematics of galaxies and their host haloes (Dutton et al., 2010; Lapi et al., 2018).

Moreover, the specific angular momentum of the stellar component increases as a function of the stellar mass, and of the halo mass. Also, halo and galaxy sizes correlate (effective radius - halo radius relation). Brighter discs are observed to be redder (e.g. van den Bosch & Dalcanton, 2000), and have smaller gas mass fractions (McGaugh & de Blok, 1997).

Scaling relations of disc-dominated galaxies usually show a weak evolution as the redshift increases (e.g. Barden et al., 2005; Trujillo et al., 2006; Bouché et al., 2007; Dutton et al., 2011a). Especially for the size - stellar mass relation, a low degree of evolution is interpreted as the evidence that disc galaxies increase their size as they grow more massive (inside-out scenario, see Section 2.4.3).

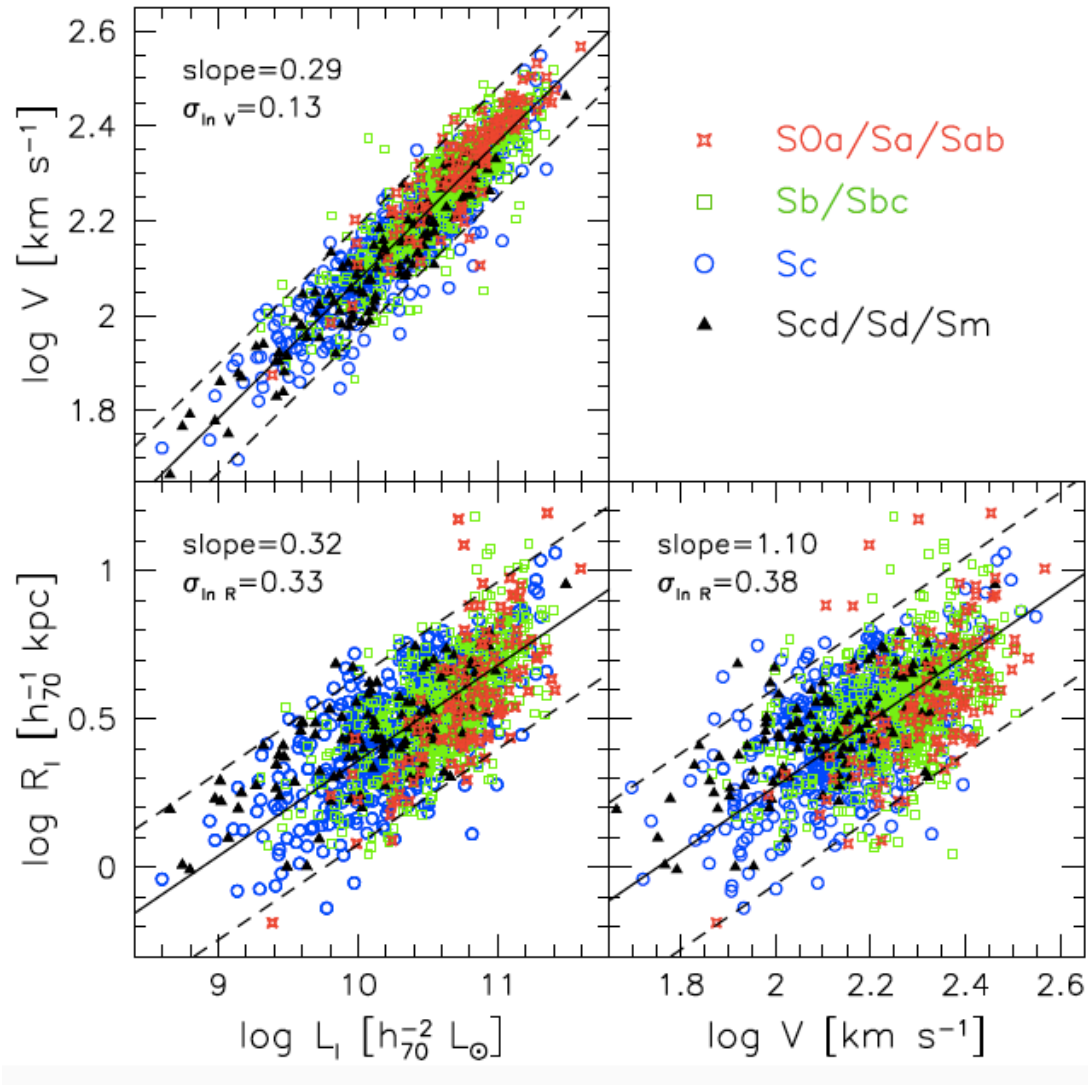

Figure 2.5: Tully-Fisher, luminosity-size, and velocity-size scaling relations for a sample of disc galaxies, colour-coded according to the galaxy morphological type (see Figure 2.2). Figure from Courteau et al. (2007).

2.4.3 Stars and their metal content

Metals are unique tracers of galaxy evolution and of the past history of feedback. Stars generally have a diverse and complex metallicity and chemical content, indicating the variety of living environments and stellar evolution paths. While having a main active role in the process of chemical enrichment of the surrounding ISM of a galaxy, stars also passively contribute to track galaxy evolution, as their chemical composition records vital information on the past events of the galactic ecosystem. The number of long-lived stars and the composition of their stellar atmospheres in terms of different metal abundances are indeed key tracers of the galaxy star formation history, of the accretion of pristine gas from the large-scale environment, and of the timing with which all these processes occurred across cosmic time (e.g. Wilson & Matteucci, 1992; Matteucci, 2012).

Before giving a short overview on the chemical properties of stars observed in spiral galaxies, I will briefly discuss how the metal content is commonly expressed and measured. Total metallicity is accurately traced by the most abundant elements, i.e. carbon, nitrogen, and oxygen. Among them, oxygen is by far the most common, even if it is difficult to retrieve (Cayrel et al., 2004).

Metal abundances are commonly investigated in terms of the overall metal content $[Z/H]$. Here, $[Z/H] = \log_{10}(Z/H) - \log_{10}(Z/H)_{\odot}$ is the logarithm of the ratio of the abundance by mass (or by number, according to the choice of different authors) of all elements heavier than helium (He or Y) over hydrogen (H or X), compared to that of the Sun[2]. The abundance of a single element $Z_{\rm i}$ is quantified through $[Z_{\rm i}/H]$, correspondingly. Sometimes, the linear (i.e. non logarithm) and absolute (i.e. not scaled to the solar values) metallicity Z is also quoted. Another widely adopted way to express the metal content is by means of the quantity $12 + \log_{10}\left(N_{\rm Z_i}/N_{\rm H}\right)$, where $N_{\rm Z_i}$ and $N_{\rm H}$ are number densities of the element $Z_{\rm i}$ and of hydrogen, respectively. This peculiar scale has the zero point set by $\log_{10} N_{\rm H} = 12$.

The metal content of gas and stars is retrieved by analysing spectra. In particular for gas and stars in nearby disc galaxies, the gas metal content is usually estimated through emission lines from H II regions and planetary nebulae, while the stellar metal content is retrieved from absorption lines in the spectra of massive stars.

Values for the current Sun's abundance in different elements are tabulated and inferred by investigating the solar photosphere or meteoritic abundances (e.g. Grevesse & Sauval, 1998; Asplund et al., 2005, 2009; Caffau et al., 2011). As for the present-day Sun's total metallicity, accurate estimates of abundances by mass are the following: $Z_{\odot} = 0.01524 \pm 0.0015$ (Caffau et al., 2011) and $Y_{\odot} = 0.2485 \pm 0.0035$ (Basu & Antia, 2004), so that $(Z/H)_{\odot} = 0.0207 \pm 0.0015$ (Bressan et al., 2012).

Historically stars have been sliced into different populations according to their metal content (Baade, 1958). Stars belonging to the so-called first population have roughly solar or supersolar metallicity ($0.002 \lesssim Z \lesssim 0.06$), are younger than ~ 10 Gyr, and are characterised by circular orbits on the galactic plane. The second generation is made up of older stars with a remarkably sub-solar metal content and eccentric orbits. Also, a third population of stars is predicted to exist, consisting of metal free or extremely metal poor stars, i.e. the first stars that have ever shone. Up to now, no metal free stars have been detected, although a few possible relics ($[Fe/H] = -5.4$) of the third population have been observed (Christlieb et al., 2002; Frebel et al., 2005).

Despite being rather outdated, this classification highlights that different components of disc galaxies are made up of stars with peculiar properties. Velocity dispersion supported stars in the halo and bulge are older and more metal poor than stars located in the disc. Therefore, the metallicity of stellar atmospheres relates directly to the local enrichment of the ISM out of which stars form. As time passes the metallicity of the ISM increases, since evolving stars synthesise metals

[2]More precisely, He and H are the symbols used to refer to helium and hydrogen, respectively, while Y and X are generally their mass fraction.

and pollute their surrounding medium. As a consequence, stars are progressively richer in heavy elements.

Observations show that stars within galaxy discs are characterised by negative radial metallicity gradients (e.g. Yong et al., 2006; Lemasle et al., 2007; Sziládi et al., 2007; Romaniello et al., 2008; Pedicelli et al., 2010; Luck et al., 2011; Luck & Lambert, 2011; Genovali et al., 2013, 2014b; Spina et al., 2017), with $[Fe/H]$ declining from $[Fe/H] \sim 0.4$ down to $[Fe/H] \sim -0.5$ when the distance from the Galaxy centre increases from 5 to 15 kpc. The aforementioned data come from samples of stars observed within the MW. Our Galaxy is by far the most investigated galaxy ever. The wealth of observational data of MW stars represents a crucial contribution to the study of chemical evolution in disc galaxies, even if more data from other nearby galaxies are being acquired. MW observations are commonly considered representative of spiral galaxies with comparable stellar mass (although see Hammer et al., 2007; Bell et al., 2017).

Radial metallicity gradients are commonly interpreted as a signature of the inside-out formation of stellar discs. Observations show that stellar discs progressively increase their size as they grow: inner regions form first, then star formation proceeds at increasing distances from the galaxy centre as new gas with higher specific angular momentum is accreted (e.g Barden et al., 2005; Magrini et al., 2009; Muñoz-Mateos et al., 2011; Patel et al., 2013; González Delgado et al., 2014).

Among flows that can affect metallicity radial profiles, stellar migration and radial gas inflows are often invoked to explain features in the observed distributions. Radial migration allows stars to move radially from their original position to another distance from the galaxy centre. As a consequence, stars observed at a given location are not the result of in situ star formation anymore, and can have properties different from the majority of surrounding stars. Radial migration is commonly considered to be a diffusive process (Brunetti et al., 2011, but see e.g. Sellwood & Binney 2002). Metal rich stars from inner and denser regions tend to move outwards on timescales shorter than those related to the motion of more metal poor stars migrating in the opposite direction from less dense regions. The main outcome of radial migration is a flattening of metallicity profiles: as time passes, stars with different properties redistribute and likely mix (Roškar et al., 2008; Schönrich & Binney, 2009; Debattista et al., 2017). Conversely, radial inflows of gas result in a steepening of (gaseous and, consequently, stellar) metallicity profiles, as they promote the flow of metals towards the inner regions (Lacey & Fall, 1985; Portinari & Chiosi, 2000; Spitoni & Matteucci, 2011; Pezzulli & Fraternali, 2016).

The initial mass function (IMF) and the stellar yields are among the elements that determine the abundance and distribution of metals. The IMF governs the mass distribution that stars had at their birth and plays a crucial role in driving the production of metals. Its shape sets the relative number of stars that enter the chemical evolution processes and those that do not, and different assumptions (e.g. Salpeter, 1955; Kroupa et al., 1993; Kroupa, 2001; Chabrier, 2003) produce different patterns of chemical enrichment.

Stellar yields quantify the mass of metals that are synthesised and released in the ISM by stars of given mass and metallicity. Since stars retain the metals of the ISM out of which they formed, the complex interplay among the aforementioned components reflects on signatures of stars such as the α-element-to-iron abundance ratio, α/Fe (see also Section 7). α-elements (usually assumed to be O, Ne, Mg, Si, S, Ar, Ca, Ti) are metals produced as a consequence of helium nucleus captures during the Si burning phase just before the SNe II core collapse. The α/Fe ratio can be used to constrain the galaxy star formation history, since the trend of α-element abundance with metallicity is determined by the timescales of star formation and chemical enrichment, by the shape of the IMF, and by the amount of stars formed at the peak of the galaxy star formation history (Tinsley, 1979). Stellar enhancement in α-elements, with respect to the solar ratio, determines the typical timescale of chemical enrichment. Massive stars exploding as SNe II pollute the ISM with α-elements over a timescale shorter than ~ 50 Myr, depending on the metallicity. On the other hand, the production of iron-peak elements is delayed with respect to α-elements, since it is mainly produced by SNe Ia originating after the thermonuclear explosion of a white dwarf within a binary system. The timescale required for SN Ia explosions and subsequent chemical feedback spans between ~ 50 Myr and several Gyr. This ratio allows us to identify different chemical evolutionary patterns for stars located in different components of our Galaxy, namely in the bulge, halo, thin or thick disc (e.g. Edvardsson et al., 1993; Cayrel et al., 2004; Zoccali et al., 2006; Meléndez et al., 2008).

2.4.4 Galactic outflows

Mass and energy flows are a crucial component of galaxy formation and evolution. Metal poor gas inflows from the IGM, is accreted by forming galaxies, and fuels star formation. As time passes, stars age and a fraction of them explode as SNe II. Besides supplying thermal energy to the ISM, SN explosions trigger galactic outflows, generating kpc-scale galactic winds. These galactic winds are driven by the kinetic energy and momentum that SN explosions provide the ISM with.

Galactic outflows have been observed both in the local Universe (e.g. Bradshaw et al., 2013; Arribas et al., 2014; Lofthouse et al., 2017; Yuma et al., 2017) and at higher ($\lesssim 6$) redshift (e.g. Heckman et al., 2000; Pettini et al., 2001; Dawson et al., 2002; Frye et al., 2002; Shapley et al., 2003; Martin, 2005; Wilman et al., 2005; Weiner et al., 2009; Rubin et al., 2010; Kornei et al., 2012; Tang et al., 2014). These multiwavelength observations suggest that outflows are multiphase, made up of both neutral and ionised gas. They extend beyond the galaxy scale, with characteristic velocities ranging from few to several hundreds of km s^{-1}, and that can be as high as 1000 km s^{-1} especially at high redshift (see e.g. the review by Veilleux et al., 2005).

The morphology of outflows varies on a galaxy-to-galaxy basis: they often have a bipolar structure, with opening angles spanning the range $\sim 10^\circ \div 45^\circ$ in the proximity of the galaxy disc, and as wide as $\sim 100^\circ$ above. Outflow structure can

reach a height of $\sim 10 \div 20$ kpc above the galactic plane (Veilleux et al., 2003; Rubin et al., 2011; Tumlinson et al., 2011). Outflowing gas often entrains ambient medium along the path. Velocity of the warm and ionised gas components in outflows are higher than that of the cold phase (e.g. Shopbell & Bland-Hawthorn, 1998; Walter et al., 2002).

As for the energetics of galactic outflows, the kinetic energy of these winds ranges between $\sim 10^{50} \div 10^{54}$ erg in dwarf galaxies, and $\sim 10^{56} \div 10^{59}$ erg in starburst galaxies characterised by high infrared luminosity. Correspondingly, powers vary between $\sim 10^{36} \div 10^{39}$ erg s^{-1} and $\sim 10^{41} \div 10^{44}$ erg s^{-1}. The mass of warm gas (i.e. the phase responsible for the bulk motion) involved in galactic outflows is about $10^5 \div 10^6$ M$_\odot$ in dwarfs and can be as high as $\sim 10^7$ M$_\odot$ in starburst systems. Outflowing gas has a typical dynamical time of $\sim 0.1 \div 10$ Myr, so that outflow rates of $\sim 0.1 \div 10$ M$_\odot$ yr^{-1} can be inferred. The higher the SFR of the galaxy, the higher the outflow rate. The mass loading factor of the outflow is a parameter that describes its mass entrainment efficiency: it can be cast as $\eta = \dot{M}/SFR$, $\dot{M}$ being the outflowing mass rate, and spans the the range $0.01 \lesssim \eta \lesssim 10$ (Veilleux et al., 2005, and references therein).

A small fraction ($\lesssim 10\%$, Rupke et al., 2005) of outflowing gas is powered to velocity high enough to escape the gravitational potential of the host galaxy; the bulk of the gas involved in the process rather remains bound to the galaxy, within its gaseous halo. It can eventually fall back towards the galaxy disc, originating the so-called galactic fountains (Shapiro & Field, 1976; Bregman, 1980).

Galactic outflows play a crucial role in galaxy evolution across cosmic time. Their are able to heat up the surrounding medium and to remove (or even deplete) gas from star-forming regions where they originate: as a consequence they have a dramatic impact on star formation. Galactic outflows are indeed thought to be one of the main mechanisms that control star formation in low- and intermediate-mass galaxies ($M_* \lesssim 10^{11}$ M$_\odot$), as they are able to hamper the galaxy growth. They are considered to be crucial to reproduce the low-mass end of the observed galaxy stellar mass function. This latter evidence has been mainly proved by quantifying the effect of stellar feedback and galactic winds in cosmological simulations (e.g. Puchwein & Springel, 2013). The key role that galactic outflows have in simulations of galaxy formation will be thouroughly discussed in Chapters 3 and 6.

Galactic outflows are a natural outcome of stellar feedback. Aging stars pollute the ISM with heavy elements synthesised during their evolution. Galactic outflows drive metal-enriched gas outwards from sites of star formation, and foster the spread and circulation of metals over galactic scales (see also Section 7). Also, they guarantee a continuous interaction between galaxies and their surrounding medium, since they are responsible of the metal enrichment of the CGM (Savage et al., 2002; Adelberger et al., 2003; Werk et al., 2016). Meanwhile, they counterbalance the accretion of pristine or metal-poor gas from the large scale environment (Tumlinson et al., 2017, and references therein).

AGN (active galactic nucleus) feedback (see Section 2.4.5) can promote galactic winds, too. As highlighted by Veilleux et al. (2005), it is hard to state whether a galactic wind is powered either by sturburst and star formation activity only or by AGN activity alone. It is likely that galactic outflows are often the result of the joint activity of stellar and AGN feedback.

2.4.5 AGN feedback

Almost every galaxy hosts a BH in its innermost regions. BHs in the centre of galaxies are usually referred to as SMBHs ($M_{\rm BH} \gtrsim 10^6$ $\rm M_\odot$), in order to distinguish them from lower mass ($M_{\rm BH} \lesssim 10^2$ $\rm M_\odot$) BHs resulting from stellar evolution. The vast majority of SMBHs are silent, while $\sim 1\%$ exhibit ongoing activity and are called AGNs, i.e. active galactic nuclei (Kormendy & Richstone, 1995; Ferrarese & Merritt, 2000). AGN feedback is the process by which a SMBH regulates and affects the evolution of its host galaxy and of the environment where they reside. The most visible evidence of AGN activity are observed in the X-ray images of elliptical galaxies and galaxy groups and clusters (e.g. Smith et al., 2002; David et al., 2009; Fabian et al., 2011), where they appear as depressions and ripples in the surface brightness maps. Spectral energy distributions and light curves of systems also show imprints of AGNs.

AGNs operate in systems with different mass residing in different environments, from isolate spiral galaxies to massive ellipticals located at the centre of bright groups and clusters of galaxies. SMBHs accrete surrounding gas; the gravitational energy that accreted matter releases provides feedback energy. AGN feedback develops through the interaction between the mechanical, thermal and radiative energy supplied by accretion and the gas in the host galaxy. BH feedback operates through two main distinct modes: radiative or quasar mode, and kinetic or radio mode (e.g. Fabian, 2012). During the quasar mode the AGN is highly luminous, its luminosity approaching the Eddington limit, i.e. $\sim 1.3 \cdot 10^{38}$ $(\rm M_{BH}/M_\odot)$ erg $\rm s^{-1}$ (Frank et al., 2002). Quasar radiation likely originates from an accretion disc; gas-rich mergers and cold flows are supposed to be the main mechanisms by which the BH is fed during this phase, as they can sustain high BH accretion rates. The bulk of feedback energy is released through winds and by radiation when AGNs are in quasar-mode. On the other hand, the accreting BH acts through the mechanical energy of its radio-emitting jets during the radio mode. These collimated jets can inflate cavities and bubbles, and entrain ambient gas resulting in massive outflows, that are sub-relativistic on kpc scales. The latter mode is dominant among low-power AGNs at redshift $z \lesssim 2$, where BHs are characterised by lower accretion rates and mainly sustained by the secular evolution of the host system (e.g. reviews by Ferrarese & Ford, 2005; McNamara & Nulsen, 2007; Fabian, 2012; Kormendy & Ho, 2013; Morganti, 2017, and references therein). Radiation pressure can also power outflows (Proga, 2007). AGN feedback energy also affects the accretion and the growth of the BH itself, thus controlling its duty-cycle and making the system reach the self-regulation.

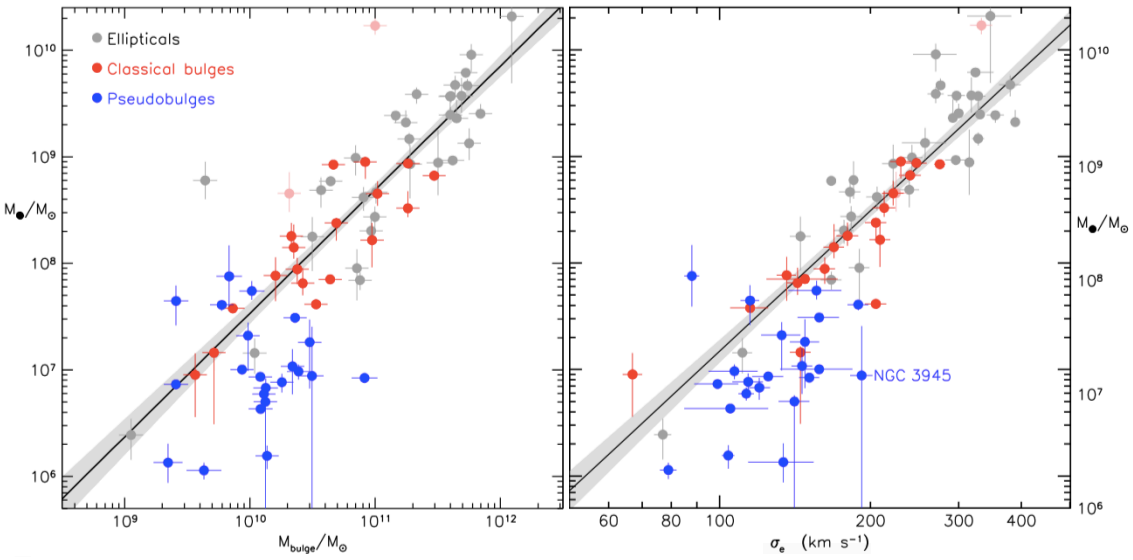

Figure 2.6: Correlations between BH mass and stellar mass of bulge (left-hand panel) and BH mass and stellar velocity dispersion (right-hand panel) for a sample of elliptical and spiral galaxies. Spiral galaxies in the sample are color coded according to whether they host a classical bulge or a pseudo-bulge. Solid lines represent the best fit to ellipticals and classical bulges. Figure from Kormendy & Ho (2013).

The most convincing indication of AGN activity across cosmic time is the existence of tight correlations between properties of SMBHs and their host galaxies. Observed correlations are the following: the larger the BH mass, the larger the mass of the host spheroid (i.e. the host elliptical galaxy or the bulge component of the host spiral) and the higher its luminosity. Also, the larger the BH mass, the higher the velocity dispersion of stars within elliptical galaxies or bulges of disc galaxies (e.g. Magorrian et al., 1998; Ferrarese & Merritt, 2000; Gebhardt et al., 2000; Merritt & Ferrarese, 2001; Tremaine et al., 2002; Marconi & Hunt, 2003; Häring & Rix, 2004). These correlations are commonly interpreted as the evidence of a coevolution of BHs and host galaxies. The host galaxy evolution, e.g. whether it experiences or not mergers, and the physical properties of its ISM regulate BH feeding and growth; conversely, feedback from BHs determines and shapes general properties of the host galaxy.

Whether all the galaxies with a spheroidal component have a bulge mass that correlates with the mass of their BH or not, has been investigated for long time. Kormendy & Ho (2013) analysed a sample of elliptical galaxies, classical bulges and pseudo-bulges (see Section 2.1). They found that classical bulges that are structurally like ellipticals and that likely formed in major mergers lie on the tight correlation that characterises elliptical galaxies. On the other hand, pseudo-bulges that most likely grew through a secular evolution within galaxy discs do not obey the same relation: they are observed to host a BH whose mass is not as large as other systems (see Figure 2.6).

The role of AGN feedback is key in controlling the star formation and the gas cooling processes. BH feedback can be negative and positive, according to whether it results in a global heating of the ISM or in hot gas cooling and consequent star formation events (see also Chapter 9). Also, BH feedback is considered one of the main mechanisms that regulate the growth of the bulge in spiral galaxies, determining its final mass (Kormendy & Kennicutt, 2004; Blanton & Moustakas, 2009; Kormendy & Ho, 2013).

3

Simulating galaxies in a cosmological context

Observations provide us with evidence that show the final results of the process of structure formation and that help in constraining galaxy evolution across cosmic time. Further insight can be gained by exploiting cosmological hydrodynamical simulations, that investigate these processes from a complementary point of view. In Sections 2.1 and 2.4 I reviewed the phenomenology of late-type galaxies, summarising their main features emerging from observations. How much of this phenomenology has been understood reliably, and is convincingly explained by simulations? What are the main difficulties that simulations encounter in matching observations? What are the open issues?

This Chapter is devoted to describe the current understanding of simulations of galaxies in a cosmological framework, and will focus on simulations of disc galaxies while proceeding through the Sections. In Section 3.1 I briefly outline how the study of structure and galaxy formation can benefit from different state-of-the-art numerical approaches, with an in-depth analysis of cosmological hydrodynamical simulations. Section 3.2 reports about some of the challenges that simulations have to face in order to prove their predictive power. Also, numerical techniques naturally come with their own virtues and limitations, and possible numerical artefacts that can enter final results. In Section 3.3 the main limitation that has long been preventing simulations of disc galaxies from succeeding in reproducing observed spiral galaxies is discussed. Finally, Section 3.4 is devoted to briefly review

the most recent progresses in the numerical modelling of the physics of the ISM that have made possible to make advancements in simulations of late-type galaxies.

Contents

3.1 Numerical approach to astrophysics and the role of simulations

The cosmological framework outlined in Section A.2 and favoured by data from CMB experiments provides the initial conditions (ICs) for the problem of structure formation. Numerical simulations that evolve a representation of a region of the early Universe forward in time are a relatively recent acquisition. They are a fundamental tool, as they constitute the only way to adequately capture the complexity of the non-linear evolution of perturbations (see Sections 2.2 and A.3).

Different numerical approaches can be pursued to investigate the formation and evolution of galaxies. Simulations represent the first approach and play a crucial role. Here, I focus on cosmological simulations, that are the ones that account for the evolution of matter in an expanding background starting from a realization of a cosmological model that reproduces the observed anisotropies of the CMB, and therefore I do not discuss simulations focussing on the scale of a single structure or even below, that start by considering the system already formed and evolve it for a limited time interval. The first cosmological simulations that have been performed aimed at investigating the evolution of the DM component, and accounted only for the gravitational interaction, that is the dominant force at very large scale (see also Section 4.1). These DM-only simulations turned out to be suitable for studying the internal structure of DM haloes (Navarro et al., 1996), and for investigating the hierarchical growth of haloes and how their distribution shapes the large scale structure (Springel et al., 2005c). However, unless attaching on top adequate prescriptions in post processing, DM-only simulations cannot help in gaining insight on the formation of galaxies and on the evolution of the baryonic component of the Universe.

A more comprehensive scenario emerges when simulations simultaneously account for the coupled evolution of DM and baryons (see also Section 4.2). Cosmological hydrodynamical simulations capture the spatial and temporal complexity of the formation and evolution of cosmic structures. They indeed follow the cosmological accretion of gas from the large-scale structure and the infall of gas into the innermost

regions of forming structures. As this gas cools, it fuels star formation, whose final result is the injection in the ISM of feedback energy and metals. All these processes can be self-consistently implemented in cosmological simulations, where also the chemical evolution is a natural outcome of galaxy evolution. Besides capturing gas dynamics, cosmological simulations that self-consistently follow the joint evolution of DM and gas are also able to account for the back-reaction of baryons on the DM (see Section 2.3 for the transformations induced by baryonic processes on the underlying DM distribution during early stages of galaxy formation).

The shortcoming is their demanding computational cost: the balance is thus between either choosing a high force and mass resolution but focussing on a single or a small number of objects (see Section 3.2), or opting for a large simulation volume but at a lower resolution. A third possibility is to halt the cosmological simulation at a redshift relatively high (e.g. as high as ~ 8 in the BlueTides simulation, Feng et al., 2016). As a consequence, the exploration of the simulations' parameter space cannot be performed in an immediate or systematic fashion.

Other approaches can be followed to study galaxy evolution. DM-only simulations can be exploited to populate haloes with galaxies either relying on the statistics of galaxy clustering available from surveys within the halo occupation distribution formalism (e.g. Peacock & Smith, 2000; Tinker et al., 2005), or assuming a correspondence between the stellar mass of galaxies and the mass of the haloes in which they reside, with statistical abundance matching techniques (e.g. Guo et al., 2010; Moster et al., 2010, 2013; Behroozi et al., 2013). A more powerful approach is constituted by semi-analytic models (e.g. White & Frenk, 1991; Cole et al., 2000; De Lucia et al., 2004; Nagashima et al., 2005; Croton et al., 2006; Yates et al., 2013; Hirschmann et al., 2016): these models take advantage of the output of DM-only simulations, i.e. the halo merging history along with properties of DM haloes such as their mass, angular momentum and circular velocity, and then populate haloes with the baryonic component according to physically motivated, still necessarily simplified, prescriptions. Baryonic processes that drive galaxy evolution are then modelled, yielding to a flexible method to investigate properties of the galaxy population over large volumes and to study the effect of several processes controlling galaxy evolution. Nevertheless, although they do not demand large computational resources, semi-analytic models are not able to include a self-consistent treatment of the gas dynamics, and rely on the assumption that initial features of the proto-galaxies depend on the properties of DM haloes, that subsequently are not perturbed by galaxy evolution.

Another useful approach to gain further insight on the evolution of galaxies is represented by chemodynamical models of galactic chemical evolution (e.g. Matteucci, 2003; Gibson et al., 2003; Pagel, 2009; Matteucci, 2012). State-of-the-art models of galactic chemical evolution are the most sophisticated tools to investigate the abundance of different metals, especially in our Galaxy, even if they are not limited to it (e.g. Calura & Matteucci, 2003). These models usually assume that gas is initially acquired by the evolving galaxy through subsequent episodes of gas infall and generally approximate the description of the system with a rather

simplified geometry. Despite being very flexible and accurate, and complex enough to account for processes such as radial gas flows (Lacey & Fall, 1985; Portinari & Chiosi, 2000; Schönrich & Binney, 2009; Spitoni & Matteucci, 2011; Mott et al., 2013) and for different formation and evolutionary paths for galactic stellar components, namely halo, thick and thin disc (Chiappini et al., 1997; Portinari et al., 1998; Romano et al., 2010), models of galactic chemical evolution are not designed to capture the full complexity of galaxy evolution in a cosmological context.

Therefore, cosmological hydrodynamical simulations play undeniably a major role in the field of galaxy formation and evolution, also because their predictions often show a remarkable agreement with observations (see also Chapters 6 and 7). Thus, simulations can be used to bracket ignorance in galaxy formation, to probe or reject different scenarios of galaxy evolution, and to interpret observations.

As for cosmological hydrodynamical simulations, they can follow two alternative, yet not necessarily self-excluding, strategies: either simulating one structure in detail, or describing the properties of the galaxy population. The first method consists of simulations targeted to follow the formation and evolution of one single galaxy at a time (e.g. Oser et al., 2010; Aumer et al., 2013; Stinson et al., 2013; Marinacci et al., 2014; Murante et al., 2015; Dutton et al., 2015; Wang et al., 2015; Grand et al., 2017; Hopkins et al., 2018), or of one single galaxy cluster (Rasia et al., 2015). These simulations can achieve a higher resolution (see Section 3.2) than those evolving simultaneously several structures, especially because their ICs are zoomed-in, i.e. they allow the re-simulation of a parent DM-only simulation (see Section 5.5 for further details). The simulations that I carried out and whose results will be presented in Chapters 6, 7, 8, and 9 follow this approach.

On the other hand, there are large scale simulations designed to have volume large enough to investigate the variety of galaxy populations along with the most massive structures in the Universe, i.e. galaxy groups and clusters. Examples of these simulations are: Horizon-AGN (Dubois et al., 2014), Illustris (Vogelsberger et al., 2014a) and Illustris-TNG (Pillepich et al., 2018), Eagle (Schaye et al., 2015), MassiveBlack-II (Khandai et al., 2015), Magneticum (Remus et al., 2017), Mufasa (Davé et al., 2016), and Bahamas (McCarthy et al., 2017). Simulations of this kind that evolve a periodic cubic portion of the Universe, are well suited to perform studies of galaxy properties in a statistical way. Also, they allow to appreciate the effect that the same process or feedback mechanism has within and on systems characterised by different properties. The associated limitation is that the resolution of these simulations is usually lower than simulations targeted to follow the evolution of a single object. A further challenge for simulations of the latter type is to reproduce a specific region of our local Universe along with the position and the properties of galaxies within it. These are known as constrained simulations, as further dynamical constraints coming from observations are added to the ICs, as in the Apostole and Clues simulations (Sawala et al., 2016; Carlesi et al., 2016, respectively).

The astrophysical processes involved in the formation and evolution of galaxies in cosmological hydrodynamical simulations span a wide dynamical range of

scales. They indeed range from the ∼parsec scales typical of star formation to the ∼Mpc scales where gravitational instabilities drive the evolution of the dark matter component and the hierarchical assembly of galaxy-sized haloes, passing through the ∼kpc scales where galactic winds distribute the stellar feedback energy to the surrounding gas, thereby regulating its accretion and subsequent star formation. The call for sub-resolution models (see also Sections 3.4 and 5.3) is thus essential: they model processes that take place at scales not resolved by cosmological hydrodynamical simulations, but that affect the evolution of the simulated structure on scales that are explicitly resolved. In general, these sub-resolution models resort to a phenomenological description of rather complex processes, through a suitable choice of parameters, that need to be carefully tuned by requiring simulations to reproduce basic observational properties of the galaxy population.

A common criticism that has been often made to numerical astrophysics deals with the number of parameters that are employed when modelling physical processes, in particular when referring to the parameters that characterise sub-resolution models. However, observed or expected results cannot be reproduced by just fine-tuning parameters. Results are rather determined by proper parametrizations of processes. For instance: when modelling star formation, results are mainly driven by the fact of correctly relating the SFR (star formation rate) to the mass of cold gas available, i.e. $\dot{M}_{\rm sf} = A\, M_{\rm c}$, rather than to the exact value of the proportionality constant A, that is the parameter which is tuned (see also equation (3.3) and discussion in Section 3.4). According to this view, parameter space esplorations are not meant to provide a best fit to observations one wants to compare with. They rather allow to better understand the dependence of the model on different elements to consider. Also, parameter calibration allows to make predictions for unknown or loosely constrained physical quantities.

3.2 Simulating galaxies: challenges

In this Section and in Sections 3.3 and 3.4, the discussion is focused on cosmological hydrodynamical simulations that adopt the Smoothed Particle Hydrodynamics (SPH) technique (although several of the issues discussed in these Sections are also relevant to Eulerian codes). These simulations represent DM, stars, and gas by means of particles of given mass, that are resolution elements. The essentials of SPH will be thoroughly discussed in Chapter 4, that is dedicated to the numerical methods used in the simulations that I carried out. Here, I only anticipate that SPH is a numerical technique to solve the equations of the hydrodynamics. Within the SPH formalism, the fluid is discretised through a finite number of gas particles. A key notion is the smoothing length, that represents the size of the characteristic volume over which the mass of each gas particle is considered to be distributed.

A challenge in cosmological simulations is to achieve a modelling of physical processes as accurate as posssible while keeping the computational resources to a feasible and affordable effort. This requirement has direct consequences on the

resolution of the simulation, and thus on the accuracy of the fluid sampling and of the numerical integration (the time-step being proportional to the smoothing length for gas particles; see Section 5.2 for details). Resolution in mass and space are indeed key quantities to define the accuracy of the simulation. Mass resolution is provided by the mass that particles have, and is usually quoted separately for DM particles, and for gas and star particles (the latter ones having smaller masses). Space resolution in particle-based codes is the scale at which gravitational and hydrodynamical interactions are smoothed, so to avoid particle overlapping. Since gravity is smoothed at a scale defined by the softening length (see Section 4.1), the latter parameter defines the force resolution of the simulation[1].

The call for resolution in cosmological hydrodynamical simulations drove the development of numerical techniques as the zoom-in and the renormalization technique (Tormen et al., 1997; Springel et al., 2008; Jenkins, 2010, and Section 5.5). They allow to focus on the regions of interest of the computational domain and to increase mass and force resolution in the innermost volume where the structures form; meanwhile, the large scale environment is also sampled, and the tidal interaction responsible for the generation of initial angular momentum in haloes is accounted for.

A numerical issue in (especially low-resolution) simulations is the two-body heating (see also Section 4.1). This artefact is due to the coarse-grained representation of fluids by means of particles and arises when two particles are close to collide. Even if the gravitational interaction is smoothed so as to overcome collisions, in cosmological simulations a close gravitational encounter between particles with different mass (DM particles are usually more massive than gas particles by a factor ~ 10) can induce an artificial transfer of energy to less massive particles. As a consequence, the random motion of the latter particles is boosted, and the structure of simulated galaxies can be distorted (see also Section 3.3).

Cosmological hydrodynamical simulations of structure formation have been struggling for long time with regulating an excessive amount of gas that cooled out of the hot phase and collapsed towards the centre of the host DM halo. This issue, known as the overcooling problem, generally arises during the early stages of structure formation and then propagates down to low redshift since the cooling intrinsically has a runaway behaviour, due to its dependence on the square of the gas density. Indeed, as gas undergoes cooling, it becomes denser and therefore experiences larger radiative losses. This loop can have catastrophic consequences if no mechanisms prevent the gas from cooling and subsequently forming stars, producing structures that are too much centrally concentrated and have star formation rates not in keeping with observations (e.g. Katz & White, 1993; Thacker & Couchman, 2000; Pearce et al., 2001).

The overcooling problem is generally ascribed to two main reasons in simulations. First, the absence of processes that counterbalance radiative losses of gas, such as the presence of an ionizing background and the feedback from massive stars and

[1]Should two interacting particles have different softening lengths, the force resolution is provided by the largest softening length.

AGN. Not only these phenomena have to be accounted for, but they also have to be implemented and numerically modelled in an effective way (see Section 3.4).

Second, the resolution in mass and space plays, once again, a major role. Low resolution simulations are indeed more heavily affected by the overcooling problem. This issue is also present (and even enhanced) in higher resolution simulations if no injection of feedback energy or ionizing background are included (Balogh et al., 2001; Tornatore et al., 2003; Borgani et al., 2006). Higher resolution simulations can indeed resolve higher gas density, while also properly account for the evolution of high-redshift smaller sub-haloes and clumps where further star formation occurs. However, this picture is changed when feedback processes are included: accounting for stellar feedback, for instance, leads towards an almost self-regulated scenario where a more enhanced high-redshift star formation also produces a larger amount of feedback energy that hampers excessive cooling. In this way, the fraction of gas that cools and is converted into stars is almost convergent or mildly decreases as the resolution increases (Borgani et al., 2006).

The resolution has also significant implications on the distribution of feedback energy provided to the ambient medium (Davé et al., 2001). One of the resolution-related weaknesses that cosmological simulations have to face when dealing with stellar feedback (especially if the thermal feedback is considered, see Section 3.4), is the energy deposit from stars (that is, from star particles representing ensembles of stars) into a large mass of gas. Star particles usually provide feedback energy to the gas residing in their surrounding resolution elements; the ratio between the mass of the gas receiving energy and that of the star particle that provided it, is by far larger than the same ratio in real systems, where the energy released by typically one SN every ~ 100 $M_\odot$ is deposited in roughly few solar masses of ejecta (Dalla Vecchia & Schaye, 2012). As a consequence of the sharing of feedback energy over a too large mass of gas, the feedback is not effective at heating gas up to a temperature that ensures that energy is not immediately radiated away (at variance with real systems where 10 $M_\odot$ of ejected gas is heated up to $\sim 2 \cdot 10^8$ K if 10^{51} erg of energy from a SN II explosion are supplied). Even if the aformentioned critical ratio between the mass of star particles and that of gas that is provided with energy does not vary significantly when the resolution changes, a higher resolution can alleviate this issue. Indeed, the sound crossing time[2] across a resolution element in SPH decreases as the resolution increases[3] ($t_\mathrm{s} \propto m^{1/6}$). A sound crossing time shorter than the cooling time ensures that the energy received is not entirely radiated away locally, and thus the effectiveness of the feedback (Schaye et al., 2015). In addition to that, high resolution allows to resolve a larger number of cold and dense clumps that result in more clustered sites of star formation: the cumulative effect of feedback energy injections is more effective than the smoother counterpart in lower resolution simulation (Keller et al., 2014). Also, once cold and dense blobs are resolved in

[2]The sound crossing time $t_\mathrm{s} \sim h/c_\mathrm{s}$, where h is the smoothing length and $c_\mathrm{s} = (\gamma\, P/\rho)^{1/2}$ is the sound speed, P and ρ being gas pressure and density, respectively.

[3]Indeed, $t_\mathrm{s} \sim h/c_\mathrm{s}$, $h \propto \rho^{-1/3}$ (see Section 4.3), and $c_\mathrm{s} \propto (T/m)^{1/2}$, T being the gas temperature. As a consequence, $t_\mathrm{s} \propto m^{-1/3}\, m^{1/2} \propto m^{1/6}$.

high resolution simulations, their dominant mass contribution is separated from the diffuse hot phase, that is therefore not as prone to cooling as in lower resolution runs.

Among other limitations, low resolution simulations lack the ability to resolve properties of cold and dense gas in the innermost regions of forming galaxies. A coarse fluid sampling leads to a smearing of cold gas properties, whose values are averaged and smoothed over large regions of the computational domain, where the hot phase is the dominant volume filling component. As a consequence, cold gas temperature results to be overestimated, while cold gas density is underestimated. This issue is especially worth to be tackled when modelling the accretion of gas onto SMBHs in the centre of galaxies, as lower densities and higher temperatures for the cold gas that is accreted result in a reduced accretion rate (usually estimated via the Bondi (1952) formula and thus generally boosted in cosmological simulations, as discussed in Springel et al. (2005a); Booth & Schaye (2009), and in Chapter 9).

Assessing the impact of resolution in simulations and inspecting the stability of results against numerical resolution is crucial to appreciate how robust they are and how powerful their predictions are. However, convergence of predictions when simulations resort to sub-resolution models is a difficult and subtle issue. Indeed, properties of the ISM vary when the resolution is changed (e.g. density and temperature, as discussed above), and so do the timing of feedback events, and quantities such as energy, momentum and mass involved. As a consequence, the calibration of parameters as the feedback efficiency at a given resolution does not ensure the same effectiveness of the feedback when the resolution is changed (see Schaye et al., 2015, for further discussion). This scenario led to the introduction of the so-called strong and weak convergence: demanding strong convergence from simulations implies that predictions from simulations with different resolution have to agree without further tuning of parameters of the sub-resolution model. Resorting to weak convergence means that requirements for numerical convergence are weakened as the resolution is varied, and recalibration of the model's parameters is allowed (see also Section 6.6.1). Actually, it is extremely difficult to conceive a sub-resolution model that produces numerically strong convergent results.

Also, the resolution of simulations determines the scale below which the sub-resolution model adopted has to account for physical processes not explicitly resolved. Sub-resolution models should therefore be resolution-dependent, at least when very high resolutions are achieved. For instance, reaching a resolution as high as ~ 100 pc or below translates in the requirement for the sub-resolution models to describe the giant molecular clouds and the processes that take place at the typical scales at which star formation occurs. This is still out of the reach of state-of-the-art cosmological simulations of galaxy formation.

Moreover, physical relations adopted within the sub-resolution models can be susceptible to change with resolution. For instance, the Schmidt-Kennicutt relation (see Section 2.4.1) that is often assumed in simulations to estimate the SFR, is usually considered to be in place when ISM properties are averaged over spatial scales of few hundreds of pc or above (e.g. Casasola et al., 2015). Should a simulation reach a

higher resolution, it is not obvious whether the calibration of the Schmidt-Kennicutt relation still holds and thus whether the estimate of SFRs continues to be reliable.

Another implication of the resolution is connected to the ability of resolving first structures. In higher resolution simulations smaller haloes are formed, and at higher redshift: they can host proto-galaxies where high-redshift star formation occurs and this can affect the overall evolution of the simulated structures due to the feedback energy supplied to the surrounding medium. Also, especially when studying the convergence of results in simulations of galaxies with zoomed-in ICs (Section 5.5), the resolution has an interplay with the accretion history of the halo in which the forming galaxy resides. Indeed, when the resolution is e.g. increased, extra power is added at small scales: as a consequence, the halo merging history can be modified, and this affects the evolution of the simulated galaxy (Springel et al., 2008; Murante et al., 2015).

This is the complex, yet stimulating framework within which state-of-the-art cosmological hydrodynamical simulations fit. The challenges and open issues discussed above require to figure out how to balance the limitations coming from computational resources, the resolution that can be reached along with the volume that can be simulated, and the detailed modelling of the sub-resolution physics.

3.3 The angular momentum problem

The low-redshift morphology of simulated galaxies is the first and most immediate prediction that can be deemed as a testing ground to asses the success of a cosmological simulation. If simulated galaxies do not resemble those that we observe in the Universe, the cosmological simulation that produced them has not fully succeeded at investigating the scenario of galaxy formation and evolution. The size and the prominence of the stellar disc are the general requirements that a simulated late-type galaxy has to fulfill by visual inspection in order to allow to consider the simulation trustworthy (or at least deserving further analysis).

Early cosmological simulations usually failed at reproducing the observed morphology of disc galaxies: simulated spiral galaxies were generally characterised by a dominant bulge component and did not exhibit an extended disc (e.g. Navarro & White, 1994). The reason of this drawback stems from the spurious angular momentum loss that gas particles suffer during their infall in the host DM halo, before settling and starting to orbit in the galaxy disc. This issue is usually referred to as the angular momentum problem or catastrophe (Navarro & Benz, 1991; Mayer et al., 2008; Mo et al., 2010). To quantify the impact of the problem, the specific angular momentum of simulated galaxy discs was estimated to be lower by up to an order of magnitude than that of observed galaxies (Steinmetz & Navarro, 1999; Sommer-Larsen et al., 1999b; Navarro & Steinmetz, 2000).

The origin of the problem has been traced back to the initial gas infalling within DM haloes and especially to the hierarchical clustering process leading to galaxy formation (D'Onghia et al., 2006; D'Onghia & Navarro, 2007). During subsequent

episodes of mergers, the gas component of two merging haloes is progressively deprived of angular momentum due to dynamical friction, i.e. the drag force that transfers energy and momentum from the moving gas clumps to the surrounding DM (Binney & Tremaine, 2008; Mo et al., 2010). Also, later gas accretion occurs with a significant loss of angular momentum to the DM along the path to reach the innermost regions of the forming galaxy. The situation gets even worse when gas is characterised by a clumpy distribution and is accreted in the form of cold and dense blobs (Navarro & Benz, 1991; Sommer-Larsen et al., 1999b).

Other numerical issues that contribute to the angular momentum loss of the gas are due to the discrete representation of the fluid by means of particles (Mayer et al., 2008). An example is the interaction between particles with considerably different temperature in the outskirts of galaxy discs: here, cold gas particles transfer angular momentum to the hotter surrounding gas because of a spurious force due to the pressure gradient, and as a consequence move towards smaller distances from the galaxy centre (Okamoto et al., 2003). The asymmetric morphology of gaseous discs appears as a further physical source of angular momentum loss: gas in the disc can be indeed deprived of angular momentum by the halo, that exerts a gravitational torque. Furthermore, the artificial viscosity, that is introduced in SPH to properly account for dissipation of energy at shock regions (see Section 4.4), also includes spurious angular momentum transport and energy dissipation. Moreover, two-body heating (Section 3.2) can be responsible for artificial angular momentum loss, since the spurious increase in energy experienced by gas particles can enhance a component of their velocity randomly, thus amplifying the velocity dispersion and producing both an angular momentum loss and a puffed-up stellar disc (Mayer et al., 2008).

Unless revising the underlying ΛCDM cosmological model and resorting to warm DM models that predict a lower number of mergers (and thus, a reduced loss of angular momentum and a smoother distribution of baryons within haloes, e.g. Sommer-Larsen & Dolgov, 2001), the main numerical effects that hamper the radial growth of the galaxy disc as gas accretion from the halo proceeds are the lack of an adequately high resolution and the absence of an effective feedback from massive stars. A proper numerical modelling of feedback mechanisms can succeed in limiting artificial angular momentum loss and in fostering the formation of more extended discs: feedback increases the thermal energy of baryons, prevent them from arranging in a clumpy distribution, and thus avoids the transfer of angular momentum to the DM (Brook et al., 2004; Robertson et al., 2006; Scannapieco et al., 2008; Governato et al., 2010; Piontek & Steinmetz, 2011; Übler et al., 2014, see also Sections 2.3 and 3.4).

The increase of resolution helps in mitigating the shortfalls discussed above, since a higher resolution allows a finer description of the fluid and avoids a large artificial dissipation of energy and momentum (Governato et al., 2004; Kaufmann et al., 2007). All the critical issues analysed in this Section are naturally alleviated once the structure of the ISM and the feedback processes are accurately modelled within simulations (see Section 3.4), and when improved hydrodynamical solvers are adopted (Sections 4.4 and 5.2).

As a concluding remark, it is worth noting that the formation of extended stellar and gaseous discs does not ensure their survival across cosmic time and in the dynamical living environment of galaxies. The presence of merging substructures, and the gravitational and tidal interactions with stellar satellites significantly perturb the morphology of galaxy discs, and generally increase the disc scale height and limit further radial growth (Kazantzidis et al., 2008; Bekki & Couch, 2011; Pillepich et al., 2015).

3.4 Modelling ISM and sub-resolution processes

In this Section, I give a brief overview of state-of-the art modelling of the ISM and the stellar feedback process within sub-resolution models adopted in cosmological simulations of galaxies. This outline is far from being complete: deeper insight can be gained from the review of Mayer et al. (2008) and from Section 2 of Murante et al. (2015).

Since it is not possible to resolve the ISM down to scales that allow to capture in full the complexity of star formation and of the physical processes related to the injection of feedback energy from exploding SNe in the ISM, these phenomena have to be included within the sub-resolution physics. An accurate description of these processes has been proved to be the main element for successfully simulating disc galaxies in a cosmological context. In fact, nowadays the challenge of simulating spiral galaxies is an achievable task (yet within the caveats and open issues overviewed in Sections 3.2 and 3.3) and simulated galaxies have often properties in broad agreement with observations (e.g. Aumer et al., 2013; Stinson et al., 2013; Marinacci et al., 2014; Vogelsberger et al., 2014a; Murante et al., 2015; Agertz & Kravtsov, 2016; Keller et al., 2015; Schaye et al., 2015; Grand et al., 2017; Hopkins et al., 2018). The situation has not always been so positive (see e.g. Figures 3.1 and 3.2). Poorly modelled and loosely constrained sub-resolution physics has indeed been affecting the predictive power of simulations for long time. Cosmological simulations of disc galaxies have undergone early stages (e.g. Cen & Ostriker, 1993; Navarro & White, 1994; Navarro & Steinmetz, 1997) where simulated galaxies were too centrally concentrated, did not have an extended disc, were characterised by centrally peaked rotation curves, and shared some of the limitations discussed in Sections 3.2 and 3.3.

Early simple modelling of star formation in cosmological simulations (Katz et al., 1996) relied on the evidence that star formation is the outcome of the gravitational collapse of clouds of dense, molecular gas. Star formation was therefore implemented according to a probabilistic formulation that allows to convert gas particles into star particles whenever the former become denser of a given density threshold, and sample a converging, Jeans unstable fluid. According to the model of Katz et al. (1996), a gas particle i becomes thus eligible to generate a star particle if the following conditions are met: the particle density $\rho_{\rm i}$ has to correspond to a number density that is higher than the threshold $n_{\rm H} = 0.1$ cm^{-3}, where $n_{\rm H}$ is the number

density of hydrogen atoms; the velocity divergence of the particle has to be less than zero, i.e. $\nabla \cdot \mathbf{v}_\mathrm{i} < 0$ (as it can be shown from the continuity equation (4.9) in order to have gas that undergoes compression, see also Section 4.4); also, to have Jeans instability, the sound crossing time of the particle $t_{\mathrm{s,\,i}} = h_\mathrm{i}/c_{s,\,i}$ (h_i and $c_{s,\,i}$ being the smoothing length and the sound speed of the particle, respectively; see Section 3.2) has to be larger than the gravitational dynamical time, so that:

$$h_\mathrm{i}/c_{s,\,i} > (4\,\pi\,G\,\rho_\mathrm{i})^{-1/2} \ . \tag{3.1}$$

The aformentioned probabilistic formulation of the star formation translates in the probability p for the eligible gas particle to generate a star particle in the time-step Δt (see also Section 5.3):

$$p = 1 - \exp(-c_*\,\Delta t/t_\mathrm{i}) \ , \tag{3.2}$$

where c_* is a dimensionless parameter and t_i is the maximum between the particle's dynamical time (see equation (3.1)) and cooling time (see equation (2.2)). In the model of Katz et al. (1996), the SFR density of the particle eligible to form stars reads:

$$\dot{\rho}_{\mathrm{sf,\,i}} = -\dot{\rho}_\mathrm{i} = c_*\,\rho_\mathrm{i}/t_\mathrm{i} \ . \tag{3.3}$$

Since in star-forming regions the cold gas cooling time is shorter than the dynamical time, then $t_\mathrm{i} \propto \rho_\mathrm{i}^{-1/2}$, so that equation (3.3) leads to $\dot{\rho}_{\mathrm{sf,\,i}} \propto \rho_\mathrm{i}^{3/2}$. As a consequence, the SFR density is related to the cold gas density with a proportionality in agreement with the Schmidt-Kennicutt relation (see Section 2.4.1), and through an efficiency that is the parameter of the model. The efficiency parameter is tuned to reproduce observations. In this simple model, the conversion of gas into star particles proceeds along with the injection of stellar feedback energy, that is provided to surrounding gas particles as thermal energy. This feedback model was not effective in preventing overcooling and excessive star formation.

Efforts have been devoted during years to achieve an improved numerical description of the ISM and a more accurate modelling of the stellar feedback processes. For instance, a multiphase modelling of the ISM (Springel & Hernquist, 2003; Marri & White, 2003; Scannapieco et al., 2006; Murante et al., 2010, 2015) has been incorporated in several sub-resolution models, attempting to account for the different components of the ISM, i.e. the hot gas, the warm ionised and the warm neutral gas, the cold neutral phase, and the cold molecular gas. Also, a variety of stellar feedback schemes has been proposed: the numerical description of the energy injection from SN explosions in the ISM has indeed a strong impact on final results (see Chapter 6). The Aquila comparison project (Scannapieco et al., 2012, see Figures 3.1 and 3.2) brought out the crucial importance of the description of the ISM below the resolution achievable in simulations and showed how different schemes for star formation and stellar feedback lead to the formation of galaxies having rather different properties. Figures 3.1 and 3.2 show projected stellar density maps and the distribution of circularities of stellar orbits for the galaxies simulated

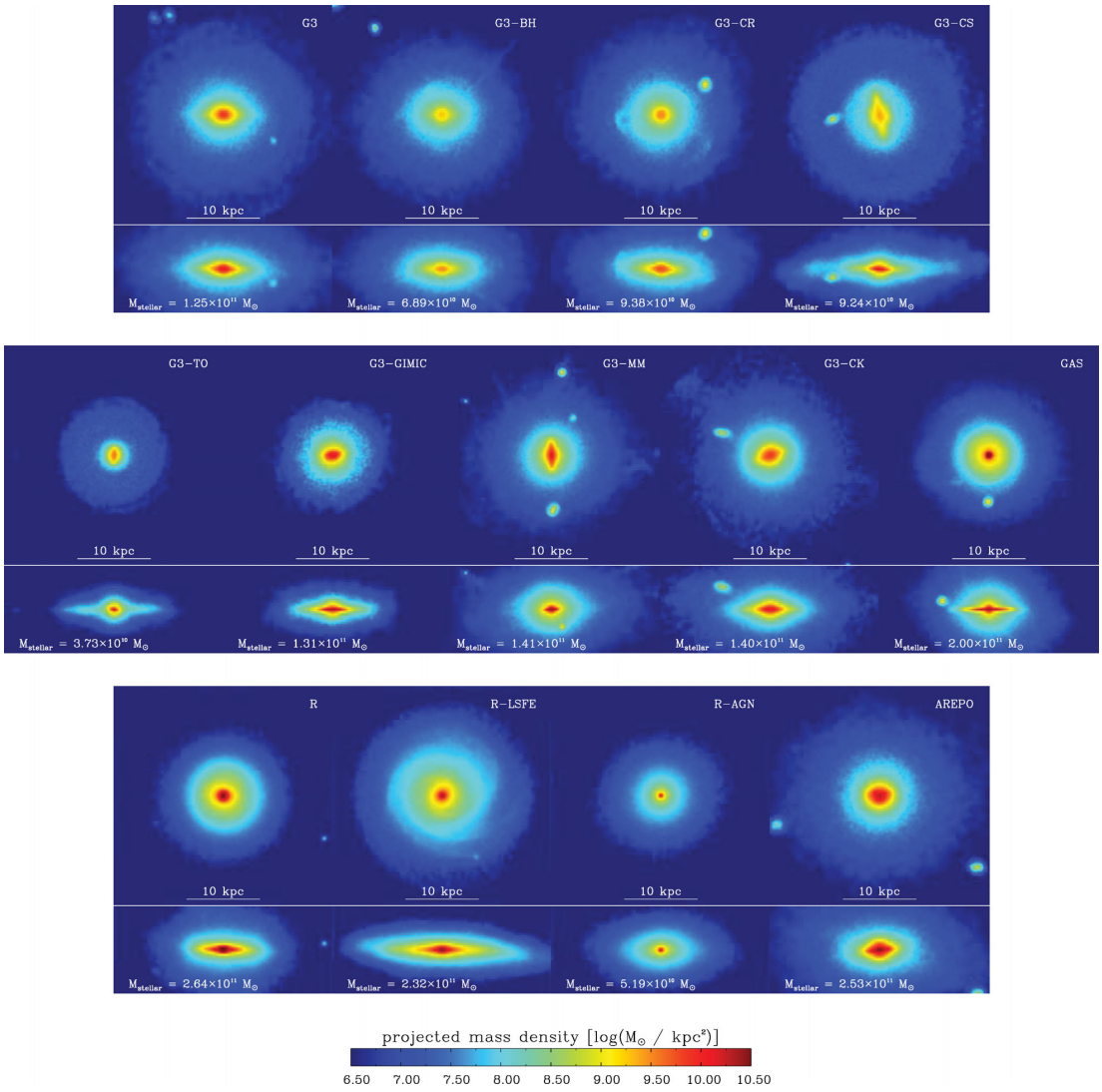

Figure 3.1: Face-on and edge-on projected stellar density maps for the galaxies simulated with different codes and sub-resolution models within the Aquila Comparison Project (Scannapieco et al., 2012, see also Section 3.4). The majority of simulated galaxies do not have extended stellar discs, especially those simulated with SPH codes (first and second rows). The relevance of the stellar disc component of these galaxies with respect to their bulge is quantified in Figure 3.2.

within the Aquila Comparison Project, highlighting the impact of the numerical technique adopted and of the sub-resolution modelling on simulation outcomes.

Springel & Hernquist (2003) introduced a model for the multiphase ISM, that accounts for star formation and stellar feedback. This model is commonly referred to as the effective model. It considers that hot and cold gas components coexist in pressure equilibrium within dense gas particles, that are the so-called multiphase particles. Properties of the cold and hot phases are assumed to represent averages over small volumes of the ISM, since molecular clouds cannot be resolved. The cold phase within the multiphase particle provides the reservoir for star formation, while being replenished by hot gas cooling. A fraction of the cold gas fuelling star

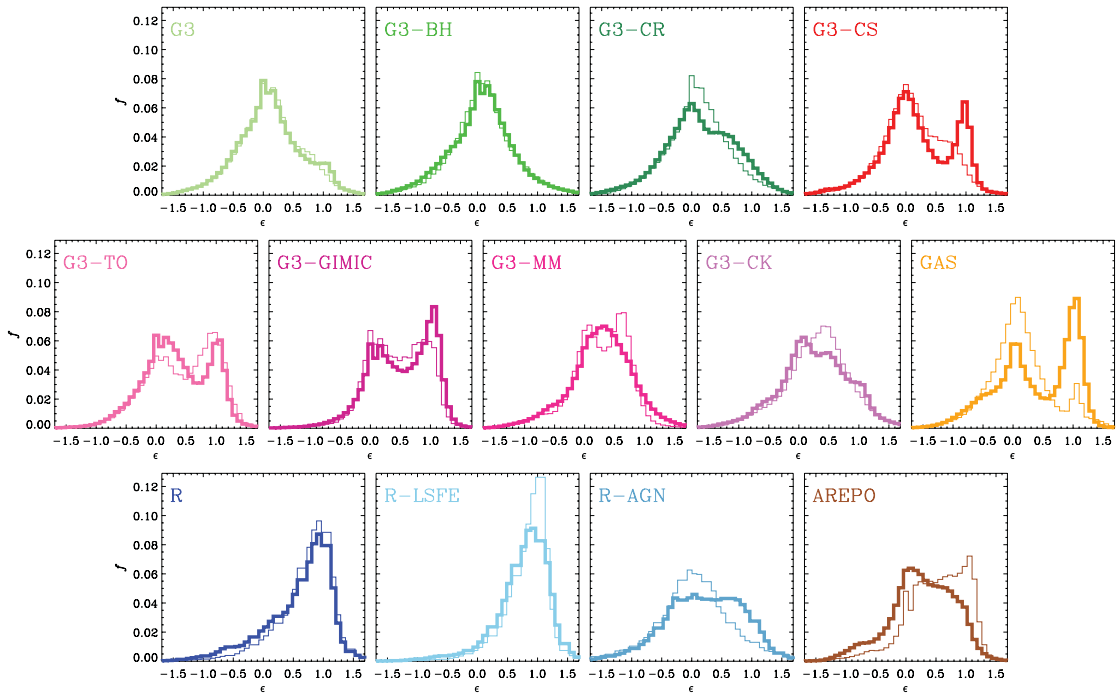

Figure 3.2: Distribution of circularities of stellar orbits for the galaxies simulated within the Aquila Comparison Project (Scannapieco et al., 2012, see also Section 3.4). The stellar circularity ε is a ratio of specific angular momenta (see Section 6.5.2 for details) that is used to split the dispersion supported stellar component (bulge, where $\varepsilon \simeq 0$) from the rotationally supported one (disc, where $\varepsilon \simeq 1$). Note that the majority of simulated galaxies do not show a predominant disc: rather, their stellar mass is dominated by the bulge. This is especially true for galaxies simulated with SPH codes (top and middle rows), that exhibit a pronounced peak at $\varepsilon \simeq 0$. The effect of the resolution can be appreciated by contrasting solid thick (higher resolution, AqC5, see Table 5.2) and thin (lower resolution, AqC6) curves. For comparison, see e.g. Figures 6.7 and 6.14.

formation is assumed to be instantaneously used to heat up the hot phase and to evaporate a share of the cold phase, mimicking the explosion of short-lived massive stars as SNe. Equations describing the evolution of the energy of the hot and cold gas phases are integrated, so that the star formation rate can be computed. Parameters of the model are, once again, calibrated to reproduce the Schmidt-Kennicutt relation (see above). This model assumes a constant temperature for the cold gas component. Also, it is characterised by a quiescent, self-regulated star formation, as the fuelling of the cold phase owing to cooling is counterbalanced by its evaporation because of SN heating. Within this model, the ISM can be described by an effective equation of state: the effective pressure of the two-phase gas particles has a functional form that is constrained by the properties of the hot and cold phases, and is expected to be constant in time due to the self-regulated star formation.

In addition, the density threshold for gas particles to become eligible to form stars can be made dependent on metallicity, based on the assumption that the higher the metallicity of the gas, the lower the density for warm and neutral gas to become cold

and molecular (Schaye, 2004; Schaye et al., 2015). Also, the SFR can be estimated from the pressure of gas particles, rather than from their density (Schaye et al., 2015).

Since the understanding of the pc-scale physics responsible for launching and driving winds is still partial and however far from being implemented directly in cosmological simulations, once again these simulations have to resort to phenomenological prescriptions to capture the effects of galactic outflows (Section 2.4.4). As for the sources of energy that power outflows and govern their kinematic, there are two commonly pursued approaches: winds can be either energy-driven or momentum-driven.

Within the energy-driven approach, galactic outflows are triggered by SN explosions. SN energy can be provided by multiphase or star-forming gas particles to surrounding gas particles in the form of thermal or kinetic energy. Injecting feedback energy as thermal, as in the model of Katz et al. (1996) introduced above, has the limitation that the feedback usually does not result effective in driving energy far from regions where it is released. Gas particles surrounding particles that provide energy have a typical temperature of $\sim 10^5$ K and density high enough to radiate energy almost immediately, their cooling time being short. As a result, feedback is not effective in counterbalancing cooling and in preventing excessive star formation. To overcome this weakness, a stochastic thermal feedback model has been proposed (Dalla Vecchia & Schaye, 2012), where gas receiving thermal feedback energy is heated up to a temperature high enough to guarantee the effectiveness of feedback (see Section 6.3.1, for further details).

Alternatively, stellar feedback energy is provided in the form of kinetic energy and used to boost the velocity of surrounding gas particles (e.g. Springel & Hernquist, 2003; Dalla Vecchia & Schaye, 2008). They are thus kicked from the original position and energy is eventually thermalised and radiated away, but not as promptly as in the thermal scenario. To enforce the effectiveness of kinetic feedback schemes, particles that receive energy and sample galactic winds are often decoupled from hydrodynamic interactions: in this way, they are prevented from being halted from surrounding particles in dense regions of galaxy discs, and from thermalising energy soon after they have been provided with.

For instance, in the effective model, the energy released by SN explosions is entirely used to heat up the hot phase within the multiphase particle and regulate the star formation cycle. As a consequence SN feedback does not foster galactic outflows within that scheme. Therefore, in addition to the prescriptions for star formation, a model for galactic winds was included. To this end, the disc mass loss rate going in winds is assumed to be proportional to the SFR, through the mass upload or mass loading factor, a (constant) parameter of the model of order unity. Winds are assumed to carry a fraction of the energy supplied by SNe, that determines the kinetic energy of the winds and their fixed velocity. Within this formalism, gas particles have a probability to enter the wind stage. While sampling winds, these particles are decoupled hydrodynamically for a given time interval, so that they do not feel hydrodynamical forces and can transport energy

away from star-forming regions where they have been launched, before radiating it. Variations include a velocity of winds that depends linearly on the DM halo circular velocity (Vogelsberger et al., 2013), and an additional dependence on the redshift (Pillepich et al., 2018).

An alternative model is represented by the so-called blast-wave feedback (Gerritsen & Icke, 1997; Stinson et al., 2006). Within this scheme, the stellar feedback energy is provided to eligible gas particles as thermal energy, but these particles are then prevented from cooling for a short period of time (typically few tens of Myr). The physical motivation behind this prescription originates from the evolution of a SN remnant (e.g. Clarke & Carswell, 2007). As soon as a SN explodes, it drives a blast wave in the ISM, that undergoes a first phase of free expansion, followed by an adiabatic stage (the Sedov-Taylor phase) where radiative losses are negligible. Soon after, the blast wave enters the radiative phase. The switch off of cooling mimics the unresolved adiabatic phase, whose duration is estimated to be of order 30 Myr; then gas particles are allowed to cool again. Alternatively, the switch off of cooling can be explained by assuming that the energy released by SN explosions generates turbulence at unresolved scales and is partially dissipated over few tens of Myr, thus hindering gas cooling (Thacker & Couchman, 2000; Governato et al., 2007). When implemented in cosmological simulations, this feedback scheme results effective in avoiding excessive star formation, as gas particles that are provided with energy are heated up to a temperature that does not allow them to be star-forming anymore shortly after. This blast-wave feedback is also successful in producing a two-phase ISM: at variance with the effective model, here the two gas components are not in pressure equilibrium locally.

The alternative approach to energy-driven outflows consists in momentum-driven winds (Murray et al., 2005; Oppenheimer & Davé, 2006, 2008; Dutton & van den Bosch, 2009). Here, winds are considered to be driven by radiation pressure of massive stars on dust grains, instead of by SN explosions. In these models the velocity of the winds is proportional to the halo circular velocity, while the mass loading factor is inversely proportional to it.

The discussion in this Section has been focused on star formation and stellar feedback since these are the most important processes whose numerical implementation determines final results in cosmological simulation of disc galaxies (see Chapters 6 and 7). Here, I have not discussed the effect of AGN feedback in simulations of disc galaxies. As for the numerical prescriptions adopted for dumping AGN feedback energy to the gas surrounding the central SMBH, the energy can be provided in the form of both thermal and kinetic energy, and considerations similar to those for the implementation of stellar feedback hold. The simulations that I carried out and whose results I am going to discuss in Chapters 6, 7, and 8 do not include the effect of AGN feedback. On the other hand, I further enhanced our sub-resolution model (Section 5.3) to account for the presence of SMBHs and AGN feedback: details on the implementation are presented in Chapter 9, where results of simulations with both stellar and AGN feedback are shown. In Chapter 9, I will also briefly discuss state-of-the-art numerical modelling for incorporating the effect of AGN feedback in cosmological simulations.

Part II

Methods

4

Numerical methods

Cosmological hydrodynamical simulations that evolve simultaneously the collisionless DM and a self-gravitating, collisional baryonic fluid are a unique tool to investigate the formation and evolution of cosmic structures. They are able to probe the evolution of the DM and gas, coupled via the gravitational interaction, in an expanding Universe and self-consistently capture the gas dynamics.

A key focus of the work presented in this Thesis is on the numerical implementation of physical processes within a complex state-of-the-art code for cosmological simulations: this kind of challenging work is fundamental to advance the capabilities of simulations of structure formation. Also, in order to achieve a full control of simulations and use them as supervised experiments, a deep knowledge of the essentials of computational fluid dynamics and of the basis of numerical cosmology is a necessary requirement.

In this Chapter I outline the main features of the numerical techniques adopted in the cosmological hydrodynamical simulations that I carried out. The goal of this Chapter is to provide an overview of how the code used for the cosmological simulations presented in the next Chapters simultaneously deals with gravity and gas dynamics.

Contents

4.1 Collisionless matter and gravity

Gravity is the force that drives structure formation. The building block of most cosmological simulations is therefore an N-body code (see e.g. Yoshikawa et al., 2013, for a discussion on alternative approaches). The goal of an N-body code is to investigate the non-linear dynamical evolution of a self-gravitating, collisionless system (Dolag et al., 2008; Springel, 2016, for reviews). A collisionless fluid is a system whose constituent elements move under the effect of the collective gravity field generated by the total mass distribution: in a collisionless system gravitational collisions and interactions between fluid elements are negligible and do not influence the motion and general properties of the constituent elements themselves. In order to establish quantitatively whether a system can be considered collisionless or not, the relaxation timescale has to be contrasted to the timescale over which the system evolves or is investigated. A system featuring $N_{\rm true}$ constituent particles moving with typical velocity v across its size L is characterised by the crossing time (Binney & Tremaine, 2008):

$$t_{\rm cross} = \frac{L}{v} \ . \tag{4.1}$$

Possible collisions with nearby particles result in a quadratic velocity perturbation $(\Delta v)^2$ of each particle's velocity, since each encounter contributes with a randomly oriented Δv. The relaxation time is the timescale over which the quadratic velocity perturbation amounts to roughly the squared velocity itself:

$$t_{\rm relax} = \frac{v^2}{(\Delta v)^2 / t_{\rm cross}} \ . \tag{4.2}$$

Here, $v^2/(\Delta v)^2$ quantifies the number of crossings required to have a velocity change of the same order as v^2 and depends on the number $N_{\rm true}$ of particles (Binney & Tremaine, 2008). Therefore, the relaxation time can be cast as:

$$t_{\rm relax} = \frac{N_{\rm true}}{8 \ln N_{\rm true}} t_{\rm cross} \ . \tag{4.3}$$

A system can be deemed as collisionless if its relaxation time exceeds by far the age of the Universe $\sim 1/H_0$. After the timescale $t_{\rm relax}$, deflections in a particle motion by interactions with other particles are expected, and the system cannot be considered collisionless anymore.

CDM and stars in galaxies can be represented as a collisionless, non-relativistic fluid made of particles located at the comoving position $\mathbf{x}$, with mass m and momentum $\mathbf{p}$. It can be described by means of the distribution function $f(\mathbf{x}, \mathbf{p}, t)$ in the phase space, whose time evolution in an expanding Universe is given by the Boltzmann (or Vlasov) equation:

$$\frac{\partial f}{\partial t} + \frac{\mathbf{p}}{m\, a^2} \nabla f - m \nabla \Phi \frac{\partial f}{\partial \mathbf{p}} = 0 \ . \tag{4.4}$$

Here, a is the expansion factor and Φ is the gravitational potential. This equation is coupled with the Poisson equation:

$$\nabla^2\Phi(\mathbf{x},t) = 4\,\pi\,G\,a^2\,[\rho(\mathbf{x},t) - \bar{\rho}(t)] \ , \tag{4.5}$$

where $\bar{\rho}(t)$ is the background density. In order to retrieve the mass density $\rho(\mathbf{x},t)$, $f(\mathbf{x},\mathbf{p},t)$ has to be integrated over the momenta $\mathbf{p} = m\,a^2\,\dot{\mathbf{x}}$, so that:

$$\rho(\mathbf{x},t) = \int f(\mathbf{x},\mathbf{p},t)\,d^3p \ . \tag{4.6}$$

Since it is arduous to deal with a six-dimensional problem, one usually prefers to resort to the N-body approximation: the initial phase space is sampled with a finite number N of discrete fluid elements. These elements are considered as tracer particles or realisations of the underlying mass distribution. Note that $N << N_{\rm true}$ by several orders of magnitude. As a consequence, $t_{\rm relax}$ of simulated systems is by far smaller than that of real systems: this is why coarse sampled systems in simulations may suffer from spurious two-body relaxation and heating (Steinmetz & White, 1997). In the N-body approximation the solution is obtained by integrating the equations of motion of the N particles in the cumulative gravity field. These equations, in comoving coordinates, read:

$$\frac{d\mathbf{p}}{dt} = -m\,\nabla\Phi \qquad \text{and} \qquad \frac{d\mathbf{x}}{dt} = \frac{\mathbf{p}}{m\,a^2} \ . \tag{4.7}$$

The equations of motion are integrated in time, adopting numerical schemes that integrate ordinary differential equations. The most demanding process is the computation of the gravitational potential to estimate particle accelerations. Different approaches can be adopted to tackle this problem.

A first method is the Particle-Particle (PP) method. It consists in computing, for each considered particle i, the contribution to the potential from the other particles j through direct summation, so that:

$$\Phi(\mathbf{r}_{\rm i}) = -G\sum_{j\neq i}\frac{m_{\rm j}}{(\,|\mathbf{r}_{\rm i}-\mathbf{r}_{\rm j}|^2+\varepsilon^2)^{1/2}} \ . \tag{4.8}$$

In equation (4.8), $\mathbf{r}_{\rm i}$, $\mathbf{r}_{\rm j}$, and $m_{\rm j}$ are the position of particle i, and the position and mass of particles j, respectively. The gravitational potential is modified using a *gravitational softening* ε, that smooths the gravitational interaction between a particle pair. The softened gravitational force is not Newtonian anymore on scales that are comparable to ε. In this way, ε preserves the collisionless property of the system, limiting spurious two-body relaxation in collisionless fluids represented with a finite number of particles. The gravitational softening translates directly into spatial resolution, as its presence implies that no scale lengths smaller than or of the order of ε can be resolved. It is usually assumed to be a fraction ($\sim 1/50$, Dolag et al., 2008) of the mean inter-particle separation within the computational domain. The PP algorithm is highly accurate, but computationally expensive, as it requires a number of N^2 operations to estimate the force. Therefore, either one chooses

to accelerate the computation using ad-hoc hardwares and dedicated devices (e.g. the GRAPE hardware (GRAvity PipE, Makino et al., 2003) and GPUs, graphic processing units), or resorts to less accurate, yet faster computational methods.

A common approach is the Particle-Mesh (PM) method (e.g. Hockney & Eastwood, 1988), that employs a grid in order to compute the force. The scheme is as follows. First, densities from particle positions are assigned to a mesh, by adopting a weighting function. Then, the Poisson equation is solved in Fourier space, so as to retrieve the gravitational potential. The force is thus computed on the grid and then interpolated back to particle positions, adopting the same weighting function as before. In the end, particle positions and velocities are updated. The PM method is computationally cheaper than the direct summation ones, as it requires a number of operations that scales as $N + N_{\rm m} \log N_{\rm m}$, $N_{\rm m}$ being the number of mesh points (thanks to the fact that the Fast Fourier Transform technique is commonly adopted). However, since the mesh points have to be recorded and stored, this method is memory demanding, and this limits the exploitable dynamical range.

Another widely diffuse approach is the hierarchical multipole method, also called Tree algorithm (Appel, 1985; Barnes & Hut, 1986; Jernigan & Porter, 1989; Springel et al., 2001). The key idea of this method is to arrange particles in groups, according to their distance from the considered particle. The smartest way to achieve this particle grouping is by means of a tree structure. The tree consists in a recursive subdivision of space: it can be characterised by different features, but it basically slices the computational domain into sub-domains (called nodes or cells), until a sub-domain which contains only one particle or none is reached. The force addition from each group of particles is then supplied by its multipole expansion, where only lowest order terms contribute as the distance from the considered particle increases. The force experienced by the considered particle is computed starting from the lowest refinement level. If the ratio between the size of the cell and the distance of its centre of mass from the considered particle is lower than a critical opening angle that encodes the precision of the algorithm, then the force contribution through the multipole expansion can be computed. Otherwise, one has to continue walking along the tree until nodes small and distant enough to provide accurate force contribution through multipole expansions are reached. The sum over the force contributed by N particles is in this way replaced by a sum over a smaller number of cells. Note that the Tree algorithm reduces to a PP method for nearby particles which are seen under an angle larger than the critical opening angle. The computational cost amounts to $N \log N$ operations. Even if this algorithm suffers from a lower accuracy in the estimate of the force with respect to the PM method, it has an almost unlimited dynamical range and no difficulties in dealing with clumpy distributions.

Hybrid extensions of the two aforementioned approaches have been developed, so as to combine their advantages. For instance, in the TreePM method (Bode et al., 2000; Bagla, 2002) the gravitational potential is decomposed into two contributions: a short-range component and a long-range one. In this way, the potential is split in the Fourier space at a characteristic scale identifying the force decomposition. Long-range interactions are retrieved via the PM method. Short-range forces are

instead computed directly in the real space. A Tree algorithm is employed for their computation, by taking advantage of the fact that their contribution dies off with distance, becoming negligible for distances slightly larger than the scale of the force split. This method allows to achieve a higher accuracy in computing long-range interactions with respect to the standard Tree algorithm, while keeping the advantages of the latter one.

Another hybrid method that is worth naming is the Particle-Particle–Particle-Mesh (PPPM or P^3M) algorithm (e.g. Efstathiou et al., 1985). It is analogous to the TreePM (although historically developed earlier), but here the short-term force is retrieved through the PP method, from direct summation over particles.

Interesting variations of the two last algorithms are their adaptive versions, ATreePM (Springel, 2005) and AP^3M (e.g. Couchman, 1991), respectively. Here, there is more than one refinement level for the mesh that is employed to slice the computational domain into sub-domains, according to particle distribution. The refinement ensures that long-range interactions are always handled by the PM algorithm and effectively computed on a grid for a large number of particles, even if a clustered and clumpy particle distribution is present.

4.2 Hydrodynamics

DM and stars are collisionless components: their evolution is driven by gravity alone. On the other hand, interactions between gas particles occur on typical timescales shorter than the dynamical time or the crossing time (equation (4.1)). As a consequence, gas is a collisional component: its evolution is ruled by hydrodynamical forces, in addition to gravity. The equations of hydrodynamics that govern the evolution of gas lie on the key assumption that gas can be approximated as a fluid and described as a continuum (Clarke & Carswell, 2007). The constitutive components of a fluid are the fluid elements, over which local variables such as density and temperature can be defined. In this way, a fluid is investigated by means of its macroscopic properties. The fluid approximation is valid as long as the scale length on which particle-by-particle interactions take place, i.e. the mean free path λ, is by far smaller than the characteristic scale length L of the fluid. This latter quantity can be estimated by analysing the spatial scale over which any relevant quantity q changes significantly, that is $L \sim q/\nabla q$, and is commonly approximated with tipical scales investigated. The mean free path of protons and electrons in a plasma where no magnetic field is present is controlled by Coulomb collisions and is $\lambda \approx 5 \cdot 10^{18}\,(T/10^6\ \mathrm{K})^2 (n/10^{-3}\ \mathrm{cm}^{-3})^{-1}$ cm (Spitzer, 1978; Sarazin, 2009). Typical values of λ in the hot ($T = 10^6$ K) ionised ISM of a disc galaxy range between a few pc and few tens of pc for gas number densities of $n = 10^{-3}$ cm^{-3} and $n = 10^{-4}$ cm^{-3},

respectively[1]. Typical mean free paths are remarkably smaller than $\sim$ kpc scales over which quantities vary significantly in the ISM, and considerably smaller than the computational domain of galaxy simulations (but see, for instance, discussion in Ritchie & Thomas (2001)). This allows to use the equations of hydrodynamics to describe the evolution of gas. Fluid elements, despite being an abstract concept that does not enter the computations, are assumed to have a typical size ℓ such that $\lambda << \ell << L$. Therefore, they are small enough to ignore changes in fluid properties within them, while they are large enough to contain a considerable number of particles that continuously interact until they reach the same temperature and their motion is represented in terms of a Maxwellian velocity distribution.

In particular, the ISM and CGM can be described as ideal fluids. Inviscid or ideal fluids are fluids in which viscosity can be neglected. In these fluids, as opposed to viscous fluids, microscopic interactions between particles do not result in any force or stress that dissipates kinetic energy and deforms the flow.

A set of hydrodynamic equations describes the evolution of a non-viscous fluid. In the Lagrangian comoving form, they can be cast as:

$$\frac{\mathrm{d}\rho}{\mathrm{d}t} = -\rho\,\nabla\cdot\mathbf{v} \ , \tag{4.9}$$

$$\frac{\mathrm{d}\mathbf{v}}{\mathrm{d}t} = -\frac{\nabla P}{\rho} + \mathbf{F}_{\mathrm{ext}} \ , \tag{4.10}$$

$$\frac{\mathrm{d}u}{\mathrm{d}t} = -\frac{P}{\rho}\,\nabla\cdot\mathbf{v} + \dot{\mathcal{Q}} \ . \tag{4.11}$$

In these equations, ρ, $\mathbf{v}$, P, and u are the gas density, velocity, pressure and specific (per unit mass) internal energy, respectively. Also, the term $\mathbf{F}_{\mathrm{ext}}$ represents the external forces per unit mass and $\dot{\mathcal{Q}}$ is the specific rate of heat exchange (see below).

The set of equations (4.9), (4.10), and (4.11) is closed by an equation of state, that expresses the pressure of the fluid as a function of its density:

$$P = (\gamma - 1)\,\rho\,u \ . \tag{4.12}$$

Here, γ is the adiabatic index, that for an ideal, monatomic gas is $\gamma = 5/3$.

In equations (4.9), (4.10), and (4.11), $\mathrm{d}/\mathrm{d}t = \partial/\partial t + \mathbf{v}\cdot\nabla$ is the Lagrangian derivative following the motion. The first contribution $\partial/\partial t$ expresses the rate of variation evaluated at a fixed position and is called Eulerian derivative. The

[1] As the gas temperature rises above $T \sim 10^5$ K the hydrogen is fully ionised and the helium almost completely. Should the temperature be lower and the gas not be considered a plasma anymore, collisions do not occur between electrons and ions, but they rather interest atoms. In the case of neutral hydrogen, the mean free path can be estimated as $\lambda = 1/(n\,\sigma) \sim 10^{15}\,(n/\mathrm{cm}^{-3})^{-1}$ cm, σ being the cross section, whose lower limit can be approximated adopting the Bohr radius $a_0 = 5.3 \cdot 10^{-9}$ cm as effective radius.

second term $\mathbf{v} \cdot \nabla$ quantifies the advection, that is the change due to the motion of the fluid element, and is called convective derivative.

Equations (4.9), (4.10), and (4.11) express the conservation of mass, momentum and energy per unit volume. Equation (4.9) is the continuity equation, that states that the flow of mass into a region of fluid determines how its density varies during its motion. Equation (4.10) is the Euler equation: it describes how the momentum of a fluid element changes as a result of pressure gradient and gravity. Equation (4.11) can be inferred from the first law of thermodynamics: $du = \delta\mathcal{Q} - \delta\mathcal{W}$. Here, $\mathcal{Q}$ is the heat lost or absorbed and $\mathcal{W}$ is the $P\,d\mathcal{V}$ work done, $\mathcal{V} = \rho^{-1}$ being the specific volume. Therefore, the variation of the specific internal energy can be expressed as:

$$\frac{\mathrm{d}u}{\mathrm{d}t} = \frac{P}{\rho^2}\frac{\mathrm{d}\rho}{\mathrm{d}t} + \dot{\mathcal{Q}} \ . \tag{4.13}$$

Hence, using equation (4.9), equation (4.11) follows directly. Here and in equation (4.11), $\dot{\mathcal{Q}} = \dot{\mathcal{H}} - \rho^{-1}\, n^2\, \Lambda$ is the specific rate of heat exchange that can be expressed as the difference between the specific heating rate $\dot{\mathcal{H}}$ and the cooling rate per unit mass $\rho^{-1}\, n^2\, \Lambda$, where Λ is the cooling function defined in Section 2.2. Equation (4.11) describes the conservation of energy. The quantity that is actually conserved is the total energy density (i.e. energy per unit volume) $\mathcal{E}$, that is related to the specific energy in equation (4.11) through: $\mathcal{E} = \rho\,(v^2/2 + u + \Phi)$.

The source term $\mathbf{F}_{\mathrm{ext}}$ accounts for the presence of external forces per unit mass exerted on the fluid elements. In the absence of magnetic fields and other forces other than gravity, $\mathbf{F}_{\mathrm{ext}} = -\nabla\Phi$, Φ being the gravitational potential. In cosmological hydrodynamical simulations where the gas component is coupled to the other collisionless components via the gravitational interaction, the total Φ governing the fluid motion is contributed by all the other components and accounts for self-gravity, too. In the majority of particle-based codes (see below) where both the DM and gas are represented by means of particles, the self-gravity of all the components is computed via one among the N-body methods discussed in Section 4.1.

There are two general approaches that can be pursued to solve the set of equations of hydrodynamics: the Eulerian approach and the Lagrangian approach. Since it is not possible to solve the equations of hydrodynamics analytically, a number of codes have been developed to integrate the system of equations numerically, following either the Eulerian or Lagrangian approach.

Numerical codes that adopt the Eulerian methodology discretise the space by means of a grid. Fluid quantities and their derivatives are evaluated within each cell of the computational domain, i.e. at fixed positions. Mass and energy flows are computed across control volumes defined by the edges of the cells. Eulerian codes such as ZEUS (Stone & Norman, 1992) and ATHENA (Stone et al., 2008) adopt a grid whose zones have an almost constant spacing. As an additional feature, mesh-based codes can be provided with adaptive mesh refinement (AMR, Berger & Colella, 1989) in order to increase resolution where needed. Examples are ENZO

(Bryan & Norman, 1997), FLASH (Fryxell et al., 2000), ART (Kravtsov et al., 2002), RAMSES (Fromang et al., 2006), and PLUTO (Mignone et al., 2007).

On the other hand, the Lagrangian approach follows the evolution of fluid elements. Numerical codes that solve the equations of hydrodynamics following the Lagrangian method are particle based, since particles are used to discretise the mass of the fluid. Derivatives of fluid properties are evaluated in the system of reference that moves along with particles. Section 4.3 is devoted to introduce the main features of smoothed particle hydrodynamics, that is the technique adopted to deal with gas dynamics in the cosmological hydrodynamical simulations presented in this Thesis.

Recently, hybrid codes that take advantage of both the Eulerian and Lagrangian approaches have been developed, where the capabilities of the moving-mesh and mesh-free methods are exploited (e.g. AREPO, Springel, 2010b).

4.3 Smoothed Particle Hydrodynamics

Smoothed Particle Hydrodynamics (hereafter SPH, Gingold & Monaghan, 1977; Lucy, 1977) is the ultimate Lagrangian technique to numerically describe the motion of a fluid by means of a collection of particles. It allows to approximate a continuum through a discrete ensemble of sampling particles.

Examples of SPH numerical codes are: GADGET (Springel et al., 2001; Springel, 2005), GASOLINE (Wadsley et al., 2004, 2017), VINE (Wetzstein et al., 2009), SEREN (Hubber et al., 2011), and PHANTOM (Price et al., 2017).

In this Section I will give a brief overview of the key concepts of SPH. This compendium is mainly devoted to introduce the SPH formalism and to outline the numerical framework within which the code GADGET (see Section 5.1) that I use for simulations reported in this Thesis fits. The overview is far from being exhaustive: excellent reviews that contributed to these Sections are e.g. Monaghan (1992, 2005); Rosswog (2009); Dolag et al. (2008); Springel (2010a); Price (2012a); Springel (2016).

Considering a scalar or vector field $F(\mathbf{x})$, its smoothed interpolated version $F_{\rm int}(\mathbf{x})$ can be defined:

$$F_{\rm int}(\mathbf{x}) \coloneqq \int F(\mathbf{x}')\, W(\mathbf{x}-\mathbf{x}', h)\, \mathrm{d}\mathbf{x}' \ , \tag{4.14}$$

once it is convolved with an interpolating kernel $W(\mathbf{x}-\mathbf{x}', h)$. The smoothing length h characterises the width of the kernel function. A suitable kernel function obeys the following requirements. It is normalised to unity, so that:

$$\int W(\mathbf{x}-\mathbf{x}', h)\, \mathrm{d}\mathbf{x}' = 1 \ , \tag{4.15}$$

and it approaches a Dirac δ function in the limit of small smoothing lengths, i.e.:

$$\lim_{h\to 0} W(\mathbf{x}-\mathbf{x}', h) = \delta(\mathbf{x}-\mathbf{x}') \ . \tag{4.16}$$

The latter property ensures that the original field is recovered whenever

$$\lim_{h\to 0} F_{\rm int}(\mathbf{x}) = F(\mathbf{x}) \ . \tag{4.17}$$

Also, the kernel is chosen to be symmetric and isotropic (for conservation of angular momentum):

$$W(\mathbf{x}-\mathbf{x}', h) = W(|\mathbf{x}-\mathbf{x}'|, h) \ , \tag{4.18}$$

and smooth enough to be differentiable at least twice.

Assuming to know the field $F(\mathbf{x})$ at a number of N points $\mathbf{x}_{\rm j}$, so that $F_{\rm j} = F(\mathbf{x}_{\rm j})$, equation (4.14) can be cast in the discrete approximation as:

$$F_{\rm sm}(\mathbf{x}) \coloneqq \sum_{\rm j} \frac{m_{\rm j}}{\rho_{\rm j}} F_{\rm j}\, W(\mathbf{x}-\mathbf{x}_{\rm j}, h) \ . \tag{4.19}$$

This equation highlights how sampling particles of mass $m_{\rm j}$ located at the position $\mathbf{x}_{\rm j}$ can be interpreted as a set of interpolation points. Note that the smoothed field $F_{\rm sm}(\mathbf{x})$ is defined everywhere, not only at the underlying sampling positions. Dropping the subscript *sm* in equation (4.19) and cosidering the density field, i.e. $F(\mathbf{x}) = \rho(\mathbf{x})$, one gets:

$$\rho(\mathbf{x}) = \sum_{\rm j} m_{\rm j}\, W(\mathbf{x}-\mathbf{x}_{\rm j}, h) \ . \tag{4.20}$$

In this way, the density of the particle i can be estimated as:

$$\rho_{\rm i} = \sum_{\rm j=1}^{\rm N_{ngb}} m_{\rm j}\, W(\mathbf{x}_{\rm i}-\mathbf{x}_{\rm j}, h) \ . \tag{4.21}$$

Equation (4.21) is key for understanding the SPH philosophy. In SPH, each particle that contributes to the fluid sampling carries hydrodynamical quantities. Values of SPH quantities are estimated by smoothing over a given number $N_{\rm ngb}$ of neighbour particles. In this way, fluid properties are evaluated statistically, by averaging over kernel-weighted contributions from neighbour particles. Neighbour particles j of particles i are a collection of the $N_{\rm ngb}$ particles closest to i. In principle, the summation in equation (4.19) spreads over all the N particles; however, since the kernel function falls off quickly with distance, only the closest surrounding particles contribute. The smoothing length h usually approaches the inter-particle separation (see below) and kernel functions are usually null beyond $\sim 2\,h$ (although this depends on conventions, see Section 5.1). In this way, the sum in equation (4.21) is restricted to the $N_{\rm ngb}$ neighbour particles that lie within a sphere of radius $2\,h$ centred at $\mathbf{x}_{\rm i}$, around the target particle. Weighting kernels are indeed required to have a compact support (i.e. vanish at a finite distance)[2], so that the number of

[2]The Gaussian kernel does not meet this condition: this is the reason why it is not considered, although useful for analytical computations.

operations required to estimate fluid quantities reduces to $N_{\rm ngb}\,N$ instead of N^2. A commonly adopted kernel function is the so-called cubic spline:

$$M_4(q) = \frac{1}{4\,\pi\,h^3}\begin{cases}(2-q)^3 - 4\,(1-q)^3 & \text{for } \; 0 \leq q \leq 1 \;\; , \\ (2-q)^3 & \text{for } \; 1 < q \leq 2 \;\; , \\ 0 & \text{for } \; q > 2 \;\; , \end{cases} \tag{4.22}$$

where $q = |\mathbf{x}_{\rm i} - \mathbf{x}_{\rm j}|/h$. This kernel function provides a second-order accurate estimate to the underlying field $F(\mathbf{x})$ through equation (4.19), assuming that interpolation points are homogeneously distributed (Springel, 2016). Different options for the smoothing kernel are feasible (e.g. Dehnen & Aly, 2012). The choice of the kernel function and of the number $N_{\rm ngb}$ has a crucial impact on the accuracy of the fluid sampling (see below and Section 4.4).

In order to capture how a Lagrangian code deals with gas dynamics, the equations of hydrodynamics have to be written for the sampling particles in the SPH formalism. Under the assumption that the kernel function is differentiable, equation (4.19) can be differentiated as follows:

$$\nabla F_{\rm sm}(\mathbf{x}) = \sum_{\rm j} \frac{m_{\rm j}}{\rho_{\rm j}}\, F_{\rm j}\, \nabla W(\mathbf{x} - \mathbf{x}_{\rm j}, h) \;\; , \tag{4.23}$$

where $\nabla = \partial/\partial\mathbf{x}$. The drawback of equation (4.23) is that the derivative in this form does not vanish if $F(\mathbf{x})$ is constant. To work around this issue, a differentiable function $\mathcal{A}$ can be used so as to cast equation (4.23) as:

$$\nabla F = \frac{1}{\mathcal{A}}\left(\nabla(\mathcal{A}\,F) - F\,(\nabla\mathcal{A})\right) \;\; . \tag{4.24}$$

In this way, the SPH estimate of ∇F at the position $\mathbf{x}_{\rm i}$ will be:

$$\begin{aligned}\nabla_{\rm i} F_{\rm i} &= \frac{1}{\mathcal{A}_{\rm i}}\left(\sum_{\rm j=1}^{\rm N_{ngb}} \frac{m_{\rm j}}{\rho_{\rm j}}\,\mathcal{A}_{\rm j}\,F_{\rm j}\,\nabla_{\rm i} W(\mathbf{x}_{\rm i} - \mathbf{x}_{\rm j}, h) - F_{\rm i}\sum_{\rm j=1}^{\rm N_{ngb}} \frac{m_{\rm j}}{\rho_{\rm j}}\,\mathcal{A}_{\rm j}\,\nabla_{\rm i} W(\mathbf{x}_{\rm i} - \mathbf{x}_{\rm j}, h)\right) \\ &= \frac{1}{\mathcal{A}_{\rm i}}\sum_{\rm j=1}^{\rm N_{ngb}} \frac{m_{\rm j}}{\rho_{\rm j}}\,\mathcal{A}_{\rm j}\,(F_{\rm j} - F_{\rm i})\nabla_{\rm i} W_{\rm ij} \;\; , \end{aligned} \tag{4.25}$$

where $W_{\rm ij} = W(\mathbf{x}_{\rm i} - \mathbf{x}_{\rm j}, h)$. By exploiting equation (4.25) and choosing $\mathcal{A} = 1$, the continuity equation (4.9) becomes:

$$\frac{{\rm d}\rho_{\rm i}}{{\rm d}t} = \rho_{\rm i}\sum_{\rm j=1}^{\rm N_{ngb}} \frac{m_{\rm j}}{\rho_{\rm j}}\,\mathbf{v}_{\rm ij}\cdot\nabla_{\rm i} W_{\rm ij} \;\; , \tag{4.26}$$

where $\mathbf{v}_{\rm ij} = (\mathbf{v}_{\rm i} - \mathbf{v}_{\rm j})$.

Within the SPH framework, the Euler equation (4.10) describes how particles move using smoothed quantities. Since:

$$\nabla_{\rm i} P_{\rm i} = \sum_{\rm j=1}^{\rm N_{ngb}} \frac{m_{\rm j}}{\rho_{\rm j}}\,P_{\rm j}\,\nabla_{\rm i} W_{\rm ij} \;\; , \tag{4.27}$$

and neglecting external forces, i.e. $\mathbf{F}_{\rm ext} = 0$, the Euler equation reads:

$$\frac{\mathrm{d}\mathbf{v}_{\rm i}}{\mathrm{d}t} = -\frac{1}{\rho_{\rm i}} \sum_{\rm j=1}^{\rm N_{ngb}} \frac{m_{\rm j}}{\rho_{\rm j}} P_{\rm j} \nabla_{\rm i} W_{\rm ij} \ . \tag{4.28}$$

However, if $P_{\rm i} \neq P_{\rm j}$, the angular momentum is not conserved, since the force experienced by the particle i due to particle j alone:

$$\mathbf{F}_{\rm ji} = \left(m_{\rm i} \frac{\mathrm{d}\mathbf{v}_{\rm i}}{\mathrm{d}t} \right)_{\rm j} = -\frac{m_{\rm i}}{\rho_{\rm i}} \frac{m_{\rm j}}{\rho_{\rm j}} P_{\rm j} \nabla_{\rm i} W_{\rm ij} \tag{4.29}$$

turns out not to be equal and opposed to:

$$\mathbf{F}_{\rm ij} = \left(m_{\rm j} \frac{\mathrm{d}\mathbf{v}_{\rm j}}{\mathrm{d}t} \right)_{\rm i} = -\frac{m_{\rm j}}{\rho_{\rm j}} \frac{m_{\rm i}}{\rho_{\rm i}} P_{\rm i} \nabla_{\rm j} W_{\rm ij} = \frac{m_{\rm i}}{\rho_{\rm i}} \frac{m_{\rm j}}{\rho_{\rm j}} P_{\rm i} \nabla_{\rm i} W_{\rm ij} \ , \tag{4.30}$$

being $\nabla_{\rm i} W_{\rm ij} = -\nabla_{\rm j} W_{\rm ij}$ (Monaghan, 2005). In order to symmetrise the derivative $\nabla P/\rho$ on the right-hand side of equation (4.10), one resorts to the identity:

$$\frac{\nabla P}{\rho} = \nabla \left(\frac{P}{\rho} \right) + \frac{P}{\rho^2} \nabla \rho \ , \tag{4.31}$$

so that:

$$\begin{aligned} \frac{\mathrm{d}\mathbf{v}_{\rm i}}{\mathrm{d}t} = -\frac{\nabla_{\rm i} P_{\rm i}}{\rho_{\rm i}} &= -\sum_{\rm j=1}^{\rm N_{ngb}} \frac{m_{\rm j}}{\rho_{\rm j}} \frac{P_{\rm j}}{\rho_{\rm j}} \nabla_{\rm i} W_{\rm ij} - \frac{P_{\rm i}}{\rho_{\rm i}^2} \sum_{\rm j=1}^{\rm N_{ngb}} \frac{m_{\rm j}}{\rho_{\rm j}} \rho_{\rm j} \nabla_{\rm i} W_{\rm ij} \\ &= -\sum_{\rm j=1}^{\rm N_{ngb}} m_{\rm j} \left(\frac{P_{\rm j}}{\rho_{\rm j}^2} + \frac{P_{\rm i}}{\rho_{\rm i}^2} \right) \nabla_{\rm i} W_{\rm ij} \ . \end{aligned} \tag{4.32}$$

In this way the contribution to pressure from the particles is explicitly symmetric, thus ensuring that the momentum is conserved. Here, the SPH version of the Euler equation has been derived in the most straightforward way. A more refined derivation can be obtained by discretising the Lagrangian in terms of the particles, $L_{\rm SPH} = \sum_{\rm i} (m_{\rm i}\, \mathbf{v}_{\rm i}^2/2 - m_{\rm i}\, u_{\rm i})$, and then retrieving the equations of motion by exploiting variational principles of classical mechanics (Gingold & Monaghan, 1982; Springel & Hernquist, 2002).

In order to write the energy equation (4.11) using the SPH formalism, it is useful to consider it as expressed in equation (4.13). Neglecting the net cooling rate, i.e. $\dot{\mathcal{Q}} = 0$:

$$\frac{\mathrm{d}u_{\rm i}}{\mathrm{d}t} = \frac{P_{\rm i}}{\rho_{\rm i}^2} \frac{\mathrm{d}\rho_{\rm i}}{\mathrm{d}t} \ . \tag{4.33}$$

By exploiting the continuity equation (4.26), the energy equation can be written as:

$$\frac{\mathrm{d}u_{\rm i}}{\mathrm{d}t} = \frac{P_{\rm i}}{\rho_{\rm i}} \sum_{\rm j=1}^{\rm N_{ngb}} \frac{m_{\rm j}}{\rho_{\rm j}} \mathbf{v}_{\rm ij} \cdot \nabla_{\rm i} W_{\rm ij} \ . \tag{4.34}$$

Finally, the equation of state (4.12) within the SPH formalism reads:

$$P_{\rm i} = (\gamma - 1)\, \rho_{\rm i}\, u_{\rm i} \ . \tag{4.35}$$

In this way, equations (4.26), (4.32), (4.34), and (4.35) constitute the set of SPH equations.

As a final remark, the smoothing scale h describes the width of the interpolating kernel: as a consequence, it is directly related to the resolution that can be achieved in estimates of fluid quantities, since characteristic scale lengths significantly smaller than h result to be smoothed out.

Assuming a constant smoothing length leads to estimate fluid quantities by interpolating on a different number of neighbour particles, depending on whether the target particle is in an overdense or underdense region. This results in an accuracy of fluid sampling that is not constant, since fluid quantities evaluated in underdense regions would suffer of a lower accuracy (the lower is $N_{\rm ngb}$, the larger is the relative error of the discrete approximation of the field). In order to take into account discrepancy in the fluid density, a smoothing length that depends on spatial coordinates is usually considered, as an additional feature of SPH. A comparable accuracy in estimate of fluid quantity all over the computational domain is indeed achieved when variable smoothing lengths $h_{\rm i} = h(\mathbf{x}_{\rm i})$ are used. Allowing the smoothing length to differ from particle to particle, SPH results to be inherently adaptive: this ability to self-consistently increase resolution where needed is one of the fundamental advantage of SPH. The value of $h_{\rm i}$ is determined by requiring either that the number of neighbours for each target particle with $|\mathbf{x}_{\rm i} - \mathbf{x}_{\rm j}| < h_{\rm i}$ is kept almost constant at $N_{\rm ngb}$, or that the mass $\rho_{\rm i}\, h_{\rm i}^3$ within the kernel is constant.

In deriving the SPH equations of hydrodynamics in this Section, a constant smoothing length has been assumed. When a variable smoothing length is considered, the Lagrangian derivation gives the following Euler and energy equations (instead of equations (4.32) and (4.34)):

$$\frac{{\rm d}\mathbf{v}_{\rm i}}{{\rm d}t} = -\sum_{\rm j=1}^{\rm N_{ngb}} m_{\rm j} \left[f_{\rm j} \frac{P_{\rm j}}{\rho_{\rm j}^2} \nabla_{\rm i} W_{\rm ij}(h_{\rm j}) + f_{\rm i} \frac{P_{\rm i}}{\rho_{\rm i}^2} \nabla_{\rm i} W_{\rm ij}(h_{\rm i}) \right] \ , \tag{4.36}$$

and

$$\frac{{\rm d}u_{\rm i}}{{\rm d}t} = f_{\rm i} \frac{P_{\rm i}}{\rho_{\rm i}} \sum_{\rm j=1}^{\rm N_{ngb}} \frac{m_{\rm j}}{\rho_{\rm j}}\, \mathbf{v}_{\rm ij} \cdot \nabla_{\rm i} W_{\rm ij}(h_{\rm i}) \ , \tag{4.37}$$

respectively, where:

$$f_{\rm i} = \left[1 + \frac{h_{\rm i}}{3\,\rho_{\rm i}} \frac{\partial \rho_{\rm i}}{\partial h_{\rm i}} \right]^{-1} \tag{4.38}$$

is a correction term that takes into account the possibility for h to vary (Springel & Hernquist, 2002).

4.4 Successes and shortfalls of SPH

Besides the adaptive resolution (Section 4.3), SPH has several advantages as a numerical technique. As a first valuable feature, SPH conserves simultaneously mass, linear and angular momenta, and energy (if no dissipative terms are included, see below). SPH can also be formulated so as to be entropy-conserving (see Springel & Hernquist (2002) and Section 5.1). The system of particles is indeed conservative and does not own intrinsic numerical dissipation (see e.g. Springel, 2010a; Price, 2012a,b, for further discussion): as a consequence, the solution of the set of hydrodynamics equations does not diffuse energy as a spurious numerical result, at variance with Eulerian codes. Moreover, SPH is Galilean invariant and can be easily coupled to N-body codes. Also, in SPH there are no advection errors. Indeed, at variance with Eulerian codes that suffer from numerical diffusion when dealing with advection[3] of fluid quantities through the computational domain, advection is computed exactly in SPH. Another advantage of the SPH is the possibility to straightforwardly track down the physical properties of the fluid or of a region of interest of the fluid by using tracer particles (relying on passively advected fluids in Eulerian codes is not as effective). A discussion on the performance of SPH codes with respect to Eulerian codes is beyond the scope of this Thesis: however, it is worth mentioning some projects aimed at the comparison of mesh- and particle-based numerical methods, that highlighted pros and cons of both, e.g. Frenk et al. (1999); O'Shea et al. (2005); Agertz et al. (2007); Scannapieco et al. (2012); Sembolini et al. (2016b).

Along with the aforementioned benefits, SPH comes with its disadvantages, as every numerical technique. The main shortfall of the SPH comes directly from one of its advantages, i.e. the ability to solve the equations of hydrodynamics with no numerical dissipation. This indeed means that dissipative terms have to be included explicitely where physically required. The most common situation where this happens is when a shock occurs. Besides shock waves, the gas dynamics can also originate contact discontinuities. Shocks and contact discontinuities cannot be properly described by the Euler equation (4.32), because hydrodynamical variables are not differentiable across them. As for shocks, one should either resort to the Rankine-Hugoniot equations (see e.g. Clarke & Carswell, 2007) describing the conservation of matter, momentum and energy across a shock, or continue to handle shocks with the usual set of equations (4.26), (4.32), and (4.34), and include in the Euler and energy equations a contribution from the so-called artificial viscosity (AV). The second option is the one adopted by traditional SPH codes. The Rankine-Hugoniot jump conditions show that the specific entropy of the fluid increases across the shock front: as a consequence the fluid cannot be considered as non viscous anymore. Numerically speaking, this justifies the inclusion of localised ad-hoc pressure-like terms in the Euler equation. The inclusion of the AV is therefore meant to broaden the shock in a region that can be still adequately described by

[3] In order to advect a scalar field $\mathcal{B}$, the equation $\partial\mathcal{B}/\partial t = -\nabla\cdot(\mathcal{B}\,\mathbf{v})$ has to be solved, $\mathbf{v}$ being the fluid velocity. This is the form of a continuity equation.

the Euler equation (4.32). Its goal is to produce entropy by dissipating kinetic energy into internal energy, while damping the relative motion of particles. If this viscosity were absent in SPH, particles would rather approach supersonically and continue to move, without spreading energy. Since dissipative terms in SPH are explicitly included, they can be translated into their physical meaning. The AV term is designed to resemble a combination of physical shear and bulk viscosity contributing to the pressure:

$$q_{\rm visc} = c_2\,\rho\,\ell^{\,2}\,(\nabla\cdot\mathbf{v})^2 - c_1\,\rho\,c_{\rm s}\,\ell\,(\nabla\cdot\mathbf{v}) \ , \tag{4.39}$$

where c_1 and c_2 are dimensionless parameters of order unity that describe the broadening of the shock layer, and $c_{\rm s} = (\gamma\,P/\rho)^{1/2}$ is the sound speed. In equation (4.39), ℓ is the minimum length scale that can be resolved and $\ell\,(\nabla\cdot\mathbf{v})$ quantify the velocity jump between close particles. The artificial viscous pressure in equation (4.39) is made up of two contributions: the first one is the Von Neumann & Richtmyer (1950) AV term, mainly acting where strong shocks[4] occur, while the second term is comparable to a bulk viscosity and is aimed at removing velocity oscillations in the post-shock regions.

This can be adapted within the SPH formalism. A commonly adopted SPH formulation for the AV (Monaghan, 1992) leads to the further contribution $\Pi_{\rm ij}$ in the Euler equation (4.32), so that:

$$\frac{{\rm d}\mathbf{v}_{\rm i}}{{\rm d}t} = -\sum_{\rm j=1}^{\rm N_{ngb}} m_{\rm j}\left(\frac{P_{\rm j}}{\rho_{\rm j}^2}+\frac{P_{\rm i}}{\rho_{\rm i}^2}+\Pi_{\rm ij}\right)\nabla_{\rm i}W_{\rm ij} \ . \tag{4.40}$$

In equation (4.40), $\Pi_{\rm ij}$ accounts for both the contributions to the viscosity in equation (4.39), and reads:

$$\Pi_{\rm ij} = \begin{cases} \frac{-\alpha\,\bar{c}_{\rm s,ij}\,\mu_{\rm ij}+\beta\,\mu_{\rm ij}^2}{\bar{\rho}_{\rm ij}} & \text{if} \quad \mathbf{x}_{\rm ij}\cdot\mathbf{v}_{\rm ij} < 0 \\ 0 & \text{otherwise} \end{cases} \ , \qquad \text{where} \quad \mu_{\rm ij} = \frac{\bar{h}_{\rm ij}\,\mathbf{x}_{\rm ij}\cdot\mathbf{v}_{\rm ij}}{x_{\rm ij}^2+\epsilon\,\bar{h}_{\rm ij}^2} \ . \tag{4.41}$$

Here, $\mathbf{x}_{\rm ij} = (\mathbf{x}_{\rm i}-\mathbf{x}_{\rm j})$, $\mathbf{v}_{\rm ij} = (\mathbf{v}_{\rm i}-\mathbf{v}_{\rm j})$, $\bar{c}_{\rm s,ij} = (c_{\rm s,i}+c_{\rm s,j})/2$, $\bar{\rho}_{\rm ij} = (\rho_{\rm i}+\rho_{\rm j})/2$, and $\bar{h}_{\rm s,\,ij} = (h_{\rm s,\,i}+h_{\rm s,\,j})/2$. Also, numerical tests provide the following estimates for these dimensionless parameters: $\alpha \simeq 1$, $\beta \simeq 2$, and $\epsilon \simeq 0.01$ (Monaghan, 1992; Rosswog, 2009). The AV only operates for particles that are approaching each other: as a consequence, $\Pi_{\rm ij} > 0$ and the entropy increases. The contribution $\propto \mu_{\rm ij}^2$ plays a key role in hampering particle penetration in strong shocks.

Once the energy equation (4.34) is modified accordingly, it reads:

$$\frac{{\rm d}u_{\rm i}}{{\rm d}t} = \frac{P_{\rm i}}{\rho_{\rm i}}\sum_{\rm j=1}^{\rm N_{ngb}}\frac{m_{\rm j}}{\rho_{\rm j}}\,\mathbf{v}_{\rm ij}\cdot\nabla_{\rm i}W_{\rm ij} + \frac{1}{2}\sum_{\rm j=1}^{\rm N_{ngb}} m_{\rm j}\,\Pi_{\rm ij}\,\mathbf{v}_{\rm ij}\cdot\nabla_{\rm i}W_{\rm ij} \ . \tag{4.42}$$

[4]Shocks develop in regions of converging flux. From equations (4.9) and (4.10), it can be easily seen that when the gas undergoes compression, i.e. ${\rm d}\rho/{\rm d}t{>}0$, then $\rho\,\nabla\cdot\mathbf{v} < 0$, also because $\rho\,\mathbf{v}(\nabla\cdot\mathbf{v}) \propto -\nabla P$.

Still, energy and linear and angular momenta are conserved within this formulation. Other beneficial features of this AV term is that it is Galilean invariant and null for rigid body rotation. However, some pitfalls arise as the aformentioned formulation of the AV may affect the fluid motion in three-dimensional simulations also away from shock regions, and add spurious viscous forces in shear flows. Balsara (1995) introduced a limiter as a possible solution to alleviate the latter drawback. The so-called Balsara switch evaluates the rate of the local compression with respect to the shear, thus figuring out where shocks occur. It can be cast as:

$$f_{\rm i} = \frac{|\langle \nabla \cdot \mathbf{v} \rangle_{\rm i}|}{|\langle \nabla \cdot \mathbf{v} \rangle_{\rm i}| + |\langle \nabla \times \mathbf{v} \rangle_{\rm i}| + 0.0001\, c_{\rm s,i}/h_{\rm i}} \ . \tag{4.43}$$

In this way, once $\Pi_{\rm ij}$ is replaced by $\Pi'_{\rm ij} = \bar{f}_{\rm ij}\, \Pi_{\rm ij}$ in equations (4.40) and (4.42), where $\bar{f}_{\rm ij} = (f_{\rm i} + f_{\rm j})/2$, AV is suppressed in purely shear flows and limited where the relative motion of gas particles results convergent because of vorticity or rotation (e.g. Keplerian flows). Indeed, in pure shear flows where $|\langle \nabla \cdot \mathbf{v} \rangle| = 0$ and $|\langle \nabla \times \mathbf{v} \rangle| \neq 0$, the action of AV is removed. On the other hand, in purely compressional flows where $|\langle \nabla \times \mathbf{v} \rangle| = 0$, the limiter approaches unity and $\Pi'_{\rm ij}$ reduces to $\Pi_{\rm ij}$.

To enforce the AV suppression where unnecessary, another possibility is to allow the viscosity strength parameter α in equation (4.41) to vary in time for each particle (Morris & Monaghan, 1997), according to:

$$\frac{d\alpha_{\rm i}}{dt} = -\frac{\alpha_{\rm i} - \alpha_{\rm min}}{\tau_{\rm i}} + S_{\rm i} \ , \tag{4.44}$$

while fixing $\beta_{\rm i} = 2\,\alpha_{\rm i}$. Here, $S_{\rm i}$ is a source term that arises whenever a shock is identified. A suitable source function is $S_{\rm i} = \max[-(\nabla \cdot \mathbf{v})_{\rm i}, 0]$. In this way, away from shock regions, the AV exponentially decays to a threshold minimum value $\alpha_{\rm min}$ on a timescale $\tau_{\rm i}$. The timescale is usually chosen to ensure that the AV operates for few smoothing lengths h behind the shock, e.g. $\tau_{\rm i} = h_{\rm i}/(0.1\, c_{\rm s,i})$ (Rosswog, 2009).

A more recent, widely adopted method to construct dissipative terms within the SPH formalism is to consider approaching particles as the left and right input state for the Riemann problem[5] (Monaghan, 1997). In this way, dissipative terms aimed at capturing discontinuities can be related to jumps in variables that occur across shocks and contact discontinuities. Following Rosswog (2009), for a conserving scalar variable $\mathcal{A}$ a dissipative term should be included as a further contribution in the equation that describes its evolution. This dissipative term is modelled for each particle as:

$$\left(\frac{{\rm d}\mathcal{A}_{\rm i}}{{\rm d}t}\right)_{\rm diss} = \sum_{\rm j=1}^{\rm N_{ngb}} \frac{m_{\rm j}}{\bar{\rho}_{\rm ij}}\, \alpha_{\rm i}^{\mathcal{A}}\, v_{\rm i}^{\rm sign}\, (\mathcal{A}_{\rm i} - \mathcal{A}_{\rm j})\, \hat{e}_{\rm ij} \cdot \nabla_{\rm i} W_{\rm ij} \ , \tag{4.45}$$

[5]The Riemann problem is an initial value problem that consists of two constant different states, separated by a single discontinuity (e.g. Toro, 1997). It is often analysed by means of the Sod shock tube test. In this case, a first dense and overpressurised medium (on the left) is initially separated by a second rarefied gas through a wall, that is later removed. The solution is represented by a shock wave moving to the right, a rarefaction fan traveling towards the opposite direction, and a contact discontinuity in between.

where $\hat{e}_{ij} = \mathbf{x}_{ij}/|\mathbf{x}|_{ij}$ is the unit vector from particle j to i, and the local signal velocity v_i^{sign} is the maximum value that the pairwise signal velocity v_{ij}^{sign} (see below) assumes within the smoothing length h_i among different particle pairs. In equation (4.45), $\alpha_i^{\mathcal{A}}$ determines the amount of dissipation (see Section 5.2 for possible formulations).

Considering equation (4.32), the term $(d\mathbf{v}_i/dt)_{diss}$ that should be added to non-dissipative contributions on the right-hand side reads:

$$\left(\frac{d\mathbf{v}_i}{dt}\right)_{diss} = \sum_{j=1}^{N_{ngb}} \frac{m_j}{\bar{\rho}_{ij}} \left(\alpha_{ij}\, v_{ij}^{sign}\, \mathbf{v}_{ij} \cdot \hat{e}_{ij}\right) \nabla_i W_{ij} \ , \tag{4.46}$$

where the signal velocity for the diffusion of the momentum can be cast as $v_{ij}^{sign} = c_{s,i} + c_{s,j} - \mathbf{v}_{ij} \cdot \hat{e}_{ij}$ (Monaghan, 1997). This term quantifies the effect of the AV and is proportional to the velocity jump along the direction that joins the particles (the component $\mathbf{v}_{ij} \cdot \hat{e}_{ij}$ is the only one that varies during a shock). Moreover, $\alpha_{ij} = (\alpha_i + \alpha_j)/2$; a possible expression for this numerical coefficient can be found in Section 5.2.

The contribution from dissipative terms to the evolution of the specific thermal energy in equation (4.34) reads:

$$\left(\frac{du_i}{dt}\right)_{diss} = -\sum_{j=1}^{N_{ngb}} \frac{m_j}{\bar{\rho}_{ij}} \left[\alpha_{ij}\, v_{ij}^{sign}\, \frac{1}{2} \left(\mathbf{v}_{ij} \cdot \hat{e}_{ij}\right)^2 + \alpha_{ij}^{c}\, v_{ij}^{sign,c} \left(u_i - u_j\right)\right] \hat{e}_{ij} \cdot \nabla_i W_{ij} \ , \tag{4.47}$$

where the signal velocity for the diffusion of thermal energy due to the AC is modelled according to Price (2008) as: $v_{ij}^{sign,c} = \sqrt{|P_i - P_j|/\bar{\rho}_{ij}}$. This latter estimate can be eventually corrected so as to account for the presence of a gravitational potential inducing pressure gradients (see Section 5.2 and Beck et al., 2016). Once again, $\alpha_{ij}^{c} = (\alpha_i^{c} + \alpha_j^{c})/2$; a viable functional form for this numerical coefficient can be found in Section 5.2. In equation (4.47), two terms contribute to the dissipation of thermal energy: the first accounts for artificial viscosity and is always positive, since the gradient of the smoothing kernel is negative.

The second contribution is an artificial conduction (AC) term. It represents an artificial thermal diffusion, as it describes an exchange of thermal energy between close particles. Its effect is a smoothing of discontinuities in thermal energy (e.g. at contact discontinuities). The inclusion of the AC turns out to be crucial to properly describe hydrodynamical instabilities in SPH. Accurately following hydrodynamical instabilities in SPH, thus ensuring the mixing of different gas components, has been challenging for long time (e.g. Agertz et al., 2007; Price, 2008). The reason for this stems from the difficulty to treat contact discontinuities: fluids with density and temperature contrast across them are indeed prevented from mixing because of a spurious surface tension. This lack of mixing prevents the development of fluid instabilities such as the Kelvin-Helmholtz instability for several characteristic timescales. The inclusion of an AC term in the energy equation (as the one in equation (4.47) discussed above; see also Section 5.2) results effective in suppressing the spurious surface tension and guarantees fluid phase mixing (Price, 2008, 2012a; Beck et al., 2016; Springel, 2016).

Another critical aspect of the SPH technique is the accuracy of the fluid sampling. Within this context, a fundamental role is played by the kernel function and number of neighbours adopted. Increasing arbitrarily the number of neighbours to reduce the error in the estimate of fluid quantities does not turn out to be the right solution: commonly adopted kernels are indeed prone to pairing instability (Schuessler & Schmitt, 1981; Price, 2012a). This instability develops when a neighbour particle is located close enough to the target particle that the repulsive force between the particle pair approaches zero (due to the shape of the kernel gradient). As a consequence, the particles merge and the fluid becomes clumpy. Therefore, higher-order kernel functions have been proposed, aimed at suppressing the possible development of pairing instability (Read et al., 2010; Dehnen & Aly, 2012; Beck et al., 2016, and Section 5.2).

In the following Chapter, I will describe the features of SPH included in the code GADGET3 that I adopt to perform cosmological hydrodynamical simulations. Also, astrophysical processes that alter the gas thermodynamics and that have not been considered so far will be taken into account.

5

The simulations setup

The aim of this Chapter is to introduce in detail the essentials of the simulations that I carried out. I will outline the main features of the code used (Section 5.1), with particular emphasis on the scheme with which it solves the equations of hydrodynamics (Section 5.2). The focus is then on the astrophysical processes that alter the hydrodynamics and that are not explicitly resolved (Sections 5.3 and 5.4): I will give an overview of the numerical modelling of radiative cooling, star formation, stellar feedback, and the chemical enrichment process, and introduce the sub-resolution model to which my simulations resort. Finally, the initial conditions of the simulations presented in the following Chapters are introduced in Section 5.5.

Contents

5.1 The code

The cosmological hydrodynamical simulations that I have carried out use a version of the GADGET3 code, a non-public evolution of the GADGET2 code

(Springel, 2005). It is a TreePM+SPH code (see Sections 4.1 and 4.3): short-range interactions are computed via a Tree algorithm, while the PM method is employed to retrieve long-range forces, and is further enhanced with an adaptive, secondary mesh level. Both collisionless (DM and stars) and collisional (gas) fluids are sampled with particles. In this Section I outline the main features of the code that are of interest for the discussion of the results that will be presented in Chapters 6, 7, 8, and 9. A thorough description of the code, of its performance and capabilities can be found in Springel (2005).

In this version of the code, the smoothing length $h_{\rm i}$ is adaptive and spatially dependent, as it varies on a particle-by-particle basis, as shown by equations (4.36), (4.37), and (4.38). Also, the formulation of SPH is symmetric with respect to the smoothing lengths of particle pairs, as explained in Section 4.4.

In its standard version (*standard* as opposite to *improved*, see Section 5.2), GADGET3 adopts an artificial viscosity (AV) term provided by equation (4.41), whose effect is controlled by the Balsara switch (equation 4.43), as discussed in Section 4.4. Also, the standard flavour of SPH does not account for artificial conduction (AC).

The density distribution function $\widetilde{\delta}(\mathbf{x}_{\rm i})$ of each particle is represented by the Dirac δ–function convolved with a normalised gravitational softening kernel $W_{\rm ij}$ of comoving length ε. To this end, $\widetilde{\delta}(\mathbf{x}_{\rm i}) = W_{\rm ij}(|\mathbf{x}_{\rm i} - \mathbf{x}_{\rm j}|, 2.8\,\varepsilon)$. A cubic spline kernel (Monaghan & Lattanzio, 1985) is employed, whose functional form is:

$$W(|\mathbf{x}_{\rm i} - \mathbf{x}_{\rm j}|, h) = W(q) = \frac{8}{\pi\, h^3} \begin{cases} 1 - 6\,q^2 + 6\,q^3 & \text{for } \; 0 \leq q \leq 1/2 \;\; , \\ 2\,(1-q)^3 & \text{for } \; 1/2 < q \leq 1 \;\; , \\ 0 & \text{for } \; q > 1 \;\; . \end{cases} \tag{5.1}$$

Here, $q = x_{\rm ij}/h$, i.e. the ratio of the module of the distance between two particles $x_{\rm ij} = |\mathbf{x}_{\rm i} - \mathbf{x}_{\rm j}|$ and the smoothing scale h. The code uses the same kernel function as smoothing kernel[1] for SPH. Therefore, the smoothing scale h is proportional to the gravitational softening ε ($h = 2.8\,\varepsilon$, for the gravitational kernel), and is represented by the smoothing length for gas particles (i.e. $h = h_{\rm i}$ for SPH, see Section 4.3). As a consequence, the actual resolution of the simulation amounts to $2.8\,\varepsilon$, where ε is the formal resolution described by the gravitational softening (Springel et al., 2001; Springel, 2005). Under this assumption, the Newtonian potential of a point mass m is $-Gm/\varepsilon$, the same as that of a Plummer sphere (Plummer, 1911; Binney & Tremaine, 2008) of Plummer scale length $\varepsilon_{\rm Pl}$. This piece of information will be exploited in Sections 8.3.1 and 8.3.4.

GADGET3 adopts an entropy-density and entropy-conserving formulation of SPH (Hernquist, 1993; Springel & Hernquist, 2002). The thermodynamical variable

[1]Note that the scale beyond which the kernel function vanishes depends on the convention adopted. For instance, the cubic spline introduced in equation (4.22) in Section 4.3 becomes null whenever $x_{\rm ij} > 2\,h$, while the cubic spline adopted in the original version of GADGET3 drops to zero when $x_{\rm ij} > h$.

that it integrates is the specific entropy s instead of the specific energy u. In particular, the entropic function $A(s)$ is what GADGET3 is designed to integrate. This is a monotonic function of the specific entropy s of each particle:

$$s = \frac{\ln(P/\rho^{\gamma})}{(\gamma - 1)} \ , \tag{5.2}$$

and is defined as:

$$A(s) \coloneqq P/\rho^{\gamma} \ , \tag{5.3}$$

P, ρ, and γ being the pressure and the density of the particle, and the adiabatic index, respectively. It is related to the specific internal energy u by:

$$u = \frac{A(s)\,\rho^{(\gamma-1)}}{\gamma - 1} \ . \tag{5.4}$$

This formulation ensures that the specific entropy only grows in time (neglecting the possible sink term from cooling), it allows to achieve a superior numerical control of entropy source and sink terms, and better captures shocks (see Springel & Hernquist, 2002, for a detailed discussion).

The choice of the time-step plays a significant role in determining the accuracy of the numerical integration, and different options affect the computational efficiency. GADGET3 allows to compute individual and adaptive time-steps for particles, and evolves fluid properties by advancing particles in bunches.

For each SPH particle, the hydrodynamical time-step reads:

$$\Delta t_{\mathrm{i,\,hydro}} = \frac{C_{\mathrm{Courant}}\, h_{\mathrm{i}}}{v_{\mathrm{i}}^{\mathrm{sign}}} \ , \tag{5.5}$$

where C_{Courant} is the Courant factor, and the local signal velocity $v_{\mathrm{i}}^{\mathrm{sign}}$ is the maximum value that the pairwise signal velocity $v_{\mathrm{ij}}^{\mathrm{sign}}$ (see Section 4.4, and also equation (5.11) and Section 5.2) assumes within the smoothing length h_{i} among different particle pairs. In all the simulations presented in this Thesis, $C_{\mathrm{Courant}} = 0.15$.

For each particle, the code considers the minimum among the constraints on the time-step. To this end, the time-step Δt_{i} of a gas particles is the minimum between the hydrodynamical time-step, the local dynamical time ($\propto (G\,\rho)^{-1/2}$), and the time proportional to the ratio $\sigma_{\mathrm{i}}/|\mathbf{a}_{\mathrm{i}}|$, where σ_{i}^2 is the local velocity dispersion and $\mathbf{a}_{\mathrm{i}}$ the particle's acceleration. Should the particle be collisionless, the minimum of the two latter times is considered.

The global simulation time τ_{tot} is decomposed in power-of-two timebins, so that the minimum allowed time-step is $\Delta t_{\mathrm{min}} = (\tau_{\mathrm{tot}} - \tau_0)/2^{\mathrm{K}}$. Here, τ_0 is the starting time of integration and K is chosen so that 2^K is the highest integer number allowed by the machine. In this way, the time-step at the step n is $\Delta t_{\mathrm{n}} = (\tau_{\mathrm{tot}} - \tau_0)/2^{k_{\mathrm{n}}}$, with $k_{\mathrm{n}} < K$.

Particles are assigned to the timebin that is the nearest to their time-step. The integration starts considering the particles in the minimum among the populated timebins. At a given step n, those particles with the smallest time-step are called *active* and have their physical properties updated, while other particles with a longer time-step are *inactive* and will be considered only for later integrations. Indeed, as the simulation time goes on, the code continues to integrate the smallest time-steps $\Delta t_{\rm n}$ until a simulation time corresponding to $\Delta t_{\rm n-1}$ is reached: from then on, particles populating the immediately larger timebin become active, too, their time-step being $\Delta t_{\rm n-1}$. If all the particles were evolved with the smallest time-step, too large computational resources would be indeed required. On the other hand, the aforementioned procedure accounts for the large dynamic range of time-steps and ensures a high accuracy of the numerical integration within higher-density and highly dynamical regions, such as the innermost regions of forming galaxies. Determining whether particles are active or inactive is remarkably important for the accuracy of the integration and, thus, of the fluid sampling (see Section 5.2).

So far, I have summarised the main features of the code that I have adopted to carry out simulations. Some of the characteristics discussed above have been improved by an advanced formulation of SPH (see Section 5.2). Also, so far I have not considered astrophysical processes that alter the thermodynamics of the gas and that will be addressed in Sections 5.3 and 5.4.

5.2 Improved SPH formulation

The simulations that I carried out benefit from an advanced formulation of SPH. In this Section I briefly recall the main features of this implementation. It has been introduced by Beck et al. (2016, where further details can be found), and improves significantly the standard SPH implemented in the original version of the code (Section 5.1).

SPH interpolation is carried out by using a Wendland C^4 kernel function (Dehnen & Aly, 2012) with $N_{\rm ngb} = 200$ neighbours, instead of the standard cubic spline (with 64 neighbours; see equation (5.1) in Section 5.1). The functional form of the new interpolating function reads:

$$C^4(q) \; = \; \frac{495}{32\,\pi}(1-q)^6(1+6\,q+\frac{35}{3}\,q^2) \; . \tag{5.6}$$

Here, $C^4(q) = h_{\rm i}^3\,W_{\rm ij}(x_{\rm ij}, h_{\rm i})$, where $q = x_{\rm ij}/h_{\rm i}$, $x_{\rm ij} = |\mathbf{x}_{\rm i} - \mathbf{x}_{\rm j}|$, and $h_{\rm i}$ is the smoothing length. $W_{\rm ij}$ is the smoothing kernel (Section 4.3). Whenever $q > 1$, $C^4(q) = 0$. The smoothing is adaptive, such that the product $h_{\rm i}^3\,\rho_{\rm i}$, with $\rho_{\rm i}$ the density of the ith particle, keeps roughly constant. Thanks to this improvement, pairing instability is avoided (Dehnen & Aly, 2012) and a gain in accuracy in quantity estimates over the standard cubic spline is achieved.

Besides the new kernel function, the most important improvements in this new formulation of SPH mainly consist in the inclusion of AC, and in an advanced treatment of AV.

The AC term is implemented so as to promote the diffusion of entropy among particles at contact discontinuities, thus removing the spurious surface tension (see Section 4.4). As a result, it allows to follow hydrodynamical instabilities more efficiently than in standard SPH. The contribution of AC to the equation of the specific internal energy (i.e. to equation (4.34)) reads:

$$\left(\frac{\mathrm{d}u_\mathrm{i}}{\mathrm{d}t}\right)_\mathrm{AC} = -\frac{1}{2}\sum_{\mathrm{j}=1}^{\mathrm{N_{ngb}}} \frac{m_\mathrm{j}}{\bar{\rho}_\mathrm{ij}} \left(u_\mathrm{i} - u_\mathrm{j}\right) \alpha_\mathrm{ij}^\mathrm{c}\, v_\mathrm{ij}^\mathrm{sign,c}\, \bar{F}_\mathrm{ij} \ , \tag{5.7}$$

where $\bar{\rho}_\mathrm{ij} = (\rho_\mathrm{i}+\rho_\mathrm{j})/2$. The term $\bar{F}_\mathrm{ij} = [F_\mathrm{ij}(h_\mathrm{i})+F_\mathrm{ij}(h_\mathrm{j})]/2$ represents the symmetrised scalar part of the kernel gradient, which is defined as $F_\mathrm{ij}(h_\mathrm{i})\,\mathbf{x}_\mathrm{ij}/x_\mathrm{ij} = \nabla_\mathrm{i} W_\mathrm{ij}(h_\mathrm{i})$.

In equation (5.7), $\alpha_\mathrm{ij}^\mathrm{c} = (\alpha_\mathrm{i}^\mathrm{c} + \alpha_\mathrm{j}^\mathrm{c})/2$ is the symmetrised AC coefficient. It depends on the gradient of thermal energy, with:

$$\alpha_\mathrm{i}^\mathrm{c} \ = \ -\frac{h_\mathrm{i}}{3}\frac{|\nabla u|_\mathrm{i}}{|u_\mathrm{i}|} \ . \tag{5.8}$$

The signal velocity $v_\mathrm{ij}^\mathrm{sign,c}$ used in the AC is given by (Price, 2008):

$$v_\mathrm{ij}^\mathrm{sign,c} = -\sqrt{\frac{|P_\mathrm{i} - P_\mathrm{j}|}{\bar{\rho}_\mathrm{ij}}} \ , \tag{5.9}$$

and a limiter on the AC is included to correct the total thermal pressure gradient for the presence of gravitationally induced pressure gradients. Indeed, the amount of the contribution of AC in equation (5.7) depends on the gradients of internal energy (equation (5.8)) and of pressure (equation (5.9)). Should the thermal pressure gradient be determined by gravitational forces (e.g. in the case of hydrostatic equilibrium), this method would lead to an unwanted conduction. Therefore, the contribution of hydrostatic equilibrium to the total thermal pressure gradient is quantified and the amount of conduction is limited (see Beck et al., 2016, for further details).

The inclusion of the AV correction (Cullen & Dehnen, 2010; Beck et al., 2016) allows to suppress AV far from shocks and where unwanted (see Section 4.4). The AV contribution to the equation of motion, that has to be added to the non-dissipative terms (i.e. to equation (4.32)), is taken into account according to:

$$\left(\frac{\mathrm{d}\mathbf{v}_\mathrm{i}}{\mathrm{d}t}\right)_\mathrm{AV} = \frac{1}{2}\sum_{\mathrm{j}=1}^{\mathrm{N_{ngb}}} \frac{m_\mathrm{j}}{\bar{\rho}_\mathrm{ij}} \left(\mathbf{v}_\mathrm{j} - \mathbf{v}_\mathrm{i}\right) \alpha_\mathrm{ij}\, \bar{f}_\mathrm{ij}\, v_\mathrm{ij}^\mathrm{sign}\, \bar{F}_\mathrm{ij} \ , \tag{5.10}$$

where $\bar{f}_\mathrm{ij}$ is the symmetrised Balsara switch (see equation (4.43) and Section 4.4). In equation (5.10), $v_\mathrm{ij}^\mathrm{sign}$ is the pairwise signal velocity, i.e.:

$$v_\mathrm{ij}^\mathrm{sign} = c_\mathrm{s,i} + c_\mathrm{s,j} + \beta\mu_\mathrm{ij} \ , \tag{5.11}$$

where $c_{s,i}$ is the sound speed of each particle, $\mu_{ij} = \mathbf{v}_{ij} \cdot \mathbf{x}_{ij}/x_{ij}$ and $\beta = 3$. Also, $\alpha_{ij} = (\alpha_i + \alpha_j)/2$, and α_i is an adaptive viscosity coefficient (Morris & Monaghan, 1997). It is time-dependent and makes viscosity decay away from shocks according to:

$$\dot{\alpha}_i = (\alpha_i^{loc} - \alpha_i) \frac{v_i^{sign}}{\ell\, h_i} , \tag{5.12}$$

$\ell = 4.0$ being the adopted decay scale length. Also, α_i^{loc} is the local value for the viscosity coefficient (Cullen & Dehnen, 2010), defined as:

$$\alpha_i^{loc} = \alpha_{max} \frac{h_i^2 A_i}{h_i^2 A_i + (v_i^{sign})^2} . \tag{5.13}$$

In equation (5.13), $\alpha_{max} = 3$, $A_i = \xi_i \max(0, -(\nabla \cdot \mathbf{v})_i)$ is a directional shock indicator, $\xi_i = |2(1 - R_i)^4 (\nabla \cdot \mathbf{v})_i|^2 / (|2(1 - R_i)^4 (\nabla \cdot \mathbf{v})_i|^2 + |\nabla \times \mathbf{v}|_i^2)$ and $R_i = (\sum_j \text{sign}(\nabla \cdot \mathbf{v})_j) m_j W_{ij})/\rho_i$ is a factor that reveals the presence of a shock (see Beck et al., 2016). However, if $\alpha_i < \alpha_i^{loc}$, then $\alpha_i = \alpha_i^{loc}$ rather than decaying according to equation (5.12). In equations (5.12) and (5.13), v_i^{sign} is the local signal velocity, that is the maximum value that the pairwise signal velocity v_{ij}^{sign} assumes within the smoothing length h_i among different particle pairs.

Moreover, new second-order estimates for velocity gradients and curl operators are adopted to improve the computation of the Balsara switch (see equation (4.43)) and of the aforementioned factors that reveal the presence of a shock, thus better controlling the action of AV.

Finally, the contribution of AV to the equation of the specific internal energy reads:

$$\left(\frac{du_i}{dt}\right)_{AV} = -\frac{1}{2} \sum_{j=1}^{N_{ngb}} \frac{m_j}{\bar{\rho}_{ij}} (\mathbf{v}_j - \mathbf{v}_i)^2 \alpha_{ij} \bar{f}_{ij} v_{ij}^{sign} \bar{F}_{ij} . \tag{5.14}$$

Moreover, in this enhanced implementation a time-step limiting particle wake-up scheme (see Beck et al., 2016, and references therein for a thorough description) has been adopted: it alleviates large differences in the size of time-steps among nearby particles. Indeed, the code integrates quantities of different particles on an individual particle time-step basis: single time-steps are computed according to hydrodynamical properties of particles, and particles are sliced into active and inactive particles (Section 5.1). However, inactive particles in underdense regions may not be able to realise an abrupt variation of entropy or velocity of a nearby active particle, and to act accordingly. As a spurious net result, inactive particles are prone to gathering and clumping in regions where they remain almost fixed. The wake-up scheme acts in the following way: by comparing the signal velocity v_{ij}^{sign} between particles i and its neighbour j to the maximum signal velocity of j and any possible contributing particle within its smoothing length (i.e. v_j^{sign}), an inactive neighbouring particle can be promoted to be active if $v_{ij}^{sign} > f_w v_j^{sign}$, where $f_w = 3$ has been adopted from hydrodynamical tests (Beck et al., 2016). In this way, time-steps of some particles that were inactive are adapted according

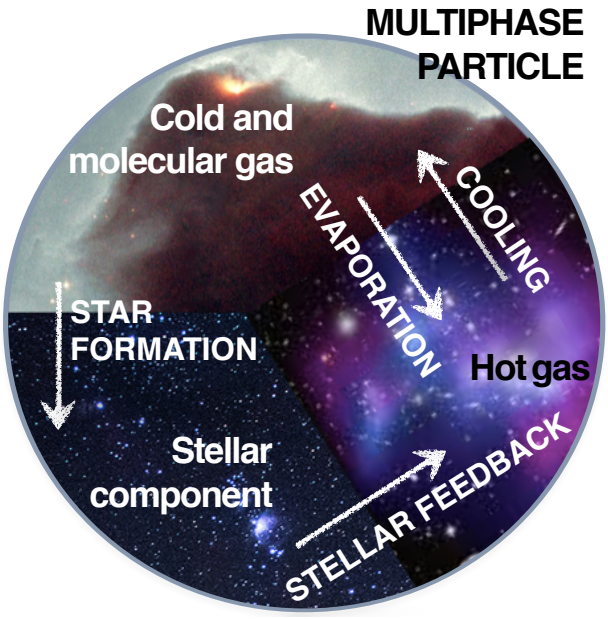

Figure 5.1: Cartoon showing the composition of a multiphase gas particle within the MUPPI model. Mass and energy flows among different components are highlighted with arrows.

to the local signal velocity $v_{\rm j}^{\rm sign}$ and just woken-up particles are then taken into account in the current time-step.

All the simulations that I carried out and whose results I will present in the following Chapters adopt the improved formulation of SPH that I have discussed in this Section, except the simulations aimed at quantifying the impact of the hydrodynamic solver in Chapter 6. These ones encode in their name the suffix *oldH*.

5.3 The model of star formation and stellar feedback

Simulations presented in this Thesis resort to the sub-resolution model MUPPI (MUlti Phase Particle Integrator) to describe processes such as hot gas cooling, star formation and stellar feedback that occur on scales not explicitly resolved. In this Section, I outline the most relevant features of the model, while a more comprehensive description and further details can be found in the introductory papers by Murante et al. (2010, 2015).

The sub-resolution model MUPPI represents a multiphase ISM and accounts for star formation and stellar feedback, both in thermal and kinetic forms. The constitutive element of the model is the multiphase particle: it is made up of a hot and a cold gas component in pressure equilibrium, and a possible further stellar component (see Figure 5.1). Considering a multiphase particle whose total mass is $M_{\rm P}$, the mass of its hot, cold, and stellar components are $M_{\rm h}$, $M_{\rm c}$, M_*, respectively. The pressure equilibrium between the hot and cold phases implies that

$$n_{\rm h}\, T_{\rm h} = n_{\rm c}\, T_{\rm c} \ , \tag{5.15}$$

where $n_{\rm h}$, $T_{\rm h}$, $n_{\rm c}$, and $T_{\rm c}$ are the number density and temperature of the hot and cold phases, respectively.

A gas particle is eligible to become multiphase whenever its density rises above a density threshold and its temperature falls below a temperature threshold ($T_{\rm thresh} = 5{\cdot}10^4$ K). We choose $n_{\rm thres} = 0.01$ cm^{-3} as the particle number density threshold (see Murante et al., 2010); adopting a mean molecular weight $\mu \sim 0.6$, such a number density threshold corresponds to $\rho_{\rm thres} \simeq 1.5 \cdot 10^5$ M$_\odot$ kpc^{-3} and to a density $n_{\rm H} \sim 0.0045$ cm^{-3} for the number density of hydrogen atoms ($\log_{10}$ (n$_{\rm H\ [cm^{-3}]}$) ~ -2.3), the assumed fraction of neutral hydrogen being 0.76. Note that within MUPPI, this is *not* the density threshold for the star formation, but for enabling the gas particle to sample the multiphase ISM (see below). When a gas particle becomes multiphase, it is considered to be made of hot gas only (so that $M_{\rm h} = M_{\rm P}$, and $T_{\rm h}$ is set to the temperature of the gas particle). This hot component then cools down according to its density and metallicity (see Section 5.4), thus generating the cold component of the multiphase particle, whose temperature is fixed to $T_{\rm c} = 300$ K. The fraction of gas mass in the hot phase within the multiphase particle, labelled $F_{\rm h}$, is related to the filling factor $f_{\rm h}$ of the hot gas through:

$$f_{\rm h} = \frac{1}{1 + \frac{F_{\rm c}}{F_{\rm h}} \frac{\mu_{\rm h}}{\mu_{\rm c}} \frac{T_{\rm c}}{T_{\rm h}}} \ , \tag{5.16}$$

where $F_{\rm c} = 1 - F_{\rm h}$ is the mass fraction of cold gas, $\mu_{\rm h}$ and $\mu_{\rm c}$ are the molecular weights of the hot and cold phase, respectively. The filling factor of the cold phase is $f_{\rm c} = 1 - f_{\rm h}$. The hot gas number density is therefore computed as:

$$n_{\rm h} = \frac{\rho\, F_{\rm h}}{f_{\rm h}\, \mu_{\rm h}\, m_{\rm p}} \ , \tag{5.17}$$

where ρ is the SPH density of the gas particle, and $m_{\rm p}$ the mass of the proton. A similar relation holds for the cold number density $n_{\rm c}$.

The following set of ordinary differential equations describes mass and energy flows between the different components:

$$\dot{M}_{\rm h} = -\dot{M}_{\rm cool} + \dot{M}_{\rm ev} \ , \tag{5.18}$$
$$\dot{M}_{\rm c} = \dot{M}_{\rm cool} - \dot{M}_{\rm sf} - \dot{M}_{\rm ev} \ , \tag{5.19}$$
$$\dot{M}_{*} = \dot{M}_{\rm sf} \ , \tag{5.20}$$
$$\dot{E}_{\rm h} = \dot{E}_{\rm fb,local} - \dot{E}_{\rm cool} + \dot{E}_{\rm hydro} \ . \tag{5.21}$$

Equations (5.18), (5.19), and (5.20) describe the evolution of the hot and cold gas masses, and of the mass of the stellar component, respectively. Equation (5.21) accounts for the evolution of the thermal energy of the hot phase $E_{\rm h}$. These equations model the following processes.

Hot gas condenses into a cold phase due to radiative cooling (see Section 5.4), so that:

$$\dot{M}_{\rm cool} = \frac{M_{\rm h}}{t_{\rm cool}} \ , \tag{5.22}$$

Table 5.1: Relevant parameters of the sub-resolution model.
Column 1: number density threshold for multiphase particles. *Column 2:* temperature of the cold phase. *Column 3:* pressure at which the molecular fraction is $f_{\rm mol} = 0.5$. *Column 4:* maximum duration of a multiphase stage in units of the dynamical time of the cold phase. *Column 5:* gas particle's probability of becoming a wind particle. *Column 6:* maximum lifetime of a wind particle. *Columns 7:* half-opening angle of the cone for thermal feedback, in degrees. As for the original version of the sub-resolution model, this is also the half-opening angle of the cone for kinetic feedback.
Second line. *Columns 8 and 9:* thermal and kinetic SN feedback energy efficiencies, respectively. *Column 10:* fraction of SN energy directly injected into the hot phase of the ISM. *Column 11:* evaporation fraction. *Column 12:* star formation efficiency, as a fraction of the molecular gas. *Column 13:* number of stellar generations, i.e. number of star particles generated by each gas particle. *Column 14:* average stellar masses of stars formed per each SN II.

$n_{\rm thresh}$ ($\rm cm^{-3}$)	$T_{\rm c}$ (K)	P_0 ($\rm k_B$ K $\rm cm^{-3}$)	$t_{\rm clock}$ ($t_{\rm dyn,c}$)	$P_{\rm kin}$	$t_{\rm wind}$ (Myr)	θ (°)
0.01	300	$2 \cdot 10^4$	1	0.05	20 - $t_{\rm clock\ [Myr]}$	30

$f_{\rm fb,therm}$	$f_{\rm fb,kin}$	$f_{\rm fb,local}$	$f_{\rm ev}$	f_*	N_*	$M_{*,\rm SN}$ ($\rm M_\odot$)
0.2	0.7	0.02	0.1	0.02	4	120

where $t_{\rm cool}$ is the cooling time of the hot phase. In turn, a tiny part $f_{\rm ev}$ of the cold gas evaporates because of the destruction of molecular clouds:

$$\dot{M}_{\rm ev} = f_{\rm ev}\, \dot{M}_{\rm sf} \ , \tag{5.23}$$

$\dot{M}_{\rm sf}$ being the star formation rate (SFR, see below). I list in Table 5.1 the values for the main model's parameters adopted in the simulations that I will present in Chapters 6, 7, 8, and 9 (should these parameters be different in various simulations, I will specify the new adopted values).

As for the SFR $\dot{M}_{\rm sf}$, a fraction $f_{\rm mol}$ of the cold gas mass $M_{\rm c}$ is expected to be in the molecular phase: a portion f_* will be converted into stars. Therefore, the SFR associated to a multiphase particle is:

$$\dot{M}_{\rm sf} = f_* \frac{f_{\rm mol}\, M_{\rm c}}{t_{\rm dyn,c}} \, . \tag{5.24}$$

Here, $t_{\rm dyn,c} = [3\,\pi/(32\,G\,\rho_{\rm c})]^{1/2}$ is the dynamical time of the cold phase. The SFR is directly proportional to the molecular fraction $f_{\rm mol}$, that is computed according to the phenomenological prescription by Blitz & Rosolowsky (2006, see Section 2.4.1):

$$f_{\rm mol} \ = \ \frac{1}{1 + P_0/P} \ , \tag{5.25}$$

where P is the hydrodynamic pressure of the gas particle and the parameter P_0 (i.e. the pressure of the ISM at which $f_{\rm mol} = 0.5$) is derived from observations. The galaxy sample of Blitz & Rosolowsky (2006), for instance, suggests that values of $P_0/{\rm k_B}$, $k_{\rm B}$ being the Boltzmann constant, range between $0.4{\cdot}10^4$ and $7.1{\cdot}10^4$ K cm^{-3}: we adopt a constant value $P_0/{\rm k_B} = 2 \cdot 10^4$ K cm^{-3} (see Table 5.1), that is in keeping with observations. According to equation (5.25), the hydrodynamic pressure of a gas particle is used to estimate the ISM pressure entering in the phenomenological relation by Blitz & Rosolowsky (2006). Equation (5.25) can be used to estimate an effective density threshold for the star formation, $n_{\rm thresh,sf}$, as follows. Assuming the latter threshold as the number density of the cold gas phase for which $f_{\rm mol} = 0.5$, and considering $P_0/{\rm k_B} = 2 \cdot 10^4$ K cm^{-3} and $T_{\rm c} = 300$ K (see Table 5.1), then equation (5.25) implies that $n_{\rm thresh,sf}\, T_{\rm c} = 2 \cdot 10^4$ K cm^{-3}, so that $n_{\rm thresh,sf} \simeq 66.7$ cm^{-3}. This number density is by far higher than $n_{\rm thres}$, that rather represents the number density threshold for a particle to become multiphase, as discussed above. As a consequence, multiphase particles with low pressure are characterised by very low SFR.

Star formation is implemented according to the stochastic model introduced by Springel & Hernquist (2003). A multiphase gas particle with initial mass $M_{\rm gas,init}$ can generate a star particle of mass $M_{*,\rm init}$ if the probability:

$$p = \frac{M_{\rm gas,init}}{M_{*,\rm init}} \left[1 - \exp\left(-\frac{\Delta M_*}{M_{\rm gas,init}} \right) \right] , \tag{5.26}$$

exceeds a randomly generated number in the interval $[0, 1]$. In equation (5.26), ΔM_* is the mass of the multiphase particle that has been converted into stars in a time-step according to equation (5.24). Each star particle is spawned with mass $M_{*,\rm init} = M_{\rm gas,init}/N_*$, N_* being the number of stellar generations, i.e. the number of star particles generated by each gas particle. Note that $M_{\rm P} < M_{\rm gas,init}$ if the gas particle has already spawned stars. Also, $M_{*,\rm init}$ is the mass of the new *star particle* that is generated and should *not* be confused with M_*, that is the mass of the *stellar component within* the multiphase particle itself. The mass of the star particle that is generated is subtracted from the mass of the stellar component M_* of the spawning multiphase particle; should M_* be smaller than $M_{*,\rm init}$, additional mass is taken from the cold phase $M_{\rm c}$ (see Murante et al., 2010, for details). The number N_* is a free parameter of the model: we choose $N_* = 4$ in order to have an accurate representation of the star formation process, but no significant variations are observed for small deviations from this number (Tornatore et al., 2007).

Equation (5.21) describes the evolution of the thermal energy of the hot gas, that is related to the hot gas temperature by:

$$T_{\rm h} = \frac{E_{\rm h}}{M_{\rm h}} \frac{(\gamma - 1)\, \mu_{\rm h}\, m_{\rm p}}{k_{\rm B}} , \tag{5.27}$$

where $\gamma = 5/3$ is the adiabatic index and $k_{\rm B}$ is the Boltzmann constant. The right-hand side of equation (5.21) shows that two sources of energy counterbalance

the cooling process ($\dot{E}_{\rm cool} = E_{\rm h}/t_{\rm cool}$). The first is the energy rate directly injected into the hot phase by SN explosions within the multiphase particle itself (therefore, *locally*):

$$\dot{E}_{\rm fb,local} = f_{\rm fb,local}\, E_{\rm SN}\, \frac{\dot{M}_{\rm sf}}{M_{*,\rm SN}} \quad , \tag{5.28}$$

where $E_{\rm SN} = 10^{51}$ erg is the energy provided by each SN, $f_{\rm fb,local}$ a feedback efficiency, and $M_{*,\rm SN}$ is the mass in stars that is required, on average, to have a single SN II event (it depends on the assumed IMF; see Table 5.1 for the adopted value).

The second source term is $\dot{E}_{\rm hydro}$: it accounts for the energy contributed by neighbour particles because of thermal and kinetic feedback from dying massive stars (see below), and also considers shocks and heating or cooling due to gravitational compression or expansion of gas.

Stellar feedback is taken into account both in thermal (Murante et al., 2010) and kinetic (Murante et al., 2015) forms. As for thermal feedback, each star-forming particle delivers to neighbours the following amount of thermal energy in a given time-step:

$$\Delta E_{\rm fb,therm} = f_{\rm fb,therm}\, E_{\rm SN}\, \frac{\Delta M_*}{M_{*,\rm SN}} \quad , \tag{5.29}$$

where ΔM_* is the mass of the multiphase star-forming particle that has been converted into stars within the time-step. The star-forming particle shares its thermal feedback energy among neighbours within a cone whose half-opening angle is θ. The origin of the cone lies on the particle itself and its axis is aligned according to minus the particle's density gradient. Each energy donor weights its contribution to eligible particles using the SPH kernel $C^4(\widetilde{q}) = h_{\rm i}^3\, W_{\rm ij}(a_{\rm ij}, h_{\rm i})$ (see equation (5.6)), $h_{\rm i}$ being the smoothing length. Here, $\widetilde{q} = a_{\rm ij}/h_{\rm i}$, where the distance $a_{\rm ij}$ of the neighbour j from the axis of the cone (aligned as $-(\nabla\rho)_{\rm i}$, see Figure 5.2 for the geometry) is considered instead of the radial distance $x_{\rm ij} = |\mathbf{x}_{\rm i} - \mathbf{x}_{\rm j}|$ between particle pairs.

A gas particle exits its multiphase stage whenever its density drops below $0.2\,\rho_{\rm thresh}$ or after a maximum allowed time ($t_{\rm clock}$) given by the dynamical time of the cold gas ($t_{\rm dyn,c}$). When a gas particle exits a multiphase stage, it has a probability $P_{\rm kin}$ of being *kicked* and to become a wind particle for a time interval $t_{\rm wind}$. Both $P_{\rm kin}$ and $t_{\rm wind}$ are free parameters of the model (Table 5.1). This scheme relies on the physical idea that galactic winds are powered by SN II explosions, once the molecular cloud out of which stars formed has been destroyed. Wind particles are decoupled from the surrounding medium for the aforementioned interval $t_{\rm wind}$. During this time, they receive kinetic energy from neighbouring star-forming gas particles, as described below. The wind stage can be concluded before $t_{\rm wind}$ whenever the particle density drops below a chosen density threshold, $0.3\,\rho_{\rm thresh}$, meaning that a wind particle has finally gone away from star-forming regions.

In the original version of the model, kinetic feedback is implemented so that each star-forming particle can provide $f_{\rm fb,kin}\, E_{\rm SN}$ as feedback energy. This amount of

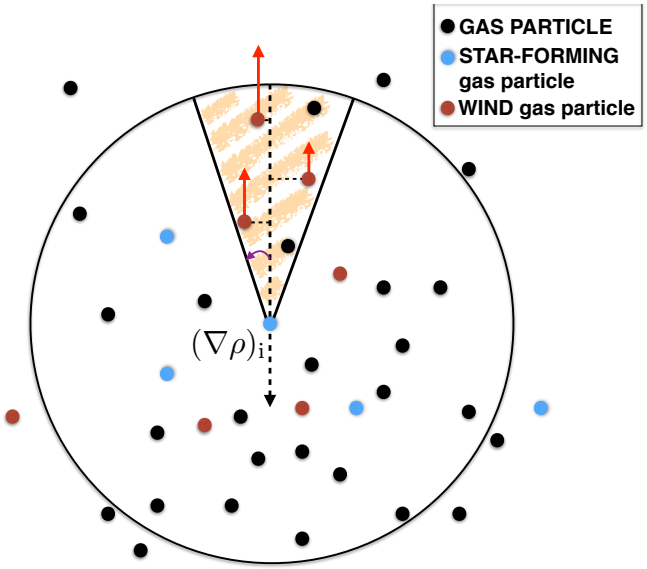

Figure 5.2: Cartoon depicting the original galactic outflow model implemented in MUPPI: each star-forming particle provides *kinetic feedback energy* to neighbour wind particles located within a cone of a given opening angle (the purple arrow highlights θ, the half-opening angle). The axis of the cone is aligned as minus the density gradient of the energy donor particle. Energy contributions are weighted according to the distance between wind particles and the axis of the cone. Figure from Valentini et al. (2017).

energy is distributed to wind particles lying inside both the cone and the smoothing length of the star-forming particle (see Figure 5.2), and the delivering mechanism is the same as the thermal scheme. Thus, outflowing energy is modelled so as to leave the star-forming particle through the least-resistance direction (Monaco, 2004). Note that only gas particles that were selected to become wind particles are allowed to receive kinetic energy. If there are no particles in the cone, the total amount of thermal energy is given to the particle nearest to the axis (Murante et al., 2010, 2015). This does not happen with the kinetic energy; in this case, if no eligible wind particle can receive it, the energy is not assigned.

The system of equations (5.18), (5.19), (5.20), and (5.21) is integrated with a Runge-Kutta algorithm within each SPH time-step (see Murante et al., 2010, 2015, for details).

The sub-resolution model that I have presented in this Section is the model that I adopted for all the simulations that I have carried out. The model has been used either in its original version or with modifications to the stellar feedback scheme: the algorithm for delivering kinetic stellar feedback energy has been indeed subject of study, as it is responsible for the triggering of galactic outflows (Chapter 6). In describing various simulation setups in the following Chapters, I will point out possible differences with respect to the reference implementation of MUPPI that I have described here.

The original release of the sub-resolution model MUPPI does not include the effect of AGN feedback. To this end, I have further enhanced the model to deal with the presence of BHs and to account for their feedback effect. I will introduce the implementation of AGN feedback within our sub-resolution model in Chapter 9.

5.4 Additional physics: cooling and chemical enrichment

Important astrophysical processes that significantly affect galaxy formation and evolution are chemical enrichment and radiative cooling, as extensively discussed in Sections 2.2 and 3.2. They are self-consistently included in the simulations that I carried out. Hot gas cooling enters the right-hand side of equation (4.11), as discussed in Section 4.2, and equations describing mass and energy flows among different gas phases within the multiphase particles, as outlined in Section 5.3.

Metal-dependent radiative cooling is implemented according to the model by Wiersma et al. (2009a). Cooling rates are estimated on an element-by-element basis, by adopting pre-computed tables where rates are functions of density, temperature, and redshift. Tables have been compiled using the spectral synthesis code CLOUDY (Ferland et al., 1998). The gas is considered to be optically thin and exposed to a spatially uniform, redshift-dependent ionising background radiation from star-forming galaxies and quasars (Haardt & Madau, 2001). When computing cooling rates, photoionization equilibrium is thus assumed (see Wiersma et al., 2009a,b, for details).

Figure 5.3 shows the contribution from different elements to the total cooling rate, as a function of the temperature. Clearly, the metal content of gas in simulations plays a crucial role: it determines the overall radiative cooling and the relative importance of different coolants. As a consequence, it impacts on the star formation (see Chapter 7).

Besides providing the ISM with energy, stellar feedback resulting from star formation and evolution also supplies heavy elements (chemical feedback), and galactic outflows foster metal spread and circulation throughout the galaxy. Our model self-consistently accounts for the chemical evolution and enrichment processes, following Tornatore et al. (2007), where a thorough description can be found. Here, I only highlight the most crucial features of the model.

Each star particle initially shares the chemical composition of the gas particle from which it has been originated. Star particles are considered to be simple stellar populations (SSPs), i.e. ensembles of coeval stars that share the same initial metallicity. By assuming an IMF (initial mass function, Section 2.4.3) and adopting predictions for stellar lifetimes and stellar yields (see below), our model carefully evaluates the number of stars aging and eventually exploding as SNe (according to a mass-dependent time-delay function), as well as the amount of

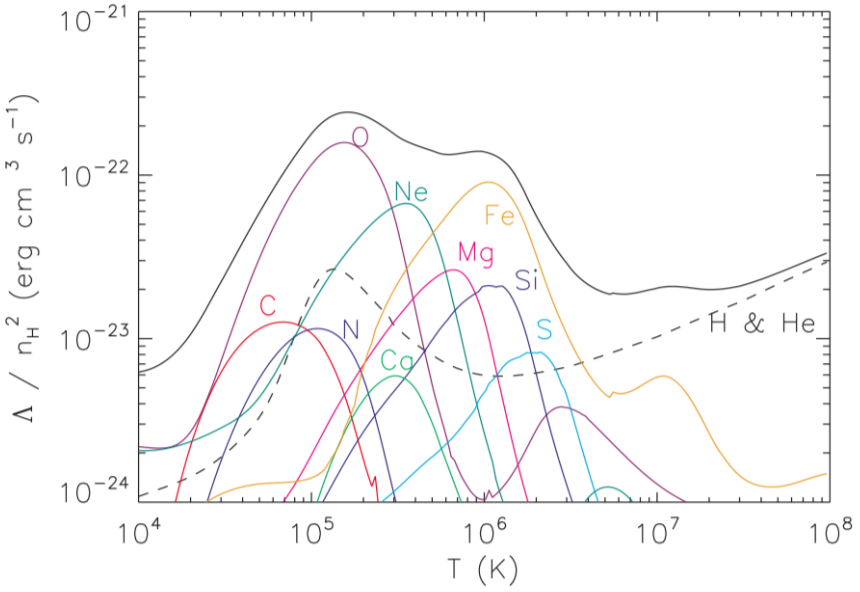

Figure 5.3: Normalised cooling rates as a function of the gas temperature, assuming photoionization equilibrium. The gas is considered to have solar abundance, hydrogen number density $n_{\rm H} = 10^{-4}$ cm^{-3}, and to be exposed to an ionising background modelled according to Haardt & Madau (2001), at redshift $z = 3$. The black solid curve shows the total cooling rate, coloured curves depict the contribution from different elements, and the black dashed curve pinpoints the hydrogen plus helium contribution. Figure from Wiersma et al. (2009a). Note that what Wiersma et al. (2009a) define as Λ is the volume cooling rate (in erg s^{-1} cm^{-3}), at variance with the formalism adopted in Sections 2.2 and 4.2.

metals polluting the surrounding ISM. The effect of the choice of the IMF is thouroughly investigated in Chapters 7 and 8.

The model accounts for different timescales of evolving stars with different masses by adopting the mass-dependent lifetimes by Padovani & Matteucci (1993). The minimum mass giving rise to stellar BHs is considered to be 8 M$_\odot$ (if not otherwise stated), and that stars that are more massive than 40 M$_\odot$ directly implode into BHs, thus not contributing to further chemical enrichment.

A fraction of stars relative to the entire mass range is assumed to be located in binary systems suitable for being progenitors of SNe Ia. The effect of the value of this fraction will be extensively explored in Chapter 7. It is set to 0.1, unless otherwise stated.

The production of different metals by aging and exploding stars is followed by assuming accurate sets of stellar yields. In simulations presented in Chapters 6, 8, and 9, for instance, I adopt the stellar yields provided by Thielemann et al. (2003) for SNe Ia and the mass- and metallicity-dependent yields by Karakas (2010) for intermediate and low mass stars that undergo the AGB (asymptotic giant branch) phase. As for SNe II, I use the mass- and metallicity-dependent yields by Woosley & Weaver (1995), combined with those provided by Romano et al. (2010). Also, the effect of adopted stellar yields will be addressed in detail in Chapter 7.

Different heavy elements produced and released by star particles are distributed to neighbouring gas particles, so that subsequently generated star particles are richer in metals. The chemical evolution process is therefore responsible for the gradual reduction of the initial mass of stellar particles, too. We follow in detail the chemical evolution of 15 elements (H, He, C, N, O, Ne, Na, Mg, Al, Si, S, Ar, Ca, Fe and Ni) produced by different sources, namely AGB stars, SNe Ia and SNe II. Each atomic species independently contributes to the cooling rate, as discussed above.

Note that the mass of gas particles is not constant throughout the simulation: the initial mass can indeed decrease due to star formation (i.e. spawning of star particles), and it can increase because of gas return by neighbour star particles.

5.5 Initial conditions

Initial conditions (ICs) for cosmological simulations consist in a distribution of particles whose positions and velocities are a realization of a density field with statistical properties set by the adopted cosmological model, i.e. in agreement with observations of the CMB. Particle positions and velocities are therefore a realization of a Gaussian random field that is completely described by the power spectrum (Section A.2). Details on the procedure adopted to generate initial conditions can be found in Dolag et al. (2008).

The ICs for all the cosmological hydrodynamical simulations whose results I will present in this Thesis describe an isolated DM halo of mass $M_{\mathrm{halo,\,DM}} \simeq 1.8 \cdot 10^{12}\ \mathrm{M}_{\odot}$ at redshift $z = 0$ (Springel et al., 2008). They are zoomed-in ICs. Zoom in is a numerical technique (see also Sections 3.1 and 3.2) that is quite convenient to achieve high resolution in cosmological simulations, while simultaneously accounting for the large scale environment and tidal interactions that influence the evolution of the simulated structure. According to this method, a parent, DM-only cosmological simulation is first carried out and evolved down to redshift $z = 0$, where the halo that one wants to focus on is identified and selected for a second, higher-resolution re-simulation. Particles out to a given distance from the centre of the target halo (generally beyond its virial radius) are pinpointed. Then they are traced back to their initial (Lagrangian) positions at high redshift: the redshift is as high as $z = 127$ for the ICs that I adopt (details in Springel et al., 2008). The positions occupied by these particles define a Lagrangian region and shape an irregular volume at high redshift, that is the volume from which the target halo formed. This volume is re-sampled with a larger number of high-resolution particles, whose mass is lower than their analogues in the parent DM-only simulation. High-resolution particles are displaced adopting the same power spectrum of the DM-only simulation, keeping both amplitudes and phases. The power spectrum adopted for generating the ICs of the parent simulation still provides the amplitude of the fluctuations, once it is extended to higher wave numbers. In the process, extra power (and thus new density fluctuations) is indeed added at small scales due to the sampling of lower frequencies with higher-resolution particles. Particles that are progressively more

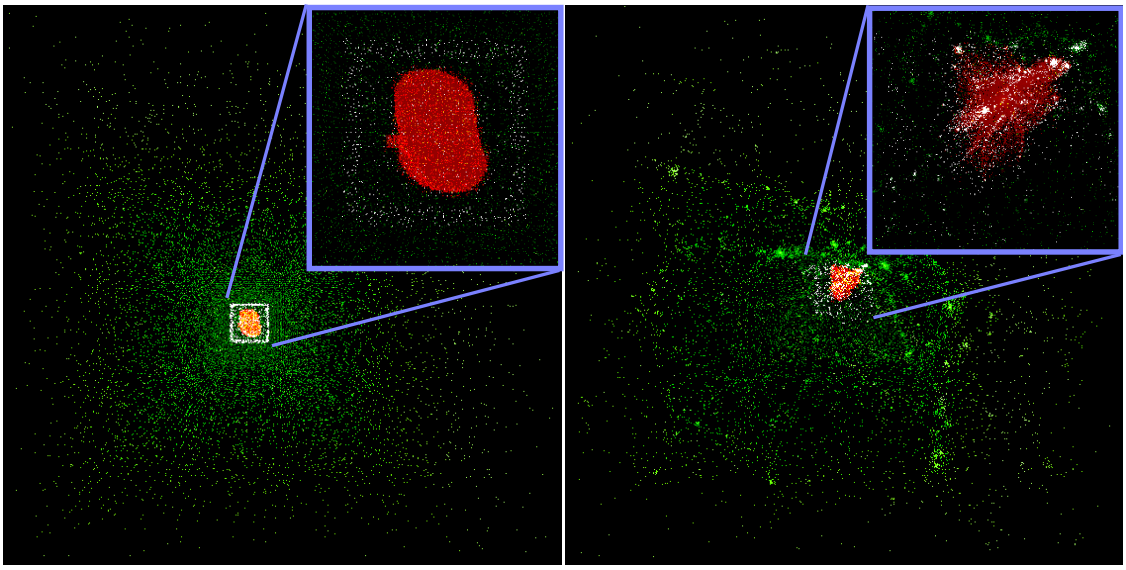

Figure 5.4: Initial ($z = 127$, *left-hand panel*) and final ($z = 0$, *right-hand panel*) density fields of the simulation box, for the simulation AqC5-newH, whose results I will show in Chapter 6. The left-hand panel illustrates the IC region for all the higher-resolution simulations that will be discussed in this Thesis (AqC5, see also Table 5.2). Green points highlight the position of the lowest-resolution DM particles. White dots pinpoint intermediate-resolution DM particles. Red points show the position of the highest-resolution DM particles. Mass of DM particles progressively decreases from green, to white, to red. The high-resolution region is the region where gas particles are added at $z = 127$. The box is 137 Mpc a side; the insets are 15 Mpc a side.

massive as the distance from the centre of the Lagrangian region increases are used to sample the remaining volume of the computational domain, in which the high-resolution particles are embedded (renormalization technique). This procedure ensures a fair accuracy in accounting for the large-scale tidal field, while saving computational resources. The mass resolution quoted for the DM component in simulations with zoomed-in ICs corresponds to the mass of the highest resolution particles. The IC region for the simulations that I carried out is shown in Figure 5.4 (left panel), where the zoom in technique is further illustrated.

Once the ICs for the DM particles are created, the baryonic component is included as follows. Each of the high-resolution DM particles is split into a DM plus a gas particle, whose relative masses are in agreement with the adopted cosmological baryon fraction ($\Omega_{\rm b}/\Omega_{\rm m} = 0.16$). In the splitting process, the centre of mass position and velocity of the new DM plus gas pairs are required to be the same as those of the parent DM particles (as in Scannapieco et al., 2012).

Our ICs are identified as *AqC* (named after the *C* halo of the *Aquarius* simulation suite) and have been first introduced by Springel et al. (2008) for the DM component. The zoomed-in region that I simulate has been selected within a cosmological volume of $100\,h^{-1}$ Mpc a side in the parent, DM-only simulation. The assumed ΛCDM cosmology is the following: $\Omega_{\rm m} = 0.25$, $\Omega_\Lambda = 0.75$, $\Omega_{\rm baryon} = 0.04$, $\sigma_8 = 0.9$,

Table 5.2: Resolution details of the ICs used for the simulations that I carried out. *Column 1:* label of the resolution level. *Column 2:* mass of DM particles. *Column 3:* initial mass of gas particles. *Column 4:* Plummer-equivalent softening length of the gravitational interaction.

Resolution level	$M_{\rm DM}$ (h^{-1} M$_\odot$)	$M_{\rm gas}$ (h^{-1} M$_\odot$)	$\varepsilon_{\rm Pl}$ (h^{-1} kpc)
AqC5	$1.6 \cdot 10^6$	$3.0 \cdot 10^5$	0.325
AqC6	$1.3 \cdot 10^7$	$4.8 \cdot 10^6$	0.650

$n_s = 1$, and $H_0 = 100\,h$ km s^{-1} Mpc^{-1} = 73 km s^{-1} Mpc^{-1}. These parameters are consistent with those provided by WMAP (Wilkinson Microwave Anisotropy Probe, Spergel et al., 2003) analysis. I adopt this cosmology throughout all the work presented in this Thesis. Albeit the adopted cosmological parameters are in tension with more recent determinations from Planck Collaboration et al. (2016a), final results of cosmological hydrodynamical simulations of galaxy formation are not sensitive to small variations of the cosmological parameters adopted. The parameter that affects the most the results is σ_8, but still, marginal variations do not impact remarkably on final results.

The *AqC* ICs are available at different resolutions: as for the simulations that I carried out, I consider an intermediate-resolution case with a Plummer-equivalent softening length for the gravitational interaction of $325\,h^{-1}$ pc (*AqC*5, according to the terminology of Springel et al. (2008)), constant in comoving units down to $z = 6$, and constant in physical units at lower redshift. Mass resolutions for DM and gas particles are as follows: DM particles have a mass of $1.6 \cdot 10^6\,h^{-1}$ M$_\odot$, while the initial mass of gas particles is $3.0 \cdot 10^5\,h^{-1}$ M$_\odot$. These pieces of information are summarised in Table 5.2.

I will also present results of lower-resolution simulations, especially to make convergence tests[2]. The ICs are referred to as *AqC*6, in this case. They have a gravitational softening of $650\,h^{-1}$ pc and the following mass resolutions: $1.3 \cdot 10^7\,h^{-1}$ M$_\odot$ for DM particles, and an initial mass of $4.8 \cdot 10^6\,h^{-1}$ M$_\odot$ for gas particles.

The mass of gas particles is not constant throughout the simulation, since the initial mass can increase due to gas return by neighbour star particles and decrease because of star formation (Section 5.3). Baryons and high-resolution DM particles occupy an irregular volume at $z = 0$ within which a sphere of radius ~ 3 Mpc can be located (this piece of information will be exploited in Section 7.4.5).

The simulated halo was selected in the parent DM-only simulation as an isolated halo, i.e. without a close massive satellite halo at redshift $z = 0$. Moreover, it does not experience major mergers at low redshift. As a consequence, it is

[2]The ICs have been generated ensuring that all the waves in the lower-resolution simulation also supply the same contribution in higher-resolution simulations. As a consequence, each structure forming in the lower resolution simulation is expected to be present at the same position also in the higher-resolution run (see Springel et al., 2008, for additional details).

expected to host a disc galaxy at redshift $z = 0$ (as predicted also by semi-analytic modelling, see Springel et al. (2008)).

Even if the mass of the *AqC* halo is similar to that of the MW ($M_{\mathrm{halo,\,DM,\,MW}} \gtrsim 1.2 \cdot 10^{12}$ $\mathrm{M}_{\odot}$ according to e.g. McMillan (2011); Zaritsky & Courtois (2017)), no specific attempts to mimic the accretion history of its dynamical environment have been made (at variance with constrained simulations, see Section 3.1). Thus, simulations that I have carried out should not be strictly interpreted as a model of our Galaxy.

Part III

Results

6

On the effect of galactic outflows in cosmological simulations of disc galaxies

The formation of disc galaxies with a limited bulge and a dominant disc component is a challenging task in cosmological simulations of galaxy formation, as discussed in Chapter 3. In this Chapter, I investigate the impact of galactic outflow modelling on the formation and evolution of a disc galaxy. Also, I quantify the strong interplay between the adopted hydrodynamical scheme and the sub-resolution model describing star formation and stellar feedback.

The key questions that I want to address in this Chapter can be summarised as follows: how much are results of a sub-resolution scheme affected by the hydrodynamic solver? How sensitive are the properties of a simulated galaxy when different galactic outflow models are implemented within the same model for star formation? What are the requirements for a galactic outflow model to lead to the formation of a late-type galaxy with a limited bulge and a dominant disc component?

This Chapter is organised as follows. Section 6.1 is devoted to outline the framework in which this Chapter fits. In Section 6.2, I provide the description of the coupling of the improved hydrodynamical scheme with the sub-resolution model that I use. I introduce the different galactic outflow models that I implemented in Section 6.3, and describe the suite of simulations in Section 6.4. In Section 6.5 I present and discuss results from cosmological simulations that lead to the formation of disc galaxies, while I draw the main conclusions in Section 6.7.

The results presented in this Chapter are described in the paper Valentini et al. (2017).

Contents

6.1 Numerical description matters

Stellar feedback triggers galactic outflows, and is a crucial component in simulations that want to investigate galaxy formation (see Section 3.4). It contributes to determine the overall evolution of galaxies (Stinson et al., 2013; Aumer et al., 2013; Marinacci et al., 2014; Murante et al., 2015), to shape their morphology (Crain et al., 2015; Hayward & Hopkins, 2017), to set their sizes and properties (Vogelsberger et al., 2014b; Schaye et al., 2015). Additionally, stellar feedback driven winds are expected to expel low angular momentum gas at high redshift from the innermost galaxy regions and to foster its following fall-back, once further angular momentum has been gained from halo gas (Brook et al., 2012; Übler et al., 2014; Teklu et al., 2015; Genel et al., 2015). Galactic outflows contribute to the continuous interaction between galaxies and their surrounding medium, and allow for the interplay between stars and different components of the ISM. Using non-cosmological simulations of isolated galaxies, Gatto et al. (2017) pointed out that strongly star-forming regions in galactic discs are indeed able to launch SN-driven outflows and to promote the development of a hot volume-filling phase. They also noted a positive correlation between outflow efficiency, i.e. the mass loading factor, and the hot gas volume-filling fraction. Moreover, Su et al. (2017) have recently shown that stellar feedback is the primary component in determining the star formation rate (SFR) and the ISM structure, and that microphysical diffusion processes and magnetic fields only play a supporting role.

Despite the general consensus on the need of stellar feedback to form spiral galaxies that are not too much centrally concentrated and have a dominant disc component, it is still unclear which are the sub-resolution models able to capture an effective description of feedback energy injection, and how to select the best ones among them. Different stellar feedback prescriptions are succeeding in promoting the formation of disc galaxies and a variety of approaches have been so far proposed to numerically describe galactic outflows (as discussed in Section 3.4).

For instance, Übler et al. (2014) contrasted galaxy formation models that adopt different stellar feedback prescriptions: a weak feedback version (Oser et al., 2010) that promotes spheroid formation, and a strong feedback scheme (Aumer et al., 2013) that favours disc formation. They also compared the predicted mass assembly histories for systems with different virial masses. Agertz & Kravtsov (2016) investigated the effect of different star formation and stellar feedback efficiencies on the evolution of a set of properties of a late-type galaxy: they highlighted that morphology, angular momentum, baryon fraction and surface density profiles are sensitively affected by the analysed parameters. A grasp on the comparison between distinct galactic outflow models would reveal vital information on the effects and consequences of diverse schemes, especially when these are implemented within the same prescriptions for star formation and cooling, in the same code.

Besides the importance of the sub-resolution prescriptions (see Section 3.4), within the Aquila comparison project Scannapieco et al. (2012) pointed out that a non-negligible role in determining the simulation results is also played by the choice of the underlying hydrodynamical scheme, either Eulerian or Lagrangian SPH.

Great effort has been therefore devoted to improving numerical techniques and enhancing hydrodynamical solvers. Advanced SPH schemes have been proposed (Price, 2008; Saitoh & Makino, 2009; Cullen & Dehnen, 2010; Dehnen & Aly, 2012; Durier & Dalla Vecchia, 2012; Pakmor et al., 2012; Price, 2012a; Valdarnini, 2012; Beck et al., 2016): modern versions of SPH adopt more accurate kernel functions, include time-step limiters and introduce correction terms, such as artificial conduction (AC) and viscosity (AV), as discussed in Section 4.4. Other enhanced SPH flavours adopt a pressure-entropy formulation, in addition (Saitoh & Makino, 2013; Hopkins, 2013; Schaller et al., 2015).

Interestingly, Schaller et al. (2015) analysed the influence of the hydrodynamic solver on a subset of the Eagle simulations. They showed that their improved hydrodynamical scheme does not affect galaxy masses, sizes and SFRs in all haloes, but the most massive ones; moreover, they highlighted that the higher the resolution is, the more responsive to the accuracy of the hydrodynamical scheme simulation outcomes are expected to be. The implementation of the SPH presented by Beck et al. (2016) has been applied to simulations of galaxy clusters by Rasia et al. (2015), who analysed the cool-core structure of clusters (see also Sembolini et al., 2016a,b; Biffi & Valdarnini, 2015).

The analysis that I present in this Chapter has been carried out with two main goals. First, the improved SPH implementation by Beck et al. (2016) has been

introduced into the code GADGET3 that I use to perform simulations of galaxy formation: I now want to test the interplay between this new SPH implementation in cosmological simulations of galaxy formation, and our sub-resolution model for star formation and stellar feedback (see Section 5.3).

Also, I explore different implementation of stellar feedback models within our scheme for star formation, to highlight the variation in the final results when only the description of galactic outflows is modified. To this end, I implement and test three different models for the production of galactic outflows (see Section 6.3), besides the standard one, and compare results.

6.2 Numerical models

In this Chapter I use the improved version of SPH presented by Beck et al. (2016), that has been implemented in the developer version of the GADGET3 code (see Sections 5.1 and 5.2), and I present simulations where the sub-resolution model MUPPI for star formation and stellar feedback is interfaced with the improved implementation of SPH. The relevant aspects of both the improved SPH scheme and of the sub-resolution model MUPPI have been introduced in Sections 5.2 and 5.3, respectively. In Sections 6.2.1 and 6.2.2, I explain how I introduced the improved version of SPH in cosmological simulations that adopt the sub-resolution model MUPPI.

6.2.1 Coupling MUPPI with the improved SPH

An important point in combining the sub-resolution model MUPPI and the SPH scheme in which an AC term is included concerns the effect of AC on the thermal structure of the ISM. I remind that AC is artificial and introduced in the energy equation to overcome intrinsic limitations of standard SPH. It does not describe a physical process involving thermal conduction. Therefore, I want to suppress, or turn-off, AC in all the unwanted situations (as described below). One of these situations concerns the description of the thermal structure of the ISM, as provided by a sub-resolution model.

In this context, I remind that our sub-resolution model MUPPI does not rely upon an effective equation of state to describe the ISM, thus I do not impose the pressure of multiphase particles to be a function of the density by adopting a polytropic equation for $P(\rho)$, as e.g. in Springel & Hernquist (2003, see also Section 3.4), and Schaye & Dalla Vecchia (2008).

Within the model MUPPI, each multiphase particle samples a portion of the ISM separately. During the multiphase stage of a particle, external properties as density and pressure can change. The hot phase of the particle can also receive energy from neighbouring star-forming particles, and from star formation occurring inside the particle itself. As a consequence, particles' average temperature can significantly

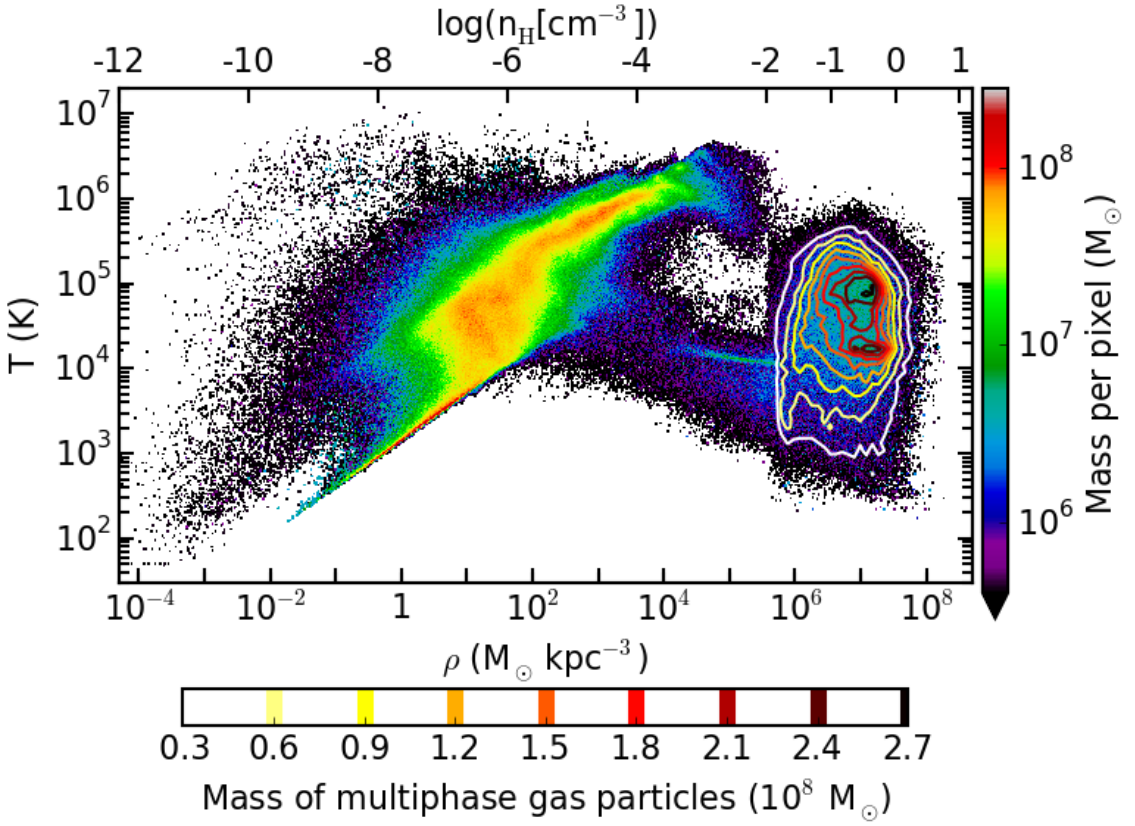

Figure 6.1: Phase diagram of all the gas particles (within the entire Lagrangian region) of the AqC5-newH simulation (see Table 6.1). Contours describe the mass distribution of multiphase particles. The phase diagram is shown at redshift $z = 0$. Colours encode the gas mass per density-temperature bin (colour scale on the right). Colours of contours are encoded as shown in the bottom colour scale. Bin size is independent for the two distributions, in order to better display the region where they overlap.

change during the multiphase stage. Since the beginning of the multiphase stage is not synchronised among neighbouring particles, they can be in different evolutionary stages and have different thermodynamical properties.

This is shown in Figure 6.1, where I analyse the mass distribution in the density-temperature phase diagram of all gas particles (within the entire Lagrangian region) for a simulation of the present suite (AqC5-newH; see Section 6.4 for a description of the simulations used in this Chapter) at redshift $z = 0$: multiphase particles (whose mass distribution is shown by contours) mainly scatter across a cloud that spans three orders of magnitude in density and almost four in temperature. The temperature plotted in Figure 6.1 is, for multiphase particles, the mass-weighted average of the (fixed) temperature of the cold phase and that of the hot phase. SPH temperature is considered for single-phase particles and the plotted density is the SPH estimate for all particles. Colours in Figure 6.1 encode the gas mass per density-temperature bin.

Clearly, such a spread would not appear if multiphase particles obeyed an effective equation of state. It is a consequence of the fact that MUPPI does not

use a solution of the equations describing the ISM obtained under an equilibrium hypothesis, as e.g. in Springel & Hernquist (2003). Instead we follow the dynamical evolution of the ISM, whose average energy depends on its past history and on the age of the sampled ISM portion. This is the reason why two neighbouring multiphase particles, having the same density, can have quite different internal energies. Note that, in the most active regions of the galaxy, the energy balance of the gas is dominated by the ISM (sub-resolution) physics, mainly via thermal feedback. The use of AC among multiphase particles would smear their properties independently of the evolution of the ISM they sample. Thus, AC must not be used when the gas particles are multiphase.

When gas particles exit their multiphase stage in MUPPI, they inherit a mean temperature that has memory of the past multiphase stage. AC between former multiphase particles and surrounding neighbours would smear local properties of the galaxy over wide regions, without preserving the peculiar thermal structure of the galaxy system that the sub-resolution model aims to account for. This is another situation where AC is clearly unwanted.

Finally, wind particles must also be excluded from AC, since we treat them as hydrodynamically decoupled from the rest of the gas. We note that, when they recouple, there can be a significant difference in internal energy with the medium where they end up.

6.2.2 A new switch for AC

Therefore, I implemented a prescription that allows AC to be active only when well-defined conditions on the physical properties of the considered particles are met:

1 - AC is switched off for both multiphase particles and wind particles as soon as they enter the wind stage.

2 - Multiphase particles that exit their multiphase stage are not allowed to artificially conduct.

3 - All the non-multiphase particles with AC off (therefore, former multiphase particles and wind particles, too) are allowed to artificially conduct again whenever their temperature differs by 20 per cent at most from the mass-weighted temperature of neighbouring particles.

Formally, the AC limiter reads as:

$$0.8 \cdot T_{\mathrm{mw,Ngb}} \leq T_{\mathrm{AC,off\rightarrow on}} \leq 1.2 \cdot T_{\mathrm{mw,Ngb}} \ , \tag{6.1}$$

where $T_{\mathrm{AC,off\rightarrow on}}$ is the temperature of the particle that is not conducting in the present time-step, while $T_{\mathrm{mw,Ngb}}$ is the mass-weighted temperature of the particle's neighbours within the smoothing length.

The physical motivation behind this switch is the following. Multiphase particles have their AC switched off, the hydrodynamics being not able to consistently describe physical processes at the unresolved scales that these particles capture. As soon as a multiphase particle exits its multiphase stage, it will retain physical properties close to the ones it had in advance for some time. For this reason, past multiphase particles keep the AC switched off. When the particle, not sampling anymore the ISM, reaches thermal equilibrium with its surrounding environment, it is allowed to artificially conduct again. We checked the dependence of our results on the exact value of the aforementioned percentage (20 per cent): we found that the precise temperature range within which a particle is allowed to conduct again (i.e. $[0.8, 1.2]$ in our default case) has not a crucial impact on the evolution of the gas, as long as it is narrow enough.

6.3 Implementation of galactic outflow models

The Murante et al. (2015) original kinetic stellar feedback implemented in MUPPI successfully produced the massive outflows required to avoid excessive star formation and resulted in a lower central mass concentration of the simulated galaxies (Barai et al., 2015; Murante et al., 2015). This stellar feedback algorithm produces realistic galactic winds, in terms of wind velocities and mass loading factor (Barai et al., 2015).

I consider here three further numerical implementations of galactic outflows: the first one (FB1 hereafter; Section 6.3.1) is based on the scheme originally proposed by Dalla Vecchia & Schaye (2012), the second one (FB2 hereafter; Section 6.3.2) is a modified version of the Murante et al. (2015) original kinetic stellar feedback in MUPPI, where particles that are eligible to produce galactic outflows are selected according to a different prescription. The third one (FB3 hereafter; Section 6.3.3) is a new and distinct model, where the mass loading factor is directly imposed. This third scheme is similar in spirit to that proposed by Springel & Hernquist (2003), adapted to our ISM model.

The main aim in introducing these three additional schemes is to verify how sensitive the general properties of the simulated galaxy are to the way in which outflows are modelled, while keeping initial conditions (ICs), simulation code, and star formation model all fixed. Moreover, I want to investigate how two popular outflow models, namely those by Dalla Vecchia & Schaye (2012) and Springel & Hernquist (2003), perform when implemented within MUPPI.

I devoted a great numerical effort to include these models within the complex code that I use to carry out simulations. The implementation has required to write large sections of the code, to heavily modify several key modules, and to perform a large number of test runs to validate the code and assess its performance.

6.3.1 FB1: Dalla Vecchia & Schaye model

The model proposed by Dalla Vecchia & Schaye (2012) assumes that thermal energy released by SN explosions is injected in the surrounding medium using a selection criterion: to guarantee the effectiveness of the feedback, the gas particles that experience feedback have to be heated up to a threshold temperature. Such a temperature increase, ΔT, ensures that the cooling time of a heated particle is longer than its sound-crossing time, so that heated gas is uplifted before it radiates all its energy. It is worth noting that stellar feedback is actually implemented as a thermal feedback in this model, since gas particles are heated as a result of the energy provided by SNe II, but the effective outcome is a galactic wind, because thermal energy is converted into momentum and hence outflows originate.

Particles have a probability to be heated by nearby star-forming particles that depends directly on the available amount $\varepsilon_{\rm SNII}$ of thermal energy per unit stellar mass released by star-forming particles of mass m_* as they explode as SNe. Once the temperature increase ΔT of gas particles receiving feedback energy has been set, the probability $p_{\rm i}$ that a gas particle is heated is determined by the fraction $f_{\rm fb,kin}$ of the total amount of SN II energy that is injected on average, i.e.:

$$p_{\rm i} = \frac{f_{\rm fb,kin}\,\varepsilon_{\rm SNII}\,m_*}{\Delta\varepsilon_{\rm i}\sum_{\rm j=1}^{N_{\rm ngb}} m_{\rm j}}\,, \tag{6.2}$$

where $\Delta\varepsilon_{\rm i}$ is the thermal energy per unit mass that corresponds to the temperature jump $\Delta T_{\rm i}$ (see below). Here, $\varepsilon_{\rm SNII}$ only refers to the fraction of SN energy that was given as *kinetic* energy in the original model. The thermal energy exchange of MUPPI remains unchanged: this is needed, since our model requires a thermal heating of the hot phase of multiphase particles. Indeed, multiphase particles have to be heated from nearby SNe to become pressurised and thus star-forming (see Section 5.3).

Eligible gas particles are all the neighbours ($N_{\rm ngb}$) of star-forming particles within their smoothing length, defined (similarly to the SPH smoothing length) as the radius of a sphere containing $N_{\rm ngb}$ gas particles[1].

The temperature increase $\Delta T_{\rm i}$, or equivalently the temperature at which the gas particle is heated when it experiences feedback, is a free parameter of the model. Dalla Vecchia & Schaye (2012) choose $\Delta T = 10^{7.5}$ K as their fiducial temperature increase and found no significative dependence among the values explored, provided that they are above a given threshold that depends on mass resolution and that ensures Bremsstrahlung to dominate the radiative cooling. They also found that cooling losses make their feedback scheme inefficient for gas density above a critical threshold, this floor mainly depending on the temperature threshold described above, on the number of neighbouring particles and on the average (initial) mass of the gas particles. Moreover, when this feedback scheme

[1]Multiphase particles are also eligible particles. If a gas particle that has been selected to receive energy was in a multiphase stage, then it is forced to exit it.

is adopted in cosmological simulations (Schaye et al., 2015; Crain et al., 2015), a $3 \cdot 10^7$ Myr delay between star formation and the release of feedback energy is adopted. Since star particles are expected to move away from the dense regions where they formed, such a time delay helps in delivering energy to gas having lower densities and thus lower radiative losses.

In my implementation of this model, I choose $\Delta T = 10^{7.5}$ K as the minimum allowed temperature increase. Then, I account for the presence of gas particles whose density is higher than the maximum density for which this feedback model is expected to be effective (see discussion above), by computing the temperature increase that is needed to guarantee effectiveness. I indeed prefer to adopt a temperature threshold (ΔT_i) that varies[2] as a function of the gas density (ρ_i) instead of introducing a delay as a further free parameter. Therefore, I calculate the temperature that each eligible particle has to reach in order to make the feedback effective (from equation 17 of Dalla Vecchia & Schaye, 2012), by taking into account the number of neighbour particles that my kernel function adopts, the average (initial) mass of gas particles and a ratio $t_\mathrm{c}/t_\mathrm{s} = 25$ between the cooling and the sound crossing time. After carrying out extensive tests, I found that this value is required to have a feedback that is effective in producing a realistic disc galaxy. The difference with respect to that adopted by Dalla Vecchia & Schaye (2012), $t_\mathrm{c}/t_\mathrm{s} = 10$, should not surprise given that the same outflow model is here applied on a completely different sub-resolution model for the ISM and star formation. Hence, in my implementation, the temperature jump of gas particles receiving energy is set to $\Delta T = \max[10^{7.5}\ \mathrm{K},\ \Delta T_\mathrm{i}]$.

I implemented the feedback efficiency adopted in the reference simulation of the Eagle set (Schaye et al., 2015), where the proposed feedback efficiency increases with the gas density n, computed as soon as a new star particle is spawned, and decreases with the metallicity Z, according to:

$$f_\mathrm{fb,kin}(n, Z) = f_\mathrm{fb,kin}^\mathrm{min} + \frac{f_\mathrm{fb,kin}^\mathrm{max} - f_\mathrm{fb,kin}^\mathrm{min}}{1 + \left(\frac{Z}{0.1\,Z_\odot}\right)^{n_\mathrm{Z}} \left(\frac{n}{n_{H,0}}\right)^{-n_\mathrm{n}}}\ , \tag{6.3}$$

where $Z_\odot = 0.0127$. Here, $n_\mathrm{H,0} = 0.67\ \mathrm{cm}^{-3}$, $n_\mathrm{Z} = 0.87$, and $n_\mathrm{n} = 0.87$ are free parameters of the model. The above analytical expression foretells a $f_\mathrm{fb,kin}$ that ranges between a high-redshift $f_\mathrm{fb,kin}^\mathrm{max}$ and a low-redshift $f_\mathrm{fb,kin}^\mathrm{min}$. The simulation AqC5-FB1 adopts equation (6.3), keeping both the aforementioned free parameters and $f_\mathrm{fb,kin}^\mathrm{max} = 3.0$ and $f_\mathrm{fb,kin}^\mathrm{min} = 0.3$, as suggested in Schaye et al. (2015, see also Section 6.6.2 for further details).

Note that, following the original scheme by Dalla Vecchia & Schaye (2012), I deliver the whole amount of SNII energy when a star is *spawned*; I do not use the continuous SFR provided by our star formation model. The reason for this choice will be detailed in Section 6.5.3.1. I verified that, in my implementation, the stochastic sampling of the SNII deposited energy is accurate to within few %, the ratio between the (cumulative) injected and expected SN feedback energy being < 4 % for all the simulations that adopt this galactic outflow model (including the lower resolution ones discussed in Section 6.6.2).

[2] I show and discuss results of a simulation where I fix the temperature jump to the reference value of $T = 10^{7.5}$ K in Section 6.6.2.

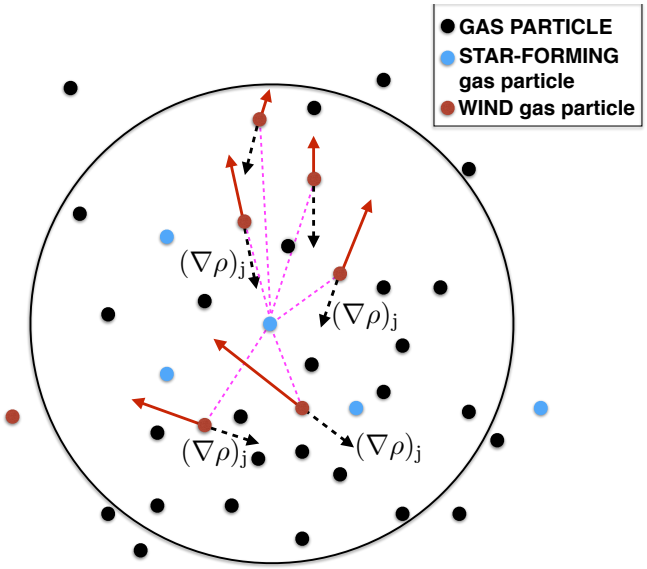

Figure 6.2: Cartoon showing the FB2 galactic outflow model implemented within the MUPPI algorithm. At variance with the original implementation, a star-forming particle provides its feedback energy to all the wind particles that are located within the smoothing sphere. Each wind particle is kicked in the direction of minus *its own* density gradient. Energy contributions are weighted according to the distance between wind particles and the energy donor star-forming particle.

6.3.2 FB2: modified MUPPI kinetic feedback

In this model, I revised the kinetic stellar feedback scheme presented in Murante et al. (2015). The original galactic outflow model was designed in order to produce outflows that are perpendicular to the forming disc, along the least-resistance direction. This is obtained by considering as eligible to receive energy only those wind particles lying in a cone centred on each star-forming particle (see Figure 5.2). Moreover, the original model required the presence of a sufficient amount of gas mass to be accelerated and produce an outflow; otherwise, the kinetic energy is considered to be lost. This may happen if no wind particles are present inside the cone.

Using the aforementioned scheme, the chosen direction of least resistance is that of the *star-forming* particle that gives energy to the wind one. However, since the new kernel (see Section 5.2) adopts a larger number of neighbours, the least-resistance direction of the *wind* particle is more likely different from that of the star-forming one. Therefore, I designed a new scheme in which the least-resistance direction is that of the wind particle *receiving* energy.

For this reason, each star-forming particle spreads its available amount of kinetic energy, $E_{\rm kin} = f_{\rm fb,\,kin}\,E_{\rm SN}$, among all wind particles within the smoothing length, with kernel-weighted contributions (see below). Figure 6.2 illustrates this scheme: a wind particle gathers energy from all star-forming particles of which it is a neighbour. The kinetic energy of the receiving particle is then updated, the wind

particle being kicked in the direction of minus *its own* density gradient. Thus, at variance with the original galactic outflow model, star-forming particles give energy isotropically and not within a cone. In this way, density gradients of star-forming particles are not used to give directionality to the outflows. Particles receiving energy use it to increase their velocity along their least-resistance path. Energy contributions are weighted according to the distance that separates each wind particle that gathers energy and the considered energy donor star-forming particle. Note that this is at variance with the original galactic outflow model, where the distance between selected wind particles and the axis of the cone is considered, instead of the radial particle pair separation.

6.3.3 FB3: fixing the mass loading factor

This model provides a new version of the original MUPPI kinetic feedback model (described above), where I directly impose the mass load, instead of using as a free parameter the probability $P_{\rm kin}$ to promote gas particles to become wind particles.

I aim at implementing a model similar to that of Springel & Hernquist (2003). In their model equilibrium is considered to be always achieved: therefore, ISM properties and consequent SFR are evaluated in an instantaneous manner for each multiphase star-forming particle. Each star-forming particle has then a probability to become a wind particle.

In my model, a multiphase particle remains in its multiphase stage for a given time: this time is related to the dynamical time of the cold phase and computed when a sufficient amount of cold gas has been produced. My model also takes into account the energy contribution from surrounding SN explosions, i.e. neighbouring star-forming particles contribute to the energy budget of each multiphase particle.

I estimate ISM properties averaged over the lifetime that each multiphase particle spends in its multiphase stage. I then use these properties to determine the probability for each multiphase particle of receiving kinetic energy and thus becoming a wind particle once it exits its multiphase stage. For this reason, I have to sum the energy contributions from SN explosions provided by star-forming particles over the multiphase stage of each gas particle receiving the energy. Moreover, I also have to estimate the mass of gas that goes in outflow, and to compute time-averaged quantities.

In what follows, I always use the index i when referring to star-forming, energy-giving particles, and the index j for particles that receive that energy.

My aim is to produce an outflow with a fixed mass loading factor η. To obtain this, I relate the wind mass-loss rate $\dot{m}_{\rm w}$ to the SFR of each star-forming particle i:

$$\dot{m}_{\rm w} \; = \; \eta \, \dot{m}_{*} \; . \tag{6.4}$$

In this FB3 model, particles that receive energy are the multiphase neighbours of multiphase star-forming particles within their entire smoothing sphere. Each

of these multiphase particles collects energy from all its neighbouring multiphase star-forming particles and stores it during its entire multiphase stage.

The wind mass-loss rate $\dot{m}_{\rm w}$ can be expressed as the outflowing mass $\widetilde{m}_{\rm w}$ in a time interval (i.e., per time-step):

$$\dot{m}_{\rm w} \;=\; \frac{\widetilde{m}_{\rm w}}{\Delta t} \;. \tag{6.5}$$

Hence, for each star-forming particle i one gets:

$$\widetilde{m}_{\rm w,\,i,\,\Delta t} \;=\; \eta\,\Delta t\,\dot{m}_{*,\,\rm i} \;, \tag{6.6}$$

where $\dot{m}_{*,\,\rm i}$ is the SFR of that same particle. Such a wind mass loss is taken out from the total gas mass contributed by all the SPH multiphase neighbours k[3] of the particle i. This mass is computed as:

$$m_{\rm tot,\,i,\,\Delta t} \;=\; \sum_{\rm k} m_{\rm k} \;, \tag{6.7}$$

$m_{\rm k}$ being the mass of each energy-receiving gas particle during the time-step interval Δt. Thus, each star-forming particle i distributes energy to the multiphase receiving particles k; it also gives to each such particles the information on the required mass loading factor, and on the total gas mass to which the mass loss is referred.

The total kinetic energy that a multiphase particle j is provided with in every time-step Δt can be expressed as:

$$E_{\rm kin\,tot,\,j,\,\Delta t} \;=\; \sum_{\rm i} f_{\rm fb,kin}\,\varepsilon_{\rm SNII}\,\frac{dm_{*,\,\rm i}}{dt}\,\Delta t \;, \tag{6.8}$$

where $\varepsilon_{\rm SNII}\frac{dm_{*,\,\rm i}}{dt}\,\Delta t$ is the kinetic energy released per time-step by each neighbour star-forming particle whose stellar mass component is $m_{*,\,\rm i}$. The sum is over all neighbouring star-forming particles i. The corresponding total kinetic energy $E_{\rm kin\,tot,j}$ that is stored during the entire multiphase stage of particle j is therefore obtained by integrating equation (6.8) over the time $t_{\rm MP,j}$ that the particle j spends in its multiphase stage (i.e., summing over all the time-steps that make up the multiphase stage). This means that I have to sum all the energy contributions $E_{\rm kin\,tot,\,j,\,\Delta t}$ during the time interval $t_{\rm MP,j}$:

$$E_{\rm kin\,tot,j} \;=\; \sum_{\Delta \rm t} E_{\rm kin\,tot,\,j,\,\Delta t} \;=\; \sum_{\Delta \rm t}\sum_{\rm i} f_{\rm fb,kin}\,\varepsilon_{\rm SNII}\,\frac{dm_{*,\,\rm i}}{dt}\,\Delta t \;. \tag{6.9}$$

The rightmost term considers that each energy contribution $E_{\rm kin\,tot,\,j,\,\Delta t}$ has already been computed during each time-step Δt in equation (6.8).

[3]The index k labels gas particles within the smoothing length of each star-forming particle i; note that each energy-receiving gas particle j can have many star-forming particles inside its smoothing length.

The required outflowing mass per time-step, sampled by particle j, is the sum over all neighbouring star-forming particles within the smoothing length of j:

$$\widetilde{m}_{\mathrm{w,\,j,\,\Delta t}} \;=\; \sum_{\mathrm{i}} \widetilde{m}_{\mathrm{w,\,i,\,\Delta t}} \;=\; \eta\,\Delta t \sum_{\mathrm{i}} \dot{m}_{*,\,\mathrm{i}} \;\; . \tag{6.10}$$

Note that each star-forming particle i gives a different contribution to particle j, being its SFR different. Therefore, the outflowing mass associated with each multiphase particle that experiences feedback can be obtained by summing all the contributions of equation (6.10) over the whole duration of the multiphase stage of particle j:

$$\widetilde{m}_{\mathrm{w,\,j}} \;=\; \sum_{\Delta \mathrm{t}} \widetilde{m}_{\mathrm{w,\,j,\,\Delta t}} \quad = \sum_{\Delta \mathrm{t}} \eta\,\Delta t \sum_{\mathrm{i}} \dot{m}_{*,\,\mathrm{i}} \;\; . \tag{6.11}$$

I want to stochastically sample the outflowing mass $\widetilde{m}_{\mathrm{w,\,j}}$. Thus, when a multiphase particle exits the multiphase stage, this particle will have a probability:

$$p_{\mathrm{j}} \;=\; \frac{\widetilde{m}_{\mathrm{w,\,j}}}{m_{\mathrm{j}}} \cdot \frac{m_{\mathrm{j}}}{m_{\mathrm{tot,\,j}}} \tag{6.12}$$

of receiving the energy:

$$E_{\mathrm{rec,\,j}} \;=\; E_{\mathrm{kin\,tot,\,j}} \cdot \frac{m_{\mathrm{j}}}{\widetilde{m}_{\mathrm{w,\,j}}} \;\; . \tag{6.13}$$

In equation (6.12), $m_{\mathrm{tot,\,j}}$ is the total mass of the multiphase gas that produces the outflow $\widetilde{m}_{\mathrm{w,\,j}}$. At each time-step:

$$m_{\mathrm{tot,\,j,\,\Delta t}} \;=\; \sum_{\mathrm{i}} m_{\mathrm{tot,\,i,\,\Delta t}} \;\; , \tag{6.14}$$

where $m_{\mathrm{tot,\,i,\,\Delta t}}$ is computed according to equation (6.7). Since the mass $m_{\mathrm{tot,\,j,\,\Delta t}}$ can vary from time-step to time-step, I evaluate a time-averaged total mass of the multiphase gas that produces the outflow, for each particle j:

$$m_{\mathrm{tot,\,j}} \;=\; \frac{\sum_{\Delta \mathrm{t}} (m_{\mathrm{tot,\,j,\,\Delta t}} \cdot \Delta \mathrm{t})}{t_{\mathrm{MP}}} \;\; ; \tag{6.15}$$

here, the sum is over the time-steps that make up the multiphase stage whose total duration is t_{MP}.

In this way, each multiphase particle j samples the SFR of its neighbours; this SFR is associated to the mass *of the star-forming particle* as far as the estimate of the mass loss is concerned, not to that of the receivers. At the same time, each multiphase particle collects the SNII energy output from the same star-forming particles. Note that each star-forming particle gives its *entire* energy budget to *all* the receivers. A particle ending its multiphase stage receives feedback energy and is uploaded into an outflow with its probability p_{j}. The kinetic energy of the receiving multiphase particle is therefore updated, the particle being kicked in the

direction of minus its own density gradient. Particles that experience feedback are hydrodynamically decoupled (for a time interval $t_{\rm wind} = 15$ Myr) from the surrounding medium as soon as they gain feedback energy.

Energy conservation reads:

$$E_{\rm tot} = \sum_{\rm j} p_{\rm j} E_{\rm rec,\,j} = \sum_{\rm j} m_{\rm j} \frac{E_{\rm kin\,tot,\,j}}{m_{\rm tot,\,j}} \,, \tag{6.16}$$

where the last equation has been obtained by plugging equations (6.12) and (6.13) into the second term. Energy conservation is proven since the total feedback energy received by all the multiphase particles ending their multiphase stage amounts to the total energy budget provided by star-forming particles exploding as SNe II, as ensured by the stochastic sampling of the energy.

I verified that the stochastic sampling correctly represents the desired mass loading factor and energy deposition to within 5% in the considered cases. This figure can slightly vary with the parameters of the model, as in the FB1 scheme; as for FB1 model, resolution leaves the accuracy of the stochastic sampling almost unaffected.

One important characteristic of this model is that the outflow velocity is fixed once η and $f_{\rm fb,kin}$ are fixed. In fact, by equating the kinetic energy given to the particle to that received from neighbouring SNe II, we find:

$$v_{\rm w} = \sqrt{2 f_{\rm fb,kin} \varepsilon_{\rm SNII} / \eta} \tag{6.17}$$

where $\varepsilon_{\rm SNII}$ is the thermal energy per unit stellar mass released by SNe II (that only depends on the chosen IMF). For this reason, this model is similar to that of Springel & Hernquist (2003). The important change is that SN II energy and SFRs are collected during the life of the portion of the ISM that is sampled, taking into account the fact that changes in the local hydrodynamics (e.g. mergers, shocks, and pressure waves) can influence these values.

Also in this model, thermal energy is still distributed according to the original MUPPI scheme.

6.4 The set of simulations

I performed cosmological simulations with the zoomed-in ICs *AqC* introduced in Section 5.5. In this Chapter, I consider both the higher-resolution level AqC5 and the lower resolution version AqC6 (see Tables 5.2 and 6.1 for details).

I list the series of simulations that I ran in order to quantify the impact of the new hydrodynamical scheme in Table 6.1. Each simulation was given a name: the identifying convention encodes the resolution of the simulation (AqC5 or AqC6) and the adopted hydrodynamical scheme, where *newH* refers to the improved SPH implementation (Beck et al. (2016); see Section 5.2) and *oldH* indicates the standard SPH scheme (see Section 5.1). Mass resolutions (for both gas and DM particles)

Table 6.1: Name and details of the simulations used in order to quantify the impact of the hydrodynamical scheme. *Column 1:* label of the run. *Column 2:* mass of DM particles. *Column 3:* initial mass of gas particles. *Column 4:* Plummer-equivalent softening length of the gravitational interaction. *Column 5:* hydrodynamical scheme. *Column 6:* galactic outflow model (original refers to Section 5.3).

Simulation	$M_{\rm DM}$ $(h^{-1}{\rm M}_\odot)$	$M_{\rm gas}$ $(h^{-1}{\rm M}_\odot)$	$\varepsilon_{\rm Pl}$ $(h^{-1}{\rm kpc})$	Hydro scheme	Stellar feedback
AqC5-newH	$1.6 \cdot 10^6$	$3.0 \cdot 10^5$	0.325	New	Original
AqC5-oldH	$1.6 \cdot 10^6$	$3.0 \cdot 10^5$	0.325	Old	Original
AqC6-newH	$1.3 \cdot 10^7$	$4.8 \cdot 10^6$	0.650	New	Original
AqC6-oldH	$1.3 \cdot 10^7$	$4.8 \cdot 10^6$	0.650	Old	Original

Table 6.2: Relevant parameters of the sub-resolution model. *Column 1:* label of the run. *Column 2:* half-opening angle of the cone, in degrees. *Column 3:* maximum lifetime of a wind particle (see Section 5.3). *Column 4:* gas particle's probability of becoming a wind particle. *Columns 5 and 6:* thermal and kinetic SN feedback energy efficiency, respectively. *Column 7:* fraction of SN energy directly injected into the hot phase of the ISM.

Simulation	θ (°)	$t_{\rm wind}$ (Myr)	$P_{\rm kin}$	$f_{\rm fb,therm}$	$f_{\rm fb,kin}$	$f_{\rm fb,local}$
AqC5-newH	30	$20-t_{\rm clock}$	0.05	0.2	0.7	0.02
AqC5-oldH	60	$30-t_{\rm clock}$	0.03	0.2	0.5	0.02
AqC6-newH	30	$20-t_{\rm clock}$	0.03	0.2	0.8	0.02
AqC6-oldH	60	$30-t_{\rm clock}$	0.03	0.2	0.5	0.02

and gravitational softenings are also provided in Table 6.1. All these simulations adopt the original galactic outflow model of MUPPI (see Section 5.3).

I ran simulations AqC5-newH and AqC6-newH adopting the advanced SPH implementation and using the values listed in the first and third rows of Table 6.2 for relevant parameters of the model MUPPI (parameters not included in Table 6.2 are set to the values reported in Table 5.1).

AqC5-oldH and AqC6-oldH are the reference simulations with the old hydrodynamical scheme; these simulations marginally differ from the runs that have been presented and described by Murante et al. (2015), as described below. Here, I adopt sets of stellar yields that are newer with respect to those used by Murante et al. (2015); they are taken from Karakas (2010) for AGB stars, from Thielemann et al. (2003) for SNe Ia, and from Woosley & Weaver (1995) and Romano et al. (2010) for SNe II (see also Section 5.4). After this change, the parameter $f_{\rm fb,kin}$ describing the fraction of SN energy directly injected into the ISM had to be slightly fine-tuned again (from 0.6 to 0.5, see Table 6.2). Such a change modifies only barely the outcome of the original simulations. Relevant parameters of the sub-resolution model that have been chosen to carry out AqC5-oldH and AqC6-oldH simulations are provided in Table 6.2 (second and fourth rows; those not listed

Table 6.3: Name and main features of the simulations performed in order to investigate the effect of the adopted galactic outflow model on final properties of the simulated galaxy. *Column 1:* label of the run. *Column 2:* hydrodynamical scheme. *Column 3:* galactic outflow model (see Section 6.3 for details). All these runs adopt the softening length and masses of DM and gas particles of the simulation AqC5-newH.

Simulation	Hydro scheme	Stellar feedback
AqC5-FB1	New	First outflow model (Section 6.3.1)
AqC5-FB2	New	Second new outflow model (Section 6.3.2)
AqC5-FB3	New	Third new outflow model (Section 6.3.3)

are set to the ones in Table 5.1). I adopt a Kroupa (2001) IMF in the mass range $[0.08, 100]$ $M_\odot$ for all the simulations carried out in this Chapter (that is defined by equation (7.2), see also Figure 7.1).

Table 6.3 lists the simulations that I carried out in order to investigate the effect of wind modelling on final properties of the simulated disc galaxy. In this Table I summarise the hydrodynamical scheme adopted and the type of galactic outflow model implemented within the sub-resolution prescriptions for cooling and star formation.

Simulations AqC5-FB1, AqC5-FB2, and AqC5-FB3 all adopt the new hydrodynamical scheme and all have the same gravitational softening and mass resolutions of AqC5-newH. I will compare results from these simulations to those of AqC5-newH in order to quantify the variation in the final results when modifying the model of stellar feedback.

6.5 Results

In this Section I present results from the simulations introduced in Section 6.4, that led to the formation of disc galaxies. After discussing the relevance of introducing a switch to suppress AC in multiphase gas particles (Section 6.5.1), I show the properties of two disc galaxies simulated by adopting the new and the old hydrodynamical schemes, respectively, and focus on the differences between the two SPH implementations (Section 6.5.2). In Section 6.5.3 I show results for the different galactic outflow models, all implemented within the new SPH scheme.

6.5.1 The importance of the AC switch

In order to assess the effect of the AC switch, I first investigate the properties of the gas particles with AC turned off. Figure 6.3 shows the density-temperature phase diagram of gas particles for the AqC5-newH simulation (see also Section 6.5.2) at redshift $z = 0$. The top panel is for all the gas particles of the simulation, while the bottom panel shows the phase diagram of the gas particles located within the virial radius of the galaxy ($R_{\rm vir} \simeq 240$ kpc). Here and in the following, I

consider virial quantities as those calculated in a sphere that is centred on the minimum of the gravitational potential of the halo and that encloses an overdensity of 200 times the *critical* density at present time.

In both panels, contours show the mass distribution of gas particles with AC switched off as a consequence of the implementation of the AC limiter. In fact, contours encircle gas particles that have just exited their multiphase stage and still keep their AC turned off, and gas particles that exited their last multiphase lapse few time-steps ago but whose temperature is not in the range (see Section 6.2.2) allowed to artificially conduct again. Note that particles encircled by contours in Figure 6.3 are not all the particles that cannot artificially conduct: multiphase and wind particles have AC switched off, too.

As expected, the majority of non-multiphase particles having AC switched off are located in high-density regions, where also multiphase particles lie. This makes it clear that the switch is acting to avoid too fast a smearing of the thermodynamical properties of the gas that here is mainly determined by the effect of our sub-grid model rather than by hydrodynamics. It is also apparent that AC is normally acting in all the remaining gas particles within the virial radius.

I also examine the position and the distribution of gas particles with AC turned off as a consequence of the implementation of our AC limiter in the AqC5-newH simulation at $z = 0$. Figure 6.4 shows, in the left column, face-on (top) and edge-on (bottom) distribution of gas particles within the galactic radius, $R_{\rm gal} \simeq 24$ kpc; the right column shows the location of gas particles within $R_{\rm gal}$ with AC switched off due to the effect of the switch, for the same simulation. Here and in the following, I define the galactic radius as one-tenth of the virial radius, i.e. $R_{\rm gal} = 0.1\,R_{\rm vir}$. I choose this radius $R_{\rm gal}$ in order to identify and select the region of the computational domain that is dominated by the central galaxy. In the four panels of Figure 6.4, I rotated the reference system in order to have the z-axis aligned with the angular momentum of stars and multiphase gas particles within 8 kpc from the location of the minimum of the gravitational potential (the same procedure has been adopted in Figures 6.5 and 6.21, and in Figures showing density maps in the following Chapters). The origin is set at the centre of the galaxy, that is defined as the centre of mass of stars and multiphase gas particles within 8 kpc from the location of the minimum of the gravitational potential.

Particles with AC switched off mainly trace the densest and the innermost regions of the simulated disc galaxy. Thus, Figures 6.3 and 6.4 show how AC is switched off for particles that are sampling the ISM, described by sub-grid physics, whose evolution strongly affects the gas thermodynamics and dominates over the resolved hydrodynamics. In particular, both the edge-on view of the AqC5-newH galaxy (bottom-right panel of Figure 6.4) and Figure 6.3 (combined with information provided by Figure 6.1) show how AC is instead normally acting outside the galaxy.

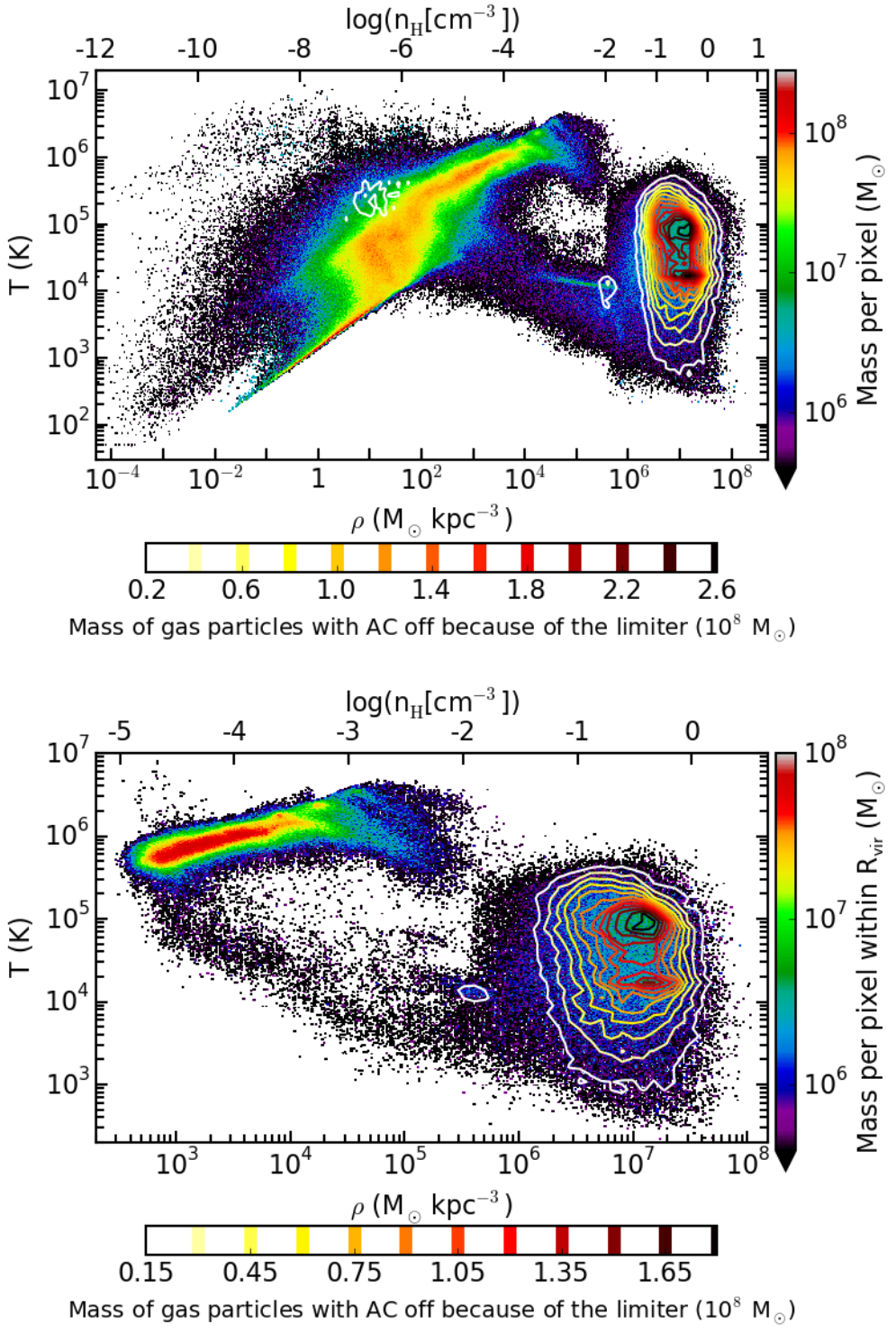

Figure 6.3: *Top panel:* phase diagram of all the gas particles (within the entire Lagrangian region) of the AqC5-newH galaxy simulation. *Bottom panel:* phase diagram of gas particles within the virial radius for the AqC5-newH run. In both panels, contours depict the mass distribution of gas particles with the AC switched off because of the effect of the new AC limiter, within the entire Lagrangian region (top panel) and within the virial radius (bottom panel). Phase diagrams are shown at redshift $z = 0$. Colour encodes the gas mass per density-temperature bin (colour scale on the right of each panel). Colours of contours are encoded as shown in the bottom colour scales. Colour scales differ for the two panels.

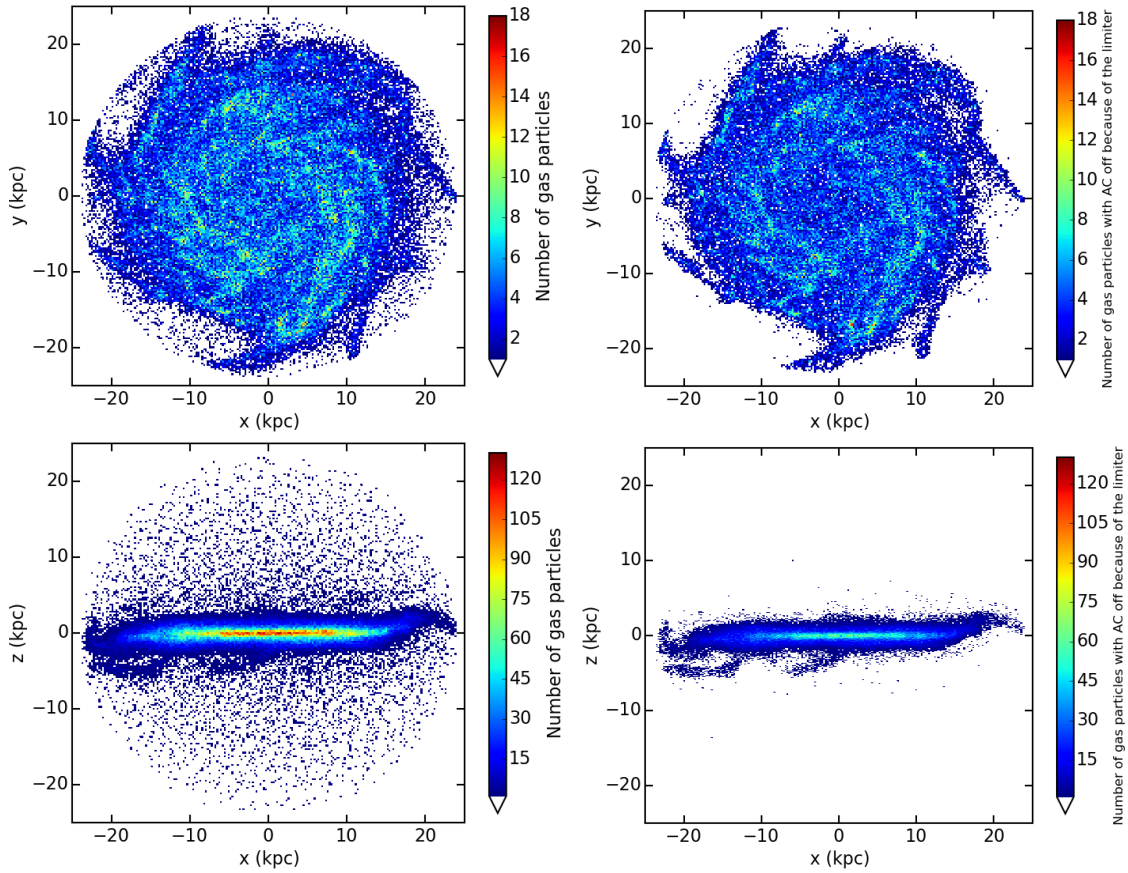

Figure 6.4: *Top panels:* face-on distribution of all the gas particles located within the galactic radius for the AqC5-newH galaxy simulation (left); face-on distribution of gas particles within $R_{\rm gal}$ with the AC switched off as a consequence of the implementation of our AC limiter, in the same run (right). *Bottom panels:* edge-on distribution of all the gas particles located within $R_{\rm gal}$ for the AqC5-newH simulation (left); edge-on distribution of gas particles within $R_{\rm gal}$ with the AC switched off because of the AC limiter (right). Plots are shown at redshift $z = 0$; the colour encodes the numerical density of the particles per bin.

6.5.2 Effect of the new SPH scheme

In this Section, I focus on the results from AqC5 simulations, just stressing few differences with respect to the low-resolution case where needed. In order to investigate the significant role played by the advanced hydrodynamical scheme in the formation and evolution of a disc galaxy, I performed the comparison at both available resolutions, i.e. between runs AqC5-oldH and AqC5-newH, and AqC6-oldH and AqC6-newH (see Table 6.1). A more detailed study of the effect of the resolution is performed in Section 6.6.1.

Figure 6.5 introduces galaxies AqC5-newH and AqC5-oldH. The first four panels show face-on and edge-on projections of gas (top panels) and stellar (third and fourth ones) density for AqC5-newH at $z = 0$. The four lower panels present face-on

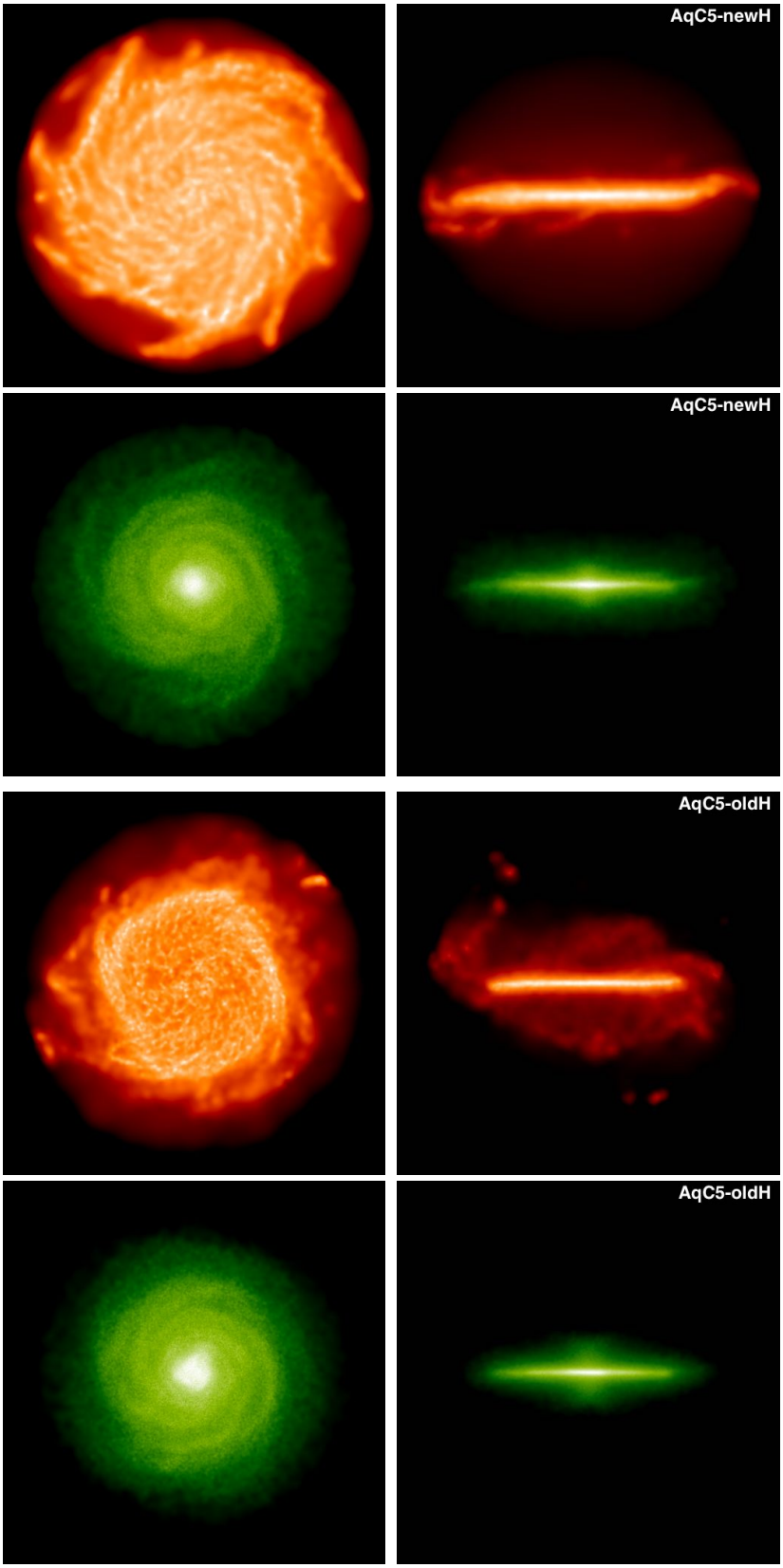

Figure 6.5: *Top four panels:* projected gas (first and second panels) and star (third and fourth) density for the AqC5-newH simulation. *Bottom four panels:* projected gas (fifth and sixth panels) and star (bottom) density for AqC5-oldH. Left- and right-hand panels show face-on and edge-on densities, respectively. All the maps are shown at redshift $z = 0$. The size of the box is 55 kpc.

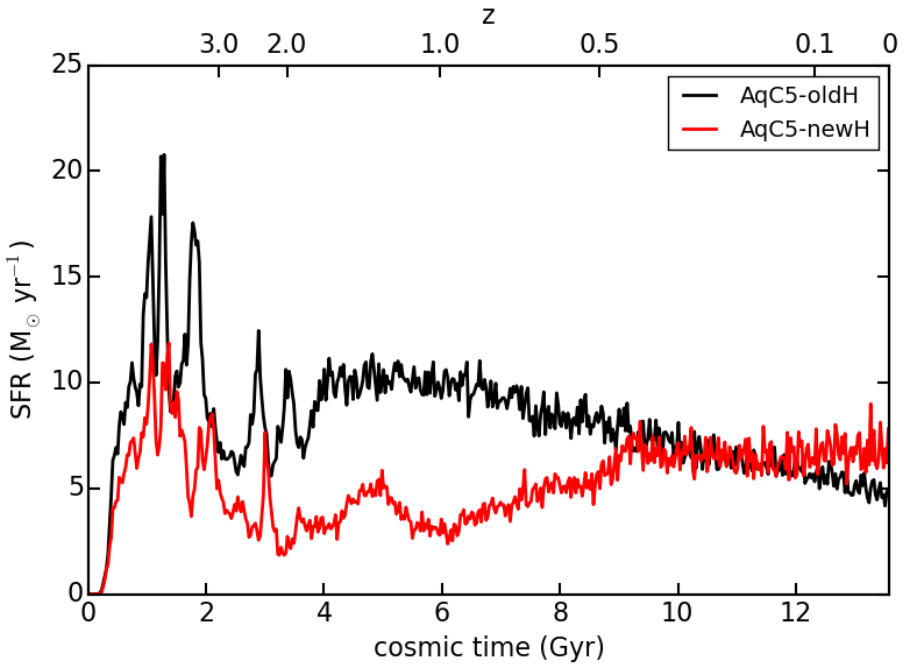

Figure 6.6: SFR as a function of cosmic time for the AqC5 simulations with the old (black) and the new (red) hydrodynamical scheme.

and edge-on projections of gas (fifth and sixth panels) and stellar (bottom ones) density for AqC5-oldH, at $z = 0$, for comparison.

The galaxy AqC5-newH has a limited bulge and a dominant disc, with a clear spiral pattern both in the gaseous and in the stellar component. The gaseous disc is more extended than the stellar one (see also the middle-left panel of Figure 6.10 and discussion below).

Figure 6.6 shows the SFR as a function of the cosmic time for AqC5-newH and AqC5-oldH simulations. Here, and in the rest of this work, we only show the SFR evaluated for all stars that at $z = 0$ are located within $R_{\rm gal}$. In all the figures presented and discussed in this Section, results of AqC5-newH are shown in red, while those referring to AqC5-oldH are in black. The burst of star formation occurring at redshift $z > 3$ builds up the bulge component (see Murante et al., 2015) in the two simulated galaxies. High redshift ($z > 3$) SFR is reduced when the new flavour of SPH is considered: as a consequence, the bulge component of AqC5-newH is slightly less massive (see Figure 6.7, described below). Below $z = 2.5$, the SFR evolves differently in the two simulations. AqC5-newH has a lower SFR till $z = 0.5$, when the two SFRs become again comparable.

One of the reasons of the discrepant SFR between AqC5-oldH and AqC5-newH for redshift that spans the range $2.5 > z > 0.5$ lies in the presence of the time-step limiting particle wake-up scheme. This feature of the improved SPH promotes the accurate treatment of feedback (Durier & Dalla Vecchia, 2012; Schaller et al., 2015; Beck et al., 2016, see also Section 5.2). When the wake-up scheme is used, energy deposited by wind particles in the surrounding medium when they hydrodynamically

recouple with the ambient gas is more accurately distributed, especially to cold inflowing gas. This slows down the gas accretion on to the galaxy (or even on to the halo) and reduces the amount of fuel that is available for the disc growth (see also Figure 6.8, and discussion below). Note that this is an interaction of the outflow model with the wake-up feature of our new hydrodynamical scheme, and depends not only on the sub-resolution model parameters but also on the details of the wake-up scheme. Here, I decided to keep the wake-up scheme and its parameter ($f_{\rm w}$, see Section 5.2) fixed. I use indeed the wake-up scheme as tested in Beck et al. (2016), where a number of hydrodynamical only tests are shown.

Besides the smaller amount of the accreted gas in AqC5-newH, inflowing gas is characterised by a lower (radial component of the) velocity than in AqC5-oldH (for $2.5 > z > 1$): as a result, the SFR drops. Moreover, gas expelled by high-redshift outflows falls back at later times in the AqC5-newH: the SFR starts to gently rise for $z < 1$, and then keeps roughly constant below $z < 0.5$, while the SFR of AqC5-oldH is moderately declining. The final SFRs slightly overestimate that observed in typical disc galaxies (see, e.g., Snaith et al., 2014, for our Galaxy). The different star formation history is the result of the lower baryon conversion efficiency of AqC5-newH (see Figure 6.11, bottom panel, described below).

I then analyse the distribution of stellar circularities in order to perform a kinematic decomposition of the simulated galaxies, by separating the dispersion supported component (bulge) from the rotationally supported one (disc). Figure 6.7 shows the distribution of stellar mass as a function of the circularity of star particles[4] at $z = 0$ for the two simulations. I consider star particles within $R_{\rm gal}$. Virial radii of the two galaxies are $R_{\rm vir} = 238.64$ kpc (AqC5-oldH) and $R_{\rm vir} = 240.15$ kpc (AqC5-newH). The circularity of a stellar orbit is defined as the ratio $J_{\rm z}/J_{\rm circ}$, i.e. the specific angular momentum in the direction perpendicular to the disc over the specific angular momentum of a reference circular orbit. This latter quantity is defined according to Scannapieco et al. (2009) as $J_{\rm circ} = r\, v_{\rm c}(r) = r(GM(< r)/r)^{1/2}$, $v_{\rm c}(r)$ being the circular velocity of each star at the distance r from the galaxy centre.

The bulk of the stellar mass is rotationally supported, thus highlighting that the disc represents the dominant component. The relative contribution to the total galaxy stellar mass from the bulge and the disc components can indeed be appreciated by weighting the heights of the peaks located at $J_{\rm z}/J_{\rm circ} = 0$ and at $J_{\rm z}/J_{\rm circ} = 1$, respectively. The total stellar mass of AqC5-newH ($4.74 \cdot 10^{10}$ M$_\odot$, within $R_{\rm gal}$) is lower than that of AqC5-oldH ($7.22 \cdot 10^{10}$ M$_\odot$); both simulated galaxies are clearly disc-dominated. Assuming that the counter-rotating stars are symmetrically distributed with zero average circularity, I estimate the bulge mass as twice the mass of counter-rotating stars. I can thus calculate the bulge-over-total stellar mass ratio within $R_{\rm gal}$, and obtain $B/T = 0.30$ and $B/T = 0.23$ for AqC5-newH and AqC5-oldH, respectively. The mass of the bulge component in AqC5-newH is marginally reduced with respect to AqC5-oldH (see Figure 6.6 and

[4]Numbers of DM, gas, and star particles within $R_{\rm vir}$ at $z = 0$ are 710150, 362648 and 692125 for AqC5-newH, respectively, and 691717, 252660 and 895657 for AqC5-oldH.

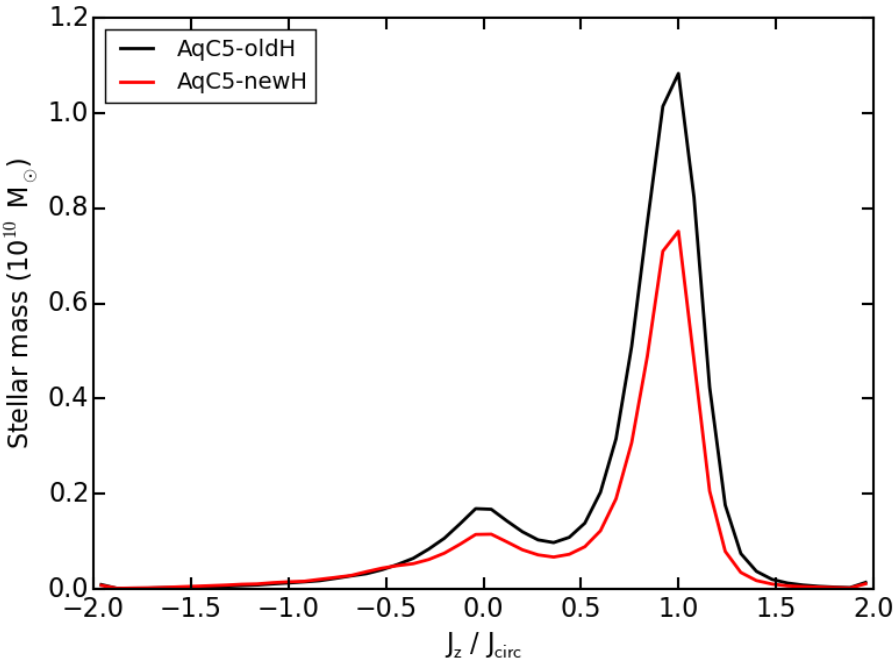

Figure 6.7: Stellar mass as a function of the circularity of stellar orbits at $z = 0$. The red curve refers to the AqC5-newH and the black curve shows the result from the AqC5-oldH simulation. The heights of the peaks located at $J_z/J_{circ} = 0$ and at $J_z/J_{circ} = 1$ describe the relative contributions to the total stellar mass of the galaxy from the bulge and the disc, respectively. $B/T = 0.30$ and 0.23 for AqC5-newH and AqC5-oldH, respectively.

discussion above); the stellar mass in the disc component is decreased as well in AqC5-newH. Gas mass within R_{gal} for AqC5-newH is $2.91 \cdot 10^{10}$ $M_\odot$, the cold ($T < 10^5$ K) gas mass being $2.54 \cdot 10^{10}$ $M_\odot$; gas mass within R_{gal} for AqC5-oldH is $1.66 \cdot 10^{10}$ $M_\odot$, the amount of cold gas being $1.55 \cdot 10^{10}$ $M_\odot$.

Figure 6.8 describes the mass accretion history (MAH), i.e. the redshift evolution of the gas mass, within the virial radius (top panel) and the galactic radius (bottom panel). Gas accretion within R_{vir} is comparable in the two reference simulations up to $z \simeq 4$; below this redshift, the gas accretion is delayed when the new SPH implementation is adopted and then, after redshift $z = 1$, continues rising down to $z = 0$. On the other hand, the old hydrodynamical scheme reduces the gas mass accretion rate below $z \simeq 2$, and this is much more evident when the gas accretion within R_{gal} is analysed, where it is stopped below $z \simeq 1$. This different gas accretion pattern is one of the reasons of the differences found between the two AqC5 simulations. The new hydrodynamical scheme is responsible for the delay of the gas inflow, by slowing down the gas fall-back within the virial and the galactic radii. Moreover, low-redshift ($z < 1$) gas accretion is faster in AqC5-newH and still ongoing at $z = 0$: as a consequence, the stellar disc forms later and it is still growing at redshift $z = 0$, when fresh gas keeps accreting on the galaxy, sustaining the star formation.

Figure 6.9 shows the density-temperature phase diagram of all the gas particles within the virial radius for the AqC5-newH simulation (top panel) and for the run

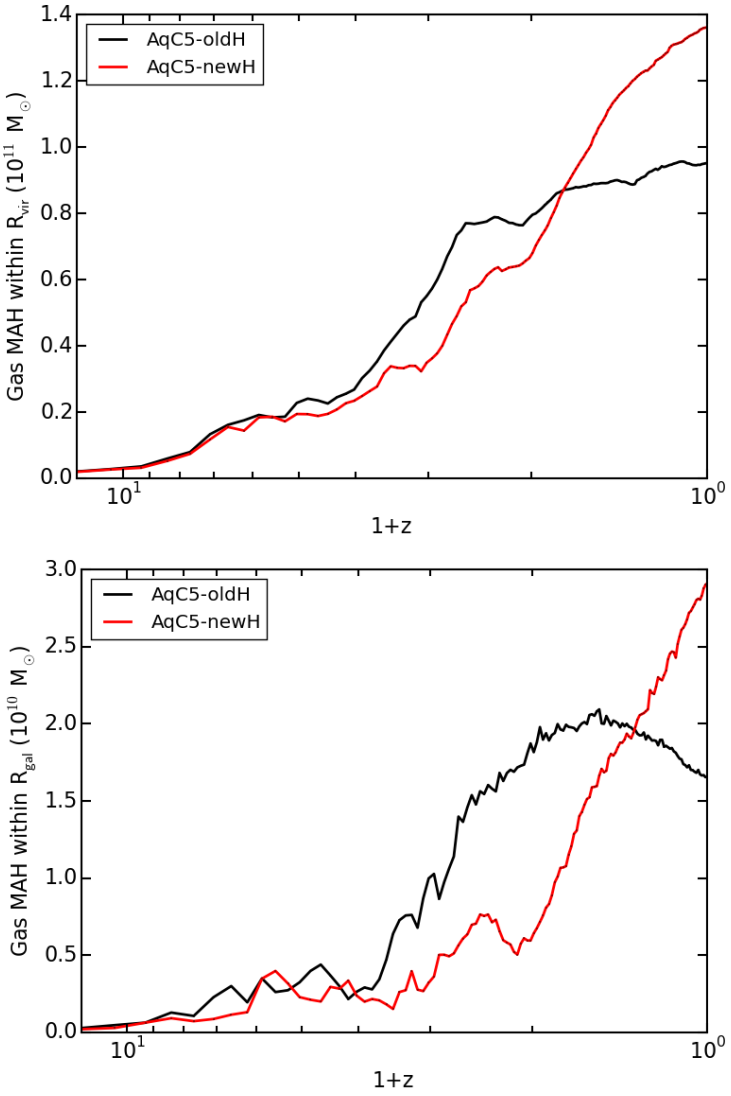

Figure 6.8: *Top panel:* MAH, i.e. the redshift evolution of the gas mass, within the virial radius. AqC5-oldH is shown in black, while the AqC5-newH simulation in red. *Bottom panel:* MAH for gas within the galactic radius.

AqC5-oldH (bottom one). The mass distribution is shown at $z = 0$ and both single-phase and multiphase particles are taken into account. As for the temperature, it is the temperature of single-phase particles and the mass-averaged temperature for the multiphase ones. The presence of AC affects the gas particle distribution in the phase diagram: cooling properties are modified, phase-mixing is promoted. When more diffuse gas is considered, i.e. $\rho < 3{\cdot}10^4$ $M_\odot$ kpc^{-3}, I find that the gas is kept hotter in the AqC5-newH simulation, with a lot of gas at temperatures $3 \cdot 10^5 < T < 4 \cdot 10^6$ K. At intermediate densities, i.e. $3 \cdot 10^4 < \rho < 4 \cdot 10^5$ $M_\odot$ kpc^{-3}, and for $T > 3 \cdot 10^5$ K, I notice the presence of a large number of gas particles that have been recently heated because of stellar feedback in the AqC5-newH simulation, while in the same density and temperature regime there is a lack of these particles in the AqC5-oldH. This feature confirms the importance of the time-step limiting particle wake-up

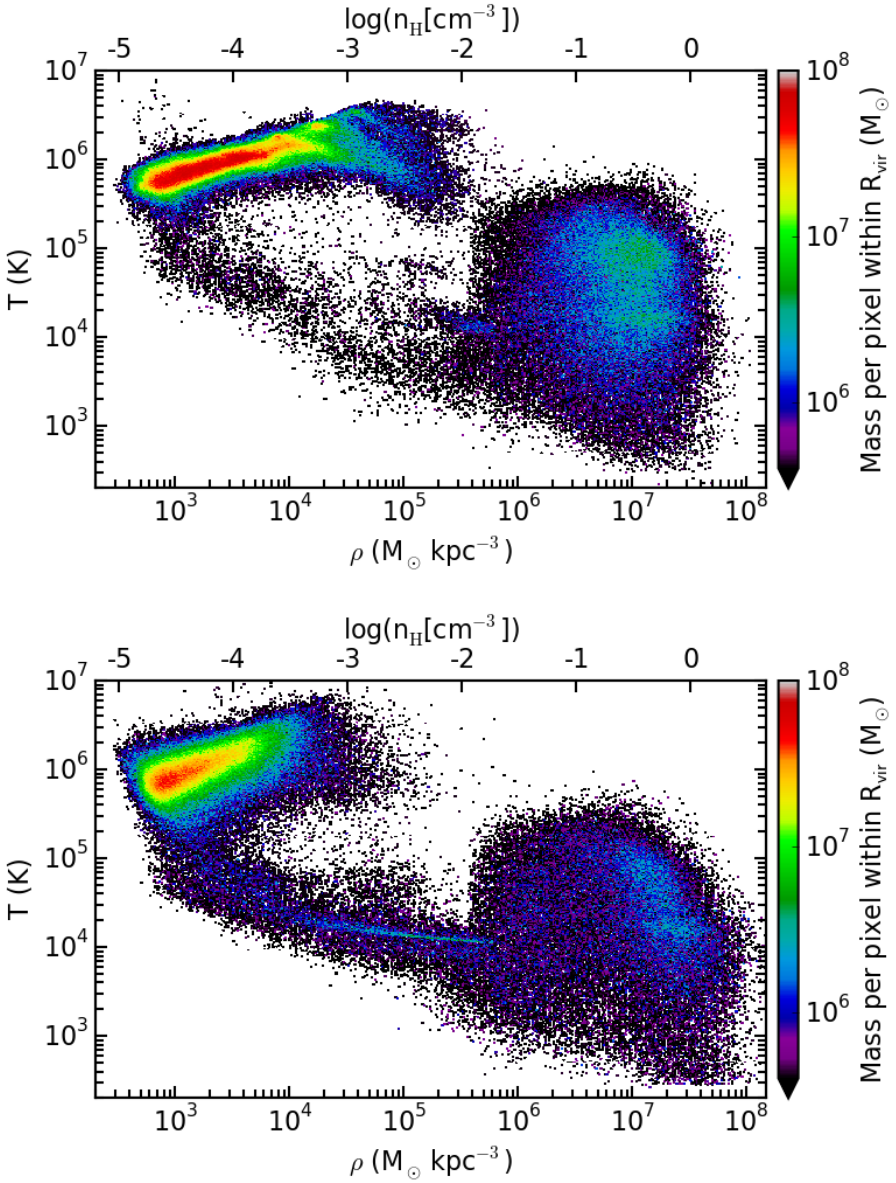

Figure 6.9: Phase diagrams of gas particles within the virial radius for the simulations AqC5-newH (*top panel*) and AqC5-oldH (*bottom panel*). Colour encodes the mass of gas particles per density-temperature bin. The colour scale is the same for both panels.

scheme in the improved SPH, as discussed above. At higher densities, above the multiphase threshold, AqC5-newH is characterised by a larger amount of multiphase and star-forming particles, as a consequence of the more active SFR at $z = 0$.

From these phase diagrams I conclude that the interplay between the hydrodynamical scheme and the sub-resolution model plays an important role in determining the thermodynamical properties of gas particles and the resulting history of star formation and feedback.

Figure 6.10 shows radial profiles at $z = 0$ of some interesting physical properties of the two galaxies obtained with the new and the original implementation of SPH. The top-left panel describes rotation curves for AqC5-oldH (black) and AqC5-newH

(red). In this panel, the solid curves describe the circular velocity due to the total mass inside a given radius, while dashed, dotted and dot-dashed curves show the different contribution of DM, stars and gas to the total curve, respectively. Both galaxies, and AqC5-newH in particular, are characterised by total rotation curves that exhibit a flat behaviour at large radii and that are not centrally peaked, thus pointing to galaxies with a limited bulge and a dominant disc component. Differences between contributions of considered components can be understood by analysing density radial profiles.

The top-right panel of Figure 6.10 shows the density radial profiles of gas (solid), stars (dotted) and DM (dashed) in the reference simulations, out to $R_{\rm vir} = 240.15$ kpc, the virial radius of AqC5-newH. Solid vertical red and black lines pinpoint the location of $R_{\rm gal}$ of AqC5-newH and AqC5-oldH, respectively. DM profiles only differ in the innermost regions, i.e. $r < 4$ kpc. Such a discrepancy is related to the different high-z ($z > 3$) SFR between the two simulated galaxies (see Figure 6.6). The lower high-z SFR in AqC5-newH produces a stellar feedback associated to the star formation burst that is not as strong as in AqC5-oldH: as a consequence, the DM component in AqC5-newH experiences a gentler adiabatic expansion, the feedback induced gas displacement being not as striking as in AqC5-oldH, at that epoch. This results in a higher central DM volume density in AqC5-newH. Gas and stellar density profiles have similar shapes but different normalizations. A higher gas content characterises the AqC5-newH simulation, while the contribution of stars is more important in AqC5-oldH, as already seen in the circularity histograms (and quantified with gas and stellar masses above).

The middle-left panel of Figure 6.10 shows surface density profiles. Solid and dashed curves refer to gas and to stars, respectively. The comparison between the gas contribution in the two simulations further shows that AqC5-newH has a higher gas content. Moreover, the size of the gas disc is more extended and the gas mass surface density is larger in the innermost regions. The higher gas content in AqC5-newH at $z = 0$ is due to the fact that a larger amount of gas is infalling towards the galaxy at $z < 1$ with the new hydrodynamic implementation (see Figure 6.8), thus being consistent with the increasing low-z SFR shown in Figure 6.6. Stellar surface density profile is higher for AqC5-oldH, and this is in agreement with the fact that high-redshift expelled gas fell back on this galaxy at earlier times and produced more stars, while this process is still ongoing in AqC5-newH.

The middle-right and bottom-left panels of Figure 6.10 show the radial profiles of gas temperature and pressure, respectively. Discs obtained with the improved SPH formalism are hotter and more pressurized in the innermost regions. The higher pressure in AqC5-newH with respect to AqC5-oldH is a direct consequence of the higher gas surface density in the galaxy simulated with the new hydrodynamical scheme (see discussion above). Temperature and pressure profiles can be further illustrated by considering the phase diagrams of gas particles shown in Figure 6.9 and discussed above: we indeed see that in AqC5-newH there is a larger number of particles having a higher temperature, when both the low- ($\rho \lesssim 5 \cdot 10^5$ M$_\odot$ kpc^{-3}) and the high-density ($\rho \gtrsim 5 \cdot 10^5$ M$_\odot$ kpc^{-3}) regimes are considered. This holds

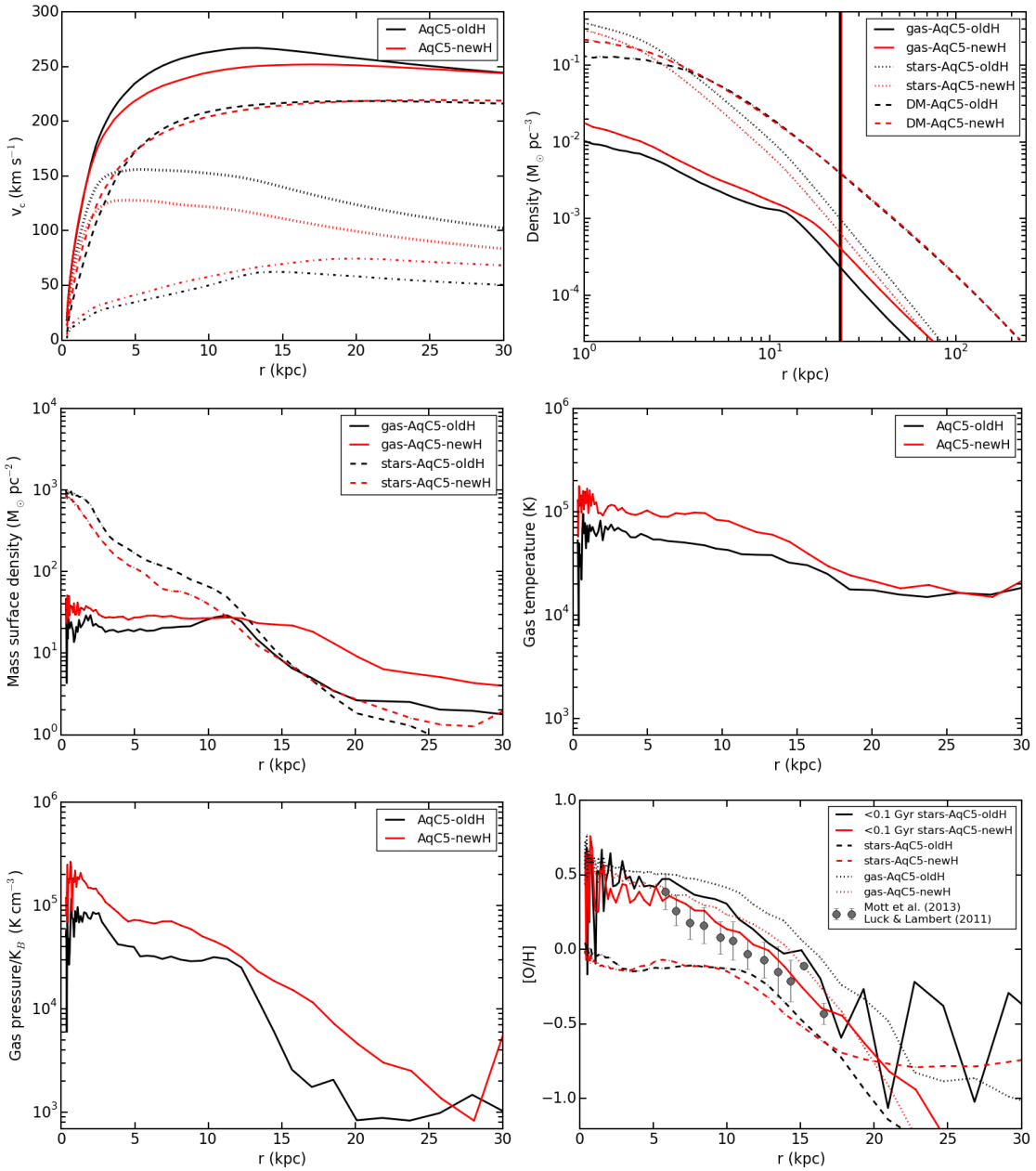

Figure 6.10: *Upper panels:* left: rotation curves for the AqC5 simulations with the old (black) and the new (red) hydrodynamical scheme. The solid curve describes the circular velocity due to the total mass inside a given radius. The split contributions of DM (dashed line), stars (dotted), and gas (dot-dashed) are shown. Right: density radial profiles of gas (solid curve), stars (dotted), and DM (dashed) for the AqC5-newH and AqC5-oldH simulations. Black and red vertical solid lines mark the galactic radii of AqC5-oldH and AqC5-newH, respectively, the x-axis extending to the virial radius of the second one. *Middle panels:* left: surface density profiles. Solid and dadhed curves describe the contribution of gas and stars, respectively. Right: gas temperature radial profiles. *Bottom panels:* left: gas pressure radial profiles. Right: radial profiles of oxygen abundance of gas (dotted curves), stars (dashed), and young stars (solid, see the text) for AqC5-newH (red) and AqC5-oldH (black). Data (grey filled circles) show the radial abundance gradient for oxygen from observations of Cepheids (Luck & Lambert, 2011), according to the division in bins performed by Mott et al. (2013). Error bars represent the standard deviation in each bin. All the profiles are analysed at $z = 0$.

in particular for multiphase particles, thus probing the higher temperature and pressure in the innermost regions of AqC5-newH.

The last panel of Figure 6.10 describes metallicity radial profiles of the two simulations. I compare the metallicity profiles from simulations with high-quality data measured for stars in our Galaxy. I stress that the current simulations are not aimed at modelling the MW; the goal of the comparison is to understand if simulated results are in broad agreement with observations of a typical disc galaxy like our MW. I consider radial profiles of oxygen abundance by number (oxygen being an accurate and reliable tracer of the total metallicity) in gas and stars for AqC5-newH (red) and AqC5-oldH (black). Data (grey filled circles) show the radial abundance gradient for oxygen from observations of Cepheids (Luck & Lambert, 2011), according to the division in bins as a function of the Galactocentric distance performed by Mott et al. (2013)[5]. Error bars represent the standard deviation computed in each bin, whose width is 1 kpc. Values for the present-day Sun's abundance are according to Asplund et al. (2009). Dotted and dashed curves depict the oxygen abundance radial profile from all the gas and star particles within $R_{\rm gal}$ at $z = 0$, respectively. I also consider oxygen abundance radial profiles (solid curves) by limiting the considered stars to those that have been formed after $z \lesssim 0.007$, i.e. less than ~ 100 Myr ago. Cepheids are indeed young stars (estimated age of $\lesssim 100$ Myr, Bono et al., 2005): solid curves allow a fair comparison with observations (I will therefore focus on them in the following analysis). I find a good agreement with observations: the slope of the radial profile predicted by considering only young stars in AqC5-newH, for distances from the galaxy centre spanning the range $5 \lesssim r \lesssim 15$ kpc, well conforms to the trend suggested by observations. The ability to recover well the slope predicted by observations highlights the effectiveness of our sub-resolution model to properly describe processes that affect the spread and the recycling of metals. I also note that there is a flattening of profiles in simulations for distances $r \lesssim 5$ kpc from the galaxy centre. The normalization of the oxygen abundance profile of young stars in AqC5-newH is consistent with observations within the error bars (despite a slight overestimate by ~ 0.05 dex, while the overestimate is about ~ 0.1 dex when AqC5-oldH is considered). However, a different normalization of the abundance profiles in simulations with respect to the observed ones is expected, as the normalization of the profiles in simulations is affected by many aspects (e.g. uncertainties related to the yields and IMF; see Chapter 7 for an extensive investigation). On the other hand, their slope can be directly compared to that of the observed abundance gradients.

The top panel of Figure 6.11 displays the stellar Tully-Fisher relation for the AqC5-newH (red) and AqC5-oldH (black) simulations. I measure the circular velocity at a distance of 8 kpc from the galaxy centre and consider the galaxy stellar mass within the galactic radius. I also plot observational data (Courteau et al., 2007; Verheijen, 2001b; Pizagno et al., 2007), the best fit to them (Dutton et al.,

[5]In this Chapter, data are the original observations by Luck & Lambert (2011): they have not been shifted by -0.17 dex as in Mott et al. (2013). Thourough discussion in Section 7.4.3.1.

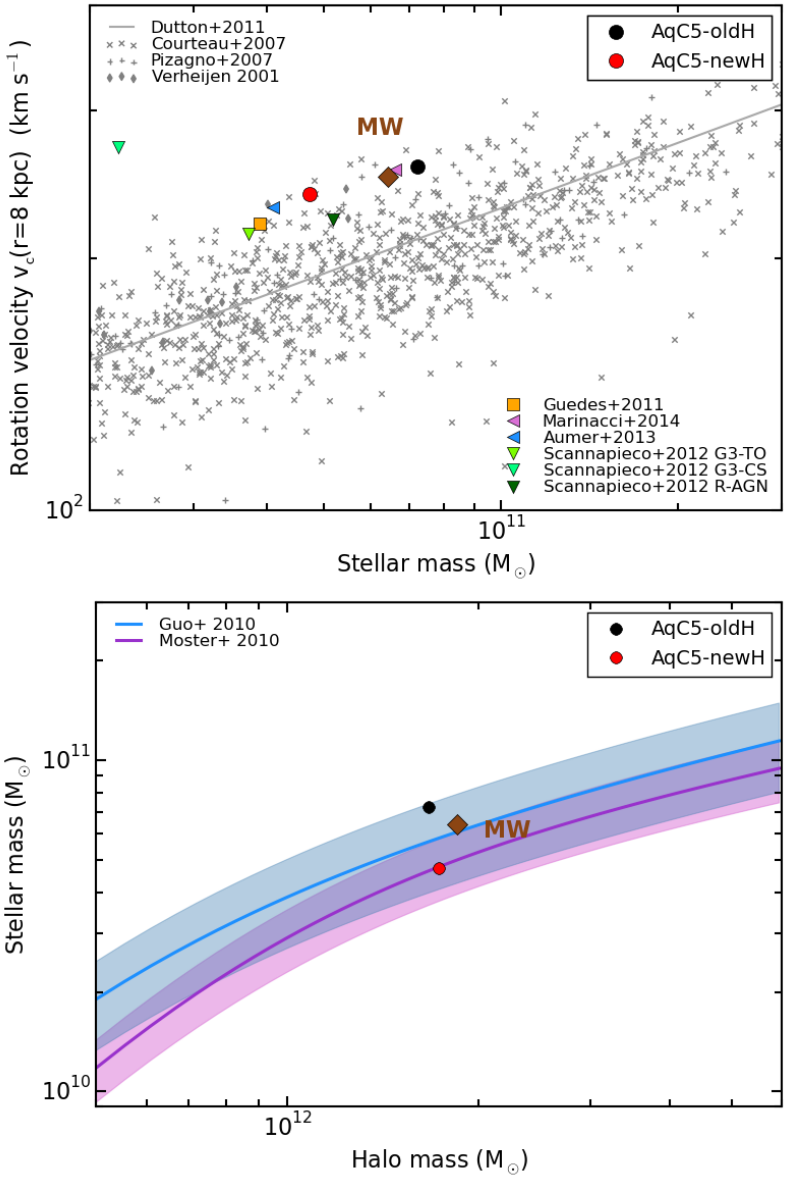

Figure 6.11: *Top panel:* Tully-Fisher relation for the AqC5-newH (red) and AqC5-oldH (black) simulations. I use the circular velocity at a distance of 8 kpc from the galaxy centre as a function of the galaxy stellar mass within the galactic radius. Grey crosses, diamonds, and plus symbols are observations from Courteau et al. (2007), Verheijen (2001b), and Pizagno et al. (2007), respectively, the solid line providing the best fit (Dutton et al., 2011b). Other coloured symbols refer to the following simulations of late-type galaxies: the purple triangle is the AqC5 from Marinacci et al. (2014), the blue triangle is the AqC5 from Aumer et al. (2013), the orange filled square shows Eris simulation from Guedes et al. (2011), and green triangles are AqC5 galaxies from the Aquila comparison project (Scannapieco et al., 2012, simulations G3-TO (light green), G3-CS (medium green) and R-AGN (dark green)). *Bottom panel:* Baryon conversion efficiency of the two disc galaxies at $z = 0$. Blue solid line shows the stellar-to-halo mass relation derived by Guo et al. (2010), with the shaded blue region representing an envelope of 0.2 dex around it. Purple solid curve describes the fit proposed by Moster et al. (2010), with 1σ uncertainty (shaded envelope) on the normalization. Brown diamonds show where the MW is located in the Tully-Fisher relation and in the stellar-to-halo mass relation plots (properties according to McMillan (2011), Bhattacharjee et al. (2014), Zaritsky & Courtois (2017)).

2011b) and results from the following simulations of late-type galaxies: the purple triangle is the AqC5 from Marinacci et al. (2014), the blue triangle is the AqC5 from Aumer et al. (2013), and the orange filled square shows Eris simulation from Guedes et al. (2011). Green triangles are AqC5 galaxies from the Aquila comparison project (Scannapieco et al., 2012, simulations G3-TO (light green), G3-CS (medium green), and R-AGN (dark green)). The brown diamond shows where the MW is placed in the Tully-Fisher relation diagram. Once again, I do not intend to claim that AqC is a model of the MW, our Galaxy being included only for completeness. As for the properties of the MW, I adopted the following values: $6.43{\cdot}10^{10}$ $M_\odot$ is the total stellar mass, 250 km s^{-1} is the circular velocity (evaluated at 8 kpc, to be consistent with our analysis), and $1.85 \cdot 10^{12}$ $M_\odot$ is the halo mass (McMillan, 2011; Bhattacharjee et al., 2014; Zaritsky & Courtois, 2017). Galaxies that I have simulated are located in the upper edge of the region traced by observational results, thus highlighting a predicted circular velocity slightly higher than the one expected from observations at the considered stellar mass. As discussed in Murante et al. (2015), this appears to be a feature shared among several similar simulations of late-type galaxies. ICs likely play a role in the aforementioned shift, rather than resolution.

The bottom panel of Figure 6.11 shows the baryon conversion efficiency of the two disc galaxies at $z = 0$. Blue solid line shows the stellar-to-halo mass relation derived by Guo et al. (2010), with the shaded blue region representing an interval of 0.2 dex around it (as done in Marinacci et al., 2014, and in Murante et al. 2015). Purple curve describes the fit (solid line) proposed by Moster et al. (2010), with 1-σ uncertainty (shaded envelope) on the normalization. The simulation performed with the new SPH implementation is characterised by a lower baryon conversion efficiency, that is in good agreement with both the predictions by Moster et al. (2010) and Guo et al. (2010). As discussed above, this reflects on the lower stellar mass of the new galaxy.

As for the comparison between AqC5-oldH and AqC5-newH simulations, the key differences can be interpreted as an effect of the different MAH: gas accretion within the virial and galactic radii is delayed in AqC5-newH. In this simulation there is still fresh gas that is infalling towards the galaxy centre at $z < 1$. In general, we are able to obtain a disc-dominated galaxy with both the old and the new hydrodynamical schemes. The free parameters of our sub-grid model had to be re-tuned when the improved SPH implementation has been adopted (see also Section 6.6.1).

6.5.3 Changing the galactic outflow model

6.5.3.1 Tuning the models

In this Section, I compare the results obtained from the three implementations of galactic outflows described in Section 6.3, and compare them to the original one presented by Murante et al. (2015). I remind that all the differences I present in this Section are only due to the change in the outflow model, being the ICs, the code, the

(improved) SPH implementation (see Section 5.2 and Table 6.3), and the MUPPI star formation model exactly the same in all cases. Note that I kept fixed the scheme for the *thermal* energy release of MUPPI. All the changes only concern the distribution of the fraction of SN energy that is provided in *kinetic* form in the original model.

For each of the three outflow models, I carried out a detailed exploration of the corresponding parameter space. To select the preferred set of parameters, I mainly focused on those simulations that produce the most prominent stellar disc component, as evaluated by visual inspection and by comparing the circularity histograms, as those shown in Figure 6.14. I also analysed the galactic SFRs, as those shown in Figure 6.15, trying to minimize the high-redshift star formation burst, in order to prevent a too large amount of late gas infall and, consequently, a too high low-redshift SFR. It was not feasible to simultaneously calibrate other properties of the simulated galaxies, such as the B/T ratio and the total stellar mass (or one between the disc or the bulge stellar mass). However, as I will show below, the main point is that galaxy properties are deeply linked to the selected outflow model: it is very difficult to obtain the same set of properties by simply tuning the model parameters.

I performed an accurate exploration of the models' parameter space mainly using the low-resolution AqC6 ICs. When needed, I slightly re-tuned some of the parameters at the higher resolution of the AqC5 ICs. In this Section, we only show results for our AqC5 best cases. The procedure for parameter tuning is described in Section 6.6.2.

The FB1 model is an implementation of the model originally introduced by Dalla Vecchia & Schaye (2012), in the context of our MUPPI star formation and ISM model. Here, the relevant parameters are the temperature jump ΔT, and the fraction of SNII energy available to power the outflows, $f_{\rm fb,kin}$, i.e. the feedback efficiency. I adopt a temperature jump that depends on the density of gas particles that are eligible to produce feedback, as detailed in Section 6.3.1 (see also Section 6.6.2 for results of a simulation where I fix the temperature jump to the value of $T = 10^{7.5}$ K). As for the feedback efficiency, I adopted the density- and metallicity-dependent feedback efficiency used in the reference Eagle simulation (Schaye et al., 2015), as discussed in Section 6.3.1. Such a choice successfully produces a disc-dominated galaxy at redshift $z = 0$, even if this galaxy is characterised by high low-redshift gas MAH and resulting SFR (see Figures 6.16, 6.15, and discussion in Section 6.5.3.2). Nonetheless, I prefer to consider the model adopting this feedback efficiency (equation 6.3) as reference FB1 simulation: I then discuss in Section 6.6.2 how different choices for $f_{\rm fb,kin}$ can reduce the amount of gas available for the low-z phase of disc formation, thus regulating the SFR at $z = 0$.

Energy provided by star formation is distributed according to Dalla Vecchia & Schaye (2012): first, I calculate the SNII energy release of the whole stellar population. Then, when a star is spawned, I use it to heat the surrounding gas. In principle, such mechanism of delivering energy contrasts with the continuous SFR of MUPPI model. In our sub-resolution model, energy provided by SNe is

indeed computed by using the energy contributed by the virtual stellar component in multiphase gas particles in each time-step, regardless of the moment in which the spawning of a star particle occurs. This results in a gradual way of distributing and releasing energy. On the other hand, if the whole amount of energy is released impulsively when a star is really spawned, the feedback turns out to be more effective. The gradual way of distributing energy does not allow us to produce disc-dominated galaxies when the FB1 galactic outflow model is adopted, since the stellar feedback is not effective enough to prevent an excessive high-redshift star formation burst. The aforementioned set of choices allows to produce an AqC5-FB1 galaxy with a dominant disc component.

The FB2 scheme is a modification of the original MUPPI outflow model. In the process of tuning this model's parameters, I had to reduce the value of the SNII energy faction down to $f_{\rm fb,kin} = 0.12$ and the probability of a gas particle to become a wind one to $P = 0.03$, in order to account for the fact that this scheme does not limit the search of available wind particles to a cone but uses the whole smoothing sphere.

Finally, results for the FB3 scheme are shown with parameters $\eta = 3.0$ and $f_{\rm fb,kin} = 2.0$. In Section 6.6.2, I discuss the choice of the parameter $f_{\rm fb,kin}$, that is the parameter to which this model is most sensitive. There, I also refer to Springel & Hernquist (2003), whose model this galactic outflow scheme is inspired. Here, I note that the higher is the value of the mass loading factor (values of η ranging between 0.5 and 8), the narrower and more reduced is the high-redshift star formation burst, thus shortening the phase of bulge formation and limiting bulge size accordingly. Observations of low-redshift kpc-scale neutral gas outflows suggest a value for the mass loading factor that slightly exceeds unity (Cazzoli et al., 2014).

6.5.3.2 Comparing results

In this Section, I discuss results obtained using my four galactic outflow models, the original one and those described in Section 6.3. Figures 6.12 and 6.13 introduce the simulated galaxies AqC5-FB1, AqC5-FB2, and AqC5-FB3, showing face-on and edge-on gas and stellar density maps, respectively. I focus on the following properties of the simulated galaxies: circularity of stellar orbits, SFRs, gas MAHs, rotation curves, Tully-Fisher relation and baryon conversion efficiencies, metallicity, and surface density profiles.

In Figure 6.14, I show the circularities for all of our models, at redshift $z = 0$. In all cases, I obtain rotationally supported galaxies. However, the bulge-over-total mass ratio changes significantly with the outflow model, with $B/T = 0.30, 0.19, 0.35$, and 0.54 for the original model, FB1, FB2 and FB3, respectively. Note that my estimate for the B/T ratio could also include satellites, stellar streams, and contribution from bars within $R_{\rm gal}$. Therefore, the B/T values that I quote throughout the Thesis should not be directly compared with observational photometric estimates, as the photometric determination for the value of B/T has been shown to be lower than the corresponding kinematic estimate (Scannapieco

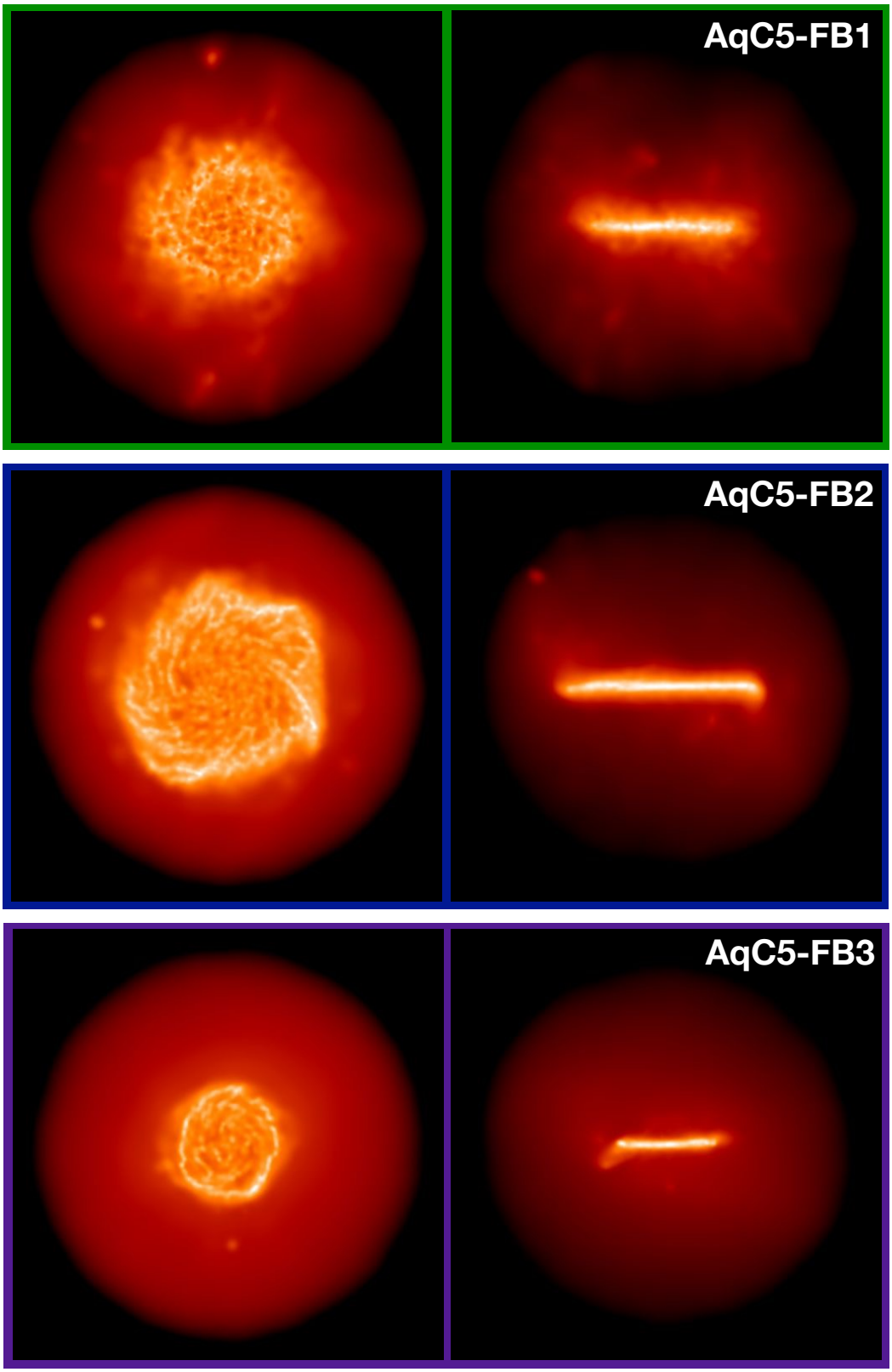

Figure 6.12: Projected gas density maps for the simulations AqC5-FB1 (*top panels*), AqC5-FB2 (*middle panels*), and AqC5-FB3 (*bottom panels*). Left- and right-hand panels show face-on and edge-on densities, respectively. All the maps are shown at redshift $z = 0$. The size of the box is 55 kpc.

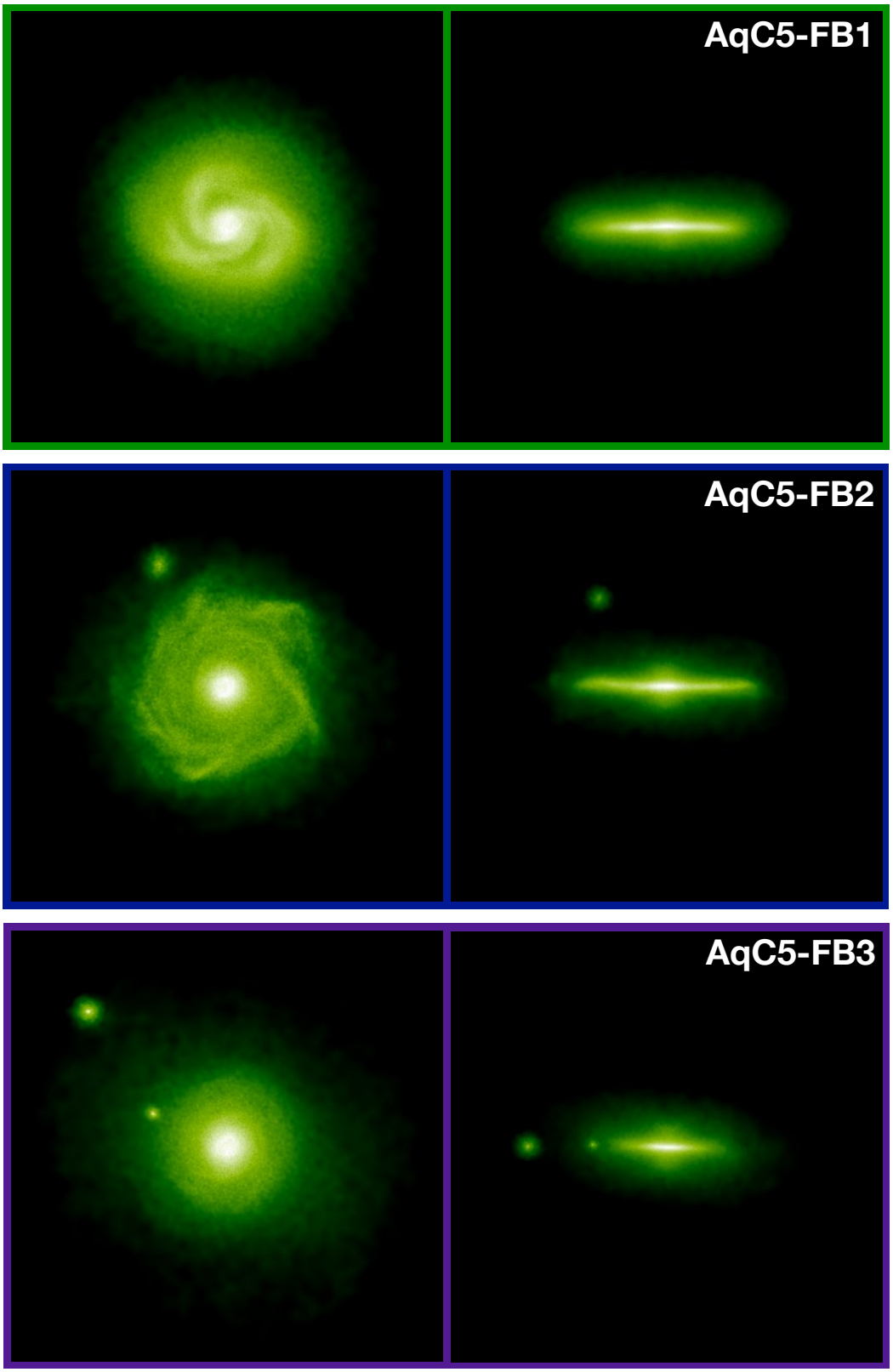

Figure 6.13: Projected stellar density maps for the simulations AqC5-FB1 (*top panels*), AqC5-FB2 (*middle panels*), and AqC5-FB3 (*bottom panels*). Left- and right-hand panels show face-on and edge-on densities, respectively. All the maps are shown at redshift $z = 0$. The size of the box is 55 kpc.

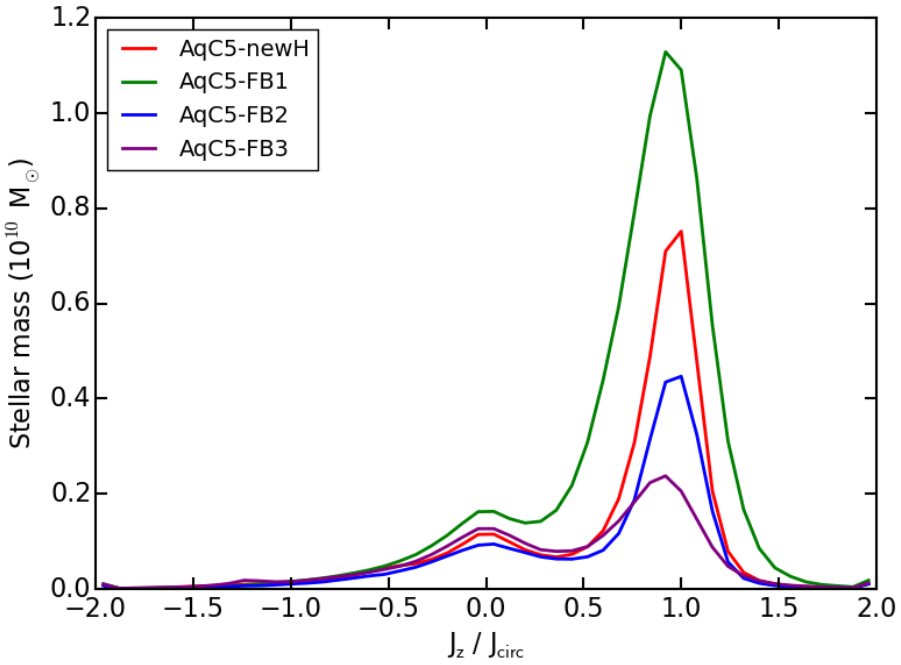

Figure 6.14: Stellar mass as a function of the circularity of stellar orbits at $z = 0$. The red curve refers to the AqC5-newH run, the green one to AqC5-FB1, the blue curve identifies AqC5-FB2 and the purple one AqC5-FB3. The values of the B/T ratios are: 0.30, 0.19, 0.35, and 0.54, respectively.

et al., 2010). The total stellar mass of the galaxy (the integral of the circularity histogram) does change, too. Total stellar masses within $R_{\rm gal}$ for AqC5-newH, AqC5-FB1, AqC5-FB2, and AqC5-FB3 are $4.74 \cdot 10^{10}$ M$_\odot$, $9.34 \cdot 10^{10}$ M$_\odot$, $3.29 \cdot 10^{10}$ M$_\odot$, and $2.94 \cdot 10^{10}$ M$_\odot$, respectively. Galactic radii are 24.01 kpc for AqC5-newH, 24.76 kpc for AqC5-FB1, 23.90 kpc for AqC5-FB2, and 23.58 kpc for AqC5-FB3. I remind that the galactic radius $R_{\rm gal} = 0.1\,R_{\rm vir}$, and it is not the scale radius of the stellar disc: the comparable size of the galactic radii of the four simulated galaxies points to fact that changing galactic outflow models does not affect significantly the large-scale dynamics.

Figure 6.15 shows the SFRs obtained for the four implementations of the outflow model, as a function of the cosmic time. SFRs are computed by considering all stars within $R_{\rm gal}$ at $z = 0$. The SFR of all models is comparable at high ($z > 3$) redshifts. Bulges of simulated galaxies form at these epochs. At later times, during the disc formation phase, the behaviour of the outflow models differs. FB1 scheme has an SFR that is slightly higher than the other models between $3 > z > 2$, thus producing a further growth of the bulge, that is the most massive one. The SFR of this model has then a drop; at $z \simeq 0.7$ it starts to rapidly increase again, and it reaches the roughly constant value of $\simeq 20$ M$_\odot$ yr^{-1} from $z \simeq 0.35$ on, i.e. over the last ~ 4 Gyr. Schaye et al. (2015) predict the SFR to be at most $\simeq 8$ M$_\odot$ yr^{-1} for a galaxy with a stellar mass slightly lower than $8 \cdot 10^{10}$ M$_\odot$ at $z = 0.1$ (this value corresponds to the upper edge of the $1-\sigma$ uncertainty of their figure 11). My galaxy (whose stellar mass is $7.39 \cdot 10^{10}$ M$_\odot$ at $z = 0.1$) has therefore an SFR in excess

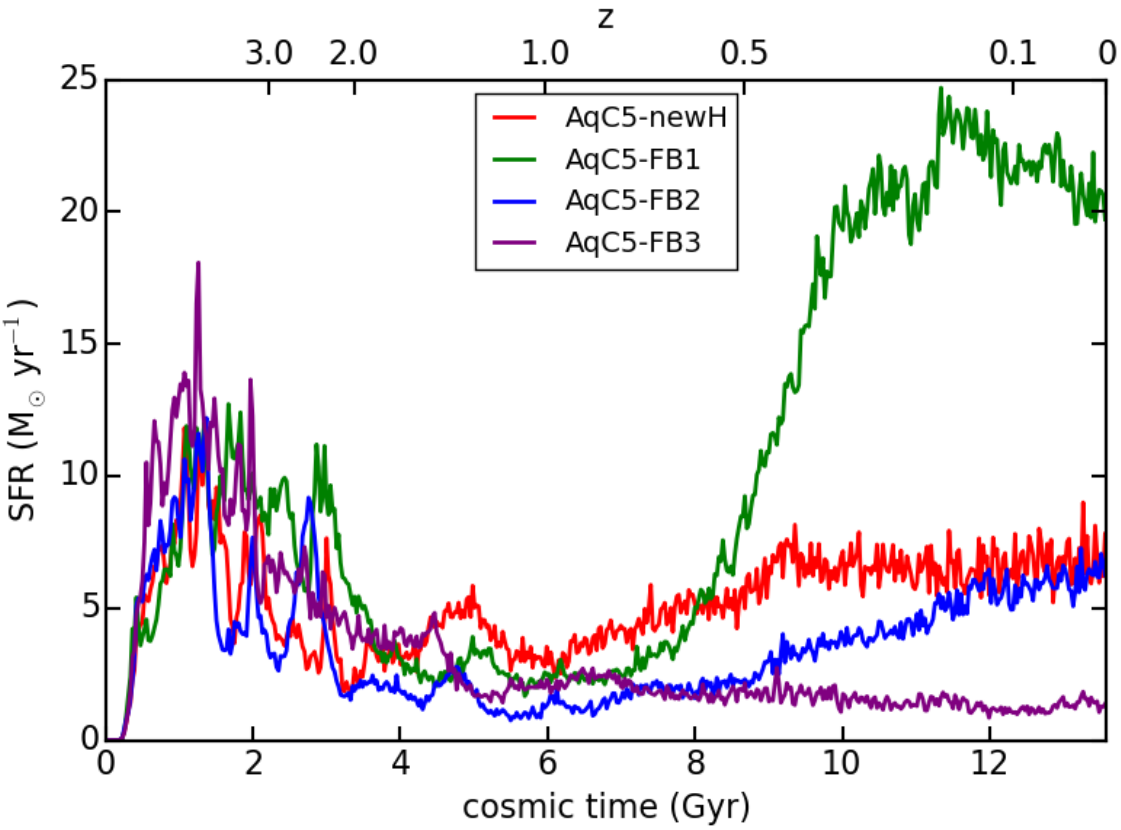

Figure 6.15: SFRs for the AqC5-FB1, AqC5-FB2, and AqC5-FB3 simulations, compared with that of AqC5-newH. Colours are as in Figure 6.14. Results refer to $z = 0$.

of that predicted by Schaye et al. (2015) by a factor of 2.5. However, unlike in Schaye et al. (2015), our simulations do not include SMBHs and the ensuing AGN feedback: AGN feedback is indeed expected to play a role in reducing low-redshift SFR (in Section 6.6.2, I show how I regulated the low-z SFR with a different choice of $f_{\rm fb,kin}$). Figure 6.15 highlights how different prescriptions for the star formation impact on final results, even when the same galactic outflow model is adopted.

Both FB2 and FB3 schemes do show a drop in the SFR below $z = 2$ with respect to AqC5-newH. In the FB2 case, SFR rises again after $z \simeq 0.5$, while it remains below ~ 2 M$_\odot$ yr^{-1} for FB3. This is clearly at the origin of the higher B/T ratios produced by these two schemes: the early-forming bulge component is similar to that of AqC5-newH, but the disc formation phase is delayed or suppressed.

The reason for the different behaviour of the SFR among models is further illustrated by Figure 6.16. Here, I show the gas MAH on to the main progenitor of the galaxy as a function of the redshift. I have already shown in Figure 6.8 a comparison of the gas MAH using the old and the new SPH implementation, and found a delay in the gas fall-back when I use the new scheme with respect to the old one. Here, the qualitative behaviour of the MAH is similar for all of the four galactic outflow models for $z \gtrsim 2$, both within the virial (top panel) and the galactic (bottom panel) radii. FB1 has the highest gas accretion rate from $z \simeq 1.5$ on. This

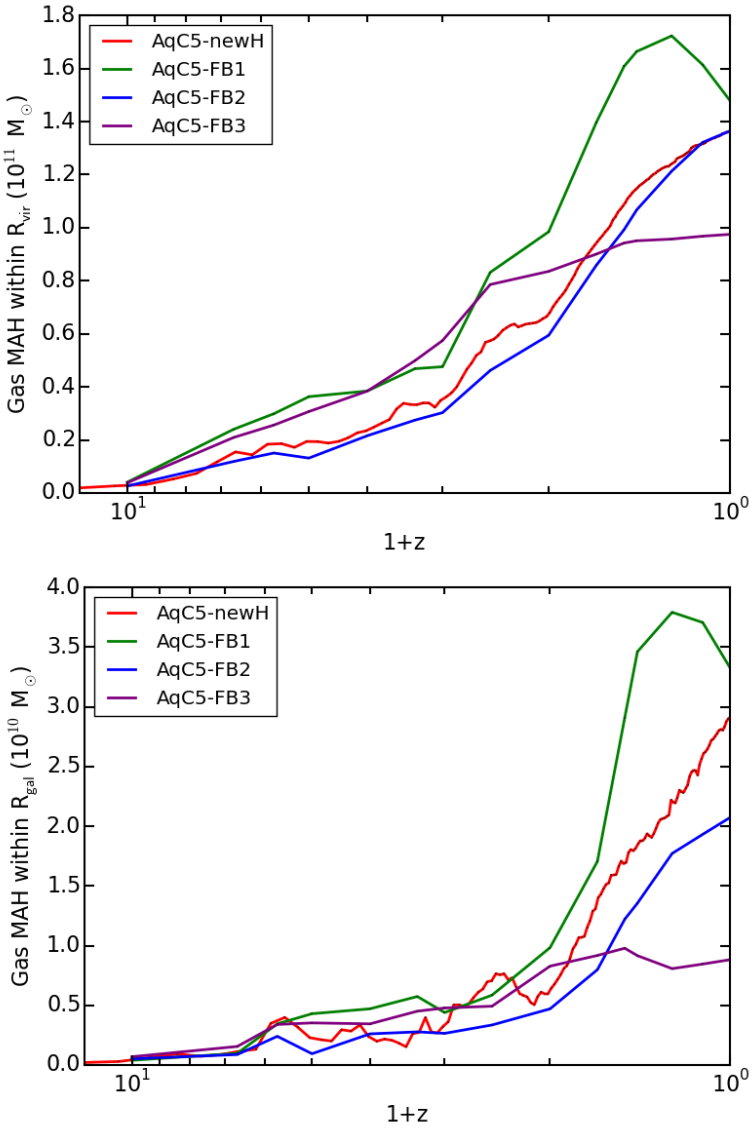

Figure 6.16: Gas MAH for AqC5-FB1, AqC5-FB2, and AqC5-FB3, compared with the result of AqC5-newH. Colours are as in Figure 6.14. Top panel shows the gas MAH within the virial radius, and bottom panel within the galactic radius.

feature highlights that this galactic outflow model is not as effective as the others in preventing gas accretion and explains the highest low-redshift SFR and final stellar mass of the galaxy simulated with this scheme. FB2 gas MAH closely follows that of the original scheme at the virial radius, but the gas accretion rate within $R_{\rm gal}$ at low redshift (below $z \sim 2$) is significantly lower. I interpret this as the evidence that this kind of feedback is more effective at low redshift, generating strong outflows that stop gas from fuelling the disc growth. FB3 is even more effective in expelling gas from the galaxy, and at $z \lesssim 1$ also from the halo. In fact, it has the lowest SFR, the smallest disc component and, as a consequence, the highest value of the B/T ratio[6].

[6]I show, for each galactic outflow model, the simulation that produces the best results in terms of circularity histogram and SFR. Any shortfall of each model is therefore a direct result of how the outflow is described and should not be ascribed to an unreliable tuning of the parameters.

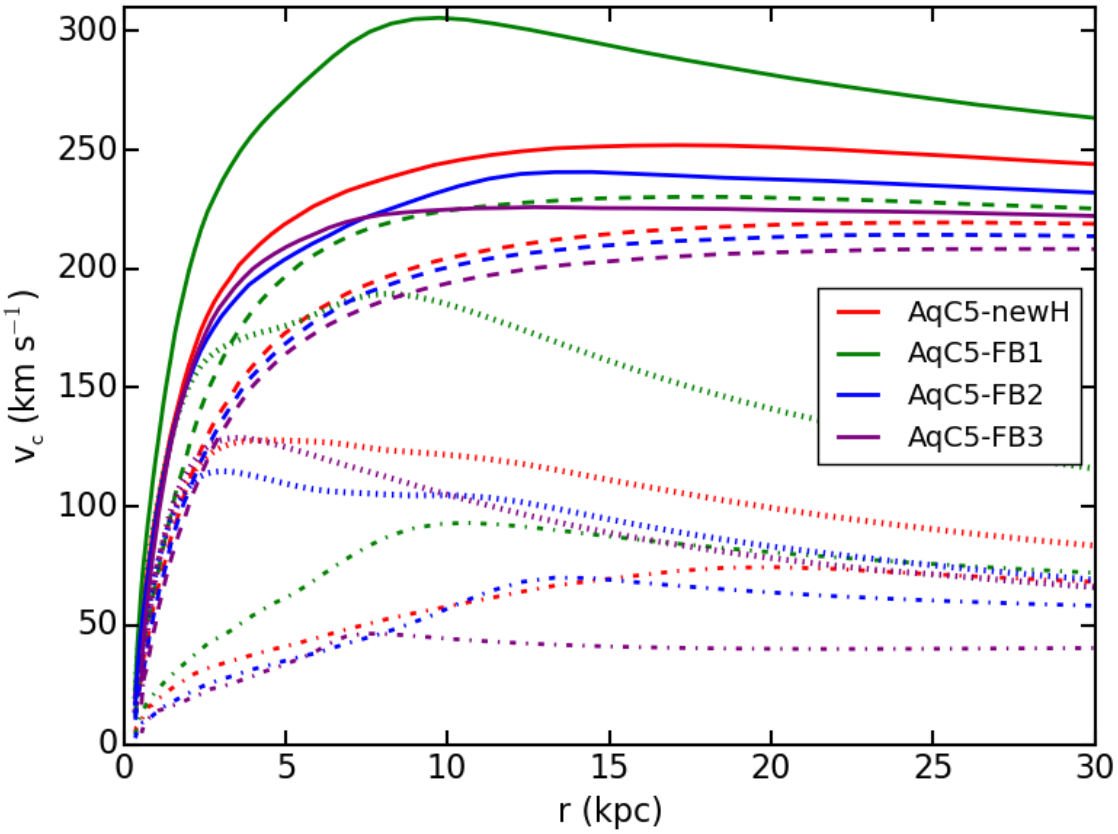

Figure 6.17: Rotation curves at $z = 0$ for AqC5-FB1, AqC5-FB2, and AqC5-FB3, compared with that of AqC5-newH. Colours as in Figure 6.14. The solid curves describe the circular velocity due to the total mass inside a given radius. The different contribution of DM (dashed line), stars (dotted) and gas (dot-dashed) to the total curve are shown.

In Figure 6.17, I show the circular velocity profiles for all the schemes. AqC5-newH, FB2, and FB3 models have profiles that are flat at large radii, thus confirming their ability to prevent the formation of a strong baryonic concentration at the centre. FB1 scheme produces a galaxy whose stellar component of the rotation curve has the most pronounced peak at small radii ($r \lesssim 5$ kpc): this is related to the larger mass of the bulge that is produced in this case. The morphology of this galaxy, with prominent stellar spiral arms, originates the peak of the velocity profile of the FB1 model, at $r \simeq 8$ kpc (see the stellar density profile in Figure 6.18, too). The normalization of the circular velocity profiles straightforwardly follows the different stellar (see above) and gas (see below) masses of the four simulations.

The top panel of Figure 6.18 shows surface density profiles of the four simulated galaxies. Dashed and solid curves refer to stars and to gas, respectively. Total gas masses within $R_{\rm gal}$ for AqC5-newH, AqC5-FB1, AqC5-FB2, and AqC5-FB3 are $2.91 \cdot 10^{10}$ M$_\odot$, $3.33 \cdot 10^{10}$ M$_\odot$, $2.07 \cdot 10^{10}$ M$_\odot$, and $8.82 \cdot 10^{9}$ M$_\odot$, respectively. Total gas masses within $R_{\rm vir}$ for AqC5-newH, AqC5-FB1, AqC5-FB2, and AqC5-FB3 are $1.36 \cdot 10^{11}$ M$_\odot$, $1.48 \cdot 10^{11}$ M$_\odot$, $1.36 \cdot 10^{11}$ M$_\odot$, and $9.75 \cdot 10^{10}$ M$_\odot$, respectively. Gas masses directly come from the different gas MAHs within $R_{\rm vir}$ and $R_{\rm gal}$ (see

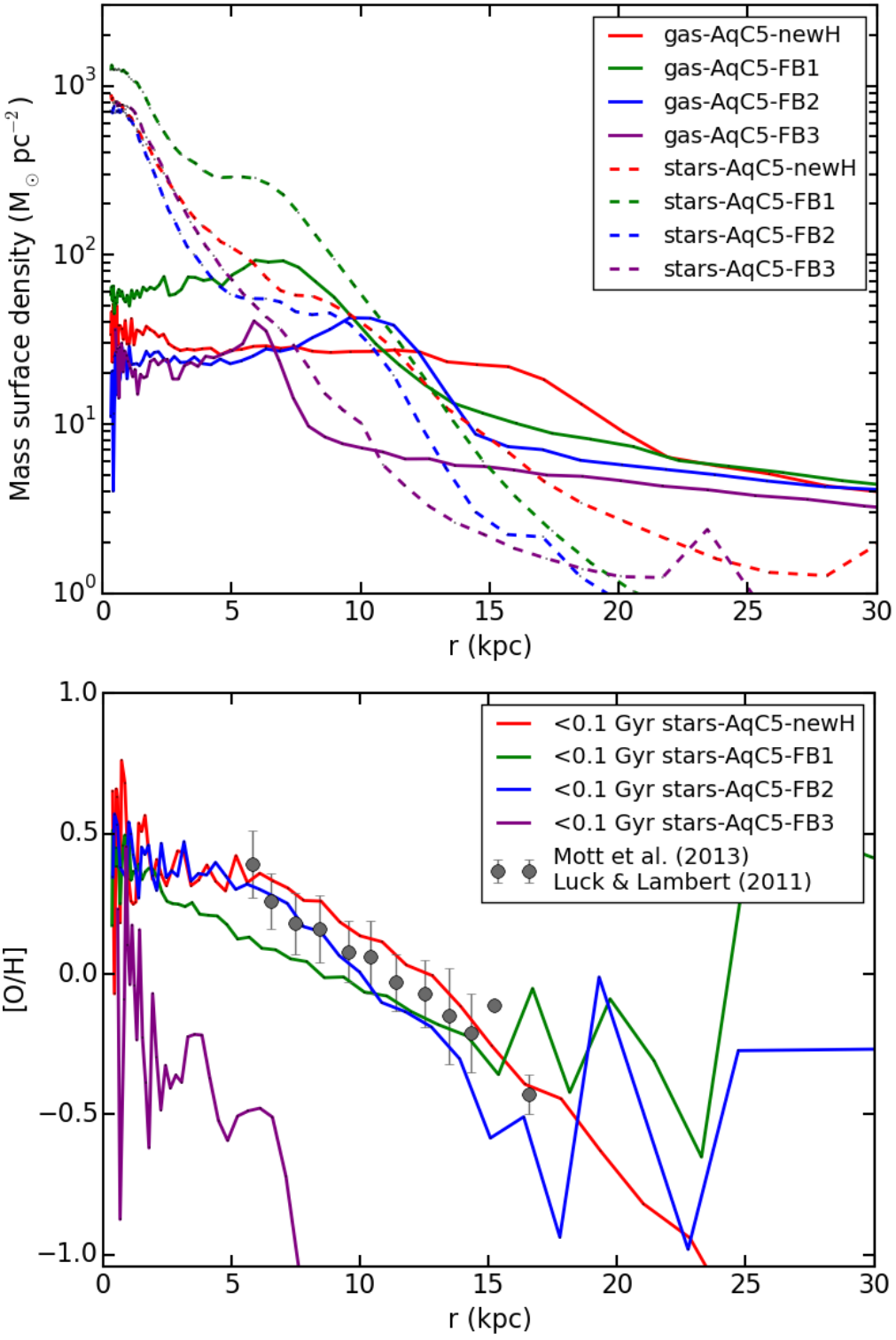

Figure 6.18: *Top panel:* surface density profiles for simulations AqC5-newH (red), AqC5-FB1 (green), AqC5-FB2 (blue) and AqC5-FB3 (purple). Solid curves describe the contribution of gas and dashed lines the one of the stars. *Bottom panel:* radial profiles of oxygen abundance in young stars (see the text) for the four simulations. Data (grey filled circles) show the radial abundance gradient for oxygen from observations of Cepheids (Luck & Lambert, 2011), according to the division in bins as a function of the Galactocentric distance performed by Mott et al. (2013). Error bars represent the standard deviation computed in each bin. All the profiles are analysed at $z = 0$.

Figure 6.16). AqC5-newH has both the most extended gas disc and the stellar component that extends farthest from the galaxy centre. AqC5-FB1 has the largest gas mass surface density in the innermost regions. Gas surface density profiles of AqC5-FB1, AqC5-FB2 and AqC5-FB3 exhibit a bump at the edge of the gas disc (at distances of 7, 10 and 6 kpc, respectively). In particular for AqC5-FB1 and AqC5-FB2, it is possible to note a corresponding excess in the stellar surface density. This is the effect of high angular momentum gas infalling within $R_{\rm gal}$ at low redshift. The shallower decrease in the stellar surface density profiles is a consequence of the enhancement of the star formation due to the recently accreted gas. The infalling gas is material ejected from the forming halo – due to the high-redshift ($z \gtrsim 3$) star formation burst that formed the bulge – with a low angular momentum. After acquiring angular momentum from halo gas (Brook et al., 2012; Übler et al., 2014; Teklu et al., 2015; Genel et al., 2015), the expelled material fell back, in a way regulated by the stellar feedback. As for AqC5-FB3, the gas fall-back occurred at earlier times than in AqC5-FB1 and AqC5-FB2 (see Figure 6.16 and discussion above), where instead the process is still ongoing.

The bottom panel of Figure 6.18 shows the metallicity radial profiles of the four simulations, where I consider radial profiles of oxygen abundance by number in stars (within $R_{\rm gal}$) that are younger than $\sim$ 100 Myr, in order to make a fair comparison with observations (as discussed in Section 6.5.2). Data (grey filled circles) are the same as in the last panel of Figure 6.10. Negative radial abundance gradients are recovered for all the models, in line with observational results. The agreement between oxygen abundance radial profiles predicted by different simulations and observations demonstrates the effectiveness of a sub-resolution model (and in particular of a galactic outflow model) to properly describe the chemical enrichment of the galaxy at different positions. We see that the galactic outflow model of AqC5-newH and FB2 well reproduces the slope of observed radial abundance profiles. The slope of the profile in AqC5-FB1 is slightly flatter than in observations. The normalization of radial abundance profiles in simulations is a delicate aspect (as discussed in Section 6.5.2); nonetheless, the normalization of the oxygen abundance profile in both the AqC5-newH and AqC5-FB2 simulations is consistent with the observed abundance gradient within the error bars. The metallicity radial profile predicted by the AqC5-FB1 simulation shows an oxygen abundance lower than observations in the inner regions ($r \lesssim 10$ kpc). The metal content of young stars throughout the galaxy is more homogeneous: this galactic outflow model is able to promote a more efficient spread of metals from stars to the surrounding gas. As for the FB3 model, it does not succeed in reproducing observations. The AqC5-FB3 galaxy has a limited stellar disc (see Figure 6.18, top panel), it is characterised by a low SFR (Figure 6.15) and a reduced gas MAH (Figure 6.16) below $z \sim 1$: as a consequence, a lower amount of metals has been produced in a confined region (subsequently generated stars being richer in heavy elements than previous ones). As for the relative difference between slopes and normalizations of profiles in simulations AqC5-newH and AqC5-FB2, metals are less locked into stars in AqC5-newH with respect to AqC5-FB2.

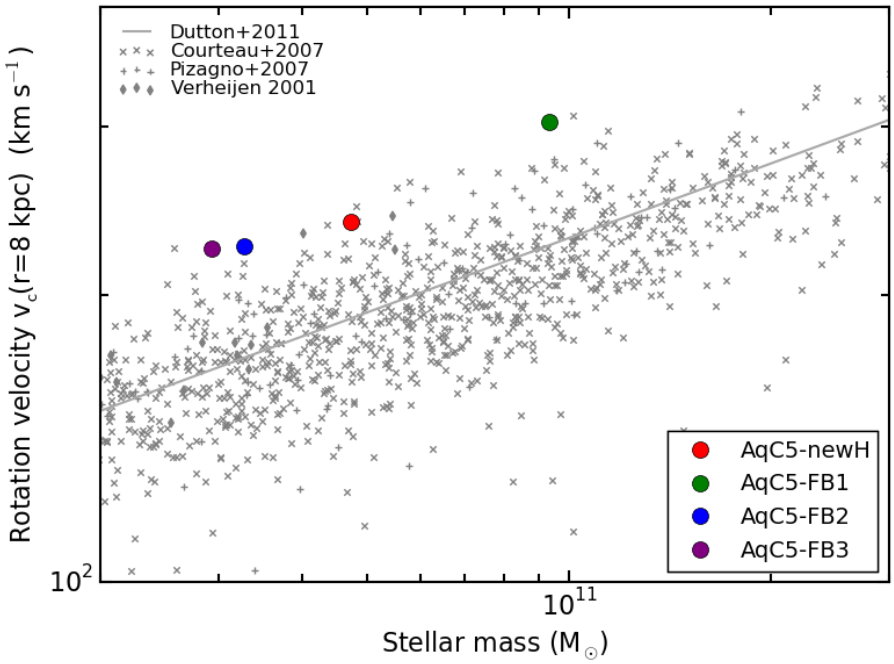

Figure 6.19: Tully-Fisher relation at $z = 0$ for AqC5-FB1, AqC5-FB2, and AqC5-FB3, compared with that of AqC5-newH. Colours are the same used in Figure 6.14. I use the circular velocity at a distance of 8 kpc from the galaxy centre as a function of the galaxy stellar mass within the galactic radius. Grey symbols are as in Figure 6.11.

Figure 6.19 shows the position of the four simulated galaxies in the Tully-Fisher diagram. Also in this case, as already discussed in Section 6.5.2, all the simulated galaxies lie close to the upper limit of the region allowed by observations. AqC5-FB1 galaxy lies just outside the region identified by the scatter of the observed data: this is a consequence of its peaked rotation curve (Figure 6.17). Rotation velocity scales with the stellar mass of the simulated galaxies, thus the position in the diagram of our four galaxies just relates with their stellar mass.

Finally, in Figure 6.20, I show the position of the simulations in the baryon conversion efficiency plot. FB1 is characterised by a baryon conversion efficiency that slightly exceeds the uncertainty contour of the prediction by Guo et al. (2010) and that overestimates the one by Moster et al. (2010). FB2 shows a baryon conversion efficiency lower than the expectations from Guo et al. (2010) and Moster et al. (2010), and also FB3 underproduces stars. Note that the lower the baryon conversion efficiency of simulated galaxies is, the larger their B/T (see Figure 6.14).

A general result of this Section is that the observational properties of the simulated galaxies are sensitive to the details of the different outflow models, even when they are implemented within the same star formation scheme. Some of these properties, for instance the bulge mass and (to a lower extent) the radial dependence of the rotation velocity (at large radii) are relatively stable against the considered implementations of galactic outflow model. On the other hand, the prominence of the disc component is highly sensitive to the implemented model and, more specifically, to the timing of the gas fall-back and to the mass of the gas involved.

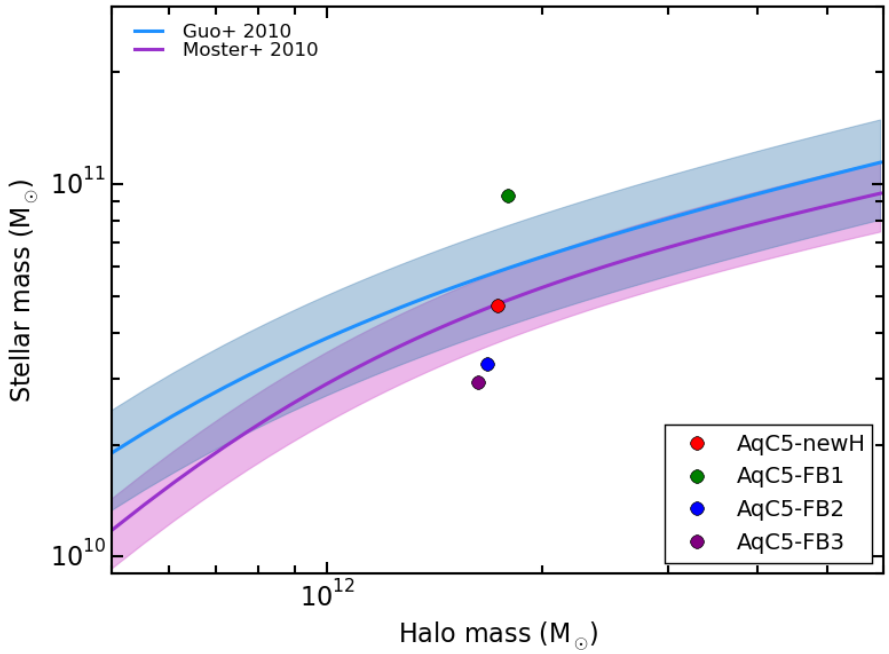

Figure 6.20: Baryon conversion efficiencies at $z = 0$ for AqC5-FB1, AqC5-FB2, and AqC5-FB3, compared with that of AqC5-newH. Colours are as in Figure 6.14. Blue solid line shows the stellar-to-halo mass relation derived by Guo et al. (2010), with the shaded blue region representing an envelope of 0.2 dex around it. Purple solid curve describes the fit proposed by Moster et al. (2010), with 1σ uncertainty (shaded envelope) on the normalization.

In fact, a feedback model that is successful in producing a disc-dominated galaxy should be able to regulate the pristine star formation, which is responsible for the creation of the bulge component, and, at the same time, not to allow a too late gas fall-back, that would turn into a too high SFR at $z = 0$. The results of my simulations confirm that this represents a non-trivial requirement on galactic outflow models to be implemented in cosmological simulations of galaxy formation.

6.6 Discussion

6.6.1 Effect of the resolution

In this Section, I discuss how the main results change when I decrease the mass resolution by a factor of ~ 10 (see Table 6.1).

Table 6.4 lists the set of simulations that I analyse in Sections 6.6.1 and 6.6.2. I do not report again here simulations already introduced in Tables 6.1 and 6.3. The simulation AqC6-newH that has been introduced in Tables 6.1 and 6.2 is now labelled as AqC6-newH_p003. The simulation AqC5-FB3 that had been introduced in Tables 6.3 is now labelled as AqC5-FB3_fk2.0.

Table 6.4: Name and details of the simulations discussed in Sections 6.6.1 and 6.6.2. *Column 1:* label of the run. *Column 2:* parameter of interest for the comparison investigated here. *Column 3:* galactic outflow model (original refers to Section 5.3). *Column 4:* hydrodynamical scheme.

Simulation	Parameter $f_{\rm fb,kin}$ or $P_{\rm kin}$	Outflow model	Hydro scheme
AqC6-newH_p003	$P_{\rm kin}$=0.03	Original	New
AqC6-newH_p005	$P_{\rm kin}$=0.05	Original	New
AqC5-FB1f2.0-1.0	Equation (6.18) with $f_{\rm fb,kin}{}^{\rm max}_{\rm min} = {}^{2.0}_{1.0}$	FB1	New
AqC6-FB1fEagle	Equation (7) of Schaye et al. (2015) for $f_{\rm fb,kin}$ (see the text)	FB1	New
AqC6-FB1- $\Delta T_{\rm fix}$	$f_{\rm fb,kin}$: equation (7) of Schaye et al. (2015); $\Delta T_{\rm fix} = 10^{7.5}$ K	FB1	New
AqC6-FB1f1.0	$f_{\rm fb,kin}$=1.0	FB1	New
AqC5-FB3_fk2.0	$f_{\rm fb,kin}$=2.0	FB3	New
AqC5-FB3_fk0.5	$f_{\rm fb,kin}$=0.5	FB3	New
AqC5-FB3_fk0.25	$f_{\rm fb,kin}$=0.25	FB3	New

I now focus on simulations AqC6-oldH, AqC6-newH_p003, AqC6-newH_p005, and contrast their results with those of AqC5-oldH and AqC5-newH that we have analysed in Section 6.5.2.

The four upper panels of Figure 6.21 show face-on and edge-on projections of gas (top panels) and stellar (third and fourth ones) density for the AqC6-newH_p003 galaxy simulation, at $z = 0$. The four lower panels depict face-on and edge-on projections of gas (fifth and sixth panels) and stellar (bottom ones) density for AqC6-oldH, at $z = 0$. The reference system has been rotated as described for Figure 6.4. AqC6-newH_p003 is a clearly disc-dominated galaxy, and a spiral pattern is evident, especially in the gas component. The gaseous disc of the galaxy produced by adopting the improved hydrodynamical scheme is more extended than the stellar one at this resolution, too. Continuing to focus on the galaxy simulated with the new SPH, it is possible to notice how the density in the outer part of the gaseous halo is no longer resolved above a given height on the disc plane (see top-right panel) at this resolution, with respect to Figure 6.5. Moreover, both the gaseous and the stellar disc of AqC6-newH_p003 are more extended than the analogous ones of AqC6-oldH when this lower resolution is considered, too.

Figures 6.22, 6.23, 6.24, and 6.25 show the impact of the hydrodynamic solver on the results of AqC6 simulations and how the main results are sensitive to the change of resolution. For the sake of completeness, besides AqC6-newH_p003, I also show results of AqC6-newH_p005, where I have set the probability $P_{\rm kin} = 0.05$

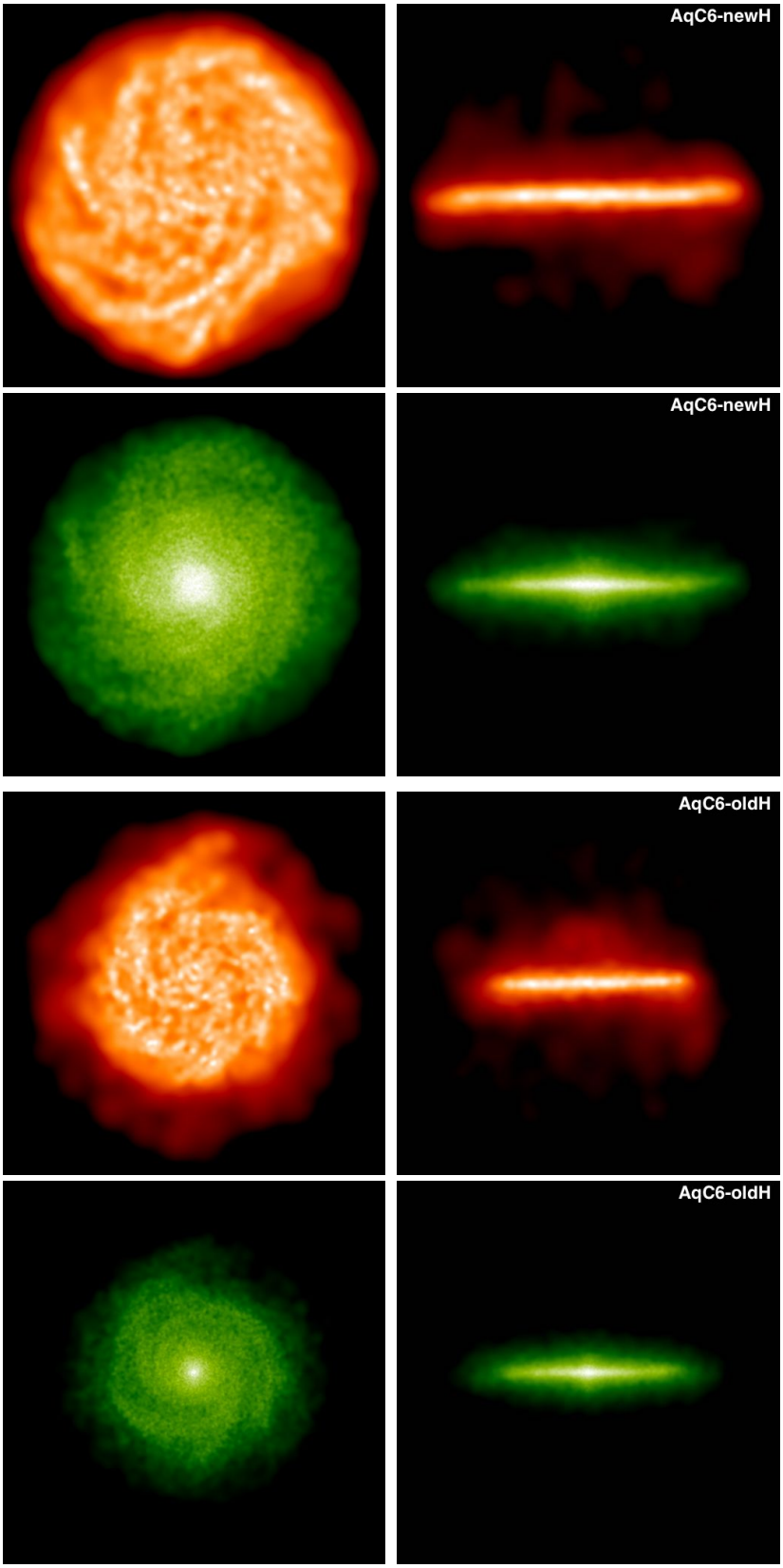

Figure 6.21: *Top four panels:* projected gas (first and second panels) and star (third and fourth) density for the AqC6-newH_p003 simulation. *Bottom four panels:* projected gas (fifth and sixth) and star (bottom) density for AqC6-oldH. Left- and right-hand panels show face-on and edge-on densities, respectively. All the maps are shown at redshift $z = 0$. The size of the box is 55 kpc.

(see Table 6.4) that is the same parameter value adopted for the reference higher resolution simulation AqC5-newH.

Figure 6.22 shows SFRs as a function of the cosmic time (and of the redshift, too). SFRs of all the analysed simulations are comparable for $z > 3$. Then, focussing on the AqC6 simulations, we see that the impact of the new hydrodynamic solver makes SFRs of AqC6-newH_p003 and AqC6-newH_p005 be lower than that of AqC6-oldH between $3 \lesssim z \lesssim 0.7$. The main reason of this discrepancy lies in the presence of the time-step limiting particle wake-up scheme, as discussed for AqC5 runs in Section 6.5.2. AqC6-newH runs then overpredict the SFR until the cosmic time reaches ~ 10 Gyr; from that moment on, the SFR of AqC6-newH_p003 starts to gently decline and matches the SFR of AqC6-oldH, while AqC6-newH_p005 keeps constantly larger than the prediction of AqC6-oldH (this is the actual reason why I prefer AqC6-newH_p003 rather than AqC6-newH_p005, though comparable). SFRs of AqC5-oldH and AqC6-oldH are relatively insensitive to mass resolution (see also Murante et al., 2015); on the other hand, the variation of resolution is quite remarkable between AqC5-newH and AqC6-newH_p003 (and AqC6-newH_p005).

Figure 6.23 describes the distribution of stellar mass as a function of the circularity of stellar orbits. All the galaxies are disc-dominated, with the hydrodynamic solver only slightly affecting the amount of stellar mass in both the bulge and the disc component. However, the different stellar mass in the disc component of AqC6-oldH and AqC6-newH_p003 (or AqC6-newH_p005, similarly) is not as pronounced as in the comparison between simulations AqC5-oldH and AqC5-newH. The effect of the resolution is much more apparent when using the new SPH scheme: a complete agreement between AqC6-newH_p003 and AqC5-newH is not reached even when the weak convergence is considered (Schaye et al., 2015, see Section 3.2). On the other hand, AqC6-oldH and AqC5-oldH show strong convergence (see Section 3.2) with numerical resolution. B/T ratios for AqC6-oldH, AqC6-newH_p003, for AqC6-newH_p005, AqC5-oldH, and AqC5-newH are: 0.23, 0.25, 0.22, 0.23, and 0.30, respectively.

Figure 6.24 shows results for the circular velocity profiles. Quite remarkably, none of the analysed profiles is centrally peaked, thus pinpointing that the adopted galactic outflow model is effective in preventing the formation of a too much centrally concentrated galaxy at both the resolutions. The different normalizations highlight the differences in the total stellar and gas mass that I obtain for the different tests. Values of the total stellar mass within the galactic radius $R_{\rm gal}$ are: $7.57 \cdot 10^{10}$ $\mathrm{M}_\odot$ ($R_{\rm gal} = 24.00$ kpc) for AqC6-oldH, $7.38 \cdot 10^{10}$ $\mathrm{M}_\odot$ ($R_{\rm gal} = 24.19$ kpc) for AqC6-newH_p003, $7.61 \cdot 10^{10}$ $\mathrm{M}_\odot$ ($R_{\rm gal} = 24.24$ kpc) for AqC6-newH_p005, $7.22 \cdot 10^{10}$ $\mathrm{M}_\odot$ ($R_{\rm gal} = 23.86$ kpc) for AqC5-oldH, and $4.74 \cdot 10^{10}$ $\mathrm{M}_\odot$ ($R_{\rm gal} = 24.01$ kpc) for AqC5-newH. Values of the gas mass within the galactic radius are: $1.85 \cdot 10^{10}$ $\mathrm{M}_\odot$ for AqC6-oldH, $4.47 \cdot 10^{10}$ $\mathrm{M}_\odot$ for AqC6-newH_p003, $4.37 \cdot 10^{10}$ $\mathrm{M}_\odot$ for AqC6-newH_p005, $1.66 \cdot 10^{10}$ $\mathrm{M}_\odot$ for AqC5-oldH, and $2.91 \cdot 10^{10}$ $\mathrm{M}_\odot$ for AqC5-newH, at $z = 0$. Note that the difference in total stellar and gas mass between AqC5-oldH and AqC6-oldH are not as prominent as in the case AqC5-newH and AqC6-newH_p003 (or AqC6-newH_p005, similarly).

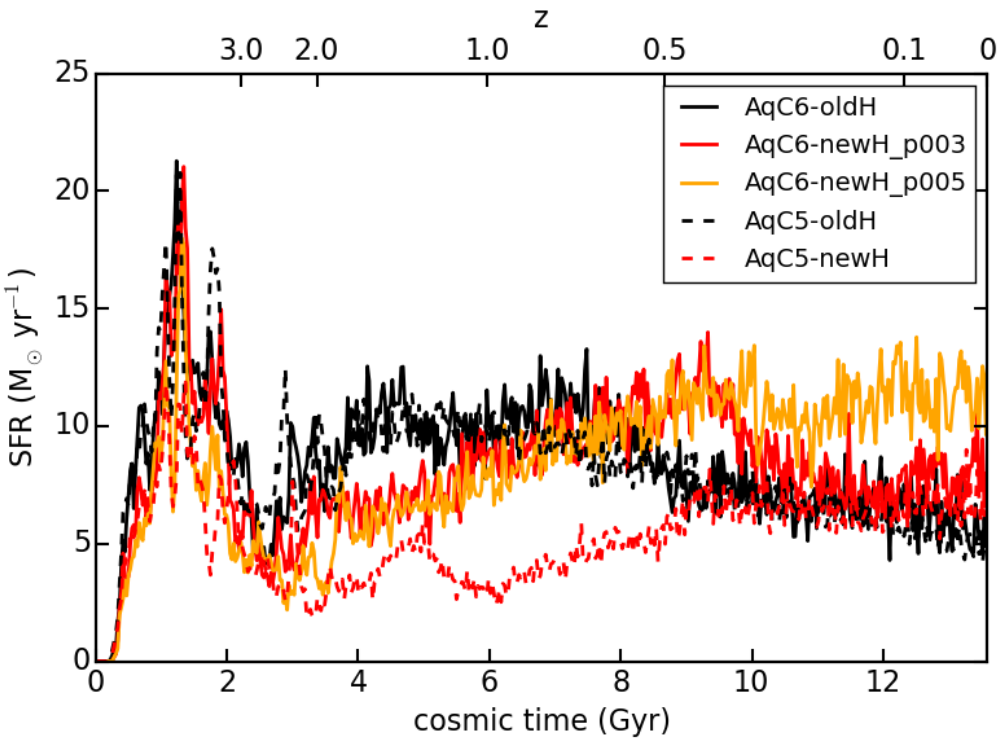

Figure 6.22: Evolution of the SFR for simulations AqC6-oldH (black solid line), AqC6-newH_p003 (red solid line), and AqC6-newH_p005 (orange solid line). Dashed lines refer to higher resolution simulations: AqC5-oldH (black) and AqC5-newH (red).

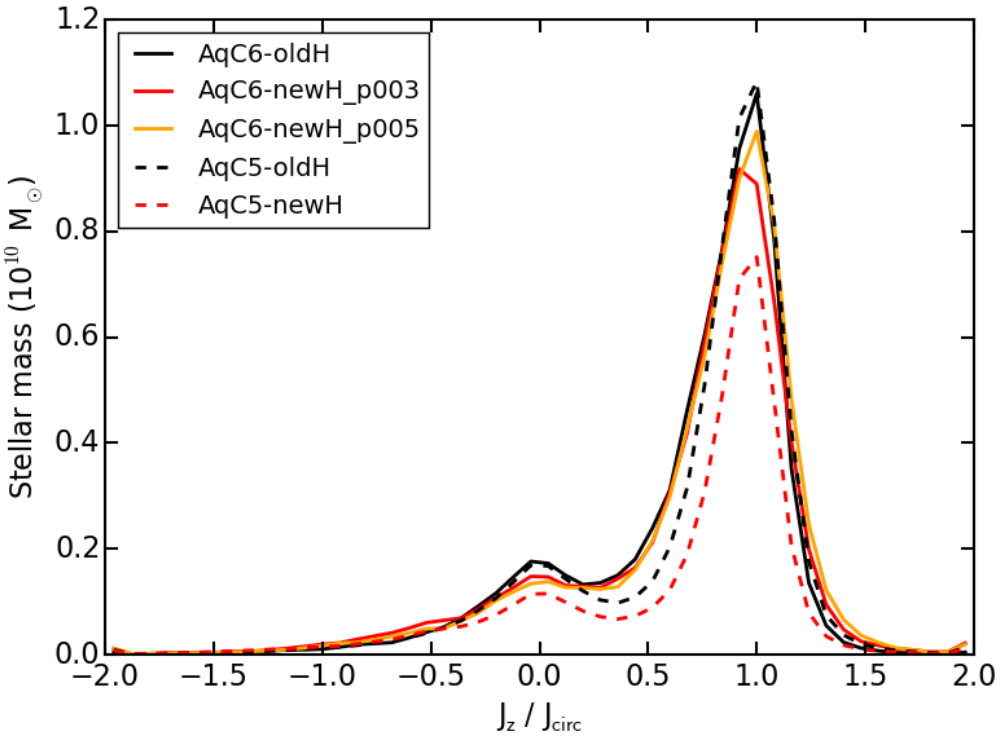

Figure 6.23: Stellar mass as a function of the circularity of stellar orbits at $z = 0$ for the following simulations: AqC6-oldH (black solid), AqC6-newH_p003 (red solid), AqC6-newH_p005 (orange solid), AqC5-oldH (black dashed) and AqC5-newH (red dashed).

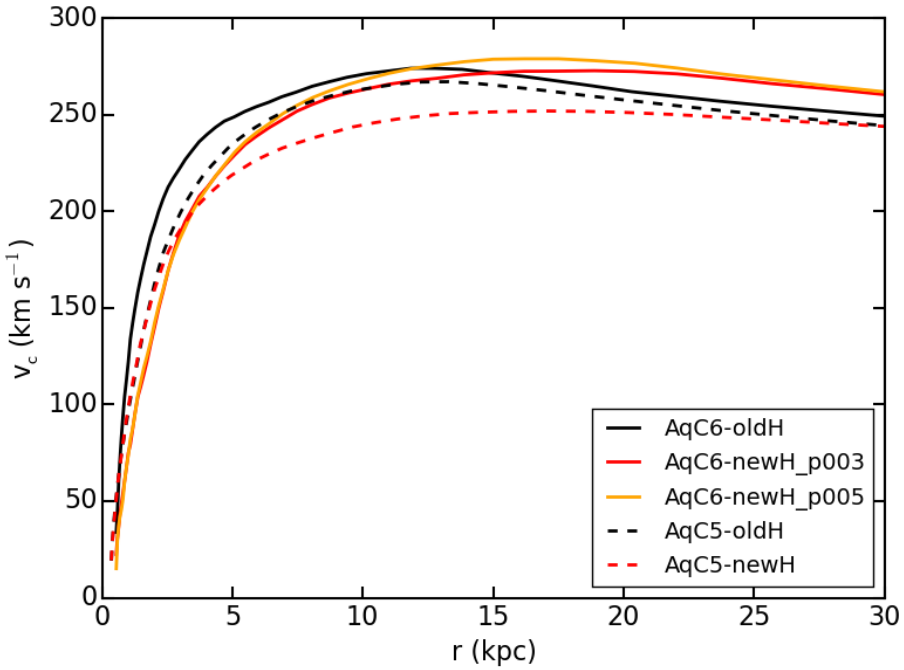

Figure 6.24: Rotation curves for simulations AqC6-oldH (black solid line), AqC6-newH_p003 (red solid line), and AqC6-newH_p005 (orange solid line). Dashed lines refer to higher resolution simulations: AqC5-oldH (black) and AqC5-newH (red). All the curves describe the circular velocity due to the total mass inside a given radius.

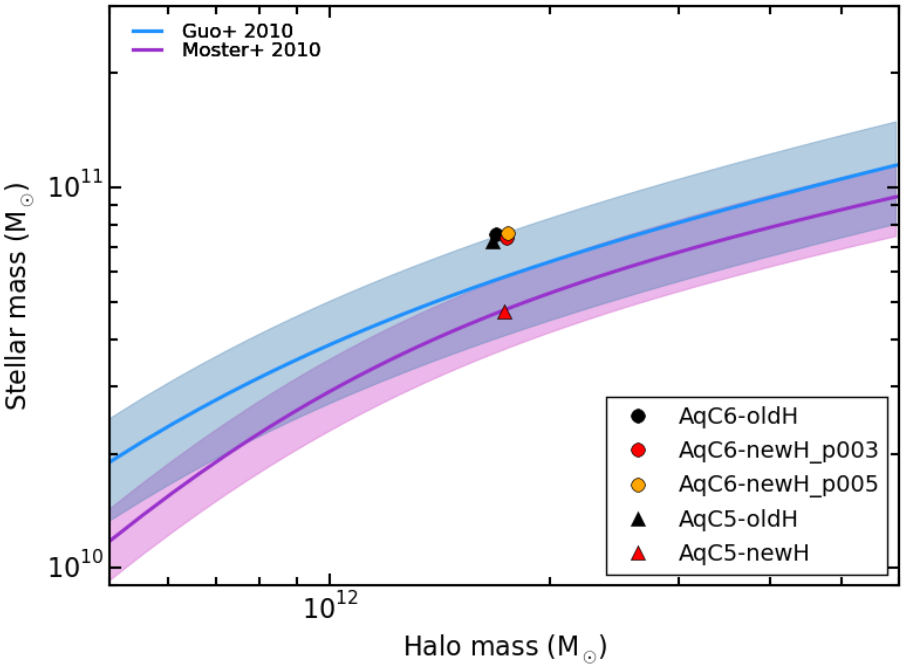

Figure 6.25: Comparison between the baryon conversion efficiency from observations and from the simulated galaxies at $z = 0$. Curves show the stellar-to-halo mass relations derived by Guo et al. (2010, blue) and by Moster et al. (2010, purple), as in the bottom panel of Figure 6.11 and in Figure 6.20. Symbols refer to simulations: AqC6-oldH (black filled circle), AqC6-newH_p003 (red filled circle), AqC6-newH_p005 (orange filled circle), AqC5-oldH (black filled triangle) and AqC5-newH (red filled triangle), respectively.

Figure 6.25 shows the position of the considered simulations in the baryon conversion efficiency plot. I find that AqC5-newH has a lower baryon conversion efficiency than AqC5-oldH, while the baryon conversion efficiency is comparable when AqC6 simulations are analysed. Moreover, the lower the resolution is, the higher the stellar content of the simulated galaxy: this is independent of the adopted SPH scheme. However, such an effect is much more evident when the new SPH scheme is considered. For completeness, total baryonic masses within $R_{\rm vir}$ for the AqC6 runs are: $1.89 \cdot 10^{11}$ M$_\odot$ for AqC6-oldH, $1.99 \cdot 10^{11}$ M$_\odot$ for AqC6-newH_p003, and $2.06 \cdot 10^{11}$ M$_\odot$ for AqC6-newH_p005, at $z = 0$.

The general result of this Section is that properties of galaxies simulated at higher resolution are significantly more sensitive to the accuracy of the hydrodynamic solver.

6.6.2 Parameter space of galactic outflow models

Feedback efficiency $f_{\rm fb,kin}$ is the most delicate parameter of galactic outflow models. I report in this Section my tests aimed at calibrating an optimal value of $f_{\rm fb,kin}$ and its impact on the resulting properties of the simulated galaxies. In particular, I concentrate here on the effect of feedback efficiency in the FB1 and FB3 outflow models.

Simulations adopting the galactic outflow model FB1 (Section 6.3.1) that I investigate in this Section are: AqC5-FB1, AqC5-FB1f2.0-1.0, AqC6-FB1fEagle, AqC6-FB1-ΔT$_{\rm fix}$, and AqC6-FB1f1.0 (see Table 6.4). Results are described in Figures 6.26 and 6.27, where I show the SFR evolution and the circularity diagram for the set of FB1 runs. The fiducial simulation AqC5-FB1 adopts equation (6.3), i.e. the density- and metallicity-dependent feedback efficiency used in the reference Eagle simulation (Schaye et al., 2015), as discussed in Section 6.3.1. The simulation AqC5-FB1f2.0-1.0 employs a redshift-dependent feedback efficiency (see below), with $f_{\rm fb,kin}$ spanning values between $f_{\rm fb,kin}^{\rm max} = 2.0$ and $f_{\rm fb,kin}^{\rm min} = 1.0$, where higher efficiency is adopted at higher redshift. The analytical expression for the redshift-dependent feedback efficiency reads:

$$f_{\rm fb,kin}(z) = f_{\rm fb,kin}^{\rm min} + (f_{\rm fb,kin}^{\rm max} - f_{\rm fb,kin}^{\rm min})\,\Theta(z-2) \ , \tag{6.18}$$

where $\Theta(z)$ is the Heaviside step function[7].

Equation (6.18) for the feedback efficiency has been introduced according to the phenomenological approach (following Schaye et al., 2015) of using a higher feedback efficiency at high redshift. The above expression for $f_{\rm fb,kin}$ is simpler than

[7] I also investigated the effect of a smoother transition for the redshift evolution of the feedback efficiency. I verified that, by adopting the following analytical expression:

$$f_{\rm fb,kin}(z) = f_{\rm fb,kin}^{\rm min} + f_{\rm fb,kin}^{\rm max}\left(0.5\,{\rm erf}\left(\frac{z-2}{0.5}\right) + 0.5\right) \ , \tag{6.19}$$

where erf(z) is the error function, instead of using equation (6.18), the SFR and the final outcome of simulations with model FB1 are left almost unaffected.

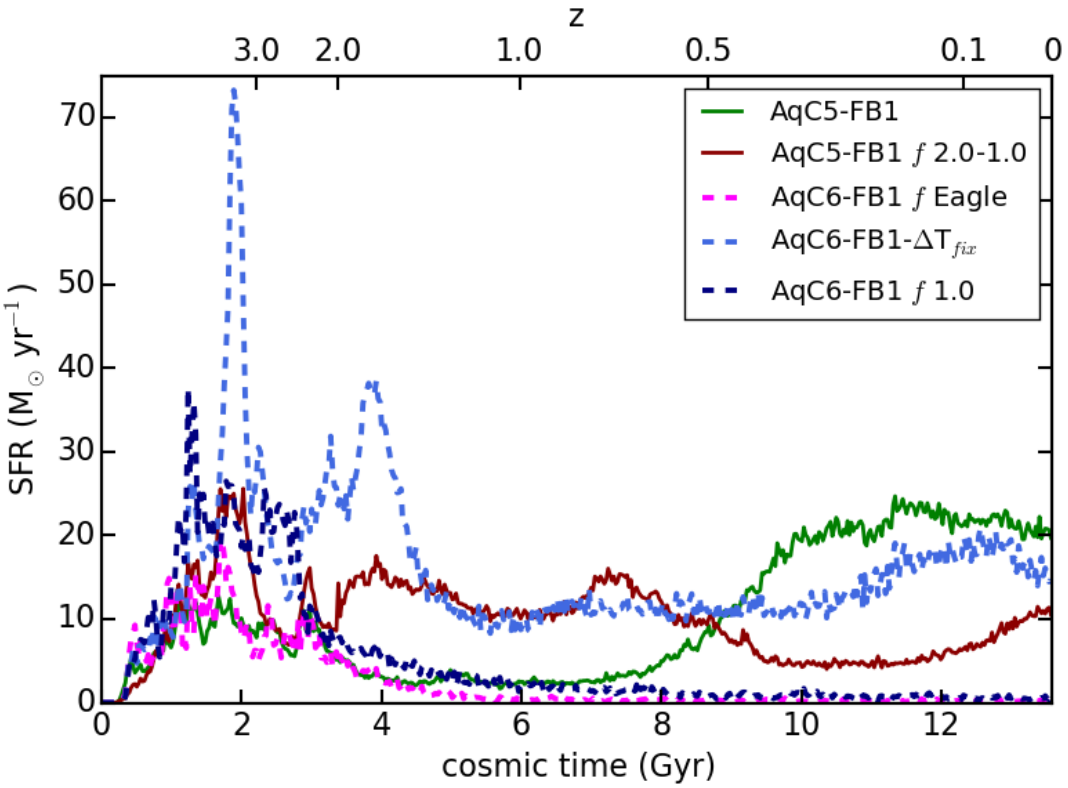

Figure 6.26: Evolution of the SFR for different simulations that adopt the FB1 outflow model.

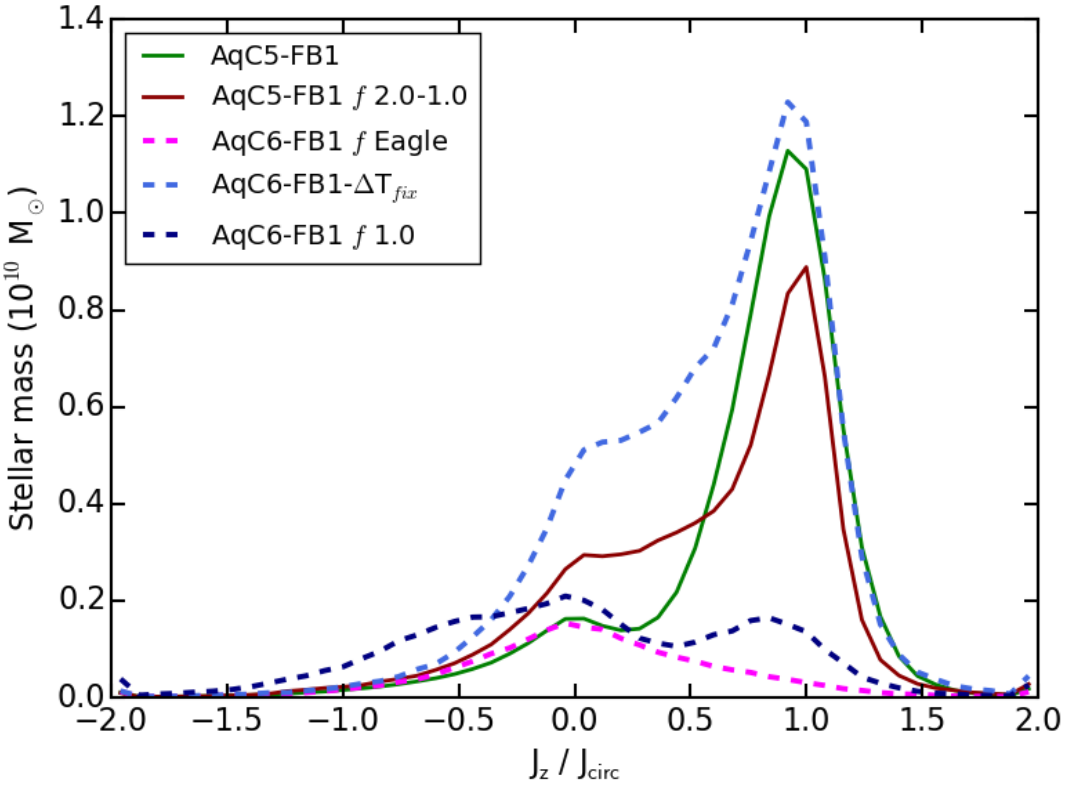

Figure 6.27: Stellar mass as a function of the circularity of stellar orbits at $z = 0$ for different simulations adopting the FB1 galactic outflow model.

equation (6.3), and has been adopted to understand how different values for high-z and low-z feedback efficiency impact on SFR. By tuning the parameters $f_{\rm fb,kin}^{\rm max}$ and $f_{\rm fb,kin}^{\rm min}$, it is possible to regulate high-z and low-z SFR.

Redshift $z = 2$ has been identified as the approximate epoch at which the bulge formation phase ends and the star formation starts building up the disc component. After an exploration of the parameter space, I found that $f_{\rm fb,kin}^{\rm max} = 2.0$ and $f_{\rm fb,kin}^{\rm min} = 1.0$ are the most suitable parameters in reproducing a typical late-type galaxy star formation history for our AqC5 simulations adopting the FB1 model. In particular, with such a choice, I am able to control low-redshift star formation (see Figure 6.26): ongoing SFR in the simulation AqC5-FB1f2.0-1.0 has been reduced by half with respect to AqC5-FB1.

Figures 6.26 and 6.27 describe the evolution of SFR and the distribution of the stellar mass as a function of the circularity of stellar orbits for the simulations adopting the galactic outflow model FB1, respectively. In these figures, I also include results from AqC6 resolution.

AqC6-FB1fEagle is a simulation analogous to AqC5-FB1. At variance with the higher resolution simulation, AqC6-FB1fEagle does not succeed to form a convincing disc galaxy, and it produces a spheroidal (see Figure 6.27). AqC6-FB1-ΔT$_{\rm fix}$ adopts the same feedback efficiency as the AqC6-FB1fEagle (i.e. equation 6.3): in this simulation, I fix the temperature jump to the reference value of $\Delta T = 10^{7.5}$ K (see Section 6.3.1). I find that this model is not able to prevent an excess of high-redshift star formation, thus ending up with a disc galaxy having an unrealistically massive bulge.

The simulation AqC6-FB1f1.0 is analogous to AqC6-FB1fEagle, but it adopts a constant $f_{\rm fb,kin} = 1.0$. In this case, a star formation burst at high redshift takes place (see Figure 6.26). As a consequence, a prominent bulge is produced, with a resulting too small stellar disc due to the drastically reduced late-time star formation. By adopting just one value for the feedback efficiency throughout the simulation, I do not succeed in producing a disc-dominated galaxy with this model (see Figure 6.27). If the parameter $f_{\rm fb,kin}$ is high enough to quench the high-redshift star formation, then it depletes the amount of gas available for a subsequent phase of disc formation at low z. This is in agreement with Crain et al. (2015), who find that disc galaxies are characterised by a compact bulge and a too low low-redshift SFR if a constant stellar feedback efficiency is adopted.

Figures 6.26 and 6.27 also show that this galactic outflow model is resolution dependent (by considering AqC5-FB1 and AqC6-FB1fEagle). AqC5 simulations have an initial mass of gas particles that is ~ 4.4 times smaller than the initial mass of baryonic particles in the reference Eagle simulation (Schaye et al., 2015), while AqC6 simulations have gas particles with a mass ~ 3.7 times larger than that of particles of the same type in the reference Eagle simulation. This result suggests that this galactic outflow model promotes the formation of disc-dominated galaxies when a resolution at least higher than AqC6 simulations is considered (unless further recalibration of parameters).

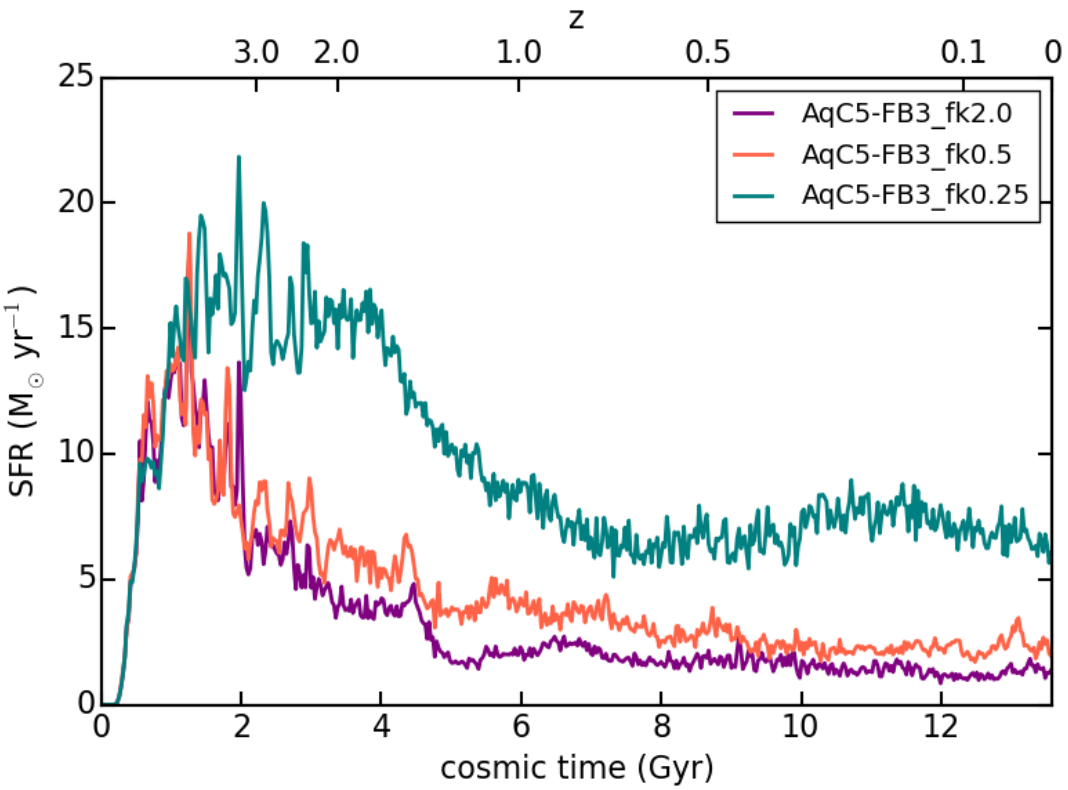

Figure 6.28: Evolution of the SFR for different simulations that adopt the FB3 outflow model.

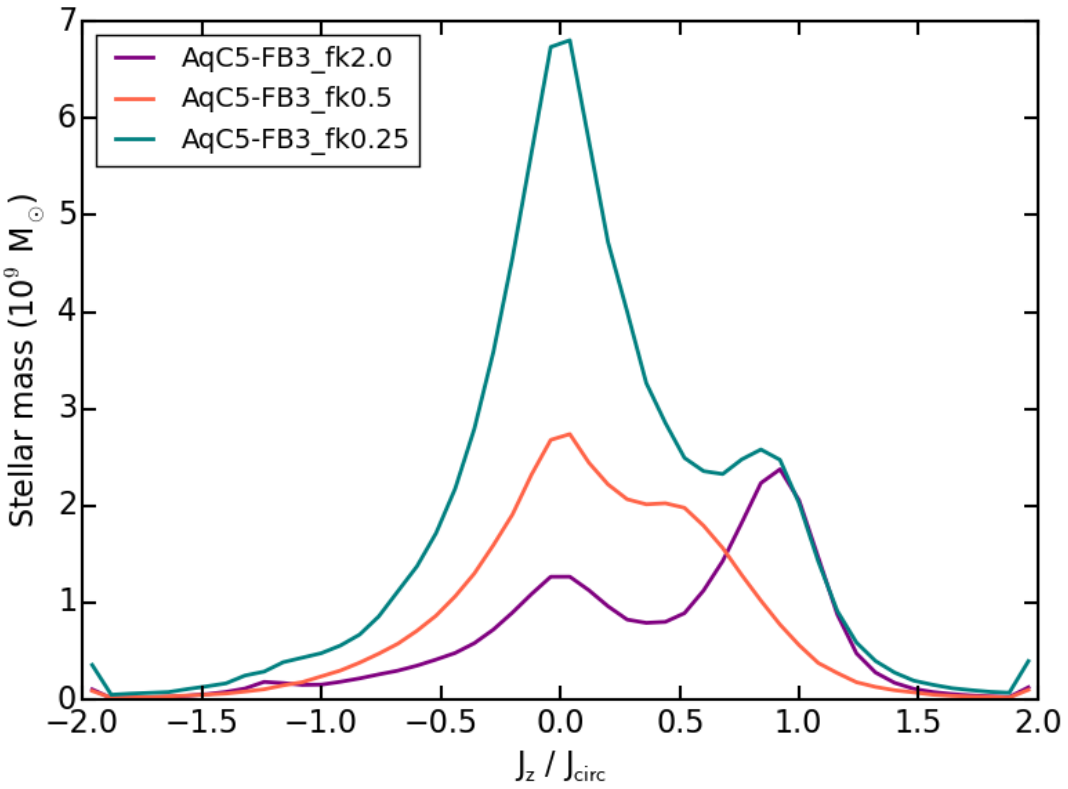

Figure 6.29: Stellar mass as a function of the circularity of stellar orbits at $z = 0$ for different simulations adopting the FB3 galactic outflow model.

As for the FB3 galactic outflow model (Section 6.3.3), I compare here the evolution of SFRs and the circularity diagrams at $z = 0$ (Figures 6.28 and 6.29, respectively) for three simulations: AqC5-FB3_fk2.0, AqC5-FB3_fk0.5, and AqC5-FB3_fk0.25. For the sake of conciseness, I present results only for the variation of the feedback efficiency $f_{\rm fb,kin}$ that spans the values 2.0, 0.5 and 0.25, respectively, while keeping the mass loading factor $\eta = 3.0$ fixed (see also Section 6.5.3.1).

I only vary the $f_{\rm fb,kin}$ parameter for two reasons: first, it is the parameter to which the model is most sensitive. Second, Springel & Hernquist (2003), whose model this galactic outflow scheme is inspired, adopted $f_{\rm fb,kin} = 0.25$ for most of their simulations, even if they admitted that this feedback efficiency can assume values of order unity or even larger. Figure 6.28 shows that a feedback efficiency larger than $f_{\rm fb,kin} = 0.25$ is needed in order to avoid a too high SFR, both at $z > 1$ – so as to quench star formation in the bulge – and at low redshift. In fact, Figure 6.29 demonstrates that simulated galaxies obtained for values of the feedback efficiency smaller than the reference value $f_{\rm fb,kin} = 2$ are mostly dominated by a dispersion-supported component ($J_{\rm z}/J_{\rm circ}$=0) rather than by a rotationally supported one ($J_{\rm z}/J_{\rm circ}$=1).

6.7 Summary and Conclusions

In this Chapter, I presented a suite of cosmological hydrodynamical simulations of a Milky-Way sized halo ($M_{\rm halo,DM} \simeq 2 \cdot 10^{12}$ M$_\odot$), using the GADGET3 code and the AqC initial conditions (ICs). As a first aim of my analysis, I coupled the sub-resolution model for star formation and stellar feedback, MUPPI (see Section 5.3), with an improved implementation of SPH that includes a high-order interpolating kernel, an improved treatment of artificial viscosity (AV) and an artificial conduction (AC) term that promotes mixing at gas interfaces (see Section 5.3). As a second goal, I implemented three different models for galactic outflows, besides the original model presented in Section 5.3, and used them to re-simulate the same ICs with the same star formation prescription. For each scheme, I tuned the relevant model parameters by carrying out an exploration of their respective parameter space (see Section 6.6.2). To choose the reference values of the parameters, I used the criterion based on maximizing the stellar disc component, both by visual inspection and by considering the circularity histograms. These simulations do not include AGN feedback.

The key features of my galactic outflow models are the following:

- In the original scheme, each particle ending its multiphase stage has a probability of receiving kinetic energy from neighbour star-forming particles, providing that it is inside a cone centred on the star-forming particles and directed towards the least-resistance direction.

- FB1 is a stochastic thermal feedback model based on Dalla Vecchia & Schaye (2012). It is here implemented within our sub-resolution model for the ISM and star formation (Section 6.3.1), different from the original one by Dalla Vecchia & Schaye (2012).

- FB2 is a kinetic stellar feedback scheme, where the ISM is isotropically provided with energy that triggers galactic outflows (Section 6.3.2).
- FB3 is a feedback model where I directly impose the mass loading factor and stochastically sample the outflowing mass. SN energy and SFRs are collected during the multiphase stage of gas particles, thus accounting for the evolution of the ISM (Section 6.3.3). This scheme is inspired by Springel & Hernquist (2003).

In order to successfully introduce the improved SPH implementation in cosmological simulations adopting the sub-resolution model MUPPI, I switched off AC for both multiphase and wind particles, and implemented a switch that allows former multiphase particles to artificially conduct whenever some conditions on their temperature are met (Section 6.2.2). Indeed, the physical state of the ISM is determined by continuous energy injections due to the sub-resolution model. This results in a particle-by-particle difference in temperature and density. AC acts in mixing internal energy, contrasting the effect of the sub-resolution model. The new switch suppresses AC for those particles that are sampling the non-uniform thermal structure of the galaxy, where the sub-resolution physics accounts for the evolution of the ISM (Section 6.5.1).

The main results can be summarized as follows.

- MUPPI is able to produce a disc galaxy using the AqC5 ICs, also when coupled with the improved SPH scheme. The simulated galaxy has a flat rotation velocity profile (flatter than the one of the galaxy simulated with the previous SPH implementation), a low value of the B/T ratio, extended gaseous and stellar discs, baryon conversion efficiency, and position on the Tully-Fisher plot in broad agreement with expectations. However, I note that significant differences arise with respect to the results obtained by adopting the standard SPH scheme. Using the new SPH solver introduces a delay in the gas fall-back that causes the stellar disc to form later, and the simulated galaxy to have a relatively higher low-redshift SFR (Section 6.5.2).
- Changing the outflow model does affect the properties of the simulated galaxies at redshift $z = 0$. Some of them are relatively stable, e.g. the high-redshift ($z \gtrsim 3$) SFR which determines the present-day stellar mass of the bulge. However, the majority of the properties, in particular the prominence of the disc component, shows a sensitive dependence on the employed outflow model (Section 6.5.3.2).
- FB1 model generates the galaxy with the largest stellar mass, a strong disc component, high SFR at redshift below $z \simeq 0.7$. FB2 model has a smaller stellar mass at $z = 0$ with respect to our reference outflow scheme, and shows a drop in SFR between $z = 2$ and $z = 0.3$. FB3 model strongly suppresses star formation after $z = 2$, producing in turn the lowest value of the B/T ratio.

- The different behaviour of my outflow models can be understood in terms of gas mass accretion history (MAH). FB1 almost always has the highest gas MAH; FB2 shows an MAH similar to that of the original model within the virial radius, but lower within the galactic radius; on the other hand, FB3 is too effective in quenching the gas fuelling of the disc. In this latter outflow model, the outflowing gas is kept inside the halo, but away from the galactic radius.

My analysis demonstrates and quantifies the strong interplay between details of the hydrodynamical scheme and the sub-resolution model describing star formation and feedback. The sub-resolution model plays a fundamental role in determining the properties of simulated galaxies and the exact values of free parameters entering into the model can significantly change with the hydrodynamic solver. The hydrodynamical scheme remarkably affects properties of simulated galaxies (stellar mass is the quantity that is affected the most) and highly regulates gas inflow and outflow across cosmic time. Moreover, the higher the resolution is, the more sensitive to the accuracy of the hydrodynamic solver properties of simulated galaxies are (see Section 6.6.1).

My results further show that the sub-resolution prescriptions adopted to generate galactic outflows are the main shaping factor of the stellar disc component at low redshift (when the hydrodynamical scheme is held fixed). In particular, the timing of the gas fall-back after its expulsion from the forming halo at high redshift is of paramount importance, together with the ability of a given model to tune or even quench the cosmological infall of gas from the large-scale environment.

For this reason, a detailed comparison between simulation results and observations of the properties of the CGM at different redshifts should provide invaluable information on the outflow/inflow gas properties and, therefore, on the history of feedback. Another interesting direction of investigation will be to compare the properties of simulated galaxy populations (instead of those of a single galaxy), obtained by adopting one or more of my outflow models, with observations.

7

Chemical evolution of disc galaxies from cosmological simulations

The distribution of metals encodes information on galaxy evolution and on the history of stellar feedback. In this Chapter, I investigate the metal content of gas and stars in a suite of cosmological simulations of disc galaxies, taking advantage of our detailed model of chemical evolution (Section 5.4). I explore the variation of the essential elements contributing to define the model of chemical evolution, and quantify their impact in determining metal abundance trends and evolutionary patterns. Particular emphasis is on the role played by the high-mass end shape of the IMF. Guided by observations, I present a detailed investigation focussing on the results at redshift $z = 0$. Comparing results with observations allows to make predictions on some of the components of the chemical evolution model in disc galaxies, such as the IMF and the fraction of stars in binary systems that are progenitors of SNe Ia.

The key questions that I want to address in this Chapter are the following: can metallicity profiles help in supporting or discarding an IMF? Can the distribution of metals around simulated galaxies shed some light on the fate of metals? What is the impact of the different components of a chemical model on the resulting abundance pattern of gas and stars?

The outline of this Chapter is as follows. I place the work developed in this Chapter in the context in Section 7.1, and I introduce the simulations in Section 7.2. In Section 7.3, I quantify the impact of two different IMFs on the predicted number of massive stars. In Section 7.4 I present and discuss results. Section 7.4.1 provides

an overview of the main features of the simulated galaxies, in Section 7.4.2 I analyse stellar ages and SN rates. I then investigate the metal content of gas and stars, focussing on metallicity profiles (Section 7.4.3) and stellar α-enhancement (Section 7.4.4). I study the distribution of metals around galaxies in Section 7.4.5, and the impact of adopted stellar yields in Section 7.4.6.

The results presented in this Chapter are fully described in the paper Valentini et al. (2018a).

Contents

7.1 Chemical evolution in simulations: an overview

Metals are a fundamental component of the galactic system, although they do not considerably contribute to the baryonic mass budget of galaxies and of their gaseous environments. Metals record earlier stages of galaxy formation, since crucial processes that shape forming galaxies and determine their evolution leave imprints on metal distribution and relative abundance of different elements (see Section 2.4.3). Stellar feedback pollutes the ISM with heavy elements synthesised during stellar evolution, galactic outflows fostered by both SN explosions and AGN activity spread metals and drive them towards the CGM, while counterbalancing and regulating the accretion of pristine or metal-poor gas from the large scale environment (see e.g. the reviews by Veilleux et al., 2005; Tumlinson et al., 2017). Some of the enriched gas that has been driven outwards from the sites of star formation within the galaxy falls then back again, eventually cooling and forming subsequent generations of stars, richer in metals than previous ones. This feedback process involves regions of the galaxy far from the original sites where outflows originated, resulting in a spread and circulation of metals over galactic scales.

A number of elements contribute to determine the present day abundance and distribution of metals: the inital mass function (IMF), the mass-dependent lifetime function, the stellar yields, the fraction of stars in binary systems originating SNe Ia,

and the efficiency and modelling of feedback processes. All these components are needed to build both chemodynamical models of galactic chemical evolution (along with the star formation history of the galaxy), and models of chemical evolution that are included in semi-analytical models and cosmological simulations of galaxy formation (e.g. Matteucci & Francois, 1989; Chiappini et al., 1997; Gibson et al., 2003; Matteucci, 2003; Nagashima et al., 2005; Tornatore et al., 2007; Borgani et al., 2008; Wiersma et al., 2009b; Yates et al., 2013; De Lucia et al., 2014; Dolag et al., 2017, and references therein).

The IMF plays a crucial role in regulating the production of metals, as discussed in Section 2.4.3. As for our Galaxy, different studies that have investigated the present-day mass function of stars located in the bulge, in the thin and thick disc agree that the IMF of MW stars, independently of their position, is compatible with a Kroupa (2001) and Chabrier (2003) IMF (see e.g. Barbuy et al., 2018, for a recent review, and references therein).

A long-standing debate concerns the universality of the IMF: observational indications suggesting that the IMF may vary depending on galaxy properties have been recently collected (e.g. Cappellari et al., 2012). The possible dependence on the metallicity, density, pressure of the gas, i.e. on the physical properties of molecular clouds, and even on the galaxy type and environment has been investigated in different studies, with no general consensus (e.g. Chiosi et al., 1998; Kroupa et al., 2013). The dependence of the IMF on the stellar mass in elliptical galaxies has been addressed with semi-analytical models. Gargiulo et al. (2015) and Fontanot et al. (2017) found that a variable IMF that depends on the instantaneous star formation rate is suited to reproduce the observed trend of increasing α-enhancement with larger galaxy stellar masses. These studies support a more top-heavy IMF in more massive systems. Similar findings are obtained by De Masi et al. (2018) using a chemical evolution model. The impact that the variation of the IMF slopes has on star formation rates, galaxy morphology, chemical properties of stars and timing of chemical enrichment has been investigated also in simulations, where different shapes of the IMF have been considered, either assuming a global IMF (Few et al., 2014) or one depending on gas density and metallicity (Bekki, 2013; Gutcke & Springel, 2017; Barber et al., 2018). Besides variations of the IMF involving the low-mass end (Conroy & van Dokkum, 2012; La Barbera et al., 2013), also the number of massive stars predicted by the IMF has long been debated. By approximating the IMF with a broken power law $\phi(m) \propto m^{-\alpha}$ (Kroupa et al., 1993; Kroupa, 2001; Chabrier, 2003, for a review), the number density of stars per mass interval can be cast as $\phi(m) \propto m^{-2.7}$ (Kroupa et al., 1993) or $\phi(m) \propto m^{-2.3}$ (Kroupa, 2001) for stars more massive than 1 $M_\odot$, whether the correction for unresolved binary systems is accounted for or not (Kroupa, 2002; Kroupa & Weidner, 2003). The impact of binary systems has been studied by Sagar & Richtler (1991), too: they found that the power-law slope α increases by ~ 0.4 if all stars are assumed to reside in binary systems.

Stellar yields contribute to determine chemical features of gas and stars, as outlined in Section 2.4.3. Elements released by stars in the surrounding medium

control radiative cooling, regulating star formation and subsequent chemical stellar feedback. Differences between available sets of stellar yields arise because of uncertainties on stellar nucleosynthesis, and due to the details of modelling stellar evolution and the structure of the star (Karakas & Lattanzio, 2007; Karakas, 2010; Romano et al., 2010; Doherty et al., 2014a). Also, the aformentioned components have a complex interaction, and leave imprints on signatures of stars such as the α/Fe (see Section 2.4.3).

Star formation and stellar deaths affect galaxies and their CGM triggering galactic outflows. Different stellar feedback models result in different star formation histories for simulated galaxies, and the way in which galactic outflows are modeled involves how metals are distributed (as thoroughly investigated in Chapter 6).

A puzzling question pertains to the location of metals in and around galaxies. Galaxies retain some metals in their innermost regions, as heavy elements are partly locked in stars and associated to different gaseous phases of the ISM and the CGM close to the galaxy itself (e.g. Oppenheimer et al., 2012, and references therein). However, a share of the total metal budget is not confined to the nearest CGM and can be even lost beyond the galaxy virial radius. Low-density, warm CGM and IGM typically escape detections, and therefore it is difficult to probe the presence of metals several hundreds of kpc far from the galaxy centre. By focussing on studies that address the so-called missing metals problem (e.g. Bouché et al., 2005; Ferrara et al., 2005; Pettini, 2006) at redshift $z = 0$, Gallazzi et al. (2008) found that the budget of metals locked up in stars ranges between $\sim 25\%$ for disc-dominated galaxies and $\sim 40\%$ in early-type galaxies. Peeples et al. (2014) investigated a sample of star-forming galaxies with stellar mass in the range $10^9 - 10^{11.5}$ $M_\odot$ in the local Universe and found that galaxies retain $20 - 30\%$ of produced metals in their ISM, dust and stars (neglecting metals locked up in stellar remnants). This fraction increases up to 50% when the CGM out to 150 kpc is accounted for, with no significant dependence on the galaxy mass. Uncertainties in the adopted nucleosynthesis yields affect predictions for missing metals, since yields determine the total budget of heavy elements that one has to look for (Peeples et al., 2014).

Studying the distribution of metals only in the innermost regions of galaxies provide us with a partial view. Investigating how gas flows into, within and out of galaxies allows to understand where the heavy elements eventually go. Cosmological hydrodynamical simulations are crucial to achieve this task, as they consistently capture the temporal and spatial complexity of gas dynamics, and account for a variety of processes, such as the chemical enrichment resulting from star formation and stellar feedback (as discussed in detail in Chapter 3). Some light on the origin and fate of metals in different systems have been shed by analysing the chemical properties of the ISM, CGM, IGM (intergalactic medium) and ICM (intra-cluster medium) in simulations, and comparing them with observations (e.g. Tornatore et al., 2007; Schaye et al., 2015; Oppenheimer et al., 2017; Torrey et al., 2017; Biffi et al., 2017; Vogelsberger et al., 2018). Also, chemical features of stars in simulated galaxies have been investigated. For instance, Dolag et al. (2017) investigated the stellar metallicity as a function of the galaxy stellar mass for a sample of

simulated galaxies: they found a stellar mass-metallicity relation shallower than suggested by observations, simulated galaxies with stellar mass above $\sim 5 \cdot 10^{10}$ $M_\odot$ being, on average, not as richer in iron as observed ones. Interestingly, Grand et al. (2016) studied how the azimuthal motion of spiral arms in simulated galaxies affect the stellar metallicity distribution, promoting metal-poor stars to move inward. Furthermore, Grand et al. (2018b) investigated the metal content and α-enhancement of stars located within galaxy discs, as a function of the distance from the galaxy centre and the height on the galactic plane, connecting chemical signatures to possible evolutionary scenarios.

7.2 Numerical simulations

In this Section, I introduce the simulations performed for the present investigation. All the simulations share the numerical setup described in Chapter 5: they have been carried out with the GADGET3 code (see Section 5.1), adopting the improved formulation of SPH introduced in Section 5.2. The ICs are the *AqC*5 ICs (higher-resolution) presented in Section 5.5: the Plummer-equivalent softening length for the computation of the gravitational force is $\varepsilon_{\rm Pl} = 325\,h^{-1}$ pc, DM particles have a mass of $1.6 \cdot 10^6\,h^{-1}$ $M_\odot$, while the initial mass of gas particles is $3.0 \cdot 10^5\,h^{-1}$ $M_\odot$.

The new SPH formulation has been introduced in cosmological simulations adopting our sub-resolution model MUPPI (see Section 5.3), as explained in Chapter 6. The key features of the sub-resolution model MUPPI and of the model for chemical evolution have been outlined in Sections 5.3 and 5.4, respectively.

At variance with the original version of the sub-resolution model MUPPI, I adopt for all the simulations carried out for the present analysis the galactic outflow model labelled *FB2* in Chapter 6 (see Section 6.3.2). Therefore, as for the kinetic stellar feedback, multiphase particles provide the ISM with kinetic feedback energy isotropically. Each star-forming particle supplies the energy $f_{\rm fb,kin}\,E_{\rm SN}$ to all wind particles within the smoothing length, with kernel-weighted contributions. I remind that $f_{\rm fb,kin}$ describes the kinetic stellar feedback efficiency. Wind particles receiving energy use it to increase their velocity along their least resistance path, since they are kicked against their own density gradient. I adopt this model for triggering galactic outflows as it promotes the formation of disc galaxies with morphological, kinematic and chemical properties in keeping with observations (see Chapters 6 and 8).

Besides those described in Section 7.2.1 and listed in Table 7.1, all the relevant parameters of the sub-resolution model that I adopt for this set of simulations can be found in Table 5.1. The only parameters that are different from those in Table 5.1 are the following: $P_{\rm kin} = 0.03$ and $t_{\rm wind} = 15 - t_{\rm clock\ [Myr]}$ Myr. Moreover, θ only identifies the value of the half-opening angle of the cone for thermal feedback when the *FB2* galactic outflow model is adopted.

It is worth noting that our sub-resolution model does not have parameters that have been calibrated to reproduce observations of metal abundances in the ISM and CGM. For instance, at variance with Vogelsberger et al. (2013); Pillepich et al.

(2018), we do not adopt a wind metal loading factor to regulate the metallicity of the wind relative to that of the ISM from where the wind originated.

Before entering in the details of the simulations that I am going to analyse, I stress that while some of the simulated galaxies are similar to our Galaxy from the morphological point of view, results of this Chapter should not be deemed as a model of the MW, as no specific attempts to reproduce the accretion history of its dynamical environment have been made (see Section 5.5).

7.2.1 The set of simulations

In this Chapter, I consider results of six simulations that I carried out. I list them in Table 7.1. These simulations have been conceived so as to investigate and quantify the effect of the adopted IMF and stellar yields, along with the impact of binary systems originating SN Ia on the chemical enrichment process.

We can define the IMF $\phi(m)$:

$$\phi(m) = \beta m^{-\alpha} \tag{7.1}$$

as the number of stars per unit mass interval, in the mass range $[M_{\rm inf}, M_{\rm sup}]$. I consider two IMFs: the Kroupa (2001) IMF and the Kroupa et al. (1993) IMF. I choose these two IMFs because one focus of this study is to investigate the impact of the number of massive stars on the metal production. I note that the Kroupa (2001) IMF is almost indistinguishable by the widely adopted Chabrier (2003) IMF (see Figure 7.1): therefore, by considering the Kroupa (2001) and the Kroupa et al. (1993) IMFs I examine the possible variation of the high-mass end shape of the IMF. The Kroupa (2001) IMF (K2s, hereafter) is characterised by the following values for the slope α of the power law in different mass intervals:

$$\begin{aligned} \alpha &= 1.3 \quad \text{for} \quad 0.08\ \mathrm{M}_\odot \leq m \leq 0.5\ \mathrm{M}_\odot, \\ \alpha &= 2.3 \quad \text{for} \quad 0.5\ \mathrm{M}_\odot < m \leq 100\ \mathrm{M}_\odot. \end{aligned} \tag{7.2}$$

I adopt $M_{\rm inf} = 0.08\ \mathrm{M}_\odot$ and $M_{\rm sup} = 100\ \mathrm{M}_\odot$ for K2s. The IMF slope $\alpha = 2.3$ for massive stars is not corrected for unresolved stellar binaries (see below). For each mass interval a normalization constant β is computed by imposing that $\int m\,\phi(m)\,dm = 1$ over the global mass range and continuity at the edges of subsequent mass intervals.

The second IMF that I adopt is the Kroupa et al. (1993) IMF (K3s, hereafter). This IMF is characterised by three slopes, as α in equation (7.1) has the following values according to the mass interval:

$$\begin{aligned} \alpha &= 1.3 \quad \text{for} \quad 0.1\ \mathrm{M}_\odot \leq m \leq 0.5\ \mathrm{M}_\odot, \\ \alpha &= 2.2 \quad \text{for} \quad 0.5\ \mathrm{M}_\odot < m \leq 1.0\ \mathrm{M}_\odot, \\ \alpha &= 2.7 \quad \text{for} \quad 1.0\ \mathrm{M}_\odot < m \leq 100\ \mathrm{M}_\odot. \end{aligned} \tag{7.3}$$

It is defined in the mass range $[0.1, 100]$ $M_\odot$ (as suggested by Matteucci & Gibson, 1995; Grisoni et al., 2017). In this case, the slope $\alpha = 2.7$ for massive stars includes the correction for unresolved stellar binary systems (Kroupa, 2002). This correction accounts for the large fraction (more than $\sim 50\%$) of stars that are located in binary systems. Surveys in our Galaxy that observe and count stars often lack the resolution to resolve pairs of close stars. The resulting statistics is therefore biased towards larger mass stars, because a fraction of them actually come from the superposition of lower mass stars. Correcting for this effect leads to a steepening of the slope in the high-mass range (Sagar & Richtler, 1991; Kroupa, 2002; Kroupa & Weidner, 2003, see also Section 7.1).

Our model for chemical evolution accounts for different evolutionary timescales of stars with different masses by adopting the mass-dependent lifetimes by Padovani & Matteucci (1993), as outlined in Section 5.4. Stars with an initial mass larger than $M_{\rm up}$ are assumed to end their life exploding as core-collapse SNe. We consider $M_{\rm up} = 8$ $M_\odot$, unless the set B of yields is used (see below). In this latter case $M_{\rm up} = 9$ $M_\odot$ (see Section 7.3, too). Stars that are more massive than 40 $M_\odot$ are assumed to implode in BHs directly, and thus do not contribute to further chemical enrichment.

A fraction of stars relative to the whole mass range is assumed to be located in binary systems that are progenitors of SNe Ia (according to the model by Greggio & Renzini, 1983). The binary system producing an SN Ia must have a total mass varying from 3 to 16 $M_\odot$ (or from 3 to 18 $M_\odot$ when using the set B of yields). The first SNe Ia explode therefore in binary systems whose components have both an initial mass of 8 $M_\odot$ (or 9 $M_\odot$), according to the single-degenerate scenario. This determines the timescale required for SN Ia explosions and consequent chemical enrichment, that ranges between ~ 50 Myr and several Gyr ($\sim 50\%$ of the total SNe Ia in an SSP explode after ~ 1 Gyr). Since SNe Ia are the main source for the production of iron-peak elements, their rate impacts directly on abundance trends and evolutionary patterns. In order to constraint the SN Ia rate, I explore the variation of the probability of the realization of a binary system hosting a SN Ia (while I do not consider to account for possible variations of stellar lifetimes or the distribution function of delay times). I consider two values for the fraction of binary systems giving rise to SN Ia: either 0.1 (case A; Greggio & Renzini, 1983; Matteucci & Greggio, 1986; Tornatore et al., 2007) or 0.03 (case B; as suggested by Grisoni et al., 2017). This parameter (that is usually called A in models) can depend on the adopted IMF, on the systems and environments investigated (Matteucci & Gibson, 1995), and other values have been adopted as well (e.g. Spitoni & Matteucci, 2011).

As discussed in Section 5.4, the production of different heavy elements by evolving and exploding stars is followed by adopting stellar yields. I consider two sets of stellar yields in order to quantify the impact that they have on final results. In the first set of yields, which I refer to as set A, I assume yields tabulated by Thielemann et al. (2003) for SNe Ia, while I adopt the mass- and metallicity-dependent yields by Karakas (2010) for AGB stars. Also, I use the mass- and metallicity-dependent yields by Woosley & Weaver (1995) for SNe II, combined with those provided by Romano et al. (2010). As for the second set of yields, labeled as set B, I adopt the

Table 7.1: Relevant features of the simulation suite. *Column 1:* simulation label. *Column 2:* adopted IMF. *Column 3:* set of yields. Set A: Thielemann et al. (2003); Karakas (2010); Woosley & Weaver (1995); Romano et al. (2010). Set B: Thielemann et al. (2003); Karakas (2010); Doherty et al. (2014a,b); Nomoto et al. (2013). See text for details. *Column 4:* fraction of binary systems originating SN Ia. *Column 5:* kinetic SN feedback energy efficiency.

Name	IMF	Set of yields	$f_{\rm bin,Ia}$	$f_{\rm fb,kin}$
K2s–yA–IaA–kA	Kroupa (2001) K2s, eq (7.2)	A	0.1	0.12
K2s–yA–IaB–kA	Kroupa (2001) K2s, eq (7.2)	A	0.03	0.12
K3s–yA–IaA–kB	Kroupa et al. (1993) K3s, eq (7.3)	A	0.1	0.26
K3s–yA–IaB–kB	Kroupa et al. (1993) K3s, eq (7.3)	A	0.03	0.26
K2s–yB–IaB–kA	Kroupa (2001) K2s, eq (7.2)	B	0.03	0.12
K3s–yB–IaB–kB	Kroupa et al. (1993) K3s, eq (7.3)	B	0.03	0.26

stellar yields provided by Thielemann et al. (2003) for SNe Ia and the mass- and metallicity-dependent yields by Nomoto et al. (2013) for SNe II. I use the mass- and metallicity-dependent yields by Karakas (2010); Doherty et al. (2014a,b) for low and intermediate mass stars that undergo the AGB and super-AGB phase ($7 - 9$ M$_\odot$). These sets of yields have been tested by state-of-the-art chemical models and well reproduce observations of different ion abundances in the MW (Romano et al., 2010, 2017, and private communications). The difference between these two sets of stellar yields is quantified in Section 7.4.6.

The key features of the simulations are listed in Table 7.1. Besides the name and the resolution of the ICs, i.e. *AqC5*, the simulation label encodes the adopted IMF, the considered set of stellar yields, and two parameters, namely the value of binary systems giving rise to SN Ia and the kinetic stellar feedback efficiency, respectively.

7.3 Impact of IMF on the number of massive stars

Stellar feedback is one of the natural outcome of star formation, but it also contributes to regulate it. Therefore, should the number of stars that mainly contribute to stellar feedback vary as a consequence of a different IMF, the amount of feedback energy is directly affected, with a dramatic impact on the star formation history of the galaxy. The number of stars that end up their life as SNe II deserves particular attention, as they mainly contribute to determine the available kinetic feedback energy and to trigger galactic outflows, expelling gas outwards.

Figure 7.1 shows the stellar number distribution per mass interval as a function of the mass for the two IMFs that I am considering for the current analysis (see equations (7.2) and (7.3) for K2s and K3s IMFs, respectively).

The number of massive ($m > M_{up}$) stars exploding as SNe II in an SSP assuming an IMF $\phi(m) = A_\phi\, m^{-\alpha}$ is:

$$N_{*\mathrm{massive}} = A_\phi \int_{M_{up}}^{M_{sup}} m^{-\alpha}\, dm \ , \tag{7.4}$$

A_ϕ being the normalization constant and α the slope of the adopted IMF in the considered mass range, respectively. In equation (7.4), M_{up} is the initial mass threshold for massive stars that explode as SN II and M_{sup} is the upper bound of the mass range in which the IMF is defined. I assume $M_{sup} = 100$ M$_\odot$.

For K2s $\phi(m) \simeq 0.22\, m^{-2.3}$ for $m > M_{up}$, while for K3s $\phi(m) \simeq 0.31\, m^{-2.7}$. Integrating equation (7.4) over the mass range and assuming $M_{up} = 8$ M$_\odot$ yields to the following numbers of massive stars: $N_{*\mathrm{massive,K2s}} \simeq 1.093 \cdot 10^{-2}$ for K2s, and $N_{*\mathrm{massive,K3s}} \simeq 0.525 \cdot 10^{-2}$ when K3s is adopted. Thus, K2s predicts roughly twice ($\simeq 2.1$) as many massive stars as K3s. This reflects directly in the amount of stellar feedback energy that the ISM is provided with. Therefore, in order to have a comparable amount of feedback energy from SN explosions, the kinetic stellar feedback efficiency $f_{\mathrm{fb,kin}}$ has to be doubled in simulations adopting the K3s IMF (i.e. $f_{\mathrm{fb,kin}} = 0.26$).

I note that marginal variations in the mass interval over which the integral in equation (7.4) is computed does not play a crucial role in assessing the ratio of massive stars when the different IMFs are considered. For instance, there is not general consensus on the exact value of M_{up} in the range $7 - 9$ M$_\odot$ mainly because of the modelling of convection within the star. Assuming $M_{up} = 9$ M$_\odot$ as the lower limit of integration in equation (7.4) leaves the relative number of $N_{*\mathrm{massive}}$ unchanged. We actually assume $M_{up} = 9$ M$_\odot$ in simulations adopting the set B of stellar yields, as Doherty et al. (2014a,b) consider that stars with initial mass ranging between $7 - 9$ M$_\odot$ undergo the super-AGB phase.

Also, variations on M_{sup} (that affect chemical feedback rather than that in energy, see Section 7.2.1) deriving from the debated fate of stars more massive than ~ 40 M$_\odot$ do not impact dramatically on the relative number of massive stars predicted by the K2s and K3s.

Accounting properly for the number of SNe II and recalibrating the feedback efficiency accordingly allows to have a comparable star formation history for simulations K2s–yA–IaA–kA and K3s–yA–IaA–kB (see Figure 7.3). I emphasise that this is the reason why I decide to contrast results from simulations adopting the K2s IMF and $f_{\mathrm{fb,kin}} = 0.12$ (*kA* in simulation names), and the ones with the K3s IMF and $f_{\mathrm{fb,kin}} = 0.26$ (*kB* in simulation labels) when analysing the effect of the varying IMF.

At variance with our aforementioned recalibration, Gutcke & Springel (2017) did not tune the stellar feedback efficiency accounting for the different number of stars produced by the adopted metallicity-dependent IMF, with a consequent overproduction of stellar mass resulting from a modified star formation history.

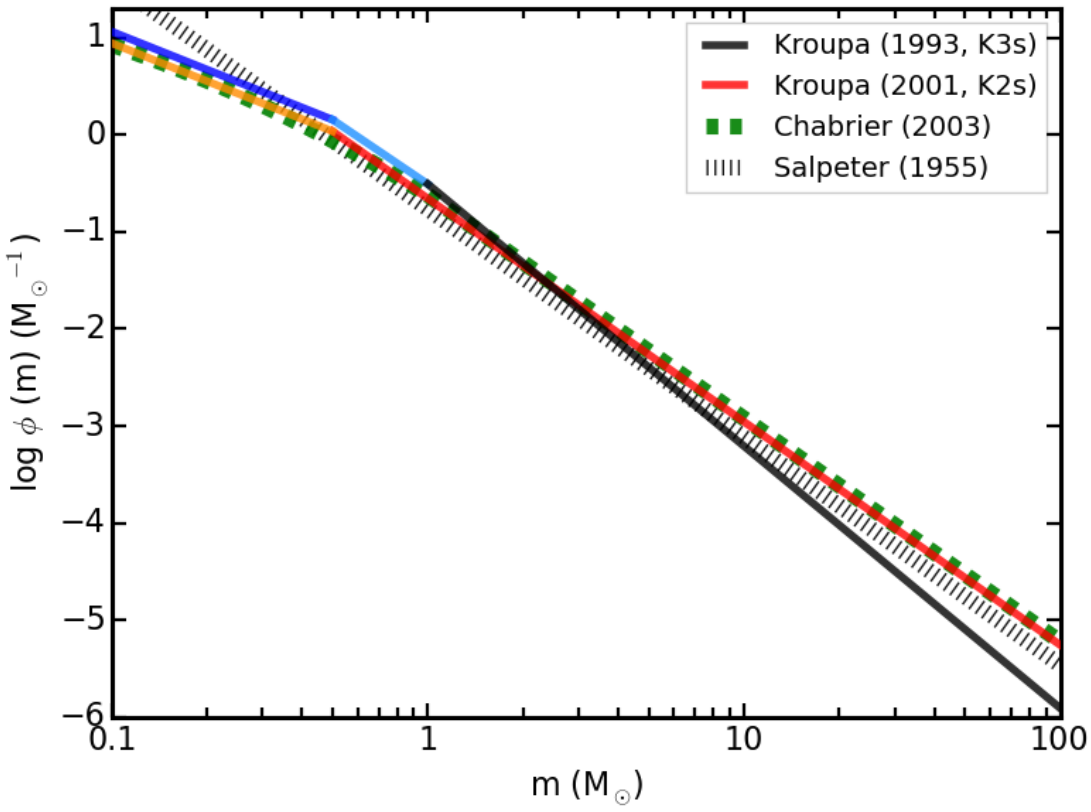

Figure 7.1: Stellar number distribution per mass interval as a function of the mass for the two IMFs that we are considering for the current analysis: K2s is the Kroupa (2001) IMF described by equation (7.2), while K3s is the Kroupa et al. (1993) IMF represented by equation (7.3). For reference, we also show the Chabrier (2003) IMF and the Salpeter (1955) IMF.

7.4 Results

In this Section, I present the results. In Section 7.4.1, I show the main properties of the simulated galaxies. In Section 7.4.2 I analyse stellar ages and SN rates, while in Section 7.4.3 I show radial abundance profiles for gas and stars in the set of galaxies. In Sections 7.4.4 and 7.4.5, I investigate the α-enhancement of stars and where metals are located within and around our galaxies. In Section 7.4.6, I investigate how stellar yields impact on final results.

Throughout this Chapter, when I mention metallicity I refer to the abundance by number of a given element or ratio between two elements. When comparing element abundance to that of Sun, I adopt values for the present-day Sun's abundance in the element X (i.e. $\log_{10}\varepsilon_{\rm X} = 12 + \log_{10}\left(N_{\rm X}/N_{\rm H}\right)$, where $N_{\rm X}$ and $N_{\rm H}$ are number densities of the element X and of hydrogen, respectively) according to Caffau et al. (2011, as for iron) and to Asplund et al. (2009, for all the other elements).

7.4.1 Main properties of the simulated galaxies

I introduce the main physical properties of the galaxies resulting from the cosmological simulations that I carried out. Figure 7.2 shows projected stellar (first and second columns) and gas (third and forth columns) density maps for each galaxy. Both edge-on (first and third columns) and face-on (second and forth columns) views are presented. Galaxies have been rotated so that the z-axis of their reference system is aligned with the angular momentum of star particles and cold and multiphase gas particles located within 8 kpc from the minimum of the gravitational potential (as done in Chapter 6). The centre of the galaxy, where the origin of the reference system is set, is assumed to be the centre of mass of the aformentioned particles. Here and in the following, I consider for the analysis star and gas particles that are located within the galactic radius[1], unless otherwise stated. The galactic radius of these galaxies is $R_{\rm gal} \sim 24$ kpc (see also Table 7.3).

Density maps in Figure 7.2 show that all the galaxies but K2s–yA–IaB–kA have a limited bulge and a dominant disc component, although the morphology and the extent of the disc varies from galaxy to galaxy. In particular, some galaxies exhibit an irregular distribution of gas around and above the galactic plane, this suggesting ongoing gas accretion (see also Figure 7.4). A clear spiral pattern is evident in the majority of the discs.

In Figure 7.3 I show the evolution of the SFR of the six galaxies. A high-redshift ($z \gtrsim 3$) star formation burst characterises the star formation history of all the galaxies, in a remarkably similar way, building up the bulk of the stellar mass in the bulge of each galaxy. Star formation occurring at lower redshift, in a more continuous way, is then responsible of the (possible) formation of the disc. General trends are as follows: the lower the fraction of binary systems originating SNe Ia, the lower the SFR below $z \sim 1$. Also, the set B of stellar yields is responsible for the reduced gas cooling and consequent lower SFR. This is particularly evident when contrasting the SFR of K3s–yA–IaB–kB and K3s–yB–IaB–kB. The reason stems from the lower amount of iron that is produced when reducing the number of SNe Ia, the iron being one of the main coolants (along with oxygen, for solar abundances, Wiersma et al., 2009a). Also, the stellar yields labeled as B predict a lower synthesis of Fe for all the considered metallicities and a lower production of O for solar metallicity (see Sections 7.4.4 and 7.4.6). Effects on the star formation are evident, as a consequence of the element-by-element metal cooling in our simulations (as discussed in Section 5.4).

A complex interplay between different processes determines and regulates the star formation histories of the galaxies in Figure 7.3: the reservoir of gas available for star formation, the cooling process, and stellar feedback. Figure 7.4 shows the

[1] As in Chapter 6, I define here the galactic radius as one tenth of the virial radius, i.e. $R_{\rm gal} = 0.1 R_{\rm vir}$. I choose the radius $R_{\rm gal}$ so as to identify and select the region of the computational domain that is dominated by the central galaxy. Moreover, virial quantities are considered as those computed in a sphere that is centred on the minimum of the gravitational potential of the halo and that encloses an overdensity of 200 times the *critical* density at present time.

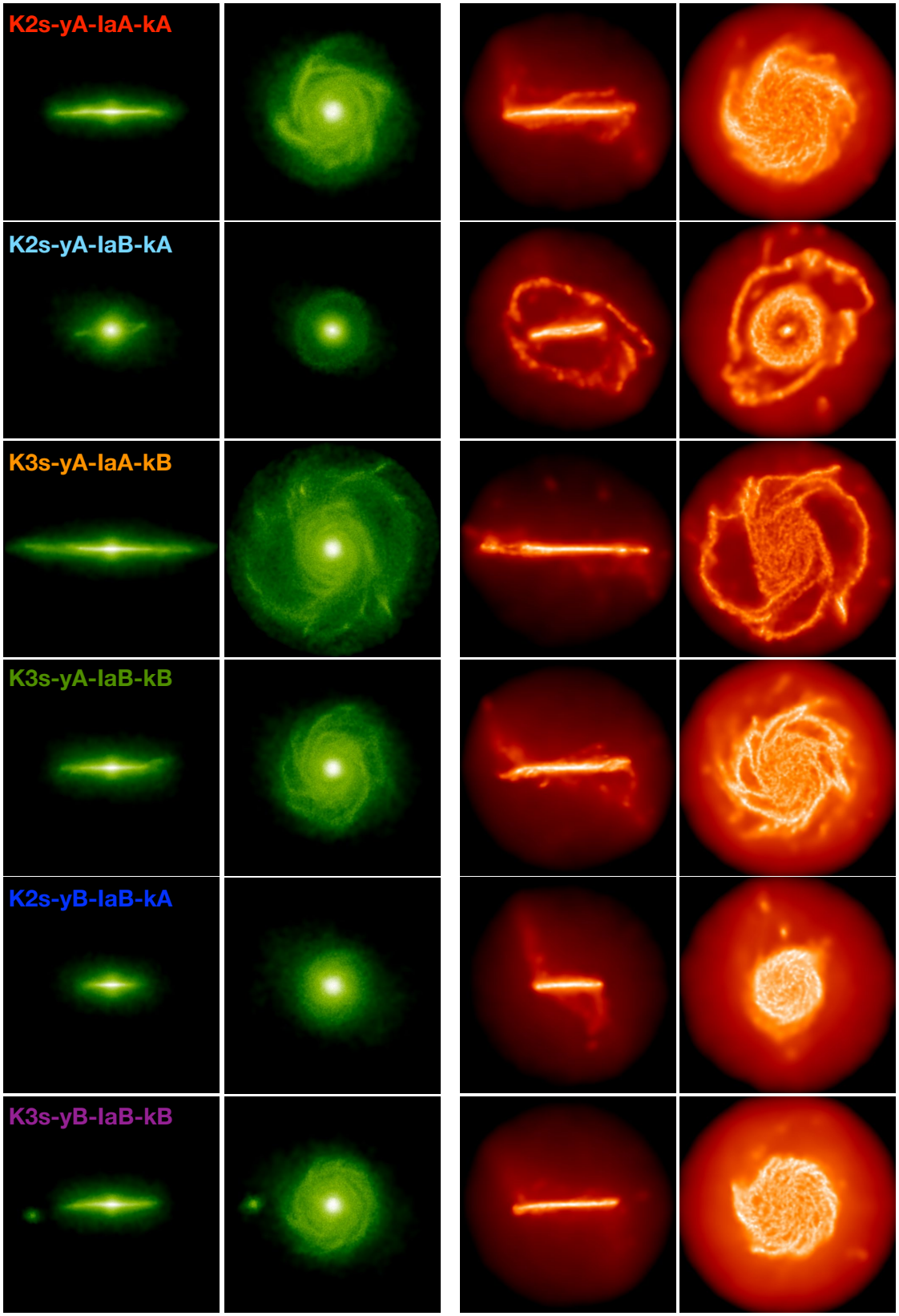

Figure 7.2: Projected stellar (first and second columns) and gas (third and forth) density maps for the set of simulated galaxies listed in Table 7.1, at $z = 0$. Each row shows a galaxy, whose name is indicated in the first column panel. First and third columns show edge-on galaxies, second and forth face-on maps. The size of each box is 48 kpc a side.

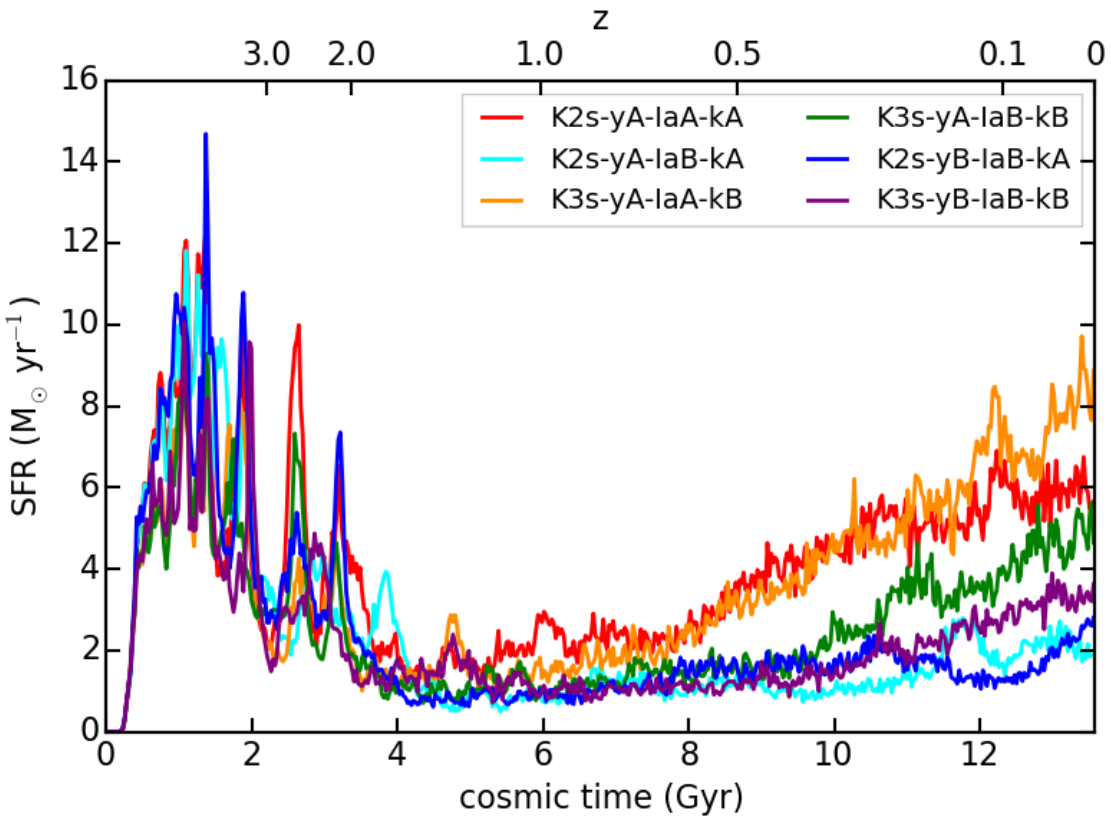

Figure 7.3: Star formation histories for the six simulated galaxies listed in Table 7.1. Red curve shows K2s–yA–IaA–kA, cyan and orange lines depict K2s–yA–IaB–kA and K3s–yA–IaA–kB, respectively. The green curve refers to K3s–yA–IaB–kB, while blue and purple lines show K2s–yB–IaB–kA and K3s–yB–IaB–kB, respectively (as shown in the legend).

mass accretion history of gas within the galactic radius for each galaxy, and can be related to the evolution of the SFR. However, there is not a direct correspondance between the amount of accreted gas and the SFR. The reason is that gas accreted becomes available for star formation as soon as it approaches the innermost regions of the forming galaxy and cools. Besides density, gas cooling depends on metallicity, that primarly shapes the cooling function. Also, massive stars trigger galactic outflows as they explode as SNe II: outflows can hamper gas that is accreted within the virial radius from flowing inwards and feed star formation. A more top-heavy IMF (i.e. K2s) would further affect this scenario if the feedback efficiency were not calibrated (see Section 7.3). I note that minor variations between low-redshift star formation histories and gas mass accretion histories of galaxies with different IMFs are present, despite the feedback efficiency calibration: this is a further evidence of how different elements enter the process of galaxy formation in a non-linear fashion. Also, the formation of the stellar disc is highly sensitive to the timing of gas accretion (see also Chapter 6).

Figure 7.5 presents a kinematic decomposition of simulated galaxies. I examine the circularity of stellar orbits in order to distinguish between the rotationally and

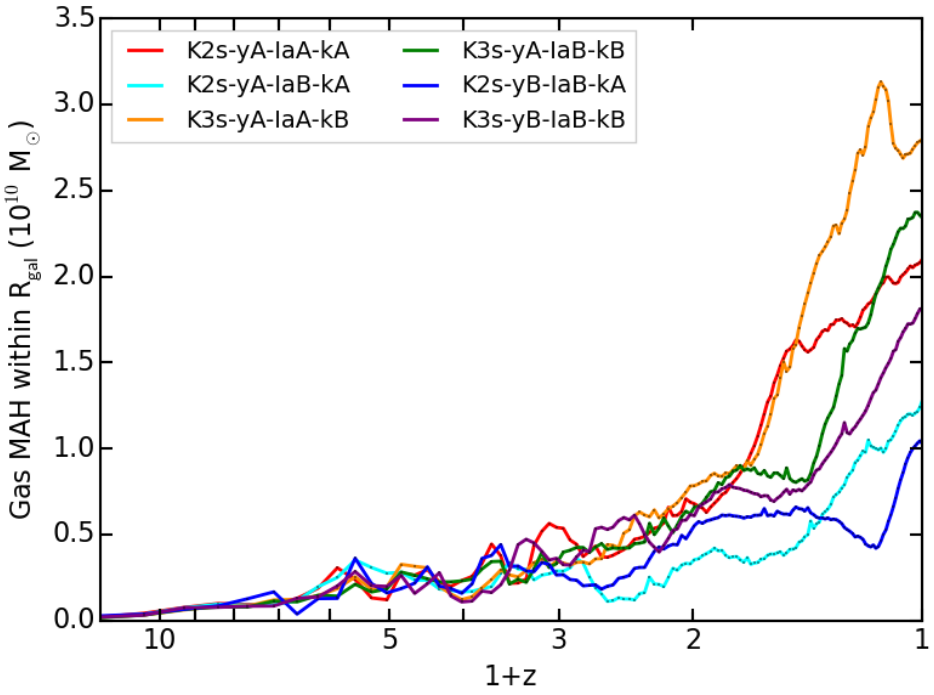

Figure 7.4: Mass accretion history (MAH) of gas within the galactic radius $R_{\rm gal}$ of galaxies. Colours as in Figure 7.3.

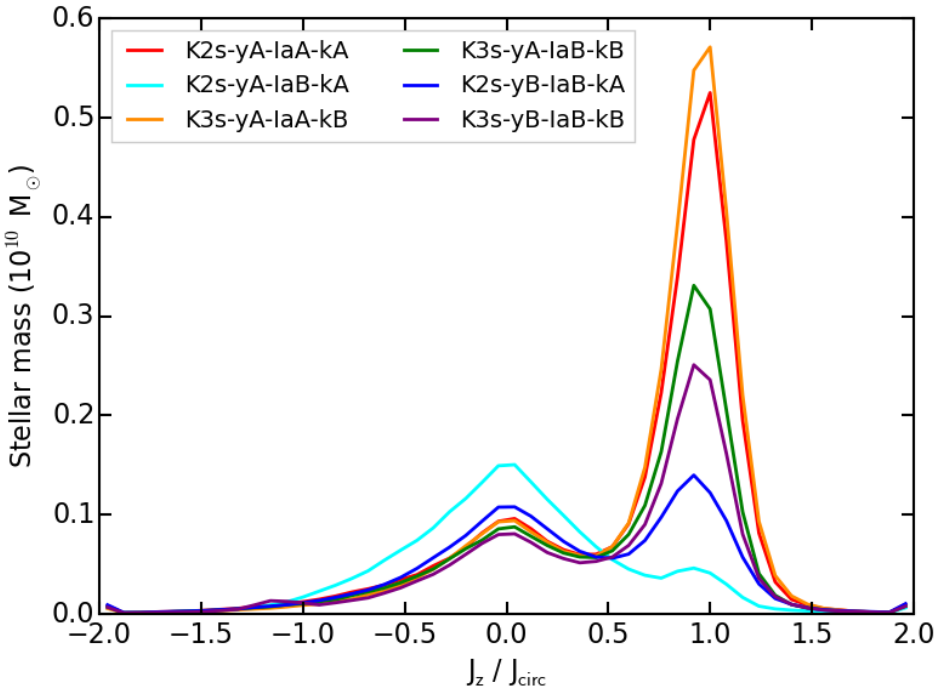

Figure 7.5: Stellar mass as a function of the circularity of stellar orbits at $z = 0$ for the set of galaxies. The height of the peaks at $J_{\rm z}/J_{\rm circ} = 0$ and at $J_{\rm z}/J_{\rm circ} = 1$ shows the relative contribution to the total stellar mass of the bulge and the disc, respectively. Bulge-over-total mass ratios are as follows: 0.33 (red), 0.97 (cyan), 0.28 (orange), 0.41 (green), 0.64 (blue), and 0.45 (purple).

Table 7.2: Success of galaxy models in matching observational constraints considered throughout Section 7.4. Each row refers to a galaxy model of the simulation suite. Columns are the observational tests.

Name	Dominant stellar disc	SN Ia & SN II rates		Gas & metallicity gradient	Stellar	α-enhancement pattern
K2s–yA–IaA–kA	✓	✓	✗	✗	✓	✗
K2s–yA–IaB–kA	✗	✓	✓	✗	✓	✓
K3s–yA–IaA–kB	✓	✓	✗	✓	✓	✗
K3s–yA–IaB–kB	✓	✓	✓	✓	✓	✓
K2s–yB–IaB–kA	✓	✓	✓	✓	✓	✓
K3s–yB–IaB–kB	✓	✓	✓	✓	✗	✓

dispersion supported components of each galaxy, thus quantifying the prominence of the disc with respect to the bulge (as done in Chapter 6, too). I remind that the circularity of stellar orbits is defined as the ratio of specific angular momenta J_z/J_{circ}, where J_z is the specific angular momentum in the direction perpendicular to the disc, and J_{circ} is the angular momentum of a reference circular orbit at the considered distance from the galaxy centre (see Section 6.5.2). Stars located in the disc contribute to the peak where $J_z/J_{circ} = 1$, while stars in the bulge are characterised by $J_z/J_{circ} \sim 0$. Galaxies K3s–yA–IaA–kB and K2s–yA–IaA–kA exhibit the most pronounced disc, as a consequence of the higher low-redshift SFR (see Figure 7.3). An extended disc where the bulk of the stellar mass is located characterises galaxies K3s–yA–IaB–kB and K3s–yB–IaB–kB, while K2s–yB–IaB–kA has a smaller, yet dominant, stellar disc component. Finally, K2s–yA–IaB–kA is an irregular galaxy with a dominant spheroidal component (as shown in Figure 7.2). Table 7.2 summarises the morphological features of different galaxy models and whether galaxy properties meet or not observational constraints that I consider during the analysis throughout Section 7.4. The prominence of the stellar disc can be easily explained by analysing the SFR below $z \sim 1$ in Figure 7.3. A higher low-redshift SFR translates directly in a more extended stellar disc component. Stellar masses of galaxies and bulge-over-total mass ratios are as follows: $3.64 \cdot 10^{10}$ $M_\odot$ and 0.33 (K2s–yA–IaA–kA), $2.02 \cdot 10^{10}$ $M_\odot$ and 0.97 (K2s–yA–IaB–kA), $3.85 \cdot 10^{10}$ $M_\odot$ and 0.28 (K3s–yA–IaA–kB), $2.68 \cdot 10^{10}$ $M_\odot$ and 0.41 (K3s–yA–IaB–kB), $2.06 \cdot 10^{10}$ $M_\odot$ and 0.64 (K2s–yB–IaB–kA), $2.24 \cdot 10^{10}$ $M_\odot$ and 0.45 (K3s–yB–IaB–kB).

7.4.2 Stellar ages and SN rates

I continue the analysis by investigating stellar ages and formation epochs for different components of simulated galaxies. Figure 7.6 shows radial profiles of the mass weighted age of stars within the galactic radius for the six simulations. The corresponding redshift at which stars form is displayed, too. Stars in the innermost regions of galaxies have, on average, an age ranging between 9.5 and 11 Gyr, depending on the simulation. The mass weighted mean age of stars progressively

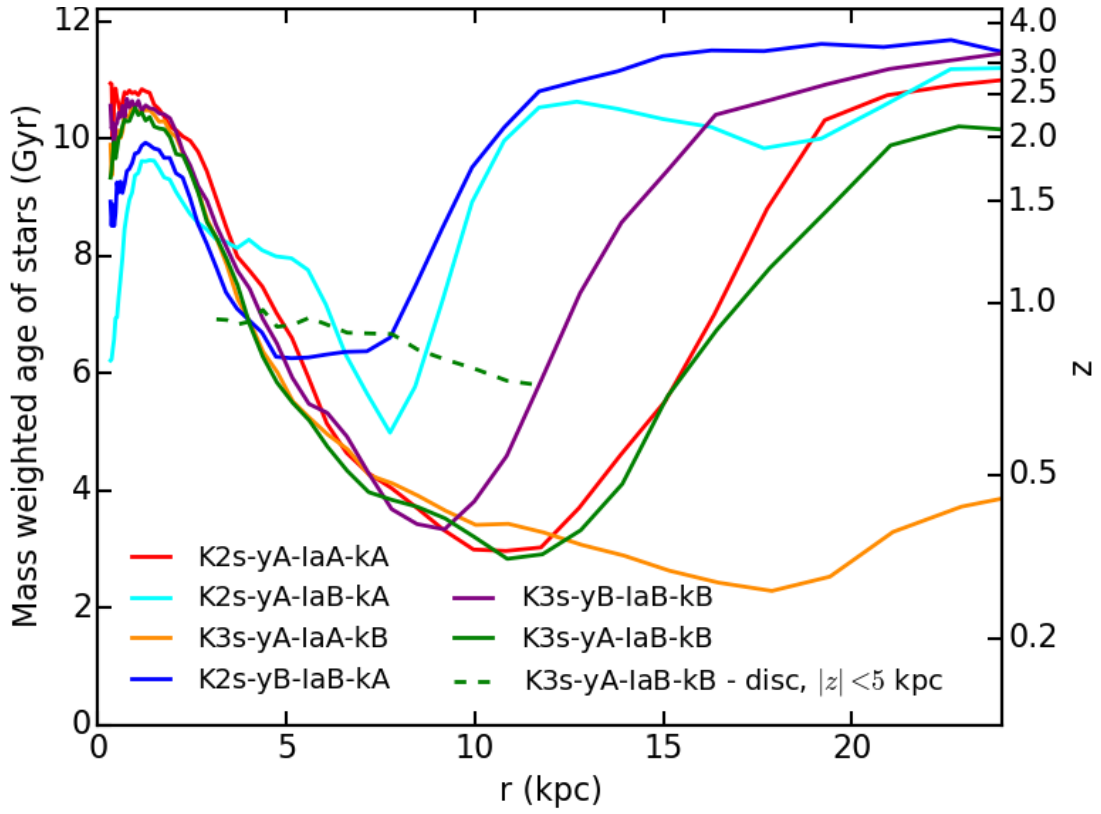

Figure 7.6: Radial profiles of the mass weighted age of stars within the galactic radii of the six simulations. For simulation K3s–yA–IaB–kB (green) I also show the mass weighted age of stars in the disc (dashed line).

decreases as the distance from the galaxy centre increases and a minimum is reached in correspondence with the extent of the stellar disc of each galaxy. Moving then outwards, the mean stellar age pinpoints stars progressively older. When computing the age of stars located at increasing distance from the galaxy centre, I consider stars within spherical shells with a given radial thickness. Therefore, albeit the identification of the innermost and outermost old stars with bulge and halo stars, respectively, is straightforward, stars that make the radial profile decline cannot be associated directly to the disc component.

For this reason, in order to further investigate stellar ages for stars in the disc, I focus on simulation K3s–yA–IaB–kB and consider a region limited as follows: $3 < r < 13$ kpc and $|z| < 5$ kpc, r and z being the radial distance from the galaxy centre and the galactic latitude, respectively. I show the mass weighted age of stars in the aformentioned volume that can be deemed as the disc (green dashed line) in Figure 7.6, too. Stars are characterised by a negative age radial gradient, and this supports the inside-out growth for the stellar disc. This scenario, where stellar discs progressively increase their size as they evolve and grow more massive (see Section 2.4.3), is corroborated by a variety of observations (e.g Barden et al., 2005; Muñoz-Mateos et al., 2011; Patel et al., 2013; González Delgado et al., 2014), and by models of chemical evolution (e.g. Chiappini et al., 2001), by semi-analytical

models (e.g. Dutton et al., 2011a), and simulations (e.g. Pichon et al., 2011; Aumer et al., 2014). I chose the K3s–yA–IaB–kB as a reference model to further investigate stellar ages in the galaxy disc. Comparable conclusions can be drawn also for other galaxy models with extended stellar discs: however, I preferred to overplot only one further radial profile in Figure 7.6 for the sake of clarity. Also, restricted regions where inspecting the age of stars located in the disc have to take into account the galaxy morphology, so that it is not trivial to define only one region for all the galaxy models where studying stars in the disc. Note that the stellar age profile of stars in the disc of K3s–yA–IaB–kB is flatter than the profile characterising all the stars in that considered range of distance from the galaxy centre, younger stars at higher latitudes on the galactic plane being not included.

Inspecting the stellar age of K3s–yA–IaB–kB further, I show the face-on and edge-on projections of all the star particles within the galactic radius $R_{\rm gal}$ at redshift $z = 0$ in Figure 7.7. The colour encodes the mean age of the star particles in each spatial bin: we can appreciate how the stellar age changes as a function of the distance from the galaxy centre across the galactic plane (top panel of Figure 7.7) and as a function of the galactic latitude (bottom panel). The youngest stars trace the spiral pattern of the galaxy, and pinpoint spiral arms as sites of recent star formation. The thickness of the stellar disc progressively increases moving outwards. The halo and the bulge are made up of the oldest stars in galaxy.

When analysing stellar ages at $z = 0$ in Figures 7.6 and 7.7, we analyse mean quantities, thus it is not trivial to deduce straightforwardly the formation scenario. If we consider the distribution in Figure 7.7 at higher-redshift simulation outputs (i.e. by evolving it backward in time), we find that high-z star formation occurs first in the innermost regions of the forming galaxy and soon after it is widespread in the galaxy, the oldest ($\sim$ 12 Gyr) stars spreading across the halo as well as in inner regions (see Clemens et al., 2009, for a similar scenario in elliptical galaxies). As time passes, star formation involves internal regions alone, as they are replenished with gas that is accreted from the large scale environment, and takes place especially in the forming bulge and at relatively larger distances from the centre with few episodes of star formation. Then, at later epochs ($z \lesssim 1.5$), star formation in the disc occurs and the disc formation proceeds inside-out.

The presence of an old ($\sim$ 12 Gyr) stellar component throughout the galaxy can be seen in Figure 7.8, where the distribution of stellar mass per bin of lookback time is shown. The galaxy stellar content has been sliced into four different regions (within the galactic radius, $r < R_{\rm gal}$), as reported in each panel. The regions can be considered as representative of the following components of the galaxy: bulge (top left), inner disc (top right), outer disc (bottom left), and halo (bottom right). Vertical lines show the median of each distribution, and highlight the formation epoch of different components.

I then analyse SN rates in our set of simulated galaxies. Figure 7.9 shows the redshift evolution of SN Ia (top panel) and SN II (bottom panel) rates, where rates are expressed as events per century and per 10^{10} $M_{\odot}$. I compute rates as SN events

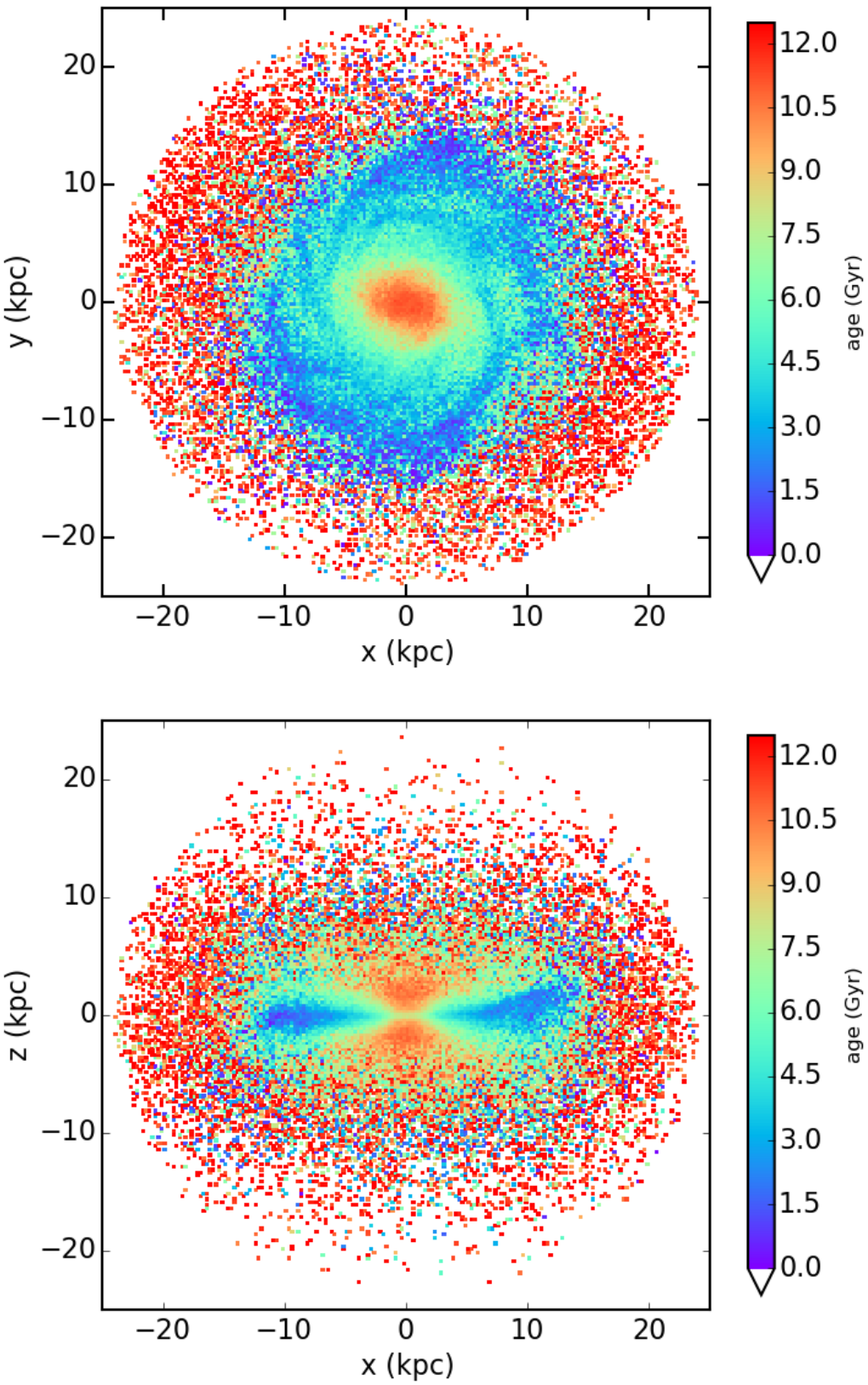

Figure 7.7: Face-on (top panel) and edge-on (bottom panel) binned distributions of all the star particles located within the galactic radius for the K3s–yA–IaB–kB (green) simulation. Plots are shown at redshift $z = 0$; the colour encodes the mean age of the star particles in the bin.

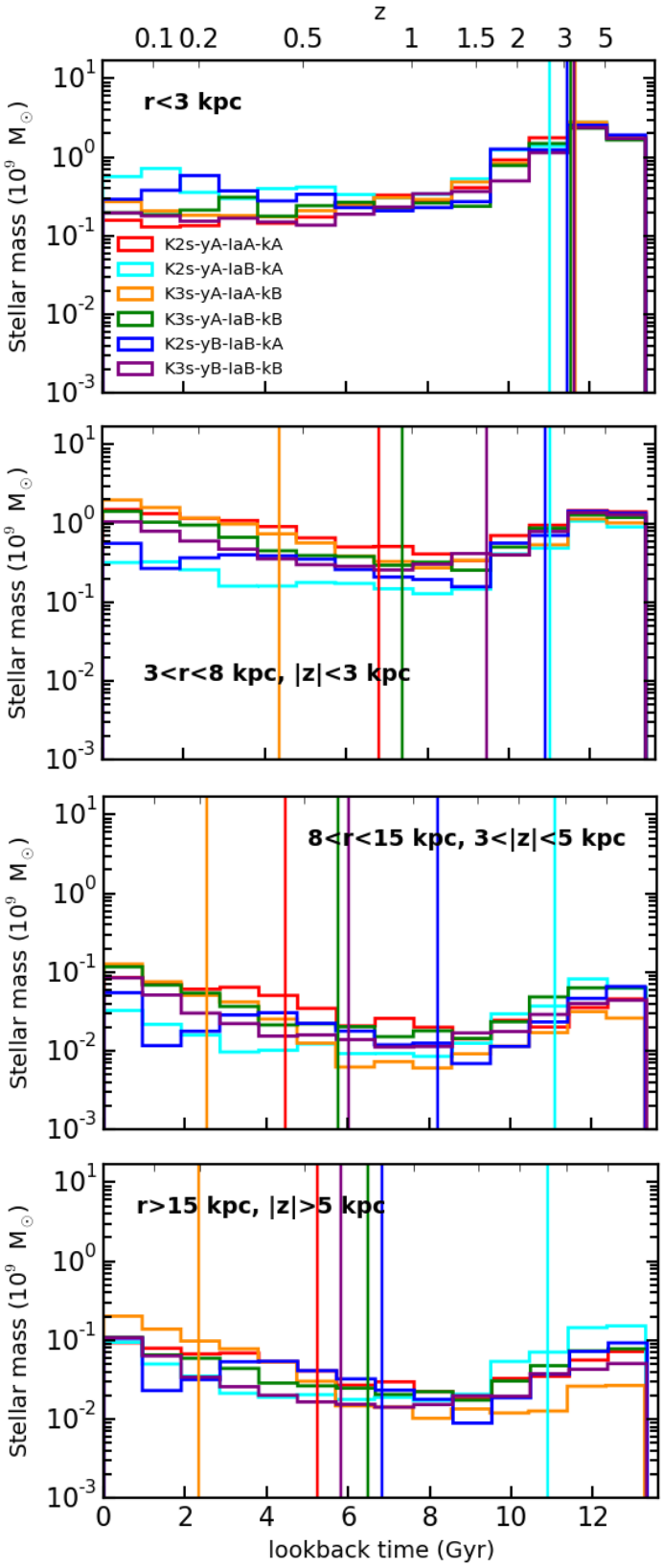

Figure 7.8: Distribution of stellar mass per bin of lookback time for all the simulations. The four panels consider different regions of the volume $r < R_{\rm gal}$, as reported in each panel, and roughly identify the following components of the galaxy *(from top to bottom)*: bulge, inner disc, outer disc, and halo. Vertical lines show the median of each distribution, and highlight the formation epoch of different component.

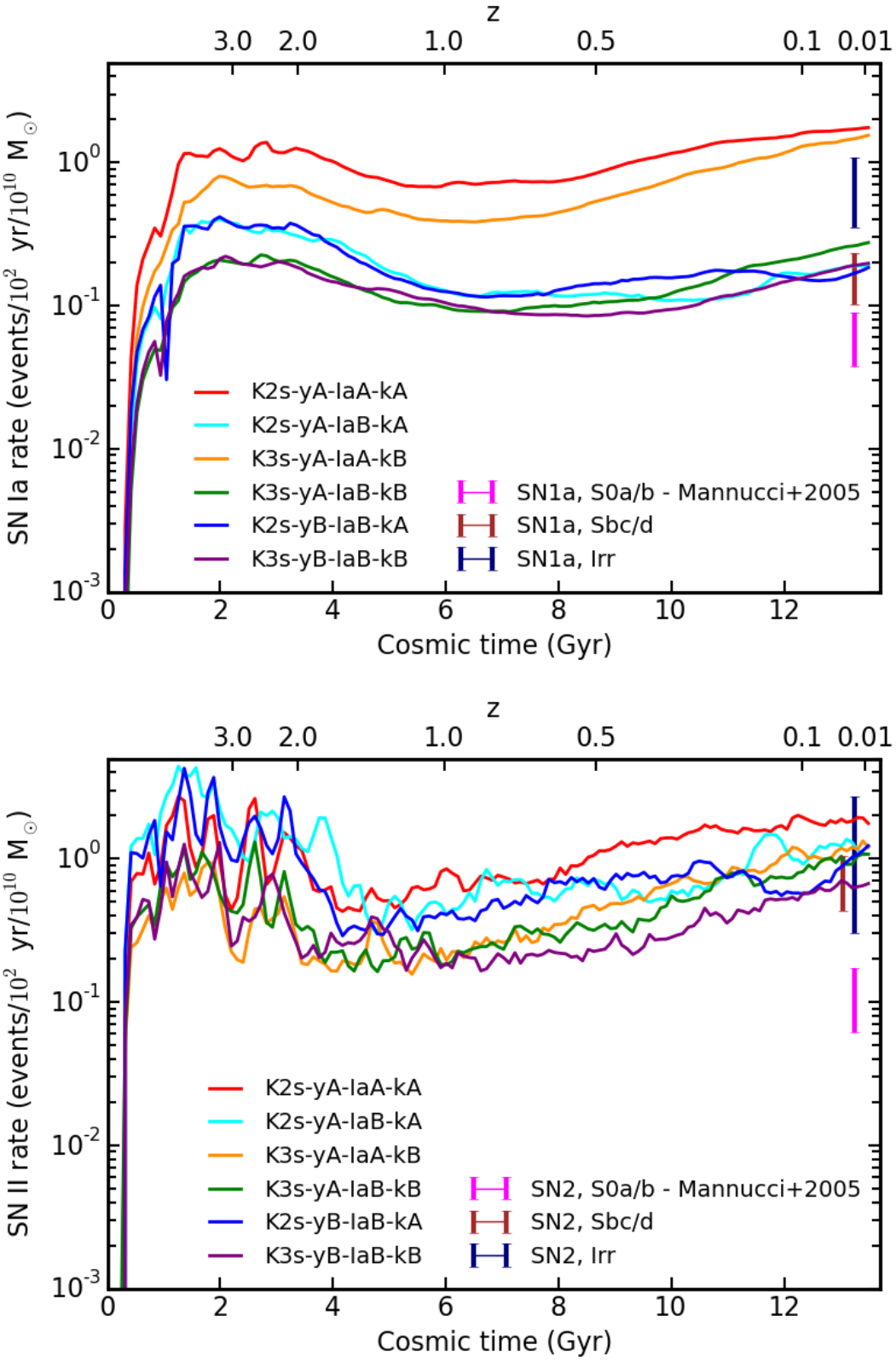

Figure 7.9: Evolution of SN Ia (left-hand side panel) and SN II (right-hand side panel) rates for the simulated galaxies. Rates are expressed as events per century and per 10^{10} $M_{\odot}$. Our predictions are compared with observations by Mannucci et al. (2005) for local Universe galaxies with different morphological type, as highlighted in the legend.

between two simulation outputs over the time between the outputs. I compare predictions from simulations with observations by Mannucci et al. (2005). These authors compute the rate of SNe for galaxies belonging to different morphological classes: here we consider SN Ia and SN II rates for galaxies classifies as irregular, S0a/b and Sbc/d in the observational sample. Error bars represent the $1-\sigma$ error (including uncertainties on SN counts, and host galaxy magnitude and inclination), but do not account for uncertainties on the estimate of the mass for galaxies in the observational sample, that is quoted to affect measurements by $\sim 40\%$.

By comparing Figures 7.9 and 7.3, we can appreciate how SN II rates trace the evolution of the SFR. We find that SN II rates of simulated galaxies are in keeping with observations from late-type Sbc/d galaxies, the galaxy model K2S–yA–IaA–kA slightly exceeding them. Also, a good agreement between SN Ia rates of simulations adopting the lower fraction of binary systems that host SNIa and observations from Sbc/d galaxies is recovered. The comparison with Mannucci et al. (2005) data supports a value for the fraction of binary systems suitable to give rise to SNe Ia of 0.03, while disfavouring the value 0.1 (at least for late-type galaxies and when the IMFs that we are adopting are considered). Matching observational data of Mannucci et al. (2005) is a valuable result of our simulations: SN rates are indeed a by-product of the chemical evolution network in our simulations, and reflect the past history of star formation and feedback of the galaxy (see also Table 7.2). Also, the comparison between computed SN rates with observations can be used as a powerful tool to predict or at least validate the morphological type of the simulated galaxies.

7.4.3 Metallicity profiles

7.4.3.1 Stellar metallicity gradient

In this Section, I analyse stellar metalicity gradients of simulated galaxies and compare predictions from simulations to observations, taking advantage of the wealth of accurate measurements available for our Galaxy. Figure 7.10 shows the iron abundance radial profile for the set of simulated galaxies. Results are compared with observations of Cepheids in MW from different authors (further detailed in the legend and caption of the Figure). Here, and in Figures 7.11 and 7.12, I consider only those stars whose age is < 100 Myr in simulated galaxies, since Cepheids are stars younger than ~ 100 Myr (Bono et al., 2005). Ages of young open clusters and star forming regions in Spina et al. (2017) are younger than ~ 100 Myr, too (see Figure 7.10). When different from ours, solar reference abundances adopted in the observational samples have been properly rescaled.

Figure 7.11 shows the radial abundance gradient for oxygen. I compare predictions from simulations with observations of Cepheids from Luck & Lambert (2011), according to the division in bins as a function of the Galactocentric distance computed by Mott et al. (2013). Error bars indicate the standard deviation computed in each bin, that is 1 kpc wide.

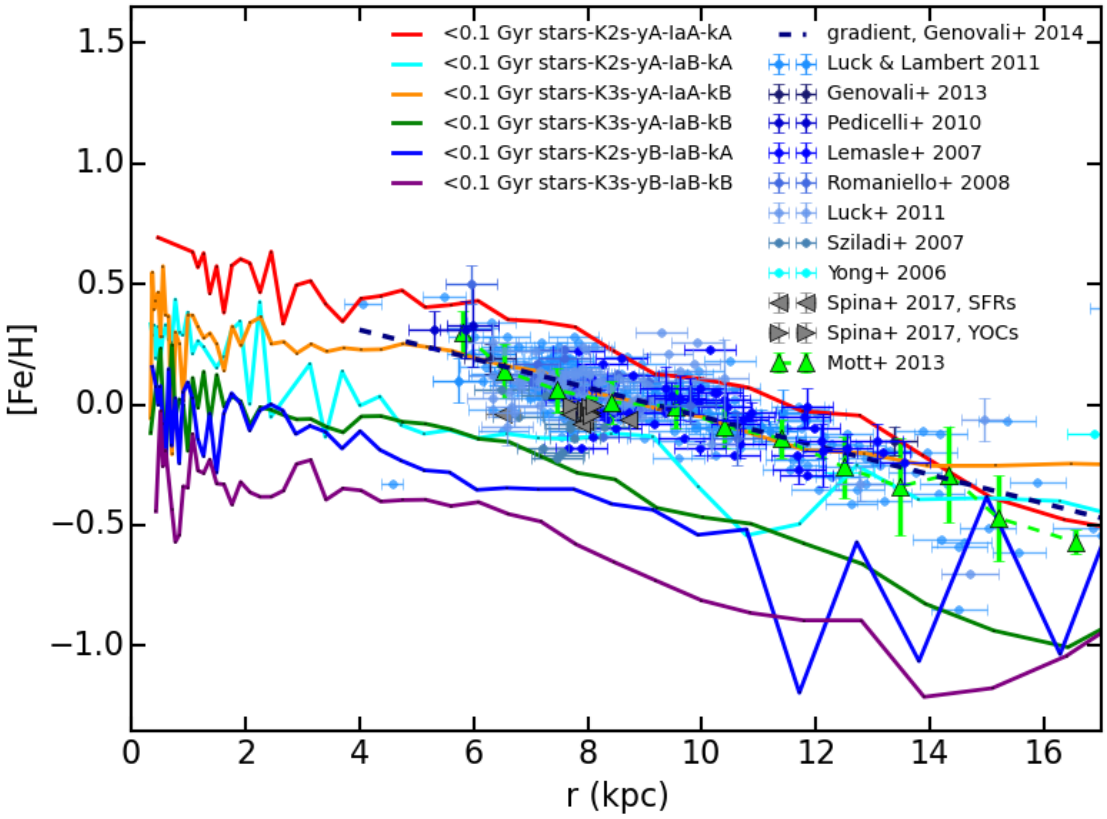

Figure 7.10: Iron abundance radial profile for young stars in the simulated galaxies (colors as in the legend and previous figures). We compare results with observations of Cepheids in the catalogue of Genovali et al. (2014a), that include data from Yong et al. (2006); Lemasle et al. (2007); Sziládi et al. (2007); Romaniello et al. (2008); Pedicelli et al. (2010); Luck et al. (2011); Luck & Lambert (2011); Genovali et al. (2013). Dashed blue line depicts the metallicity gradient for the whole sample (Genovali et al., 2014b). We also consider data for young open clusters (YOCs) and star forming regions (SFRs) in MW from Spina et al. (2017). Green symbols highlight observations of Luck & Lambert (2011) according to the binning by Mott et al. (2013).

Figure 7.12 compares radial profiles for the abundance ratio $[O/Fe]$ in simulations with observations of Cepheids (Luck & Lambert, 2011; Mott et al., 2013). Observations show that stars in the disc of MW are not α-enhanced, on average, with respect to solar values. Data of Mott et al. (2013) have been shifted by the authors themselves (by the following amounts: -0.17 dex for $[O/H]$, -0.07 for $[Fe/H]$) with respect to the original data of Luck & Lambert (2011), due to the discrepancy of the dataset of Luck & Lambert (2011) with previous observations by the same authors (see below).

Negative radial abundance gradients are recovered for all the galaxies, thus in agreement with observations (Figures 7.10 and 7.11). The slope of the profiles (for distances form the galaxy centre larger than $r > 4$ kpc) is in keeping with observations, this indicating the effectiveness of our sub-resolution model to properly describe the chemical enrichment of the galaxy at different positions.

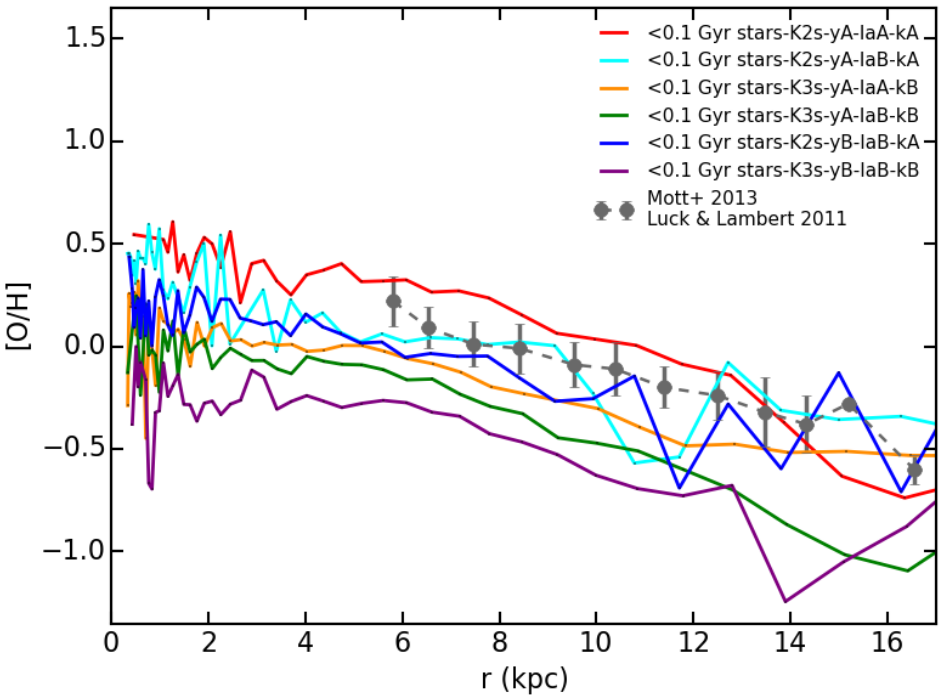

Figure 7.11: Oxygen abundance radial profile for young stars in the set of galaxies. Data show the radial gradient for oxygen from observations of Cepheids (Luck & Lambert, 2011), according to the division in bins computed by Mott et al. (2013). Error bars show the standard deviation in each bin.

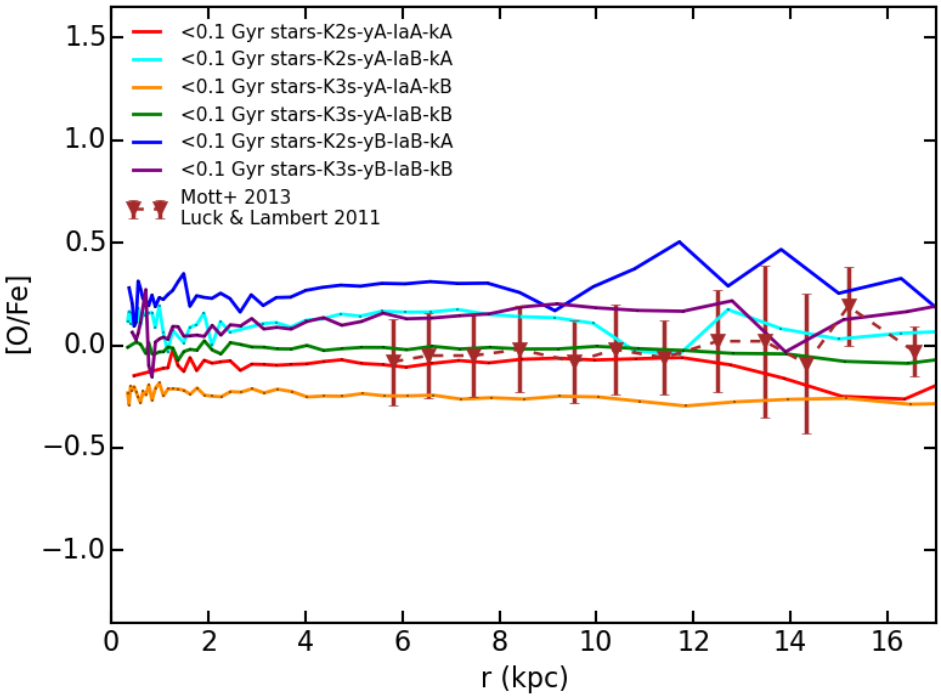

Figure 7.12: Oxygen-over-iron abundance profile for young stars in simulated galaxies. Observations of Cepheids from Luck & Lambert (2011), according to the binning performed by Mott et al. (2013).

Focussing on the normalization of oxygen profiles, comparison with Cepheids supports a K2s IMF. The K2s IMF leads to a fair agreement with observations also when the normalization of iron profiles is considered: however, in this case, a value of 0.1 for the fraction of binary systems with characteristics suitable to host SNe Ia is the driver for matching observations. Indeed, when the value of 0.03 is considered, the amount of iron produced is not enough to agree with data. The set B of stellar yields lowers the normalization of metallicity gradients, as a lower amount of oxygen and iron are synthesised (see Section 7.4.6). Iron profiles in galaxies simulated adopting this set of yields underestimate observations by $\gtrsim 0.5$ dex (Figure 7.10). Also, there exists a degeneracy between the adopted IMF and the set of yields, the galaxy models K3s–yA–IaB–kB and K2s–yB–IaB–kA providing comparable results. Peaks at distances $r > 10$ kpc for galaxies K2s–yA–IaB–kA and K2s–yB–IaB–kA are due to the reduced amount of stars as the outermost regions of the stellar disc are reached.

Figures 7.10 and 7.11 suggest that young stars in these simulated galaxies are more metal poor than observed ones in MW, when both the iron and the overall metal content ($\sim$ oxygen) are considered. This is especially true for those models of galaxies that best fit observations in Figure 7.13, and in particular for K3s–yA–IaB–kB (green). A possible reason for that stems from the star formation history of our galaxies. MW-like galaxies often assemble a considerable part of the stellar mass in the disc in the redshift range $2.5 \lesssim z \lesssim 1$ (van Dokkum et al., 2013; Snaith et al., 2014). Our galaxies are instead characterised by a quiescent star formation in the redshift range $2 \lesssim z \lesssim 1$, as shown in Figure 7.3. Should a more continuous and sustained star formation at $2.5 \lesssim z \lesssim 1$ occur, a higher quantity of metals is produced and provided to the ISM, so that stars born after $z \sim 1$ would be much metal richer than they actually are.

However, I would like to emphasise two relevant aspects that cannot be neglected and that could alleviate the tension between our predictions and observations. These are the uncertainties that affect metallicity determinations in observations and the peculiarity of Cepheids.

First, abundance estimate reliability is a delicate topic, as different sources of error enter final determinations (see e.g. Luck & Lambert, 2011). The quoted typical uncertainties for values of $[Fe/H]$ in Cepheids catalogues considered in Figure 7.10 are 0.1 dex (Romaniello et al., 2008) or 0.2 dex (Yong et al., 2006). Also, Luck & Lambert (2011) found a discrepancy of 0.07 dex between the $[Fe/H]$ derived from their sample and that computed for common objects in previous works by Luck et al. (2006, 2011). In these works they used equivalent analysis techniques, eventually tracing back to the changed surface gravity of stars the most plausible reason of the mismatch (see the discussion in Section 4.1.1 of Luck & Lambert, 2011, for further details). The discrepancy was even larger (~ 0.17 dex) when $[O/H]$ is taken into account. Besides, variability of Cepheids can enter final estimates, that can suffer an uncertainty as high as ~ 0.1 dex due to the observed phase (Luck & Lambert, 2011).

Also, different procedures adopted for metallicity calibrations yield remarkably different results. For instance, Kewley & Ellison (2008) quantified that different

techniques aimed at determining abundances from metallicity-sensitive emission line ratios affect the normalization of profiles by up to 0.7 dex. This, along with parameters in the sub-resolution physics that enter the modeling of the chemical enrichment process in simulations, usually lead different authors not to consider at all the normalization of the metallicity profiles or of the mass-metallicity relation. They rather focus on slopes only and, in case, on the evolution of the normalization of metallicity profiles (e.g. Torrey et al., 2017). Therefore, differences in the normalization of profiles by up to few tens of dex should not be considered as indicative of a serious disagreement between predictions from simulations and observations.

The second aspect concerns the possibility that Cepheids are stars with a metal content that is, on average, higher than what usually observed in nearby disc galaxies. This issue will be thoroughly addressed in Section 7.4.3.2.

7.4.3.2 Gas metallicity gradient

I continue the analysis by further investigating the metal content of gas in simulated galaxies. Figure 7.13 shows the gas metal content of simulated galaxies. I analyse oxygen abundance gradients, oxygen being one of the most accurate tracers of the total metallicity. I compare results from the set of simulations with the oxygen abundance radial profiles of the 130 disc galaxies that make up the observational sample of Pilyugin et al. (2014). The gas metal content of these late-type galaxies in the local Universe has been inferred from spectra of H II regions. Since I am not simulating our Galaxy, the comparison with properties of a set of disc galaxies is a key test.

All the simulated galaxies are characterised by negative gradients, in agreement with the majority of observed galaxies and with the scenario that outer regions of the galaxy discs are younger than inner ones (see also Section 7.4.2). Also, the slope of profiles of simulated galaxies is in keeping with the bulk of observations: this feature highlights the ability of our sub-resolution model to describe properly the local chemical enrichment process, as well as the circulation of metals driven by galactic outflows.

As for the amount of oxygen in the gas (i.e. the normalization of profiles), I find that the K2s IMF overproduces massive-star related metals. The oxygen profile of the galaxy K2s–yA–IaA–kA lies ~ 0.3 dex above the highest observed metallicity gradients, and the K2s–yB–IaB–kA model traces the upper edge of the observed metallicity range (see also below). On the other hand, we see that assuming the K3s IMF leads to a better agreement with observations by Pilyugin et al. (2014). The K3s IMF limits the number of massive stars, thus resulting in a lower amount of massive-star related metals produced and provided to the ISM.

The set B of stellar yields drifts towards a better agreement with observations (compare, for instance, K2s–yB–IaB–kA and K3s–yB–IaB–kB models with K2s–yA–IaA–kA and K3s–yA–IaB–kB ones, respectively), as a lower amount of oxygen

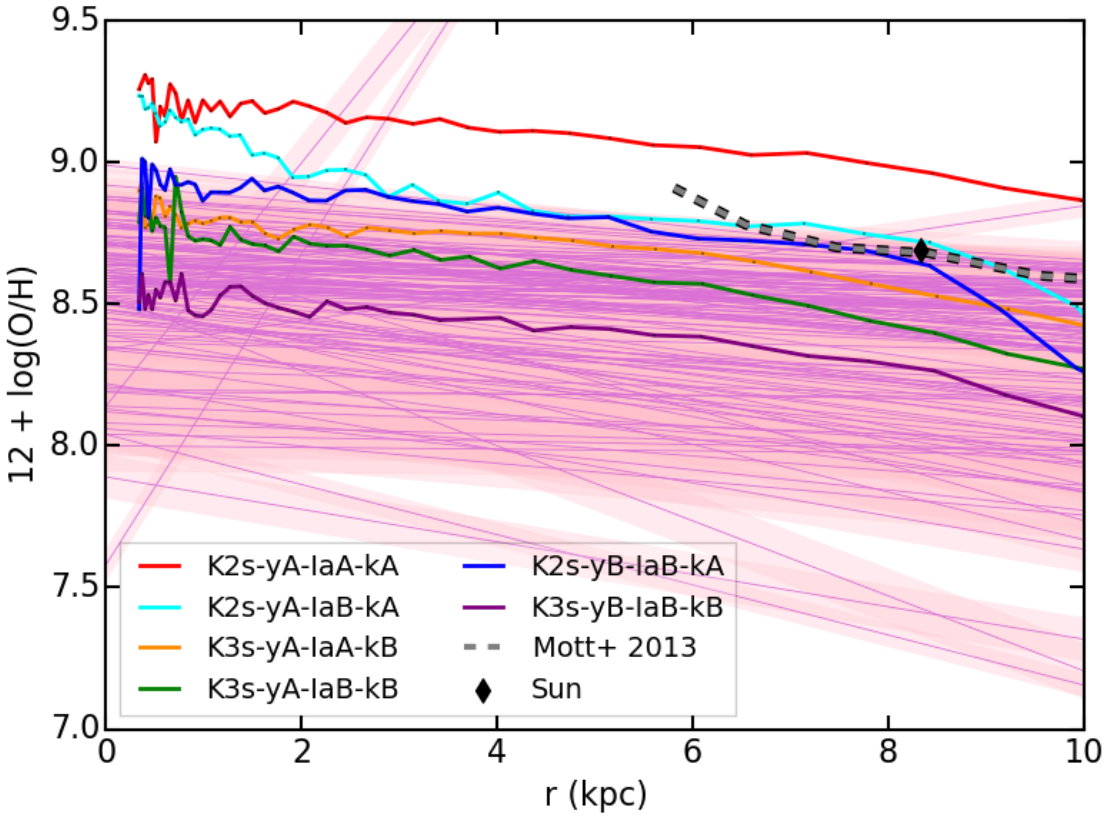

Figure 7.13: Oxygen abundance radial profile for gas in the simulated galaxies (colors as in the legend and previous figures). Pink profiles are observed metallicity gradients from the sample of 130 nearby late-type galaxies of Pilyugin et al. (2014). The shaded envelope around each profile depicts the scatter of oxygen abundance around the trend. I also show the metallicity gradient of MW (dashed curve) as deduced from observations of young stars in our Galaxy, and the position of the Sun on the plane (see the text for details).

is produced. This result is more striking when contrasting the green and purple galaxies, that experience similar star formation histories.

A robust result of this work is that a Kroupa et al. (1993) (K3s) IMF leads to a better agreement with metallicity profiles of late-type galaxies in the nearby Universe shown in Figure 7.13. The comparison with the sample of Pilyugin et al. (2014) suggests that an IMF more top-light than Kroupa (2001) (K2s) and Chabrier (2003) has to be preferred for local disc galaxies.

However, the scenario becomes puzzling and the interpretation of results more challenging when we consider metallicity determinations for MW along with measurements in the sample of Pilyugin et al. (2014). I overplot in Figure 7.13 the oxygen abundance gradient of Cepheids in MW by Mott et al. (2013, see the dashed grey line in Figure 7.11). Considering that the metal content of stars reflects directly that of gas out of which they formed, the metal content of young stars should be comparable to that of gas at redshift $z = 0$, or should fall slightly

below, at most. Also, I show where the Sun is located in Figure 7.13, considering $R_{\odot} = 8.33$ kpc as the distance of the Sun from the Galaxy centre (Gillessen et al., 2009; Bovy et al., 2009), and $\log_{10} \varepsilon_{\rm O} = 12 + \log_{10}\left(O/H\right)_{\odot} = 8.69$ (Asplund et al., 2009). We see that the metal content of young stars in MW (that is a lower limit for the gas metallicity) outlines the extreme upper edge of the region where observations by Pilyugin et al. (2014) locate.

This points out that either there are some issues with calibrations of metallicities in the considered observational samples, or Cepheids are stars with a metal content that is, on average, higher than what usually observed in nearby disc galaxies. If we deem the metallicity estimates of both samples as reliable, then we can conclude that the K2s IMF is more suitable for MW, while a K3s IMF should be preferred for other disc galaxies in the local Universe.

Also, it is striking that the Sun is characterised by an oxygen abundance comparable to that of Cepheids at the same distance from the Galaxy centre, although it is by far older than them (this possibly points towards a weak evolution of the solar neighbourhood during the last Gyrs). I envisage that the availability of more accurate observational determinations in the near future will alleviate the tension between discordant results and corroborate more robust conclusions. In Section 7.4.5, I further discuss how metals are retained and distributed in and around galaxies.

7.4.4 Stellar α-enhancement

I further analyse the metal content of the stellar component of our galaxies focussing on the stellar enhancement in α-elements with respect to the solar ratio. Figure 7.14 shows $[O/Fe]$ ratios as a function of $[Fe/H]$ for the set of simulated galaxies. Each row refers to a galaxy model. Panels of the left column represent the distribution of all the star particles in the volume we are analysing ($r < R_{\rm gal}$, see Section 7.4.1). Central and right columns show the distribution $[O/Fe]$ ratios versus $[Fe/H]$ for two subsamples of star particles, representative of stars located in the bulge and in the disc of galaxies, respectively.

I sliced the whole sample of star particles according to the kinematic diagnostic indicator $J_{\rm z}/J_{\rm circ}$ (see Section 7.4.1). I selected star particles with $-0.1 < J_{\rm z}/J_{\rm circ} < 0.1$ as belonging to the bulge, and star particles with $0.9 < J_{\rm z}/J_{\rm circ} < 1.1$ as located in the galaxy disc. Then, I also verified the position of selected particles, restricting the bulge subsample to star particles located at $r < 3$ kpc from the galaxy centre, and the disc subsample to star particles whose distance from the galaxy centre is $3 < r < 13$ kpc and whose galactic latitude is $|z| < 5$ kpc (as done in Figure 7.6, for instance). The number of star particles considered in second- and third-column panels of Figure 7.14 is not always the same, as galaxies have different stellar mass in the disc and the bulge (see Figure 7.5).

Particles selected according to these criteria sample specific components of the galaxy: their chemical features will be compared to observed stars that are

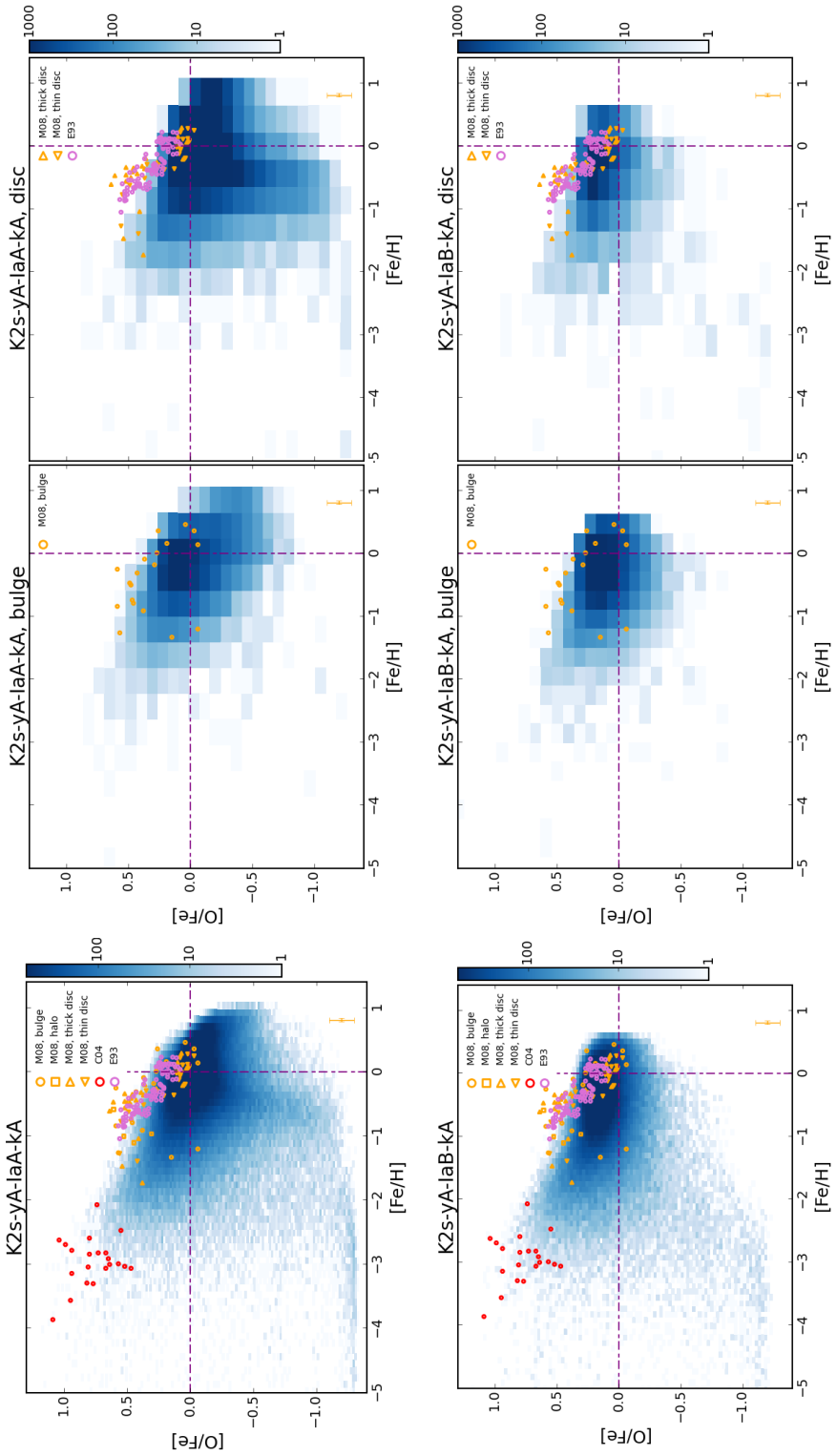

Figure 7.14: $[O/Fe]$ as a function of $[Fe/H]$ for star particles in our simulations, at $z = 0$. Each row corresponds to a galaxy model. We show the $[O/Fe]$ versus $[Fe/H]$ for all the star particles within $R_{\rm gal}$ (left-hand column), for star particles belonging to the bulge (centre), and for star particles in the disc (right-hand column). Each color bar encodes the number of star particles per pixel. We contrast our results with observations of Meléndez et al. (2008, M08), of Cayrel et al. (2004, C04), and of disc stars by Edvardsson et al. (1993, E93). Dash-dotted violet lines highlight solar values. A representative error bar for Meléndez et al. (2008, M08) data is shown.

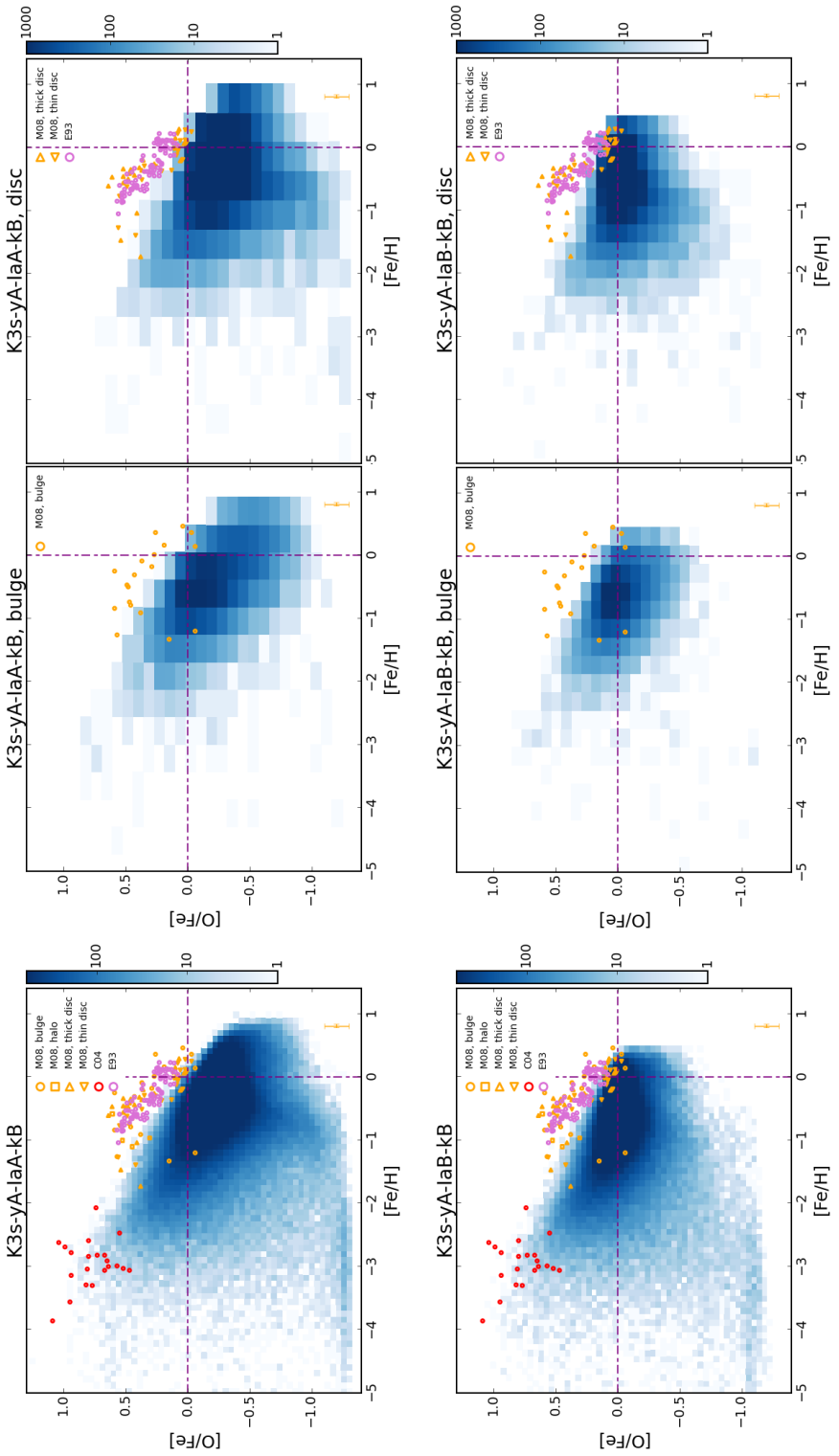

Figure 7.14: continued

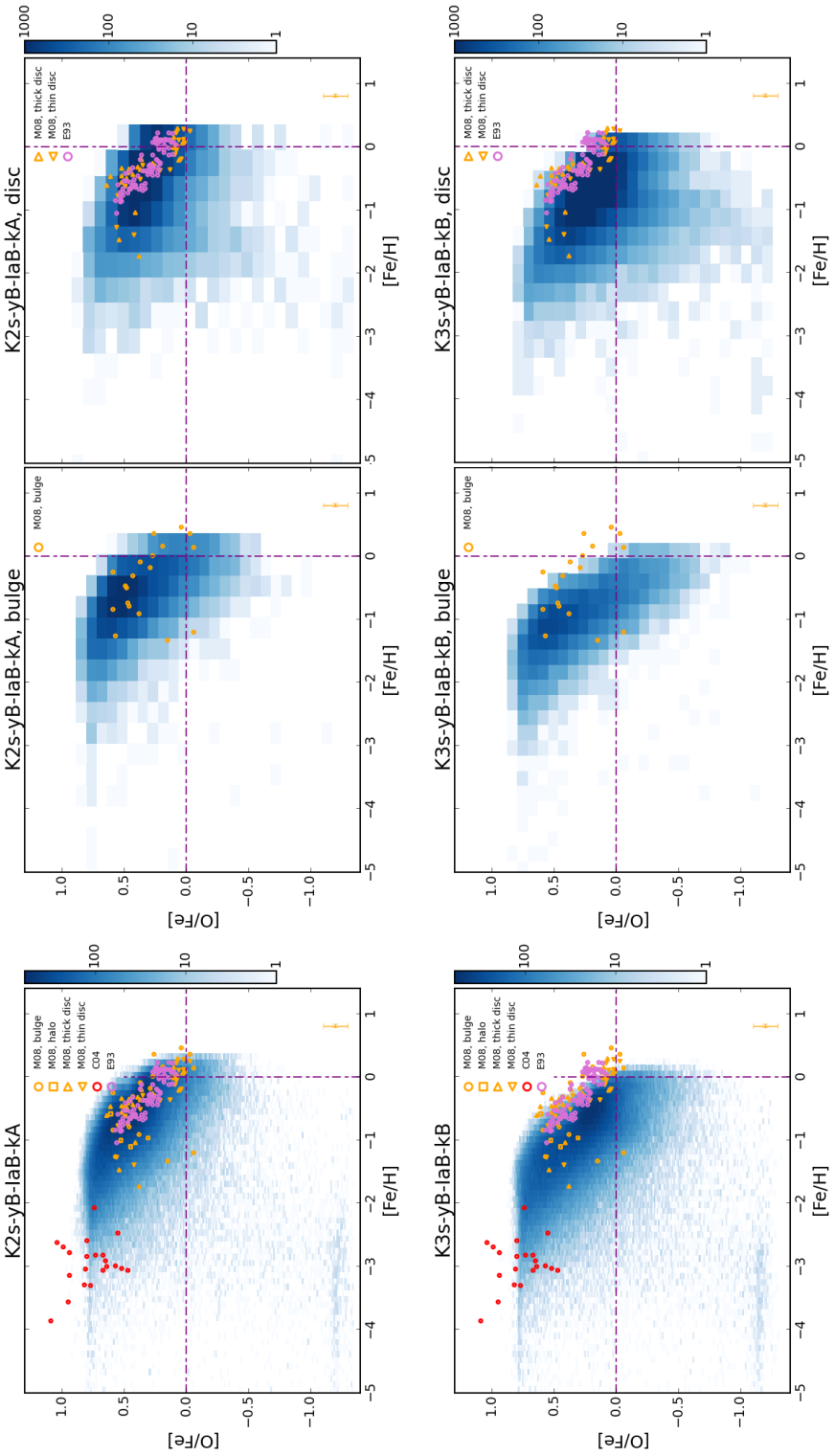

Figure 7.14: continued

located in the bulge or the disc of MW and that are characterised by peculiar evolutionary patterns.

Predictions from simulated galaxies are compared with the following observational data set: *i)*- Meléndez et al. (2008): they observed bulge, halo, thin and thick[2] disc giant stars; the quoted uncertainties of their data are 0.03 dex in Fe and 0.1 dex in $[O/Fe]$. *ii)*- Cayrel et al. (2004): they investigated very metal-poor halo giant stars, and state that the error in their abundance estimates can be as large as ~ 0.2 dex. *iii)*- Edvardsson et al. (1993): they observed dwarf stars in the disc of MW; quoted errors are 0.1 dex for abundances relative to hydrogen, and uncertainties comparable or even smaller for abundances relative to iron. In second- and third-column panels, I only consider observations for stars in the bulge or disc, respectively.

When different from ours, solar reference abundances adopted in the observational samples have been properly rescaled and homogenised.

The background two-dimensional histograms in Figure 7.14 consider the distribution of star particles in the plane $[O/Fe]$ versus $[Fe/H]$. I compare results from simulations to observations of single stars under the assumption that the metal content of a star particle in simulations statistically reproduces the mean metallicity of the SSP that the star particle samples. I will introduce another possible method in Chapter 8 (see also Grand et al., 2018a).

General trends that we observe by investigating results shown in Figure 7.14 and comparing galaxy models are the following. Adopting the K3s IMF leads to an overall reduction of oxygen that is in contrast with observations of stars in MW. This is strikingly evident when contrasting results from K2s–yA–IaA–kA (first row) and from K3s–yA–IaA–kB (third row). Decreasing the number of systems suitable for hosting SNe Ia does not shift the bulk of star particles towards values of $[O/Fe]$ high enough to alleviate the tension.

As for the fraction of binary systems originating SNe Ia, the comparison with observations in Figure 7.14 definitively rules out the value 0.1, as it produces an excess of stars with low $[O/Fe]$ and super-solar $[Fe/H]$ that is not in keeping with observations.

A result that emerges from this analysis is that stellar yields control the cooling process and are therefore a key driver of star formation, especially at high redshift. As a consequence, changing the adopted yields results in peculiar chemical evolutionary patterns. Two main features appear when the set B of stellar yields is adopted, regardless of the considered IMF: *(i)* a lower amount of iron is produced (see Section 7.4.6), and *(ii)* the galaxy bulge is more α-enhanced and forms over shorter timescales. By comparing second and fifth rows in Figure 7.14, we see that the bulk of stellar mass in the bulge of K2s–yB–IaB–kA (blue model) forms at earlier epochs (i.e. lower $[Fe/H]$) than K2s–yA–IaB–kA (cyan model), as also highlighted in the first panel of Figure 7.8. Also, it has been highly enriched by the chemical feedback

[2]Given the resolution of our simulations, we do not attempt to resolve the structure of the simulated galaxy disc by distinguishing between thick and thin disc.

from massive stars (see below). A similar picture holds when K3s–yA–IaB–kB and K3s–yB–IaB–kB are considered, too.

The set B of stellar yields allows to obtain the best agreement with observations, especially when the K2s IMF is assumed (fifth row of Figure 7.14). Results for the galaxy model K2s–yB–IaB–kA are in remarkable agreement with data: I find that stars in the bulge have $[O/Fe]$ that span from typical values of halo stars ($[O/Fe] \sim 0.4 \div 0.6$) to slightly sub-solar values as the iron abundance approaches $[Fe/H] = 0$. This trend is in keeping with findings by Zoccali et al. (2006); Meléndez et al. (2008). Also, the location of the break at $[Fe/H] \sim -1 \div -0.5$ is in agreement with observations. Bulge stars that shape this break highlight that the formation of the bulge occurred over a time longer than ~ 1 Gyr, so that SN Ia contributed with iron to the enrichment of the ISM. This feature is remarkably evident when the set B of stellar yields is adopted, while the transition to the regime where SN Ia contribute to the enrichment is smoother for the set A. The bulk of stars in the disc with $[Fe/H] \gtrsim -0.5$ are characterised, on average, by a lower α-enhancement with respect to stars in the bulge. This is in agreement with the scenario according to which the formation of the disc in late-type galaxies occurs over longer timescales than the bulge component, that is conversely mainly affected by early feedback from massive stars (see e.g. Lecureur et al., 2007). However, observed stars belonging to the bulge or to the disc of MW do not occupy distinct regions in the $[O/Fe]$-$[Fe/H]$ plane, they rather overlap for almost all the considered values of $[Fe/H]$ (see e.g. Meléndez et al., 2008). Adopting the set B of stellar yields also reduces the number of star particles characterised by sub-solar values of both $[O/Fe]$ and $[Fe/H]$, that do not have an observational counterpart. The lack of an observational counterpart may be ascribed to the fact that these stars are rather rare. These results can be considered predictions from my simulations.

Interestingly, Few et al. (2014) explored the impact of the adopted IMF and binary fraction on the chemical evolution of a field environment disc galaxy having a virial mass approximately half of that of my galaxies. They found that the slope of the $[O/Fe]$-$[Fe/H]$ relation for stars characterised by $[Fe/H] \gtrsim -1$ is regulated by the value of the binary fraction, and that the more top-heavy Kroupa (2001) IMF produces $[O/Fe]$ larger by ~ 0.2 dex with respect to the Kroupa et al. (1993) IMF, in keeping with my results.

Figure 7.15 further investigates the stellar α-enhancement focussing on the $[Mg/Fe]$ ratios as a function of $[Fe/H]$, for three galaxies selected out of the set. I contrast our results with observations of the AMBRE project (de Laverny et al., 2013; Mikolaitis et al., 2017), and of disc stars by Edvardsson et al. (1993). Trends observed and discussed for the stellar $[O/Fe]$ versus $[Fe/H]$ relation in Figure 7.14 are confirmed. Once again, I find a remarkable agreement with observations for the galaxy model K2s–yB–IaB–kA.

Results in this Section show a better agreement with observations of stars in our Galaxy when the K2s IMF is assumed. On the other hand, the comparison of gas metallicity profiles with observations of a sample of disc galaxies in the local

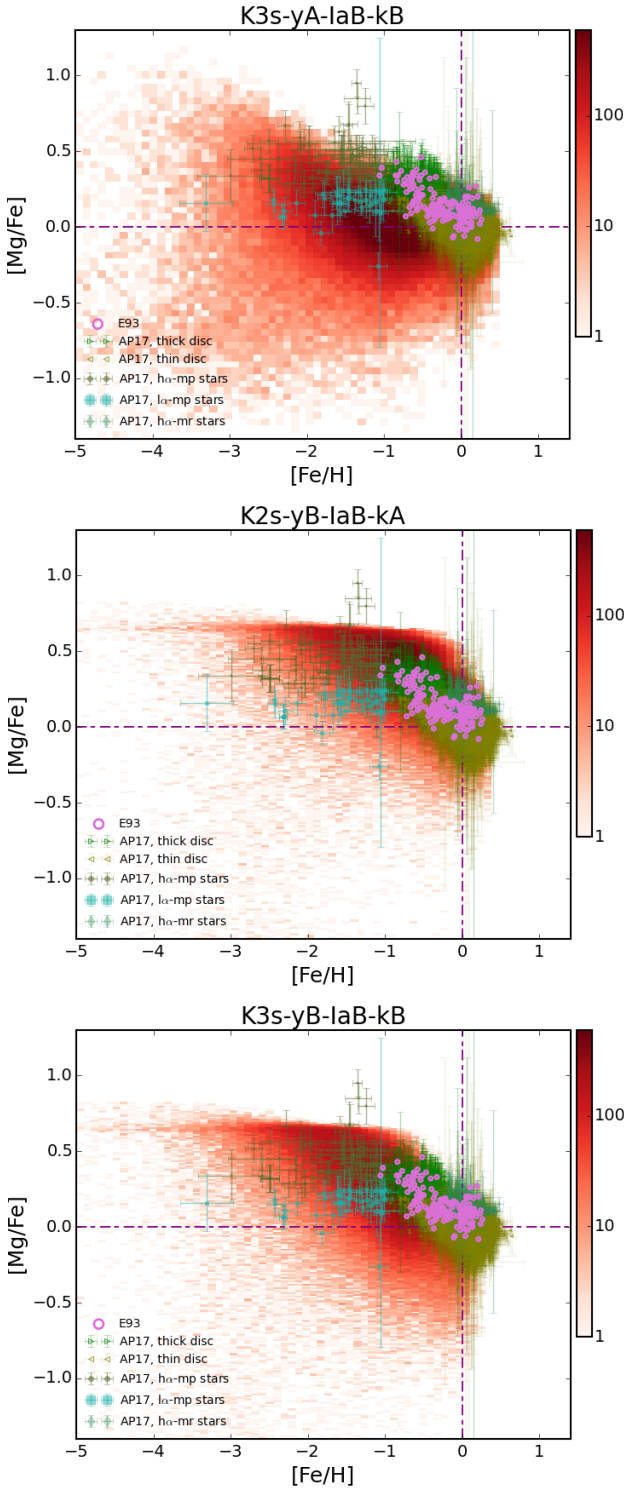

Figure 7.15: $[Mg/Fe]$ as a function of $[Fe/H]$ for star particles in three simulations, at $z = 0$. Each panel corresponds to a galaxy model (green, blue and purple from top to bottom). We show the $[Mg/Fe]$ versus $[Fe/H]$ for all the star particles within $R_{\rm gal}$. Each color bar encodes the number of star particles per pixel. Results are compared with observations of the AMBRE project (Mikolaitis et al., 2017, AP17), and of disc stars by Edvardsson et al. (1993, E93). Dash-dotted violet lines highlight solar values. Data from the AMBRE project are split into thick and thin disc stars, high- and low-α metal-poor population, and high-α metal-rich population. They are provided with error bars.

Table 7.3: Relevant quantities of the simulated galaxies. *Column 1:* simulation label. *Column 2:* virial radius. Note that the galactic radius $R_{\rm gal} = 0.1\,R_{\rm vir}$. *Column 3:* ratio between gas mass and gas plus stellar mass within $R_{\rm vir}$. *Column 4:* mass of metals in gas over gas plus stellar mass within $R_{\rm vir}$. *Column 5:* mass of metals in stars over gas plus stellar mass within $R_{\rm vir}$. *Column 6:* ratio between gas mass and gas plus stellar mass within $R_{\rm gal}$. *Column 7:* mass of metals in gas over gas plus stellar mass within $R_{\rm gal}$. *Column 8:* mass of metals in stars over gas plus stellar mass within $R_{\rm gal}$.

Name	$R_{\rm vir}$ (kpc)	$\frac{M_{\rm gas}}{M_{\rm gas+*}}$	$\frac{M_{\rm Z,gas}}{M_{\rm gas+*}}$ (10^{-3})	$\frac{M_{\rm Z,*}}{M_{\rm gas+*}}$ (10^{-3})	$\frac{M_{\rm gas}}{M_{\rm gas+*}}$	$\frac{M_{\rm Z,gas}}{M_{\rm gas+*}}$ (10^{-3})	$\frac{M_{\rm Z,*}}{M_{\rm gas+*}}$ (10^{-3})
		within $R_{\rm vir}$			within $R_{\rm gal}$		
K2s–yA–IaA–kA	238.7	0.77	2.8	5.6	0.37	7.6	17
K2s–yA–IaB–kA	236.8	0.84	1.4	2.6	0.39	4.9	11
K3s–yA–IaA–kB	241.5	0.81	1.5	1.9	0.42	3.9	6.0
K3s–yA–IaB–kB	240.3	0.85	0.83	0.99	0.47	2.7	3.9
K2s–yB–IaB–kA	236.9	0.84	1.1	1.9	0.33	3.7	8.9
K3s–yB–IaB–kB	239.6	0.87	0.58	0.69	0.47	2.0	3.2

Universe (Section 7.4.3.2) strongly supports the K3s IMF. Therefore, in agreement with previous findings in Section 7.4.3.1, I predict that MW stars exhibit a higher metal content with respect to other nearby late-type galaxies. Interestingly, stars of MW are found to be more α-enhanced than stars in nearby dwarf galaxies, and not representative of stellar populations in dwarfs (Venn et al., 2004, and references therein), even if different formation scenarios can enter this result.

I stress once again that our goal is not to reproduce observations of the MW and that I simulate a disc galaxy that should not be considered as a model for the MW. I am rather interested in investigating whether an accurate and controlled model of chemical evolution as the one we adopt in our simulations is able to yield chemical evolutionary patterns that are associated to specific components and timescales by observations.

7.4.5 Metals in and around galaxies

In this Section, I focus on the spatial distribution of metals in and around galaxies as the result of chemical feedback from outflows. Comparing predictions from our simulations with observations of the CGM is beyond the scope of this Chapter, as this kind of analysis would require an accurate modelling of the ionization state of the gas. Here I want to show that the high galactic metal content reached when the K2s IMF is assumed (see Figure 7.13) is not due to the ineffectiveness of galactic outflows in removing metals from sites of star formation, within the innermost regions of galaxies. To pursue that, I analyse how the mass budget of metals is distributed at increasing distance from the galaxy centre.

Figure 7.16 shows the cumulative distribution of metals in gas and stars of simulated galaxies as a function of the distance from the galaxy centre. I consider

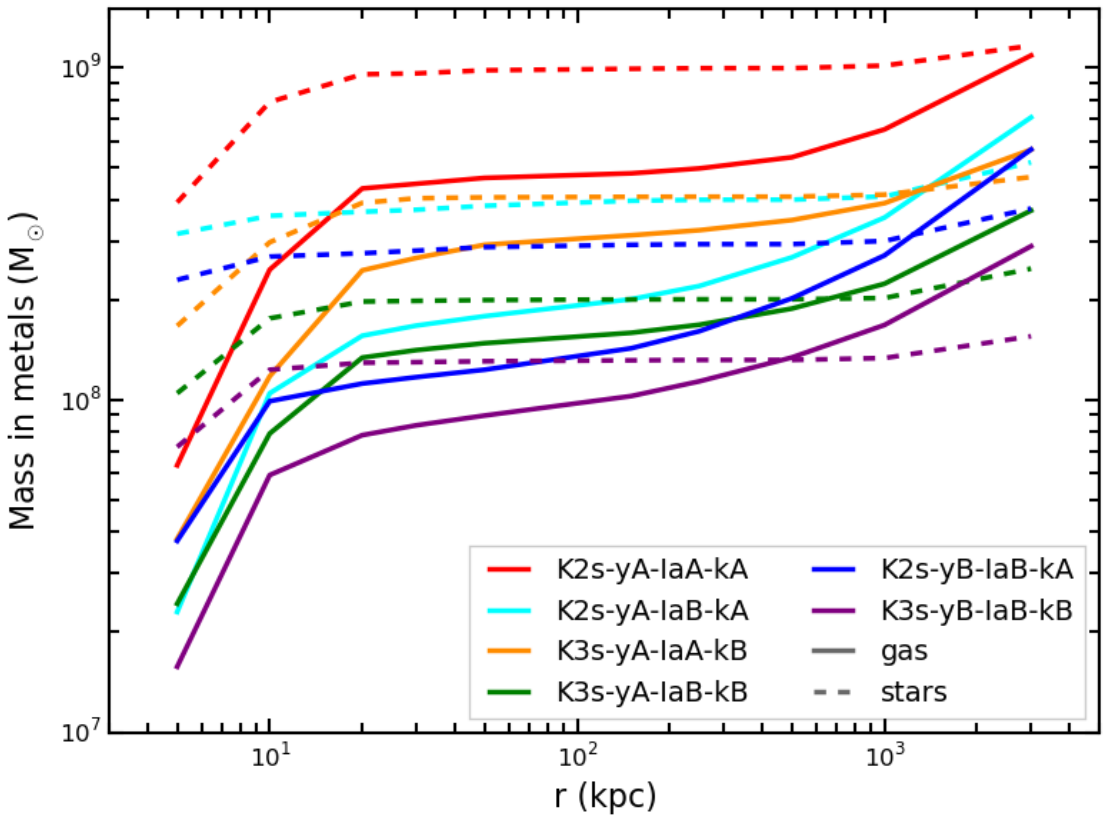

Figure 7.16: Cumulative radial distribution of metals in gas (solid lines) and stars (dashed lines) in simulated galaxies.

3 Mpc as the outermost distance within which compute the mass of metals as this is the radius of the largest sphere that can be contained in the volume with high resolution particles (see Section 5.5).

Metals have been produced by stars in the main galaxy sitting at the centre of the simulated halo and by stars in satellites and few small field galaxies. The latter stars are responsible for the mild increase of the mass of metals in stars at distances larger than the galactic radius ($R_{\rm gal} \simeq 24$ kpc) of the main galaxies. Radial profiles of mass of metals in stars in Figure 7.16 smoothly increase up to reach the stellar extent of galaxies, and then marginally rise when other stars not associated to the main galaxies are met in the volume.

Radial distribution of metals in gas show how galactic outflows are effective in driving metals outwards from star-forming regions in galaxies and in promoting the metal enrichment of the ISM and CGM. The mass of metals in gas rapidly increases in the ISM of the galaxy up to distances $r \simeq 20$ kpc; from there outwards the mass of metals in gas increases by up to a factor $\sim 2 \div 3$. Outside $R_{\rm gal}$ metals are retained by the diffuse CGM. I find that the mass of metals in gas within a distance of 20 kpc from the galaxy centre is $18 \pm 4\%$ of the total amount of metals produced (within 3 Mpc[3]) and $31 \pm 9\%$ of the metals produced which belong to the

[3]We are therefore quoting upper limits.

gaseous phase. Metals in gas and stars within 20 kpc account for at least $\sim 40\%$ of the metals produced within 3 Mpc. The mass of metals in gas and stars within 150 kpc from the galaxy centre constitutes $57 \pm 9\%$ of the metals produced. This result is in remarkable agreement with Peeples et al. (2014), which investigated a sample of nearby star-forming galaxies with stellar mass in the range $10^9 - 10^{11.5}$ $M_\odot$ and found that galaxies retain $\sim 50\%$ of produced metals in their ISM/CGM and stars out to 150 kpc, with no significant dependence on the galaxy mass (see also Section 7.1). Our results are also in keeping with the predictions of Calura & Matteucci (2004), who found that $\sim 50\%$ of metals are locked up in stars, while an additional $\sim 10\%$ is in the ISM of their galaxy population.

By analysing the mass distribution of metals in gas and stars of our galaxies, I find the following results. The mass of metals locked in stars within 10 kpc from the galaxy centre is at least twice as high as that in gas (mass ratios range between 2.22 and 3.42). The mean star-over-gas metal mass ratio 20 kpc far from the galaxy centre is 1.96 ± 0.40, while at 50 kpc it is 1.80 ± 0.41. A minimum distance of ~ 500 kpc (i.e. beyond the galaxy virial radius) has to be reached in order to have a comparable mass of metals retained by stars in the galaxy and present in the ISM and CGM of the galaxy. Table 7.3 summarises relevant quantities of the simulated galaxies.

Also, the radial distribution of metals in gas shown in Figure 7.16 sheds further light on the metal content of gas within the galaxies shown in Figure 7.13. Galaxy models assuming the K2s IMF are characterised by an oxygen abundance of gas that is higher than commonly observed in disc galaxies in the local Universe. This feature cannot be ascribed to the inability of galactic outflows to drive metals outward from sites of star formation within the galaxy. Conversely, outflows in galaxies adopting the K2s IMF are as effective as those in models with the K3s IMF, but an overproduction of metals occurs when the K2s IMF is assumed (see Section 7.4.3.2). Thus, our prediction that a Kroupa et al. (1993) IMF has to be preferred when dealing with nearby late-type galaxies is further corroborated.

7.4.6 Stellar yields

In this Section, I quantify the impact of the adopted set of stellar yields. I analyse the mass of oxygen and iron that is produced by an SSP according to the two different yield tables, once an IMF is assumed. I consider the K3s IMF in this Section.

Figure 7.17 shows the normalised cumulative mass in oxygen (top panel) and iron (bottom panel) that is produced by an SSP as a function of the mass of stars in the SSP. I consider newly produced elements for three values of the SSP metallicity Z: $2 \cdot 10^{-5}$, $1.2 \cdot 10^{-3}$, and $2 \cdot 10^{-2}$. The mass range spans between the minimum mass of the K3s IMF, that is 0.1 $M_\odot$ and 40 $M_\odot$ (see Section 7.2.1). In each panel, solid curves identify the set A of stellar yields, dashed curves pinpoint the set B. As for the normalization, each curve is normalised to the maximum of the curve of that metallicity referred to the set A. In this way, it is possible to appreciate which set of yields predict a larger amount of the considered element, at a given abundance.

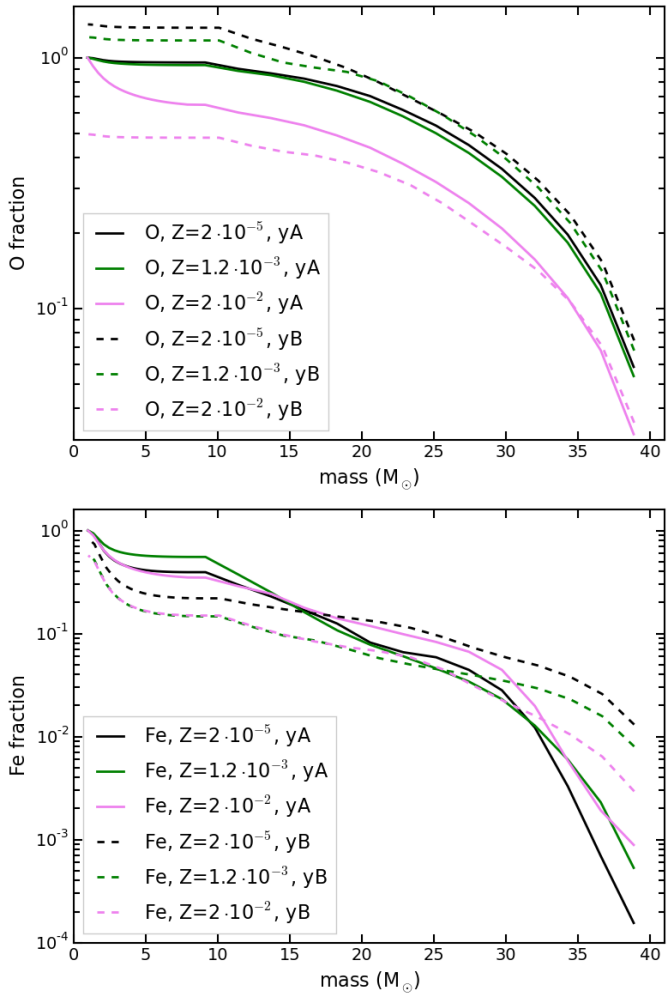

Figure 7.17: Cumulative mass in oxygen (top panel) and iron (bottom panel) that is (newly) produced by an SSP as a function of the mass of stars in the SSP. Solid and dashed curves refer to the sets A and B of stellar yields, respectively. Curve of each considered metallicity are normalised to the maximum of the curve of the set A. I consider the K3s IMF. I analyse three possible values for the metallicity Z: $2 \cdot 10^{-5}$ (black), $1.2 \cdot 10^{-3}$ (green), and $2 \cdot 10^{-2}$ (pink).

Considering a star of a given mass, these figures describe the cumulative mass of an element (oxygen or iron) that is produced by stars with mass equal or larger than the considered one. For instance, stars more massive than 15 $M_\odot$ and with a roughly solar metallicity $Z = 2 \cdot 10^{-2}$ have produced $\sim 55\%$ of the oxygen that has been synthesised, when the set A is considered.

The effect of changing yields on the metals produced by stars of different mass and initial metallicity is evident: different amounts of heavy elements are produced and this has significant consequences on the gas cooling and subsequent star formation. The lower the metal budget, the lower the cooling rate and the star formation rate, as discussed in Section 7.4.1. When the set B of stellar yields is adopted, a lower amount of iron is produced for all the considered metallicities.

The mass of synthesised oxygen is lower than in the set A for SSPs with solar abundance, and slightly higher for lower values of Z. However, note that the bulk of young stars are characterised, on average, by a roughly solar metallicity (see Figure 7.11): as a consequence, also a lower amount of oxygen is produced when the set B is adopted, at least at low redshift. Total masses of oxygen and iron produced by SSPs with increasing metallicity increase when the set A of yields is adopted. When considering the set B of stellar yields, the total mass of iron keeps almost unaltered as a function of the metallicity Z, while the cumulative mass of oxygen slightly decreases as the metallicity increases.

7.5 Discussion and Conclusions

In this Chapter, I carried out a set of cosmological hydrodynamical simulations of disc galaxies, with zoomed-in initial conditions leading to the formation of a halo of mass $M_{\rm halo,\,DM} \simeq 2 \cdot 10^{12}$ M$_\odot$ at redshift $z = 0$. These simulations have been designed to investigate the distribution of metals in galaxies and to quantify the effect of *(i)* the assumed IMF, *(ii)* the adopted stellar yields, and *(iii)* the impact of binary systems originating SNe Ia on the process of chemical enrichment. I considered either a Kroupa et al. (1993, K3s) or a Kroupa (2001, K2S) IMF, either a value 0.1 or 0.03 for the fraction of binary systems suitable to give rise to SNe Ia, and two sets of stellar yields.

The most relevant results of this study can be summarised as follows.

- I examined stellar ages and naturally predict that star formation in the disc always takes place later than in the bulge, and the disc formation proceeds inside-out (Section 7.4.2).
- I evaluated the evolution of SN rates in the set of simulated galaxies and compared them to observations of Mannucci et al. (2005). I found that SN II rates of our galaxies agree with observations from late-type Sbc/d galaxies. Also, SN Ia rates of simulations adopting 0.03 as the fraction of binary systems that host SNe Ia are in keeping with observations of Sbc/d galaxies (Section 7.4.2).
- I investigated stellar and gas metallicity gradients in simulations: negative radial abundance profiles are recovered, thus in agreement with observations. Slopes of profiles agree with observations, pointing to the effectiveness of our model to properly describe the chemical enrichment of the galaxy at different positions (Section 7.4.3).
- I compared gas metallicity profiles from our set of simulations with the oxygen abundance radial profiles of 130 nearby disc galaxies (Pilyugin et al., 2014). I found that a Kroupa et al. (1993) IMF leads to a lower amount of metals produced by massive stars and supplied to the ISM, resulting in a better agreement with observations. Therefore, we can argue that an IMF more top-light than Kroupa (2001) and Chabrier (2003) has to be preferred for local disc galaxies (Section 7.4.3.2).

- I investigated the stellar α-enhancement of star particles in our simulations, and considered also chemical patterns associated to disc and bulge, separately. The best agreement with observations of MW stars is retrieved when the Kroupa (2001) IMF is assumed (Sections 7.4.4).

- I quantified the effect of chemical feedback from outflows, investigating the mass of metals that is distributed at increasing distance from the galaxy centre. I verified that galactic outflows in our simulations are effective in driving metals out from the sites of star formation: if a high amount of metals in the ISM is present, this cannot be ascribed to the inability of outflows to move enriched gas outwards. I found that the mass of metals in gas within a distance of 20 kpc from the galaxy centre is $\sim 20\%$ of the metals produced, while about as many metals are associated to stars within the same distance. The mass of metals in gas and stars within 150 kpc from the galaxy centre increases to the $\sim 60\%$ of the synthesised metals. Therefore, an amount of metals as large as $\sim 40\%$ has been driven beyond 150 kpc by galactic outflows, that have promoted the circulation of metals in the CGM at high redshift, during the galaxy formation process (Section 7.4.5).

In the light of these results, I can draw the following conclusions on the different ingredients entering in the adopted model of stellar evolution.

- Assuming either a Kroupa et al. (1993) IMF or a Kroupa (2001) IMF results in different star formation histories, stellar feedback and scenarios of chemical evolution.

- If observational metallicity estimates are not affected by significant uncertainties, the Kroupa (2001) IMF is more suitable for our Galaxy, while a Kroupa et al. (1993) IMF (more top-light) should be preferred for other disc galaxies in the local Universe. I predict that MW stars exhibit a higher metal content with respect to other nearby late-type galaxies.

- The analysis performed supports a value for the fraction of binary systems suitable to give rise to SNe Ia of 0.03. This rules out the commonly adopted value 0.1, at least for late-type galaxies and when the IMFs that we are adopting are considered. Evidence that corroborate this finding come from the comparison of predicted SN rates and stellar α-enhancement with observations.

- Adopted stellar yields are a key component of the chemical model, as they control cooling and drive star formation. Different yields lead to different chemical features. The pattern of chemical enrichment for stars located in the galaxy bulge shows that the bulge component is the most sensitive to stellar yields.

As already pointed out, the availability of further accurate data from ongoing surveys could alleviate the tension between discrepant results and lead to firmer conclusions. As a concluding remark, I stress that an emerging piece of evidence of my work is that it is not trivial to simulate galaxies with a dominant disc component and an almost quiescent low-redshift star formation rate that simultaneously match all the available observational constraints on the pattern of metal enrichment of both the gas and stellar components. Also, results are far from being predictable when a single ingredient entering in the model for chemical evolution is varied, as its effect has a complex interplay with processes regulating the star formation history and shaping the morphology of simulated galaxies. These results highlight that it is challenging to reproduce at the same time observations of metal abundance in gas and stars. Observational uncertainties and issues with the calibration of metallicity estimates could definitely enter and complicate the comparison with simulation predictions. However, my analysis also highlights that the numerical modelling of the share of metals between stars and the surrounding gas is of paramount importance, and should be further investigated. To pursue that, higher resolution simulations are mandatory, as well as a proper treatement of the diffusion of metals associated to turbulent gas motions (see e.g. Pilkington et al., 2012; Williamson et al., 2016).

The detailed and accurate investigation of the chemical evolution of a single galaxy that I have presented in this Chapter is the starting point of a systematic analysis that I plan to accomplish in the near future. A natural and desirable extension of this study is indeed the simulation of cosmological boxes, where statistical properties of a population of galaxies can be examined.

As a word of caution, I note that the simulations presented in this Chapter do not include the effect of the AGN feedback. Albeit the AGN feedback is not expected to play a major role in the overall evolution of late-type galaxies nor to influence the history of chemical enrichment of the galaxy significantly, it can however play a supporting role in fostering outflows and promoting the circulation of metals over galactic scales. The investigation of the effect of the AGN feedback is postponed to Chapter 9.

8

Colour-magnitude diagram in simulations of galaxy formation

Star particles in simulations represent a simple stellar population (SSP), while observations provide us with estimates of properties of single stars. An accurate and fair comparison between predictions from simulations and observations is a crucial task. In this Chapter, I introduce a novel tool that allows to consistently generate a population of stars associated to a single star particle, which is characterised by a metallicity, age and IMF. This tool takes properties of star particles from simulations as input, along with their position and an IMF; a theoretical catalogue of mock stars whose characteristics are drawn from the input features is then generated, by using the TRILEGAL code, that is able to reproduce the photometric properties of mock stars. The ultimate goal of this tool is to generate (in post-processing) a database of synthetic stars from the properties of parent star particles in simulations: such a database can be deemed as the observable stellar content corresponding to observational data. It translates the populations of star particles of a simulation into stellar populations, providing masses, ages, metallicities and magnitudes of individual stars, thereby enabling a direct comparison with observations. The method is flexible, can be easily tailored to fit outputs of different codes used for cosmological simulations, and of paramount importance with ongoing survey data releases (e.g. GAIA and surveys of resolved stellar populations).

The key questions that I want to address in this Chapter are the following: is it possible to bridge the gap between the typical mass of stellar particles in simulations and that of observed single stars? In other words, would that be

achievable to develop a robust method that allows to compare simulation outcome with observations of explicitly resolved stars?

The outline of this Chapter is as follows. In Section 8.1, I introduce the context that triggered the development of the novel approach that I am going to present. In Section 8.2, I give an overview of the simulations used. I introduce the new methodology adopted in Section 8.3, while Section 8.4 provides the main features of the observational sample that I choose to compare results with. Results are presented in Section 8.5. I discuss the main findings in Section 8.6.

The results presented in this Chapter are described in the paper Valentini et al. (2018b).

Contents

8.1 The need for going from star particles to stars

Chemical evolution is one natural outcome of galaxy evolution in cosmological simulations, as outlined in Section 3.1. Models of chemical evolution have been included in cosmological hydrodynamical simulations of cosmic structure formation to properly address the study of the chemical enrichment process (see Chapter 7 and also Section 5.4). The distribution of metals in the ISM and in the CGM are indeed crucial features of hydrodynamical simulations (e.g. Oppenheimer et al., 2017; Torrey et al., 2017). Albeit less frequently investigated, the comparison with the observed stellar metallicity distribution poses a strong constraint for simulations of galaxy formation (see below), and the metal content of stars predicted by models is crucial to interpret a wide range of observations (see Chapter 7). Furthermore, a

great effort has been recently devoted to simulate the actual star counts in several regions and toward different directions within a galaxy, along with the possibility of mimicking photometric properties of stars (Girardi et al., 2005; Vanhollebeke et al., 2009). In this context, a consistent prediction of physical and photometric properties of stellar populations can put constraints on different evolutionary scenarios, and help in validating or ruling out viable theoretical models, when predictions are compared with observations.

Our Galaxy is a crucial laboratory where the validity of different models of stellar evolution and chemical enrichment in comparison with observations can be rigorously assessed. Observations especially in the solar neighbourhood and in the Milky Way (MW), but also in a limited number of nearby galaxies in the Local Universe provide us with large catalogues of stars, featuring accurate determinations of their chemical composition and stellar age, along with careful estimates of their physical and photometric properties (e.g. Strömgren, 1987; Edvardsson et al., 1993; Holmberg & Flynn, 2000; Battinelli et al., 2003; Nordström et al., 2004; Meléndez et al., 2008).

However comparing these data with simulations in a fully consistent way is a non trivial and delicate task. State-of-the-art cosmological hydrodynamical simulations of both large cosmological volumes and individual galaxies have star particles whose mass typically ranges between $\sim 10^8$ and $\sim 10^3$ $M_\odot$ according to resolution (Dubois et al., 2014; Vogelsberger et al., 2014a; Khandai et al., 2015; Rasia et al., 2015; Schaye et al., 2015; McCarthy et al., 2017; Remus et al., 2017; Pillepich et al., 2018; Oser et al., 2010; Aumer et al., 2013; Stinson et al., 2013; Marinacci et al., 2014; Murante et al., 2015; Dutton et al., 2015; Hopkins et al., 2018; Valentini et al., 2017). In these simulations star particles are resolution elements and are treated as SSPs, as discussed in Section 5.4.

When comparing simulation predictions for the stellar metal content with observational data, the commonly pursued approach consists in analysing the total metallicity or different ion abundances that characterise the stellar mass of a system (e.g. a galaxy or a galaxy group), or of a portion of it. Such a method relies on the hypothesis that the mean metallicity of a star particle in simulations statistically reproduces the mean metal content of the SSP that the star particle samples (as I assumed in Chapter 7). A straightforward comparison with observational data is indeed fair when investigating the stellar metal content as a single quantity per galaxy, as for instance for the metallicity of stars as a function of the stellar mass of galaxies (Schaye et al., 2015; Bahé et al., 2017; Dolag et al., 2017), and for the stellar α-enhancement as a function of galaxy stellar mass (Segers et al., 2016).

However, inconsistencies can arise when contrasting directly simulation output to observations of resolved stars. Surveys in the solar neighbourhood (e.g. the Geneva-Copenhagen Survey, Nordström et al., 2004; RAVE, Steinmetz et al., 2006; SEGUE-1 and SEGUE-2, Yanny et al., 2009, Rockosi et al., 2009; LEGUE, Deng et al., 2012; the GAIA-ESO survey, Gilmore et al., 2012; the AMBRE Project, de Laverny et al., 2013; APOGEE, Majewski et al., 2016; the SkyMapper Southern Survey, Wolf et al., 2018) and observations in Local Universe galaxies resolve indeed individual stars and provide us with accurate determinations of single star properties.

Going from star particles in simulations to observed stars is therefore crucial to accurately compare simulation predictions with data.

8.2 Cosmological simulations of a disc galaxy

To introduce the new tool, I first perform cosmological hydrodynamical simulations that provide an accurate model of a disc galaxy. Since careful observations are mostly available for our Galaxy, I conceived simulations of a galaxy that turns out to have similar properties to the MW ones. It is worth noting once again that, despite of the similarity between the simulated galaxies and our Galaxy from the morphological point of view, results should not be considered as a model of the MW. In fact, no specific attempts to reproduce the accretion history of its dynamical environment have been made.

8.2.1 Simulations

The simulations that I will use for further analysis in this Chapter have been already presented in Chapters 6 and 7, as detailed below. Here, I remind that they have been performed with the GADGET3 code (see Section 5.1), featuring the improved formulation of SPH introduced in Section 5.2. The ICs are the *AqC*5 ICs (higher-resolution) introduced in Section 5.5: the softening length for the gravitational force is $\varepsilon_{\rm Pl} = 325\,h^{-1}$ pc, DM particles have a mass of $1.6 \cdot 10^6\,h^{-1}$ $M_\odot$, the initial mass of gas particles is $3.0 \cdot 10^5\,h^{-1}$ $M_\odot$. These simulations resort to our sub-resolution model MUPPI, whose key features have been outlined in Section 5.3, and take advantage of our accurate model for the chemical enrichment process (see Section 5.4).

In this work I consider results of three simulations that I carried out: AqC5–fid (the reference simulation), AqC5–cone, and AqC5–3sIMF (see Table 8.1). These simulations have been introduced in Chapters 6 and 7: the simulation labelled AqC5–fid in this Chapter is the simulation AqC5–FB2 (Chapter 6); the simulation called here AqC5–cone is the run AqC5–newH (Chapter 6); the simulation labelled AqC5–3sIMF in this Chapter is the simulation K3s–yA–IaB–kB (Chapter 7, where it is identified by the green colour).

The major differences between the simulations are the following: AqC5–fid and AqC5–cone share the same IMF but have a different galactic outflow model (see below); AqC5–fid and AqC5–3sIMF have the same galactic outflow model but are characterised by a different IMF.

Both the simulations AqC5–fid and AqC5–cone adopt a Kroupa (2001) IMF that is defined by equation (7.2) and is characterised by two slopes (K2s, hereafter; this IMF is a variation of the Kroupa et al. 1993 IMF, see Figure 7.1). Note the use of the IMF exponent $\alpha = 2.3$ for massive stars, not corrected for unresolved stellar binaries (see Section 7.2.1).

The third simulation, AqC5–3sIMF, is a simulation that is similar to the reference AqC5–fid, but for the adopted IMF. In AqC5–3sIMF I adopt the Kroupa et al. (1993) IMF (see equation (7.3) and Figure 7.1), as suggested by Grisoni et al. (2017). This IMF is characterised by three slopes (K3s, hereafter) and is defined in the

Table 8.1: Relevant parameters of the sub-resolution model and features of the simulations. *Column 1:* simulation name. *Column 2:* adopted IMF. K2s is Kroupa IMF with two slopes, while K3s is Kroupa IMF with three slopes (see the text). *Column 3:* gas particle's probability of becoming a wind particle. *Column 4:* maximum lifetime of a wind particle (see Section 5.3). *Column 5:* kinetic SN feedback energy efficiency. *Column 6:* half-opening angle of the cone for thermal feedback, in degrees. As for the original version of the sub-resolution model, this is also the half-opening angle of the cone for kinetic feedback. *Column 7:* fraction of binary systems originating SN Ia. *Column 8:* corresponding simulation in Chapters 6 and 7.

Name	IMF	$P_{\rm kin}$	$t_{\rm wind}$ (Myr)	$f_{\rm fb,kin}$	θ (°)	$f_{\rm bin,Ia}$	Corresponding simulation
AqC5–fid	K2s	0.03	15 - $t_{\rm clock}$	0.12	30	0.1	AqC5–FB2 (Ch. 6)
AqC5–cone	K2s	0.05	20 - $t_{\rm clock}$	0.7	30	0.1	AqC5–newH (Ch. 6)
AqC5–3sIMF	K3s	0.03	15 - $t_{\rm clock}$	0.26	30	0.03	K3s–yA–IaB–kB (Ch. 7)

mass range $[0.1, 100]$ $M_\odot$. In this case, the slope $\alpha = 2.7$ for massive stars includes the correction for unresolved stellar binary systems (see Section 7.2.1).

As for the kinetic stellar feedback that is responsible for triggering galactic outflows, it is modelled as follows in the three simulations. ISM is isotropically provided with kinetic feedback energy in simulations AqC5–fid and AqC5–3sIMF. Therefore, each star-forming particle supplies kinetic feedback energy to all wind particles within the smoothing length, with kernel-weighted contributions (see Sections 6.3.2 and 7.2, where $f_{\rm fb,kin}$ describes the kinetic stellar feedback efficiency). Wind particles (see Section 5.3) receiving energy use it to boost their velocity along their least resistance path, since they are kicked against their own density gradient. In simulation AqC5–cone the kinetic feedback energy is provided to wind particles located within a cone (see Section 5.3), whose half-opening angle is θ (see Table 8.1), aligned towards the least resistance path of the energy donor particle. In this case particles are launched toward the direction opposite to the density gradient of the star-forming particle that provides them with feedback energy.

Besides those described in Table 8.1, all the relevant parameters of the sub-resolution model that I adopt for this set of simulations can be found in Tables 5.1 and 7.1.

In all the simulations I consider 8 $M_\odot$ as the minimum mass giving rise to stellar BHs, and that stars that are more massive than 40 $M_\odot$ implode in BHs directly and do not contribute to further chemical enrichment. As discussed in Section 7.2.1, I assume that a fraction of stars relative to the entire mass range is located in binary systems suitable for being progenitors of SNe Ia. Such a fraction is 0.03 in the simulation AqC5–3sIMF; this parameter was set to 0.1 in simulations AqC5–fid and AqC5–cone. Finally, all the simulations adopt the set A of stellar yields (details in Section 7.2.1).

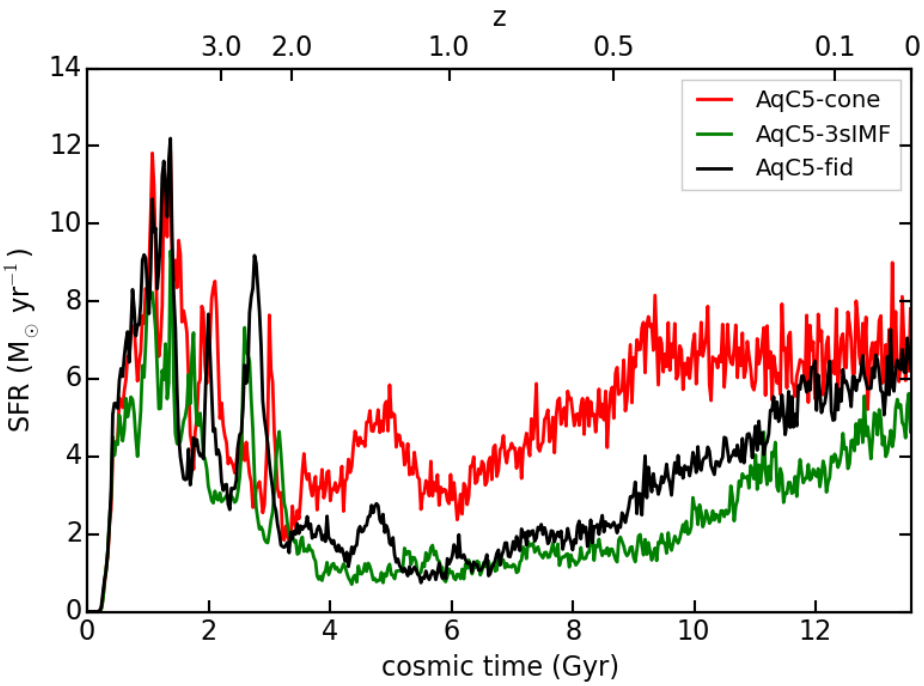

Figure 8.1: Star formation histories of the three simulated galaxies: our reference simulation in shown in black, red and green curves describe the evolution of the star formation rate (SFR) for AqC5–cone and AqC5–3sIMF, respectively.

8.2.2 Main features of the simulated galaxies

In this Section, I recall the main physical properties of the three simulated galaxies. Galaxies AqC5–fid and AqC5–cone have been extensively analysed in Chapter 6, and the properties of the galaxy AqC5–3sIMF have been studied in Chapter 7.

This work is aimed at presenting a novel approch that can be used regardless of the peculiar features of a simulated galaxy: as a consequence, providing a detailed comparison of all the characteristics of the three galaxies is beyond the scope of the present methodological Chapter. Here I only highlight some features of the galaxies, such as their star formation history, that are useful to understand and interpret the results that I will discuss in Section 8.5.2.

In Figure 8.1 I show the star formation history of the three galaxies. The bulk of the stellar mass in the bulge of each galaxy builds up at high-redshift ($z \gtrsim 3$), as a consequence of a star formation burst. Star formation in the disc occurs at later epochs, in a more continuous way. AqC5–fid and AqC5–3sIMF are characterised by a lower SFR below $z \lesssim 2$ with respect to AqC5–cone, as a consequence of the reduced amount of gas that has been accreted within the galactic radius[1]. The

[1]I define here the galactic radius as one tenth of the virial radius, i.e. $R_{\rm gal} = 0.1 R_{\rm vir}$, as in Chapters 6 and 7. I remind that I consider virial quantities as those computed in a sphere that is centred on the minimum of the gravitational potential of the halo and that encloses an overdensity of 200 times the *critical* density at present time.

low-redshift ($z \lesssim 1.5$) SFR of AqC5–3sIMF is $\lesssim 5$ $M_\odot$ yr^{-1}, in agreement with the estimate provided by Snaith et al. (2014) for our Galaxy.

Face-on and edge-on projected stellar density maps of star particles within the galactic radius of the three galaxies can be found in Figure 6.13 (middle panels) for AqC5–fid and in Figure 7.2 (fourth row, first and second columns) for AqC5–3sIMF. Figure 6.5 (second row) shows stellar density maps of the galaxy AqC5–cone.

In the following, I summarise some properties of the galaxy AqC5–3sIMF that have not been detailed explicitly in Chapter 7. The galaxy AqC5–3sIMF has a galactic radius $R_{\rm gal} = 24.0295$ kpc, at redshift $z = 0$. It has a limited bulge component and a dominant disc, where spiral arms are evident. Although defining the extent of the gaseous and stellar disc is a difficult task, I note that the stellar surface density declines outwards down to 15 $M_\odot$ pc^{-2} at a distance of ~ 11 kpc from the galaxy centre, whereas the gas surface density decreases to that same value when the radius is ~ 15 kpc. The galaxy is characterised by a rotation curve that is not centrally peaked and that is flat at large radii, the circular velocity at $r = 8$ kpc being $v_c \simeq 220$ km s^{-1}. Here, I list some of the global properties of the AqC5–3sIMF galaxy. The virial radius of the galaxy at redshift $z = 0$ is $R_{\rm vir} = 240.295$ kpc. DM, stellar and gas masses within $R_{\rm vir}$ are $1.532 \cdot 10^{12}$ $M_\odot$, $2.957 \cdot 10^{10}$ $M_\odot$, and $1.709 \cdot 10^{11}$ $M_\odot$, respectively. DM, stellar and gas masses within $R_{\rm gal}$ are $2.539 \cdot 10^{11}$ $M_\odot$, $2.679 \cdot 10^{10}$ $M_\odot$, and $2.342 \cdot 10^{10}$ $M_\odot$, respectively. A kinematic decomposition of the stellar mass within $R_{\rm gal}$ based on the circularity of stellar orbits (Scannapieco et al., 2009) yields $1.108 \cdot 10^{10}$ $M_\odot$ as the stellar mass in the bulge, $1.571 \cdot 10^{10}$ $M_\odot$ as the stellar mass rotationally supported and located in the disc, and a bulge-over-total stellar mass ratio $B/T = 0.41$.

Analogous properties of AqC5–fid and AqC5–cone can be found in Chapter 6.

8.3 Building the stellar content of star particles: method

In this Section I accurately detail all the steps that make up the methodology developed in this work. I use this identifying convention here and in the following: star particles in the simulation are referred to as *parent particles*, while mock stars that are generated by each parent particle are *child particles* or, simply, *stars*.

Our methods aims at generating the observational properties of the mock stars in a volume of a simulated galaxy. To achieve that, I produce for each parent particle of given mass, age, and metallicity a stellar population of that age and metallicity, and with the same total initial mass. For this purpose, I first select parent particles that meet specific criteria within the simulation output (Section 8.3.1). These parent particles define an age-metallicity distribution that is exploited to generate a catalogue of synthetic stars (Sections 8.3.2 and 8.3.3). These stars are then displaced to a suitable distance and among them I extract the final catalogue of mock stars (Section 8.3.4) that will be compared with observations in Section 8.5.

Throughout this Chapter, I refer to metallicity as overall metal content $[Z/H]$. Here, $[Z/H] = \log_{10}(Z/H) - \log_{10}(Z/H)_\odot$ is the logarithm of the ratio of the abundance by mass of all elements heavier than helium (He or Y) over hydrogen (H or X), compared to that of the Sun. As for the present-day Sun's metallicity, we adopt $Z_\odot = 0.01524(\pm 0.0015)$ (Caffau et al., 2011) and $Y_\odot = 0.2485(\pm 0.0035)$ (Basu & Antia, 2004), so that $(Z/X)_\odot = 0.0207(\pm 0.0015)$ and $\log_{10}(Z/H)_\odot = -1.684$ (Bressan et al., 2012).

8.3.1 Parent particle selection

I start by considering the output of our cosmological hydrodynamical simulation AqC5–fid described in Section 8.2.1. I analyse the distribution of star particles at redshift $z = 0$, i.e. the distribution that produces the smoothed stellar density maps analysed in Figure 6.13 (middle panels). As a first step of our post-processing analysis (and as done for the stellar density maps shown in Figure 6.13), we rotate the galaxy reference system so as the z-axis is aligned with the angular momentum of star particles and multiphase gas particles located within 8 kpc from the minimum of the gravitational potential. The axes of the galaxy frame are therefore defined by the eigenvectors of the angular momentum tensor. The origin of the reference system is taken to be the centre of the galaxy, that is determined as the centre of mass of star particles and multiphase gas particles within 8 kpc from the location of the minimum of the gravitational potential.

I then select the parent particles for our analysis. Since the purpose of the present study is to introduce a tool that allows the comparison between the properties of stars predicted by simulations and observed stars, I identify a volume resembling the solar neighbourhood in our simulation snapshot. Star particles located within this volume (the so called *selected region*) will be considered for the construction of the parent particle sample.

The selected region in the simulated galaxy is a sphere centred on the galactic plane at a distance $r_{\rm Sun} = 8.33$ kpc from the galaxy centre. Such a distance can be deemed as the distance of the Sun from the Galactic Centre of our Galaxy, according to state-of-the-art determinations (Gillessen et al., 2009; Bovy et al., 2009). I locate the centre of the sphere on the plane where the z coordinate is $z = 0$. I verified that the angular distance from the x-axis, $\vartheta_{\rm Sun}$, does not affect final results (see Section 8.6.1).

To estimate the size of the sphere, I determine its radius as follows. The actual resolution of our simulation amounts to 2.8 times the formal resolution described by the gravitational softening (Springel et al., 2001, see Section 5.1), and hence slightly exceeds 1 kpc ($\varepsilon_{\rm Pl} = 325\,h^{-1}$ pc, see Section 8.2.1). Since we cannot rely on the sampling of the statistical properties of particles in smaller volumes, that represent our smaller possible solar neighbourhood (star particles keep their own properties, that have been set where and when they were originated). To illustrate how this size compares with the observational requirements, I compute the distance modulus

$d_{[\mathrm{pc}]}$ of the brightest stars that can be seen within an apparent-magnitude limited survey. The associated distance defines a tentative size for the solar neighbourhood. If I consider the Geneva-Copenhagen Survey (see Section 8.4), with an apparent-magnitude limit in the Johnson V passband $m_V \sim 8.3$ and an absolute magnitude $M_V \sim 1$ (from figure 12 of Casagrande et al., 2011), I end up with an estimate of a characteristic radius of the survey that is $d = 288$ pc[2].

Selecting a sphere of radius 1 kpc, I maximise the sampling of the statistical quantities that determine our results, while using a proper volume accordingly with my simulations' properties.

The parent particles selected for our analysis are all the star particles residing within the aforementioned volume of the simulated galaxy that can be compared to the solar neighbourhood. The typical number of star particles located in this volume is $\sim$ 1000. For instance, in the reference selected sphere of AqC5–fid centred at $r_{\mathrm{Sun}} = 8.33$ kpc and $\vartheta_{\mathrm{Sun}} = 60°$ we have 891 parent particles. When considering the different volumes analysed in Section 8.6.1 for AqC5–fid, I find a mean value (and standard deviation) of 1018($\pm$186) parent particles. The number of star particles depends on the stellar mass of the simulated galaxy, and marginally varies with the position on the galactic plane.

Each stellar particle is treated as a parent particle characterised by the following properties:

- the initial mass, that is the mass that the star particle had when it was generated;
- the current mass, i.e. the mass of the parent particle when the analysis is performed (that is at redshift $z = 0$, in our case)[3];
- the age;
- the distance from the centre of the selected region;
- the initial mass fraction of metals.

Note that the fraction of mass in metals represents the metallicity (i.e. Z linear and absolute, meaning that it is not scaled according to the solar metallicity $Z_{\odot}$) of the parent particles, that is the metallicity that star particles had when they were originated. Along with this quantity, I also compute $[Z/H]$ for each parent particle: this is the way to express the metallicity that can be most easily related to data[4].

[2]Note that if I adopted $m_V \sim 7.6$, that is the apparent magnitude of the Geneva-Copenhagen Survey where incompleteness sets (see Section 8.4), I would end up with a distance modulus $d = 209$ pc. However, the procedure is not sensitive to the exact values assumed for m_V and M_V.

[3]I remind that our star particles lose mass as they evolve as SSPs, see Section 5.4.

[4]I remind the reader that we know the mass in hydrogen, helium and other elements for each parent particle in our simulation.

8.3.2 Generation of synthetic stars: the TRILEGAL Code

The second building block that makes up the tool that I have developed consists in using the TRILEGAL code to produce a catalogue of mock stars.

The TRILEGAL code (TRIdimensional modeL of thE GALaxy, Girardi et al., 2005) is a population-synthesis code. It produces mock stellar catalogues for a parent object (i.e. for each star particle, in our case) with given characteristics and simulates the corresponding photometric properties of the generated stars. The key goals of the TRILEGAL code are indeed to predict the expected star counts in different photometric systems and to mimic the photometric properties of stars located towards a given direction. Interesting examples of how this tool can be used to investigate the characteristics of stars in the bulge of MW as well as in external galaxies can be found in Vanhollebeke et al. (2009) and Girardi & Marigo (2007), respectively. Here we detail the most relevant features of the TRILEGAL code for the current study. For further technical information, we refer the reader to the aforementioned papers.

The TRILEGAL code assembles collections of stars by assuming an IMF and defines their photometric properties by using a library of stellar evolutionary tracks. First, it performs a Monte Carlo simulation to produce stars according to input features, that are the age-metallicity distribution (AMD) and the star formation rate (SFR). The IMF, SFR and AMD determine mass, age and metallicity of each single synthetic star. The code then carries out an interpolation within grids of theoretical evolutionary models, i.e. within isochrone sets, so as to generate the absolute photometry and provide the absolute bolometric magnitude of mock stars. This latter value is hence converted to absolute magnitudes in different passbands by taking advantage of tables of bolometric corrections, that have been constructed from a library of syntethic spectra. The photometric system according to which magnitudes in different passbands are computed can be defined as an input requirement.

A further input specification in the TRILEGAL code deals with the geometry of the system where mock stars are generated, i.e. with its stellar density as a function of the position. This information is needed to retrieve the number counts of stars towards an element of given coordinates subtending a certain solid angle, and in a given bin of magnitude (see Girardi et al., 2005, for more details). The tool allows to choose either a defined component of our Galaxy (for instance the bulge, the thin or thick disc, the halo) or additional objects at known distance. I adopt the latter choice and we explain why in Section 8.3.3.

The TRILEGAL code generates a catalogue of stars as output. For each star, the following properties are provided: age, metallicity, initial mass, luminosity along with effective temperature, surface gravity, absolute bolometric magnitude, and absolute magnitudes in different passbands. Although the TRILEGAL code lets optionally assume a known foreground interstellar absorption, in this study

I rely neither on a detailed modelling of distribution of dust nor on absorption curves. I rather assume a simple distance-dependent dust extinction law and a resulting color excess, as explained in Section 8.3.4.

I describe in Sections 8.3.3 and 8.3.4 how I use the TRILEGAL code by providing it with properties of star particles from simulations as input, and how mock photometric properties of generated stars are used to derive a colour-magnitude diagram (CMD).

8.3.3 Producing the star catalogue

Once the parent particles have been selected (see Section 8.3.1), their properties are provided to the TRILEGAL code as input values, together with the adopted IMF, in the following way.

- I exploit the age of parent particles and their metallicity to provide the TRILEGAL code with the AMD of star particles (see Figure 8.2 and discussion below).
- I require the TRILEGAL code to use the same IMF adopted in the cosmological simulation, that is a Kroupa IMF (either a K3s IMF (Kroupa et al., 1993) or a K2s IMF (Kroupa, 2001) according to the simulated galaxy that I consider for the analysis, see Table 8.1).
- I further use the age and mass of parent particles to supply the TRILEGAL code with an SFR.

The TRILEGAL code is hence provided with a table describing the number of parent particles, with given (initial and current) mass, per age and metallicity bin. I adopt logarithmic age bins spanning the range $0 - 13.56$ Gyr, in order to have a finer sampling of stellar ages at low redshift z and a corser one at higher z. Metallicity bins are 0.05 dex wide each. For instance, I can investigate age and metallicity properties of the parent particles within the volume centred at $r_{\rm Sun} = 8.33$ kpc and $\vartheta_{\rm Sun} = 60°$ for the reference AqC5–fid simulation. Figure 8.2 shows the AMD for all the star particles in this selected sphere. Parent particles are colour-coded according to their age: star particles younger than 1 Gyr are shown in blue, parent particles having age between 1 and 5 Gyr are identified by green filled circles, whereas red triangles pinpoint stars older than 5 Gyr. This age classification reflects the one adopted by Casagrande et al. (2011) and further discussed in Section 8.5.2. I show the metal content of the star particles in terms of overall metal content $[Z/H]$. Old parent particles have a spread in metallicity that is remarkably wider (~ 3 dex) than younger star particles ($\lesssim 1.5$ dex), and the metallicity distribution progressively narrows as we approach the youngest ones.

As for the SFR, I assume an impulsive SFR for all the parent particles in each age and metallicity bin, so that I can deal with an SSP of that age and metallicity, and of

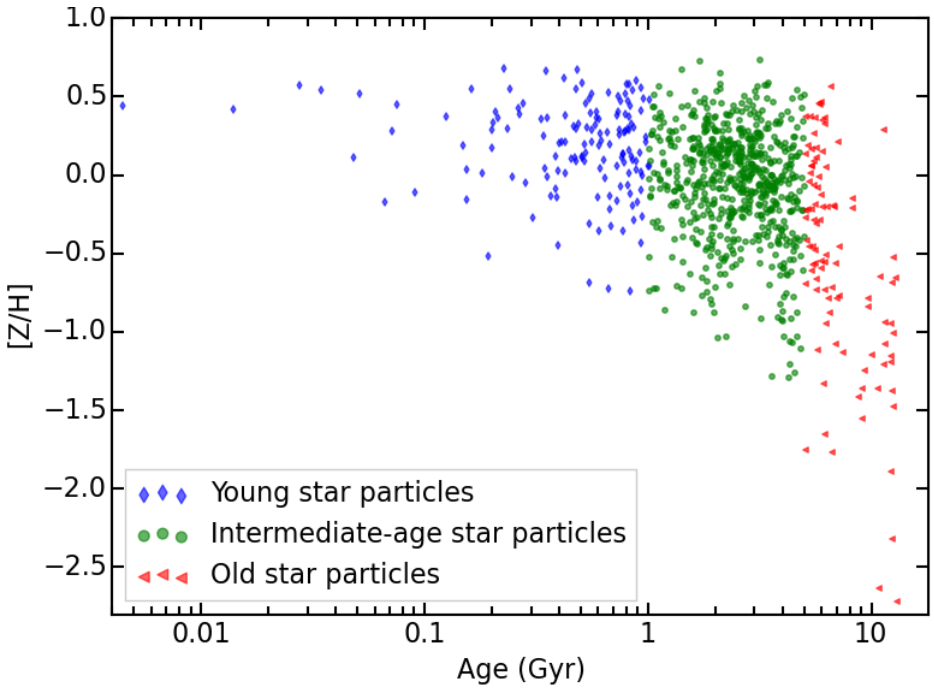

Figure 8.2: Age-metallicity distribution for star particles divided into different age intervals, at redshift $z = 0$. Metallicity is analysed in terms of $[Z/H]$. Star particles are colour-coded according to their age (see text): blue diamonds show star particles younger than 1 Gyr, green circles depict star particles with age between 1 and 5 Gyr, while star particles older than 5 Gyr are identified by red triangles.

given initial mass. The TRILEGAL code considers our parent particles as objects at known distance (see Section 8.3.2): each particle is located at a given distance from the centre of the sphere, that is the volume within which we perform our analysis. I know indeed the position of each parent particle from the numerical simulation.

Each age and metallicity bin is then populated with stars. Since age and metallicity determinations in observations are affected by non negligible uncertainties, we generate stars for stellar populations whose age and metallicity are the ones of the bin. Different options are possible, such as the generation of stars for each star particle, i.e. for each stellar population with a peculiar age and metallicity. We prefer the first choice, that also has the advantage of speeding up the procedure and will be convenient in view of higher resolution simulations and larger-area coverage surveys. While generating stars according to the input IMF, I choose to produce as many stars as needed to reach a stellar mass of $M_{*\,\mathrm{Age,Z}} \simeq 10^5$ $\mathrm{M}_\odot$ per age and metallicity bin. The TRILEGAL code requires the total stellar mass to be generated in each age and metallicity bin. We adopted this value after carrying out extensive tests. Our choice has been mainly driven by the fact that the stellar mass in each age and metallicity bin is at least as large as $\sim 10^5$ $\mathrm{M}_\odot$, in case only a few star particles occupy an age and metallicity bin. $M_{*\,\mathrm{Age,Z}}$ is defined as $M_{*\,\mathrm{Age}}/N_{\mathrm{Z\,bins}}$, that is the stellar mass per age bin over the number of metallicity bins in the considered age bin. $M_{*\,\mathrm{Age,Z}}$ can be considered as the current default IMF normalization in

each age and metallicity bin (see Section 8.3.4). I will only consider stars with mass larger than 0.6 $M_\odot$ for the current analysis: the reason stems from the mass range of stars that are typically observed in the solar neighbourhood (in particular, see Section 8.4 for the Geneva-Copenhagen Survey and Casagrande et al., 2011, figure 16 *b*). Therefore, generated stars with mass lower than our adopted threshold contribute to the total budget of stellar mass produced per age bin, but are not taken into account for further analysis. In this way, I end up with a catalogue of mock stars with simulated photometric properties as output.

8.3.4 Construction of the CMD

The most powerful tool to analyse a star cluster is the colour-magnitude diagram (CMD). A CMD is the observational plane where stars locate according to their apparent magnitude and their effective temperature, that is related to and expressed as the difference between magnitudes in two different bands, i.e. a colour. The final goal of this analysis is the construction of a CMD, starting from the star catalogue that I have generated.

Mock stars are produced with the following properties: mass, metallicity or $[Z/H]$, surface gravity, luminosity, effective temperature, absolute bolometric magnitude, and absolute magnitudes in the V band and in the *uvby* bands of the Strömgren photometric system. I choose this system since it has been shown to be particularly accurate and suited for determining stellar properties from colour indices (see e.g. Casagrande et al., 2011, and Section 8.4). The metallicity of stars is the $[Z/H]$ of the metallicity bin they belong to.

The next step towards the construction of the CMD is to identify the stars generated by each parent particle. This procedure allows to assign to each star the appropriate distance from the observer, that is the distance of its parent particle from the centre of the sphere, and thus the corresponding apparent magnitude. Stars in a given age and metallicity bin whose metallicity $[Z/H]$ differs by ± 0.05 dex at most from the $[Z/H]$ of a parent particle in the same age interval are identified as generated from that parent particle. The choice of 0.05 dex reflects the typical observational uncertainty on metallicity estimates (see Section 8.4). While doing this assignment, I discard low surface gravity stars, i.e. stars with $\log g < 3.0$, to limit the sample to MS stars, as in the observational data set (see Section 8.4; in Section 8.5 I will show the impact of the threshold surface gravity). Stars in each age bin are in this way attributed to their own parent particles.

TRILEGAL provides for each set (Age, Z) identifying bins an ensemble of stars generated from a stellar population whose *initial* mass is $M_{*\,\mathrm{Age,Z}}$ and whose *current* number of stars is $N_{*\,\mathrm{Age,Z}}$, the latter quantity neglecting stars with mass smaller than 0.6 $M_\odot$ and surface gravity $\log g < 3.0$. A number $N_{*\,\mathrm{extr}}$ of stars is then

attributed to each parent particle proportionally to its initial mass $M_{\rm parent,init}$, by randomly extracting among the $N_{*\,\rm Age,Z}$ stars[5]. Therefore:

$$N_{*\,\rm extr} \propto \frac{M_{\rm parent,init}}{M_{*\,\rm Age,Z}} \cdot N_{*\,\rm Age,Z}\,. \tag{8.1}$$

Such a procedure accomplishes the mass normalization, overcoming the initial generation of a fixed stellar mass per age and metallicity bin, regardless of the actual number of parent particles in each age and metallicity interval. Moreover, in this way more massive parent particles contribute to the final sample with a larger number of stars.

Once I populated star particles with stars, these stars have to be put to a suitable distance in order to construct a proper CMD. Since the TRILEGAL code provides mock stars with absolute magnitudes, the distance modulus has to be computed in order to retrieve apparent magnitudes and construct the CMD. In keeping with the notion that hydrodynamical quantities in simulations are characterised by smoothing distances (see e.g. Section 5.1), I also express the location of stars around each parent particle with a probability distribution function. I assume for this distribution a Plummer profile (see below). In this way, first stars are assigned the distance $d_{0,\rm parent}$ of their own parent particle from the centre of the selected sphere. I then displace stars marginally around their position before estimating the apparent magnitude: I take a random number in the range $(d_{0,\rm parent} - \varepsilon_d,\, d_{0,\rm parent} + \varepsilon_d)$ for the actual value of $d_{0,*}$, i.e. the distance of each star from the centre of the selected sphere.

The random extraction is weighted according to the differential mass distribution $dM_{\rm Pl}(r)/dr$ relative to a Plummer profile, since the mass represented by a star particle in the simulation is assumed to be distributed over a non-zero volume through a Plummer density profile[6] (see also Section 5.1). The density corresponding to the Plummer potential (Plummer, 1911; Binney & Tremaine, 2008) is:

$$\rho_{\rm Pl}(r) = \frac{3\,m}{4\,\pi\,\varepsilon_{\rm Pl}} \left(1 + \frac{r^2}{\varepsilon_{\rm Pl}^2}\right)^{-5/2}, \tag{8.2}$$

where m is the mass of the system, i.e. a parent particle in our case, needed for the normalization, and r is the distance from the centre. I use the Plummer-equivalent softening length for the gravitational interaction of the simulation for the Plummer scale length $\varepsilon_{\rm Pl}$ (see Section 8.2.1). I fix $\varepsilon_d = 3 \cdot \varepsilon_{\rm Pl} = 1.335$ kpc. Equation (8.2) is therefore used to retrieve $dM_{\rm Pl}(r)/dr$ and compute weights, by considering the fraction of mass of a parent particle within a given shell. This is a key step, because it allows the association between parent particles and individual stars.

[5] I verified that the mass distribution of the randomly extracted stars is in agreement with the IMF.

[6] Extensive tests show that adopting other possible profiles for the mass distribution, e.g. constant weights corresponding to a uniform distribution of stars around the star particle position, does not affect significantly the CMD.

I then compute m_V, i.e. the apparent magnitude in the Johnson V passband:

$$m_V = M_V - 5 + 5 \cdot \log_{10} d_{0,*\,[\mathrm{pc}]} \ , \tag{8.3}$$

and introduce a distance-dependent dust extinction, so that:

$$m_{V,\mathrm{obs}} = m_V + 1 \text{ magn} \cdot \frac{d_{0,*\,[\mathrm{kpc}]}}{1\,\mathrm{kpc}} \ . \tag{8.4}$$

I do not attempt to provide a self-consistent model for the distribution of dust in the solar neighbourhood here: I just consider an attenuation of 1 magnitude per kpc (see e.g. Vergely et al., 1998), in order to mimic the presence of dust. We adopt this choice because a negligible number of stars ends up to have an apparent magnitude larger than the magnitude limit of the survey due to dust extinction. However, refinements to the procedure are possible, also exploiting quantities provided by the simulation itself: for instance, a dust-to-gas mass ratio can be assumed or estimated from gas metallicity, a dust cross section can be adopted, and the gas density can be used to compute the optical depth, and thus the attenuation.

Then, I compute the colour $b - y$ by making the difference between the b and y magnitudes[7] in the two passbands of the Strömgren photometry. I also consider the effect of reddening $E(b - y)$ on the colour index:

$$(b-y)_{\mathrm{obs}} = (b-y) + E(b-y) = (b-y) + 0.32 \text{ magn} \cdot \frac{d_{0,*\,[\mathrm{kpc}]}}{1\,\mathrm{kpc}} \ . \tag{8.5}$$

In equation (8.5), the coefficient 0.32 comes from the adopted extinction law (Cardelli et al., 1989).

To allow a fair comparison with the observational data set, I then remove stars whose apparent magnitude $m_{V,\mathrm{obs}}$ exceeds the apparent-magnitude limit of the CGS. When making the final star catalogue that I use to compare my predictions to observed properties, I select 6670 stars, by randomly extracting out of our star collection the same number of stars that makes up the $irmf$ sample (see Section 8.4) of the CGS. The CMD is then accomplished.

8.4 Observational data set for the comparison

A precise determination of observed star properties is crucial to validate models of chemical enrichment and predictions of heavy-element abundance. The MW, and in particular the solar neighbourhood, are the places where this task can be most easily and accurately achieved.

In Section 8.5.2, I will compare my simulation predictions to observational data of stars in the solar neighbourhood from the Geneva-Copenhagen Survey (GCS hereafter, Nordström et al., 2004; Holmberg et al., 2007, 2009; Casagrande et al.,

[7] Note that the colour $b-y$ is remarkably similar to the colour $B-V$ of the Johnson photometry.

2011). Here I summarise the most important features of this survey for the current work, referring the interested reader to the aforementioned papers for further details.

The CGS is one among the most comprehensive investigations of nearby stars in the solar neighbourhood. This survey is an apparent-magnitude limited survey, as it observes stars brighter than $m_V \sim 8$. The CGS provides an ideal accurate database: ages, metallicities, kinematics and galactic orbits are determined for a sample of low-mass main sequence (MS) stars. Observed stars have masses spanning the range $0.6 - 2.3$ $M_\odot$ and are long-lived objects: the age probability distribution for all stars in the GCS peaks around 2 Gyr. Therefore, the atmospheres of these dwarf MS stars carry key information on the chemical composition of the ISM out of which they formed in a certain position of the disc of our Galaxy. The peaked age distribution (see Casagrande et al., 2011, figure 13) reflects the bias that the CGS has towards very young and very old stars. A number of reasons contribute to that, such as the apparent-magnitude limit, and the removal of very blue and giant stars. Distances of observed stars have been determined based on *Hipparcos* parallaxes, while their ages have been estimated by using BASTI and Padova isochrones (Pietrinferni et al., 2006; Bertelli et al., 2008, 2009, and references therein).

Among the $\sim$ 17000 stars observed in the CGS, we focus our attention on a sub-sample of them for our analysis, that is the so-called *irmf* sample. It is a sample of 6670 stars, containing stars with the best photometry. Additionally, they are mostly single MS stars (surface gravity $\log g \geq 3.0$).

Effective temperature and metallicity were determined using homogeneous Strömgren photometry, being the *uvby* photometric system (Strömgren, 1963) well suited to derive stellar atmospheric parameters through different colour indices.

Uncertainties on metallicity estimates range between $0.04 - 0.05$ dex both in terms of overall metal content $[Z/H]$ and iron abundance $[Fe/H]$, and slightly depend on colours, increasing towards the blue-most and the red-most indices. Stellar age determination is considered correct whenever either the absolute error is lower than 1 Gyr or the relative uncertainty is higher than 0.25. Therefore, uncertainties on stellar ages are usually larger for older objects, the aforementioned criteria leading to good determination of absolute ages for young objects and to fair assessment of relative age determination for older stars.

The majority of stars in the GCS resulted unaffected by the extinction due to interstellar dust, these stars being located in the solar neighbourhood. A reddening correction is assumed for stars with a color excess $E(b-y) \geq 0.01$ mag and farther than 40 pc from the observer, otherwise no correction was applied. Only $\sim 25\%$ of the sample needed such a reddening correction, the mean reddening being 0.0025 mag (see Holmberg et al., 2007; Casagrande et al., 2011, for further details).

As for the completeness of the survey, the GCS is volume-complete to a distance of 40 pc. While the commonly quoted apparent-magnitude limit of the sample is $m_V = 8.3$, the magnitude at which incompleteness sets depends on colour. The CGS begins to lose completeness near an apparent-magnitude $m_V = 7.6$ and below 1 $M_\odot$.

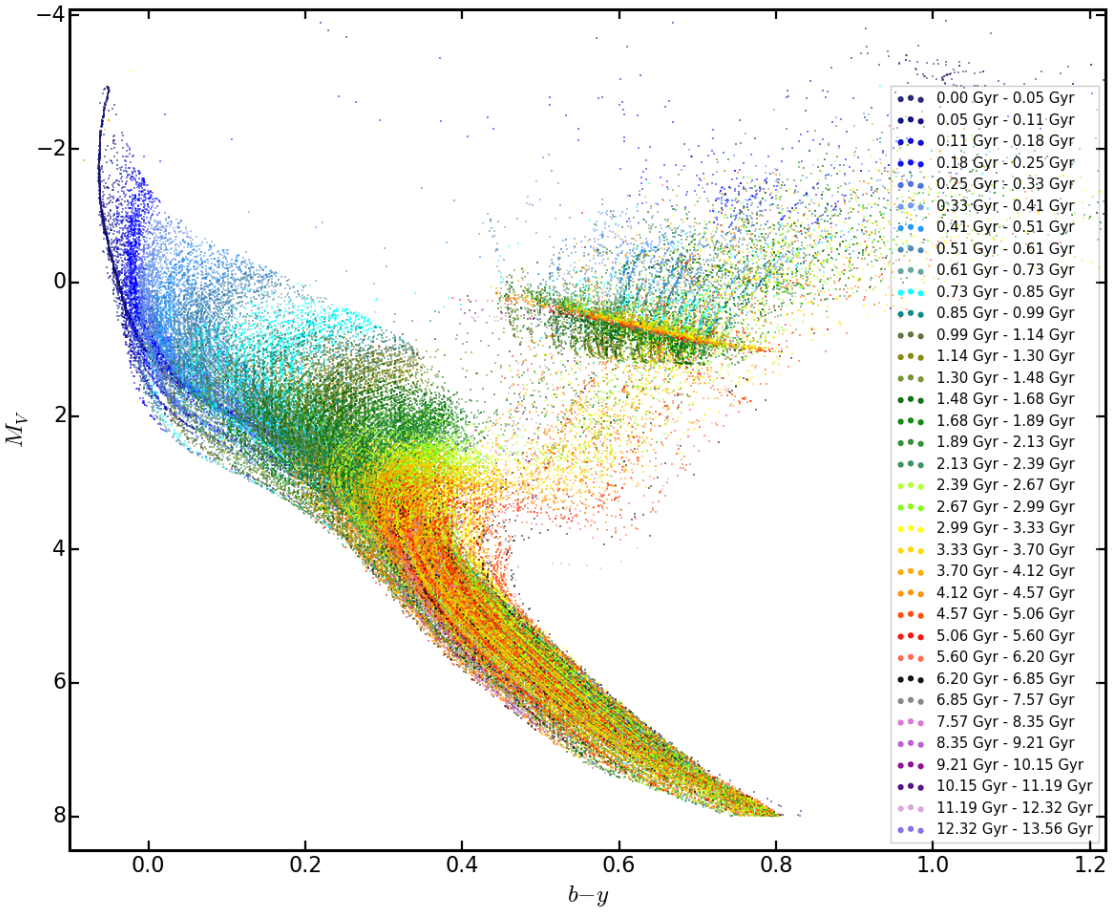

Figure 8.3: Colour-absolute magnitude diagram for all the stars brighter than the apparent-magnitude limit of the GCS ($m_V = 7.6$), i.e. the observational survey we want to compare our results with. I show the absolute Johnson M_V magnitude as a function of the colour $b - y$, and consider stars evolving beyond the MS, too. Stars are colour-coded according to their age, as highlighted in the legend.

8.5 Results

In this Section, I present the results. In Section 8.5.1, I show the CMDs that can be obtained by applying the approach I have developed to the output of a cosmological simulation of a disc galaxy. In Section 8.5.2, I investigate several properties of our catalogue of synthetic stars and address the comparison with observations.

Throughout Sections 8.5.1 and 8.5.2, I focus on our reference simulation AqC5–fid, and in particular on the sub-volume across its galactic disc (centred at $r_{\rm Sun} = 8.33$ kpc and $\vartheta_{\rm Sun} = 60°$) that I have selected to analyse a solar neighbourhood-like region (see Section 8.3.1). Simulations AqC5–cone and AqC5–3sIMF will be considered for comparison when I analyse the metallicity distribution function (Figure 8.7).

8.5.1 CMD from cosmological simulations

We start our analysis by investigating properties of mock stars in the aforementioned selected region of AqC5–fid. Figure 8.3 introduces the colour-absolute magnitude diagram. I show the absolute Johnson M_V magnitude as a function of the colour $b-y$ for all the stars in our catalogue that are brighter than the apparent-magnitude limit of the survey. I consider $m_V = 7.6$ for the GCS apparent-magnitude limit. Here, I do not restrict the sample of stars to those whose surface gravity is larger than $\log g \geq 3.0$, so as to appreciate all the possible evolutionary stages and not to limit to MS stars alone. Stars are colour-coded according to their age, that is the age of their own parent particles. The various filters and bands in which magnitudes are considered reflect the ones adopted in the GCS (see Casagrande et al., 2011). Stars sharing the same colour can be deemed as an ensemble of stars lying on a set of isochrones characterised by similar ages (ranging between each age bin). Isochrones are curves on the luminosity (or absolute magnitude)-temperature (or colour) plane that link evolutionary stages of stars with different mass at a given time. Each isochrone is identified by age and chemical composition. In Figure 8.3 we can appreciate the spread in metallicity of quasi-coeval stars by analysing how stars of the same age that are experiencing the MS stage extend over the colour index. Assuming the same age, stars with a higher metal content have both a larger colour index and a larger mass at the turn-off (TO) point. Also, the TO becomes fainter and redder (higher $b-y$) as the matallicity increases. Above the TO, the extent across the colour index of coeval stars is mainly due to the different evolution that stars with different mass undergo. Figure 8.3 shows how stars of different colours describe different shapes: as time passes, stars of different mass indeed evolve out of the MS, thus revealing striking features of aging stellar populations. For instance, the TO progressively dims and reddens as the stellar age increases; the red giant branch (RGB) becomes well populated and more extended for stars older than ~ 1 Gyr; also, the luminosity of the horizontal branch (HB) is roughly constant ($M_V \sim -1 \div 0$) after ~ 1 Gyr. Stars characterised by the lowest values of M_V show an interesting feature: their M_V progressively decreases as their colour index decreases. The reason for this behaviour stems from the threshold mass of our sample (0.6 $M_\odot$, see Section 8.3.3 and Figure 8.6): stars having the same mass but lower metallicity (i.e. left edge of the MS wideness) have a higher temperature and a lower M_V, due to their lower opacity.

I then analyse properties of the 6670 stars that make up the final stellar catalogue, i.e. the one that matches the observational data set of the GCS (see Section 8.4). Figure 8.4 shows the colour-absolute magnitude diagram (top panel) and the CMD (colour-apparent magnitude diagram, bottom panel) for the sample of 6670 stars. Stars are colour-coded according to their age, as described in the legend. I adopted $m_V = 7.6$ as GCS apparent-magnitude limit and $\log g \geq 3.0$ as threshold surface gravity. In the top panel of Figure 8.4, I consider the absolute Johnson M_V magnitude as a function of the colour $b-y$: we can appreciate the effect of the surface gravity limit in restricting the sample to unevolved stars alone by contrasting

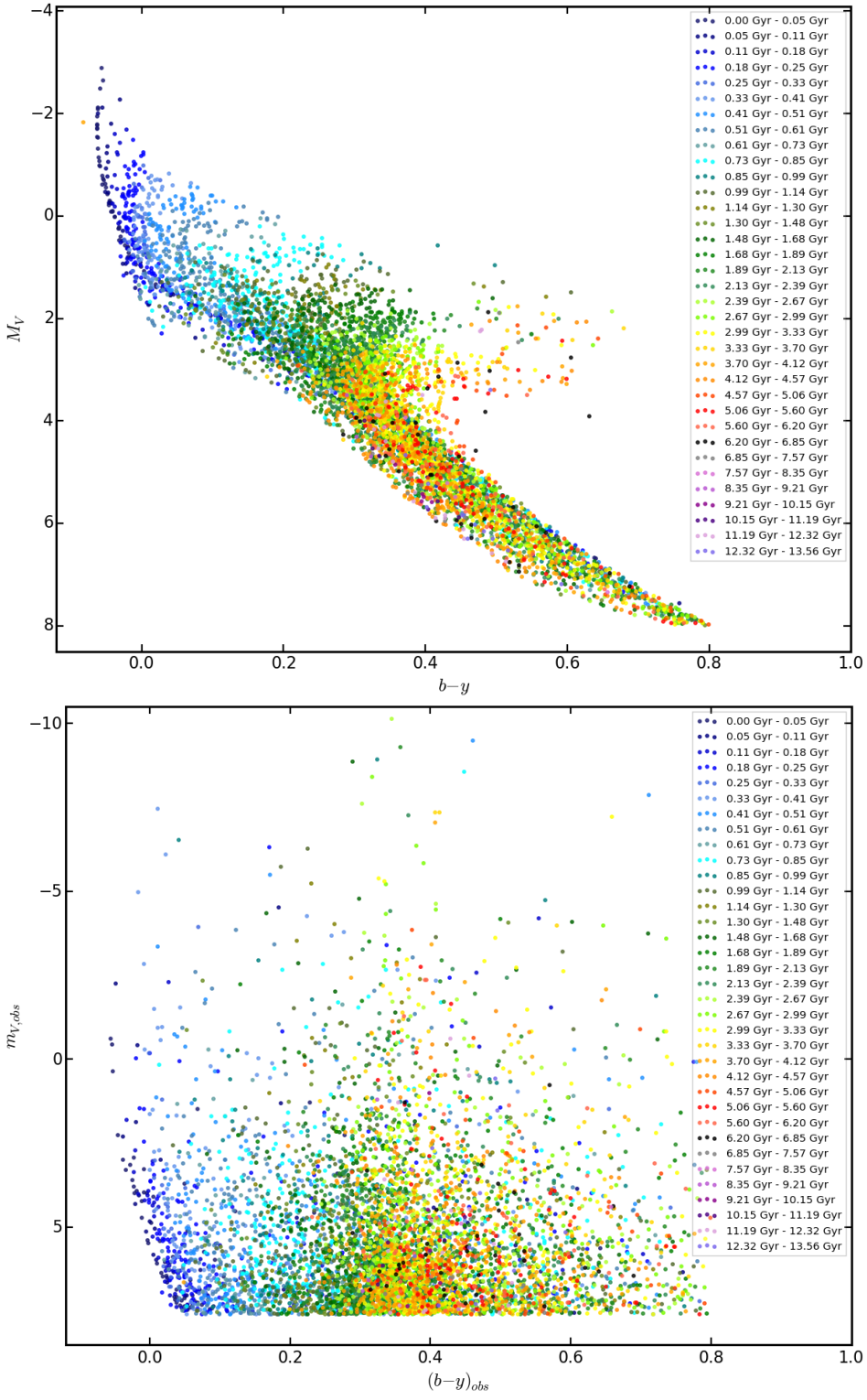

Figure 8.4: Colour-absolute magnitude diagram (top panel) and CMD (i.e. colour-apparent magnitude diagram, bottom panel) for the sample (6670 stars) that matches the observational data set of the GCS. Stars are colour-coded according to their age, as highlighted in the legend. These stars are brighter than the apparent-magnitude limit of the survey ($m_V = 7.6$) and have a surface gravity typical of MS stars ($\log g \geq 3.0$). In the top panel we show the absolute Johnson M_V magnitude as a function of the colour $b-y$. In the bottom panel we consider the apparent Johnson $m_{\rm V,obs}$ magnitude (accounting for dust extinction, too) as a function of the reddened colour $(b-y)_{\rm obs}$.

with Figure 8.3, where the low-magnitude portion of the plane is well populated for $b - y \gtrsim 0.4$. The bottom panel of Figure 8.4 illustrates the CMD of our star sample. Here, the Johnson $m_{\mathrm{V,obs}}$ magnitude has been corrected for the effect of dust (see equation (8.4), Section 8.3.4) and the color index $(b - y)_{\mathrm{obs}}$ is reddened according to equation (8.5). The effect of the apparent-magnitude limit is evident here, since the diagram is not populated below $m_{\mathrm{V,obs}} = 7.6$. The majority of stars locate where $m_{\mathrm{V,obs}} \lesssim 3$ and is characterised by a colour index $0 \lesssim b - y \lesssim 0.6$. The distribution of stars gets sparser as the magnitude decreases and as the colour index depicts lower temperatures. These CMDs show the observable stellar content of a volume of the simulated galaxy.

8.5.2 Properties of synthetic stars

We continue our analysis by further investigating properties of the catalogue of 6670 mock stars. Figure 8.5 illustrates the AMD for the sample of 6670 stars. Stars are colour-coded according to their age. The identifying colour convention is the same adopted for parent particles in Figure 8.2. Metallicity is here analysed in terms of $[Z/H]$. Stars have been generated according to the input properties of the selected parent particles: therefore, stars have the same age and a similar metallicity of their own parent particles. In particular, the $[Z/H]_{\mathrm{stars}}$ ranges between $[Z/H]_{\mathrm{parent\ particle}} \pm 0.05$ dex (see Section 8.3.4). This explains why stars and star particles share an almost indistinguishable AMD (and proves the accuracy of the stochastic sampling, too). In Figure 8.5, the shade of each symbol is proportional to the number of stars sharing properties on the age-$[Z/H]$ plane: thicker symbols identify stars coming from more sampled parent particles (see equation (8.1)). The reason why the AMDs of parent particles and stars are not exactly the same is twofold: first, stars associated to the same star particle can have sligthly different $[Z/H]$ (see, for instance, the youngest stars on the left of Figure 8.5). This is due to the fact that stars in two contiguous metallicity bins can have an $[Z/H]_{\mathrm{stars}}$ within $[Z/H]_{\mathrm{parent\ particle}} \pm 0.05$ dex. Also, some parent particles can be not represented at all by the final 6670 stars, either because they are not massive enough to generate stars that pass the selection and extraction procedures, or because their child stars have an apparent magnitude that is higher than the apparent-magnitude limit of the GCS (for instance, by comparing Figures 8.2 and 8.5, we see that the star particles with a $[Z/H]_{\mathrm{parent\ particle}} < -2$ are not represented by stars).

Figure 8.6 shows the mass-metallicity distribution for our star sample. The 6670 star sample has been sliced into three subsamples – young, intermediate-age, and old stars – according to the aformentioned age classification. The young (blue), intermediate-age (green) and old (red) star subsamples consist of the following number of stars: 2047, 4351, and 272, respectively. The background two-dimensional histogram represents the distribution of young stars in this plane. Mass-metallicity bins are colour-coded according to the fraction of stars in the bin with respect to the total number of young stars, the fraction of stars increasing from ligther- to darker-blue bins. Green contours show the distribution of intermediate stars: from

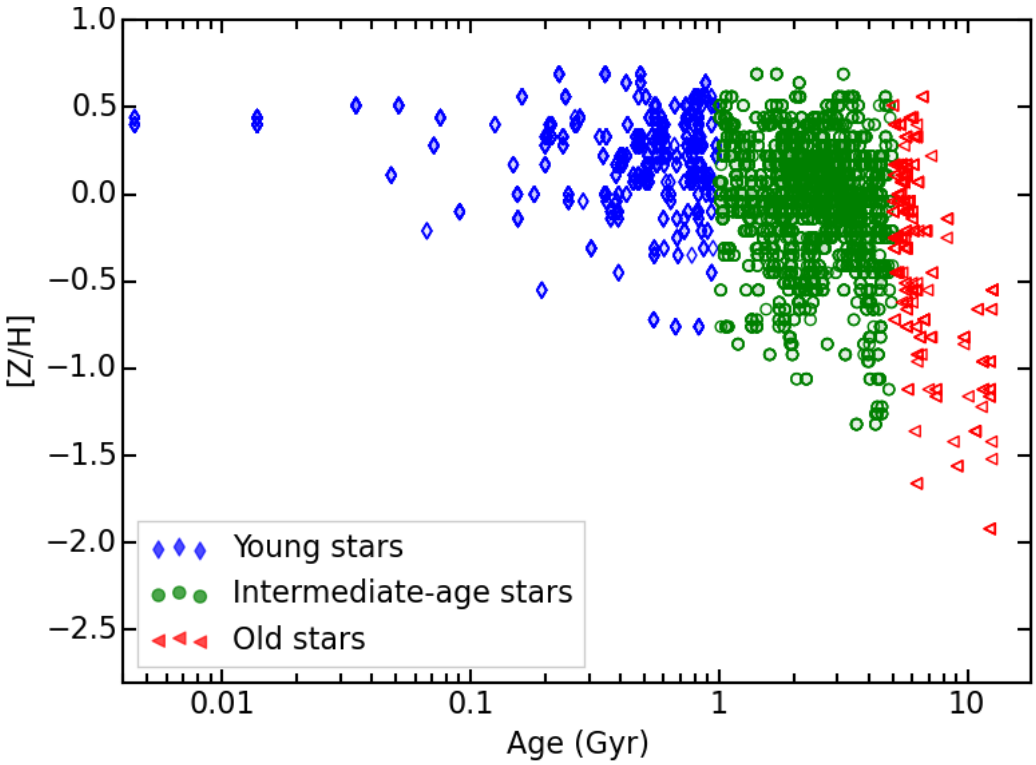

Figure 8.5: Age-metallicity distribution for the sample of 6670 stars, divided into different age intervals. Metallicity is analysed in terms of $[Z/H]$. Stars are colour-coded according to their age (i.e. the age of their own parent particles, see text): blue diamonds show stars younger than 1 Gyr, green circles depict stars with age between 1 and 5 Gyr, while stars older than 5 Gyr are identified by red triangles. Stars share age and a similar metallicity with their parent star particles: darker-filled symbols with thicker edges identify stars coming from more populated parent particles.

outwards to inwards contours enclose mass-metallicity bins with a fraction of $8 \cdot 10^{-4}$, $5 \cdot 10^{-3}$, and $2 \cdot 10^{-2}$ stars with respect to the total number of intermediate-age stars, respectively. Red triangles describe the distribution of old stars. This figure displays the mass distribution of stars that make up our sample: the majority of stars have a mass ranging between 0.6 $M_\odot$ and ~ 1.5 $M_\odot$, with mass never exceeding 7 $M_\odot$. Mass distribution is more clustered going from young to intermediate-age to old stars, only few old stars having a mass larger than 1 $M_\odot$. Young stars have on average a higher $[Z/H]$, although the region of the plane with $-0.1 \lesssim [Z/H] \lesssim 0.3$ is almost equally populated by young and intermediate-age stars (note that the blue and green subsamples differ by a factor of ~ 2 in terms of number of stars, so numbers expressing fractions almost immediately translate in number of stars). As the stellar age increases, stars tend to move towards smaller masses (as a consequence of stellar evolution) and lower metallicities. As a consequence, higher-metallicity stars spread over the entire mass range, while the lower the $[Z/H]$ is, the smaller is the mass of the star and the older is the star.

Figure 8.7 introduces the metallicity distribution function (MDF) for models and observations. I consider here three different star samples, one for each simulation

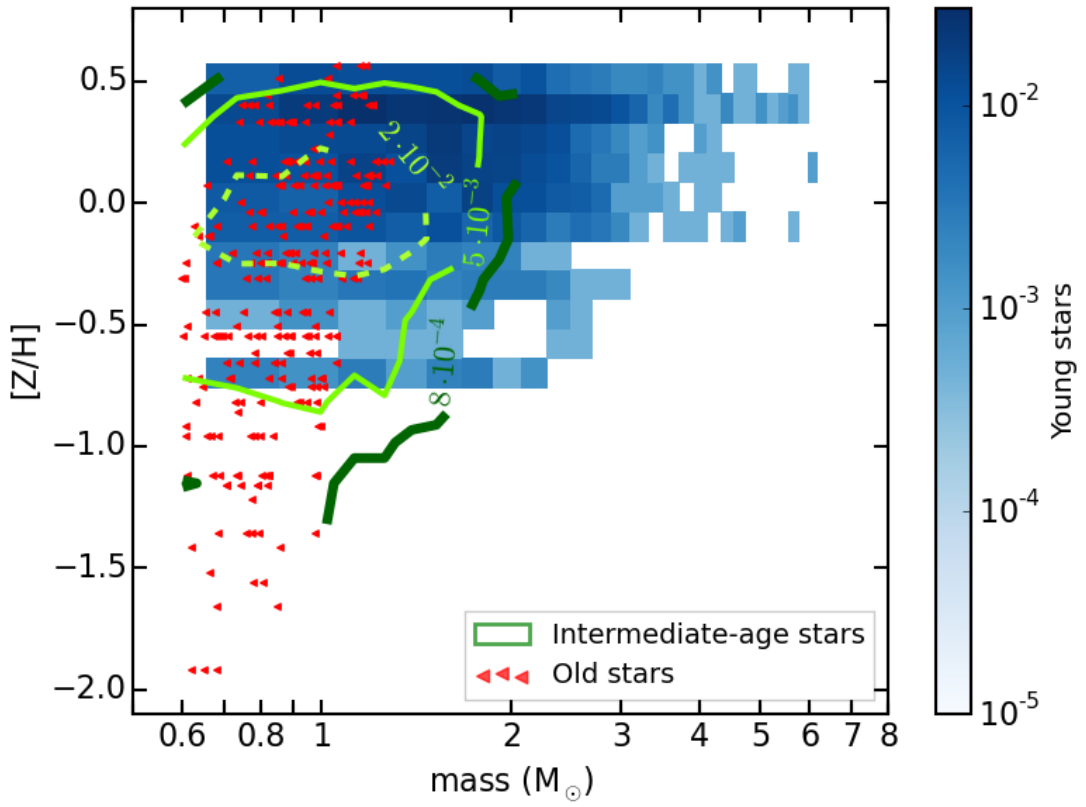

Figure 8.6: Mass-metallicity distribution for the 6670 star catalogue, once it has been split into three subsamples according to stellar age. The background two-dimensional blue histogram represents the distribution of young stars, the bins being colour-coded according to the fraction of stars with respect to the total number of young stars. Green contours describe the distribution of intermediate stars: from outwards to inwards contours enclose bins with a fraction of $8 \cdot 10^{-4}$, $5 \cdot 10^{-3}$, and $2 \cdot 10^{-2}$ stars with respect to the total number of intermediate stars, respectively. Red triangles show the distribution of old stars.

that I carried out (see Section 8.2.1 and Table 8.1). The three star samples represent the observable stellar content of three volumes, each centred at $r_{\rm Sun} = 8.33$ kpc and $\vartheta_{\rm Sun} = 60°$ in the reference simulation AqC5–fid, in AqC5–cone and in AqC5–3sIMF. The black histogram in Figure 8.7 depicts the MDF of the star catalogue of AqC5–fid, violet and pink histograms describing the MDFs of the star samples of AqC5–3sIMF and AqC5–cone, respectively. I also show the MDF obtained by Casagrande et al. (2011) for the GCS (in light blue), and I report their median and mean values ($[Z/H] = -0.01$, $[Z/H] = -0.02$, respectively).

Before drawing any strong conclusion from this comparison, I caution that the metallicity scale in observations and simulations could be different. The former is derived from photometry, the latter is inferred directly from our chemical evolution network and then accounts for the binning discussed in Section 8.3.3. This caveat has to be considered when comparing our models with observations. For this reason, I will focus on the overall shape and mean values of predicted and observed MDFs. I choose a bin size that roughly matches that of the histogram in Casagrande et al.

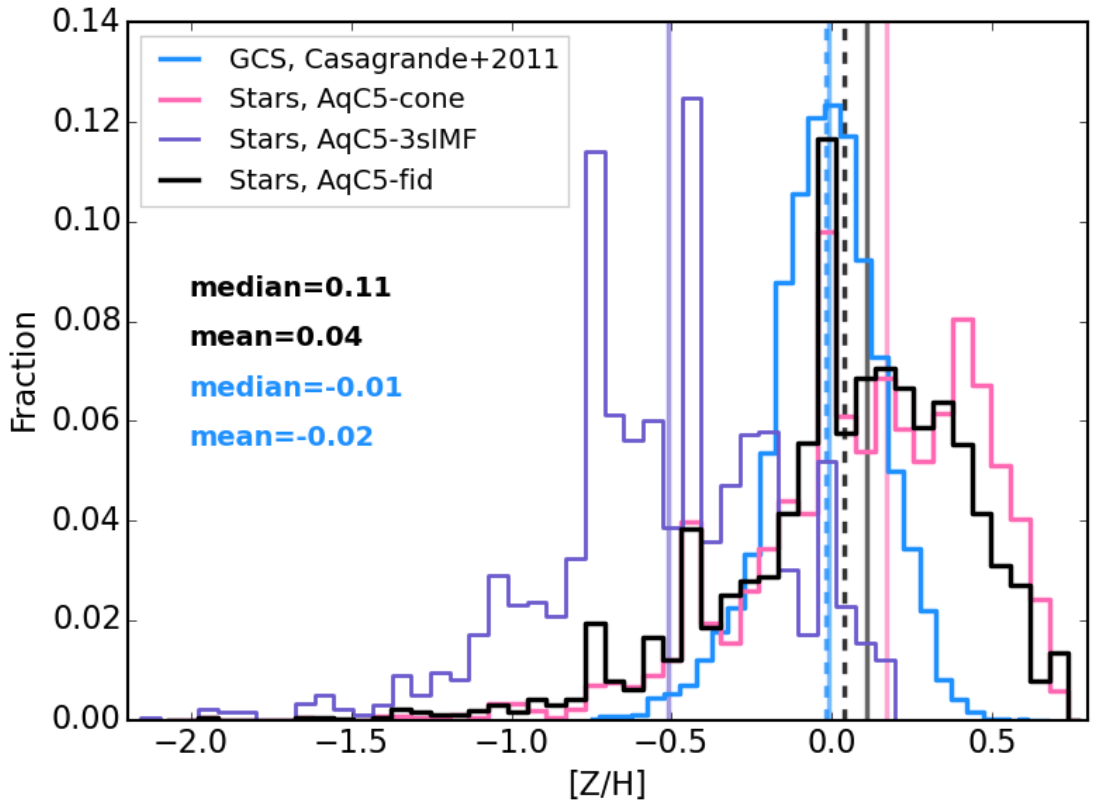

Figure 8.7: MDF for the star sample of 6670 stars in AqC5–fid (black histogram), in AqC5–cone (pink histogram), and AqC5–3sIMF (violet histogram). Solid (and dashed) vertical lines indicate the median (and the mean) of each distribution. I also show the MDF obtained for the GCS by Casagrande et al. (2011), for comparison (light blue histogram). Solid and dashed light blue vertical lines describe the median and the mean of the latter distribution, respectively.

(2011) for the MDF of our models. The MDF of the solar neighbourhood-like volume in AqC5–fid (median $[Z/H] = 0.11$, mean $[Z/H] = 0.04$) agrees well with observations. The means and medians of the two distributions differ by only 0.06 dex and 0.12 dex, respectively (see also Figures 8.9 and 8.10, and Section 8.6.1). The difference between the means of the two MDFs implies that stars of our sample are on average richer in metals than observed ones by $\sim 15\%$. The considered star sample of AqC5–fid is characterised by a low-metallicity tail that is more extended than the MDF of the GCS, and that is mainly populated by old stars (see Figure 8.8). Also, a larger fraction of mock stars has a super-solar metallicity with respect to the observed sample. Despite these differences, the peaks of the two MDFs perfectly overlap and pinpoint a solar metallicity.

The peak at solar metallicity in the MDF of AqC5–fid is not within the Poisson errors computed on the number of mock stars in metallicity bins (this is true for the main peaks in the MDFs of AqC5–cone and AqC5–3sIMF, too). By fitting the MDF of AqC5-fid with a Gaussian (mean 0.117, standard deviation 0.317) I find that this peak is 11.7σ above the value predicted by the fit ($\sigma \sim 0.004$ being the Poisson

error of the considered bin). The peak in the MDF of mock stars is due to the properties of the parent particles closer to the centre of the solar neighbourhood-like volume. These parent particles generate mock stars that are more likely to pass the apparent magnitude limit cut. The metallicity of the peak therefore traces the metallicity of the innermost region of the galactic disc.

When associating mock stars to their parent particles, I take a possible uncertainty in metallicity into account (i.e. 0.05 dex, see Section 8.3.4). This uncertainty in metallicity means that we distribute the same mock stars to star particles located into two contiguous metallicity bins (see above in this Section). However, it can happen that some parent particles are isolated in the age-metallicity plane, without other particles populating metallicity bins directly above or below. For parent particles located into these isolated bins, mock stars will be associated with a precise value of metallicity. This means that the uncertainty on metallicity estimates for mock stars whose metallicity is that of these isolated bins will be underestimated with respect to observations. This is reflected on the fact that when we derive the MDF for our mock stars with the same binning as in observations we are recovering into a single bin mock stars that should populate also adjacent metallicity bins. This can be solved by introducing a slight smoothing in our distribution. If I add to the metallicity of each mock star an uncertainty drawn from a normal distribution (centred on the metallicity of the considered mock star and with standard deviation 0.025 dex), the peaks of predicted MDFs in Figure 8.7 are considerably reduced.

I also consider the MDFs of synthetic star catalogues in AqC5–cone and AqC5–3sIMF. Stars in the selected sphere of AqC5–cone have a MDF with slightly super-solar median and mean values ($[Z/H] = 0.17$, $[Z/H] = 0.10$, respectively). The excess of metal-rich stars is a consequence of the low-redshift SFR (higher than in the other galaxies, see Figure 8.1), that affects outer regions of the galaxy disc, further enriching them in metals. The higher metal content of stars in AqC5–cone with respect to AqC5–fid is also supported by the radial metallicity profiles of these two galaxies shown in Figure 6.18 (bottom panel). As for AqC5–3sIMF, the peak of the MDF is subsolar (median $[Z/H] = -0.51$, mean $[Z/H] = -0.53$). The distribution is left-skewed and is characterised by a pronounced low-metallicity tail. The comparison with the GCS suggests that stars in the solar neighbourhood are metal richer than those in AqC5–3sIMF by a factor of ~ 2.5 (the medians of the two distributions differ by 0.4 dex). The tension between predictions from AqC5–3sIMF and the reference AqC5–fid is due to the different IMF (see Section 8.2.1): the K3s produces a smaller number of massive stars than K2s, thus limiting the metal enrichment contributed by SNe II (the role of different IMFs has been thoroughly addressed in Chapter 7). However, I note that Casagrande et al. (2011) also cautioned that it is not straightforward to compare directly their MDF with theoretical predictions, since it is affected by sample selection effects. For instance, they provide the MDF for a reduced number of stars (5976) with respect to their *irfm* sample. They indeed consider for the MDF analysis only those stars that meet the criteria needed for their metallicity calibration. While doing that, they exclude some of the stars whose colour index is in the range $0.43 \leq (b - y) \leq 0.63$: it is

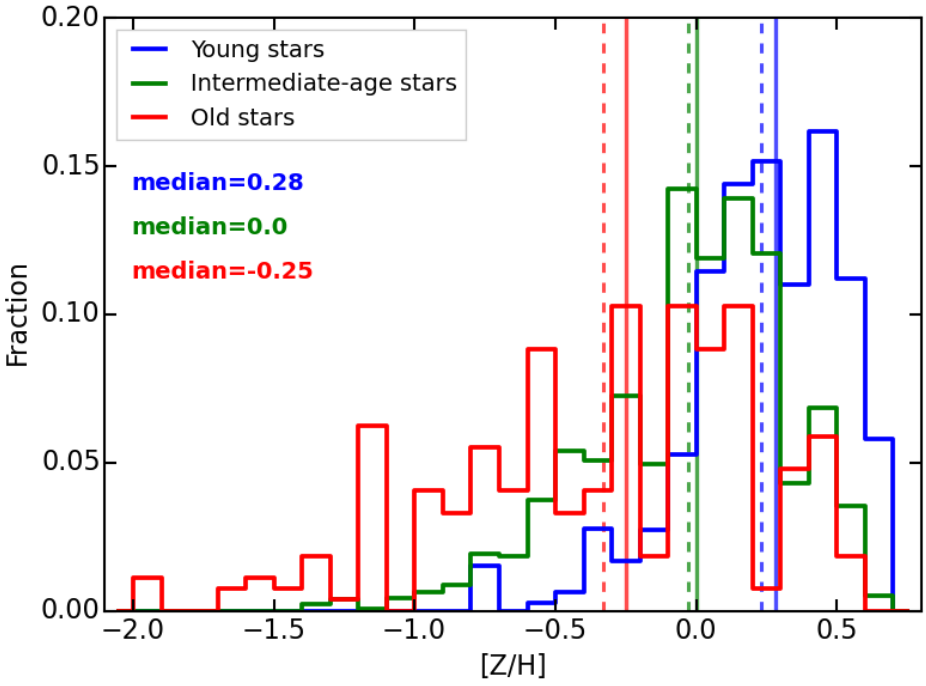

Figure 8.8: MDF for the three subsamples of stars in which the 6670 star catalogue has been sliced according to stellar age. Solid and dashed vertical lines pinpoint the median and the mean of each distribution, respectively. The 6670 star catalogue is made up of 2047 young stars, 4351 stars with age between 1 and 5 Gyr, and 272 old stars.

not trivial to figure out how the aforementioned sample selection effect affects the MDF of observed stars. In Section 8.6.1 I discuss how the shape and the peak of the MDF are affected by the position in the simulated galaxy of the volume where we carry out our analysis.

I then consider how the three subsamples of young, intermediate-age, and old stars in which I split the whole star catalogue contribute to the total MDF. Here I focus the analysis on stars within the volume centred at $r_{\rm Sun} = 8.33$ kpc and $\vartheta_{\rm Sun} = 60°$ in the reference simulation AqC5–fid. Figure 8.8 shows the MDF for the three subsamples. The age classification is the same adopted in Figures 8.2, 8.5, and 8.6, and discussed above in this Section. The reason why in Figure 8.8 I prefer to show split MDFs in terms of fraction of stars with given metallicity relative to each entire subsample lies in the uneven contribution by different subsamples. The old star MDF (mean $[Z/H] = -0.33$, median $[Z/H] = -0.25$) shows that the low-metallicity tail of the total MDF of AqC5–fid in Figure 8.7 is mainly contributed by old stars. As already pointed out by the mass-metallicity distribution in Figure 8.6, young stars are characterised by the narrowest distribution; the MDF of intermediate-age stars (mean $[Z/H] = -0.03$, median $[Z/H] = 0.00$) has a broader barely-populated wing that extends towards very low $[Z/H]$. Moreover, the blue MDF (mean $[Z/H] = 0.23$, median $[Z/H] = 0.28$) shows that young stars are the main responsible for the quasi-totality of stars with highly super-solar metallicity, i.e. $[Z/H] > 0.3$. Also, young and intermediate-age stars are the main contributors to stars with the $[Z/H]$ value where the total MDF peaks (see Figure 8.7).

8.6 Discussion

8.6.1 Solar neighbourhood sampling variance

In this Section, I address the impact of the assumed position of the solar neighbourhood in the simulated galaxy on final results. Do my conclusions change if I choose different positions for the centre of the volume in which I perform my analysis? In Section 8.2.1 I stressed that disc galaxies I simulated should not be considered as a model of the MW, in spite of similar morphological properties and several features shared by them. Also, when I selected the sphere where I carried out the analysis (Section 8.3.1), I did not make any particular attempt to reproduce the actual location of the solar neighbourhood with respect to the bar orientation and the spiral pattern of the MW, nor I considered the exact radial extent or the scale radius of the stellar disc of the simulated galaxies. However, I compare my predictions with results from a typical survey in the solar neighbourhood: thus, I assume that the variation of properties of star samples at marginally different positions is not dramatic once a star sample large enough to be representative of a typical region of the galactic disc is chosen.

In order to investigate if sample selection effects modify final results, I select different spheres in the AqC5–fid galaxy, I extract from each a star catalogue made up of 6670 stars (as I did for the reference case in previous Sections), and I compare MDFs of different star samples. All the volumes where I perform the analysis have origins on the galactic plane: I first fix a distance $r_{\rm Sun}$ and consider different $\vartheta_{\rm Sun}$. Then, I rather choose a position angle $\vartheta_{\rm Sun}$ for their centres and allow their distance from the galaxy centre to vary by 0.5 kpc from time to time. In all the considered cases, I keep the size of the sphere constant (i.e. 1 kpc).

Figure 8.9 highlights that MDFs of stars located on the galactic plane of the simulated galaxy are comparable, whatever is the angle $\vartheta_{\rm Sun}$ that identifies the location of the centre of the volume in which I perform the analysis. I introduce the MDFs for six different star samples. These star samples are all located in spheres whose origin is $r_{\rm Sun} = 8.33$ kpc far from the galaxy centre. On the other hand, their position angle varies on the galactic plane of the simulated galaxy. I consider $\vartheta_{\rm Sun} = 0°$, $\vartheta_{\rm Sun} = 45°$, $\vartheta_{\rm Sun} = 60°$, $\vartheta_{\rm Sun} = 90°$, $\vartheta_{\rm Sun} = 120°$, and $\vartheta_{\rm Sun} = 180°$, respectively. The median of each distribution is as follows: 0.07, 0.11, 0.11, 0.07, 0.00, and −0.04, respectively, the medians of some MDFs overlapping. Note that the black MDF identifies the same distribution shown in Figures 8.7 and 8.10. Also, I notice that in Section 8.5.2, Figure 8.7, I have analised the MDF for the star sample in the reference volume ($r_{\rm Sun} = 8.33$ kpc, $\vartheta_{\rm Sun} = 60°$): that MDF is characterised by a median value that is among the ones that differ the most by the median of the observed MDF in the GCS, and this highlights the agreement of our results with observations. All the MDFs in Figure 8.9 peak around solar metallicities, the median values of different distributions differing by 0.15 dex at most. I can therefore conclude that sample selection effects do not affect significantly my results.

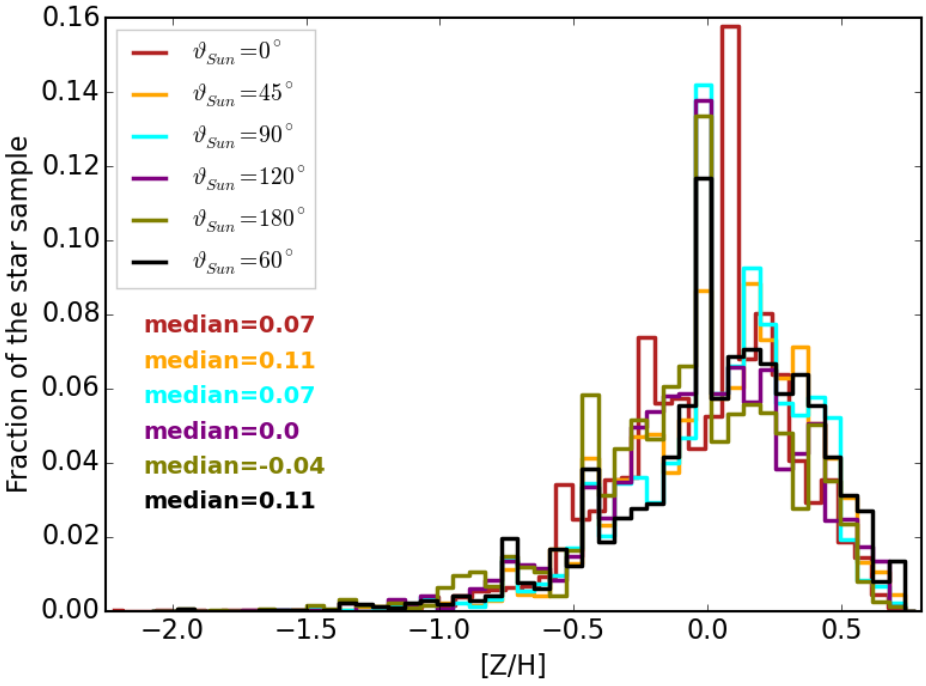

Figure 8.9: MDFs for six different star samples of 6670 stars each for the AqC5–fid galaxy. These star samples are located in volumes whose origin is at fixed distance from the galaxy centre, i.e. $r_{\rm Sun} = 8.33$ kpc, whereas their position angle varies on the galactic plane of the simulated galaxy. I consider $\vartheta_{\rm Sun} = 0°$, $\vartheta_{\rm Sun} = 45°$, $\vartheta_{\rm Sun} = 60°$, $\vartheta_{\rm Sun} = 90°$, $\vartheta_{\rm Sun} = 120°$, and $\vartheta_{\rm Sun} = 180°$, respectively. I also indicate the median of each distribution. The black MDF identifies the same distribution shown in Figures 8.7 and 8.10.

I note that the result shown in Figure 8.9 also ensures that differences in metal content among star particles (and thus among stars) within regions whose radius is 1 kpc are trustworthy. Since our formal resolution is ~ 1 kpc, we are relying on a single sampling of the interested volume when we analyse stellar properties in one sphere. However, retrieving comparable MDFs within different volumes shows that statistical fluctuations cannot be responsible for the analysed chemical features.

Figure 8.10 shows the MDFs for three different star samples of 6670 stars each. The volumes where these star samples are located are centred at $r_{\rm Sun} = 7.83$ kpc, $r_{\rm Sun} = 8.33$ kpc, and $r_{\rm Sun} = 8.83$ kpc, respectively. The centre of all these spheres is on the galactic plane of the simulated galaxy, at a fixed position angle, i.e. $\vartheta_{\rm Sun} = 60°$. Each distribution is characterised by the following median: 0.11, 0.11, and 0.07, respectively. Stars in selected spheres centred at increasing distance from the galaxy centre share very similar MDFs. As already discussed, the reason for similar values of metallicity for the peak of the MDFs stems from the properties of parent particles located within the innermost regions of the solar neighbourhood-like volume, i.e. on the inner galactic disc. The stellar chemical homogeneity shared by the analysed regions of the stellar disc can be understood by analysing the metallicity maps in Figure 8.11. I show face-on and edge-one distribution of all the star particles located within the galactic radius $R_{\rm gal}$ of the AqC5–fid galaxy

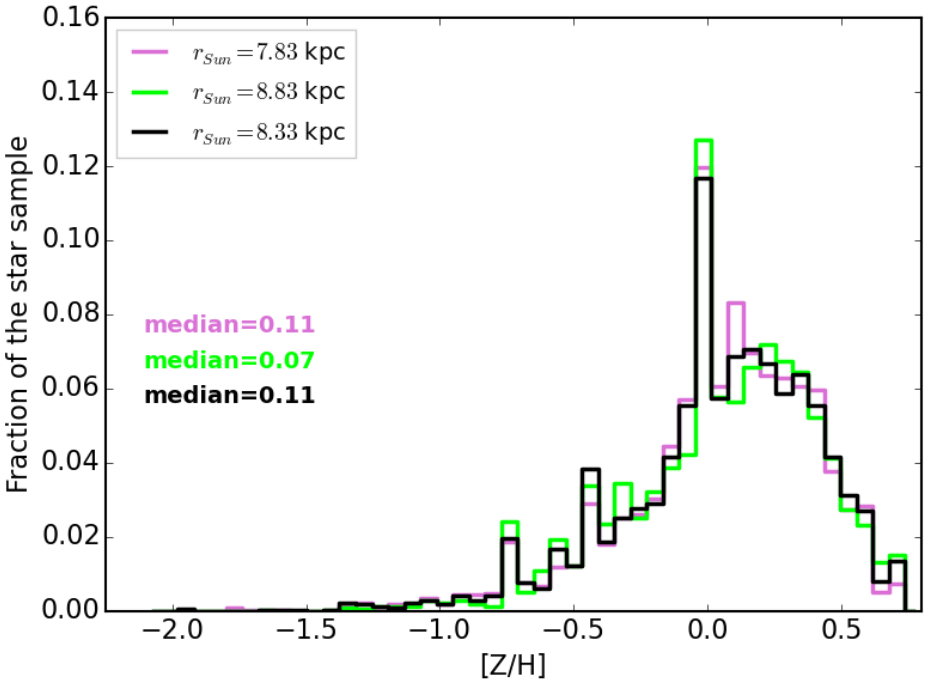

Figure 8.10: MDFs for three different star samples of 6670 stars each for the AqC5–fid galaxy. These star samples are located in spheres whose origin is at increasing distance from the galaxy centre, i.e. $r_{\rm Sun} = 7.83$ kpc, 8.33 kpc, and 8.83 kpc, respectively. The centre of all these volumes is on the galactic plane of the simulated galaxy, at a fixed position angle ($\vartheta_{\rm Sun} = 60°$). The black MDF identifies the same distribution shown in Figures 8.7 and 8.9.

simulation, at redshift $z = 0$. The colour encodes the mean $[Z/H]$ of the star particles in each spatial bin: we can appreciate how the metal content in stars changes as a function of the distance from the galaxy centre across the galactic plane (top panel of Figure 8.11) and as a function of the height over it (bottom panel). Stars on the galactic disc within a distance of $r \lesssim 10$ kpc from the galaxy centre have on average a solar metallicity, the mean $[Z/H]$ rapidly decreasing as one moves towards larger distances and higher galactic latitudes.

Also, in Chapter 6 I have shown that radial metallicity profiles of all the stars are almost flat for $r \lesssim 10$ kpc (see Figure 6.10, last panel, for AqC5–cone, this feature being shared with AqC5–fid)[8]; on the other hand, a radial metallicity gradient (for $r > 5$ kpc) is evident and in keeping with observations when only younger stars are considered (see Figure 6.18, bottom panel, for both AqC5–fid and AqC5–cone).

The general result is that properties of mock stars originated from star particles that are located in marginally different regions of the simulated galaxy are

[8]This is also the reason why I decide not to evaluate a scaled position for the centre of our volume $r_{\rm Sun}$ according to an effective radius of the simulated galaxy. For the sake of completeness, by fitting the stellar surface density profile of AqC5–fid with an exponential law $\Sigma(r) \propto \exp(-r/r_s)$, r_s being the scale radius, we find $r_s = 3.25$ kpc. For instance, McMillan (2011) found $r_s = 3.29 \pm 0.56$ kpc for the thick disc ($r_s = 3.00 \pm 0.22$ kpc for the thin disc) of MW.

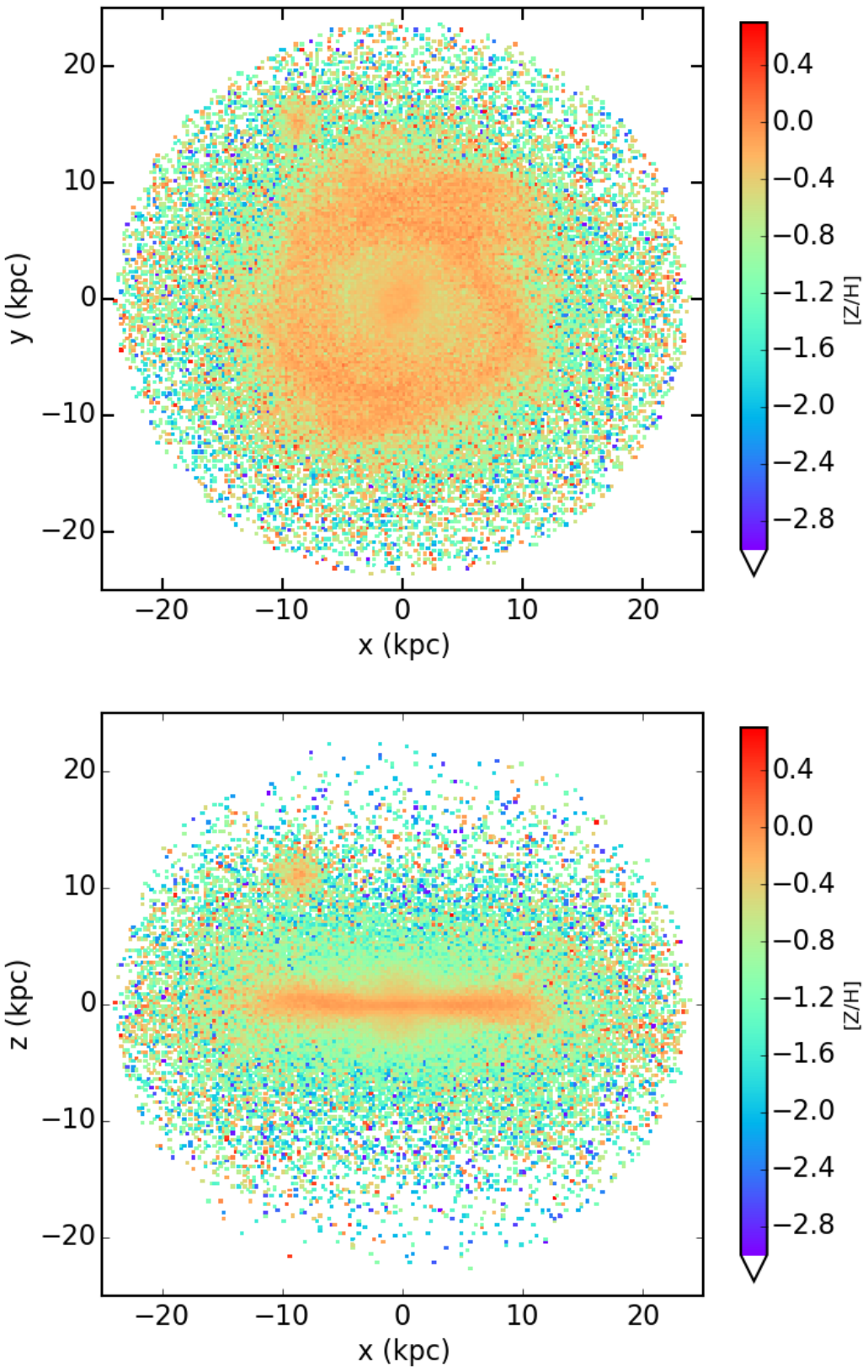

Figure 8.11: Face-on (top panel) and edge-on (bottom panel) binned distributions of all the star particles located within the galactic radius for the AqC5–fid galaxy simulation. Plots are shown at redshift $z = 0$; the colour encodes the mean $[Z/H]$ of the star particles in the bin.

remarkably similar. I indeed find that stars at a given distance from the galaxy centre share a considerably comparable MDF, regardless of their exact position angle on the galactic plane. The stellar chemical homogeneity is preserved when considering stars located within a torus and when we marginally increase or decrease the distance of the volume where we carry out the analysis from the galaxy centre on the galactic plane. Thus, my model predicts that chemical features of stars observed in the solar neighbourhood are likely shared by stars on the Galactic plane at a similar distance from the MW centre, and to some extent by stars beyond the conventional extension of the solar neighbourhood.

8.6.2 Comparison with results from the GCS

I outlined in Section 8.4 the reasons that led me to choose the GCS for the comparison with observational data. I want here to stress that the comparison between my results and observational findings is not meant to validate my method. The simulated galaxy is not indeed a model for the MW. Also, different results are found from different observational star catalogues, as we discuss in Section 8.6.3, and marginally contrasting conclusions can be drawn when peculiar sample selection effects affect different data sets. I rather selected one survey among the many others in order to show how the features of the observational sample one wants to compare with enter the procedure we developed. One could mimic observational selection effects so as to overcome biases intrinsic to a survey, but this is beyond the scope of the present work.

There are several interesting features that the star sample that I produced shares with stars in the GCS composing the *irfm* sample. The mass-metallicity distribution of both the present study and the GCS is characterised by high-metallicity stars spreading throughout the complete mass range, whereas lower metallicity stars are mainly old stars and some intermediate-age stars. Making a direct comparison between values of metallicity is difficult, since I analyse the metal content of stars in terms of $[Z/H]$, while they consider both the mass- and age-metallicity distribution in terms of $[Fe/H]$. Translating one quantity into the other is not straightforward for stars of different age.

As for the AMD, I find that my star sample shares the same trend as in observations. Young and intermediate stars have, on average, a higher metal content than older ones. Also, the metallicity distribution progressively narrows when moving from old to younger stars.

Albeit Casagrande et al. (2011) do not provide us with the exact number of stars that make up each of the three subsamples, by analysing the normalised age probability distribution for all the stars in their catalogue it is possible to see that the intermediate star sample is the one that by far contributes the most (see their Figure 13). This feature is shared with our reference star catalogue, where stars having age in the range $1 - 5$ Gyr are 4389 out of 6670. Contributions to the catalogue from young and old stars follow, thus in keeping with the GCS data set.

I have already discussed the MDF of my star sample in comparison with the one of Casagrande et al. (2011) in Sections 8.5 and 8.6.1 (see Figure 8.7). Here I note that Nordström et al. (2004) found a mean of $[Z/H] = -0.14$ for the MDF of stars in the GCS, and a dispersion of 0.19 dex around the mean: therefore, the mean of the MDF can vary by more than 0.1 dex when different authors analyse slightly different subsamples of the same survey, by assuming their own calibrations for physical properties. By further investigating the role of subsamples of different age in the MDF, I notice that I have a negligible contribution by old stars to the metal-rich wing of the MDF (see Figure 8.8). The MDFs of young and intermediate-age stars roughly overlap in our sample for $-0.1 \leq [Z/H] \leq 0.3$. The distribution of intermediate-age stars extends toward lower metallicity down to $[Z/H] \sim -1.3$ and toward higher metallicity to $[Z/H] \sim 0.7$, whereas the metallicity of young stars covers the range $-0.5 \leq [Z/H] \leq 0.7$ and has a super-solar mean due to recent star formation. Young stars in the GCS sample have a much narrower distribution than intermediate stars: still, the comparison is not trivial being the split MDF analysed only in term of $[Fe/H]$ in Casagrande et al. (2011).

When performing the analysis presented in this work, I did not tune any parameter of our cosmological hydrodynamical simulation in order to attempt to match observational findings. As for the simulation AqC5-3sIMF I stress here that, in contrast with the tension between the predicted MDF and the one observed in the GCS (see Figure 8.7), I found a good agreement between observations and our results concerning both radial abundance gradients in the gas of this galaxy and different metal abundances in stars (as discussed in Chapter 7).

8.6.3 Comparison with the MDF of other surveys

Stars in the *irfm* sample of the GCS have a comparable MDF in terms of $[Z/H]$ and $[Fe/H]$. The former is characterised by the following values for the mean, the median, and the full width at half maximum (FWHM): -0.02, -0.01, and 0.34, respectively. The latter has a mean $[Fe/H] = -0.06$, a median value of -0.05, and the FWHM is 0.38.

Other authors have investigated the MDF of different samples of nearby stars in the MW. Results are usually shown in terms of $[Fe/H]$, being the oxygen abundance (oxygen is the most common metal and an accurate tracer of the total metallicity) difficult to retrieve (see e.g. Cayrel et al., 2004). For instance, Gilmore et al. (1995) investigated the $[Fe/H]$ distribution for a sample of stars located in the thick disc of MW, finding that it peaks at -0.7 dex. Studies by Rocha-Pinto & Maciel (e.g. 1996, 1998), Favata et al. (1997), and Holmberg et al. (2007) agree on a $[Fe/H]$ distribution peaking around $-0.2 \div -0.3$.

A slightly sub-solar value for the mean of the MDF is supported by studies of e.g. Haywood (2001) and Taylor & Croxall (2005); for instance, Allende Prieto et al. (2004) found that luminous stars within 15 pc from the Sun in their sample have a $[Fe/H]$ distribution with a mean $[Fe/H] = -0.11$, the standard deviation

being ~ 0.2 dex. On the other hand, investigations by e.g. Luck & Heiter (2006) confirm a marginally super-solar peak value of the MDF. Reasons why different results are found are claimed to be due to systematic errors, different calibrations especially in the effective temperature of stars, sample selection effects.

As for more recent results, the MDF of stars of the AMBRE Project (de Laverny et al., 2013) located in the thin disc of the MW spans the range $-0.5 \lesssim [Fe/H] \lesssim 0.5$, the mean value being roughly solar; stars in this survey located in the thick disc have $-1 \lesssim [Fe/H] \lesssim -0.2$, and a $[Fe/H] \simeq -0.5$ mean value (see Grisoni et al., 2017, for instance). However, if stars with high metallicity and high α-elements are included when considering stars in the thick disc (the AMBRE Project considers these components separately), the MDF peaks around a $[Fe/H]$ value that is slightly sub-solar.

8.7 Summary and Conclusions

In this Chapter I have introduced a novel approach to link star particles in simulations with observed stars. The key goal of this new method is to compare as fairly as possible the outcome of cosmological simulations, that provide a coarse sampling of stellar populations by means of star particles corresponding to simple stellar populations (SSPs), with observations, that explicitly resolve single stars within stellar populations. The procedure that I have developed consists in populating star particles with stars, according to input properties that star particles consistently inherit from a cosmological simulation. In this way, it is possible to bridge the gap between the mass resolution of state-of-the-art cosmological simulations, with star particles that have a typical mass ranging between $\sim 10^8$ and $\sim 10^3$ $M_\odot$, and the mass suitable for an appropriate comparison with observations of single stars. Features of parent star particles such as mass, position, and their age-metallicity distribution are supplied to a code named TRILEGAL, along with an IMF. TRILEGAL then generates a catalogue of stars that share properties with their parent population and that have a mass ranging between ~ 0.5 and few $M_\odot$. Also, stars are provided with photometric properties, so that I know their absolute magnitude and can retrieve their apparent magnitude in different bands.

I focused on a possible application of this new approach: I simulated the observable stellar content of a volume that is comparable to the solar neighbourhood of the Milky Way (MW). First, I carried out a cosmological hydrodynamical simulation of a disc galaxy and selected star particles located within a sphere around the galactic plane, ~ 8 kpc far from the galaxy centre. This region can be approximately deemed as a representation of the solar neighbourhood. I then provided the TRILEGAL code with properties of these parent star particles, and it generated a catalogue of mock stars. I conceived a procedure to select generated stars in order to match the main observational constraints of one of the survey, namely the Geneva-Copenhagen Survey (GCS), that recently collected informations of several thousands of nearby stars, deriving accurate determinations of their physical properties.

The most relevant results of this Chapter can be summarised as follows.

- I constructed and presented colour-absolute magnitude and colour-apparent magnitude diagrams for mock stars in the sample, showing the observational features that stars originated from selected star particles in a cosmological simulation would have (Section 8.5.1).
- I investigated the age-metallicity distribution for this mock star sample. I find that young and intermediate-age stars are characterised, on average, by a higher metal content than old stars. Moreover, old stars have a spread in metallicity that is remarkably wider (~ 2.5 dex) than younger stars (~ 1.5 dex), and the metallicity distribution progressively narrows towards the youngest ones, thus in keeping with indications from observational data.
- As for the mass-metallicity distribution, I find that stars tend to move towards smaller masses and lower metallicities as the stellar age increases, in agreement with observations. Also, I successfully generated a wide spectrum of low- and intermediate-mass stars. The bulk of stars in my sample have a mass ranging between 0.6 $M_\odot$ and 1.5 $M_\odot$, their mass never being larger than 7 $M_\odot$. Stellar mass distribution is more clustered as one moves from young to intermediate-age to old stars, only few old stars being more massive than 1 $M_\odot$ (Section 8.5.2).
- I examined the metallicity distribution function (MDF) of stars in three different cosmological simulations that I carried out: the considered star samples represent the observable stellar content of three solar neighbourhood-like volumes. I compared my predictions with chemical properties of stars in the solar neighbourhood in the GCS, whose MDF has a slightly sub-solar mean value of $[Z/H] = -0.02$ (Casagrande et al., 2011). The MDF of the star catalogue of my reference simulation AqC5–fid has a mean $[Z/H] = 0.04$, that is in good agreement with observations. The means of the two distributions differ by only 0.06 dex, such difference implying that stars of my sample are on average richer in metals than observed ones by $\sim 15\%$. The considered star sample of AqC5–fid is characterised by a low-metallicity tail that is more extended than the MDF of the GCS, and that is mainly populated by old stars. My results are in keeping with observations, the peaks of the two MDFs perfectly overlapping and pinpointing a solar metallicity. I also consider the MDFs of synthetic star catalogues in simulations AqC5–cone and AqC5–3sIMF. Stars in AqC5–cone have a MDF with slightly super-solar median and an excess of metal-rich stars, due to the moderate low-redshift star formation rate, that further enriches in metals outer regions of the galaxy disc. As for the simulation AqC5–3sIMF, characterised by a Kroupa IMF with a third slope limiting the number of massive stars, the peak of the MDF is subsolar (mean $[Z/H] = -0.53$). The comparison with the GCS suggests that stars in the solar neighbourhood are metal richer than those in AqC5–3sIMF by a factor of ~ 2.5. A straightforward comparison between predicted and observed MDFs can be however not trivial, because of sample selection effects that affect observational data sets. When slicing my star samples into different subsamples according to stellar age, I find that old stars are responsible for the low-metallicity tail of the MDF, in agreement with observations.

- Properties of stars that are originated from star particles in marginally different regions of the simulated galaxy are remarkably similar. Stars at fixed distance from the galaxy centre are characterised by comparable MDFs, despite their exact position angle on the galactic plane. Also, I find that stars within volumes centred at marginally different distances (i.e. within 1 kpc, on the galactic plane) from the galaxy centre with respect to the reference $r_{\rm Sun}$ share very similr MDFs. A natural prediction of this investigation is that chemical properties of stars observed in the solar neighbourhood are typical of MW stars at a similar distance from our Galaxy centre. Moreover, chemical features of nearby stars are shared to some extent by stars beyond the conventional extension of the solar neighbourhood (Section 8.6.1).

In the present work I explored the feasibility of the approach I have developed and I showed its capabilities and possible applications. Its ultimate goal is to introduce a new technique that allows us to perform a comparison as accurate as possible between simulation output and observations of stars. This method is versatile and can be tailored to fit output of different particle based codes. I envisage that it will have interesting applications when comparing simulations of galaxy formation, reaching an ever increasing resolution, with ongoing and future survey data releases, such as Gaia-ESO and especially GAIA.

Here I would like to highlight another possible future application of this tool. Cosmological simulations allow us to identify peculiar classes of stars at different redshifts, during the formation of a galaxy. For instance, stars belonging to substructures of the galaxy disc or halo, to captured or destroyed stellar satellites, or stars being members of stellar streams: these stars likely have chemical features and patterns that are different from the ones shared by the bulk of stars in a component of the galaxy, since they did not take part to the general galaxy evolutionary path. These stars can be tracked during the simulation. In this way, it could be interesting to construct the CMDs of stars that have had a unique life. Therefore, the approach that I have conceived can have a significant comparative and predictive power. Also, it could be used to evaluate selection effects and sample completeness of observed catalogues.

Another possible interesting direction of future investigation will be to predict properties of stars with distinguishing chemical features and to compare predictions from hydrodynamical models with data: for instance, we can study peculiar classes of stars by selecting generated stars according to physical criteria (e.g. surface gravity) that different tracers of stellar populations (e.g. AGB stars, horizontal branch stars, dwarf stars, variable stars) meet. Also, we could select star particles according to chemical properties on the age-metallicity relation plane, thus identifying parent particles of peculiar stars, and then retrieve information on their evolution and past history.

9

AGN feedback in simulations of disc galaxies

The role of AGN feedback is fundamental in regulating the formation and evolution of galaxies. The properties of the ISM surrounding SMBHs (supermassive black holes) in the centre of galaxies, galaxy groups and clusters are thought to regulate the BH feeding. Also, the presence of a multiphase medium in the innermost regions of cosmic structures poses a challenging question: how different gas phases experience AGN feedback?

In this Chapter, I describe how I introduced BHs and the ensuing AGN feedback in the simulations setup presented in Chapter 5. This Chapter aims at investigating the interaction between the central SMBH and the various gas phases which coexist in the ISM of the host galaxy, focussing on late-type galaxies.

The key questions that I want to address in this Chapter are the following: how do accreting BHs transfer feedback energy to the surrounding ISM? How do they determine the properties of their host galaxy? How do different models and regimes of gas accretion affect the BH-galaxy coevolution? Does AGN feedback affect significantly the circulation of heavy elements within the galaxy?

This Chapter is organised as follows. In Section 9.1, I outline the context in which the work presented in this Chapter fits, from a numerical perspective. Section 9.2 is devoted to introduce the AGN feedback model that I implemented within the code and the sub-resolution model adopted for cosmological simulations. In Section 9.3,

I introduce the suite of simulations that I carried out, and in Section 9.4 I present and discuss results. The main conclusions are drawn in Section 9.5.

The results presented in this Chapter will be extensively described in the paper Valentini et al., in preparation.

Contents

9.1 AGN feedback in cosmological simulations

Simulations that model structure formation and evolution in a cosmological context have to take into account the effect of AGN. Indeed, nuclear galactic activity has been deemed fundamental to simulate structures whose properties are in agreement with observations at different redshifts (see also Sections 2.4.5 and 3.2).

In particular, AGN feedback is of crucial importance in regulating cooling and star formation in galaxies across cosmic time (see Section 2.4.5). AGNs can have both a positive and a negative impact on the star formation of their hosts. They can stimulate some degree of cooling, enhancing the star formation (the so-called positive feedback), or they can produce an overall heating of the system, ultimately quenching the formation of stars (e.g. Peterson & Fabian, 2006; McNamara & Nulsen, 2007; McNamara et al., 2016). The relative importance of these processes is still under debate.

In recent years, a wealth of multiwavelength observations has revealed the presence of gas spanning a wide range of densities, temperatures, and ionisation states in and around galaxies. This multiphase gas is ubiquitous not only in spiral

galaxies, commonly recognised as systems rich in cold gas, but also in ellipticals and in the innermost regions of galaxy groups and clusters, environments commonly known to be dominated by X-ray emitting, hot gas (e.g. Werner et al., 2014; David et al., 2014). This multiphase component has been observed to be present also in galactic-scale outflows, which represent one of the most characteristic imprints of AGN presence in a system (e.g. Chartas et al., 2003; Rupke & Veilleux, 2011; Cicone et al., 2014; Feruglio et al., 2015; Tombesi et al., 2015; Morganti et al., 2016).

Multiphase outflows powered by AGNs are a direct consequence of the fact that the energy generated by the accreting SMBH is coupled to the surrounding ISM in what is commonly referred to as AGN feedback. As it is unlikely that outflowing cold gas is the result of entrainment by a hot gas phase outflow, the AGN feedback energy has to be transferred to both the diffuse and cold phases. This complex process is still far from being fully understood, and thus an accurate modelling in cosmological hydrodynamical simulations is still missing.

Another key point which is under debate is the best way to capture an effective description of AGN feeding and feedback in cosmological simulations. Both the mechanism through which the gas is accreted onto the SMBH and the way of releasing energy are burning issues. As for AGN feedback, the commonly pursued approaches consist in providing the feedback energy to the surrounding medium in the form of thermal or kinetic energy (e.g. Springel et al., 2005b; Sijacki et al., 2007; Dubois et al., 2010), or with a combination of the two (and a discussion similar to that about stellar feedback in Section 3.4 holds). The recently pursued direction of investigation aims at simulating the effect of the radiative power of the AGN via the injection of thermal energy, while modelling the outcome of the mechanical power of the AGN by means of outflows in the form of kinetic feedback (e.g. Steinborn et al., 2015; Barai et al., 2016; Weinberger et al., 2017, and references therein).

As for AGN feeding, the most common way to model gas accretion onto SMBHs is to assume the Bondi accretion (see Section 9.2.2 for details). However, due to the inability of resolving the Bondi radius in cosmological hydrodynamical simulations, the estimate of the Bondi accretion needs to be done by sampling gas properties over quite large volumes in the proximity of the BH. Indeed, so as to resolve the Bondi accretion, the Bondi radius $r_{\rm B} = G\,M_{\rm BH}/c_{\rm s}^2 \sim 0.04\,(M_{\rm BH}/10^6\,{\rm M}_\odot)\,(c_{\rm s}/10\,{\rm km\ s^{-1}})^{-2}$ kpc, where G, $M_{\rm BH}$, and $c_{\rm s}$ are the gravitational constant, the BH mass and the sound speed of the ambient gas, respectively, needs to be resolved (Edgar, 2004; Booth & Schaye, 2009); on the other hand, cosmological simulations generally have spatial resolutions spanning from few kpc down to few hundreds of pc. As a consequence, gas density results to be underestimated, while gas temperature is overestimated. This leads to an underestimation of the accretion rate, that is commonly boosted in order to have an effective AGN feedback and to match the observations (Di Matteo et al., 2005; Booth & Schaye, 2009; Negri & Volonteri, 2017). Moreover, cold gas that accretes onto SMBHs is expected to deviate considerably from the idealised Bondi assumptions (e.g. Gaspari et al., 2013, and Section 9.2.3).

In addition to this, further uncertainties, such as those coming from the prescriptions for seeding BHs at high redshift within simulations (see Section 9.2.1), enter in the physical description and the numerical modelling of AGN feedback. This framework opens to new challenging tasks.

As this Thesis is focused on late-type galaxies, I will introduce my AGN feedback model and explore how it works within the scenario of disc galaxy formation and evolution, that has been extensively studied in previous Chapters. The investigation of the effect of AGN feedback in elliptical galaxies is postponed to a forthcoming work (see also Section 9.5).

9.2 AGN feedback modelling

In this Section, I describe in detail the AGN feedback model that I adopt to carry out the simulations whose results are presented in this Chapter. BH accretion and ensuing feedback are modelled resorting to sub-resolution prescriptions, as for star formation and stellar feedback (see Section 5.3).

While the prescriptions adopted for BH seeding and accretion are predominantly based, despite a number of differences that are detailed in the following, on the original model by Springel et al. (2005b) and largely inherited from simulations of galaxy clusters (e.g. Fabjan et al., 2010; Ragone-Figueroa et al., 2013; Rasia et al., 2015), the modelling of the release of AGN feedback energy is original.

In particular, since the sub-resolution model MUPPI describes a multiphase ISM, I exploit this feature in order to study the coupling of AGN feedback energy to different phases of the ISM over cosmic time. This has been achieved for the first time in cosmological hydrodynamical simulations. In what follows, I describe the implementation of AGN feedback that I have included within the simulations setup outlined in Chapter 5.

I devoted a great effort to implement this original AGN feedback model within the code that I use to carry out my simulations. The implementation has required to write large sections of the code, to heavily modify several key modules, and to perform a large number of test runs to validate the code and assess its performance.

9.2.1 Introducing BHs: seeding and pinning

BHs in cosmological hydrodynamical simulations are represented by means of collisionless sink particles[1] of mass $M_{\rm BH}$. The commonly quoted mass $M_{\rm BH}$ is the *theoretical mass* of the BH, modelled at the sub-resolution level (as opposite

[1]Sink particles are particles that can absorb neighbour particles, and that are commonly implemented to allow the removal of other particles from their surroundings. They have been introduced to numerically deal with collapsing regions and to avoid spurious effects due to a considerable increase of mass density (e.g. Bate et al., 1995).

to its *dynamical* mass, that is the actual gravitational mass of the BH particle in the simulation, see Section 9.2.2).

BH particles are introduced in massive haloes at relatively high-redshift in cosmological simulations, and they are then allowed to grow and increase their initial or *seed* mass. As we are still lacking a solid understanding of the formation scenario of first SMBHs (see Volonteri & Bellovary, 2012, for a review), BHs are first inserted according to the so-called seeding prescriptions.

In the simulations presented in this Chapter, a BH of mass $M_{\rm BH,\,seed}$ is seeded within DM haloes whose mass exceeds the threshold mass $M_{\rm DM,thresh}$, and that do not already have a BH. I adopt $M_{\rm BH,\,seed} = 1.1{\cdot}10^5$ M$_\odot$ and $M_{\rm DM,thresh} = 1.7{\cdot}10^{10}$ M$_\odot$ for the fiducial simulations (see Table 9.1 and Section 9.3). Also, the eligible DM halo is required to have a minimum stellar mass fraction ($f_{\star,\,\rm seed} = 0.02$) for BH seeding. The latter requirement ensures that BHs are seeded only within haloes that host adequately resolved proto-galaxies (Hirschmann et al., 2014).

DM haloes are identified by means of the Friends-of-Friends (FoF) algorithm[2]. The FoF is performed on DM particles alone, and a linking length of 0.16 times the mean inter-particle spacing is adopted.

To achieve an accurate centering of the BH particle in the pinpointed halo, the BH is seeded in the position of the minimum potential of the halo, by identifying the star particle which has the highest binding energy. The selected star particle is thus converted into a BH sink particle of (theoretical) mass $M_{\rm BH,\,seed}$.

The location of the BH is crucial to determine physical properties of the gas that undergoes accretion and to compute quantities involved in the ensuing feedback. In simulations, BHs can generally move away from the innermost regions of the forming galaxy and wander becuse of numerical artefacts (Wurster & Thacker, 2013): indeed, they can be dragged by surrounding particles, especially in highly-dynamical, high-redshift environments. Also, the dynamical friction that is expected to promote the settling of massive BHs in the centre of halos usually is not adequately captured at the resolution achieved in cosmological simulations (Weinberger et al., 2017). In order to avoid the fact that BHs move from the centre of the halo in which they reside because of numerical spurious effects, the BH is re-positioned on the minimum of the gravitational potential. To this end, at each time-step the BH is shifted towards the position of the particle (DM, stellar or gas particle) with the absolute minimum value of the local gravitational potential within the gravitational softening of the BH (as done, among others, by Ragone-Figueroa et al., 2013; Schaye et al., 2015; Weinberger et al., 2017; Barai et al., 2018; Pillepich et al., 2018).

[2]A Friends-of-Friends (FoF) algorithm (Davis et al., 1985) is a numerical technique to group particles that are closer together than a threshold, the so-called *linking length*, that is usually expressed in terms of the mean inter-particle separation. Particles identified are considered to belong to the same structure. This method is commonly employed in numerical simulations as a halo finder, to identify bound structures based on particle proximity.

Table 9.1: Relevant parameters of the AGN model.
Column 1: BH seed mass in the reference simulations. *Column 2:* halo mass for BH seeding. *Column 3:* minimum stellar mass fraction for BH seeding. *Column 4:* threshold temperature to distinguish between hot and cold accreting gas. *Column 5:* radiative efficiency. *Column 6:* feedback efficiency. *Column 7:* reference value for the parameter regulating the angular momentum dependent accretion of cold gas.

$M_{\rm BH,\,seed}$ ($\rm M_\odot$)	$M_{\rm DM,\,thresh}$ ($\rm M_\odot$)	$f_{\star,\,\rm seed}$	$T_{\rm split}$ (K)	$\epsilon_{\rm r}$	$\epsilon_{\rm f}$	$C_{\rm visc}$
$1.1 \cdot 10^5$	$1.7 \cdot 10^{10}$	0.02	$5 \cdot 10^5$	0.1	0.01	$2\,\pi$

9.2.2 AGN feeding

BHs grow because of gas accretion and mergers with other BHs.

Gas accretion onto the central BH is commonly modelled through the Bondi-Hoyle-Lyttleton accretion solution (Hoyle & Lyttleton, 1939; Bondi & Hoyle, 1944; Bondi, 1952). The Bondi accretion rate reads:

$$\dot{M}_{\rm B} = \frac{4\,\pi\,\lambda\,G^2\,M_{\rm BH}^2\,\rho_\infty}{c_{\rm s,\,\infty}^3}\ , \tag{9.1}$$

where G is the gravitational constant, and λ is a dimensionless parameter of order unity, that is a function of the adiabatic index γ. In equation (9.1), ρ_∞ and $c_{\rm s,\,\infty}$ are the density and the sound speed of the gas, respectively, evaluated at very large distance (formally infinity) from the accreting BH, where the gas is also supposed to be at rest.

Following Springel et al. (2005b), the Bondi-like BH accretion rate is numerically estimated as:

$$\dot{M}_{\rm B} = \frac{4\,\pi\,G^2\,M_{\rm BH}^2\,\langle\rho\rangle}{(\langle c_{\rm s}\rangle^2 + \langle v\rangle^2)^{3/2}}\ , \tag{9.2}$$

where the density of the gas ρ, its sound speed $c_{\rm s}$, and the velocity v of the BH relative to the gas is computed by averaging over SPH quantities of the gas particles within the smoothing length of the BH, with kernel-weighted contributions. I do not assume any boost factor, neither for the hot nor for the cold gas accretion. Extensive tests have shown that the BHs in the simulations that I will present in Section 9.4 grow to masses that are in agreement with observations without the need for boosting the accretion. Rather, I will explore the possibility to accrete cold gas only, thus neglecting hot gas accretion, as discussed in Section 9.3.

Although the smoothing length usually pertains only to gas particles, a smoothing length for the BH particle is generally defined to estimate hydrodynamical quantities in the proximity of the BH. In analogy to gas particles, the mass within the sphere whose radius is the BH smoothing length $h_{\rm i}$ is required to be constant (and equal to that enclosed within the gas particles' smoothing sphere).

As suggested by Steinborn et al. (2015), gas accretion is estimated by considering separately hot and cold gas. The temperature $T_{\rm split} = 5 \cdot 10^5$ K is assumed to distinguish between hot and cold accreting gas. The accretion rates for the hot and cold phases are thus computed according to equation (9.2), and $\dot{M}_{\rm B,\,h}$ and $\dot{M}_{\rm B,\,c}$ are estimated.

The accretion rate cannot exceed the Eddington accretion rate:

$$\dot{M}_{\rm Edd} = \frac{4\,\pi\,G\,M_{\rm BH}\,m_{\rm p}}{\epsilon_{\rm r}\,\sigma_{\rm T}\,c} \quad , \tag{9.3}$$

where $m_{\rm p}$, $\sigma_{\rm T}$, and c are the proton mass, the Thompson cross-section, and the speed of light, respectively, and $\epsilon_{\rm r}$ is the radiative efficiency. As for the radiative efficiency, I adopt a constant value $\epsilon_{\rm r} = 0.1$ (see also Table 9.1), which corresponds to the mean value for the radiatively efficient accretion onto a Schwarzschild BH (Shakura & Sunyaev, 1973).

Therefore, the accretion rate of the BH is given by the sum of both hot and cold gas accretion, and is capped to the Eddington accretion rate, i.e.:

$$\dot{M}_{\rm BH} = \min(\dot{M}_{\rm B,\,h} + \dot{M}_{\rm B,\,c}, \dot{M}_{\rm Edd}) \quad . \tag{9.4}$$

Computing a separated accretion rate for hot and cold gas drives a faster BH growth during the quasar mode (see Section 2.4.5) of AGNs, when they are expected to be surrounded mainly by cold gas. Indeed, averaging velocities and sound speeds of (almost completely) cold gas and hot gas separately leads to a higher estimate for $\dot{M}_{\rm B}$ in equation (9.2) (Steinborn et al., 2015).

Gas accretion is modelled according to the stochastic scheme originally proposed by Springel et al. (2005b). Should the theoretical mass of the BH exceed the dynamical one, the BH can absorb gas particles. Each BH neighbouring gas particle has a probability to be swallowed, which is proportional to the difference between the theoretical and dynamical mass of the BH over the kernel-smoothed mass of the gas particle itself. The original model was marginally modified in order to achieve a more continuous sampling of the accretion process: each selected gas particle contributes to BH feeding with a fraction of its mass (Fabjan et al., 2010; Hirschmann et al., 2014). In this way, a larger number of gas particles are involved in sampling the accretion and selected gas particles are not always swallowed, their mass being rather decreased. I assume a value of 1/4 for the slice of the gas particle mass to be accreted.

The stochastic accretion scheme determines the increase of the dynamical mass of the BH. On the other hand, the sub-resolution continuous increase of the theoretical mass of the BH is smooth and computed according to equation (9.2). The accurate numerical description of the accretion process ensures that the increase of the dynamical mass faithfully reproduces that of the theoretical mass, with marginal fluctuations around it.

As for BH merging which contributes to BH growth, two BHs are merged whenever their distance is smaller than twice their gravitational softening length,

and if their relative velocity is smaller than a fraction (assumed to be 0.5) of the sound speed of the surrounding gas (i.e. the average of the sound speed of gas particles within the smoothing length of the BH, with kernel-weighted contributions). The resulting BH is located at the position of the most massive one between the two BHs that undergo merging[3].

9.2.3 Controlling BH accretion

The Bondi model for gas accretion onto BHs relies, among others, on the assumptions of spherical simmetry and of zero angular momentum for the inflowing gas. However, accreting gas does have some angular momentum: therefore, it settles onto a circular orbit whose radius is determined by its angular momentum, and the accretion proceeds through an accretion disc (King, 2010; Hobbs et al., 2011). This is especially true for cold gas, that is expected to depart significantly from the Bondi assumptions because of cooling and turbulence (Booth & Schaye, 2009; Gaspari et al., 2012, 2013, 2015, and Section 9.1). The angular momentum represents a natural barrier to accretion: as a consequence, only gas with the lowest angular momentum is effectively accreted and feeds the BHs (Power et al., 2011).

For this reason, I consider the possibility of reducing the gas accretion onto the central BH for gas which has a high angular momentum. To this end, our implementation of BH feeding allows to adopt an angular momentum dependent accretion rate for the cold gas, following the phenomenological correction introduced by Rosas-Guevara et al. (2015) and also adopted by Schaye et al. (2015). Note that the limiter to the gas accretion reduces the overall BH accretion rate in Rosas-Guevara et al. (2015); Schaye et al. (2015), as they do not distinguish between hot and cold gas accretion. On the other hand (see Section 9.2.2), I prefer to limit only cold gas accretion, for the reasons outlined above. Also, as I will extensively discuss in Section 9.4.7, properties of the warm and cold ISM are expected to crucially impact on the evolution of the accretion rate of SMBHs in the centre of late-type galaxies, where cold gas is rotationally supported.

When I suppress the BH accretion rate according to the angular momentum of the cold gas, the contribution to the BH accretion rate from the cold gas (entering in equation (9.9)) reads:

$$\dot{M}_{\mathrm{B,c}} = \dot{M}_{\mathrm{B,c}} \cdot \min(1, \mathcal{L}_{\mathrm{AM}}) \ , \tag{9.5}$$

where $\mathcal{L}_{\mathrm{AM}}$ is the BH accretion rate limiter, i.e.:

$$\mathcal{L}_{\mathrm{AM}} = \frac{1}{C_{\mathrm{visc}}} \left(\frac{c_{\mathrm{s,c}}}{V_{\phi}} \right)^3 \ . \tag{9.6}$$

[3]This scheme for repositioning the merged BH leads to a violation of the momentum conservation law (see e.g. Hirschmann et al., 2014).

In equation (9.6), $C_{\rm visc}$ is a constant parameter (see below), $c_{\rm s,\,c}$ is the sound speed of the cold ($T < T_{\rm split} = 5{\cdot}10^5$ K, see Section 9.2.2) gas, and V_ϕ is the rotational velocity of the cold gas surrounding the BH, that can be cast as (Rosas-Guevara et al., 2015):

$$V_\phi = \left| \sum_{\rm i=0}^{N_{\rm ngb}} \mathbf{x}_{\rm i} \times \mathbf{v}_{\rm i}\, m_{\rm i}\, W(x_{\rm i}, h)\, \frac{1}{\rho_{\rm c}\, h} \right| \ . \tag{9.7}$$

In equation (9.7), $W(x_{\rm i}, h)$ is the smoothing kernel (see Section 5.2), h is the smoothing length of the BH, and the sum spreads over the BH neighbour gas particles whose position with respect to the BH is $\mathbf{x}_{\rm i}$ and whose velocity is $\mathbf{v}_{\rm i}$. Also, $\rho_{\rm c}$ is the smoothed density of the cold gas surrounding the BH. Note that only gas particles whose SPH temperature is lower than $T_{\rm split} = 5 \cdot 10^5$ K (see Section 9.2.2) enter in the computation of equation (9.7).

$C_{\rm visc}$ is a constant parameter that has been introduced to parametrise at the sub-resolution level the viscosity of the accretion disc (see Section 9.4.7, and Rosas-Guevara et al., 2015, for further details). This parameter regulates how the BH accretion rate is sensitive to the angular momentum of the accreting gas.

As a consequence, the limiter to the cold gas accretion rate is switched off unless $C_{\rm visc}^{1/3}\, V_\phi > c_{\rm s,\,c}$. I adopt $C_{\rm visc}/2\,\pi = 1,\ 10^2,\ 10^3$ (as suggested by Schaye et al., 2015, see also Table 9.1). In Section 9.4.7, I will discuss how variations of this parameter impact on final results. Note that the suppression of the accretion rate is controlled by the ratio $V_\phi / c_{\rm s,\,c}$ (see also Rosas-Guevara et al., 2015).

9.2.4 AGN feedback

Each BH radiates away a small part $\epsilon_{\rm r}$ of its accreted rest-mass energy. Its bolometric luminosity can be thus cast as:

$$L_{\rm r} = \epsilon_{\rm r}\, \dot{M}_{\rm BH}\, c^2 \ . \tag{9.8}$$

A tiny fraction of the radiated luminosity $L_{\rm r}$ is provided to the ISM in the form of AGN feedback energy, so that the feedback energy per unit time is:

$$\dot{E}_{\rm fb,tot}^{\rm AGN} = \epsilon_{\rm f}\, L_{\rm r} = \epsilon_{\rm f}\, \epsilon_{\rm r}\, \dot{M}_{\rm BH}\, c^2 \ , \tag{9.9}$$

where $\epsilon_{\rm f}$ is the feedback efficiency, quantifying the radiated luminosity that is actually coupled to the surrounding gas. I assume $\epsilon_{\rm f} = 0.01$ in all the simulations presented in this Chapter (see also Table 9.1). This AGN feedback energy is coupled thermally and isotropically to the BH neighbouring gas particles, as detailed in Section 9.2.5.

The rate of total AGN feedback energy $\dot{E}_{\rm fb,tot}^{\rm AGN}$ available is distributed to all gas particles within the smoothing kernel of the BH, and kernel-weighted contributions are assigned to both single-phase and multiphase particles. The rate of AGN feedback energy pertaining to each considered particle is $\dot{E}_{\rm fb}^{\rm AGN}$.

For single-phase particles, the AGN feedback energy received in the SPH time-step is a source term contributing to the heating rate: it enters the right-hand side of

equation (4.11), as discussed in Section 4.2. AGN feedback energy is therefore used to increase their specific internal energy, and hence their entropy (see Section 5.1).

Multiphase particles selected to receive feedback energy pose a challenging question: how does AGN feedback energy couple to the different components of a multiphase ISM? In Section 9.2.5, I introduce a model that allows to investigate this issue.

9.2.5 Including AGN feedback within MUPPI

The sub-resolution model MUPPI accounts for the evolution of multiphase particles that have been provided with AGN feedback energy. In particular, I consider that a fraction $\mathcal{A}_\mathrm{h}$ of the rate of feedback energy $\dot{E}_\mathrm{fb}^\mathrm{AGN}$ is coupled with the hot phase of each multiphase particle, while the remaining fraction $\mathcal{A}_\mathrm{c} = 1 - \mathcal{A}_\mathrm{h}$ of the energy budget per unit time is supplied to the cold component. The values and modelling of $\mathcal{A}_\mathrm{h}$ and $\mathcal{A}_\mathrm{c}$ are extensively discussed in Section 9.2.6. In this way, the feedback energy per unit time available to the hot phase is:

$$\dot{E}_\mathrm{h}^\mathrm{AGN} = \mathcal{A}_\mathrm{h}\, \dot{E}_\mathrm{fb}^\mathrm{AGN} \quad , \tag{9.10}$$

while the rate of feedback energy of the cold phase is:

$$\dot{E}_\mathrm{c}^\mathrm{AGN} = \mathcal{A}_\mathrm{c}\, \dot{E}_\mathrm{fb}^\mathrm{AGN} \quad . \tag{9.11}$$

The energy contributions $E_\mathrm{h}^\mathrm{AGN}$ and $E_\mathrm{c}^\mathrm{AGN}$ corresponding to equations (9.10) and (9.11) are used as follows: the AGN feedback energy $E_\mathrm{h}^\mathrm{AGN}$ provided to the hot gas is used to increase its temperature T_h. On the other hand, the AGN feedback energy $E_\mathrm{c}^\mathrm{AGN}$ coupled to the cold phase is employed to bring cold gas mass to the hot phase. As a consequence, the initial mass of cold gas M_c of the multiphase particle (whose temperature remains fixed at $T_\mathrm{c} = 300$ K, see Section 5.3) is progressively eroded because of the effect of AGN.

When the effect of AGN feedback is included within the sub-resolution model MUPPI, the following set of ordinary differential equations describes mass and energy flows between the different components:

$$\dot{M}_\mathrm{h} = -\dot{M}_\mathrm{cool} + \dot{M}_\mathrm{ev} + \dot{M}_\mathrm{c\to h}^\mathrm{AGN} \quad , \tag{9.12}$$

$$\dot{M}_\mathrm{c} = \dot{M}_\mathrm{cool} - \dot{M}_\mathrm{sf} - \dot{M}_\mathrm{ev} - \dot{M}_\mathrm{c\to h}^\mathrm{AGN} \quad , \tag{9.13}$$

$$\dot{M}_* = \dot{M}_\mathrm{sf} \quad , \tag{9.14}$$

$$\dot{E}_\mathrm{h} = \dot{E}_\mathrm{fb,local} - \dot{E}_\mathrm{cool} + \dot{E}_\mathrm{hydro} + \dot{E}_\mathrm{h}^\mathrm{AGN} + \dot{E}_\mathrm{c\to h}^\mathrm{AGN} \quad , \tag{9.15}$$

$$\dot{E}_\mathrm{c,\,used}^\mathrm{AGN} = \dot{E}_\mathrm{c\to h}^\mathrm{AGN} \quad . \tag{9.16}$$

Equations (9.12), (9.13), (9.14), (9.15), and (9.16) are integrated instead of equations (5.18), (5.19), (5.20), and (5.21) introduced in Section 5.3. The new contributions that account for the AGN feedback are labelled with the superscript *AGN*. I will now detail each of the new terms.

The term $\dot{M}_{\mathrm{c}\to\mathrm{h}}^{\mathrm{AGN}}$ in equation (9.12) accounts for the mass of cold gas that is brought to the hot phase due to the AGN feedback energy $E_{\mathrm{c}}^{\mathrm{AGN}}$ coupled to the cold component.

Being this fundamental to fully understand the implementation of the AGN feedback model, I remind that the set of equations (9.12), (9.13), (9.14), and (9.15) is integrated with a Runge-Kutta algorithm (whose time-step I refer to as $\Delta t_{\mathrm{MUPPI}}$) within each SPH time-step $\Delta t_{\mathrm{SPH}} > \Delta t_{\mathrm{MUPPI}}$, as explained in Section 5.3 (see Murante et al., 2010, 2015, for details).

Therefore, first, the code evaluates the amount of the cold gas mass that can be brought to the hot phase within the SPH time-step Δt_{SPH} using the entire energy budget $E_{\mathrm{c}}^{\mathrm{AGN}}$ available, i.e.:

$$\dot{M}_{\mathrm{c,\,th}}^{\mathrm{AGN}} = \dot{E}_{\mathrm{c}}^{\mathrm{AGN}} \frac{(\gamma-1)\,\mu\,m_{\mathrm{p}}}{k_{\mathrm{B}}\,(T_{\mathrm{h}}-T_{\mathrm{c}})} \quad . \tag{9.17}$$

Then, should the cold gas mass to be (in *theory*) evaporated $\dot{M}_{\mathrm{c,\,th}}^{\mathrm{AGN}}$ exceed the gas of the cold phase M_{c} available in the MUPPI time-step $\Delta t_{\mathrm{MUPPI}}$, I limit $\dot{M}_{\mathrm{c,\,th}}^{\mathrm{AGN}}$ to:

$$\dot{M}_{\mathrm{c}\to\mathrm{h}}^{\mathrm{AGN}} = \frac{M_{\mathrm{c}}}{\Delta t_{\mathrm{MUPPI}}} \quad . \tag{9.18}$$

Therefore:

$$\dot{M}_{\mathrm{c}\to\mathrm{h}}^{\mathrm{AGN}} = \begin{cases} \dot{M}_{\mathrm{c,\,th}}^{\mathrm{AGN}} & \text{for} \quad \dot{M}_{\mathrm{c,\,th}}^{\mathrm{AGN}}\,\Delta t_{\mathrm{MUPPI}} \leq M_{\mathrm{c}} \quad , \\ M_{\mathrm{c}}/\Delta t_{\mathrm{MUPPI}} & \text{for} \quad \dot{M}_{\mathrm{c,\,th}}^{\mathrm{AGN}}\,\Delta t_{\mathrm{MUPPI}} > M_{\mathrm{c}} \quad , \end{cases} \tag{9.19}$$

and $\dot{M}_{\mathrm{c}\to\mathrm{h}}^{\mathrm{AGN}}$ is lower than or equal to $\dot{M}_{\mathrm{c,\,th}}^{\mathrm{AGN}}$. $\dot{M}_{\mathrm{c}\to\mathrm{h}}^{\mathrm{AGN}}$ in equation (9.16) represents a source term for the evolution of the hot gas mass in equation (9.12), and a sink term for the evolution of the mass of the cold phase in equation (9.13).

Once $\dot{M}_{\mathrm{c}\to\mathrm{h}}^{\mathrm{AGN}}$ is retrieved, it is adopted to compute the amount of AGN feedback energy $E_{\mathrm{c}\to\mathrm{h}}^{\mathrm{AGN}}$ that is actually used to evaporate cold gas. It reads:

$$\dot{E}_{\mathrm{c}\to\mathrm{h}}^{\mathrm{AGN}} = \dot{M}_{\mathrm{c}\to\mathrm{h}}^{\mathrm{AGN}} \frac{k_{\mathrm{B}}\,(T_{\mathrm{h}}-T_{\mathrm{c}})}{(\gamma-1)\,\mu\,m_{\mathrm{p}}} \quad , \tag{9.20}$$

where $\gamma = 5/3$ is the adiabatic index, and k_{B} and m_{p} are the Boltzmann constant and the mass of the proton, respectively. The energy contribution $E_{\mathrm{c}\to\mathrm{h}}^{\mathrm{AGN}}$ accounts for the energy that is supplied to the hot component by the cold mass that is evaporated and enters in the hot phase. In this way, besides the term $\dot{E}_{\mathrm{h}}^{\mathrm{AGN}}$ described in equation (9.10), $\dot{E}_{\mathrm{c}\to\mathrm{h}}^{\mathrm{AGN}}$ also increases the hot gas energy (see equation (5.27)).

Equation (9.16) describes the evolution of the AGN feedback energy that the cold gas is provided with and that is actually consumed to evaporate cold gas. The energy rate $\dot{E}_{\mathrm{c,\,used}}^{\mathrm{AGN}}$ records the rate of consumed energy $\dot{E}_{\mathrm{c}\to\mathrm{h}}^{\mathrm{AGN}}$, that is lower than or equal to $\dot{E}_{\mathrm{c}}^{\mathrm{AGN}}$ (see equation (9.11)) due to the fact that $\dot{M}_{\mathrm{c}\to\mathrm{h}}^{\mathrm{AGN}}$ is lower than or equal to $\dot{M}_{\mathrm{c,\,th}}^{\mathrm{AGN}}$.

Then, at the end of the SPH time-step, $\dot{E}^{\rm AGN}_{\rm c,\,used}$ from equation (9.16) is contrasted to the originally available $\dot{E}^{\rm AGN}_{\rm c}$. Should:

$$\dot{E}^{\rm AGN}_{\rm c,\,extra} = \dot{E}^{\rm AGN}_{\rm c} - \dot{E}^{\rm AGN}_{\rm c,\,used} > 0 \ , \tag{9.21}$$

the corresponding further energy contribution $E^{\rm AGN}_{\rm extra,c}$ is provided to the energy of the hot gas component $E^{\rm AGN}_{\rm h}$. This addition amounts to the energy that has not been used during the entire SPH time-step to bring cold gas from the cold to the hot phase, because the multiphase particle was already devoid of the cold gas mass. Also, this contribution ensures that no feedback energy is lost: indeed, whenever $E^{\rm AGN}_{\rm c}$ exceeds the maximum energy that can be used to lead all the available cold gas to the hot phase, the remaining energy is coupled to the hot gas, that is the only component left. I decided to integrate equation (9.16) and then to provide the extra energy $E^{\rm AGN}_{\rm c,\,extra}$ to the hot gas at the end of the SPH time-step rather then estimating the extra energy budget at the beginning of the SPH time-step for the following reason: the temperature $T_{\rm h}$ of the hot gas changes during the integration of the equations (9.12), (9.13), (9.14), and (9.15), so that the precise amount of $M^{\rm AGN}_{\rm c\to h}$ is known only at the end of the integration.

The general description of the AGN feedback model that I outlined so far accounts for AGN feedback energy that is distributed to both the hot and the cold gas. The way in which the feedback energy is shared among the different phases of the multiphase ISM is established by the coupling parameters $\mathcal{A}_{\rm h}$ and $\mathcal{A}_{\rm c}$ (see equations (9.10) and (9.11)), and different scenarios arise when specific values or parametrizations for them are adopted. I will discuss this point in Section 9.2.6.

9.2.6 Coupling AGN feedback energy to a multiphase ISM

As explained in Section 9.2.5, the AGN feedback energy assigned to multiphase particles can be shared between their hot and cold components. Therefore, by designing different ways of distributing the available feedback energy to the hot and cold gas phases, it is possible to investigate how feedback energy couples to a multiphase ISM, and how various possibilities impact on the BH-galaxy coevolution. The way in which feedback energy is distributed between the hot and cold gas is controlled by the coupling parameters $\mathcal{A}_{\rm h}$ and $\mathcal{A}_{\rm c} = 1 - \mathcal{A}_{\rm h}$ (see equations (9.10) and (9.11)).

Different combinations can be explored, and they can be broadly divided into two different categories: *(i)* constant values of the coupling parameters (Section 9.2.6.1), and *(ii)* coupling parameters modelled according to physical properties of the ISM, i.e. of the multiphase particle which is provided with feedback energy (Section 9.2.6.2).

9.2.6.1 Constant coupling parameters

I will consider three different possibilities as test cases to investigate how AGN feedback energy couples to the surrounding multiphase ISM:

- All the energy is provided to the hot gas phase ($\mathcal{A}_{\rm h} = 1$ and $\mathcal{A}_{\rm c} = 0$).
- AGN feedback energy is entirely supplied to the cold component ($\mathcal{A}_{\rm h} = 0$ and $\mathcal{A}_{\rm c} = 1$).
- The energy assigned to each multiphase particle is evenly shared among the hot and cold gas ($\mathcal{A}_{\rm h} = 0.5$ and $\mathcal{A}_{\rm c} = 0.5$).

When $\mathcal{A}_{\rm h} = 1$ and $\mathcal{A}_{\rm c} = 0$, the system of equations (9.12), (9.13), (9.14), and (9.15) reduces to:

$$\dot{M}_{\rm h} = -\dot{M}_{\rm cool} + \dot{M}_{\rm ev} \ , \tag{9.22}$$
$$\dot{M}_{\rm c} = \dot{M}_{\rm cool} - \dot{M}_{\rm sf} - \dot{M}_{\rm ev} \ , \tag{9.23}$$
$$\dot{M}_{*} = \dot{M}_{\rm sf} \ , \tag{9.24}$$
$$\dot{E}_{\rm h} = \dot{E}_{\rm fb,local} - \dot{E}_{\rm cool} + \dot{E}_{\rm hydro} + \dot{E}_{\rm h}^{\rm AGN} \ , \tag{9.25}$$

and there is no need anymore for integrating equation (9.16).

On the other hand, if $\mathcal{A}_{\rm h} = 0$ and $\mathcal{A}_{\rm c} = 1$, the system of equations to be integrated is:

$$\dot{M}_{\rm h} = -\dot{M}_{\rm cool} + \dot{M}_{\rm ev} + \dot{M}_{\rm c\rightarrow h}^{\rm AGN} \ , \tag{9.26}$$
$$\dot{M}_{\rm c} = \dot{M}_{\rm cool} - \dot{M}_{\rm sf} - \dot{M}_{\rm ev} - \dot{M}_{\rm c\rightarrow h}^{\rm AGN} \ , \tag{9.27}$$
$$\dot{M}_{*} = \dot{M}_{\rm sf} \ , \tag{9.28}$$
$$\dot{E}_{\rm h} = \dot{E}_{\rm fb,local} - \dot{E}_{\rm cool} + \dot{E}_{\rm hydro} + \dot{E}_{\rm c\rightarrow h}^{\rm AGN} \ , \tag{9.29}$$
$$\dot{E}_{\rm c,\,used}^{\rm AGN} = \dot{E}_{\rm c\rightarrow h}^{\rm AGN} \ , \tag{9.30}$$

where the only source term $\dot{E}_{\rm h}^{\rm AGN}$ is missing in equation (9.29).

When $\mathcal{A}_{\rm h} = 0.5$ and $\mathcal{A}_{\rm c} = 0.5$, the general description of the model outlined in Section 9.2.5 is valid. Interestingly, in this case when

$$E_{\rm c}^{\rm AGN} = E_{\rm h}^{\rm AGN} = \frac{1}{2} E_{\rm fb}^{\rm AGN} \ , \tag{9.31}$$

it is worth to analytically quantify the mass of initially cold gas that can be evaporated and brought to the hot phase, i.e. $M_{\rm c\rightarrow h}^{\rm AGN}$, and cast it as a function of the initial mass of the hot gas in the multiphase particle, $M_{\rm h,\,init}$, i.e. before receiving AGN feedback energy.

Under the simplified assumptions that there is enough cold gas to receive all the feedback energy $E_{\rm c}^{\rm AGN}$, so that $M_{\rm c\rightarrow h}^{\rm AGN} = M_{\rm c,\,th}^{\rm AGN}$ (see equation (9.19)) and $E_{\rm c,\,extra}^{\rm AGN} = 0$ (see equation (9.21)), and that contributions from cooling and evaporation are

neglected, in order to focus on the mass flow induced by the AGN feedback, it is possible to proceed as follows. From equation (9.17):

$$M_{\mathrm{c}\to\mathrm{h}}^{\mathrm{AGN}} = E_{\mathrm{c}}^{\mathrm{AGN}} \frac{(\gamma-1)\,\mu\,m_{\mathrm{p}}}{k_{\mathrm{B}}\,(T_{\mathrm{h,\,fin}} - T_{\mathrm{c}})} \quad ; \tag{9.32}$$

the final temperature of the hot phase after the energy contribution by the AGN, $E_{\mathrm{h}}^{\mathrm{AGN}}$, reads:

$$T_{\mathrm{h,\,fin}} = T_{\mathrm{h,\,init}} + E_{\mathrm{h}}^{\mathrm{AGN}} \frac{(\gamma-1)\,\mu\,m_{\mathrm{p}}}{k_{\mathrm{B}}\,M_{\mathrm{h,\,init}}} \quad . \tag{9.33}$$

By approximating $(T_{\mathrm{h,\,fin}} - T_{\mathrm{c}}) \simeq T_{\mathrm{h,\,fin}}$ and plugging equation (9.33) into equation (9.32):

$$\begin{aligned} M_{\mathrm{c}\to\mathrm{h}}^{\mathrm{AGN}} &= E_{\mathrm{c}}^{\mathrm{AGN}} \frac{(\gamma-1)\,\mu\,m_{\mathrm{p}}}{k_{\mathrm{B}}\left(T_{\mathrm{h,\,init}} + E_{\mathrm{h}}^{\mathrm{AGN}} \frac{(\gamma-1)\,\mu\,m_{\mathrm{p}}}{k_{\mathrm{B}}\,M_{\mathrm{h,\,init}}}\right)} \\ &= E_{\mathrm{c}}^{\mathrm{AGN}} \frac{(\gamma-1)\,\mu\,m_{\mathrm{p}}\,M_{\mathrm{h,\,init}}}{k_{\mathrm{B}}\,T_{\mathrm{h,\,init}}\,M_{\mathrm{h,\,init}} + E_{\mathrm{h}}^{\mathrm{AGN}}\,(\gamma-1)\,\mu\,m_{\mathrm{p}}} \\ &= E_{\mathrm{c}}^{\mathrm{AGN}} \frac{M_{\mathrm{h,\,init}}}{k_{\mathrm{B}}\,T_{\mathrm{h,\,init}} \frac{M_{\mathrm{h,\,init}}}{(\gamma-1)\,\mu\,m_{\mathrm{p}}} + E_{\mathrm{h}}^{\mathrm{AGN}}} \\ &= M_{\mathrm{h,\,init}} \frac{E_{\mathrm{c}}^{\mathrm{AGN}}}{E_{\mathrm{h}}^{\mathrm{AGN}} + M_{\mathrm{h,\,init}} \frac{k_{\mathrm{B}}\,T_{\mathrm{h,\,init}}}{(\gamma-1)\,\mu\,m_{\mathrm{p}}}} \quad . \end{aligned} \tag{9.34}$$

Then, using equation (9.31):

$$M_{\mathrm{c}\to\mathrm{h}}^{\mathrm{AGN}} = M_{\mathrm{h,\,init}} \frac{E_{\mathrm{fb}}^{\mathrm{AGN}}}{E_{\mathrm{fb}}^{\mathrm{AGN}} + 2\,M_{\mathrm{h,\,init}} \frac{k_{\mathrm{B}}\,T_{\mathrm{h,\,init}}}{(\gamma-1)\,\mu\,m_{\mathrm{p}}}} < M_{\mathrm{h,\,init}} \quad . \tag{9.35}$$

As a consequence, assuming $\mathcal{A}_{\mathrm{h}} = \mathcal{A}_{\mathrm{c}} = 0.5$, the hot gas mass and thus the hot gas density can increase by up to a factor of $\lesssim 2$, at most. Therefore, the hot gas phase will not experience a runaway cooling, and the SPH temperature of the multiphase particle is not expected to change significantly due to the AGN-induced transfer of cold gas to the hot phase.

9.2.6.2 Locally varying energy coupling

Another powerful possibility is to determine the coupling factors according to the physical properties of the multiphase particles. Here, I will explore an AGN feedback energy coupling driven by the covering factors of the hot and cold phases. The physical idea behind this modelling considers that the larger is the volume occupied by the cold gas, the larger is the amount of energy that it can absorb.

In Section 5.3, I introduced the filling factor f_{h} of the hot gas (see equation (5.16)), that is related to the fraction of gas mass in the hot phase within the multiphase

particle, labelled $F_{\rm h}$, and that quantifies its clumpiness. Note that the formulation provided by equation (5.16) is equivalent to express the filling factor of the hot phase as the ratio between the volume filled by the hot gas and the volumes occupied by both the hot and cold components.

Being the filling factor of the cold phase $f_{\rm c} = 1 - f_{\rm h}$, the covering factor of the cold phase can be cast as:

$$\mathcal{C}_{\rm c} = f_{\rm c} \frac{L_{\rm P}}{\ell_{\rm MC}} \ . \tag{9.36}$$

In equation (9.36), $\ell_{\rm MC}$ is the typical size of molecular (cold) clouds, while $L_{\rm P}$ is the size of the multiphase particle, i.e.:

$$L_{\rm P} = \left(\frac{3}{4\,\pi} V_{\rm P} \right)^{1/3} = \left(\frac{3}{4\,\pi} \frac{M_{\rm P} - M_*}{\rho} \right)^{1/3} \ , \tag{9.37}$$

where $V_{\rm P}$, $M_{\rm P}$, M_*, and ρ are the volume of the multiphase particle occupied by the gas phases, the mass of the multiphase particle, the mass of its stellar component, and the SPH density of the multiphase particle, respectively. $\ell_{\rm MC}$ is a parameter of the model: observations suggest that it ranges between few pc and a few tens of pc. After carrying out extensive tests, I adopt $\ell_{\rm MC} = 20$ pc for the fiducial runs.

Equation (9.36) can be interpreted by considering that the filling factor can be expressed as $f_{\rm c} = N\,\ell_{\rm MC}^3 / L_{\rm P}^3$, N being the number of cold clouds within the multiphase particle, while $\mathcal{C}_{\rm c} = N\,\ell_{\rm MC}^2 / L_{\rm P}^2$, and by dividing the latter equation by the former one. The covering factor of the hot phase is: $\mathcal{C}_{\rm h} = 1 - \mathcal{C}_{\rm c}$.

Therefore, within this model I assume: $\mathcal{A}_{\rm h} = \mathcal{C}_{\rm h}$ and $\mathcal{A}_{\rm c} = \mathcal{C}_{\rm c}$.

As a side note, when computing $\mathcal{C}_{\rm c}$, I first check whether $f_{\rm h} < 1$; should the multiphase particle be entirely filled by hot gas (i.e. $f_{\rm h} = 1$), then $\mathcal{C}_{\rm c} = 0$. An unwanted situation may occur when $\mathcal{C}_{\rm c} > 1$ (it can be associated to the situation in which cold clouds overlap with each other), if $L_{\rm P} \gg \ell_{\rm MC}$. Should this happen, the covering factor is limited to unity, i.e. $\mathcal{C}_{\rm c} = 1$, and thus $\mathcal{C}_{\rm h} = 0$.

9.3 The suite of simulations

In this Section, I introduce the set of simulations carried out to investigate the impact of AGN feedback on the evolution of late-type galaxies. The numerical setup is the same as the one described in Chapter 5: simulations have been performed with the GADGET3 code (see Section 5.1), using the improved formulation of SPH presented in Section 5.2. The ICs are the *AqC*5 ICs described in Section 5.5: the Plummer-equivalent softening length for the computation of the gravitational force is $\varepsilon_{\rm Pl} = 325\,h^{-1}$ pc, DM particles have a mass of $1.6 \cdot 10^6\,h^{-1}$ M$_\odot$, and the initial mass of gas particles is $3.0 \cdot 10^5\,h^{-1}$ M$_\odot$. As explained in Chapters 6 and 7, the new SPH formulation has been introduced in cosmological simulations adopting the sub-resolution model MUPPI (see Section 5.3). The key features of the

model MUPPI and of the model for chemical evolution have been outlined in Sections 5.3 and 5.4, respectively.

As for the stellar feedback scheme, I adopt for all the simulations involved in the present analysis the galactic outflow model labelled *FB2* in Chapter 6 (see Section 6.3.2), as done for the simulations discussed in Chapter 7. I remind that according to this model the ISM is isotropically provided with kinetic stellar feedback energy. Apart from those related to the AGN feedback model (see below), all the relevant parameters of the sub-resolution model that I adopt for the simulations in this Chapter are the same ones adopted for the simulations presented in Chapter 7. In particular, the simulations introduced in Section 7.2.1 constitute the reference simulations without SMBH feedback that I consider to quantify the impact of the AGN in this Chapter. Therefore, further details and parameter values can be recovered in Section 7.2.1, and in Tables 5.1 and 7.1.

Besides reference simulations without BHs and the ensuing feedback used as control simulations, the simulations carried out for the present analysis include the implementation of AGN that I described in Section 9.2.

I designed a number of simulations aimed at investigating the effect of the following aspects of the numerical implementation (I highlight within brackets the reference acronym encoded in the simulation label, that I will further explain later):

- *Gas accretion:* I consider the possibility for the BH to accrete:
  - *(hcA)* – both hot and cold gas, according to equation (9.9);
  - *(ocA)* – cold gas only, according to $\dot{M}_{\rm BH} = \min(\dot{M}_{\rm B,c}, \dot{M}_{\rm Edd})$.

  In addition, I explore the effect of the *angular momentum limiter* to cold gas accretion introduced in Section 9.2.3, taking into account:
  - *(hcAL)* – both cold (limited) plus hot accretion;
  - *(ocAL)* – only cold gas accretion, limited by $\mathcal{L}_{\rm AM}$ (equations (9.5) and (9.6)).
- *Energy coupling:* I explore the different possibilities described in Sections 9.2.6.1 and 9.2.6.2, considering:
  - *(both)* – $\mathcal{A}_{\rm h} = 0.5$ and $\mathcal{A}_{\rm c} = 0.5$;
  - *(hot)* – $\mathcal{A}_{\rm h} = 1$ and $\mathcal{A}_{\rm c} = 0$;
  - *(cold)* – $\mathcal{A}_{\rm h} = 0$ and $\mathcal{A}_{\rm c} = 1$;
  - *(cf)* – $\mathcal{A}_{\rm h} = \mathcal{C}_{\rm h}$ and $\mathcal{A}_{\rm c} = \mathcal{C}_{\rm c}$.
- *BH seed mass:* To investigate the effect of the initial BH mass on the BH-galaxy coevolution and select the fiducial value, I choose the following BH seed masses:
  - *(Sref)* – $M_{\rm BH,seed} = 1.1 \cdot 10^5$ M$_\odot$, reference value;

Table 9.2: Relevant parameters of the simulations with AGN feedback.
Column 1: simulation label. *Column 2:* AGN feedback: included or not. *Column 3:* AGN feedback energy coupling to the multiphase ISM. *Column 4:* hot and/or cold gas accretion. *Column 5:* angular momentum limiter: included or not. *Column 6:* BH seed mass. *Column 7:* adopted IMF. *Column 8:* fraction of binary systems giving rise to SNe Ia. Other parameters as in Table 9.1.

Label	AGN	Energy coupling	$\dot{M}_{\rm BH}$	$\mathcal{L}_{\rm AM}$ $\frac{C_{\rm visc}}{2\,\pi}$	$M_{\rm BH,\,seed}$ ($\rm M_\odot$)	IMF	$f_{\rm bin,Ia}$
noAGN–K3s–IaB	✗					K3s	0.03
AGN–hot–hcA	✓	$\mathcal{A}_{\rm h}=1$, $\mathcal{A}_{\rm c}=0$	hot+ cold	✗	$1.1{\cdot}10^5$	K3s	0.03
AGN–both–hcA	✓	$\mathcal{A}_{\rm h}=0.5$, $\mathcal{A}_{\rm c}=0.5$	hot+ cold	✗	$1.1{\cdot}10^5$	K3s	0.03
AGN–cold–hcA	✓	$\mathcal{A}_{\rm h}=0$, $\mathcal{A}_{\rm c}=1$	hot+ cold	✗	$1.1{\cdot}10^5$	K3s	0.03
AGN–both–hcAL	✓	$\mathcal{A}_{\rm h}=0.5$, $\mathcal{A}_{\rm c}=0.5$	hot+ cold	✓ 1	$1.1{\cdot}10^5$	K3s	0.03
AGN–both–hcAL2	✓	$\mathcal{A}_{\rm h}=0.5$, $\mathcal{A}_{\rm c}=0.5$	hot+ cold	✓ 10^2	$1.1{\cdot}10^5$	K3s	0.03
AGN–both–hcAL3	✓	$\mathcal{A}_{\rm h}=0.5$, $\mathcal{A}_{\rm c}=0.5$	hot+ cold	✓ 10^3	$1.1{\cdot}10^5$	K3s	0.03
AGN–both–ocA	✓	$\mathcal{A}_{\rm h}=0.5$, $\mathcal{A}_{\rm c}=0.5$	cold	✗	$1.1{\cdot}10^5$	K3s	0.03
AGN–both–ocAL	✓	$\mathcal{A}_{\rm h}=0.5$, $\mathcal{A}_{\rm c}=0.5$	cold	✓ 1	$1.1{\cdot}10^5$	K3s	0.03
AGN–cf–hcA	✓	$\mathcal{A}_{\rm h}=\mathcal{C}_{\rm h}$, $\mathcal{A}_{\rm c}=\mathcal{C}_{\rm c}$	hot+ cold	✗	$1.1{\cdot}10^5$	K3s	0.03
AGN–cf–ocA	✓	$\mathcal{A}_{\rm h}=\mathcal{C}_{\rm h}$, $\mathcal{A}_{\rm c}=\mathcal{C}_{\rm h}$	cold	✗	$1.1{\cdot}10^5$	K3s	0.03
AGN–both–hcA–S0.5x	✓	$\mathcal{A}_{\rm h}=0.5$, $\mathcal{A}_{\rm c}=0.5$	hot+ cold	✗	$5.5{\cdot}10^4$	K3s	0.03
AGN–both–hcA–S2x	✓	$\mathcal{A}_{\rm h}=0.5$, $\mathcal{A}_{\rm c}=0.5$	hot+ cold	✗	$2.7{\cdot}10^5$	K3s	0.03
AGN–both–ocA–S0.5x	✓	$\mathcal{A}_{\rm h}=0.5$, $\mathcal{A}_{\rm c}=0.5$	cold	✗	$5.5{\cdot}10^4$	K3s	0.03
AGN–both–ocA–S2x	✓	$\mathcal{A}_{\rm h}=0.5$, $\mathcal{A}_{\rm c}=0.5$	cold	✗	$2.7{\cdot}10^5$	K3s	0.03
noAGN–K2s–IaB	✗					K2s	0.03
AGN–both–hcA–K2s–IaB	✓	$\mathcal{A}_{\rm h}=0.5$, $\mathcal{A}_{\rm c}=0.5$	hot+ cold	✗	$1.1{\cdot}10^5$	K2s	0.03
noAGN–K3s–IaA	✗					K3s	0.1
AGN–both–hcA–K3s–IaA	✓	$\mathcal{A}_{\rm h}=0.5$, $\mathcal{A}_{\rm c}=0.5$	hot+ cold	✗	$1.1{\cdot}10^5$	K3s	0.1
noAGN–K2s–IaA	✗					K2s	0.1
AGN–both–hcA–K2s–IaA	✓	$\mathcal{A}_{\rm h}=0.5$, $\mathcal{A}_{\rm c}=0.5$	hot+ cold	✗	$1.1{\cdot}10^5$	K2s	0.1

  - *(S0.5x)* – $M_{\rm BH,\,seed} = 5.5 \cdot 10^4$ M$_\odot$;
  - *(S2x)* – $M_{\rm BH,\,seed} = 2.7 \cdot 10^5$ M$_\odot$.

- *IMF:* To quantify the impact of AGN feedback on metallicity profiles, I consider the two IMFs that have been taken into account in Chapter 7, i.e.:
  - *(K3s)* – the Kroupa et al. (1993) IMF, see equation (7.3);
  - *(K2s)* – the Kroupa (2001) IMF, see equation (7.2).

- *SN Ia fraction:* Also, I examine two possible values for the fraction of binary systems with characteristics suitable for originating SNe Ia, i.e.:
  - *(IaA)* – $f_{\rm bin,Ia} = 0.1$ and
  - *(IaB)* – $f_{\rm bin,Ia} = 0.03$, as in Section 7.2.1.

All the simulations are listed in Table 9.2. The name of the simulations encodes the implementation options described above and uses the following template: simulation names are in the form *(no)AGN-cccc-aaA(L)-(Snnx-IMF-IaX)*.

The label AGN denotes the fact that the simulations described in this Chapter include AGN feedback, becoming *noAGN* only for the control ones where AGN feedback is not active. The label *cccc* refers to the coupling, and it can take the values *both*, *cold*, *hot*, or *cf*. The label *aaA(L)* stands for the modelling of the accretion: *hcA* if both hot and cold gas are accreted, *ocA* if only cold gas is accreted. In addition, should the simulations include the angular momentum *limiter* for the cold gas accretion, their label reads *hcAL* or *ocAL*, with the possibility of showing a number that encodes the value of the parameter $C_{\rm visc}$ (see Section 9.2.3). In this way, *hcAL2* refers to $C_{\rm visc}/2\,\pi = 10^2$, *hcAL3* refers to $C_{\rm visc}/2\,\pi = 10^3$, while *hcAL* and *ocAL* assume $C_{\rm visc}/2\,\pi = 1$.

The coupling and accretion labels are missing only for the control simulations with no AGN feedback. The seed label is in the form *Sssx*, where *ss* can take the values $ss = 2$ or $ss = 0.5$. The seed label is absent if the reference seed is used ($M_{\rm BH,\,seed} = 1.1 \cdot 10^5$ M$_\odot$). *IMF* stands for the IMF used and follows the convention (*K3s* or *K2s*) explained above. When not present, the K3s IMF is assumed. Finally, *IaX* represents the fraction of binary systems giving rise to SNe Ia, i.e. $f_{\rm bin,Ia}$, and can be either *IaA* or *IaB*. Unless otherwise stated, I assume $f_{\rm bin,Ia} = 0.03$ (IaB).

9.4 Results

In this Section, I present the results. I show how the coupling of AGN feedback energy to the multiphase ISM determines the main features of simulated galaxies (Section 9.4.1), the evolution of BHs (Section 9.4.2), and the BH-galaxy coevolution (Section 9.4.3). In Section 9.4.4, I explore the effect of the BH seed mass on final results, while Section 9.4.5 is devoted to investigate the effect of AGN feedback on metallicity profiles. In Section 9.4.6, I show how AGN feedback energy can be coupled according to the physical properties of the multiphase ISM, while in Section 9.4.7 I discuss the effect of the modelling BH gas accretion on final results.

9.4.1 Disc galaxies with AGN feedback

I start to investigate the BH-galaxy coevolution by focussing on four galaxies:

- *noAGN–K3s–IaB:* this is the fiducial simulation without BHs and their ensuing feedback (see Table 9.2). This galaxy has been introduced in Section 7.4.1, and its properties have been thouroughly analysed in Chapter 7, in which it was labelled K3s–yA–IaB–kB. It has been also considered in Chapter 8, where it was referred to as AqC5–3sIMF. Throughout this Chapter, this simulation is identified by the black colour, and it is used to quantify the effect of AGN feedback, that is included in the other simulations involved in the comparison.
- *AGN–hot–hcA:* identified by the red colour, this galaxy includes the AGN feedback, and the AGN feedback energy is coupled entirely to the hot gas;
- *AGN–both–hcA:* for this galaxy model (green) the AGN feedback energy is evenly provided to the hot and cold phases;
- *AGN–cold–hcA:* pinpointed by the blue colour, the AGN supplies all the feedback energy to the cold gas.

The BHs of all these galaxies accrete both hot and cold gas (see also Table 9.2), according to equation (9.9). First, I introduce the projected stellar and gas density maps for each galaxy. Figure 9.1 shows the face-on (first column) and edge-on (second column) gas density maps, while Figure 9.2 presents the corresponding views for the stellar density. Using the same procedure adopted in Chapters 6 and 7, galaxies have been rotated in order to have the z-axis of their reference system aligned with the angular momentum of star particles and cold and multiphase gas particles located within 8 kpc from the minimum of the gravitational potential. The origin of the reference system is set at the centre of the galaxy, that is considered to be the centre of mass of the aformentioned cold and multiphase gas particles. Here and in the following, I consider for the analysis star and gas particles that are located within the galactic radius, defined as one tenth of the virial radius, i.e. $R_{\rm gal} = 0.1 R_{\rm vir}$. I choose $R_{\rm gal}$ in order to identify the region of the computational volume that is dominated by the central galaxy. In analogy with previous Chapters, virial quantities are considered as those computed in a sphere that is centred on the minimum of the gravitational potential of the halo and that encloses an overdensity of 200 times the *critical* density today. The galactic radius of these galaxies is $R_{\rm gal} \sim 24$ kpc. When analysing radial profiles (see Figure 9.12), I will consider gas and star particles out to a distance of $r = 30$ kpc.

Density maps in Figures 9.1 and 9.2 show that all the galaxies have a dominant, extended disc and a limited bulge component. Gaseous discs are more extended than stellar ones. A well-defined spiral pattern is evident in the majority of the discs. The morphology and the extent of the disc vary: with respect to the fiducial simulation noAGN–K3s–IaB, galaxies simulated accounting for AGN feedback have more

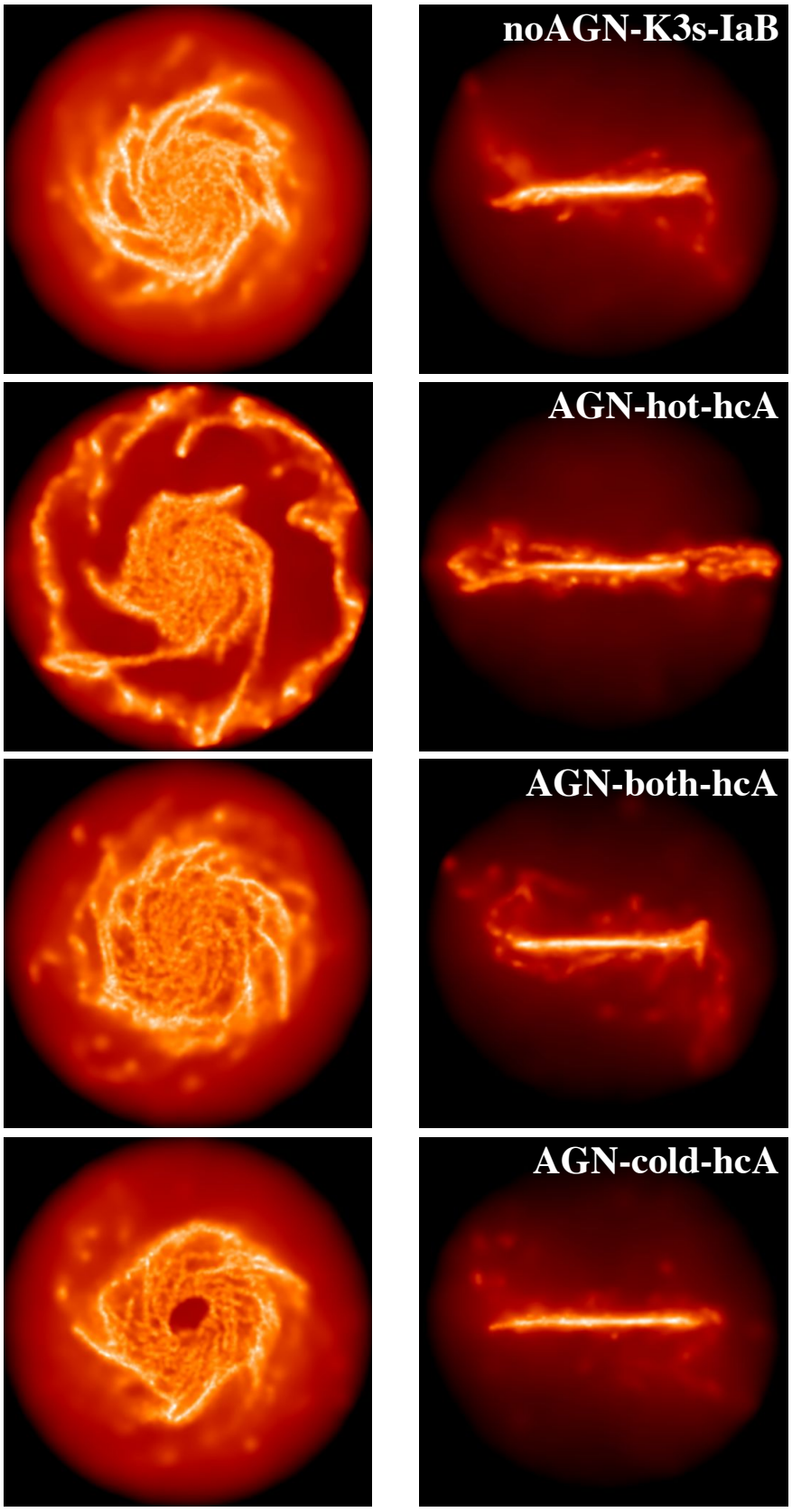

Figure 9.1: Face-on (left-hand panels) and edge-on (right-hand panels) projected gas density maps. Each row shows a galaxy, as highlighted in the label. Plots are shown at redshift $z = 0$. Particles within $R_{\rm gal} = 0.1\,R_{\rm vir}$ are considered. The size of each box is 50 kpc a side.

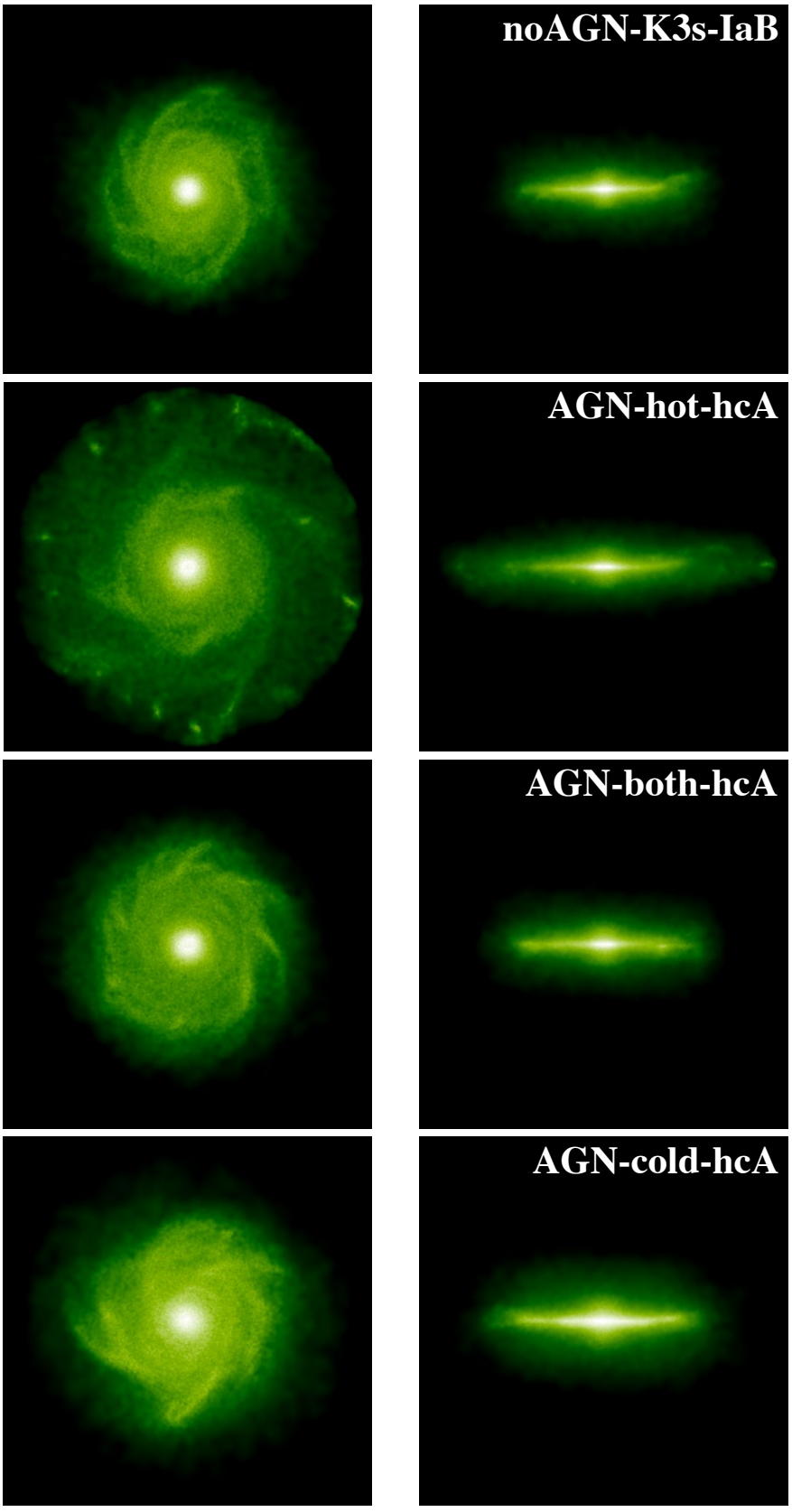

Figure 9.2: Face-on (left-hand panels) and edge-on (right-hand panels) projected stellar density maps. Each row shows a galaxy, as highlighted in the label. Plots are shown at redshift $z = 0$. Particles within $R_{\rm gal} = 0.1\,R_{\rm vir}$ are considered. The size of each box is 50 kpc a side.

extended gaseous and stellar discs (see also Figure 9.12). However, the morphology of these galaxies usually appear more disturbed, especially in the outermost regions. This is the result of a highly dynamical environment. The most characteristic case is represented by the galaxy AGN–hot–hcA, that exhibits a regular, inner disc and an outer ring-like structure, which appears as the natural extension of the internal disc. The outermost gas is the result of recently accreted (and re-accreted, see Section 2.3 and Chapter 6) gas, that still has to settle down on the disc and that is characterised by a high angular momentum. The recent accretion phase experienced by this galaxy can be seen also by analysing the mass accretion of gas below $z \lesssim 0.5$ (see Figure 9.9, that I will further discuss later).

The galaxy AGN–both–hcA, with a more regular morphology, also has an irregular distribution of gas above and around the galactic plane, suggesting ongoing gas accretion (see also Figure 9.9). As for the galaxy AGN–cold–hcA, it certainly has the most evident signature of the presence of a SMBH, that accreted all the available gas in its surrounding, leaving a hole in the gas density map. The radius of the central region deficient in gas is $r \sim 2.5$ kpc (see also Figure 9.12). Before presenting an extensive analysis of the main features of the simulated galaxies (Section 9.4.3), I will investigate the properties and the evolution of the central BHs, that drive their host galaxy evolution.

9.4.2 BH evolution

In this Section, I study the evolution and the properties of the SMBHs of the galaxies: AGN–hot–hcA, AGN–both–hcA, and AGN–cold–hcA. I will focus on the evolution of their mass and their accretion rate, and consider whether they fulfil observed scaling relations.

Figure 9.3 shows the evolution of the BH accretion rates. The top panel describes the redshift evolution of the accretion rate (in units of 10^{-2} $M_\odot$ yr^{-2}) of the most massive BH within each galaxy (i.e. located within 100 kpc from the galaxy centre). The most massive BH within each galaxy in these simulations is always located at the galaxy centre (see Section 9.4.1), as a consequence of the procedure adopted for the BH pinning (see Section 9.2.1) and of the relatively quite dynamical environment within which the galaxy forms. The bottom panel shows the same evolution in units of the Eddington accretion rate $\dot{M}_{\rm Edd}$. The central BH is seeded at $z \simeq 8.5$ in all the galaxies. By focussing on the bottom panel of Figure 9.3, it is possible to see that BHs experience a high-redshift quasar-mode phase (see Section 2.4.5) and then they enter a radio-mode stage at a redshift spanning the range $3 \lesssim z \lesssim 2$. The commonly adopted threshold to discriminate between quasar- and radio-mode feedback is $\dot{M}_{\rm BH}/\dot{M}_{\rm Edd} = 0.01$ (e.g. Churazov et al., 2005; Sijacki et al., 2007). During the quasar phase, the BHs in AGN–both–hcA and and AGN–cold–hcA experience a few episodes of enhanced accretion, with $\dot{M}_{\rm BH}/\dot{M}_{\rm Edd} \sim 1$. In particular, the SMBH in AGN–cold–hcA is characterised by several episodes of accretion where $0.1 \lesssim \dot{M}_{\rm BH}/\dot{M}_{\rm Edd} \lesssim 1$, while the accretion is remarkably suppressed later.

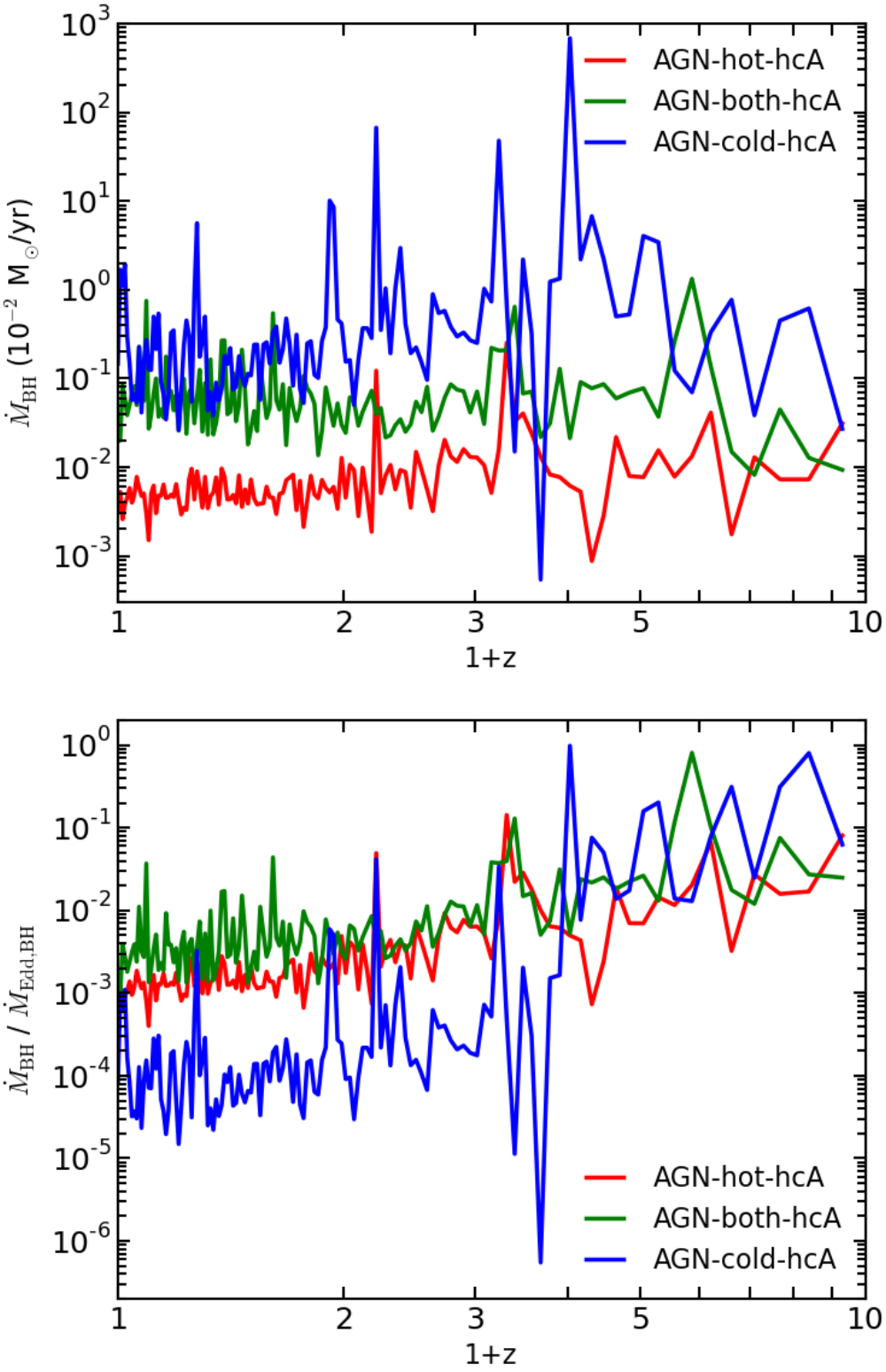

Figure 9.3: Evolution of the accretion rate of the most massive BH in AGN–hot–hcA (red), AGN–both–hcA (green), and AGN–cold–hcA (blue). The same evolution is shown both in units of 10^{-2} $M_\odot$ yr^{-2} *(top panel)* and in units of the Eddington accretion rate $\dot{M}_{\rm Edd}$ *(bottom panel)*.

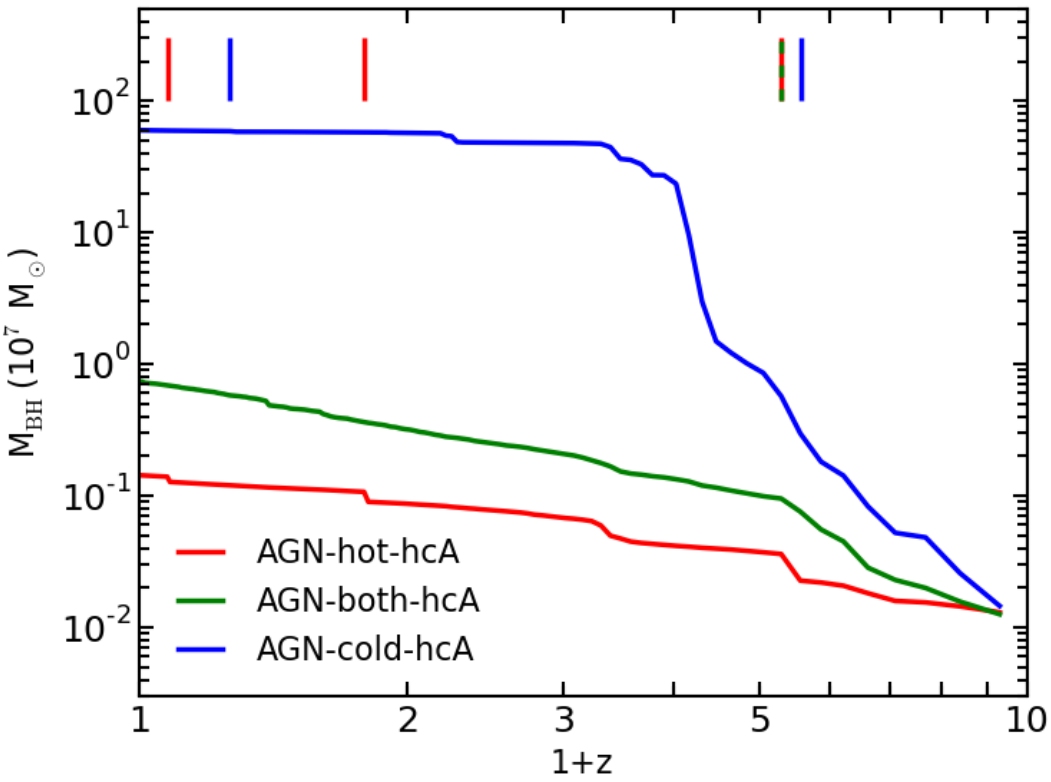

Figure 9.4: Evolution of the BH mass growth for the most massive BH in each of the simulated galaxies. Segments at the top of the Figure highlight the redshift at which the considered BH experienced a BH merger. Note that at $z \sim 4.2$ both the BHs in AGN–hot–hcA and in AGN–both–hcA have a merger.

The evolution of the BH accretion rates shown is Figure 9.3 produces the growth of BH masses, as illustrated in Figure 9.4. Figure 9.4 describes the evolution of the mass of the most massive BH within the simulated galaxies. Vertical segments highlight the redshift at which BH mergers involving the central SMBH occur. Mergers usually appear as jumps in the track of the BH mass evolution, unless the merger is between a low-mass BH which has just been seeded, and an already massive one, thus contributing a negligible increase to the BH growth (see for instance the slight jump at $z \lesssim 0.2$ for the BH of AGN–cold–hcA). The mass of the BHs at $z = 0$ are $1.43 \cdot 10^6$ $M_\odot$ (AGN–hot–hcA), $7.37 \cdot 10^6$ $M_\odot$ (AGN–both–hcA), and $5.99 \cdot 10^8$ $M_\odot$ (AGN–cold–hcA).

Even if the ICs are the same, the timing of BH mergers can be different from simulation to simulation, due to the perturbations that the BHs themselves introduce within the system.

The different evolution of the three BHs is due to the effect of the AGN when different models for coupling feedback energy to the multiphase ISM are adopted. In order to understand how feedback energy coupling affects the BH accretion and growth, I focus on the extreme cases represented by AGN–hot–hcA and AGN–cold–hcA. The reason for the intermediate behaviour of AGN–both–hcA follows directly.

When the AGN feedback energy is entirely coupled to the hot phase of the ISM, it increases the temperature of the hot phase (see Section 9.2.5). The corresponding thermal energy increase is converted into momentum for the multiphase particles, and thus can originate outflows. Multiphase particles are hence displaced from the innermost regions of the galaxy: as a consequence, the density of the central regions feeding the BH decreases and the BH accretion rate is moderate. On the other hand, when all the feedback energy supplied to the multiphase ISM is provided to the cold component of multiphase particles, it is used to evaporate cold gas and to move its mass to the hot phase. However, this AGN-induced mass transfer does not produce a significant increase of the SPH temperature of the multiphase particle (see Section 9.2.6.1). As a consequence, the multiphase gas remains close to the BH and enhances its accretion. Therefore, the BH experiences a rapid phase of mass growth, that will be halted when all the gas available within its surroundings is consumed. The BH mass growth is stopped (see Figure 9.4, below $z \lesssim 2$) and the central region of the galaxy appears devoid of gas (see the density map of AGN–cold–hcA in Figure 9.1, where the central density depression has a radius which is comparable to the smoothing length of the BH at $z = 0$, see below). In this way, it is possibe to explain why the evolution of the BH masses of AGN–hot–hcA and AGN–cold–hcA starts to differ significantly from each other at redshift $z \sim 4$. From then on, the way in which the BH impacts on the overall evolution of the galaxy is remarkably different, especially because of the feedback energy budget involved.

I provide a more quantitative explanation by computing the mass of the gas that is located within 5 kpc from the galaxy centre and that is outflowing (i.e. with $v_{\rm r} > 0$, $v_{\rm r}$ being the radial component of the particle velocity). The size of the region (a sphere with $r = 5$ kpc) that I chose to study the gas dynamics is roughly twice as large as the smoothing length of the BHs in AGN–hot–hcA and AGN–cold–hcA in the redshift range that I consider, i.e. $3 \lesssim z \lesssim 4$. This redshift range identifies the time interval within which the discrepancy between the evolution of the BH mass of AGN–hot–hcA and AGN–cold–hcA is magnified. Note that the BH smoothing length decreases below this redshift, reaching a size of ~ 2.3 kpc at $z = 0$ for AGN–cold–hcA, while it is as small as 0.8 kpc at $z = 0$ for AGN–hot–hcA. The total mass of gas outflowing from the innermost regions at $z = 4$ and $z = 3$ for AGN–hot–hcA is detailed in Table 9.3, together with the corresponding shares of multiphase and single-phase outflowing gas.

Table 9.3 also shows the same quantities for AGN–cold–hcA. These latter values are lower than those of AGN–hot–hcA by roughly a factor ~ 2. This supports the interpretation that I provided.

Figure 9.5 shows the position of the BHs of the three simulated galaxies on the plane of the so-called Magorrian relation (Magorrian et al., 1998), that describes the correlation existing between the mass of the BH and that of the bulge of the host galaxy (see Section 2.4.5). I compare results from simulations with observations from the sample by Kormendy & Ho (2013, see also Figure 2.6) and from the sample of McConnell & Ma (2013), which is made of 35 early-type galaxies (and whose best fit is provided the red solid line). In their sample, Kormendy & Ho (2013) distinguish

Table 9.3: Mass of gas outflowing from the innermost regions of AGN–hot–hcA and AGN–cold–hcA.
Column 1: simulation label. *Column 2:* redshift. *Column 3:* total mass of gas outflowing from $r \leq 5$ kpc. *Column 4:* mass of multiphase gas outflowing from $r \leq 5$ kpc. *Column 5:* mass of single-phase gas outflowing from $r \leq 5$ kpc.

Simulation	z	$M_{\mathrm{outf,\,tot}}$ ($\mathrm{M}_\odot$)	$M_{\mathrm{outf,\,mp}}$ ($\mathrm{M}_\odot$)	$M_{\mathrm{outf,\,sp}}$ ($\mathrm{M}_\odot$)
AGN–hot–hcA	$z = 4$	$1.4 \cdot 10^9$	$1.2 \cdot 10^9$	$2.1 \cdot 10^8$
	$z = 3$	$1.5 \cdot 10^9$	$1.3 \cdot 10^9$	$1.6 \cdot 10^8$
AGN–cold–hcA	$z = 4$	$7.4 \cdot 10^8$	$6.2 \cdot 10^8$	$1.2 \cdot 10^8$
	$z = 3$	$6.2 \cdot 10^8$	$4.9 \cdot 10^8$	$1.3 \cdot 10^8$

between elliptical galaxies, classical bulges in late-type galaxies and pseudo-bulges in late-type galaxies. Classical bulges are scaled-down versions of ellipticals, with which they share the formation scenario. On the other hand, pseudo-bulges are the outcome of the secular evolution they experienced within galaxy discs and do not obey the same relation as the elliptical galaxies (as discussed in Section 2.4.5). This is evident from Figure 9.5, where the majority of pseudo-bulges is located below the best-fit to ellipticals only (red solid line), and are responsible for the bending of the M_{bulge}-M_{BH} relation at $M_{\mathrm{bulge}} \lesssim 5 \cdot 10^{10}$ $\mathrm{M}_\odot$.

The bulges of the galaxies that I have simulated have a formation history more similar to that of pseudo-bulges rather than to that of classical bulges: they indeed have grown within the galaxy as the galaxy itself grew more massive[4]. Therefore, I consider as in agreement with observations those BHs that are located below the fit to the sample of elliptical galaxies only. Predictions from simulations are indicated by stars in Figure 9.5. For each simulated galaxy, I consider the mass of the BH, at $z = 0$, and the mass of the bulge of the galaxy. The mass of the bulge is estimated from the total stellar galaxy mass within R_{gal} (see Section 9.4.3) by means of the bulge-over-total mass ratio B/T: the B/T is computed as twice the mass of the counter-rotating ($J_{\mathrm{z}}/J_{\mathrm{circ}} < 0$, see Figure 9.8) star particles, thus assuming that half of the bulge mass is made up of all the counter-rotating stars. The mass of the bulge for the considered galaxies at $z = 0$ is as follows: $1.17 \cdot 10^{10}$ $\mathrm{M}_\odot$ for AGN–hot–hcA, $1.10 \cdot 10^{10}$ $\mathrm{M}_\odot$ for AGN–both–hcA, and $1.06 \cdot 10^{10}$ $\mathrm{M}_\odot$ for AGN–cold–hcA. Figure 9.5 shows that the BHs of the AGN–hot–hcA and AGN–both–hcA galaxies are in good agreement with observations. On the other hand, the AGN–cold–hcA galaxy hosts a BH that is too massive for the bulge (and thus, the galaxy) in which it resides.

BHs are indeed expected to grow mainly at high-redshift ($z \gtrsim 2$), while at later times the AGN reaches a quasi self-regulated state, with AGN feedback roughly counterbalancing gas accretion and cooling. At approximately that point, the BH approaches the Magorrian relation, the BH accretion rate drops to lower values and

[4]Note that I postpone to a forthcoming work a proper classification and an extensive investigation of the formation path of the bulges of the galaxies that I have simulated.

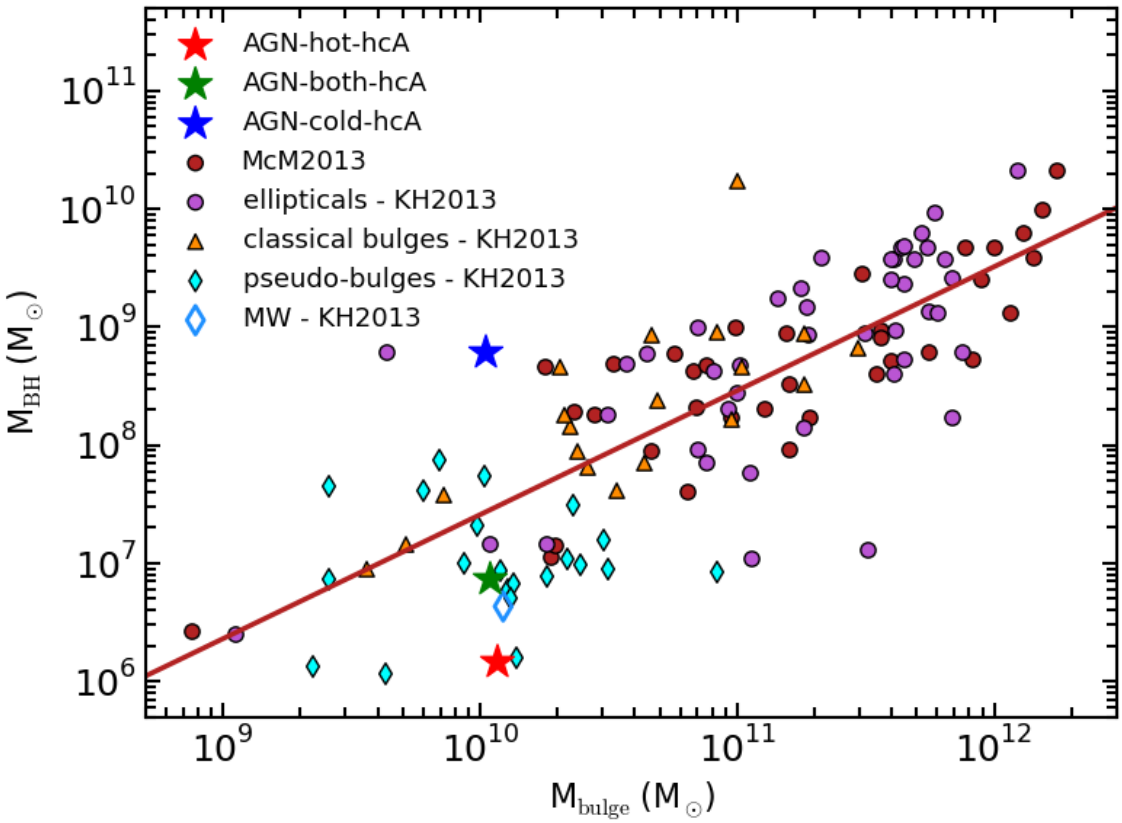

Figure 9.5: $M_{\rm bulge}$-$M_{\rm BH}$ relation for BHs in the simulated galaxies AGN–hot–hcA (red starlet), AGN–both–hcA (green starlet), and AGN–cold–hcA (blue starlet). Observations are from Kormendy & Ho (2013, KH2013) and from McConnell & Ma (2013, McM2013). The red solid line depicts the best fit to the 35 elliptical galaxies in the sample of McConnell & Ma (2013). The light-blue empty diamond shows the position of the BH in our Galaxy.

the AGN experiences the radio-mode. BHs of the simulated galaxies AGN–hot–hcA and AGN–both–hcA set on the Magorrian relation at $z \sim 1$, approaching by that time a position close to that where they are at $z = 0$. The way in which BHs climb the plane of the Magorrian relation proceeds along with the evolution of their mass shown in Figure 9.4. Indeed, the mass of the bulge of these galaxies does not grow significantly at $z \lesssim 2$, and this almost fixes the position of the galaxies on the x-axis of Figure 9.5. For instance, considering the AGN–both–hcA galaxy, the mass of its bulge increases from $9.10 \cdot 10^9$ $M_\odot$ at $z = 1.5$, to $9.27 \cdot 10^9$ $M_\odot$ at $z = 1$, to $9.77 \cdot 10^9$ $M_\odot$ at $z = 0.5$, reaching then $1.10 \cdot 10^{10}$ $M_\odot$ at $z = 0$. Matching observations when the Magorrian relation is considered is a valuable benchmark for simulated galaxies, as this relation involves the BH mass and the stellar mass of the bulge of the host galaxy, that are quantities integrated throughout the galaxy evolution. In addition, the BH mass is also highly sensitive to details of the feedback process.

In Section 9.4.4, I will show how the final results are sensitive to BH seed mass and to the details of gas accretion, and how I exploited the Magorrian relation to choose the reference $M_{\rm BH,\,seed}$.

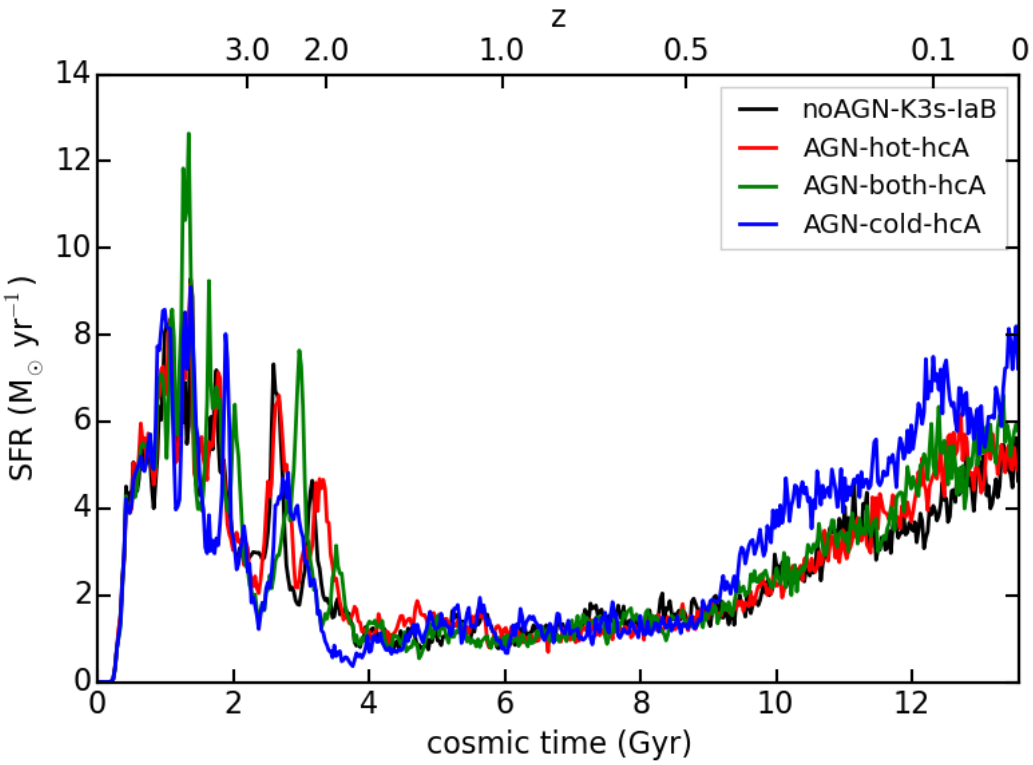

Figure 9.6: Star formation history for galaxies simulated with and without AGN feedback, colour-coded as explained in the legend.

9.4.3 BH-galaxy coevolution

In this Section, I introduce the most important properties of the simulated galaxies presented in Section 9.4.1, i.e. AGN–hot–hcA, AGN–both–hcA, and AGN–cold–hcA, focussing on the effect that AGN feedback has on their evolution. I will contrast results with properties of the galaxy noAGN–K3s–IaB, where the AGN is not included.

Figure 9.6 shows the star formation history of the four galaxies. With respect to the simulation noAGN–K3s–IaB (black curve), the three galaxies including AGN feedback experience a comparable star formation history at early epochs ($z \gtrsim 3$), when the galaxy bulge forms. The comparison between some of the most pronounced star formation peaks highlights how the AGN usually has a positive feedback: for instance, the peak at $z > 3$ of AGN–both–hcA is a clear evidence of this. Also, bursts in the evolution of the star formation can be related, relatively easily for AGN–both–hcA and AGN–cold–hcA, to peaks in the evolution of the BH accretion rate (see Figure 9.3). Nonetheless, a number of episodes where the AGN is found to have a negative feedback, suppressing star formation, are also present. The inclusion of the AGN clearly produces a positive feedback at low redshift ($z \lesssim 0.5$), where the SFR is higher for simulations with AGN. The reason for the enhanced star formation stems from the fact that AGN feedback energy over-pressurises the gas (see equations (5.24) and (5.25), and Section 5.3).

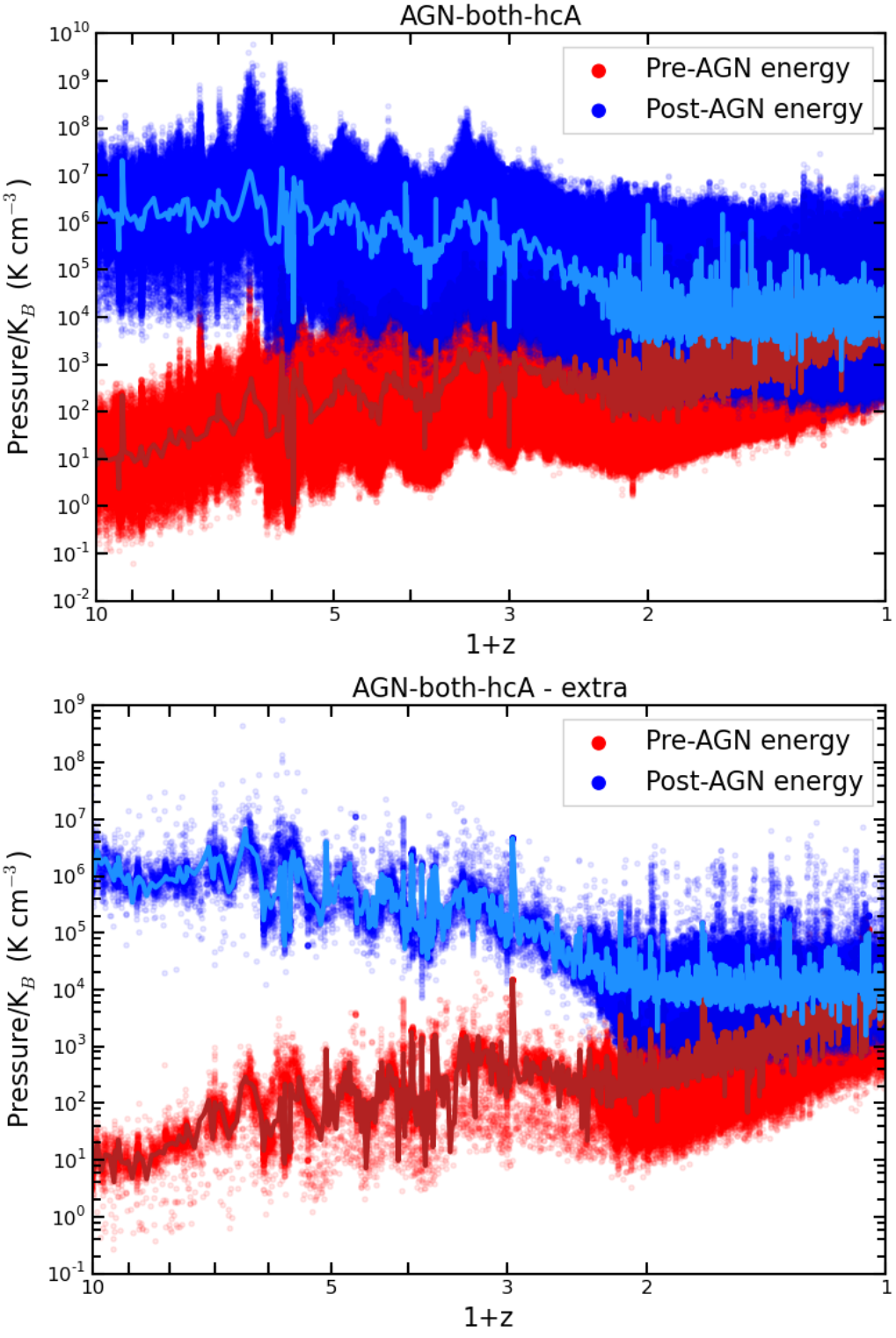

Figure 9.7: Pressure of multiphase gas particles before and soon after the feedback energy injection, as a function of redshift, for the simulation AGN–both–hcA. Solid curves show the median evolution. *Top panel:* evolution of gas particles for which all the feedback energy supplied to the cold gas is used for the evaporation of the cold gas mass. *Bottom panel:* evolution of gas particles for which a fraction of the energy initially allocated to the cold phase is provided to the hot phase, as an additional contribution that ensures that no feedback energy is lost.

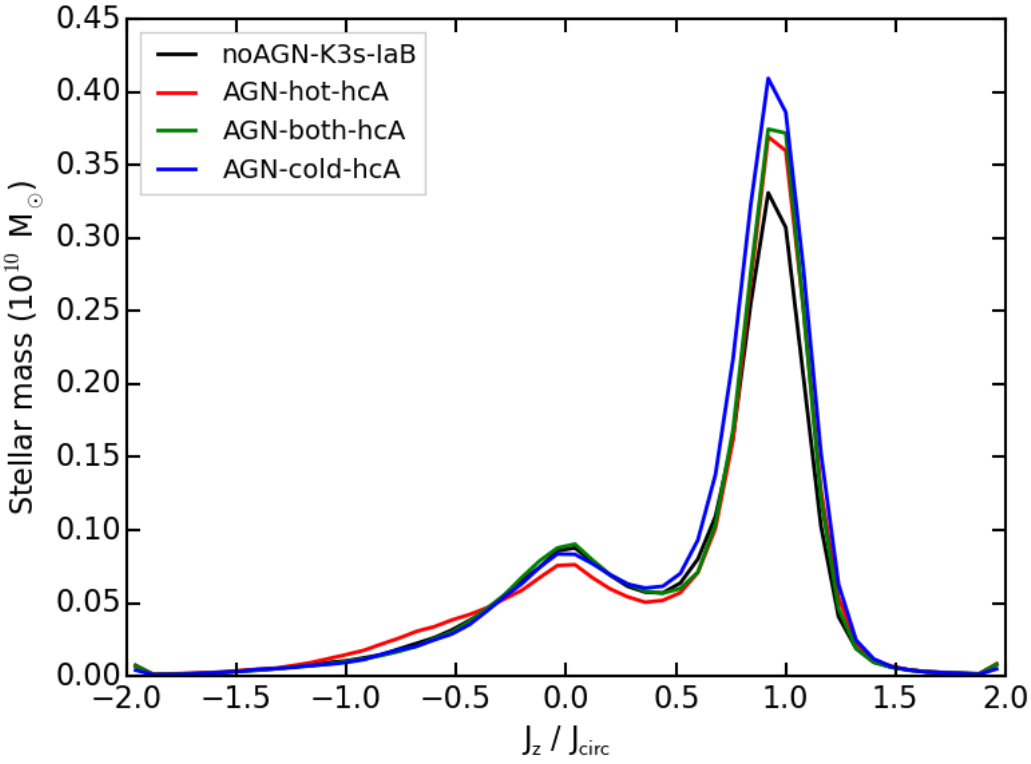

Figure 9.8: Circularity of star particles' orbits for galaxies simulated with and without AGN feedback, colour-coded as explained in the legend.

Table 9.4: Relevant features of the galaxies analysed in Sections 9.4.1, 9.4.2, and 9.4.3. *Column 1:* simulation label. *Column 2:* bulge-over-total mass ratio. *Column 3:* total stellar mass within $R_{\rm gal}$. *Column 4:* stellar mass of the galaxy bulge. *Column 5:* galactic radius $R_{\rm gal}$.

Simulation	B/T	$M_{*,\,\rm tot}$ ($\rm M_\odot$)	$M_{*,\,\rm bulge}$ ($\rm M_\odot$)	$R_{\rm gal}$ (kpc)
noAGN–K3s–IaB	0.41	$2.68 \cdot 10^{10}$	$1.11 \cdot 10^{10}$	24.03
AGN–hot–hcA	0.41	$2.83 \cdot 10^{10}$	$1.17 \cdot 10^{10}$	24.18
AGN–both–hcA	0.38	$2.87 \cdot 10^{10}$	$1.10 \cdot 10^{10}$	24.15
AGN–cold–hcA	0.34	$3.14 \cdot 10^{10}$	$1.06 \cdot 10^{10}$	24.16

AGN-induced over-pressurisation of gas can be quantified by comparing the pressure of multiphase gas particles that received feedback energy. Figure 9.7 considers the simulation AGN–both–hcA and analyses the pressure of multiphase gas particles before and soon after the feedback energy injection (i.e. at the beginning and at the end of the SPH time-step), as a function of redshift. The top panel of Figure 9.7 considers the multiphase particles for which all the feedback energy supplied to the cold gas is used for the evaporation of the cold gas mass. The bottom panel describes the evolution of gas particles for which a fraction of the energy initially allocated to the cold phase is provided to the hot phase (see equation (9.21) and Section 9.2.5), as an additional contribution that ensures that no feedback

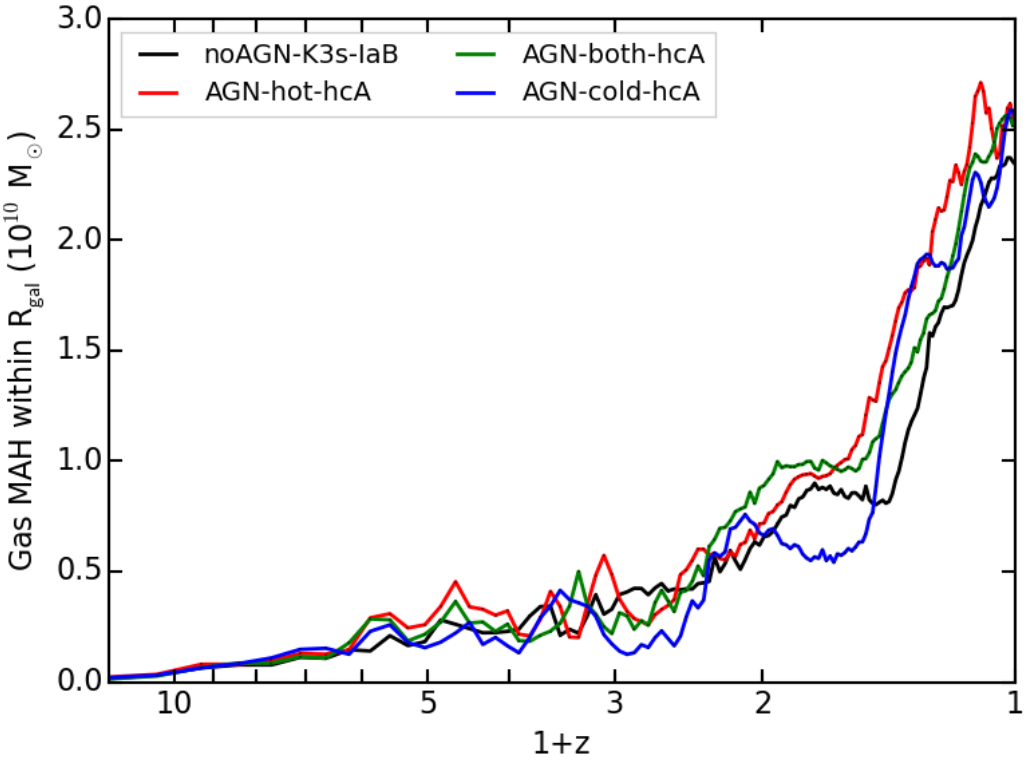

Figure 9.9: Gas mass accretion history for galaxies simulated with and without AGN feedback. Evolution of the gas accreted within the galactic radius, i.e. $R_{\rm gal} = 0.1\,R_{\rm vir}$.

energy is lost. Solid curves depict the median evolution. The trend is the same for the two sub-samples of particles: nevertheless, in this way it is possible to appreciate the impact of the condition that guarantees that all the feedback energy is actually used (even if the multiphase gas particle that is provided with it has not enough mass of cold gas) and the number of particles that this condition involves (1/10 of the total number of multiphase particles selected for receiving feedback energy). For the sake of concision, I show how the pressure of gas particles increases due to AGN feedback for the simulation AGN–both–hcA only. Similar conclusions can be drawn when considering the other simulations, with the AGN-induced over-pressurisation of gas particles always becoming less significant as the redshift decreases.

The over-pressurisation of gas shown in Figure 9.7 does not result in an enhanced SFR at all the redshifts (see Figure 9.6, where the star formation history of galaxies with and without the AGN feedback is comparable in the redshift range $2 \gtrsim z \gtrsim 0.5$): this is due to the complex effect of AGN feedback, that also produces a concurrent overall heating of the forming galaxy and promotes massive outflows, thus reducing the gas reservoir available for star formation. These findings favour a scenario where the BH feedback can reach the self-regulation.

The low-redshift enhanced star formation in galaxies simulated with AGN feedback with respect to the noAGN–K3s–IaB simulation is responsible for more extended galaxy stellar discs (see also Figure 9.2). Figure 9.8 shows the distribution of stellar mass as a function of the circularity of the orbits of star particles, at

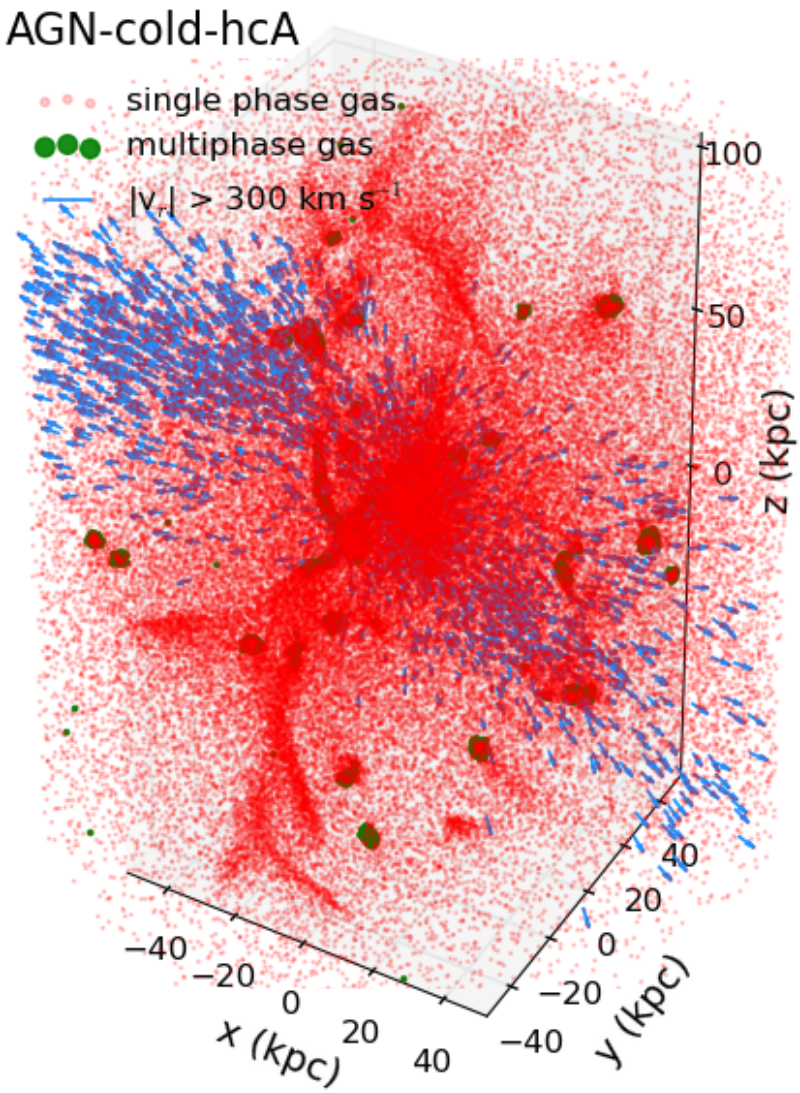

Figure 9.10: Geometry of the outflowing gas in the AGN–cold–hcA simulation, at $z = 2$. Single-phase gas is shown by red points, multiphase gas by green dots, and is mostly embedded within the innermost regions of the forming galaxy. Light blue arrows pinpoint gas that is outflowing with a radial velocity larger than the escape velocity of the halo.

$z = 0$, for the different simulations. The circularity of a stellar orbit is quantified by means of the ratio of specific angular momenta J_z/J_{circ}, as explained in Section 6.5.2 (see also Sections 6.5.3.2 and 7.4.1). The stellar disc component ($J_z/J_{circ} \sim 1$) is remarkably larger in AGN–hot–hcA, AGN–both–hcA, and especially in AGN–cold–hcA with respect to noAGN–K3s–IaB. Bulge-over-total mass ratios are lower (or equal, at most); their values, along with total and bulge stellar masses within R_{gal} are detailed in Table 9.4.

Figure 9.9 shows the mass accretion history of the four galaxies, i.e. the evolution of the mass of gas that is accreted within their galactic radius. Galaxies share comparable accretion histories, except for some episodes where differences are

evident. These discrepancies are the result of the internal gas dynamics: powerful outflows fostered by the joint activity of stellar and AGN feedback can reduce or even suppress for a while the accretion of gas from the large scale environment towards the innermost regions of galaxies. As an example, strong outflows at $z = 2$ in the AGN–cold–hcA simulation are responsible for the dip in the mass accretion history of the galaxy, since they hinder gas accretion (note that I am now considering a different redshift range with respect to that analysed in Section 9.4.2). Outflow geometry in the aformentioned case is shown in Figure 9.10: from the forming galaxy, at $z = 2$, a powerful bipolar outflow is launched, as shown by the light blue arrows pinpointing single-phase gas that is outflowing with a radial velocity that exceeds the escape velocity of the halo (i.e. $v_{\rm r} > 300$ km s^{-1}). Single-phase outflowing gas has a mass of $1.8 \cdot 10^{10}$ M$_{\odot}$, while the mass of multiphase outflowing gas amounts to $1.5 \cdot 10^{9}$ M$_{\odot}$; single-phase outflowing gas powered at velocity $v_{\rm r} > 300$ km s^{-1} has a mass of $7.4 \cdot 10^{8}$ M$_{\odot}$.

Also, by focussing on the mass accretion history of AGN–both–hcA and AGN–cold–hcA in Figure 9.9, at $z \sim 1$, it is possible to see how outflows powered within galaxies that are experiencing a coevolution with SMBHs of different masses and accretion rates (see Figures 9.4 and 9.3, top panel) have a different interaction with the large scale environment. Figure 9.11 shows the radial component of the velocity for both single-phase and multiphase gas particles, as a function of their distance from the galaxy centre, at $z = 1$. AGN feedback launches a larger amount of gas to higher velocities in the AGN–cold–hcA than in AGN–both–hcA, and this results in a slow-down and a reduction of gas accretion from the large scale. Total outflowing gas masses involved in the process are as follows: $3.8 \cdot 10^{10}$ M$_{\odot}$ for AGN–both–hcA, and $4.2 \cdot 10^{10}$ M$_{\odot}$ for AGN–cold–hcA. The contribution to the outflowing gas mass from the single-phase gas is larger by an order of magnitude than that coming from the multiphase gas. In line with the interpretation proposed in Section 9.4.2, when the AGN feedback energy provided to the multiphase gas is entirely coupled to the cold phase, a lower amount of multiphase gas is outflowing ($4.1 \cdot 10^{9}$ M$_{\odot}$ for AGN–both–hcA, with respect to $2.8 \cdot 10^{9}$ M$_{\odot}$ for AGN–cold–hcA).

For reference, in Figure 9.11, I also show the radial velocity for single-phase and multiphase gas particles when the AGN is not included. With respect to the case in which SMBHs are considered, in noAGN–K3s–IaB a lower amount of gas is fostered to outflow, the total mass of outflowing gas being $3.5 \cdot 10^{10}$ M$_{\odot}$ (the same is true when focussing on the outflowing gas which is located within a distance of $r = 15$ kpc from the galaxy centre).

Finally, Figure 9.12 shows the radial profiles of gas and stellar surface density for the set of simulated galaxies, and provides complementary evidence to the gas and stellar density maps discussed in Section 9.4.1 (see Figures 9.1 and 9.2). The most striking features are the drop in the gas density profiles of AGN–cold–hcA for $r \lesssim 2.5$ kpc, and the external bump ($25 \gtrsim r \gtrsim 18$ kpc) in the gas density profile of AGN–hot–hcA. The latter property is the outcome of recent gas accretion (as extensively discussed in Section 6.5.3.2).

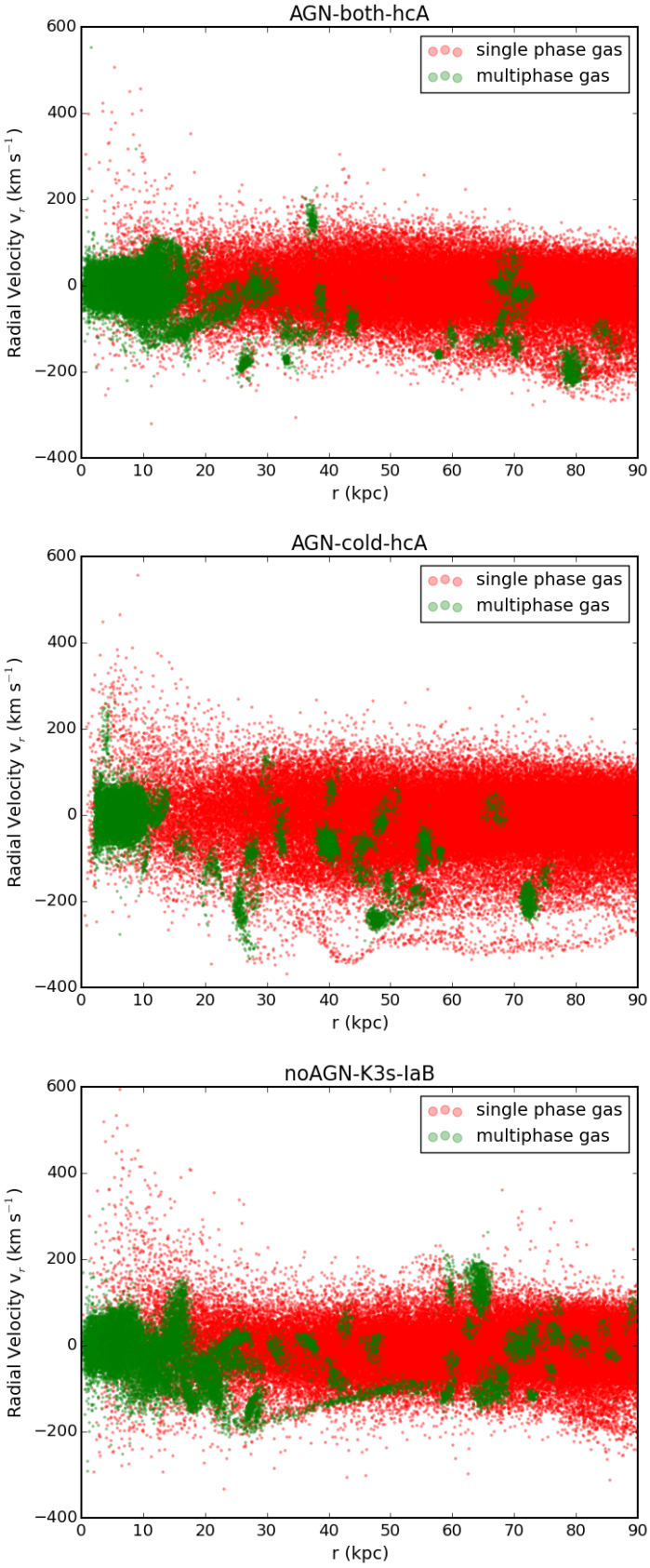

Figure 9.11: Radial component of the velocity for single-phase (red) and multiphase (green) gas particles as a function of their distance from the galaxy centre, at $z = 1$. *From top to bottom:* simulations AGN–both–hcA, AGN–cold–hcA, and noAGN–K3s–IaB.

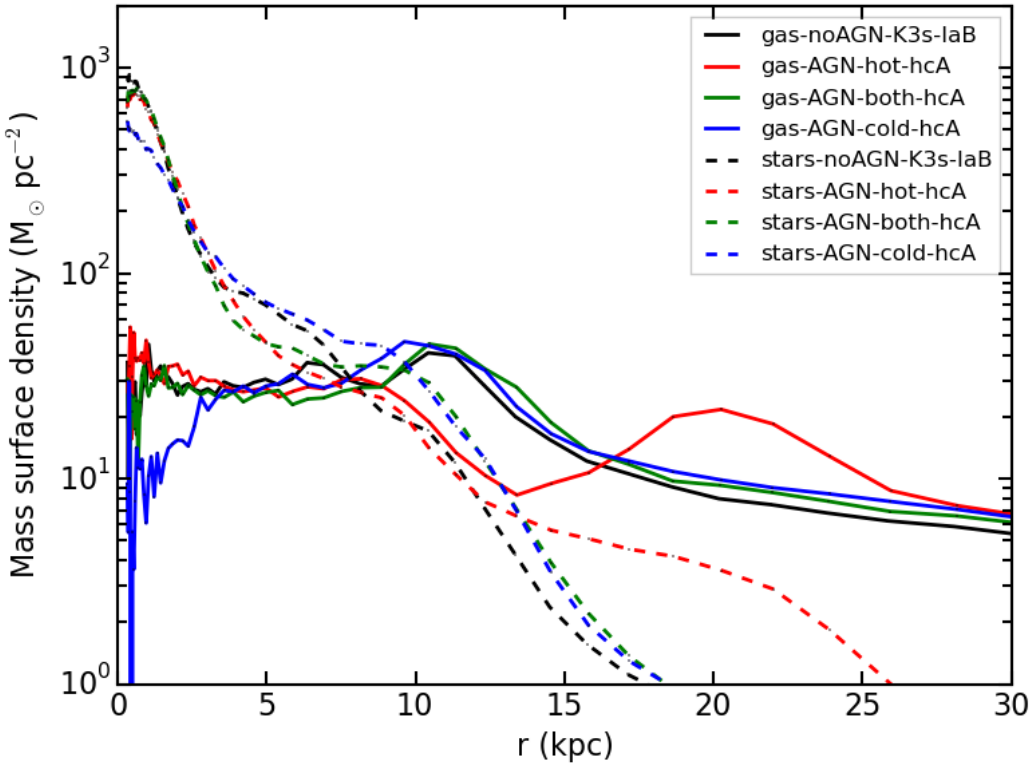

Figure 9.12: Gas (solid curves) and stellar (dashed lines) surface density profiles for galaxies simulated with and without AGN feedback.

9.4.4 Effect of BH seed mass

The initial mass assumed for BHs in cosmological simulations (see Section 9.2.1) is rather important, and has fundamental implications for theoretical models, as it is linked to the mass of SMBH progenitors and to viable scenarios of SMBH formation. The value adopted for the BH seed mass is remarkably crucial when simulating MW-sized galaxies (i.e. $M_{\rm halo,\,DM} \simeq 10^{12}$ M$_\odot$ at redshift $z = 0$, see Section 5.5) in a cosmological context: indeed, since BH growth due to gas accretion is relatively moderate in these galaxies, final results are quite sensitive to the value adopted for $M_{\rm BH,\,seed}$.

The adopted value of $M_{\rm BH,\,seed}$ is closely connected to the choice of $M_{\rm DM,thresh}$, according to the prescriptions that I adopt for seeding BHs (see Section 9.2.1). Indeed, a lower mass threshold $M_{\rm DM,thresh}$ for the DM halo within which BHs can be seeded translates directly to the introduction of the BH at higher redshift. In this Section, I explore the impact that the value assumed for $M_{\rm BH,\,seed}$ has on final results. The values for BH seed masses that I explore are: $M_{\rm BH,\,seed} = 1.1 \cdot 10^5$ M$_\odot$ (reference value), $M_{\rm BH,\,seed} = 5.5 \cdot 10^4$ M$_\odot$ (*S0.5x*), and $M_{\rm BH,\,seed} = 2.7 \cdot 10^5$ M$_\odot$ (*S2x*) (see Table 9.2). BH seeds as massive as $\sim 10^5$ M$_\odot$ would correspond to a formation scenario for SMBHs by direct collapse (e.g. Begelman et al., 2006).

I consider a first set of three simulations: the reference AGN–both–hcA (analysed in Sections 9.4.1, 9.4.2, and 9.4.3), AGN–both–hcA–S0.5x, and AGN–both–hcA–

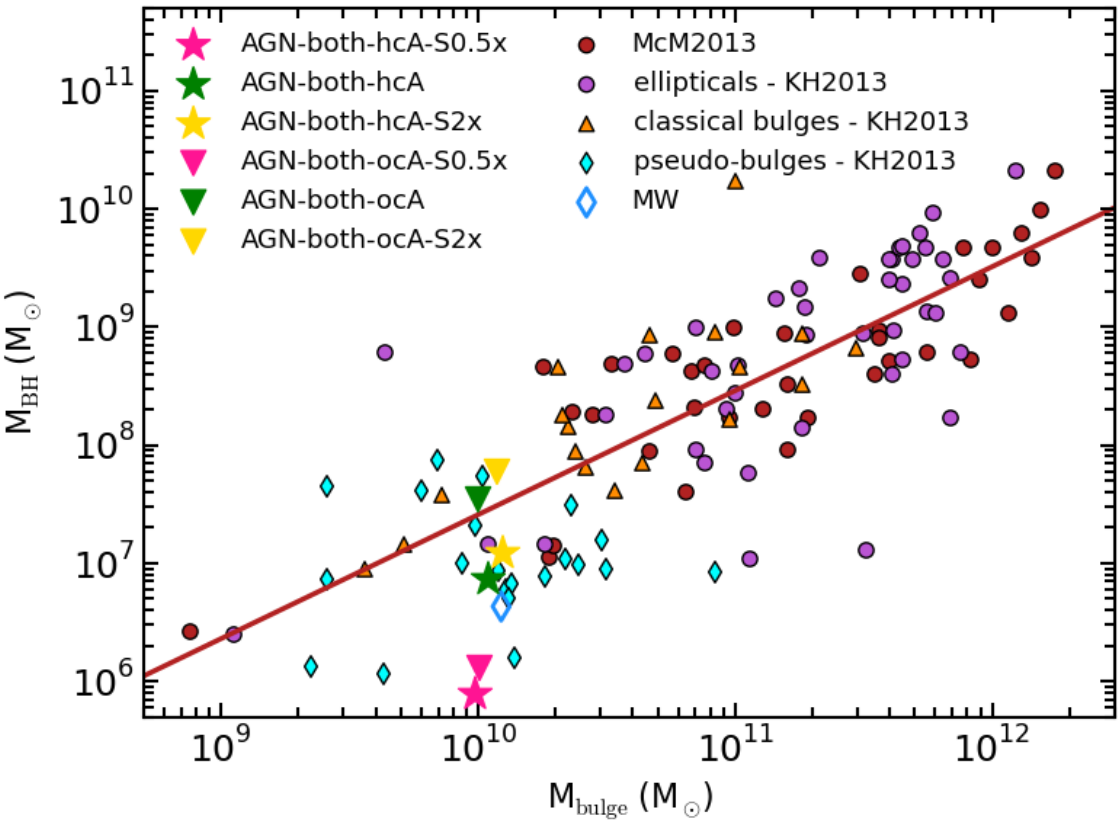

Figure 9.13: $M_{\rm bulge}$-$M_{\rm BH}$ relation for BHs in the simulated galaxies where different BH seed masses are considered (see Table 9.2). Simulations pinpointed by starlets assume both cold and hot gas accretion (*hcA*), while simulations identified by triangles assume only cold gas accretion (*ocA*). Observations are from Kormendy & Ho (2013, KH2013) and from McConnell & Ma (2013, McM2013), as in Figure 9.5.

S2x (see Table 9.2). They share the same setup and physics, and they only differ for the assumed $M_{\rm BH,\,seed}$.

Masses of their BHs at $z = 0$ are as follows: $M_{\rm BH} = 7.4 \cdot 10^6$ M$_\odot$ (AGN–both–hcA), $M_{\rm BH} = 7.7 \cdot 10^5$ M$_\odot$ (AGN–both–hcA–S0.5x), and $M_{\rm BH} = 1.2 \cdot 10^7$ M$_\odot$ (AGN–both–hcA–S2x). Figure 9.13 shows the $M_{\rm bulge}$-$M_{\rm BH}$ relation for the simulated galaxies. I compare the outcome of the three simulations (identified by stars) to observations. Observational samples for the comparison have been introduced in Section 9.4.2 and in Figure 9.5. Indeed, the seed mass of the BHs is commonly calibrated in order to reproduce observed scaling relations at redshift $z = 0$.

The simulation adopting $M_{\rm BH,\,seed} = 1.1 \cdot 10^5$ M$_\odot$ is the one that best agrees with observations. A BH seed mass as large as twice the reference value also leads to a good agreement with observations. On the other hand, decreasing $M_{\rm BH,\,seed}$ by a factor of ~ 2 with respect to the fiducial value, would decrease the $M_{\rm BH}$ at $z = 0$ by an order of magnitude. This worsens significantly the matching with observations in Figure 9.13.

I also consider three additional simulations: AGN–both–ocA, AGN–both–ocA–S0.5x, and AGN–both–ocA–S2x. They are analogous to the first set as for the

adopted BH mass seeds and model of the coupling of AGN feedback energy, but the BH in these simulations only accretes cold gas (see Table 9.2 and Section 9.3). In this way, I can explore how a different model for the BH mass growth impacts on final results. Also, I can investigate whether the prediction for the most suitable value of $M_{\rm BH,\,seed}$ is unchanged when the details of the gas accretion modelling are varied.

At $z = 0$, the most massive BH within each of the simulated galaxy has the following mass: $3.5 \cdot 10^7$ M$_\odot$ (AGN–both–ocA), $1.3 \cdot 10^6$ M$_\odot$ (AGN–both–ocA–S0.5x), and $6.0 \cdot 10^7$ M$_\odot$ (AGN–both–ocA–S2x). The stellar mass of the bulge of simulated galaxies does not depend on whether only cold or both hot and cold gas is accreted.

For this second set of simulations (triangles), the lowest value for $M_{\rm BH,\,seed}$ leads to a simulated galaxy on the edge of the region of the $M_{\rm bulge}$-$M_{\rm BH}$ relation where observations are found. The reference and the highest values for $M_{\rm BH,\,seed}$ predict a SMBH that is located in the upper edge of the region of the plane occupied by pseudo-bulges.

When only cold gas accretion is assumed, BHs grow more massive than the case in which both hot and cold gas accretion is considered. Also, if the SMBH only accretes cold gas, it usually experiences a faster growth at low redshift ($z \lesssim 1$).

The location at $z = 0$ of a SMBH on the plane of the Magorrian relation loosely constrains the way in which it coevolved with its host galaxy. However, when $M_{\rm BH,\,seed} = 1.1 \cdot 10^5$ M$_\odot$ is adopted, the BH is required to roughly increase its mass by an order of magnitude or slightly more between the redshift z at which it has been seeded and $z = 0$. Such a requirement seems to favour the scenario according to which SMBHs accrete both hot and cold gas, at least when the reference seed mass is adopted and when the AGN feedback energy provided to the multiphase ISM is evenly shared by the hot and the cold phase. Another direction of investigation comes from the possibility of limiting cold gas accretion (see Sections 9.2.3 and 9.4.7).

All the BHs in the simulations that I consider in this Section are seeded at $z \sim 8.5$: this redshift is closely related to the (fixed) value of $M_{\rm DM,thresh}$.

As a consequence, I adopt $M_{\rm BH,\,seed} = 1.1 \cdot 10^5$ M$_\odot$ as the fiducial value for the BH mass seed. Albeit the exploration of the parameter space for $M_{\rm BH,\,seed}$ has been carried out for a single galaxy rather than for galaxies in a cosmological box, and even if resolution effects can enter the calibration, the reference value for $M_{\rm BH,\,seed}$ can be considered as representative of typical progenitors of MW-sized BHs at $z = 0$. According to predictions from the simulations considered here, SMBH progenitors as massive as $\sim 10^5$ M$_\odot$ should already be in place at redshift $z \gtrsim 8$. This poses a challenging question from a theoretical perspective (Begelman et al., 2006), given the age of the Universe at that time ($\sim 0.6 \div 0.7$ Gyr).

9.4.5 Does AGN feedback affect metallicity profiles?

The goal of this Section is to address the question of whether AGN feedback has an impact on the distribution of heavy elements within galaxies.

At variance with stellar feedback, the feedback from SMBHs is limited to energy injection, while it does not supply metals to the surrounding medium. However, AGN feedback promotes powerful outflows: they can foster the circulation of gas in and around galaxies, thus resulting in a modification of the heavy elements distribution. In addition, while launching outflows, SMBHs can modify the chemo-galactic ecosystem because they could either expel pristine gas at high redshift, that later falls back and dilutes the local metal content of the galaxy; or they could eject outwards gas enriched from stellar feedback, depriving of metals the innermost regions of galaxies. In order to assess the possible importance of these processes, the slopes and the normalizations of metallicity gradients can reveal vital information.

In this Section, I consider two sets of simulations: the first set assumes $f_{\rm bin,Ia} = 0.03$ as for the fraction of binary systems originating SNe Ia (as for all the simulations analysed so far), in the second set $f_{\rm bin,Ia} = 0.1$. Each set is constituted of four simulations, two for each considered IMF (either Kroupa (2001), i.e. K2s or Kroupa et al. (1993), i.e. K3s), one of them with AGN feedback included, the other one without AGN feedback. In this way, I can explore the relative role of the AGN feedback and the assumed IMF in determining metallicity profiles. Predictions from simulations are compared with the oxygen abundance radial profiles of gas of the 130 nearby late-type galaxies in the observational sample of Pilyugin et al. (2014), introduced in Section 7.4.3.2.

First, I analyse the four simulations: *noAGN–K3s–IaB* (black), *AGN–both–hcA–K3s–IaB* (green), *noAGN–K2s–IaB* (cyan), and *AGN–both–hcA–K2s–IaB* (brown). The first two simulations are the ones considered also, for instance, in Section 9.4.1, and the color choice is self-consistent throughout the Chapter. Here, for the sake of clarity, I also specified *–IaB* in their label, as the fraction of binary systems hosting SNe Ia is what distinguishes the first set of simulations from the second one in this Section. The simulation labeled *noAGN–K2s–IaB* is the simulation K2s–yA–IaB–kA (cyan) presented in Chapter 7. I remind that, as thouroughly discussed in Section 7.3 and in agreement with the work presented in Chapter 7, all the simulations adopting the K2s IMF have a feedback efficiency ($f_{\rm fb,kin} = 0.12$) roughly halved with respect to simulations where the K3s IMF is assumed (where $f_{\rm fb,kin} = 0.26$).

The left-hand panel of Figure 9.14 shows the star formation history of the set of galaxies, while the right-hand panel describes the distribution of stellar mass as a function of the circularity of star particles' orbits (see Section 9.4.1, and Chapters 6 and 7). Galaxies noAGN–K3s–IaB (black) and AGN–both–hcA–K3s–IaB (green) have been already analysed in Section 9.4.1. Galaxies noAGN–K2s–IaB (cyan) and AGN–both–hcA–K2s–IaB (brown) present a striking difference: noAGN–K2s–IaB is a bulge-dominated galaxy with a reduced stellar disc (see Figure 7.2 and further analysis in Section 7.4.1), while AGN–both–hcA–K2s–IaB is a disc

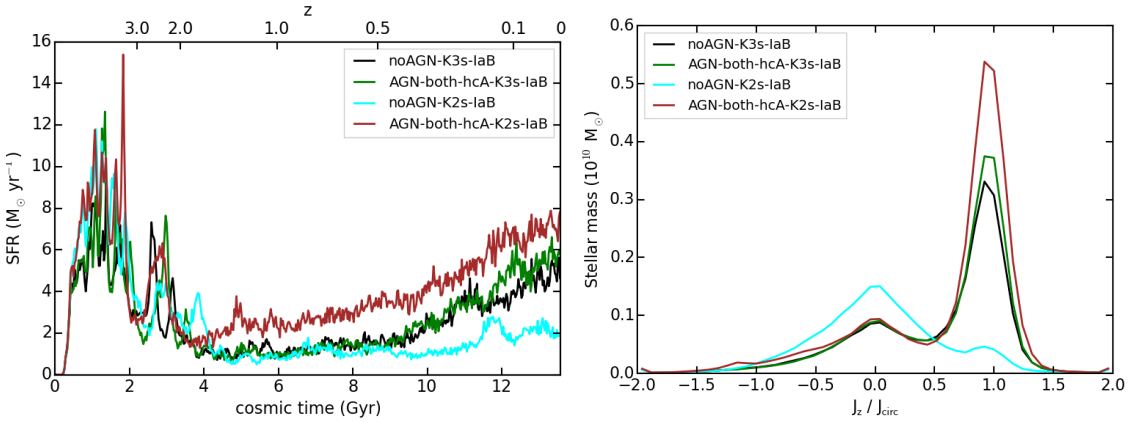

Figure 9.14: Star formation history *(left-hand panel)* and stellar mass as a function of the circularity of stellar orbits *(right)* for the simulated galaxies characterised by $f_{\rm bin,Ia} = 0.03$.

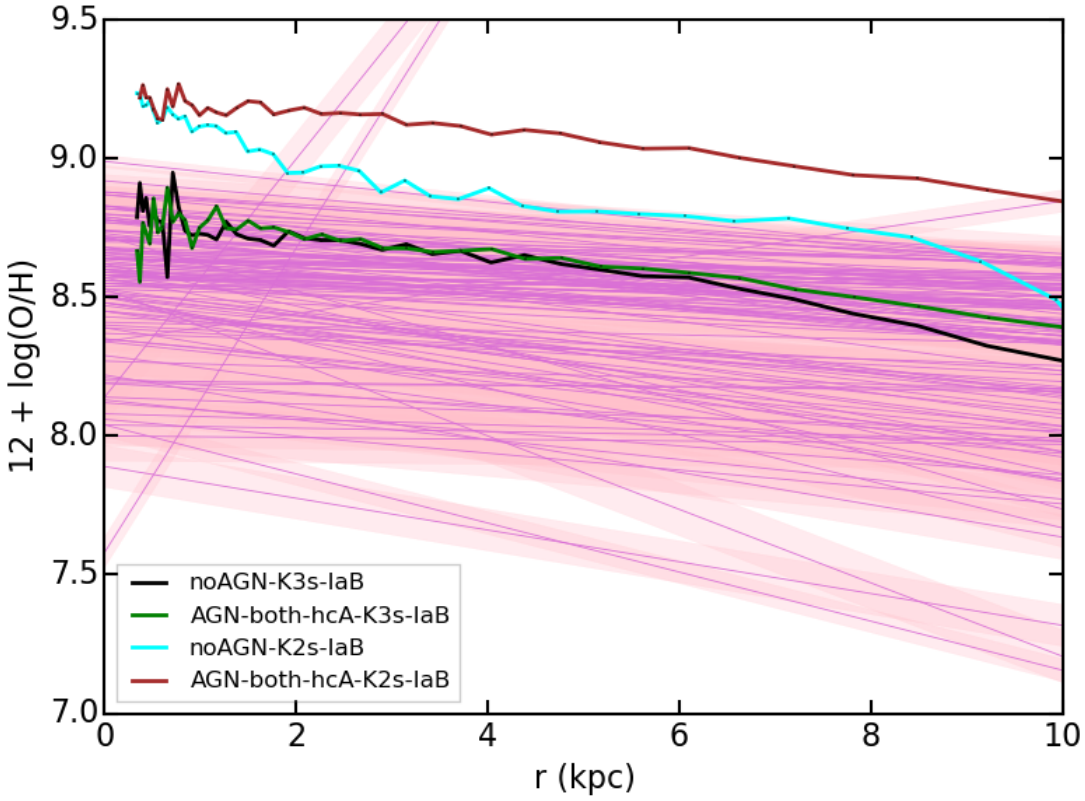

Figure 9.15: Oxygen abundance gradients of gas in the simulated galaxies having $f_{\rm bin,Ia} = 0.03$. Pink profiles are observations from the sample of disc galaxies of Pilyugin et al. (2014), with shaded envelopes depicting the scatter of oxygen abundance around the trend.

dominated galaxy, its stellar disc extending out to $\gtrsim$ 15 kpc from the galaxy centre. The clear peak at $J_z/J_{circ} \sim 1$ (Figure 9.14, right panel) is the consequence of the sustained star formation occurring below $z \lesssim 2$ (Figure 9.14, left panel). The higher low-redshift SFR is the result of the positive AGN feedback, and of the larger amount of gas accreted within both the virial and the galactic radii of the AGN–both–hcA–K2s–IaB galaxy. The AGN feedback is responsible for over-pressurising the gas located within the forming galaxy disc, and thus for enhancing and promoting the star formation. Also, the presence of the SMBH is responsible for a different gas dynamics within the galaxy. For instance, at $z = 2$, powerful outflows characterise the noAGN–K2s–IaB galaxy (that has just experienced a burst of star formation), single-phase outflowing gas with velocities as high as 1000 km s^{-1} and even more being present out to $r \gtrsim 30$ kpc from the galaxy centre. This high-velocity outflowing gas is responsible for quenching or strongly suppressing gas accretion in noAGN–K2s–IaB. On the other hand, outflows are less powerful in AGN–both–hcA–K2s–IaB at $z \sim 2$; in addition, its central BH has an accretion rate of $\dot{M}_{BH} \simeq 10^{-2} \div 10^{-3}$ M$_\odot$ yr^{-1} at $z \sim 2$. Such a redshift can be identified as the redshift from which the star formation histories of the galaxies noAGN–K2s–IaB and AGN–both–hcA–K2s–IaB start to differ significantly. Although counterintuitive, it can happen that outflows powered by stellar activity only are more powerful than the situation in which AGN feedback is included; this is especially true if the AGN comes from a long period of quasar-like accretion (powered by inflow), while in the corresponding period the same galaxy without SMBH has experienced a burst of star formation.

Figure 9.15 shows the oxygen abundance radial profiles of gas in the simulated galaxies. Predictions from simulations are compared with observations of Pilyugin et al. (2014, see above and Section 7.4.3.2). Simulations noAGN–K3s–IaB (black) and AGN–both–hcA–K3s–IaB (green) have almost indistinguishable metallicity profiles, that only show a slight discrepancy beyond $r \gtrsim 6$ kpc from the galaxy centre (the discrepancy being as high as 0.1 dex at $r = 10$ kpc). The two profiles share comparable slopes and normalization, this indicating that the AGN feedback does not affect significantly the distribution of heavy elements in the galaxy. Profiles of both the simulated galaxies are in agreement with observations. The marginal discrepancy at $r \gtrsim 6$ kpc highlighted above is due to the AGN-stimulated star formation at $z \lesssim 0.1$ (see Figure 9.14, left-hand panel), that results in recent star formation occurring in the outer regions of the galaxy disc (see also Figure 9.14, right-hand panel). The stellar mass surface density of AGN–both–hcA–K3s–IaB at $r = 10$ kpc is twice as high as that of noAGN–K3s–IaB.

As for the metallicity profiles of galaxies noAGN–K2s–IaB (cyan) and AGN–both–hcA–K2s–IaB (brown), they show a discrepancy that amounts to $\sim 0.2 \div 0.3$ dex from $r = 2$ kpc outwards. This difference, however, directly results from the different star formation history that the galaxies experience (see Figure 9.14, left-hand panel) and from their consequently different morphologies (see Figure 9.14, right-hand panel). The galaxy noAGN–K2s–IaB has a dominant bulge component and a

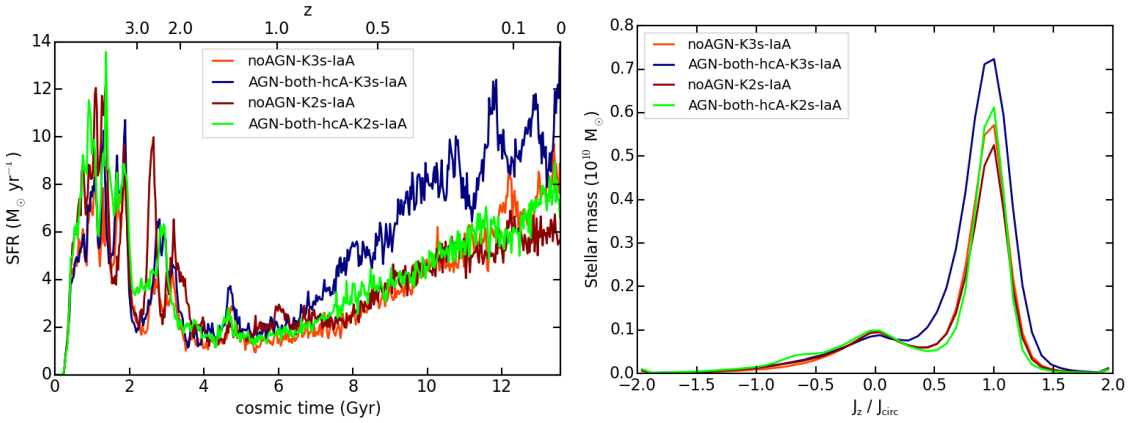

Figure 9.16: Star formation history *(left-hand panel)* and stellar mass as a function of the circularity of stellar orbits *(right)* for the simulations adopting $f_{\rm bin,Ia} = 0.1$.

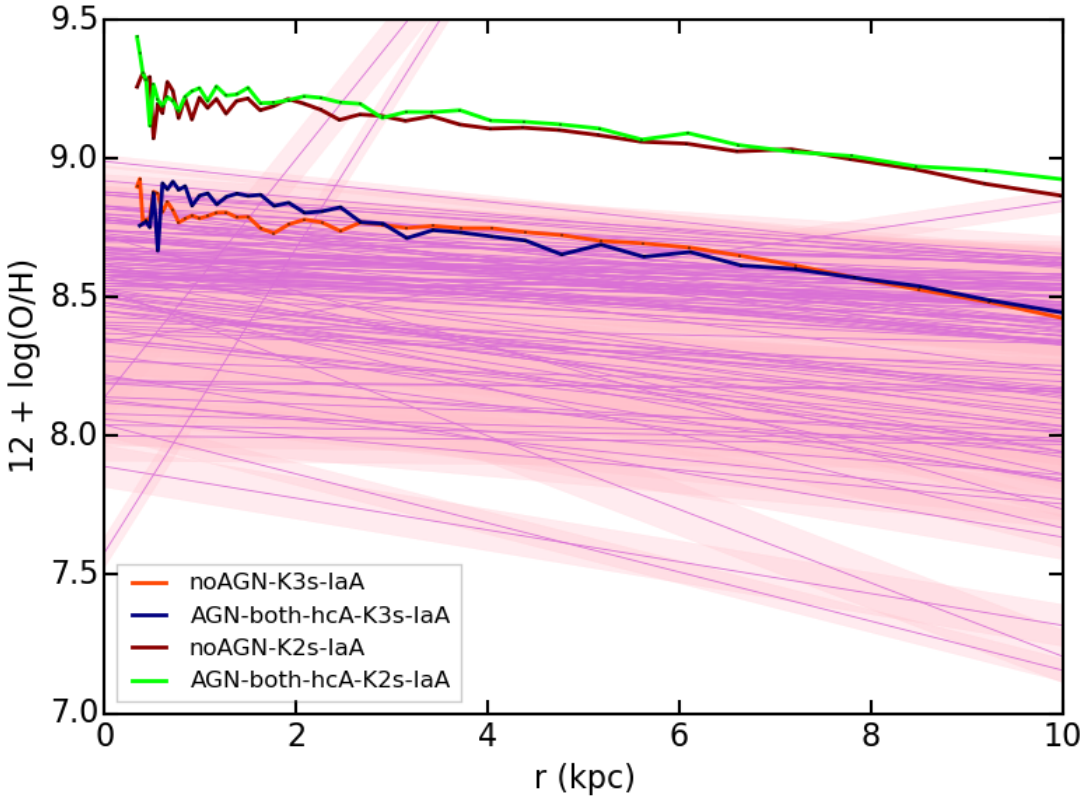

Figure 9.17: Oxygen abundance radial profile of gas in the simulated galaxies having $f_{\rm bin,Ia} = 0.1$. Pink profiles are observed metallicity gradients from the sample of Pilyugin et al. (2014).

reduced stellar disc (see Figure 7.2 and Section 7.4.1). On the other hand, AGN–both–hcA–K2s–IaB has a dominant disc component, that has grown in size with time as it progressively became more massive (inside-out scenario, see Section 7.4.2). As a consequence, the star formation that took place in the disc across all its extent is responsible for the higher metal content in the AGN–both–hcA–K2s–IaB galaxy. Therefore, the difference between the two profiles cannot be ascribed to the direct effect of the AGN on the circulation of metals within the galaxy; it is rather due to the coevolution of the galaxy and the SMBH, whose final outcome is the enhanced star formation history of the AGN–both–hcA–K2s–IaB galaxy at redshift $z \lesssim 2$. Metallicity profiles of galaxies simulated assuming the K2s IMF highlight an over-production of heavy elements with respect to observations of Pilyugin et al. (2014) and to predictions by simulations adopting the K3s IMF, due to the larger number of massive stars predicted by the K2s IMF (as explained in Section 7.3 and thouroughly discussed in Chapter 7).

The picture emerging is that the normalization of the metallicity profiles is driven by the IMF, while the AGN feedback has a negligible, direct effect on them.

Simulations analysed so far adopt $f_{\rm bin,Ia} = 0.03$ as for the fraction of binary systems with properties suitable for originating SNe Ia: this value has been indeed found to be preferred for late-type galaxies in the local Universe (see Chapter 7). However, since Figure 9.15 is not a proof beyond argument of the lack of influence of AGN feedback on metallicity profiles, due to the effect ascribed to the different morphology of the galaxies, further evidence is needed.

Taking advantage of the simulations carried out to explore the different parameters entering the chemical model (see Chapter 7), I consider a second set of simulations. For all of them $f_{\rm bin,Ia} = 0.1$ is assumed. The simulated galaxies in the second suite are: *noAGN–K3s–IaA* (orange), *AGN–both–hcA–K3s–IaA* (dark blue), *noAGN–K2s–IaA* (dark red), and *AGN–both–hcA–K2s–IaA* (bright green). The simulations labeled *noAGN–K3s–IaA* and *noAGN–K2s–IaA* are the simulations K2s–yA–IaA–kA (red) and K3s–yA–IaA–kB (orange) presented in Chapter 7.

The left-hand panel of Figure 9.16 shows the star formation history of the four galaxies: with respect to simulations with no AGN (extensively discussed in Section 7.4.1), the most striking difference is the positive AGN feedback at low redshift ($z \lesssim 1$), due to the (marginally) larger mass of gas that is accreted by the forming galaxy and (especially) to the pressurisation of gas (see also Section 9.4.1). At higher redshift, it is worth noting some episodes of negative feedback, especially if we focus on the redshift range $3 \gtrsim z \gtrsim 1.8$ and consider simulations noAGN–K2s–IaA (dark red) and AGN–both–hcA–K2s–IaA (bright green): the SFR of the latter galaxy exhibits less pronounced peaks. The right-hand panel of Figure 9.16 shows the distribution of stellar mass as a function of the circularity of stellar orbits, and clearly demonstrates that all the analysed galaxies are spirals with a dominant, rotation-supported disc component. The stellar mass in the disc is larger when the AGN is accounted for, due to its positive feedback at low redshift. Bulge-over-total

mass ratios are: $B/T = 0.28$, 0.22, 0.33, and 0.38 for for galaxies noAGN–K3s–IaA, AGN–both–hcA–K3s–IaA, noAGN–K2s–IaA, and AGN–both–hcA–K2s–IaA, respectively. The quite high B/T quoted for the AGN–both–hcA–K2s–IaA galaxy is due to the presence of a counter-rotating satellite[5], while the galaxy morphology is regular, with an extended disc and no bars.

Figure 9.17 confirms that the normalization of metallicity gradients is driven by the assumed IMF alone. The AGN feedback has a negligible effect in shaping the metallicity gradients: simulations where the AGN is included predict that the distribution of metals within galaxies is not altered by the AGN feedback. As a consequence, the analysis performed in Section 7.4.3.2 is still valid when BHs and the ensuing feedback are included in simulations, and the results are even more robust. Therefore, the conclusions drawn in Chapter 7 as for the indication to prefer a Kroupa et al. (1993) IMF (more top-light) for disc galaxies in the local Universe is confirmed and further corroborated.

9.4.6 Coupling AGN feedback energy according to ISM properties

In simulations presented so far, AGN feedback energy was coupled to the multiphase ISM in a straightforward way (see Section 9.2.6.1). Besides this possibility, I also conceived a model where the AGN feedback energy allocated to the multiphase ISM is coupled to its phases according to their physical properties (see Section 9.2.6.2). In this Section, I present the results of the simulation AGN–cf–hcA (see Table 9.2): I consider that AGN feedback energy is provided to the hot and cold components of the multiphase particles selected to receive it, according to the covering factors of the two phases. Thus, $\mathcal{A}_{\rm h} = \mathcal{C}_{\rm h}$, $\mathcal{A}_{\rm c} = \mathcal{C}_{\rm c}$, and $\ell_{\rm MC} = 20$ pc (see Section 9.2.6.2). Results are contrasted to the fiducial simulation AGN–both–hcA (green) analysed in previous Sections.

Figure 9.18 introduces the gas and stellar projected density maps for the galaxy AGN–cf–hcA. This galaxy has a disc-dominated morphology, and shares the majority of its properties at $z = 0$ with AGN–both–hcA and AGN–hot–hcA (see Section 9.4.3). At variance with the latter ones, it is characterised by a lower SFR ($\sim 3 \div 4$ M$_\odot$ yr^{-1}) at low-redshift ($z \lesssim 0.5$; see Figure 9.6). This is the result of the delayed and reduced accretion of gas within the galactic radius. The total stellar mass of the galaxy is $2.5 \cdot 10^{10}$ M$_\odot$, and its bulge-over-total stellar mass ratio is $B/T = 0.5$.

Figure 9.19 shows the distribution of the coupling factors for the hot and cold phase of all the multiphase particles that have been selected to receive AGN feedback energy down to $z = 0$. In this way, it is possible to quantify how AGN feedback energy is coupled to the multiphase ISM. The two histograms presented in Figure 9.19

[5]The mass of the bulge that enters the computation of the B/T is estimated as twice the mass of the counter-rotating ($J_{\rm z}/J_{\rm circ} < 0$) star particles, under the hypothesis that half of the bulge mass is constituted by all the counter-rotating stars (see also Sections 9.4.2 and 6.5.3.2).

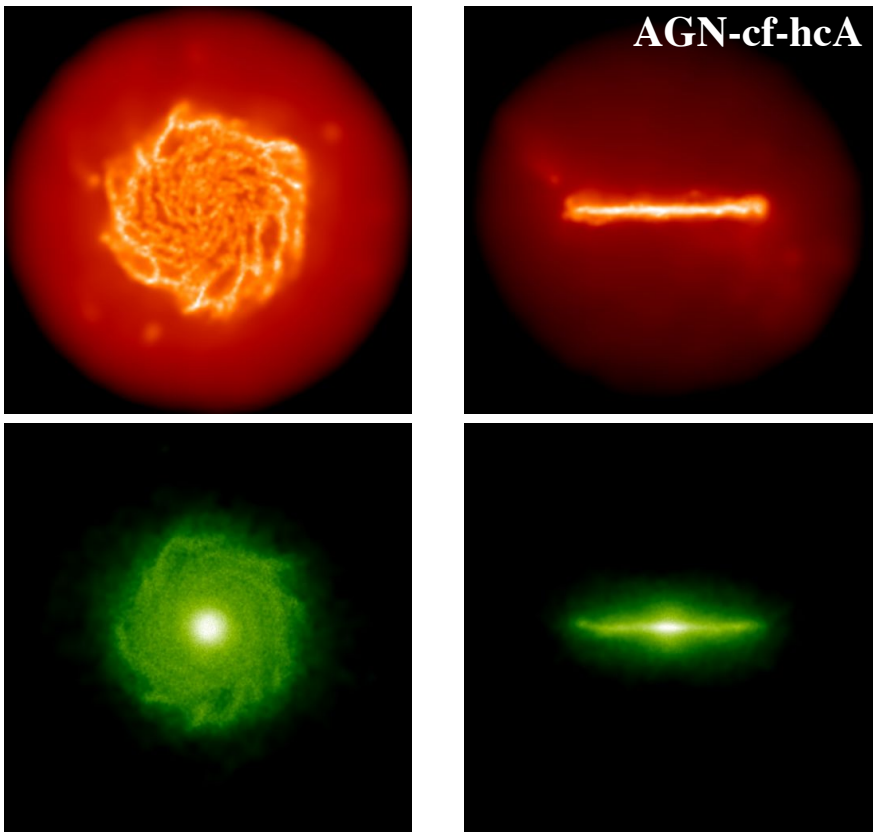

Figure 9.18: Face-on (left-hand panels) and edge-on (right-hand panels) projected gas (top) and stellar (bottom) density maps of the galaxy AGN–cf–hcA, at redshift $z = 0$. This galaxy is simulated assuming that AGN feedback energy couples to the multiphase ISM according to its properties. The size of each box is 50 kpc a side.

represent the same distribution, since $\mathcal{C}_{\rm h}$ and $\mathcal{C}_{\rm c}$ sum to 1, by definition. They show that for the majority of the multiphase particles receiving feedback energy, the bulk of the available energy budget is assigned to the diffuse, volume filling phase. The origin of the two peaks of the distribution has been discussed in Section 9.2.6.2. Median values for the covering factors predict an evolution for the galaxy and for its SMBH that is close to that experienced by AGN–hot–hcA (see Section 9.4.2).

The median value of the histograms does not exhibit a definite trend with redshift. On the other hand, it depends on the adopted parameter $\ell_{\rm MC}$, describing the typical size assumed for molecular clouds. Adopting $\ell_{\rm MC} = 30$ pc results in a median value for $\mathcal{C}_{\rm h}$ of ~ 0.97, while $\ell_{\rm MC} = 5$ pc leads to 0.81 as median value of $\mathcal{C}_{\rm h}$. This trend can be understood by considering that the lower $\ell_{\rm MC}$, the larger $\mathcal{C}_{\rm c}$, when a particle with given physical properties is considered (see equation (9.36)).

Focussing on the evolution of the BH and on the way in which it coevolves with its host, I analyse the evolution of the SMBH mass and its location on the $M_{\rm bulge}$-$M_{\rm BH}$ relation at $z = 0$ (Figure 9.20). In line with the investigation presented in Section 9.4.4, I consider the simulation AGN–cf–ocA (which is analogous, but with

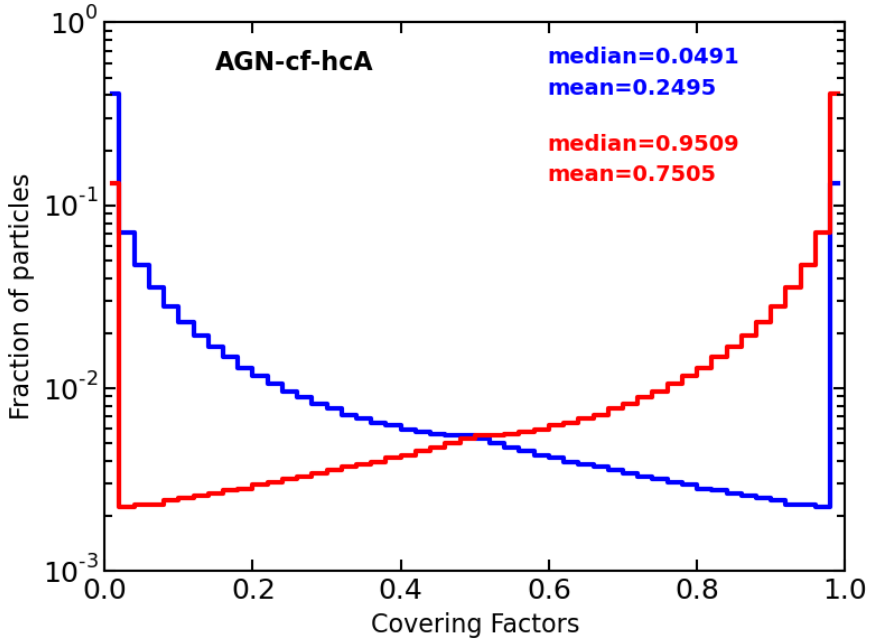

Figure 9.19: Distribution of the covering factors of the hot (red) and cold (blue) components for all the multiphase particles that have received AGN feedback energy down to $z = 0$, for the galaxy AGN–cf–hcA. Mean and median values for the two distributions are indicated. The two distributions are specular, since $\mathcal{C}_{\rm h}$ and $\mathcal{C}_{\rm c}$ are complementary by definition.

only cold gas accretion, see Table 9.2) in addition to the simulation AGN–cf–hcA, to explore the impact of different BH gas accretion on final results.

The left panel of Figure 9.20 shows the evolution of the mass of the most massive BH within the simulated galaxies; vertical segments indicate the redshift at which BH mergers involving the central SMBH take place. The evolution of the SMBHs in AGN–cf–hcA and AGN–cf–ocA is similar and rather moderate: it spans roughly an order of magnitude in mass from $z \sim 8.5$ (redshift at which the BH is seeded) to $z = 0$, and proceeds mainly via gas accretion. It is comparable to the mass evolution of the SMBH in AGN-hot-hca (see Figure 9.4), but for the lower number of mergers that the BHs experienced. The mass of the BHs at $z = 0$ are $1.84 \cdot 10^6$ $\mathrm{M}_\odot$ (AGN–cf–hcA) and $1.49 \cdot 10^6$ $\mathrm{M}_\odot$ (AGN–cf–ocA). Despite being comparable, the final mass of the BH when only cold gas accretion is taken into account (AGN–cf–ocA) is marginally lower than that of the SMBH in AGN–cf–hcA, at variance with results in Figure 9.13.

The right panel of Figure 9.20 shows the position of the BHs of the simulated galaxies on the plane of the Magorrian relation. The comparison with observations highlights that AGN–cf–hcA and AGN–cf–ocA lie on the lower edge of the region occupied by pseudo-bulges. This suggests that a larger seed mass $M_{\rm BH,\,seed}$ can be considered, if this model for the coupling of AGN feedback energy to the multiphase ISM is adopted.

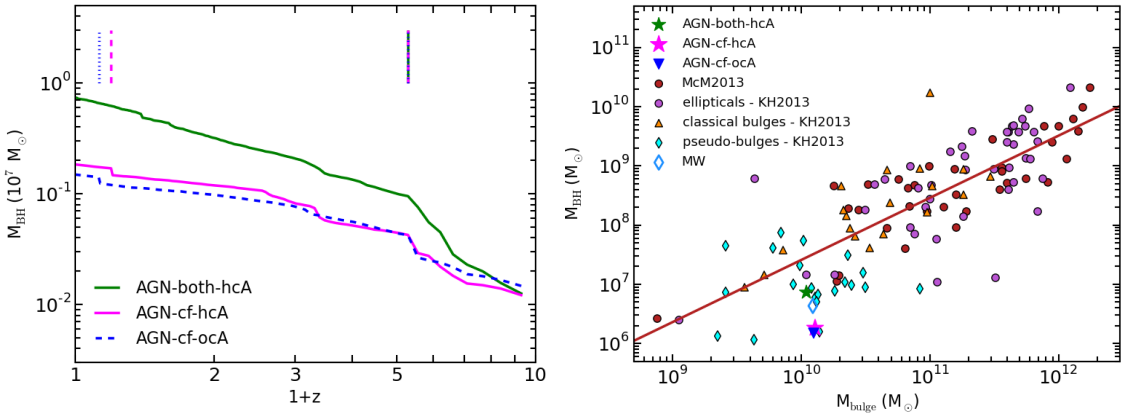

Figure 9.20: Evolution of the BH mass growth for the most massive BH in the galaxy (*left-hand panel*) and $M_{\rm bulge}$-$M_{\rm BH}$ relation (*right-hand panel*) for each one of the considered simulations. Solid curves refer to simulations in which the SMBH accretes both hot and cold gas (*hcA*), while the dashed curve identifies the case of cold gas accretion only (*ocA*). The green curve is the same as in Figure 9.4.

9.4.7 Angular momentum dependent accretion

In this Section, I investigate the effect of modelling gas accretion onto SMBHs. In particular, I study the impact that limiting accretion of cold gas that is supported by rotational velocity has on the BH mass at $z = 0$ and on the scaling relation $M_{\rm bulge}$-$M_{\rm BH}$.

To this end, I consider the results of six simulations: AGN–both–hcA (in green, the reference simulation investigated throughout this Chapter), AGN–both–ocA (different from the fiducial simulation because the SMBH only accretes cold gas), AGN–both–hcAL, AGN–both–hcAL2, AGN–both–hcAL3, and AGN–both–ocAL (see Table 9.2).

The last four simulations account for the reduction of the accretion of cold gas that is in rotational support onto the BH (as explained in Section 9.2.3 and further discussed below). The simulations AGN–both–hcAL, AGN–both–hcAL2, and AGN–both–hcAL3 only differ from each other because of the parameter $C_{\rm visc}$ that describes the viscosity of the cold gas that is supported by rotational velocity, at the sub-resolution level.

The values of $C_{\rm visc}$ that I explore are the following: $C_{\rm visc}/2\,\pi = 1$ (AGN–both–hcAL) $C_{\rm visc}/2\,\pi = 10^2$ (AGN–both–hcAL2), and $C_{\rm visc}/2\,\pi = 10^3$ (AGN–both–hcAL3).

The simulation AGN–both–ocAL assumes $C_{\rm visc}/2\,\pi = 1$, but only cold gas accretion: as a consequence, in this simulation, all the gas that contributes to accretion is controlled by the limiter $\mathcal{L}_{\rm AM}$ (see Section 9.2.3). On the other hand, should the BH accrete both hot and cold gas, the limiter only controls cold gas accretion.

The values of $C_{\rm visc}$ that I consider correspond to those explored by Schaye et al. (2015); Crain et al. (2015).

Before diving into the results, I provide a brief explanation for the sub-resolution parametrisation of the viscosity encoded in $C_{\rm visc}$. Rosas-Guevara et al. (2015) showed that the factor $\mathcal{L}_{\rm AM} = C_{\rm visc}^{-1} \, (c_{\rm s,\,c}/V_\phi)^3$ (see equation (9.6)), which reduces the Bondi accretion rate (see equation (9.5)), is equivalent to the ratio between the Bondi timescale and the viscous timescale ($t_{\rm visc}$, see below). Indeed, the presence of gas with a given amount of angular momentum introduces a characteristic spatial scale when modelling BH accretion, that is the size of the disc on which gas orbits before infalling onto the BH. Depending on the angular momentum of the gas, a typical timescale is set. This viscous timescale enters the problem in addition to the Bondi timescale, that is valid for gas accretion under the assumption that accreting gas does not rotate while infalling. The Bondi timescale reads: $t_{\rm B} = r_{\rm B}/c_{\rm s}$, where $r_{\rm B}$ is the Bondi radius, i.e. the scale where the BH dominates over hydrodynamical processes (see Section 9.1), and $c_{\rm s}$ is the sound speed of gas. The viscous timescale is proportional to the dynamical time (see e.g. Section 2.2), and can be cast as: $t_{\rm visc} = [\alpha_{\rm visc} \, (H/R)^2]^{-1} \, t_{\rm dyn}$ (see Rosas-Guevara et al., 2015, for further details). Here, R and H are the radius and the scale height of the accretion disc, respectively, while $\alpha_{\rm visc}$ is a dimensionless parameter that is related to the kinematic viscosity (see equation (4.39)). If the transport processes through the viscous accreting disc were fully understood, adequately accurate values for R, H, and $\alpha_{\rm visc}$ would be inserted to model the effective accretion process. However, since we lack a full understanding of viscosity and accretion, and also considering that the accretion disc is far from being resolved in cosmological simulations, the ignorance is parametrised by means of $C_{\rm visc} = 2\,\pi \, [\alpha_{\rm visc} \, (H/R)^2]^{-1}$. In this way, a parameter is introduced in order to numerically capture the viscosity of gas in rotational support on a notional accretion disc, at the sub-resolution level.

The (highly uncertain) value of the effective viscosity parameter $C_{\rm visc}$ has been first explored by Rosas-Guevara et al. (2015), who proposed for it the range $10^3 \div 10^8$. They adopted $C_{\rm visc} = 2 \cdot 10^6$ as fiducial value, and found that the larger is the value of $C_{\rm visc}$, the smaller is the mass of the hosted SMBH, for DM haloes as massive as $\sim 10^{12}$ $\rm M_\odot$.

Note that $C_{\rm visc} \to \infty$ would correspond to the case in which (cold) gas accretion onto the SMBH is not included. Also, note that large variations in $C_{\rm visc}$ are required in order to have remarkable differences in the final results, since the suppression of the gas accretion by angular momentum needs $C_{\rm visc}^{1/3} \, V_\phi > c_{\rm s}$ to result effective (see equation (9.6)).

Decreasing $C_{\rm visc}$ corresponds to the situation in which the viscosity of the disc is higher and the gas accretion proceeds faster: indeed, viscosity transports angular momentum outward, enabling accreting gas to spiral in towards the BH.

Figure 9.21 illustrates the evolution of the BH mass as a function of the redshift. As in previous Sections, I consider the most massive BH within a distance of 100 kpc

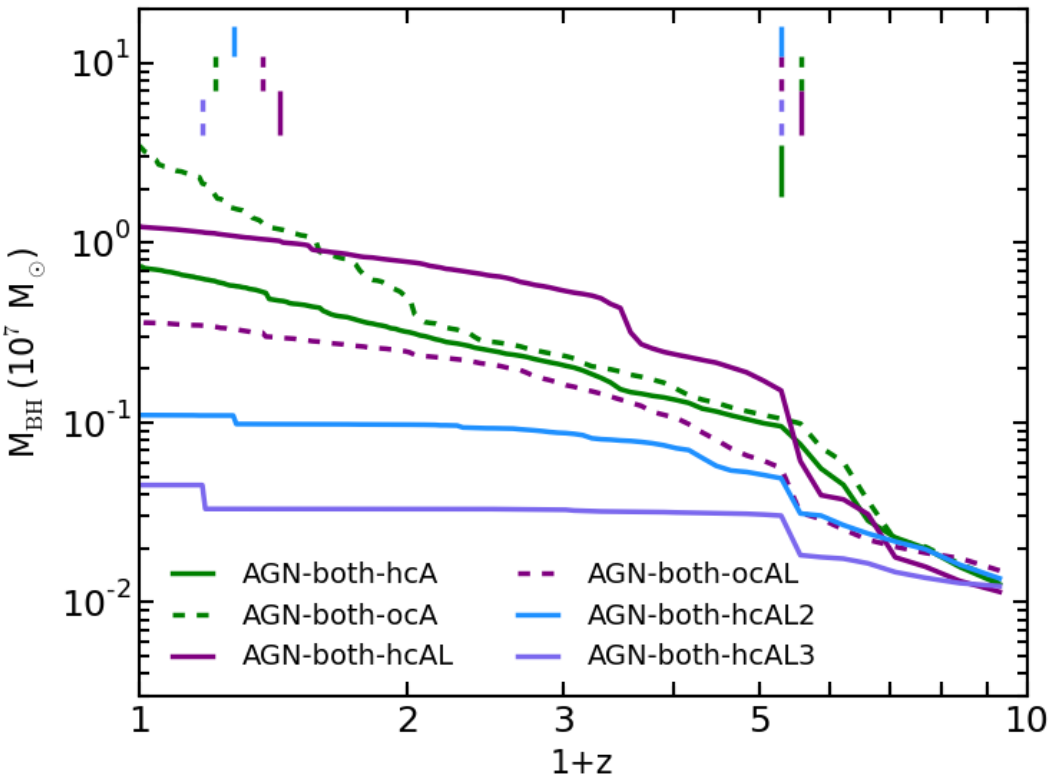

Figure 9.21: Evolution of the BH mass growth for the most massive BH in each of the simulated galaxies. Segments at the top of the Figure highlight the redshift at which the considered BH experienced a BH merger. Solid curves refer to simulations in which the SMBH accretes both hot and cold gas (*hcA*), while dashed curves identify the case of cold gas accretion only (*ocA*).

from the galaxy centre. Vertical segments at the top of Figure 9.21 record the redshift at which a BH merger occurred.

The evolution of the BH mass of AGN–both–hcA has been already considered in Figure 9.4 and in Section 9.4.2. When the limiter to the accretion of cold gas that is supported by rotational velocity is accounted for, the evolution of the BH mass changes as described by AGN–both–hcAL, AGN–both–hcAL2, and AGN–both–hcAL3. The purple solid line (AGN–both–hcAL) shows that a value for $C_{\rm visc}$ as low as $2\,\pi$ is not enough to limit the total growth of the BH mass effectively. The hot gas that is accreted can have a role in boosting the BH mass growth when the viscosity of the disc is high (see below) or the BH is not able to reach self-regulation as soon as in the reference case (AGN–both–hcA).

When higher values of $C_{\rm visc}$ are adopted, the growth of the BH mass is significantly reduced. Focussing on AGN–both–hcAL2, the BH mass growth is hindered below $z \sim 4$; finally, the BH is prevented from growing below $z \sim 2$, aside from a BH merger at $z \sim 0.2$. The BH growth by gas accretion is even stopped when $C_{\rm visc}/2\,\pi = 10^3$ (AGN–both—hcAL3) is adopted. With respect to the reference simulation AGN–both—hcA, the BH at $z = 0$ is reduced by an order of magnitude

or even more, the BH masses being $1.10 \cdot 10^6$ $M_\odot$ (AGN–both—hcAL2) and $4.48 \cdot 10^5$ $M_\odot$ (AGN–both—hcAL3).

The values of $C_{\rm visc}$ for AGN–both—hcAL2 and AGN–both—hcAL3 are the ones adopted in the Eagle simulations. They adopt $C_{\rm visc}/2\,\pi = 10^2$ for the simulation of their suite at lower resolution (in which the initial mass of gas particles is larger than that of AqC5 by a factor 4.4, see Table 5.2), and $C_{\rm visc}/2\,\pi = 10^3$ for their higher resolution run (where the initial mass of gas particles is smaller than that of AqC5 by a factor 1.8). Indeed, Crain et al. (2015) explored the variation on galaxy scaling relations produced by different values of $C_{\rm visc}$ (they considered the following values: $C_{\rm visc}/2\,\pi = 0.01,\ 1,\ 100$), to quantify the impact of the sub-resolution viscosity in calibrating the EAGLE simulation. They found that their model for AGN feedback is primarily dependent on $C_{\rm visc}$. Also, they found that larger values of $C_{\rm visc}$ delay the BH growth via gas accretion and the quenching of star formation by AGN feedback. Also, they observed that the higher is the value of $C_{\rm visc}$, the lower is the BH mass corresponding to a determined stellar mass (of the bulge) of the host galaxy. Results presented in Figures 9.21 and 9.22 are thus in agreement with Crain et al. (2015).

Interestingly, when I consider only cold gas accretion (AGN–both–ocA), the limiter that I implemented yields desirable results also for $C_{\rm visc} = 2\,\pi$: indeed, in the simulated galaxy AGN–both–ocAL, the final BH mass is reduced (from $3.46 \cdot 10^7$ $M_\odot$ to $3.61 \cdot 10^6$ $M_\odot$) and its growth at low redshift ($z \lesssim 2$) is slowed down.

Figure 9.22 shows the impact of limiting accretion from cold gas in rotational support on the $M_{\rm bulge}$-$M_{\rm BH}$ relation. The position of the simulated galaxies AGN–both—hcAL2, AGN–both—hcAL3, and AGN–both—ocAL highlight how reducing the accretion of cold gas delays or even suppresses the BH growth.

The scenario that emerges from Figure 9.21 is quite important within the context of the formation and evolution of disc galaxies. Indeed, according to the widely known scenario, the fundamental connection between the $M_{\rm BH}$ and $M_{\rm bulge}$ implies that the growth of the BH is tightly linked to the formation of galaxy bulges (Kormendy & Ho, 2013). Even if the coevolution with pseudo-bulges is not as close as for classical bulges, BHs do not correlate with the properties of galaxy discs (Kormendy & Gebhardt, 2001; Kormendy et al., 2011; Kormendy & Ho, 2013). As a consequence, the SMBH in a late-type galaxy is expected to grow mainly at high-redshift, while the formation of the bulge of the galaxy proceeds. On the contrary, the BH growth is limited at low-redshift, when the formation of the galaxy disc occurs.

Figure 9.21 shows that this is the case for AGN–both–hcAL2: below redshift $z \sim 3 \div 2$ the growth of the BH through gas accretion is completely insignificant. Below redshift $z \sim 2$, the BH mass only grows as a consequence of mergers with other BHs. The effect of the limiter $\mathcal{L}_{\rm AM}$ is clearly evident when considering the simulated galaxy AGN–both–hcAL3: below redshift $z \sim 4$, the growth of the BH by gas accretion is suppressed, and the BH mass evolution is driven by mergers alone.

Interestingly, the scenario of BH merging as the most viable channel for BH growth in galaxies within haloes of $\sim 10^{12}$ $M_\odot$ has been pointed out by Bonoli

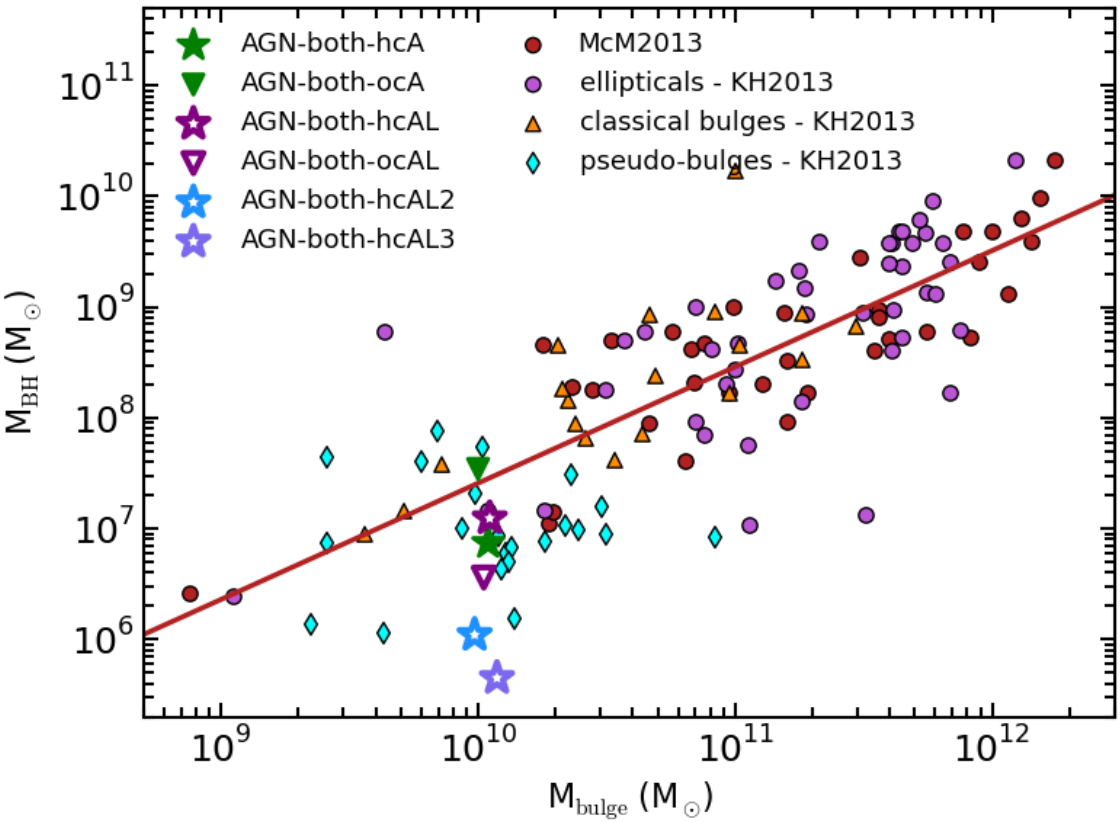

Figure 9.22: $M_{\rm bulge}$-$M_{\rm BH}$ relation for BHs in the simulated galaxies where different accretion models are considered (see Table 9.2). Starlets pinpoint simulations in which the SMBH accretes both hot and cold gas (*hcA*), while triangles refer to the case of cold gas accretion only (*ocA*, as in Figure 9.13). Empty symbols identify simulations in which the accretion of cold gas in rotational support is reduced. Observations are from Kormendy & Ho (2013, KH2013) and from McConnell & Ma (2013, McM2013), as in Figure 9.5.

et al. (2016), who presented a detailed study of the coevolution of a MW-sized simulated galaxy and its SMBH. They found that the SMBH growth is mainly due to the mergers with other BHs located within satellites approaching the forming galaxy, rather than to gas accretion. At $z = 0$, their simulated galaxy hosts a BH as massive as $2 \cdot 10^6$ $M_\odot$.

Since I have shown in Chapters 6 and 7 and in Section 9.4.3 that the formation of the bulge and of the disc of the galaxies that I simulate typically occurs above and below $z \sim 3 \div 2$, respectively, what emerges from Figure 9.21 is that once the angular momentum of the cold gas that is accreting onto the central BH is taken into account, the commonly recognised scenario for BH-disc galaxy coevolution is successfully reproduced.

Finally, Figure 9.23 shows the gas and stellar projected density maps for the galaxy AGN–both–hcAL2, for which I have discussed above the evolution of the hosted SMBH. The galaxy has a dominant disc component: its stellar mass (within $R_{\rm gal}$) is $3.53 \cdot 10^{10}$ $M_\odot$, and its bulge-over-total mass ratio is $B/T = 0.27$.

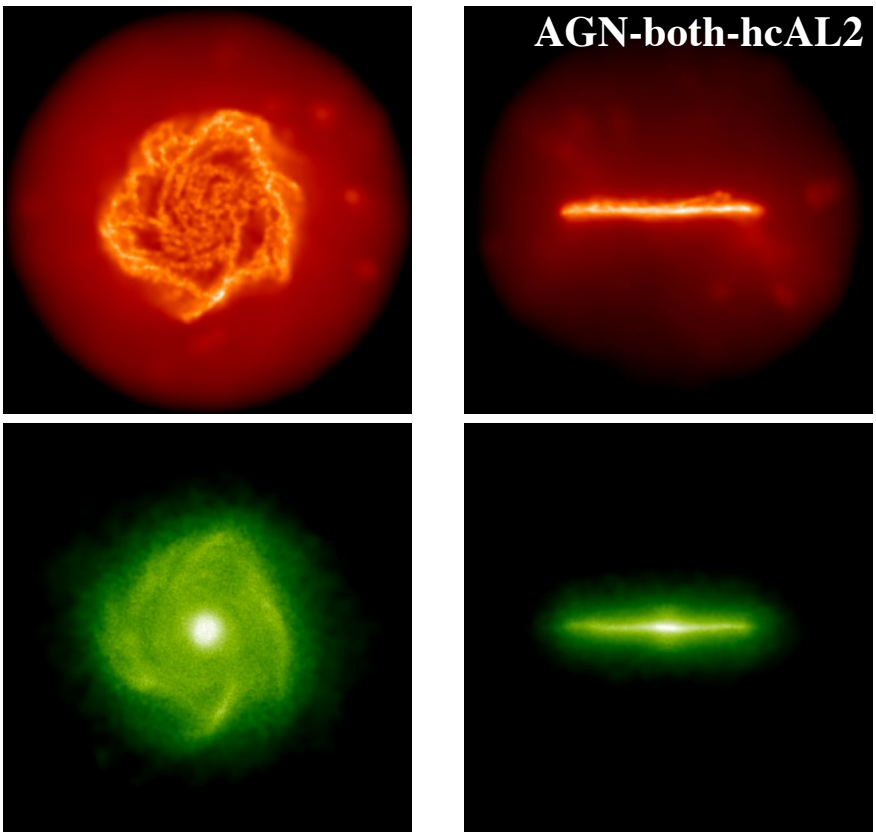

Figure 9.23: Face-on (left-hand panels) and edge-on (right-hand panels) projected gas (top) and stellar (bottom) density maps of the galaxy AGN–both–hcAL2, at redshift $z = 0$. In this galaxy the accretion of cold gas in rotational support is reduced. The size of each box is 50 kpc a side.

9.5 Concluding remarks

In this Chapter, I introduced a novel model for AGN feedback and I implemented it within the sub-resolution model MUPPI, already featuring cooling, star formation, stellar feedback and chemical enrichment.

I carried out a suite of cosmological hydrodynamical simulations of disc galaxies, with zoomed-in initial conditions leading to the formation of a halo of mass $M_{\rm halo,\,DM} \simeq 2 \cdot 10^{12}$ M$_\odot$ at redshift $z = 0$. These simulations have been designed to investigate:

(i) - the impact of different models of gas accretion, namely only cold gas, both cold and hot gas, with the additional possibility of limiting gas accretion from cold gas that is supported by rotational velocity;

(ii) - the effect of different ways of coupling AGN feedback energy to the hot and cold phases of the multiphase ISM;

(iii) - how different models of gas accretion and AGN feedback energy coupling affect the evolution of SMBHs;

(iv) - the overall BH-galaxy coevolution.

The most relevant results of this Chapter can be summarised as follows.

- I investigated the effect that coupling AGN feedback energy to the different phases of the ISM has on the evolution of SMBHs. Providing to the hot phase the entire budget of feedback energy, or a considerable fraction of it, produces a SMBH that grows in mass by up to one or two order of magnitudes from $z \sim 8.5$ to $z = 0$. Its final mass ranges between $\sim 10^6$ $M_\odot$ and $\sim 10^7$ $M_\odot$. On the other hand, when the AGN feedback energy is entirely supplied to the cold phase, the multiphase ISM does not result to be highly dynamical and remains close to the BH: as a consequence, the BH experiences a rapid phase of mass growth (in the redshift range $3 \lesssim z \lesssim 5$) during which it deprives of gas the centre of the host galaxy, and then its growth is suppressed. The BH mass at $z = 0$ can be as high as $\sim 10^9$ $M_\odot$ in this case. Therefore, a prediction of my model is that at least a share of the AGN feedback energy has to couple with the diffuse gas (Section 9.4.2).

- Gas accretion is the process that contributes the most to the BH growth, rather than mergers with other BHs (Section 9.4.2). This is true unless cold gas rotationally supported is prevented from accreting (see below).

- Simulations that include AGN feedback produce spiral galaxies with a more extended stellar disc component. The SMBH mainly produces a positive feedback, pressurising the multiphase gas and ultimately enhancing the star formation (Section 9.4.3).

- I find that when the BH only accretes cold gas, it experiences a growth by gas accretion that is faster than (or at most comparable to) the case in which both cold and hot gas are accreted. As for the galaxy $M_{\rm bulge}$-$M_{\rm BH}$ scaling relation, predictions from simulations are in keeping with observations, considering a BH seed mass as large as $\sim 10^5$ $M_\odot$ (Section 9.4.4).

- Including AGN feedback does not affect the slope nor the normalization of metallicity gradients. As a consequence, I can conclude that the energy injection and especially the outflows driven by the SMBH do not alter significantly the circulation of metals within galaxies (Section 9.4.5).

- I examined the effect of coupling the AGN feedback energy injected in a multiphase ISM to its phases according to their physical properties. I considered a model where feedback energy coupling is driven by the covering factors of the hot and cold phases, assuming that the larger is the volume occupied by the cold gas, the larger is the amount of energy that it absorbs (see Section 9.2.6.2). A prediction of this model is that the bulk of AGN feedback energy is transferred and couples to the warm, diffuse ISM (Section 9.4.6).

- I find that when the accretion of cold gas that is supported by rotational velocity is reduced, the BH mass growth is delayed and the BH mass at $z = 0$ is reduced by up to an order of magnitude with respect to the case in which both hot and cold gas accretion proceed unimpeded. Within the scenario emerging from this model, the SMBH in MW-sized galaxies is prevented from growing by gas accretion below $z \lesssim 2$, aside from possible BH mergers. Also, the lower is the viscosity assumed for the cold gas which is accreting (i.e. the larger $C_{\rm visc}$), the more the BH mass growth is reduced. Moreover, when only cold gas accretion is considered, the delay and suppression of the BH mass growth is obtained by assuming a higher viscosity for the disc on which the accreting gas is settled, i.e. by assuming an accretion not as impeded as if it involved both hot and cold gas (Section 9.4.7).

AGN feedback operates in a wide class of systems, from galactic bulges to massive galaxy clusters. In this Chapter, I started to study the way in which AGN feedback energy is coupled to the different components of the ISM focussing on late-type galaxies: however, AGN feedback is expected to play a supporting role in MW-sized galaxies, where the central BH primarily determines the properties of the bulge and shape the galaxy innermost regions. A forthcoming extension of this study is to include elliptical galaxies in the analysis, so as to investigate how the AGN affects the formation and evolution of systems characterised by more massive BHs accreting at higher rates.

At the same time, it would be interesting to further investigate hot gas haloes in massive spiral galaxies. Indeed, I have already studied the hot gas cooling process triggered by AGN feedback in models of low mass ellipticals (Valentini & Brighenti, 2015); provided the similarity between the hot ISM of these systems and detected hot coronae around disc galaxies, it appears likely that any outburst from the central BH could promote cooling of the hot corona, generating cold clouds that would accrete on the galactic disc.

A desirable spin-off result concerns the investigation of the effect of stellar and AGN feedback on the properties of simulated galaxy populations, instead of those of single galaxies.

Also, it would be a quite interesting challenge to compare predictions from these simulations to observations at high redshift, in order to better constrain the BH growth across cosmic time and interpret possible scenarios of galaxy evolution.

10

Conclusions and future perspective

This Thesis has been devoted to the study of the formation of late-type galaxies, and the role that feedback from stars and supermassive black holes (SMBHs) plays in galaxy evolution across cosmic time. The main goal of this work has been to investigate how different processes, such as the cosmological gas accretion from the large scale environment, star formation and chemical enrichment, stellar and AGN (Active Galactic Nucleus) feedback, affect the early stages of forming galaxies, contributing to determine their present-day properties. I focused especially on gas inflow and outflow, and on understanding how these mechanisms drive galaxy formation and evolution, while guaranteeing a continuous interaction with the surrounding, dynamical environment. Particular emphasis has been devoted to connect chemical evolution and gas dynamics, to interpret observations of metal abundance in the interstellar medium (ISM) and circumgalactic medium (CGM). I investigated these issues from a theoretical and numerical perspective, making extensive use of cosmological hydrodynamical simulations. To this end, I improved the sub-resolution model for star formation and stellar feedback to which my simulations resort, and I also included a novel implementation of AGN feedback within it.

In what follows, I will discuss the most relevant results of this Thesis and the main implications arising from them.

Interplay between hydrodynamical scheme and sub-resolution physics

Numerical techniques adopted to solve the equations of hydrodynamics have a crucial impact on final results. To carry out all the simulations presented in

this Thesis, I introduced an advanced implementation of smoothed particle hydrodynamics (SPH) in cosmological simulations of galaxy formation that adopt the sub-resolution model MUPPI (Murante et al., 2010, 2015). This improved SPH implementation (Beck et al., 2016) ensures a more accurate fluid sampling and a better description of gas mixing and hydrodynamical instabilities. In order to successfully introduce the improved SPH formalism in simulations, I implemented a limiter that suppresses artificial conduction for those particles that are sampling the non-uniform thermal structure of the galaxy, where the evolution of the ISM is mainly driven by the sub-resolution physics rather than by hydrodynamics. Indeed, the galaxy ISM state is determined by continuous energy injections accounted for by the sub-resolution model. This originates particle-by-particle differences in temperature and density. Artificial conduction acts by mixing internal energy, thus contrasting the effect of the sub-resolution model.

The analysis I carried out demonstrates and quantifies the strong interplay between the features of the hydrodynamical scheme and the sub-resolution model. *The hydrodynamical scheme remarkably affects properties of simulated galaxies (stellar mass is the quantity that is affected the most) and gas inflow and outflow across cosmic time. The interaction between the hydrodynamical scheme and the features of sub-resolution physics changes gas cooling properties and affects the way in which energy is distributed in the ISM and CGM, thus impacting on the gas accretion history. Moreover, the higher the resolution is, the more sensitive to the accuracy of the hydrodynamical solver simulation outcomes are.*

Impact of galactic outflows on the formation of disc galaxies

Galactic outflows are triggered by stellar feedback and they are a crucial component in regulating the interplay between galaxies and the CGM. Despite the general consensus on the need of stellar feedback to form spiral galaxies that are not too much centrally concentrated and have a dominant disc component, it is still debated how reliable different sub-resolution models are in capturing an effective description of feedback energy injection. I therefore carried out a comparative study of the effects of different outflow models on the formation of disc galaxies by performing a suite of cosmological simulations.

I implemented three different galactic outflow models, besides the original one included in MUPPI (Murante et al., 2015), within the same sub-resolution model and compared results. Among these galactic outflow models, the original one considers that energy from supernova explosions is injected in the ISM within a cone directed toward the least resistance path; in another scheme the ISM is isotropically provided with stellar feedback energy. A third model is a stochastic thermal feedback scheme based on the model originally developed by Dalla Vecchia & Schaye (2012), while the last model is inspired to that of Springel & Hernquist (2003) and is characterised by stellar winds with constant velocity.

My work highlights that the observational properties of simulated galaxies are sensitive to the details of the different outflow models, even when they are implemented within the same scheme for cooling and star formation, and when the hydrodynamical solver is unchanged. My results show that the numerical prescriptions adopted for generating galactic outflows are the main shaping factor of the stellar disc component at low redshift. *I found that galactic outflows regulate the timing of gas accretion, by fostering or even quenching the cosmological infall of gas from the large-scale environment, and determine the star formation history of the forming galaxy.* By comparing galaxies simulated with different galactic outflow models, *I demonstrated that a feedback model that is successful in producing a disc-dominated galaxy should be able to regulate the pristine star formation (which is responsible for the creation of the bulge component) while, at the same time, avoiding a too late gas fall-back, that would turn into a too high star formation rate at redshift* $z = 0$.

Chemical evolution of disc galaxies

I carried out a suite of cosmological hydrodynamical simulations of disc galaxies, aiming at investigating the chemical evolution and the distribution of metals in a disc galaxy, and at quantifying the effect of *(i)* the assumed IMF, *(ii)* the adopted stellar yields, and *(iii)* the impact of binary systems originating SNe Ia on the process of chemical enrichment. I considered either a Kroupa et al. (1993) or a more top-heavy Kroupa (2001) IMF, two sets of stellar yields and different values (either 0.1 or 0.03) for the fraction of binary systems suitable to give rise to SNe Ia. I investigated stellar ages, SN rates, stellar and gas metallicity gradients, and stellar α-enhancement in simulations, and compared predictions with observations. *Stellar ages show that star formation in the disc always takes place later than in the bulge, and that the disc formation proceeds inside-out.* I evaluated the evolution of SN rates in the set of simulated galaxies and compared them to observations of Mannucci et al. (2005). *I found that SN II rates of simulated galaxies agree with observations from late-type Sbc/d galaxies.* Also, SN Ia rates of simulations adopting 0.03 as the fraction of binary systems that host SNe Ia are in keeping with observations of Sbc/d galaxies.

The adopted stellar yields are crucial in regulating cooling and star formation, and in determining the chemical enrichment of stars, especially of those located in the galaxy bulge. Also, *I investigated stellar and gas metallicity gradients in simulations: negative radial abundance profiles are recovered, thus in agreement with observations.* Slopes of profiles agree with observations, pointing to the *effectiveness of the model of chemical enrichment and of galactic outflows that I use in simulations to properly describe the amount of produced metals and their circulation within and around the simulated galaxies.*

The IMF in late-type galaxies

Assuming either a Kroupa et al. (1993) IMF or a Kroupa (2001) IMF results in different star formation histories, stellar feedback and scenarios of chemical evolution. I compared *gas metallicity profiles* from my set of simulations with the oxygen abundance radial profiles of 130 nearby disc galaxies (Pilyugin et al., 2014). I found that a Kroupa et al. (1993) IMF leads to a lower amount of metals produced by massive stars and supplied to the ISM, resulting in a better agreement with observations. In the light of these results, I can draw the following conclusion: if observational metallicity estimates are not affected by significant uncertainties, *a Kroupa et al. (1993) IMF, more top-light than Kroupa (2001) and Chabrier (2003), has to be preferred when modelling late-type galaxies in the local Universe. On the other hand, the comparison of stellar metallicity profiles with observations of Milky Way (MW) stars shows a better agreement when a Kroupa (2001) IMF is assumed.* Also, I predict that MW stars exhibit a higher metal content with respect to other nearby late-type galaxies.

I investigated the stellar α-enhancement of star particles in my simulations, and considered also chemical patterns associated to disc and bulge, separately. The *best agreement with observations of MW stars is retrieved when the Kroupa (2001) IMF is assumed. In agreement with the predictions from SN rates in my simulations, this analysis further supports a value for the fraction of binary systems suitable to give rise to SNe Ia of* 0.03, at least for late-type galaxies and when the adopted IMFs are considered.

Galactic outflows drive the chemical enrichment of ISM and CGM

I studied the effect of chemical feedback from outflows and quantified the mass of metals that is distributed at increasing distance from the galaxy centre. Galactic outflows in my simulations are effective in driving metals out from the sites of star formation. A high amount of metals in the ISM cannot be ascribed to the inability of outflows to move enriched gas outwards: rather, the ISM has been massively enriched by generations of stars. I found that the mass of metals in gas within a distance of 20 kpc from the galaxy centre is $\sim 20\%$ of the metals produced, and about as many metals are associated to stars within the same distance. The mass of metals in gas and stars within 150 kpc from the galaxy centre increases to $\sim 60\%$ of the synthesised metals. Thus, *an amount of metals as large as* $\sim 40\%$ *has been driven beyond* 150 *kpc by galactic outflows, that have promoted the circulation of metals in the CGM at high redshift, during the galaxy formation process.*

A novel method to generate synthetic stars from star particles

State-of-the-art cosmological hydrodynamical simulations have star particles with typical mass between $\sim 10^8$ and $\sim 10^3$ $M_\odot$ according to resolution, and treat them as simple stellar populations (SSPs). On the other hand,

observations in nearby galaxies resolve individual stars and provide single star properties. When comparing simulation predictions for the stellar metal content with observational data, the commonly pursued approach assumes that the mean metallicity of a star particle in simulations statistically reproduces the mean metal content of the SSP that the star particle samples. Aiming at accurately comparing predictions from simulations and observations, I introduced a novel approach to link star particles in simulations with observed stars.

The technique that I have developed consists in populating star particles with mock stars, according to input properties that star particles consistently inherit from a cosmological simulation. The properties of parent star particles such as mass, position, and their age-metallicity distribution are supplied to the code TRILEGAL (Girardi et al., 2005), along with an IMF. By exploiting a library of stellar evolutionary tracks and synthetic spectra, TRILEGAL generates a catalogue of stars that share features with their parent population and that have a mass ranging between ~ 0.5 and few $M_{\odot}$. Also, stars are provided with photometric properties, so that their absolute and apparent magnitudes in different bands can be retrieved.

Using this original approach, *I produced a database of synthetic stars from the properties of parent star particles in simulations.* With this new method, *I introduced a technique to compare as fairly as possible the outcome of cosmological simulations, that provide a coarse sampling of stellar populations by means of star particles corresponding to SSPs, with observations, that explicitly resolve single stars within stellar populations.*

Colour-magnitude diagram from a cosmological simulation

I have focused on a possible application of this method to generate synthetic stars: I have simulated the observable stellar content of a volume that is comparable to the solar neighbourhood of our Galaxy. I carried out a cosmological hydrodynamical simulation of a disc galaxy and selected star particles located within a region that can be deemed as a representation of the solar neighbourhood. I applied the technique introduced and generated a catalogue of mock stars. I also conceived a procedure to select generated stars in order to match the main observational constraints of a specific survey of stars in the solar neighbourhood, namely the Geneva-Copenhagen Survey (GCS, Casagrande et al., 2011).

I constructed and showed colour-absolute magnitude and colour-apparent magnitude diagrams for synthetic stars in the sample, showing the observational features that stars originated from selected stellar particles in the cosmological simulation would have. I investigated the age-metallicity distribution for the mock star catalogue, and found that young (< 1 Gyr) and intermediate-age stars ($1 \div 5$ Gyr) are characterised, on average, by a higher metal content than old stars (> 5 Gyr). Old stars have a spread in metallicity

that is wider (~ 2.5 dex) than younger stars (~ 1.5 dex), and the metallicity distribution progressively narrows towards the youngest ones, thus in keeping with indications from observational data. Also, I successfully generated a wide spectrum of low- and intermediate-mass stars. The bulk of stars in my sample have a mass ranging between 0.6 $M_\odot$ and 1.5 $M_\odot$. As for the mass-metallicity distribution, I find that stars tend to move towards smaller masses and lower metallicities as the stellar age increases, in agreement with observations. *I examined the metallicity distribution function (MDF) of mock stars and compared my predictions with chemical properties of stars in the solar neighbourhood in the GCS. The MDF of the star catalogue of my reference simulation has a mean* $[Z/H] = 0.04$*, that is in good agreement with the MDF of observations,* the peaks of the two MDFs perfectly overlapping and pinpointing a solar metallicity. A difference of 0.06 dex in the means of the observed and of the simulated MDF implies that stars of my synthetic sample are on average richer in metals than observed ones by $\sim 15\%$. When slicing my star sample into different subsamples according to stellar age, *I find that old stars are responsible for the low-metallicity tail of the MDF, in agreement with observations.* Properties of stars that are originated from star particles in different regions of the simulated galaxy are remarkably similar. *A natural prediction of this investigation is that chemical properties of stars observed in the solar neighbourhood are typical of MW stars at a similar distance from our Galaxy centre, and that chemical features of nearby stars are shared by stars beyond the extension of the solar neighbourhood.*

AGN feedback operating in a multiphase ISM

I introduced a novel model for AGN feedback and I implemented it within the sub-resolution model MUPPI adopted for all the simulations presented in this Thesis. Since this sub-resolution model describes a multiphase ISM, accounting for the presence of a hot and a cold phase in pressure equilibrium within the same particle (i.e. within the same resolution element), I exploit this feature to investigate which is the most suitable way to couple AGN feedback energy to different phases of the ISM over cosmic time.

As for the effect that coupling AGN feedback energy to the different phases of the ISM has on the evolution of SMBHs, I found that when the entire budget of feedback energy, or a considerable fraction of it, is provided to the hot phase, the SMBH grows in mass by up to one or two order of magnitudes from $z \sim 8.5$ to $z = 0$. Its final mass ranges between $\sim 10^6$ $M_\odot$ and $\sim 10^7$ $M_\odot$. On the other hand, when the AGN feedback energy is entirely supplied to the cold phase, the BH experiences a rapid phase of mass growth (in the redshift range $3 \lesssim z \lesssim 5$), during which it deprives of gas the centre of the host galaxy, and then its growth is suppressed. The BH mass at $z = 0$ can be as high as $\sim 10^9$ $M_\odot$ in this case. Therefore, *a prediction of my model is that at least a share of the AGN feedback energy has to be coupled with the diffuse gas. I found that gas accretion is the process that contributes the most*

to the BH growth, rather than mergers with other BHs, at least in late-type galaxies. Also, when the BH only accretes cold gas, it experiences a growth by gas accretion that is faster than (or at most comparable to) the case in which both cold and hot gas are accreted.

Furthermore, I considered the possibility of coupling the AGN feedback energy injected in a multiphase ISM to its phases according to their physical properties. In particular, I developed a prescription where feedback energy coupling is driven by the covering factors of the hot and cold phases, assuming that the larger is the volume occupied by the cold gas, the larger is the amount of energy that it absorbs. *A prediction of this model is that the bulk of AGN feedback energy is transferred and naturally couples to the warm, diffuse ISM.*

AGN feedback and metallicity gradients

I investigated the impact of AGN feedback on the metallicity profiles of gas within galaxies. Including AGN feedback does not affect the slope nor the normalization of metallicity gradients. As a consequence, *I can conclude that the energy injection and the powerful outflows driven by the SMBH do not influence or alter significantly the circulation of metals within spiral galaxies.*

AGN feedback in disc galaxies: SMBH-galaxy coevolution

Simulations including AGN feedback lead to the formation of spiral galaxies with a more extended stellar disc. While coevolving with its host galaxy, the SMBH mainly produces a positive feedback, as it pressurises the multiphase gas that receives AGN feedback energy and ultimately enhances the star formation. *As for the galaxy $M_{\rm bulge}$-$M_{\rm BH}$ scaling relation, predictions from simulations are in keeping with observations*, considering a BH seed mass as large as $\sim 10^5$ $M_\odot$.

By further investigating the impact of different models of gas accretion, besides considering accretion of only cold gas and both cold and hot gas, I also accounted for the possibility of limiting gas accretion from cold gas that is supported by rotational velocity. *Should the accretion of rotationally supported cold gas be reduced, I found that the BH mass growth is delayed and the BH mass at $z = 0$ is reduced by up to an order of magnitude with respect to the case in which both hot and cold gas accretion proceed unimpeded.* Within the scenario emerging from this model, the SMBH in MW-sized galaxies is prevented from growing by gas accretion below $z \lesssim 2$, aside from possible BH mergers. Also, the lower is the viscosity assumed for the cold gas which is accreting, the more the BH mass growth is reduced. As a consequence, *the SMBH in late-type galaxies is expected to grow more massive mainly at high-redshift, while the galaxy bulge forms. On the contrary, the BH growth is limited at low-redshift, when the formation of the galaxy disc occurs.*

Summarising, *feedback has been the leitmotif of this Thesis: feedback from stars and from SMBHs, feedback in energy and in metals.* The key idea behind this main theme is that the various processes entering in the galaxy formation and evolution are not only important per se. Rather, they are fundamental for what they produce within the system over quite long timescales, they are crucial as they foster or prevent mechanisms that result in establishing the present-day properties of late-type galaxies. This is the case, for instance, of galactic outflows, that are the main mechanism through which feedback effects propagate inside and around galaxies. This Thesis highlights the crucial role played by outflows in shaping the formation of late-type galaxies and in determining their evolution. Outflows are powered by the joint activity of stellar and AGN feedback, they guarantee a continuous interaction with the surrounding medium of the galaxy and are responsible for setting galaxy properties. Their crucial role is evident throughout the process of galaxy evolution. Indeed, they control the reservoir of gas available for star formation: they regulate gas inflow and thus the accretion of pristine, low-metallicity gas from the large scale environment, while driving gas heavily enriched in metals outwards from the sites of star formation. Also, they regulate the gas dynamics, controlling how the gas falls back on the forming galaxy and how it circulates within the galaxy itself: this has a remarkable impact on both the size of gaseous and stellar discs, and on the slope of metallicity profiles. Moreover, outflowing gas from the innermost regions of the galaxy can have a striking impact on the nuclear activity, as it affects the availability of gas feeding the SMBH, and thus the ensuing AGN feedback. Implementing in cosmological hydrodynamical simulations this complex circulation of cosmic baryons in a self-regulated fashion is extremely challenging.

Clearly, to quantify the impact of the astrophysical phenomena described above, it is extremely important the way in which they are modelled. *A key result of this Thesis is that the physical and numerical description of mechanisms that trigger feedback processes (e.g. kinetic stellar feedback and gas accretion onto the SMBH) is of paramount importance in order to investigate feedback processes themselves and how they affect galaxy evolution.* To this end, it is possible to appreciate how powerful cosmological hydrodynamical simulations are: they allow to explore different, possible scenarios and to bracket our ignorance on what currently still lacks a full physical understanding. Numerical effort is thus essential to move forward.

The galaxy scale that I have investigated in this Thesis represents a key framework and a unique test laboratory to understand and probe larger scales. The study of how SMBHs grow and AGN feedback energy couples to the components of a multiphase ISM, focused on late-type galaxies, can be profitably applied in simulations of elliptical galaxies, as well as of galaxy groups and clusters. In this way, it is possible to explore how the AGN affects the formation and evolution of systems characterised by more massive BHs accreting at higher rates. A natural and immediate extension of this investigation is the simulation of cosmological boxes, where statistical properties of evolving galaxies and their CGM can be explored. When simulating large cosmological volumes, results from galaxy targeted

simulations deserve consideration in order to assess the role of processes that also occur in larger-scale environments at a more complex level.

Meanwhile, another interesting direction of investigation is represented by the increase of resolution in simulations of single galaxies: this desirable achievement is mandatory in order to understand whether new physical processes have to be included in the description of galaxy formation, together with an even more correct representation of those that are already implemented. The call for higher resolution would also turn out to have important consequences for sub-resolution models: indeed, a larger number of processes that are now accounted for by sub-resolution models would be modelled above the resolution limit of cosmological simulations, while sub-resolution schemes would in turn be left with a more accurate description of processes occurring on scales still not explicitely resolved. The increase of resolution in simulations can be of paramount importance also for the comparison with observations. I indeed envisage that the method that I developed to generate catalogues of synthetic stars from star particles in cosmological simulations will have interesting applications when comparing the outcome of simulations, reaching an even higher resolution, with ongoing and future survey data releases, such as Gaia-ESO and especially GAIA.

The detailed and accurate investigation of the chemical evolution that I have presented is the starting point of a systematic analysis that I plan to accomplish in the near future. To this end, a first possible development is represented by a thourough exploration of the numerical modelling of the share of metals between stars and the surrounding gas. Also, to pursue that, a proper treatement of the diffusion of metals associated to turbulent gas motions is mandatory, as well as an accurate modelling of the ionization state of the gas. An interesting benchmark would be then represented by observations of metal and ion abundances in the CGM. Indeed, combined multiwavelength observations show the simultaneous and persistent presence of a warm and a cold phase embedded in the hotter CGM of low-redshift galaxies. Observations of CGM absorption systems have provided evidence that the distribution and abundance of highly ionized metals (such as O VI) follow the star-forming/passive galaxy dichotomy: it would be of interest investigating how AGN and stellar feedback energy affect the ionization state of different metals during galaxy evolution, and also possible definite trends with the central BH duty cycle. I also plan to continue to examine metal distribution with joint numerical studies and observation driven analysis, investigating the metal content of gas moving further from the simulated galaxies, at different redshift. This will let me explore the relative contribution to gas enrichment over cosmic time between the cosmological accretion of metal-poor gas and the outflow of enriched gas fostered by stellar feedback.

Moreover, an unexplored direction of investigation would concern the comparison between predictions from simulations and observations at high redshift, in order to test evolutionary scenarios emerging from simulations and better constrain processes such as the BH growth across cosmic time. As for the modelling of AGN feedback, a

further direction for improvement is provided by the additional work that is required to numerically account for the mechanical component of AGN-triggered outflows.

Also, the mutual interaction between the large scale structure and galaxies inhabiting it represents a challenging aspect to be further investigated. The large scale structure determines galaxy, group and cluster formation and evolution over cosmic time, as it continuously fuels collapsing structures with baryons. However, where the intergalactic medium merges with the CGM, astrophysical processes connected with galaxy evolution strongly impact on the thermo- and chemo-dynamical properties of the diffuse baryons. Cosmological hydrodynamical simulations are the ideal tools to investigate the coevolution of the cosmic web and galaxy groups and clusters. It would be of paramount relevance to assess the relative importance of large scale structure driven galaxy evolution and of galactic feedback imprints on the cosmic web over cosmic time.

As new upcoming observational instruments (e.g. the James Webb Space Telescope, JWST and the European-Extremely Large Telescope, E-ELT) will allow us to probe the very high-redshift Universe, it is of even more paramount importance to have numerical codes as complete as possible as for the inclusion of physical processes implemented and very efficient from the computational point of view (e.g. partly or entirely ported to GPUs, graphics processing units), so as to produce simulations able to shed new light on what drives the formation of the first structures and their subsequent evolution.

Appendix

A

Essentials of cosmology

This Appendix presents fundamental concepts to which I refer throughout the Thesis. In Section A.1, I briefly recall the basics of cosmology and introduce essential quantities such as cosmological parameters and redshift. Section A.2 is devoted to introduce the power spectrum and the density fluctuations from which the growth of cosmic structures reviewed in Section 2.2 develops. Finally, in Section A.3, I summarise the theory of the top-hat spherical collapse and define virial quantities.

Contents

A.1 Basics of our Universe

Cosmology applies relativity and gravity theories to the history of the Universe, investigating how it evolves and how the present-day cosmic structures such as galaxies originated. Modern cosmology relies on the Einstein's theory of general relativity and on the Cosmological Principle, that is the assumption of a homogeneous and isotropic Universe. Homogeneity of the Universe is a property

that is retrieved over large scales, i.e. hundreds of Mpc today, with respect to the kpc scale across which galaxies extend. Therefore, it is worth considering the dynamical evolution of the Universe in terms of mean quantities, at least over large scales. Later on (Section A.2), the growth of perturbations originating structures will be addressed.

First, I introduce a framework to geometrically describe the Universe. Assuming the Cosmological Principle, the Friedmann-Robertson-Walker (FRW) metric characterises the infinitesimal distance between two spacetime points:

$$ds^2 = c^2\,dt^2 - a^2(t)\left[\frac{dr^2}{1-K\,r^2} + r^2(d\theta^2 + \sin^2\theta\,d\phi^2)\right] \ , \tag{A.1}$$

r, θ, and ϕ being spatial spherical coordinates and c the speed of light. In equation (A.1), K is the curvature of the Universe and it can be equal, lower or larger than zero according to whether a flat, hyperbolic or spherical geometry is assumed, respectively. The expansion or scale factor $a(t)$ describes the size of the Universe and factors out its temporal evolution. Once the expansion factor is determined, the Hubble parameter H relates the velocity of two spacetime points receding one from another to their proper distance (Hubble & Humason, 1931), and is defined as $H(t) = \dot{a}(t)/a(t)$. At present time, $H_0 = 67.81 \pm 0.92$ km s^{-1} Mpc^{-1} (Planck Collaboration et al., 2016b); it is usually expressed in terms of the dimensionless parameter h, where $H_0 = 100\,h$ km s^{-1} Mpc^{-1}.

Due to space expansion, photons travelling across the Universe are observed today (t_0) with frequencies lower than those they were emitted with (at time t). The redshift z quantifies this discrepancy. It is defined as:

$$z = \frac{a(t_0)}{a(t)} - 1. \tag{A.2}$$

How the Universe evolves is determined by its energetic content. According to Einstein's field equation the structure of spacetime is shaped and regulated by its matter-energy content. Assuming the FRW metric and a perfect relativistic fluid as the Universe's matter content, Einstein's field equation reduces to the Friedmann's equations:

$$\ddot{a} = -\frac{4\,\pi}{3}\,G\left(\rho + \frac{3\,P}{c^2}\right)a + \left(\frac{\Lambda\,c^2}{3}\right)a \ , \tag{A.3}$$

$$\dot{a}^2 + K\,c^2 = \frac{8\,\pi}{3}\,G\,\rho\,a^2 + \left(\frac{\Lambda\,c^2}{3}\right)a^2 \ , \tag{A.4}$$

Λ being the cosmological constant. In equations (A.3) and (A.4), p and ρ are the pressure and the density of the fluid, and they are related according to the equation of state, that can be cast as: $p(\rho) = w\,\rho\,c^2$. Examples of w for different components are as follows: $w = 0$ for matter, $w = 1/3$ for radiation, and $w = -1$ for the cosmological constant Λ.

In order to determine the geometry of the Universe, one compares the present-day density $\rho_0 = \rho(t_0)$ to a characteristic density. This is the so-called critical density: $\rho_{0,\,\mathrm{crit}} = 3\,H_0^2/(8\,\pi\,G)$. By writing the various density components in dimensionless form, one gets the present-day density parameter for each component i: $\Omega_{0,\,\mathrm{i}} = \rho_{0,\,\mathrm{i}}/\rho_{0,\,\mathrm{crit}}$. The various components are: the radiation (photons, neutrinos if massless), the matter (baryons, DM or both), the cosmological constant. Each of them is characterised by a peculiar equation of state and dominates over the others in a specific cosmological era.

Following Coles & Lucchin (2002), equation (A.4) can be rearranged in the form:

$$H_0^2\,(1 - \Omega_{0,\mathrm{tot}}) = -\frac{K\,c^2}{a_0^2} \quad , \tag{A.5}$$

where $\Omega_{0,\mathrm{tot}}$ amounts to the sum of the density parameters of the various components. The geometry of the Universe, encoded within K, is flat, hyperbolic or spherical depending on whether $\Omega_{0,\mathrm{tot}}$ is equal, smaller or larger than one, respectively.

Also, by using equation (A.2) and rewriting equation (A.4) in terms of $\Omega_{0,\,\mathrm{i}}$, the evolution of the Hubble parameter can be cast as:

$$\begin{aligned} H(z) &= H_0\,(1+z)\,[\Omega_{0,\,\mathrm{m}}(1+z) + \Omega_{0,\,\mathrm{r}}(1+z)^2 + \Omega_{0,\,\Lambda}(1+z)^{-2} + (1 - \Omega_{0,\mathrm{tot}})]^{1/2} \\ &= H_0\,E(z) \quad , \end{aligned} \tag{A.6}$$

where the subscripts m, r, and Λ refer to matter, radiation, and cosmological constant, respectively. The former equation is fundamental in order to compute the comoving distance d_c, i.e. the distance that does not vary as a consequence of the Universe expansion (Hogg, 1999):

$$d_\mathrm{c} = \frac{c}{H_0} \int_0^z \frac{dz'}{E(z')} \quad . \tag{A.7}$$

Observations indicate that $\Omega_\Lambda > 0$, thus suggesting that the Universe is experiencing an accelerated expansion (Riess et al., 1998; Perlmutter et al., 1999).

Free parameters of the cosmological model are determined via different observations, such as supernova (SN) surveys (Riess et al., 1998; Perlmutter et al., 1999), galaxy cluster number counts (e.g. Borgani et al., 2001; Reiprich & Böhringer, 2002), gravitational lensing (e.g. Koopmans et al., 2003), and probes of galaxy clustering, as for example baryon acoustic oscillations (e.g. Percival et al., 2010; Ross et al., 2015), and redshift-space distortions (e.g. Samushia et al., 2014). The most powerful way to constrain the present-day Universe's parameters is the analysis of the cosmic microwave background (CMB), the relic radiation of our Universe. State-of-the-art determinations (Planck Collaboration et al., 2016b) provide the following values for the most relevant parameters: $H_0 = 67.81 \pm 0.92$ km s^{-1} Mpc^{-1}, $\Omega_\Lambda = 0.692 \pm 0.012$, $\Omega_\mathrm{m} = 0.308 \pm 0.012$, and the baryon density parameter is $\Omega_\mathrm{b} h^2 = 0.02226 \pm 0.00023$. Also, observations support the scenario according to which our Universe is flat, being $\Omega_{0,\mathrm{tot}} \simeq 1$ (de Bernardis et al., 2002; Spergel et al., 2003; Planck Collaboration et al., 2016b).

A.2 Origin of cosmic structures

In this Section, I outline the processes that lead to the formation of the cosmic structures that we observe today, starting from an almost homogeneous Universe. I introduce the theoretical picture where galaxy formation fits and quantities that I deal with throughout the Thesis. A thorough description of how perturbations grow and evolve to form structures is beyond the aim of this Section. Exhaustive explanations can be found in the following books, that have contributed to this overview: Peebles (1980); Padmanabhan (1993); Mukhanov (2005); Weinberg (2008).

The history of the Universe can be described as a thermal history. The Big Bang represents a virtual discontinuity of infinite temperature and density: from then on, the Universe cools down as a consequence of its expansion. At first the Universe is dominated by radiation (being Ω_r larger than other Ω_i), then it enters a matter-dominated era ($z \sim 3000$). At $z \sim 1100$, protons and electrons that make up the ionised plasma filling the Universe finally combine into hydrogen atoms. As a consequence, photons are not coupled anymore to the hot medium through scattering processes: they decouple from matter and travel freely across space. The surface of last-scattering between radiation and matter is the CMB and constitutes the farthest observable of our Universe. The originating radiation can be described through an almost perfect blackbody emission, whose $T_\mathrm{CMB} \simeq 2.73$ K today, with temperature (or density, correspondingly) fluctuations amounting to $\Delta T_\mathrm{CMB}/T_\mathrm{CMB} \simeq 10^{-5}$ imprinted on it (see Figure 2.3). How do we describe these fluctuations? And how do they evolve?

Density fluctuations are investigated by means of the overdensity field, that at a given time reads:

$$\delta(\mathbf{x}) = \frac{\rho(\mathbf{x})}{\bar{\rho}} - 1 \ , \tag{A.8}$$

where $\rho(\mathbf{x})$ is the matter density distribution at the position $\mathbf{x}$, and $\bar{\rho}$ is the mean background density. The density contrast $\delta(\mathbf{x})$ can be described through its decomposition in modes of wavenumber k in the Fourier space:

$$\delta(\mathbf{x}) = \frac{1}{(2\,\pi)^3} \int \hat{\delta}(\mathbf{k}) \exp(i\,\mathbf{k}\cdot\mathbf{x})\, d^3\mathbf{k} \ , \tag{A.9}$$

$\hat{\delta}(\mathbf{k})$ being the Fourier transform of $\delta(\mathbf{x})$. The spatial dependence of $\delta(\mathbf{x})$, that is interchangeable with the dependence on $\mathbf{k}$ in the Fourier space, is usually investigated as a statistical distribution of the amplitude of perturbation modes. This leads to define the power spectrum $P(\mathbf{k})$ of the density fluctuation field as:

$$\langle \hat{\delta}^*(\mathbf{k})\, \hat{\delta}(\mathbf{k}') \rangle = (2\,\pi)^3\, P(\mathbf{k})\, \delta_\mathrm{D}^{(3)}(\mathbf{k} - \mathbf{k}') \ , \tag{A.10}$$

i.e. as the average product of fluctuation amplitudes in two different points of the Fourier space. In equation (A.10), $\delta_\mathrm{D}^{(3)}$ is the three-dimensional Dirac delta function.

Since $P(\mathbf{k}) \propto \langle|\hat{\delta}(\mathbf{k})|^2\rangle$, the power spectrum quantifies the mean square fluctuation on the scale $\mathbf{k}$, assessing the contribution of each wave of given $\mathbf{k}$ to the overdensity field $\delta(\mathbf{x})$. Under the assumption of statistical isotropy of the Universe, $P(\mathbf{k}) = P(k)$. Inflation theory yields a model according to which the overdensity field originated from early gaussian quantum fluctuations in a scalar field (Guth, 1981). The power spectrum fully describes a gaussian stochastic process, since different modes are assumed not to be correlated. Therefore, once we know the shape and the amplitude of the power spectrum of the density fluctuations in the early Universe, we are provided with a statistical description of the seed perturbations that originated the present-day cosmic structures. The power spectrum encodes indeed the initial conditions for the problem of structure formation (see Section 5.5).

In order to determine the amplitude of the power spectrum, the variance of the density field $\delta(\mathbf{x})$:

$$\sigma^2 = \frac{1}{(2\,\pi)^3} \int P(k)\, d^3k \tag{A.11}$$

is conveniently smoothed by means of a window function, in order to obtain the mass variance, that is defined as:

$$\sigma^2_{\rm M} = \frac{1}{(2\,\pi)^3} \int P(k)\, \hat{W}^2(k, R)\, d^3k \ . \tag{A.12}$$

Here, $\hat{W}^2(k, R)$ is the Fourier transform of the window function $W^2(k, R)$, that depends on a characteristic resolution scale R. Adopting a spherical top-hat as window function, where $W = 1$ within a sphere of radius R and zero outside, the smoothed density field quantifies the mass fluctuations within a sphere of radius R. The amplitude of the present-day power spectrum (see below) is analysed through the mass variance σ_8, that is the measure of its amplitude on a scale of $R = 8\ h^{-1}$ Mpc and accounts for its normalization.

The most recent determinations for parameters describing the power spectrum are the following: the primordial spectral index of fluctuations is $n_{\rm s} = 0.968 \pm 0.006$, and $\sigma_8 = 0.8149 \pm 0.0093$ (Planck Collaboration et al., 2016b). Observations are consistent with a nearly scale-invariant (i.e. $P(k) \sim k$, Harrison, 1970; Zeldovich, 1972) power spectrum for initial density fluctuations, in line with the predictions of standard inflationary models.

The primordial power spectrum (see equation A.10) that has been discussed so far gets then modified, especially at large k, as a consequence of causal processes taking place within the cosmological horizon. As a result, the processed power spectrum $P(k)$ is not described by a power law anymore. The discrepancy between the primordial power spectrum $P_{\rm prim}(k)$ and the final one $P(k)$ is encoded in the so-called transfer function $T(k)$, so that $P(k) \propto P_{\rm prim}(k)\, T^2(k)$.

As long as $\delta(\mathbf{x}) \ll 1$, the evolution of density perturbations can be described within the linear regime. Under the assumptions that matter can be treated as

a perfect fluid and that fluctuations are adiabatic, the temporal evolution of $\delta(\mathbf{x})$ reads (Coles & Lucchin, 2002):

$$\ddot{\delta}(\mathbf{x},t) + 2\,H(t)\,\dot{\delta}(\mathbf{x},t) - \frac{c_\mathrm{s}^2}{a(t)^2}\,\nabla^2\delta(\mathbf{x},t) - 4\,\pi\,G\,\bar{\rho}\,\delta(\mathbf{x},t) = 0 \ , \tag{A.13}$$

c_s being the sound speed of the component whose fluctuations are considered. This equation shows how density perturbations evolve as a consequence of the expansion of the Universe (second term), of their own pressure support (third term), and of gravity (fourth term). Gravity would lead to the gravitational collapse of the perturbations, contrasting expansion and pressure. Assuming that the pressure term is negligible (e.g. non-collisional DM dominated Universe), equation (A.13) has two solutions, where a generic spatial dependence can be factorised out: $\delta(\mathbf{x},t) = D_+(t)\,A(\mathbf{x}) + D_-(t)\,B(\mathbf{x})$. The growing mode D_+ is of cosmological interest, since it dominates over the decaying one D_- as time passes. It describes how the perturbation grows and possibly collapses (see Sections 2.2 and A.3). The solution is usually normalised by the growing mode at present time, so that one can define the growth factor $D(a) = D_+(a)/D_+(a_0)$. Since the shape of the power spectrum is not affected during the linear regime, if one assumed the linear approximation until now, the present-day power spectrum would read: $P(k) = D(a)\,P_\mathrm{prim}(k)\,T^2(k)$. However, despite the linear regime is useful to understand general processes and their evolution, the growth of cosmic structure departs soon from linearity.

A.3 The spherical collapse

If one relaxes the assumption $\delta(\mathbf{x}) \ll 1$ and leaves the linear regime, equation (A.13) does not hold anymore. Since it is impossible to capture analytically the complex evolution of perturbations beyond the linear regime, there is no way to further investigate their growth but resorting to numerical simulations. The only possible analytical approach to the evolution of density perturbations beyond the linear regime is the spherical collapse of a perturbation. The basic assumption of this model considers a positive spherical perturbation, with a top-hat distribution of uniform density and null peculiar velocity. The perturbation is deemed as a small universe embedded itself within a background universe. The background universe is assumed to be flat and without cosmological constant (Einstein – De Sitter universe): as long as the redshift is high, this is a fair approximation also when curve universes with the contribution of Λ are considered. Final results can be then generalised. The perturbation is instead treated as a close universe. Equation (A.4) describes the following evolution for a close universe: it expands as long as its scale factor reaches a maximum; after that, it experiences a contraction, collapsing ideally into a point. The dynamical evolution of the considered perturbation can be described in an analogous way: after a first expansion it undergoes a collapse, but this contraction will not end into a point, as the perturbation leads to a structure

with finite dimensions. When reaching its maximum expansion at the time $t_{\rm max}$, the perturbation has the density (Coles & Lucchin, 2002):

$$\rho(t_{\rm max}) = -\frac{3\,\pi}{32\,G\,t_{\rm max}^2} \ , \tag{A.14}$$

while the mean density of the background universe reads:

$$\bar{\rho}(t_{\rm max}) = -\frac{1}{6\,\pi\,G\,t_{\rm max}^2} \ . \tag{A.15}$$

By plugging equations (A.14) and (A.15) in equation (A.8), one finds that an overdensity $\delta(t_{\rm max}) \simeq 4.6$ (i.e. far beyond the linear approximation) characterises the perturbation at the so-called turn around point.

After the perturbation turned around, it undergoes collapse in a timescale $t_{\rm eq} = 2\,t_{\rm max}$. This contraction will be hindered either by radiation pressure or velocity dispersion according to whether a baryonic or DM fluctuation is considered. Therefore, approximately at $t_{\rm eq}$, the collapsing perturbation starts oscillating until it reaches an equilibrium configuration. The radius of this spherical parturbation at $t_{\rm eq}$ can be evaluated by means of the virial theorem, yielding $r(t_{\rm eq}) = 1/2\,r(t_{\rm max})$. As a consequence, the density of the collapsing region increases by a factor 8. The ratio between the density of the perturbation over the density of the expanding background at $t_{\rm eq}$ amounts to $18\,\pi^2 \simeq 180$ (Peebles, 1980).

Approximating $t_{\rm eq}$ with the (following) moment $t_{\rm vir}$ in which the collapsing perturbation reaches the virial configuration, one finds that virialised structures have reached an overdensity as high as

$$\delta_{\rm vir} \simeq 200 \ . \tag{A.16}$$

Extrapolating the predictions from linear theory yields to the following underestimates: $\delta(t_{\rm max}) \simeq 1.07$ and $\delta(t_{\rm eq}) \simeq 1.68$.

Therefore, first the perturbation takes part to the overall expansion of the Universe: its density decreases and its volume increases up to reach a maximum value. Meanwhile, the self-gravity of the perturbation stands in the way of the Universe expansion. Then, the overdensity turns around, detaches definitively from the Hubble flow and collapses. In the end, it is a virialised structures characterised by a typical overdensity of ~ 200 times the mean (or critical, upon definitions) density of the Universe at that time. Its size can be described by the virial radius $R_{\rm vir}$, that is the radius enclosing the overdensity $\delta_{\rm vir}$. The virial mass $M_{\rm vir}$ is the mass within $R_{\rm vir}$.

The spherical collapse model is a simplified approach, yet its predictions turn out to be useful to gain accurate insight of halo properties. Generalising the result, the typical overdensity of virialised structures in a flat Universe can be cast (Bryan & Norman, 1998):

$$\Delta_{\rm vir} = 18\,\pi^2 + 82\,(\Omega_{\rm m}(z) - 1) - 39\,(\Omega_{\rm m}(z) - 1)^2 \ , \tag{A.17}$$

where $\Omega_{\rm m}(z) = \Omega_{0,\,\rm m}(1+z)^3/E^2(z)$ and a negligible contribution from $\Omega_{0,\,\rm r}$ is assumed (see equation (A.6)). The virial radius of a halo of mass M ending its collapse at redshift z reads (Barkana & Loeb, 2001):

$$R_{\rm vir} = 0.784 \left(\frac{M}{10^8 h^{-1}{\rm M}_\odot}\right)^{1/3} \left[\frac{\Omega_{0,\,\rm m}}{\Omega_{\rm m}(z)}\,\frac{\Delta_{\rm vir}}{18\,\pi^2}\right]^{-1/3} \left(\frac{1+z}{10}\right)^{-1} h^{-1}{\rm kpc}\ . \qquad \text{(A.18)}$$

Bibliography

Abel T., Stebbins A., Anninos P., Norman M. L., 1998, ApJ, 508, 530
Abel T., Bryan G. L., Norman M. L., 2000, ApJ, 540, 39
Adelberger K. L., Steidel C. C., Shapley A. E., Pettini M., 2003, ApJ, 584, 45
Agertz O., Kravtsov A. V., 2016, ApJ, 824, 79
Agertz O., et al., 2007, MNRAS, 380, 963
Allende Prieto C., Barklem P. S., Lambert D. L., Cunha K., 2004, A&A, 420, 183
Appel A. W., 1985, SIAM J. Sci. Stat. Comp., 6, 85
Arribas S., Colina L., Bellocchi E., Maiolino R., Villar-Martín M., 2014, A&A, 568, A14
Asplund M., Grevesse N., Sauval A. J., 2005, in Barnes III T. G., Bash F. N., eds, Astronomical Society of the Pacific Conference Series Vol. 336, Cosmic Abundances as Records of Stellar Evolution and Nucleosynthesis. p. 25
Asplund M., Grevesse N., Sauval A. J., Scott P., 2009, ARA&A, 47, 481
Aumer M., White S. D. M., Naab T., Scannapieco C., 2013, MNRAS, 434, 3142
Aumer M., White S. D. M., Naab T., 2014, MNRAS, 441, 3679
Baade W., 1958, Ricerche Astronomiche, 5, 3
Bagla J. S., 2002, Journal of Astrophysics and Astronomy, 23, 185
Bahé Y. M., Schaye J., Crain R. A., McCarthy I. G., Bower R. G., Theuns T., McGee S. L., Trayford J. W., 2017, MNRAS, 464, 508
Balogh M. L., Pearce F. R., Bower R. G., Kay S. T., 2001, MNRAS, 326, 1228
Balsara D. S., 1995, Journal of Computational Physics, 121, 357
Barai P., Monaco P., Murante G., Ragagnin A., Viel M., 2015, MNRAS, 447, 266
Barai P., Murante G., Borgani S., Gaspari M., Granato G. L., Monaco P., Ragone-Figueroa C., 2016, MNRAS, 461, 1548
Barai P., Gallerani S., Pallottini A., Ferrara A., Marconi A., Cicone C., Maiolino R., Carniani S., 2018, MNRAS, 473, 4003
Barber C., Crain R. A., Schaye J., 2018, preprint, (arXiv:1804.09079)
Barbuy B., Chiappini C., Gerhard O., 2018, preprint, (arXiv:1805.01142)
Barden M., et al., 2005, ApJ, 635, 959
Barkana R., Loeb A., 2001, PhR, 349, 125
Barnes J., Efstathiou G., 1987, ApJ, 319, 575
Barnes J., Hut P., 1986, Nature, 324, 446
Basu S., Antia H. M., 2004, ApJL, 606, L85
Bate M. R., Bonnell I. A., Price N. M., 1995, MNRAS, 277, 362
Battinelli P., Demers S., Letarte B., 2003, AJ, 125, 1298
Beck A. M., et al., 2016, MNRAS, 455, 2110
Begelman M. C., Volonteri M., Rees M. J., 2006, MNRAS, 370, 289
Behroozi P. S., Wechsler R. H., Conroy C., 2013, ApJ, 770, 57
Bekki K., 2013, MNRAS, 436, 2254
Bekki K., Couch W. J., 2011, MNRAS, 415, 1783
Bell E. F., de Jong R. S., 2001, ApJ, 550, 212
Bell E. F., McIntosh D. H., Katz N., Weinberg M. D., 2003, ApJS, 149, 289
Bell E. F., Monachesi A., Harmsen B., de Jong R. S., Bailin J., Radburn-Smith D. J., D'Souza R., Holwerda B. W., 2017, ApJL, 837, L8
Berger M. J., Colella P., 1989, Journal of Computational Physics, 82, 64
Bertelli G., Girardi L., Marigo P., Nasi E., 2008, A&A, 484, 815
Bertelli G., Nasi E., Girardi L., Marigo P., 2009, A&A, 508, 355

Bhattacharjee P., Chaudhury S., Kundu S., 2014, ApJ, 785, 63
Biffi V., Valdarnini R., 2015, MNRAS, 446, 2802
Biffi V., et al., 2017, MNRAS, 468, 531
Bigiel F., Leroy A., Walter F., Brinks E., de Blok W. J. G., Madore B., Thornley M. D., 2008, AJ, 136, 2846
Binney J., Tremaine S., 2008, Galactic Dynamics: Second Edition. Princeton University Press
Bizyaev D., et al., 2017, ApJ, 839, 87
Blanton M. R., Moustakas J., 2009, ARA&A, 47, 159
Blitz L., Rosolowsky E., 2006, ApJ, 650, 933
Blumenthal G. R., Lin D. N. C., Yang L. T., 1984, ApJ, 287, 774
Blumenthal G. R., Faber S. M., Flores R., Primack J. R., 1986, ApJ, 301, 27
Bode P., Ostriker J. P., Xu G., 2000, ApJS, 128, 561
Bondi H., 1952, MNRAS, 112, 195
Bondi H., Hoyle F., 1944, MNRAS, 104, 273
Bono G., Marconi M., Cassisi S., Caputo F., Gieren W., Pietrzynski G., 2005, ApJ, 621, 966
Bonoli S., Mayer L., Kazantzidis S., Madau P., Bellovary J., Governato F., 2016, MNRAS, 459, 2603
Booth C. M., Schaye J., 2009, MNRAS, 398, 53
Borgani S., et al., 2001, ApJ, 561, 13
Borgani S., et al., 2006, MNRAS, 367, 1641
Borgani S., Fabjan D., Tornatore L., Schindler S., Dolag K., Diaferio A., 2008, Space Sci. Rev., 134, 379
Bosma A., 1981, AJ, 86, 1825
Bosma A., 2017, in Knapen J. H., Lee J. C., Gil de Paz A., eds, Astrophysics and Space Science Library Vol. 434, Outskirts of Galaxies. p. 209
Bouché N., Lehnert M. D., Péroux C., 2005, MNRAS, 364, 319
Bouché N., et al., 2007, ApJ, 671, 303
Bovy J., Hogg D. W., Rix H.-W., 2009, ApJ, 704, 1704
Bradshaw E. J., et al., 2013, MNRAS, 433, 194
Bregman J. N., 1980, ApJ, 236, 577
Bressan A., Marigo P., Girardi L., Salasnich B., Dal Cero C., Rubele S., Nanni A., 2012, MNRAS, 427, 127
Bromm V., Coppi P. S., Larson R. B., 1999, ApJL, 527, L5
Brook C. B., Kawata D., Gibson B. K., Flynn C., 2004, MNRAS, 349, 52
Brook C. B., Stinson G., Gibson B. K., Roškar R., Wadsley J., Quinn T., 2012, MNRAS, 419, 771
Brooks A. M., Governato F., Quinn T., Brook C. B., Wadsley J., 2009, ApJ, 694, 396
Brunetti M., Chiappini C., Pfenniger D., 2011, A&A, 534, A75
Bryan G. L., Norman M. L., 1997, in Clarke D. A., West M. J., eds, Astronomical Society of the Pacific Conference Series Vol. 123, Computational Astrophysics; 12th Kingston Meeting on Theoretical Astrophysics. p. 363 (arXiv:astro-ph/9710186)
Bryan G. L., Norman M. L., 1998, ApJ, 495, 80
Buat V., 1992, A&A, 264, 444
Buat V., Deharveng J. M., Donas J., 1989, A&A, 223, 42

Bullock J. S., Dekel A., Kolatt T. S., Kravtsov A. V., Klypin A. A., Porciani C., Primack J. R., 2001, ApJ, 555, 240
Caffau E., Ludwig H.-G., Steffen M., Freytag B., Bonifacio P., 2011, Sol. Phys., 268, 255
Calura F., Matteucci F., 2003, ApJ, 596, 734
Calura F., Matteucci F., 2004, MNRAS, 350, 351
Cappellari M., et al., 2012, Nature, 484, 485
Cardelli J. A., Clayton G. C., Mathis J. S., 1989, ApJ, 345, 245
Carlesi E., et al., 2016, MNRAS, 458, 900
Casagrande L., Schönrich R., Asplund M., Cassisi S., Ramírez I., Meléndez J., Bensby T., Feltzing S., 2011, A&A, 530, A138
Casasola V., Hunt L., Combes F., García-Burillo S., 2015, A&A, 577, A135
Cayrel R., et al., 2004, A&A, 416, 1117
Cazzoli S., Arribas S., Colina L., Piqueras-López J., Bellocchi E., Emonts B., Maiolino R., 2014, A&A, 569, A14
Cen R., Ostriker J. P., 1993, ApJ, 417, 415
Chabrier G., 2003, PASP, 115, 763
Chartas G., Brandt W. N., Gallagher S. C., 2003, ApJ, 595, 85
Chiappini C., Matteucci F., Gratton R., 1997, ApJ, 477, 765
Chiappini C., Matteucci F., Romano D., 2001, ApJ, 554, 1044
Chiosi C., Bressan A., Portinari L., Tantalo R., 1998, A&A, 339, 355
Christlieb N., et al., 2002, Nature, 419, 904
Churazov E., Sazonov S., Sunyaev R., Forman W., Jones C., Böhringer H., 2005, MNRAS, 363, L91
Ciardi B., Ferrara A., 2005, SSRv, 116, 625
Cicone C., et al., 2014, A&A, 562, A21
Clarke C., Carswell B., 2007, Principles of Astrophysical Fluid Dynamics
Clemens M. S., Bressan A., Nikolic B., Rampazzo R., 2009, MNRAS, 392, L35
Codis S., Pichon C., Pogosyan D., 2015, MNRAS, 452, 3369
Cole S., Lacey C. G., Baugh C. M., Frenk C. S., 2000, MNRAS, 319, 168
Coles P., Lucchin F., 2002, Cosmology: The Origin and Evolution of Cosmic Structure, Second Edition
Colless M., et al., 2001, MNRAS, 328, 1039
Conroy C., van Dokkum P. G., 2012, ApJ, 760, 71
Couchman H. M. P., 1991, ApJL, 368, L23
Courteau S., Dutton A. A., van den Bosch F. C., MacArthur L. A., Dekel A., McIntosh D. H., Dale D. A., 2007, ApJ, 671, 203
Crain R. A., et al., 2015, MNRAS, 450, 1937
Croton D. J., et al., 2006, MNRAS, 365, 11
Cullen L., Dehnen W., 2010, MNRAS, 408, 669
D'Onghia E., Navarro J. F., 2007, MNRAS, 380, L58
D'Onghia E., Burkert A., Murante G., Khochfar S., 2006, MNRAS, 372, 1525
Dalgarno A., McCray R. A., 1972, ARA&A, 10, 375
Dalla Vecchia C., Schaye J., 2008, MNRAS, 387, 1431
Dalla Vecchia C., Schaye J., 2012, MNRAS, 426, 140
Davé R., et al., 2001, ApJ, 552, 473

Davé R., Thompson R., Hopkins P. F., 2016, MNRAS, 462, 3265
David L. P., Jones C., Forman W., Nulsen P., Vrtilek J., O'Sullivan E., Giacintucci S., Raychaudhury S., 2009, ApJ, 705, 624
David L. P., et al., 2014, preprint, (arXiv:1407.3235)
Davis M., Efstathiou G., Frenk C. S., White S. D. M., 1985, ApJ, 292, 371
Dawson S., Spinrad H., Stern D., Dey A., van Breugel W., de Vries W., Reuland M., 2002, ApJ, 570, 92
De Lucia G., Kauffmann G., White S. D. M., 2004, MNRAS, 349, 1101
De Lucia G., Tornatore L., Frenk C. S., Helmi A., Navarro J. F., White S. D. M., 2014, MNRAS, 445, 970
De Masi C., Matteucci F., Vincenzo F., 2018, MNRAS, 474, 5259
Debattista V. P., Ness M., Gonzalez O. A., Freeman K., Zoccali M., Minniti D., 2017, MNRAS, 469, 1587
Dehnen W., Aly H., 2012, MNRAS, 425, 1068
Deng L.-C., et al., 2012, Research in Astronomy and Astrophysics, 12, 735
Di Cintio A., Brook C. B., Dutton A. A., Macciò A. V., Stinson G. S., Knebe A., 2014, MNRAS, 441, 2986
Di Matteo T., Springel V., Hernquist L., 2005, Nature, 433, 604
Doherty C. L., Gil-Pons P., Lau H. H. B., Lattanzio J. C., Siess L., 2014a, MNRAS, 437, 195
Doherty C. L., Gil-Pons P., Lau H. H. B., Lattanzio J. C., Siess L., Campbell S. W., 2014b, MNRAS, 441, 582
Dolag K., Borgani S., Schindler S., Diaferio A., Bykov A. M., 2008, SSRv, 134, 229
Dolag K., Mevius E., Remus R.-S., 2017, Galaxies, 5, 35
Dressler A., 1980, ApJ, 236, 351
Dubois Y., Devriendt J., Slyz A., Teyssier R., 2010, MNRAS, 409, 985
Dubois Y., et al., 2014, MNRAS, 444, 1453
Durier F., Dalla Vecchia C., 2012, MNRAS, 419, 465
Dutton A. A., van den Bosch F. C., 2009, MNRAS, 396, 141
Dutton A. A., van den Bosch F. C., 2012, MNRAS, 421, 608
Dutton A. A., van den Bosch F. C., Dekel A., Courteau S., 2007, ApJ, 654, 27
Dutton A. A., Conroy C., van den Bosch F. C., Prada F., More S., 2010, MNRAS, 407, 2
Dutton A. A., et al., 2011a, MNRAS, 410, 1660
Dutton A. A., et al., 2011b, MNRAS, 416, 322
Dutton A. A., Macciò A. V., Stinson G. S., Gutcke T. A., Penzo C., Buck T., 2015, MNRAS, 453, 2447
Edgar R., 2004, NewAR, 48, 843
Edvardsson B., Andersen J., Gustafsson B., Lambert D. L., Nissen P. E., Tomkin J., 1993, A&A, 275, 101
Efstathiou G., Jones B. J. T., 1980, Comments on Astrophysics, 8, 169
Efstathiou G., Davis M., White S. D. M., Frenk C. S., 1985, ApJS, 57, 241
Epinat B., et al., 2008, MNRAS, 388, 500
Fabian A. C., 2012, ARA&A, 50, 455
Fabian A. C., et al., 2011, MNRAS, 418, 2154
Fabjan D., Borgani S., Tornatore L., Saro A., Murante G., Dolag K., 2010, MNRAS, 401, 1670

Fall S. M., 1979, Nature, 281, 200
Fall S. M., Efstathiou G., 1980, MNRAS, 193, 189
Favata F., Micela G., Sciortino S., 1997, A&A, 323, 809
Feng Y., Di-Matteo T., Croft R. A., Bird S., Battaglia N., Wilkins S., 2016, MNRAS, 455, 2778
Ferland G. J., Korista K. T., Verner D. A., Ferguson J. W., Kingdon J. B., Verner E. M., 1998, PASP, 110, 761
Ferrara A., Scannapieco E., Bergeron J., 2005, ApJL, 634, L37
Ferrarese L., Ford H., 2005, SSRv, 116, 523
Ferrarese L., Merritt D., 2000, ApJL, 539, L9
Feruglio C., et al., 2015, A&A, 583, A99
Few C. G., Courty S., Gibson B. K., Michel-Dansac L., Calura F., 2014, MNRAS, 444, 3845
Fontanot F., De Lucia G., Hirschmann M., Bruzual G., Charlot S., Zibetti S., 2017, MNRAS, 464, 3812
Frank J., King A., Raine D. J., 2002, Accretion Power in Astrophysics: Third Edition
Franx M., et al., 2000, The Messenger, 99, 20
Frebel A., et al., 2005, Nature, 434, 871
Frenk C. S., et al., 1999, ApJ, 525, 554
Fromang S., Hennebelle P., Teyssier R., 2006, A&A, 457, 371
Frye B., Broadhurst T., Benítez N., 2002, ApJ, 568, 558
Fryxell B., et al., 2000, ApJS, 131, 273
Fukugita M., Peebles P. J. E., 2006, ApJ, 639, 590
Fuller T. M., Couchman H. M. P., 2000, ApJ, 544, 6
Gadotti D. A., 2008, MNRAS, 384, 420
Gadotti D. A., 2009, MNRAS, 393, 1531
Gadotti D. A., Kauffmann G., 2009, MNRAS, 399, 621
Gallazzi A., Brinchmann J., Charlot S., White S. D. M., 2008, MNRAS, 383, 1439
Gardner J. P., 2001, ApJ, 557, 616
Gargiulo I. D., et al., 2015, MNRAS, 446, 3820
Gaspari M., Brighenti F., Temi P., 2012, MNRAS, 424, 190
Gaspari M., Ruszkowski M., Oh S. P., 2013, MNRAS, 432, 3401
Gaspari M., Brighenti F., Temi P., 2015, A&A, 579, A62
Gatto A., et al., 2017, MNRAS, 466, 1903
Gebhardt K., et al., 2000, ApJL, 539, L13
Genel S., Fall S. M., Hernquist L., Vogelsberger M., Snyder G. F., Rodriguez-Gomez V., Sijacki D., Springel V., 2015, ApJL, 804, L40
Genovali K., et al., 2013, A&A, 554, A132
Genovali K., et al., 2014a, VizieR Online Data Catalog, 356
Genovali K., et al., 2014b, A&A, 566, A37
Gerritsen J. P. E., Icke V., 1997, A&A, 325, 972
Gibson B. K., Fenner Y., Renda A., Kawata D., Lee H.-c., 2003, PASA, 20, 401
Gillessen S., Eisenhauer F., Trippe S., Alexander T., Genzel R., Martins F., Ott T., 2009, ApJ, 692, 1075
Gilmore G., Wyse R. F. G., Jones J. B., 1995, AJ, 109, 1095

Gilmore G., et al., 2012, The Messenger, 147, 25
Gingold R. A., Monaghan J. J., 1977, MNRAS, 181, 375
Gingold R. A., Monaghan J. J., 1982, Journal of Computational Physics, 46, 429
Girardi L., Marigo P., 2007, in Kerschbaum F., Charbonnel C., Wing R. F., eds, Astronomical Society of the Pacific Conference Series Vol. 378, Why Galaxies Care About AGB Stars: Their Importance as Actors and Probes. p. 20
Girardi L., Groenewegen M. A. T., Hatziminaoglou E., da Costa L., 2005, A&A, 436, 895
González Delgado R. M., et al., 2014, A&A, 562, A47
Governato F., et al., 2004, ApJ, 607, 688
Governato F., Willman B., Mayer L., Brooks A., Stinson G., Valenzuela O., Wadsley J., Quinn T., 2007, MNRAS, 374, 1479
Governato F., et al., 2010, Nature, 463, 203
Grand R. J. J., et al., 2016, MNRAS, 460, L94
Grand R. J. J., et al., 2017, MNRAS, 467, 179
Grand R. J. J., et al., 2018a, preprint, (arXiv:1804.08549)
Grand R. J. J., et al., 2018b, MNRAS, 474, 3629
Greggio L., Renzini A., 1983, A&A, 118, 217
Grevesse N., Sauval A. J., 1998, SSRv, 85, 161
Grisoni V., Spitoni E., Matteucci F., Recio-Blanco A., de Laverny P., Hayden M., Mikolaitis Ŝ., Worley C. C., 2017, MNRAS, 472, 3637
Guedes J., Callegari S., Madau P., Mayer L., 2011, ApJ, 742, 76
Guo Q., White S., Li C., Boylan-Kolchin M., 2010, MNRAS, 404, 1111
Gutcke T. A., Springel V., 2017, preprint, (arXiv:1710.04222)
Guth A. H., 1981, Phys. Rev. D., 23, 347
Haardt F., Madau P., 2001, in Neumann D. M., Tran J. T. V., eds, Clusters of Galaxies and the High Redshift Universe Observed in X-rays. CEA, Saclay, p.64. (arXiv:astro-ph/0106018)
Hall M., Courteau S., Dutton A. A., McDonald M., Zhu Y., 2012, MNRAS, 425, 2741
Hammer F., Flores H., Elbaz D., Zheng X. Z., Liang Y. C., Cesarsky C., 2005, A&A, 430, 115
Hammer F., Puech M., Chemin L., Flores H., Lehnert M. D., 2007, ApJ, 662, 322
Häring N., Rix H.-W., 2004, ApJL, 604, L89
Harrison E. R., 1970, Phys. Rev., 1, 2726
Hayward C. C., Hopkins P. F., 2017, MNRAS, 465, 1682
Haywood M., 2001, MNRAS, 325, 1365
Heckman T. M., Lehnert M. D., Strickland D. K., Armus L., 2000, ApJS, 129, 493
Hernquist L., 1993, ApJ, 404, 717
Heyer M., Dame T. M., 2015, ARA&A, 53, 583
Hirschmann M., Dolag K., Saro A., Bachmann L., Borgani S., Burkert A., 2014, MNRAS, 442, 2304
Hirschmann M., De Lucia G., Fontanot F., 2016, MNRAS, 461, 1760
Hobbs A., Nayakshin S., Power C., King A., 2011, MNRAS, 413, 2633
Hockney R. W., Eastwood J. W., 1988, Computer simulation using particles
Hogg D. W., 1999, ArXiv Astrophysics e-prints,
Holmberg J., Flynn C., 2000, MNRAS, 313, 209
Holmberg J., Nordström B., Andersen J., 2007, A&A, 475, 519

Holmberg J., Nordström B., Andersen J., 2009, A&A, 501, 941
Hopkins P. F., 2013, MNRAS, 428, 2840
Hopkins P. F., et al., 2018, MNRAS,
Hoyle F., Lyttleton R. A., 1939, Proceedings of the Cambridge Philosophical Society, 35, 405
Huang K.-H., et al., 2017, ApJ, 838, 6
Hubber D. A., Batty C. P., McLeod A., Whitworth A. P., 2011, A&A, 529, A27
Hubble E. P., 1936, Realm of the Nebulae
Hubble E., Humason M. L., 1931, ApJ, 74, 43
Jenkins A., 2010, MNRAS, 403, 1859
Jernigan J. G., Porter D. H., 1989, ApJS, 71, 871
Jiang X.-J., Wang Z., Gu Q., Wang J., Zhang Z.-Y., 2015, ApJ, 799, 92
Karakas A. I., 2010, MNRAS, 403, 1413
Karakas A., Lattanzio J. C., 2007, PASA, 24, 103
Katz N., White S. D. M., 1993, ApJ, 412, 455
Katz N., Weinberg D. H., Hernquist L., 1996, ApJS, 105, 19
Kauffmann G., White S. D. M., 1993, MNRAS, 261
Kaufmann T., Mayer L., Wadsley J., Stadel J., Moore B., 2007, MNRAS, 375, 53
Kazantzidis S., Bullock J. S., Zentner A. R., Kravtsov A. V., Moustakas L. A., 2008, ApJ, 688, 254
Keller B. W., Wadsley J., Benincasa S. M., Couchman H. M. P., 2014, MNRAS, 442, 3013
Keller B. W., Wadsley J., Couchman H. M. P., 2015, MNRAS, 453, 3499
Kennicutt Jr. R. C., 1989, ApJ, 344, 685
Kennicutt Jr. R. C., 1998a, ARA&A, 36, 189
Kennicutt Jr. R. C., 1998b, ApJ, 498, 541
Kennicutt Jr. R. C., et al., 2007, ApJ, 671, 333
Kewley L. J., Ellison S. L., 2008, ApJ, 681, 1183
Khandai N., Di Matteo T., Croft R., Wilkins S., Feng Y., Tucker E., DeGraf C., Liu M.-S., 2015, MNRAS, 450, 1349
King A. R., 2010, MNRAS, 402, 1516
Koopmans L. V. E., Treu T., Fassnacht C. D., Blandford R. D., Surpi G., 2003, ApJ, 599, 70
Kormendy J., Bender R., 2012, ApJS, 198, 2
Kormendy J., Gebhardt K., 2001, in Wheeler J. C., Martel H., eds, American Institute of Physics Conference Series Vol. 586, 20th Texas Symposium on relativistic astrophysics. pp 363–381 (arXiv:astro-ph/0105230)
Kormendy J., Ho L. C., 2013, ARA&A, 51, 511
Kormendy J., Kennicutt Jr. R. C., 2004, ARA&A, 42, 603
Kormendy J., Richstone D., 1995, ARA&A, 33, 581
Kormendy J., Bender R., Cornell M. E., 2011, Nature, 469, 374
Kornei K. A., Shapley A. E., Martin C. L., Coil A. L., Lotz J. M., Schiminovich D., Bundy K., Noeske K. G., 2012, ApJ, 758, 135
Kravtsov A. V., Klypin A., Hoffman Y., 2002, ApJ, 571, 563
Kroupa P., 2001, MNRAS, 322, 231
Kroupa P., 2002, Science, 295, 82
Kroupa P., Weidner C., 2003, ApJ, 598, 1076

Kroupa P., Tout C. A., Gilmore G., 1993, MNRAS, 262, 545
Kroupa P., Weidner C., Pflamm-Altenburg J., Thies I., Dabringhausen J., Marks M., Maschberger T., 2013, The Stellar and Sub-Stellar Initial Mass Function of Simple and Composite Populations. p. 115
La Barbera F., Ferreras I., Vazdekis A., de la Rosa I. G., de Carvalho R. R., Trevisan M., Falcón-Barroso J., Ricciardelli E., 2013, MNRAS, 433, 3017
Lacey C., Cole S., 1993, MNRAS, 262, 627
Lacey C. G., Fall S. M., 1985, ApJ, 290, 154
Lapi A., Salucci P., Danese L., 2018, ApJ, 859, 2
Lecureur A., Hill V., Zoccali M., Barbuy B., Gómez A., Minniti D., Ortolani S., Renzini A., 2007, A&A, 465, 799
Lemasle B., François P., Bono G., Mottini M., Primas F., Romaniello M., 2007, A&A, 467, 283
Lemson G., Kauffmann G., 1999, MNRAS, 302, 111
Leroy A. K., Walter F., Brinks E., Bigiel F., de Blok W. J. G., Madore B., Thornley M. D., 2008, AJ, 136, 2782
Lin D. N. C., Pringle J. E., 1987, MNRAS, 225, 607
Lisenfeld U., et al., 2011, A&A, 534, A102
Lofthouse E. K., Houghton R. C. W., Kaviraj S., 2017, MNRAS, 471, 2311
Luck R. E., Heiter U., 2006, AJ, 131, 3069
Luck R. E., Lambert D. L., 2011, AJ, 142, 136
Luck R. E., Kovtyukh V. V., Andrievsky S. M., 2006, AJ, 132, 902
Luck R. E., Andrievsky S. M., Kovtyukh V. V., Gieren W., Graczyk D., 2011, AJ, 142, 51
Lucy L. B., 1977, AJ, 82, 1013
Macciò A. V., Dutton A. A., van den Bosch F. C., Moore B., Potter D., Stadel J., 2007, MNRAS, 378, 55
Magorrian J., et al., 1998, AJ, 115, 2285
Magrini L., Sestito P., Randich S., Galli D., 2009, A&A, 494, 95
Majewski S. R., APOGEE Team APOGEE-2 Team 2016, Astronomische Nachrichten, 337, 863
Makino J., Fukushige T., Koga M., Namura K., 2003, PASJ, 55, 1163
Maller A. H., Dekel A., 2002, MNRAS, 335, 487
Mannucci F., Della Valle M., Panagia N., Cappellaro E., Cresci G., Maiolino R., Petrosian A., Turatto M., 2005, A&A, 433, 807
Marconi A., Hunt L. K., 2003, ApJL, 589, L21
Marinacci F., Pakmor R., Springel V., 2014, MNRAS, 437, 1750
Marri S., White S. D. M., 2003, MNRAS, 345, 561
Martin C. L., 2005, in Braun R., ed., Astronomical Society of the Pacific Conference Series Vol. 331, Extra-Planar Gas. p. 305
Martínez-Delgado D., et al., 2010, AJ, 140, 962
Matteucci F., 2003, The Chemical Evolution of the Galaxy
Matteucci F., 2012, Chemical Evolution of Galaxies
Matteucci F., Francois P., 1989, MNRAS, 239, 885
Matteucci F., Gibson B. K., 1995, A&A, 304, 11
Matteucci F., Greggio L., 1986, A&A, 154, 279
Matthews L. D., Wood K., 2003, ApJ, 593, 721

Mayer L., Governato F., Kaufmann T., 2008, Advanced Science Letters, 1, 7
McCarthy I. G., Schaye J., Bird S., Le Brun A. M. C., 2017, MNRAS, 465, 2936
McConnell N. J., Ma C.-P., 2013, ApJ, 764, 184
McGaugh S. S., de Blok W. J. G., 1997, ApJ, 481, 689
McGaugh S. S., Schombert J. M., Bothun G. D., de Blok W. J. G., 2000, ApJL, 533, L99
McMillan P. J., 2011, MNRAS, 414, 2446
McNamara B. R., Nulsen P. E. J., 2007, ARA&A, 45, 117
McNamara B. R., Russell H. R., Nulsen P. E. J., Hogan M. T., Fabian A. C., Pulido F., Edge A. C., 2016, ApJ, 830, 79
Meléndez J., et al., 2008, A&A, 484, L21
Merritt D., Ferrarese L., 2001, ApJ, 547, 140
Mignone A., Bodo G., Massaglia S., Matsakos T., Tesileanu O., Zanni C., Ferrari A., 2007, ApJS, 170, 228
Mikolaitis Š., de Laverny P., Recio-Blanco A., Hill V., Worley C. C., de Pascale M., 2017, A&A, 600, A22
Mo H. J., Mao S., White S. D. M., 1998, MNRAS, 295, 319
Mo H., van den Bosch F. C., White S., 2010, Galaxy Formation and Evolution
Monaco P., 2004, MNRAS, 352, 181
Monaghan J. J., 1992, ARA&A, 30, 543
Monaghan J. J., 1997, Journal of Computational Physics, 136, 298
Monaghan J. J., 2005, Reports on Progress in Physics, 68, 1703
Monaghan J. J., Lattanzio J. C., 1985, A&A, 149, 135
Morganti R., 2017, Frontiers in Astronomy and Space Sciences, 4, 42
Morganti R., Veilleux S., Oosterloo T., Teng S. H., Rupke D., 2016, A&A, 593, A30
Morris J. P., Monaghan J. J., 1997, Journal of Computational Physics, 136, 41
Moster B. P., Somerville R. S., Maulbetsch C., van den Bosch F. C., Macciò A. V., Naab T., Oser L., 2010, ApJ, 710, 903
Moster B. P., Naab T., White S. D. M., 2013, MNRAS, 428, 3121
Mott A., Spitoni E., Matteucci F., 2013, MNRAS, 435, 2918
Muñoz-Mateos J. C., Boissier S., Gil de Paz A., Zamorano J., Kennicutt Jr. R. C., Moustakas J., Prantzos N., Gallego J., 2011, ApJ, 731, 10
Mukhanov V., 2005, Physical Foundations of Cosmology
Murante G., Monaco P., Giovalli M., Borgani S., Diaferio A., 2010, MNRAS, 405, 1491
Murante G., Monaco P., Borgani S., Tornatore L., Dolag K., Goz D., 2015, MNRAS, 447, 178
Murray N., Quataert E., Thompson T. A., 2005, ApJ, 618, 569
Nagashima M., Lacey C. G., Okamoto T., Baugh C. M., Frenk C. S., Cole S., 2005, MNRAS, 363, L31
Navarro J. F., 1998, in Zaritsky D., ed., Astronomical Society of the Pacific Conference Series Vol. 136, Galactic Halos. p. 409 (arXiv:astro-ph/9801073)
Navarro J. F., Benz W., 1991, ApJ, 380, 320
Navarro J. F., Steinmetz M., 1997, ApJ, 478, 13
Navarro J. F., Steinmetz M., 2000, ApJ, 538, 477
Navarro J. F., White S. D. M., 1994, MNRAS, 267, 401
Navarro J. F., Frenk C. S., White S. D. M., 1996, ApJ, 462, 563
Negri A., Volonteri M., 2017, MNRAS, 467, 3475

Nishi R., Susa H., 1999, ApJL, 523, L103
Nomoto K., Kobayashi C., Tominaga N., 2013, ARA&A, 51, 457
Nordström B., et al., 2004, A&A, 418, 989
O'Brien J. C., Freeman K. C., van der Kruit P. C., 2010, A&A, 515, A62
O'Shea B. W., Nagamine K., Springel V., Hernquist L., Norman M. L., 2005, ApJS, 160, 1
Okamoto T., Jenkins A., Eke V. R., Quilis V., Frenk C. S., 2003, MNRAS, 345, 429
Oosterloo T., Fraternali F., Sancisi R., 2007, AJ, 134, 1019
Oppenheimer B. D., Davé R., 2006, MNRAS, 373, 1265
Oppenheimer B. D., Davé R., 2008, MNRAS, 387, 577
Oppenheimer B. D., Davé R., Katz N., Kollmeier J. A., Weinberg D. H., 2012, MNRAS, 420, 829
Oppenheimer B. D., Schaye J., Crain R. A., Werk J. K., Richings A. J., 2017, preprint, (arXiv:1709.07577)
Oser L., Ostriker J. P., Naab T., Johansson P. H., Burkert A., 2010, ApJ, 725, 2312
Padmanabhan T., 1993, New Scientist, 1876, 52
Padovani P., Matteucci F., 1993, ApJ, 416, 26
Pagel B. E. J., 2009, Nucleosynthesis and Chemical Evolution of Galaxies
Pakmor R., Edelmann P., Röpke F. K., Hillebrandt W., 2012, MNRAS, 424, 2222
Patel S. G., et al., 2013, ApJ, 778, 115
Peacock J. A., Smith R. E., 2000, MNRAS, 318, 1144
Pearce F. R., Jenkins A., Frenk C. S., White S. D. M., Thomas P. A., Couchman H. M. P., Peacock J. A., Efstathiou G., 2001, MNRAS, 326, 649
Pedicelli S., et al., 2010, A&A, 518, A11
Peebles P. J. E., 1969, ApJ, 155, 393
Peebles P. J. E., 1980, The large-scale structure of the universe
Peeples M. S., Werk J. K., Tumlinson J., Oppenheimer B. D., Prochaska J. X., Katz N., Weinberg D. H., 2014, ApJ, 786, 54
Penzias A. A., Wilson R. W., 1965, ApJ, 142, 419
Percival W. J., et al., 2010, MNRAS, 401, 2148
Perlmutter S., et al., 1999, ApJ, 517, 565
Peterson J. R., Fabian A. C., 2006, Physics Reports, 427, 1
Pettini M., 2006, in Le Brun V., Mazure A., Arnouts S., Burgarella D., eds, The Fabulous Destiny of Galaxies: Bridging Past and Present. p. 319 (arXiv:astro-ph/0603066)
Pettini M., Shapley A. E., Steidel C. C., Cuby J.-G., Dickinson M., Moorwood A. F. M., Adelberger K. L., Giavalisco M., 2001, ApJ, 554
Pezzulli G., Fraternali F., 2016, MNRAS, 455, 2308
Pichon C., Pogosyan D., Kimm T., Slyz A., Devriendt J., Dubois Y., 2011, MNRAS, 418, 2493
Pierce M. J., Tully R. B., 1992, ApJ, 387, 47
Pietrinferni A., Cassisi S., Salaris M., Castelli F., 2006, ApJ, 642, 797
Pilkington K., et al., 2012, MNRAS, 425, 969
Pillepich A., Madau P., Mayer L., 2015, ApJ, 799, 184
Pillepich A., et al., 2018, MNRAS, 473, 4077
Pilyugin L. S., Grebel E. K., Kniazev A. Y., 2014, AJ, 147, 131
Piontek F., Steinmetz M., 2011, MNRAS, 410, 2625

Pizagno J., et al., 2007, AJ, 134, 945
Planck Collaboration et al., 2016a, A&A, 594, A1
Planck Collaboration et al., 2016b, A&A, 594, A13
Plummer H. C., 1911, MNRAS, 71, 460
Porciani C., Dekel A., Hoffman Y., 2002, MNRAS, 332, 339
Portinari L., Chiosi C., 2000, A&A, 355, 929
Portinari L., Chiosi C., Bressan A., 1998, A&A, 334, 505
Power C., Nayakshin S., King A., 2011, MNRAS, 412, 269
Press W. H., Schechter P., 1974, ApJ, 187, 425
Price D. J., 2008, Journal of Computational Physics, 227, 10040
Price D. J., 2012a, Journal of Computational Physics, 231, 759
Price D. J., 2012b, in Capuzzo-Dolcetta R., Limongi M., Tornambè A., eds, Astronomical Society of the Pacific Conference Series Vol. 453, Advances in Computational Astrophysics: Methods, Tools, and Outcome. p. 249
Price D. J., et al., 2017, preprint,
Proga D., 2007, ApJ, 661, 693
Puchwein E., Springel V., 2013, MNRAS, 428, 2966
Putman M. E., Peek J. E. G., Joung M. R., 2012, ARA&A, 50, 491
Ragone-Figueroa C., Granato G. L., Murante G., Borgani S., Cui W., 2013, MNRAS, 436, 1750
Rasia E., et al., 2015, ApJL, 813, L17
Read J. I., Hayfield T., Agertz O., 2010, MNRAS, 405, 1513
Reiprich T. H., Böhringer H., 2002, ApJ, 567, 716
Remus R.-S., Dolag K., Naab T., Burkert A., Hirschmann M., Hoffmann T. L., Johansson P. H., 2017, MNRAS, 464, 3742
Renzini A., 1999, in Carollo C. M., Ferguson H. C., Wyse R. F. G., eds, The Formation of Galactic Bulges. p. 9
Reyes R., Mandelbaum R., Gunn J. E., Pizagno J., Lackner C. N., 2011, MNRAS, 417, 2347
Riess A. G., et al., 1998, AJ, 116, 1009
Ritchie B. W., Thomas P. A., 2001, MNRAS, 323, 743
Rix H.-W., et al., 2004, ApJS, 152, 163
Robertson B., Bullock J. S., Cox T. J., Di Matteo T., Hernquist L., Springel V., Yoshida N., 2006, ApJ, 645, 986
Rocha-Pinto H. J., Maciel W. J., 1996, MNRAS, 279, 447
Rocha-Pinto H. J., Maciel W. J., 1998, A&A, 339, 791
Rockosi C., Beers T. C., Majewski S., Schiavon R., Eisenstein D., 2009, in astro2010: The Astronomy and Astrophysics Decadal Survey. (arXiv:0902.3484)
Romaniello M., et al., 2008, A&A, 488, 731
Romano D., Karakas A. I., Tosi M., Matteucci F., 2010, A&A, 522, A32
Romano D., Matteucci F., Zhang Z.-Y., Papadopoulos P. P., Ivison R. J., 2017, MNRAS, 470, 401
Rosas-Guevara Y. M., et al., 2015, MNRAS, 454, 1038
Ross A. J., Percival W. J., Manera M., 2015, MNRAS, 451, 1331
Rosswog S., 2009, NewAR, 53, 78
Roškar R., Debattista V. P., Quinn T. R., Stinson G. S., Wadsley J., 2008, ApJL, 684,

L79
Rubin K. H. R., Weiner B. J., Koo D. C., Martin C. L., Prochaska J. X., Coil A. L., Newman J. A., 2010, ApJ, 719, 1503
Rubin K. H. R., Prochaska J. X., Ménard B., Murray N., Kasen D., Koo D. C., Phillips A. C., 2011, ApJ, 728, 55
Rupke D. S. N., Veilleux S., 2011, ApJL, 729, L27
Rupke D. S., Veilleux S., Sanders D. B., 2005, ApJS, 160, 115
Sagar R., Richtler T., 1991, A&A, 250, 324
Saintonge A., et al., 2011, MNRAS, 415, 32
Saitoh T. R., Makino J., 2009, ApJL, 697, L99
Saitoh T. R., Makino J., 2013, ApJL, 768, 44
Salpeter E. E., 1955, ApJ, 121, 161
Samushia L., et al., 2014, MNRAS, 439, 3504
Sancisi R., 1976, A&A, 53, 159
Sancisi R., Fraternali F., Oosterloo T., van der Hulst T., 2008, A&ARv, 15, 189
Sarazin C. L., 2009, X-Ray Emission from Clusters of Galaxies
Savage B. D., Sembach K. R., Tripp T. M., Richter P., 2002, ApJ, 564, 631
Sawala T., et al., 2016, MNRAS, 457, 1931
Scannapieco C., Tissera P. B., White S. D. M., Springel V., 2006, MNRAS, 371, 1125
Scannapieco C., Tissera P. B., White S. D. M., Springel V., 2008, MNRAS, 389, 1137
Scannapieco C., White S. D. M., Springel V., Tissera P. B., 2009, MNRAS, 396, 696
Scannapieco C., Gadotti D. A., Jonsson P., White S. D. M., 2010, MNRAS, 407, L41
Scannapieco C., et al., 2012, MNRAS, 423, 1726
Schaller M., Dalla Vecchia C., Schaye J., Bower R. G., Theuns T., Crain R. A., Furlong M., McCarthy I. G., 2015, MNRAS, 454, 2277
Schaye J., 2004, ApJ, 609, 667
Schaye J., Dalla Vecchia C., 2008, MNRAS, 383, 1210
Schaye J., et al., 2015, MNRAS, 446, 521
Schmidt M., 1959, ApJ, 129, 243
Schönrich R., Binney J., 2009, MNRAS, 396, 203
Schuessler I., Schmitt D., 1981, A&A, 97, 373
Segers M. C., Schaye J., Bower R. G., Crain R. A., Schaller M., Theuns T., 2016, MNRAS, 461, L102
Sellwood J. A., Binney J. J., 2002, MNRAS, 336, 785
Sembolini F., et al., 2016a, MNRAS, 457, 4063
Sembolini F., et al., 2016b, MNRAS, 459, 2973
Sersic J. L., 1968, Atlas de Galaxias Australes
Shakura N. I., Sunyaev R. A., 1973, A&A, 24, 337
Shapiro P. R., Field G. B., 1976, ApJ, 205, 762
Shapley A. E., Steidel C. C., Pettini M., Adelberger K. L., 2003, ApJ, 588, 65
Sheth R. K., Tormen G., 2002, MNRAS, 329, 61
Shopbell P. L., Bland-Hawthorn J., 1998, ApJ, 493, 129
Sijacki D., Springel V., Di Matteo T., Hernquist L., 2007, MNRAS, 380, 877
Smith D. A., Wilson A. S., Arnaud K. A., Terashima Y., Young A. J., 2002, ApJ, 565, 195

Snaith O. N., Haywood M., Di Matteo P., Lehnert M. D., Combes F., Katz D., Gómez A., 2014, ApJL, 781, L31
Sofue Y., Rubin V., 2001, ARA&A, 39, 137
Sommer-Larsen J., Dolgov A., 2001, ApJ, 551, 608
Sommer-Larsen J., Gelato S., Vedel H., 1999a, ApJ, 519, 501
Sommer-Larsen J., Gelato S., Vedel H., 1999b, ApJ, 519, 501
Spergel D. N., et al., 2003, ApJS, 148, 175
Spina L., et al., 2017, A&A, 601, A70
Spitoni E., Matteucci F., 2011, A&A, 531, A72
Spitzer L., 1978, Physical processes in the interstellar medium
Springel V., 2005, MNRAS, 364, 1105
Springel V., 2010a, ARA&A, 48, 391
Springel V., 2010b, MNRAS, 401, 791
Springel V., 2016, Star Formation in Galaxy Evolution: Connecting Numerical Models to Reality, Saas-Fee Advanced Course, Volume 43. ISBN 978-3-662-47889-9. Springer-Verlag Berlin Heidelberg, 2016, p. 251, 43, 251
Springel V., Hernquist L., 2002, MNRAS, 333, 649
Springel V., Hernquist L., 2003, MNRAS, 339, 289
Springel V., Yoshida N., White S. D. M., 2001, New Astron., 6, 79
Springel V., Di Matteo T., Hernquist L., 2005a, MNRAS, 361, 776
Springel V., Di Matteo T., Hernquist L., 2005b, MNRAS, 361, 776
Springel V., et al., 2005c, Nature, 435, 629
Springel V., et al., 2008, MNRAS, 391, 1685
Stark D. V., McGaugh S. S., Swaters R. A., 2009, AJ, 138, 392
Steinborn L. K., Dolag K., Hirschmann M., Prieto M. A., Remus R.-S., 2015, MNRAS, 448, 1504
Steinmetz M., Navarro J. F., 1999, ApJ, 513, 555
Steinmetz M., White S. D. M., 1997, MNRAS, 288, 545
Steinmetz M., et al., 2006, AJ, 132, 1645
Stinson G., Seth A., Katz N., Wadsley J., Governato F., Quinn T., 2006, MNRAS, 373, 1074
Stinson G. S., Brook C., Macciò A. V., Wadsley J., Quinn T. R., Couchman H. M. P., 2013, MNRAS, 428, 129
Stone J. M., Norman M. L., 1992, ApJs, 80, 753
Stone J. M., Gardiner T. A., Teuben P., Hawley J. F., Simon J. B., 2008, ApJS, 178, 137
Strömgren B., 1963, QJRAS, 4, 8
Strömgren B., 1987, in Gilmore G., Carswell B., eds, NATO Advanced Science Institutes (ASI) Series C Vol. 207, NATO Advanced Science Institutes (ASI) Series C. pp 229–246
Su K.-Y., Hopkins P. F., Hayward C. C., Faucher-Giguère C.-A., Kereš D., Ma X., Robles V. H., 2017, MNRAS, 471, 144
Sutherland R. S., Dopita M. A., 1993, ApJs, 88, 253
Sziládi K., Vinkó J., Poretti E., Szabados L., Kun M., 2007, A&A, 473, 579
Tang Y., Giavalisco M., Guo Y., Kurk J., 2014, ApJ, 793, 92
Taylor B. J., Croxall K., 2005, MNRAS, 357, 967
Teklu A. F., Remus R.-S., Dolag K., Beck A. M., Burkert A., Schmidt A. S., Schulze F., Steinborn L. K., 2015, ApJ, 812, 29

Thacker R. J., Couchman H. M. P., 2000, ApJ, 545, 728
Thielemann F.-K., et al., 2003, in Hillebrandt W., Leibundgut B., eds, From Twilight to Highlight: The Physics of Supernovae. p. 331
Tinker J. L., Weinberg D. H., Zheng Z., Zehavi I., 2005, ApJ, 631, 41
Tinsley B. M., 1979, ApJ, 229, 1046
Tombesi F., Meléndez M., Veilleux S., Reeves J. N., González-Alfonso E., Reynolds C. S., 2015, Nature, 519, 436
Tonini C., Lapi A., Salucci P., 2006, ApJ, 649, 591
Tormen G., Bouchet F. R., White S. D. M., 1997, MNRAS, 286, 865
Tornatore L., Borgani S., Springel V., Matteucci F., Menci N., Murante G., 2003, MNRAS, 342, 1025
Tornatore L., Borgani S., Dolag K., Matteucci F., 2007, MNRAS, 382, 1050
Toro E. F., 1997, Riemann Solvers and Numerical Methods for Fluid Dynamics
Torres-Flores S., Epinat B., Amram P., Plana H., Mendes de Oliveira C., 2011, MNRAS, 416, 1936
Torrey P., et al., 2017, preprint, (arXiv:1711.05261)
Tremaine S., et al., 2002, ApJ, 574, 740
Tremonti C. A., et al., 2004, ApJ, 613, 898
Trujillo I., et al., 2006, ApJ, 650, 18
Tully R. B., Fisher J. R., 1977, A&A, 54, 661
Tumlinson J., et al., 2011, ApJ, 733, 111
Tumlinson J., Peeples M. S., Werk J. K., 2017, ARA&A, 55, 389
Übler H., Naab T., Oser L., Aumer M., Sales L. V., White S. D. M., 2014, MNRAS, 443, 2092
Valdarnini R., 2012, A&A, 546, A45
Valentini M., Brighenti F., 2015, MNRAS, 448, 1979
Valentini M., Murante G., Borgani S., Monaco P., Bressan A., Beck A. M., 2017, MNRAS, 470, 3167
Valentini M., Borgani S., Bressan A., Murante G., Tornatore L., Monaco P., 2018a, MNRAS
Valentini M., Bressan A., Borgani S., Murante G., Girardi L., Tornatore L., 2018b, MNRAS, 480, 722
Vanhollebeke E., Groenewegen M. A. T., Girardi L., 2009, A&A, 498, 95
Veilleux S., Shopbell P. L., Rupke D. S., Bland-Hawthorn J., Cecil G., 2003, AJ, 126, 2185
Veilleux S., Cecil G., Bland-Hawthorn J., 2005, ARA&A, 43, 769
Venn K. A., Irwin M., Shetrone M. D., Tout C. A., Hill V., Tolstoy E., 2004, AJ, 128, 1177
Vergely J.-L., Ferrero R. F., Egret D., Koeppen J., 1998, A&A, 340, 543
Verheijen M. A. W., 2001a, ApJ, 563, 694
Verheijen M. A. W., 2001b, ApJ, 563, 694
Vogelsberger M., Genel S., Sijacki D., Torrey P., Springel V., Hernquist L., 2013, MNRAS, 436, 3031
Vogelsberger M., et al., 2014a, MNRAS, 444, 1518
Vogelsberger M., et al., 2014b, MNRAS, 444, 1518
Vogelsberger M., et al., 2018, MNRAS, 474, 2073

Vogt N. P., Haynes M. P., Giovanelli R., Herter T., 2004, AJ, 127, 3325
Volonteri M., Bellovary J., 2012, Reports on Progress in Physics, 75, 124901
Von Neumann J., Richtmyer R. D., 1950, Journal of Applied Physics, 21, 232
Wadsley J. W., Stadel J., Quinn T., 2004, New Astronomy, 9, 137
Wadsley J. W., Keller B. W., Quinn T. R., 2017, MNRAS, 471, 2357
Walter F., Weiss A., Scoville N., 2002, ApJL, 580, L21
Wang L., Dutton A. A., Stinson G. S., Macciò A. V., Penzo C., Kang X., Keller B. W., Wadsley J., 2015, MNRAS, 454, 83
Weinberg S., 2008, Cosmology. Oxford University Press
Weinberger R., et al., 2017, MNRAS, 465, 3291
Weiner B. J., et al., 2009, ApJ, 692, 187
Werk J. K., et al., 2016, ApJ, 833, 54
Werner N., et al., 2014, MNRAS, 439, 2291
Wetzstein M., Nelson A. F., Naab T., Burkert A., 2009, ApJS, 184, 298
White S. D. M., Frenk C. S., 1991, ApJ, 379, 52
White S. D. M., Rees M. J., 1978, MNRAS, 183, 341
Wiersma R. P. C., Schaye J., Smith B. D., 2009a, MNRAS, 393, 99
Wiersma R. P. C., Schaye J., Theuns T., Dalla Vecchia C., Tornatore L., 2009b, MNRAS, 399, 574
Williamson D., Martel H., Kawata D., 2016, ApJ, 822, 91
Wilman R. J., Gerssen J., Bower R. G., Morris S. L., Bacon R., de Zeeuw P. T., Davies R. L., 2005, Nature, 436, 227
Wilson T. L., Matteucci F., 1992, A&Ar, 4, 1
Wolf C., et al., 2018, preprint, (arXiv:1801.07834)
Wong T., Blitz L., 2002, ApJ, 569, 157
Woosley S. E., Weaver T. A., 1995, ApJs, 101, 181
Wurster J., Thacker R. J., 2013, MNRAS, 431, 2513
Yanny B., et al., 2009, AJ, 137, 4377
Yates R. M., Henriques B., Thomas P. A., Kauffmann G., Johansson J., White S. D. M., 2013, MNRAS, 435, 3500
Yong D., Carney B. W., Teixera de Almeida M. L., Pohl B. L., 2006, AJ, 131, 2256
York D. G., et al., 2000, AJ, 120, 1579
Yoshida N., Omukai K., Hernquist L., 2008, Science, 321, 669
Yoshikawa K., Yoshida N., Umemura M., 2013, ApJ, 762, 116
Yuma S., Ouchi M., Drake A. B., Fujimoto S., Kojima T., Sugahara Y., 2017, ApJ, 841, 93
Zaritsky D., Courtois H., 2017, MNRAS, 465, 3724
Zeldovich Y. B., 1972, MNRAS, 160, 1P
Zoccali M., et al., 2006, A&A, 457, L1
de Bernardis P., et al., 2002, ApJ, 564, 559
de Laverny P., Recio-Blanco A., Worley C. C., De Pascale M., Hill V., Bijaoui A., 2013, The Messenger, 153, 18
de Vaucouleurs G., 1948, Annales d'Astrophysique, 11, 247
van Dokkum P. G., et al., 2013, ApJL, 771, L35
van den Bosch F. C., Dalcanton J. J., 2000, ApJ, 534, 146

van den Bosch F. C., Abel T., Croft R. A. C., Hernquist L., White S. D. M., 2002, ApJ, 576, 21

Acknowledgements

I have been lucky enough to meet people who taught me what has made possible to reach this stage in this journey of mine, and to go even beyond.

I want to warmly thank my supervisors Stefano Borgani, Giuseppe Murante, and Alessandro Bressan, for the unique way in which they have contributed to my scientific growth.

I thank the scientists with which I have had the opportunity to collaborate and interact during these years: Luca Tornatore, Pierluigi Monaco, Gian Luigi Granato, Andrea Lapi, Elena Rasia, Klaus Dolag, Gabriella De Lucia.

I am deeply grateful to SISSA, and to the professors and researchers of the Astrophysics Sector, for having provided me with a scientifically stimulating environment where to work and grow.

I wish to thank Fabrizio Brighenti, for always finding the time to discuss with me, for scientific advice, and to whom I owe my passion for hydrodynamics and numerical astrophysics.

Also, I would like to thank the external referees Lucio Mayer and Francesco Calura, who accepted to read this Thesis and provided me with valuable comments.

Many thanks to my colleagues in SISSA and in the Astronomical Observatory of Trieste: in particular, a big thank you to Andrej Obuljen, Elias Kammoun, Francesca Lepori, Gor Oganesyan, David Goz and Alex Beck.

I am especially grateful to Cristiana Spingola and Veronica Biffi, close friends outside science, for (Skype) teas, chats, support, and for the path shared together.

Special thanks to Nicola and my family, for their support and for always being there. Ringrazio i miei genitori, per avermi sempre sostenuta e perché a loro devo molto di quel che sono; e mio fratello Valerio, per il suo incoraggiante ottimismo e per riuscire sempre a propormi un altro punto di vista. Grazie a Vania e Paolo, per il loro affetto e supporto. E a Ilaria, l'amica di sempre.

A Nicola, semplicemente, grazie grazie: di tutto, di te, di noi.

Un pensiero non può non andare all'ubiquo complice Bobby, per la sua educata, discreta e tristemente sventurata compagnia.

Non chi comincia,
ma quel che persevera.